



**HAL**  
open science

# Development of metal-organic framework carbon composites for carbon dioxide and methane separation

Nurul Khaliesah Mohd Kamal Azhari

► **To cite this version:**

Nurul Khaliesah Mohd Kamal Azhari. Development of metal-organic framework carbon composites for carbon dioxide and methane separation. Chemical and Process Engineering. Ecole nationale supérieure Mines-Télécom Atlantique; Université de technologie de Petronas (1997-..; Seri Iskandar, Perak, Malaisie), 2020. English. NNT : 2020IMTA0201 . tel-03506929

**HAL Id: tel-03506929**

**<https://theses.hal.science/tel-03506929>**

Submitted on 3 Jan 2022

**HAL** is a multi-disciplinary open access archive for the deposit and dissemination of scientific research documents, whether they are published or not. The documents may come from teaching and research institutions in France or abroad, or from public or private research centers.

L'archive ouverte pluridisciplinaire **HAL**, est destinée au dépôt et à la diffusion de documents scientifiques de niveau recherche, publiés ou non, émanant des établissements d'enseignement et de recherche français ou étrangers, des laboratoires publics ou privés.

# THÈSE DE DOCTORAT DE

L'ÉCOLE NATIONALE SUPÉRIEURE MINES-TÉLÉCOM ATLANTIQUE  
BRETAGNE PAYS DE LA LOIRE - IMT ATLANTIQUE

UNIVERSITI TEKNOLOGI PETRONAS  
SERI ISKANDAR - PERAK - MALAYSIA

ÉCOLE DOCTORALE N° 602

*Sciences pour l'ingénieur*

Spécialité : Systèmes énergétiques et environnement

Par

**Nurul Khaliesah MOHD KAMAL AZHARI**

**Development of metal-organic framework carbon composites  
for carbon dioxide and methane separation**

Thèse présentée et soutenue à Nantes, le 17/09/2020

Unité de recherche : CNRS GEPEA

Thèse N° : 2020IMTA0201

## Rapporteurs avant soutenance :

Jean-Pierre BELLAT    Professeur, Université de Bourgogne Franche-Comté  
Cécile VALLIERES    Professeure, Université de Lorraine

## Composition du Jury :

Président	: Johnny DESCHAMPS	Professeur, ENSTA Institut Polytechnique de Paris
Examineurs	: Thomas DEVIC	Charge de recherche, Institut des Matériaux Jean Rouxel
	Thanabalan MURUGESAN	Professeur, Universiti Teknologi PETRONAS
	Su Shiung LAM	Professeur Associé, Universiti Malaysia Terengganu
	Jean-Pierre BELLAT	Professeur, Université de Bourgogne Franche-Comté
	Cécile VALLIERES	Professeure, Université de Lorraine
Dir. de thèse	: Pascaline PRÉ	Professeure, IMT Atlantique
Co-dir. de thèse:	Mohamad Azmi BUSTAM	Professeur Associé, Universiti Teknologi PETRONAS

## Invité(s) :

Denys GRÉKOV (co-encadrant)	Maitre-assistant, IMT Atlantique
Azmi MOHD SHARIFF (co-encadrant)	Professeur, Universiti Teknologi PETRONAS



### Acknowledgement

Foremost, I would like to express the sincerest gratitude to my supervisors, Prof. Pascaline Pré and Assoc. Prof. Mohamad Azmi Bustam for their good care and kindness, patient guidance, enthusiastic encouragement and valuable advices of this research for three years. Their willingness to assist me tirelessly in every way possible is greatly appreciated. I'm deeply grateful to have them as my supervisors.

I'd also like to extend my gratitude to my co-supervisor, Dr. Denys Grekov, who was very kind and patient with me. His guidance, insightful comments and encouragement helped me in all the time of the research and the writing of this thesis. He was a good teacher and his explanations were very detailed and helpful.

I would like to express my great appreciation to Dr. Lomig Hamon for his assistance in the lab work and his willingness to share his resources of modelling as a guidance for me. His technical contribution in computational mathematics is truly acknowledged.

I would like also to thank the other members of my thesis committee, Prof. Johnny Deschamps and Prof. Azmi Mohd Shariff for their useful suggestions of their immense knowledge. The discussions with them were always meaningful and encouraging.

I'm grateful to Prof. Jean-Pierre Bellat, Prof. Cécile Vallieres, Assoc. Prof. Thomas Devic, Prof. Thanabalan Murugesan and Assoc. Prof. Su Shiung Lam who accepted to participate in my defence committee.

I would give my thanks to all staffs of IMT Atlantique and Universiti Teknologi PETRONAS especially to Mr. Eric Chevrel, Ms. Shahidah Zakariya and Mr. Samad Zainal for their valuable technical support to ease my experimental work on this research.

I am also grateful to all my friends who have always been a major source of support when things would get a bit discouraging.

Most importantly, I wish to acknowledge the support and great love of my husband and family. They kept me going on and this work would not have been possible without their motivational support.

### Résumé

La demande mondiale d'énergie s'est déplacée vers le gaz naturel en raison de l'efficacité énergétique et de plus faibles impacts des émissions de gaz à effet de serre par la combustion de ces hydrocarbures par rapport à d'autres ressources fossiles (charbon, produits pétroliers). La production de biogaz est aussi fortement encouragée en Europe par les politiques menées en faveur du développement des énergies renouvelables, guidées par les enjeux économiques, environnementaux et climatiques. Par conséquent, les chercheurs travaillent à développer des solutions technologiques permettant d'augmenter la faisabilité économique de l'exploitation de ces ressources. Le dioxyde de carbone ( $\text{CO}_2$ ) est le principal contaminant gazeux présent dans les gaz naturel extraits des gisements et dans le biogaz. Sa teneur pouvant atteindre jusqu'à 70% en volume, donc il est nécessaire de l'extraire pour enrichir les gaz en méthane ( $\text{CH}_4$ ) avec une pureté suffisante en vue de sa valorisation. Parmi les technologies de séparation du  $\text{CO}_2$  de gaz naturels ou de biogaz, l'adsorption par modulation de pression « PSA, Pressure Swing Adsorption » est mise en œuvre à l'échelle industrielle et est considérée comme une alternative intéressante par rapport aux technologies d'absorption, membranaires ou cryogéniques.

Au cours des dernières décennies, une famille de matériaux nanoporeux constitués de réseaux organométalliques « MOF, Metal Organic Frameworks » a fait l'objet de recherches intenses en raison de leurs grands volumes microporeux et d'immenses surfaces spécifiques. Les MOFs sont l'assemblage de nœuds contenant des métaux coordonnés à des ligands organiques donnant naissance à des structures cristallines caractéristiques tridimensionnelles ordonnées. En raison d'une structure cristalline bien définie et d'un réseau régulier de pores, les MOFs sont reconnus avoir des propriétés d'adsorption des gaz modulables suivant la nature du ligand, la substitution des centres métalliques, leur permettant d'atteindre des performances en termes de capacité d'adsorption et de sélectivité très élevées par rapport à d'autres adsorbants conventionnels, tels charbons actifs et zéolites. À ce jour, la famille des MOF-74, et en particulier le matériau Mg-MOF-74 figurent parmi les adsorbants les plus prometteurs pour la séparation du  $\text{CO}_2$  de mélanges  $\text{CO}_2/\text{CH}_4$  et  $\text{CO}_2/\text{CH}_4/\text{N}_2$  dans le contexte de la purification du gaz naturel et du biogaz. L'excellente sélectivité d'adsorption vis-à-vis du  $\text{CO}_2$  provient des interactions intermoléculaires privilégiées du moment quadripolaire porté par le  $\text{CO}_2$  avec les centres métalliques exposés,

conduisant à la stabilisation de leur sphère de coordination et donc à un ordre élevé de molécules de CO<sub>2</sub> adsorbées au sein de la maille élémentaire.

Une amélioration des performances d'adsorption de gaz dans ces matériaux peut être escomptée en modifiant la texture et la morphologie du solide de façon à développer leur microporosité et une porosité interstitielle secondaire. Ceci doit augmenter l'accessibilité et faciliter le transport du gaz vers les sites d'adsorption. Récemment, des recherches ont examiné l'incorporation de composés à base de carbone dans les structures cristallines de MOFs. En raison de la formation de porosité additionnelle, les matériaux MOFs dopés au carbone ont été signalés capables d'avoir de meilleures capacités d'adsorption par rapport à leur homologue non-dopé. Les nanotubes de carbone (CNT) et l'oxyde de graphène (GO) ont été considérés comme les agents prometteurs dans la synthèse des matériaux dopés MOF-carbone.

Les CNT sont une forme allotropique de carbone appartenant à la famille des fullerènes, dont les parois permettent aux ligands et fonctionnels organiques de se fixer. Le GO contient une densité élevée d'atomes de carbone suivant un agencement de structure en couches, ainsi que des fonctionnalités d'oxygène. Celles-ci étant des groupes hydroxyle, carboxyle, époxy et cétone sont capables de se coordonner avec les centres métalliques des MOFs, pour former des cristaux de MOFs s'insérant entre les couches de graphène. Depuis que le Mg-MOF-74 a été introduit en 2005, aucun travail publié ne s'est intéressé au développement de matériaux dopés Mg-MOF-74-carbone malgré les avantages potentiels que ces nouveaux matériaux peuvent offrir pour la séparation sélective de gaz. Cette étude propose de synthétiser de nouveaux types de matériaux dopés Mg-MOF-74-carbone, utilisant comme agents dopants des CNT à parois multiples ou du GO monocouche. Les propriétés thermodynamiques et cinétiques d'adsorption des matériaux synthétisés ont été caractérisés pour les cas particuliers du CO<sub>2</sub> et du CH<sub>4</sub> dans une gamme de pressions jusqu'à 35 bar et à des températures entre l'ambiante et 75°C. Ces données sont nécessaires afin d'évaluer leurs performances pour une mise en œuvre en procédé PSA traitant de mélanges de types gaz naturel ou biogaz.

Le matériau Mg-MOF-74 a été synthétisé par réaction solvothermique améliorée. Cette technique de préparation consiste en la préparation d'un mélange de réactifs sous ultrasons, suivie d'une réaction solvothermique, d'un lavage et d'une extraction du solvant. Grâce à une cinétique de réaction rapide, cette technique permet de produire des particules MOFs de qualité uniforme, de petite taille et présentant avec un taux de cristallinité et une

## RÉSUMÉ

---

pureté élevées. Cependant, le processus de lavage est délicat car l'évacuation incomplète du milieu réactif engendre le blocage partiel des pores du matériau produit. Une amélioration de l'étape de lavage a été proposée en introduisant une série de séparations centrifuges dont les paramètres ont été optimisés. L'échantillon issu de la voie de synthèse optimisée montre une capacité d'adsorption pour le CO<sub>2</sub> significativement plus élevée que celle obtenue avec l'échantillon obtenu suivant le protocole de base. Un protocole analogue de synthèse optimisée a ensuite été appliqué à l'élaboration des matériaux dopés Mg-MOF-74@CNT et Mg-MOF-74@GO, les précurseurs réactifs étant initialement mélangés avec les agents dopants. Les teneurs en CNT et GO des matériaux composites ont été rapportées en masse par rapport à celle du Mg-MOF-74 non-dopé. Cette teneur a été optimisée à une valeur de 0,3% en masse, en prenant en compte leur cristallinité et leur capacité d'adsorption pour le CO<sub>2</sub> mesurée à 1 bar.

Les trois matériaux synthétisés ont été caractérisés par diffraction aux rayons X (DRX), spectrométrie infrarouge à transformée de Fourier (IRTF), microscopie électronique à balayage (MEB), analyse thermogravimétrique (ATG) et physisorption d'azote à 77 K. Les résultats de caractérisation ont montré que la cristallinité de Mg-MOF-74 était bien préservée dans les deux matériaux dopés. Les composites Mg-MOF-74@CNT et Mg-MOF-74@GO font apparaître des tailles moyennes de cristallites plus grandes, 82 nm et 73 nm respectivement comparées à 67 nm pour le matériau d'origine. L'analyse morphologique a montré que les tailles moyennes de particules du Mg-MOF-74@CNT et du Mg-MOF-74@GO étaient aussi plus grandes, 23 µm et 37 µm respectivement contre 10 µm pour le matériau non-dopé. Les agents dopants ont ainsi favorisé l'agglomération de la structure polycristalline du matériau, se combinant avec les réseaux des MOFs ou s'empilant à la surface des cristallites. La modification de la structure par adjonction d'agents carbonés confère non seulement une meilleure stabilité thermique, mais développe aussi la microporosité des matériaux. La surface spécifique BET est ainsi augmentée de 1111 m<sup>2</sup>·g<sup>-1</sup> pour le Mg-MOF-74 à 1340 m<sup>2</sup>·g<sup>-1</sup> (+21%) et 1393 m<sup>2</sup>·g<sup>-1</sup> (+25%) pour le Mg-MOF-74@CNT et le Mg-MOF-74@GO respectivement. L'analyse des isothermes d'adsorption d'azote par la théorie de la densité fonctionnelle (DFT), indique une augmentation du volume de micropores cohérente avec celle de la surface spécifique des matériaux : de 0,40 cm<sup>3</sup>·g<sup>-1</sup> pour le Mg-MOF-74 à 0,48 cm<sup>3</sup>·g<sup>-1</sup> (+18%) et 0,49 cm<sup>3</sup>·g<sup>-1</sup> (+24%) pour le Mg-MOF-74@CNT et le Mg-MOF-74@GO, respectivement.

Les équilibres d'adsorption monocomposés du CO<sub>2</sub> et du CH<sub>4</sub> ont été étudiés sur le Mg-MOF-74 et ses dérivés dopés. Les données d'équilibre mesurées à basse pression (1 bar) et à 25 °C ont indiqué une amélioration de la capacité d'adsorption du CO<sub>2</sub> de 18% en mole et de 23% en mole pour le Mg-MOF-74@CNT et le Mg-MOF-74@GO, respectivement par rapport au matériau non-dopé. Ces améliorations sont reliées à l'augmentation de la surface spécifique et à celle du volume microporeux dans les deux matériaux dopés. De même, il a été mesuré une augmentation de la capacité d'adsorption en CH<sub>4</sub> de 27% en moles et de 36% en moles pour le Mg-MOF-74@CNT et le Mg-MOF-74@GO, respectivement. Les performances des matériaux pour la séparation des gaz ont été évaluées non seulement en terme de capacité de traitement mais aussi en terme d'efficacité de séparation. A partir de la théorie de la solution adsorbée idéale « IAST, Ideal Adsorbed Solution Theory », la sélectivité en mélange équimolaire CO<sub>2</sub>/CH<sub>4</sub> a été évaluée. A 1 bar et 25 °C, le matériau Mg-MOF-74@GO apparaît donner ainsi le meilleur compromis entre capacité et sélectivité d'adsorption vis-à-vis du CO<sub>2</sub>.

Les données d'équilibre d'adsorption ont ensuite été mesurées dans une gamme de pressions élevées, jusqu'à 35 bars, et pour différentes températures : 25 °C, 50 °C et 75 °C. Des gains en terme de capacité d'adsorption pour le CO<sub>2</sub> ont été observés dans cette région de pression pour les deux matériaux dopés par rapport au matériau non-dopé, et ceux-ci sont augmentés avec l'augmentation de la température. La capacité d'adsorption du CO<sub>2</sub> sur le matériau non-dopé est significativement dégradée avec l'élévation de la température du système, tandis qu'elle l'est moins pour les deux matériaux dopés. Cette propriété est d'intérêt pour la mise en œuvre en procédé, car elle indique une moindre influence de l'échauffement local résultant du processus exothermique d'adsorption sur la capacité dynamique des lits. La sélectivité en mélange a été prédite à partir du modèle IAST dans la gamme de pression limitée à 10 bars tenant compte de la forme des isothermes de type II. À 50 °C et 75 °C, les matériaux composites offrent simultanément une meilleure capacité de traitement alliée à une meilleure efficacité de séparation. Les données expérimentales de chaleur isostérique d'adsorption des gaz montrent que celles-ci sont susceptibles de varier en fonction du taux de recouvrement des adsorbants et qu'elles se situent en deçà de 76 kJ·mol<sup>-1</sup>. Les valeurs plus élevées obtenues pour le CO<sub>2</sub> par rapport au CH<sub>4</sub> ont été attribuées à la polarisabilité et à la plus grande accessibilité des molécules de CO<sub>2</sub> à l'intérieur des micropores.

## RÉSUMÉ

---

La cinétique de sorption du CO<sub>2</sub> et du CH<sub>4</sub> sur les matériaux a été étudiée à partir d'expériences de manométrie par la méthode dite « ZLC, Zero Length Column », aux températures de 25 °C, 50 °C et 75 °C. Les données cinétiques ont été ajustées aux modèles de la force motrice linéaire « LDF, Linear Driving Force » et suivant la loi de diffusion de Fick, en tenant compte de l'influence de la température et du taux d'adsorption qui affecte la diffusivité des gaz dans le domaine de pression au-delà de la région de Henry. Les résultats montrent que les vitesses de diffusion des molécules du CO<sub>2</sub> dans les deux matériaux dopés sont significativement plus lentes que celles dans le matériau non-dopé. Elles révèlent en revanche une plus forte sélectivité cinétique du CO<sub>2</sub> vis-à-vis du CH<sub>4</sub> à toutes les températures.

Les deux méthodes de mesure fournissent des résultats précieux pour comprendre la cinétique d'adsorption du CO<sub>2</sub> et du CH<sub>4</sub> sur les matériaux synthétisés pour une large gamme de pression et de température. Cependant, la différence dans l'ordre de grandeur des diffusivités dérivées expérimentalement peut être attribuée aux différents mécanismes contrôlant le transfert de masse pendant les processus d'adsorption et de désorption opérés dans des conditions où les barrières externes peuvent ou non avoir une contribution significative contre la diffusion intra-cristalline. Par conséquent, des études cinétiques plus approfondies nécessiteraient de mettre en œuvre des modèles cinétiques basés sur les connaissances dérivées des données de diffusivité mesurées et de tester leur capacité à simuler correctement la dynamique des processus d'adsorption et de désorption à l'échelle du lit.

Les performances montrées par les matériaux dopés Mg-MOF-74 au carbone ont encouragé à poursuivre les recherches vers une meilleure compréhension de ces structures et le développement de nouveaux matériaux dopés MOF-carbone comme candidats potentiels pour la séparation du CO<sub>2</sub> des flux de gaz CO<sub>2</sub>/CH<sub>4</sub> dans le contexte de la purification du gaz naturel et du biogaz.

## Table of contents

List of abbreviations .....	13
List of symbols .....	15
List of figures .....	18
List of tables .....	24
<b>CHAPTER 1: INTRODUCTION</b> .....	<b>27</b>
1.1. General introduction .....	27
1.2. Problem statements .....	28
1.3. Objectives of the study .....	29
1.4. Scopes of the study .....	30
<b>CHAPTER 2: CONTEXT OF THE STUDY</b> .....	<b>32</b>
2.1. Global energy demands .....	32
2.1.1. Natural gas .....	32
2.1.2. Biogas and biomethane .....	34
2.2. CO <sub>2</sub> problems in natural gas and biogas productions .....	36
2.3. CO <sub>2</sub> removal technologies .....	37
2.3.1. CO <sub>2</sub> removal from natural gas streams .....	37
2.3.2. Comparison of different technologies: Advantages and challenges .....	40
2.3.3. Operation conditions at different stages of gas treatment .....	42
2.4. Pressure Swing Adsorption (PSA) .....	44
2.4.1. Introduction to adsorption .....	44
2.4.2. Pressure Swing Adsorption .....	45
2.4.3. MOFs for Pressure Swing Adsorption .....	47
2.5. Metal-organic frameworks (MOF) for CO <sub>2</sub> capture .....	50
2.5.1. Selection of MOFs over other adsorbents .....	50
2.5.2. MOF structure and families .....	51
2.5.3. Selection of MOF-74 for CO <sub>2</sub> /CH <sub>4</sub> separation .....	56
2.5.4. Performance of MOF-carbon composites for gas separation .....	64
2.6. Conclusion .....	73
<b>CHAPTER 3: SYNTHESIS AND CHARACTERIZATION OF MATERIALS</b> .....	<b>75</b>
3.1. Synthesis of MOFs and MOF composites: Review .....	75
3.2. Synthesis of MOF-74: Materials and methodology .....	79
3.2.1. Materials .....	79
3.2.2. Solvothermal synthesis technique .....	79
3.2.3. Improvement of conditions of solvent evacuation .....	80
3.2.4. Improvement of washing processes .....	80
3.2.5. Metal nodes tuning .....	81
3.2.6. Reproducibility and storage .....	81

<b>3.3. Synthesis of MOF-74-carbon composites: Materials and methodology</b> .....	<b>82</b>
3.3.1. Materials.....	82
3.3.2. <i>In situ</i> synthesis method.....	82
3.3.3. Extraction of graphene oxide.....	83
3.3.4. Optimization of concentration of carbon doping agent.....	84
<b>3.4. Characterization of synthesized materials: Methodology</b> .....	<b>84</b>
<b>3.5. Synthesis of MOF-74: Results and discussions</b> .....	<b>86</b>
3.5.1. Characterization for improving the synthesis.....	86
3.5.2. Production yield.....	96
<b>3.6. Synthesis of MOF-74-carbon composites: Results and discussions</b> .....	<b>96</b>
3.6.1. Characterization for optimizing the concentration.....	96
3.6.2. Production yield.....	100
<b>3.7. Characterization of selected materials: Results and discussions</b> .....	<b>100</b>
3.7.1. Crystal structure of materials.....	100
3.7.2. Chemical functionality of materials.....	103
3.7.3. Morphology of materials.....	106
3.7.4. Thermal properties of materials.....	108
3.7.5. Pore textural properties of materials.....	109
3.7.6. Ageing effects of materials.....	113
<b>3.8. Conclusion</b> .....	<b>114</b>
<b>CHAPTER 4: ADSORPTION EQUILIBRIA</b> .....	<b>118</b>
<b>4.1. Adsorption mechanisms: Principles</b> .....	<b>118</b>
4.1.1. Mass transfer phenomena from bulk gas phase to solid surface.....	118
4.1.2. Intermolecular interactions of CO <sub>2</sub> .....	121
4.1.3. Equilibrium interactions of CO <sub>2</sub> in MOF-74.....	122
<b>4.2. Adsorption isotherms: Principles</b> .....	<b>126</b>
4.2.1. IUPAC adsorption isotherm types.....	126
4.2.2. Isosteric heat of adsorption.....	129
4.2.3. Equilibrium selectivities for gas separation.....	131
<b>4.3. Manometric measurements: Methodology</b> .....	<b>137</b>
4.3.1. Experimental approaches and data treatment.....	137
4.3.2. Temperature-dependent dead volumes estimation for high temperatures.....	141
4.3.3. Pressure-dependent dead volumes estimation for high pressures.....	143
4.3.4. Absolute and relative experimental errors.....	147
4.3.5. Procedure of measurements.....	149
<b>4.4. Adsorption isotherms at low pressures: Results and discussions</b> .....	<b>151</b>
4.4.1. CO <sub>2</sub> adsorption isotherms and modelling.....	151
4.4.2. CH <sub>4</sub> adsorption isotherms and modelling.....	156
4.4.3. Equilibrium selectivities of CO <sub>2</sub> /CH <sub>4</sub> .....	158

---

4.4.4. Cycling performance of CO <sub>2</sub> adsorption/desorption.....	160
<b>4.5. Adsorption isotherms at high pressures: Results and discussions.....</b>	<b>162</b>
4.5.1. CO <sub>2</sub> adsorption isotherms and modelling.....	162
4.5.2. CH <sub>4</sub> adsorption isotherms and modelling.....	172
4.5.3. Equilibrium selectivities of CO <sub>2</sub> /CH <sub>4</sub> .....	178
4.5.4. Isosteric heat of adsorption.....	182
<b>4.6. Conclusion.....</b>	<b>187</b>
<b>CHAPTER 5: ADSORPTION KINETICS.....</b>	<b>190</b>
<b>5.1. Mass transfer by diffusions: Principles.....</b>	<b>190</b>
5.1.1. Fick's laws.....	190
5.1.2. Gradient of chemical potential.....	191
5.1.3. Non-isothermal diffusion system.....	194
<b>5.2. Diffusion mechanisms in porous solid: Principles.....</b>	<b>195</b>
5.2.1. External mass transfers.....	195
5.2.2. Internal mass transfers.....	196
<b>5.3. Sorption kinetic based on the context of the study.....</b>	<b>200</b>
<b>5.4. Manometric method: Methodology.....</b>	<b>202</b>
5.4.1. Experimental approaches.....	202
5.4.2. Mathematical modelling of sorption kinetic.....	202
5.4.3. Procedure of measurements.....	207
<b>5.5. Zero Length Column method: Methodology.....</b>	<b>208</b>
5.5.1. Experimental approaches.....	208
5.5.2. Mathematical modelling of sorption kinetic.....	209
5.5.3. Procedure of measurements.....	211
<b>5.6. Manometric method: Results and discussions.....</b>	<b>213</b>
5.6.1. Regeneration of adsorbent after CO <sub>2</sub> adsorption.....	213
5.6.2. CO <sub>2</sub> and CH <sub>4</sub> adsorption kinetics at different temperatures.....	214
5.6.3. Determination of diffusion coefficients.....	219
5.6.4. Kinetic selectivity of CO <sub>2</sub> /CH <sub>4</sub> .....	228
<b>5.7. Zero Length Column method: Results and discussions.....</b>	<b>228</b>
5.7.1. CO <sub>2</sub> and CH <sub>4</sub> adsorption kinetics at different temperatures.....	228
5.7.2. Determination of diffusion coefficients.....	234
5.7.3. Comparison with manometric method.....	239
<b>5.8. Conclusion.....</b>	<b>241</b>
<b>GENERAL CONCLUSIONS.....</b>	<b>243</b>
<b>PERSPECTIVES.....</b>	<b>247</b>
<b>Annex I.....</b>	<b>249</b>
<b>Annex II.....</b>	<b>250</b>
<b>Annex III.....</b>	<b>254</b>

**Annex IV** ..... 261

**Annex V** ..... 270

**Annex VI** ..... 274

**References**..... 279

## List of abbreviations

AC	Activated carbon
Ba	Barium
BBC	1,3,5-tris(4'-carboxy[1,1'-biphenyl]-4-yl)benzoate
BDC	1,4-benzenedicarboxylate
BE	Binding energy of adsorbate–adsorbent
BET	Brunauer–Emmett–Teller
BPDC	4,4-biphenyldicarboxylate
BPTC	3,3',5,5'-biphenyltetracarboxylate
BTB	1,3,5-benzenetriyltribenzoate
BTC	1,3,5-benzenetricarboxylate
BTE	1,3,5-triscarboxyphenylethynyl benzoate
BTTri	1,3,5-tri(1,2,3-triazol-4-yl)benzene
C	Carbon
CH <sub>4</sub>	Methane
CNT	Carbon nanotubes
CO	Carbon monoxide
CO <sub>2</sub>	Carbon dioxide
CPDF	Chemical potential driving force
CPO	Coordination Polymer of Oslo
Cr	Chromium
Cu	Copper
DFT	Density Functional Theory
DOBDC	2,5-dioxido-1,4-benzene-dicarboxylate
DHTP	2,5-dihydroxyterephthalic acid
DMF	Dimethylformamide
DOBDC	2,5-dioxido-1,4-benzene-dicarboxylate
DOT	2,5-dioxidoterephthalate ligand
DVS	Dynamic Vapour Sorption vacuum
EDXS	Energy dispersive X-ray spectroscopy
EOS	Equations of states
EU	The European Union
FESEM	Field emission scanning electron microscopy
FTIR	Fourier-transform infrared spectroscopy
Ga	Gallium
GO	Graphene oxide
H	Hydrogen
H <sub>2</sub> BDC	Benzene-1,4-dicarboxylic acid
H <sub>2</sub> BPDC	4,4-biphenyldicarboxylic acid
H <sub>2</sub> DHBDC	2,5-dihydroxy-1,4-benzene-dicarboxylic acid
H <sub>2</sub> NDC	1,4-naphthalenedicarboxylic acid
H <sub>2</sub> O	Water or humidity
H <sub>2</sub> PDC	Pyridine-2,6-dicaboxylic acid
H <sub>2</sub> S	Hydrogen sulfide
H <sub>2</sub> TPDC	4,4-triphenyldicarboxylic acid
H <sub>3</sub> BBC	1,3,5-tris(4'-carboxy[1,1'-biphenyl]-4-yl)benzene
H <sub>3</sub> BTB	1,3,5-tri(4carboxyphenyl)benzene

H <sub>3</sub> BTC	Benzene-1,3,5-tricarboxylic acid
H <sub>3</sub> BTE	1,3,5-triscarboxyphenylethynyl benzene
H <sub>4</sub> BPTC	3,3',5,5'-biphenyltetracarboxylic acid
H <sub>4</sub> DSBDC	2,5- disulfhydrylbenzene-1,4-dicarboxylic acid
HK	Horvath-Kawazoe model
HKUST	Hong Kong University of Science and Technology
HP	High pressure
HPDC	Pyridine-2,6-dicaboxylate
IAST	Ideal adsorbed solution theory
IGCC	Integrated gasification combined cycle
In	Indium
IRMOF	Isorecticular metal-organic frameworks
IUPAC	International Union of Pure and Applied Chemistry
LDF	Linear Driving Force
LNG	Liquified natural gas
LP	Low pressure
MEA	Monoethanolamine
Mg	Magnesium
MIL	Matériau Institut Lavoisier
MOF	Metal-organic frameworks
N <sub>2</sub>	Nitrogen
NaX	Zeolites 13X
NDC	1,4-naphthalenedicarboxylate
NGCC	Natural gas combined cycle
NGL	Natural gas liquids
NH <sub>3</sub>	Ammonia
Ni	Nickel
NO	Nitrogen oxide
NO <sub>2</sub>	Nitrogen dioxide
O	Oxygen
OH <sup>-</sup>	Hydroxide
Pd	Palladium
PSA	Pressure Swing Adsorption
PXRD	Powder X-ray diffraction
QDF	Quadratic Driving Force
SBU	Secondary Building Unit
SC/PCC	Supercritical pulverized coal combustion
Sr	Strontium
TEPA	Tetraethylenepentamine
TGA	Thermogravimetric analysis
Th	Thorium
Ti(OiPr)	Titanium isopropoxide
TSA	Thermal Swing Adsorption
U	Uranium
VBA	Visual Basic for Applications
VPSA	Vacuum Pressure Swing Adsorption
ZIF	Zeolitic imidazolate framework
ZLC	Zero Length Column
Zn	Zinc

## List of symbols

$\alpha^{INT}$	Intrinsic selectivity
$\alpha^{IAST}$	Ideal Adsorbed Solution Theory selectivity
$\beta$	Similarity constant (Eq. A-6); roots of solution of Eq. 5-47
$\delta$	External surface thickness of an adsorbent crystal
$\eta$	Fluid (gas) viscosity
$\lambda$	Mean free path of gas molecule
$\varepsilon$	Porosity of adsorbent solid
$\varepsilon_{AB}$	Maximum energy of attraction between molecules A and B
$\mu$	Net moment value (Section 4.1.2); chemical potential (Section 5.1.2)
$\mu^0$	Standard chemical potential for pure phase
$\pi$	Spreading pressure
$\pi^*$	Reduced spreading pressure
$\rho_{ads}$	Adsorbed phase density
$\rho_g$	Adsorbate gas density
$\rho_{liquid}$	Adsorbate phase liquid density
$\rho_s$	Adsorbent solid density
$\sigma_{AB}$	Average diameter of Lennard-Jones collision between molecules A and B
$\sigma_{cum}^2$	Calculations of cumulative variances
$\sigma_{cum}^2$	Cumulative variances of absolute experimental errors
$\sigma^2$	Variance of absolute experimental errors
$\theta$	Fractional adsorption loading / adsorption coverage ratio
$\Omega_D$	Dimensionless Lennard-Jones parameter
$A$	Solid specific surface area
$ARE$	Average relative error
$a$	Adsorbate activity
$a_s$	Specific surface of an adsorbent crystal
$B$	Molecular mobility which equals to $1/f$
$b$	Theoretical affinity parameter of adsorption site–adsorbate of isotherm model
$c$	Adsorbate concentration in bulk gas phase
$\partial c / \partial t$	Accumulation of adsorbate in fluid phase
$c_0$	Initial adsorbate concentration in bulk gas phase
$c_s^*$	Adsorbate concentration in bulk gas phase that would be in equilibrium with the concentration at the surface of adsorbent particle
$d_c$	Adsorbent crystal diameter
$d_{pore}$	Pore diameter
$D$	General Fickian diffusivity
$D_0$	Fickian diffusivity at zero surface (adsorption) coverage
$D_c$	Intracrystalline diffusivity
$D_c / r_c^2$	Intracrystalline diffusion time constant
$D_{eff}$	Effective diffusivity
$D_{eff,0}$	Effective diffusivity at zero surface (adsorption) coverage
$D_{eff} / r_c^2$	Effective diffusivity time constant
$D_{AB}$	Molecular diffusivity in a binary mixture of species A and B
$D_K$	Knudsen diffusivity
$D_L$	Axial dispersion coefficient
$D_m$	Molecular diffusivity

$D_p$	Poiseuille or viscous diffusivity
$D_s$	Surface diffusivity
$D_{s,0}$	Surface diffusivity at zero surface (adsorption) coverage
$E$	Characteristic energy of adsorption of Dubinin–Radushkevitch (DR) model
$E_o$	Characteristic energy of adsorption towards a reference adsorbate of DR model
$E_a$	Activation energy of diffusion of Arrhenius law equation
$E_{a,s}$	Activation energy of surface diffusion of Arrhenius law equation
$E_{MOF+CO_2}$	Total energy of adsorbate–substrate of MOF–CO <sub>2</sub> at equilibrium
$E_{CO_2}$	Total energy of CO <sub>2</sub> adsorbate
$E_{MOF}$	Total energy of MOF substrate
$ERRSQ$	Sum squares errors
$F$	Total volume flow rate of purging gas
$f$	Molecular friction coefficient which equals to $1/B$
$Q_{st}$	Isosteric heat of adsorption
$J$	Diffusive flux
$K$	Henry’s constant expressed as a proportionality factor of adsorbed amount per unit mass of adsorbent to adsorbate gas pressure at equilibrium ( $\text{mol}\cdot\text{g}^{-1}\cdot\text{bar}^{-1}$ )
$K_H$	Henry’s constant expressed as a ratio of adsorbate concentration in adsorbed phase per unit mass of adsorbent to adsorbate concentration in gas phase in ( $\text{mol}\cdot\text{g}^{-1}/\text{mol}\cdot\text{m}^{-3}$ )
$K'_H$	Dimensionless Henry’s constant expressed as a ratio of adsorbate concentration in adsorbed phase per unit volume of adsorbent to adsorbate concentration in gas phase in ( $\text{mol}\cdot\text{m}^{-3}/\text{mol}\cdot\text{m}^{-3}$ )
$Kn$	Knudsen number
$k, k_{ext}$	Overall external mass transfer coefficient, $k$ in $\text{m}\cdot\text{s}^{-1}$ and $k_{ext}$ in $\text{s}^{-1}$
$k_b$	Boltzmann constant
$k_f$	External film mass transfer coefficient
$k_s$	External surface permeability coefficient
$k_L$	External mass transfer coefficient in Linear Driving Force expressed as $a_s \cdot k$
$L$	Dimensionless parameter of Eq. 5-46, Eq. 5-47 and Eq. 5-48
$M$	Adsorbate molar mass
$m_s$	Adsorbent sample mass
$1/n$	Empirical heterogeneity factor of adsorption system of isotherm model
$n$	Number of moles
$n_{ads}, \Delta n$	Amount of adsorbate adsorbed at equilibrium
$n_{abs}, n_{total}$	Absolute (or total) adsorption capacity
$n_{ex}$	Excess adsorption capacity
$n_{net}$	Net adsorption capacity
$\Delta P$	Pressure drop / variation of pressure between reservoir and sample cell
$P, p, p_T$	Pressure of adsorption system (definition depends on the equation)
$p^o$	Gas saturation pressure at temperature of adsorption
$p/p^o$	Relative pressure expressed as a ratio of total pressure of pure gas to its saturation pressure at temperature of adsorption
$p_i^o$	Hypothetical pressure of species $i$ in Ideal Adsorbed Solution Theory
$p_i$	Partial pressures of species $i$ in Ideal Adsorbed Solution Theory
$\frac{\partial \ln p}{\partial \ln q}$	Darcken thermodynamic corrective factor
$\Delta q$	Working adsorption capacity
$q$	Amount of adsorbate adsorbed per unit mass (or per unit volume) of adsorbent at equilibrium
$\partial q/\partial t$	Accumulation of adsorbate in adsorbed phase

$q_0$	Initial value of $q$ when $t < 0$
$q_\infty$	Final value of $q$ when $t \rightarrow \infty$
$q_{exp}$	Amount of adsorbate adsorbed per unit mass of adsorbent at equilibrium measured experimentally
$q_{model}$	Amount of adsorbate adsorbed per unit mass of adsorbent at equilibrium calculated by isotherm model
$q_s$	Adsorbate actual concentration at the boundary of an adsorbent crystal
$q_{sat}$	Theoretical saturation capacity of adsorbate of isotherm model
$q_i^o(p)$	Amount of species $i$ adsorbed on the surface when in equilibrium with the gas phase of pure species $i$ in Ideal Adsorbed Solution Theory
$q_i^o(p_T)$	amount of species $i$ adsorbed on the surface when in equilibrium with the gas phase of the mixture in Ideal Adsorbed Solution Theory
$R$	Gas constant, $R = 8.314 \text{ J}\cdot\text{mol}^{-1}\cdot\text{K}^{-1}$
$R^2$	Coefficient of determination
$r$	Radius coordinate in an adsorbent crystal
$r_c$	Thickness radius of an adsorbent crystals
$r_{pore}$	Pore radius
$r_{vdw}$	Minimum distance of Van der Waals
$S^{PSA}$	Adsorbent selection parameter in Pressure Swing Adsorption
$1/t$	Empirical heterogeneity factor of adsorption system of Toth model
$t$	Time
$T$	Temperature of adsorption
$T_1$	Reservoir temperature
$T_2$	Sample cell temperature
$T_{ref}$	Reference temperature of Arrhenius law equation
$u$	Gas flow velocity
$V$	Volume; volume of $\text{N}_2$ adsorbed at STP per unit mass of adsorbent (Section 3.7.5)
$\Delta V$	Change in volume
$V_a, V_{ads}$	Adsorbed phase volume
$V_2$	Dead volume of sample cell
$V_{2,T_1}$	Dead volumes of sample cell with sample inside calibrated using helium at $T_1$
$V_{2,T_2}$	Dead volumes of sample cell with sample inside calibrated using helium at $T_2$
$V_U$	Dead volume in upper compartment of sample cell
$V_D$	Dead volume in lower compartment of sample cell
$V_{cell}$	Empty sample cell volume
$V_{NA}$	Non-accessible volume by adsorbate
$V_g$	Bulk gas phase volume
$V_{pore}$	Total pore volume
$V_s$	Adsorbent sample volume
$x_{Gibbs}$	Imaginary line called the ‘‘Gibbs dividing surface’’
$x_i$	Adsorbate mole fractions in adsorbed phase
$y_i$	Adsorbate mole fractions in bulk gas phase
$Z$	Gas compressibility factor
$z$	Axial coordinate in a column

## List of figures

Figure 2-1. (left) World energy consumption by energy resource in quadrillion British Thermal Unit (BTU) from 1990 with the projection to 2040 [1]. (right) World energy-related CO <sub>2</sub> emissions by fuel type in billion metric tons from 1990 with the projection to 2040 [1].	32
Figure 2-2. (left) Development of biogas production in European countries in mega British Thermal Unit (MBTU) from 2004 to 2015 [68]. (right) The number of existing upgrading plant producing biomethane worldwide in 2019 [69].	35
Figure 2-3. Schematic figure of natural gas treatment at processing plant [49].	39
Figure 2-4. Schematic pathways of CO <sub>2</sub> capture approaches in fuel-fired power plants [6].	40
Figure 2-5. Pressure swing adsorption technology for biogas production [99].	46
Figure 2-6. Separation factor vs. working capacity of different adsorbents for biogas separation of 50:50 mixtures of CO <sub>2</sub> /CH <sub>4</sub> . The adsorption was carried out at $p_{ads}=10$ bar and $p_{des}=1$ bar [107].	50
Figure 2-7. Chemical structure of linear carboxylate ligands used in MOF synthesis.	54
Figure 2-8. Chemical structure of trigonal and imidazolate carboxylate ligands used in MOF synthesis.	54
Figure 2-9. The formation of SBU and consequently the framework by copolymerization of metal ions with organic linkers [14, 121].	54
Figure 2-10. The formation of hexagonal array of M-MOF-74 formed from one-dimensional channels of M <sub>2</sub> O <sub>2</sub> (CO <sub>2</sub> ) <sub>2</sub> SBU and DOBDC linker [121].	57
Figure 2-11. (left) CO <sub>2</sub> sorption isotherm at 296 K and 1 atm (main figure) and 0.1 atm (sub-figure) by comparing M/DOBDC series (filled markers: adsorption points; open markers: desorption points) [18]. (right) CO <sub>2</sub> uptake of various MOF families at 0.1 bar at 293-298 K [123].	58
Figure 2-12. (left) One unit cell of Mg-MOF-74 occupied by 12 molecules of CO <sub>2</sub> ; Mg (green), O (red), C (grey) and CO <sub>2</sub> (blue) [18]. (right) The geometry of adsorption of (a) CO, (b) N <sub>2</sub> and (c) CO <sub>2</sub> in Mg-MOF-74; Mg (cyan), O (red), C (grey) and N (blue); distances in Å [16].	59
Figure 2-13. Statistic of publication number on MOF-carbon composites according to carbonaceous doping agent from 2009 to 2015 [27].	65
Figure 2-14. (left) Schematic comparison of the coordination between GO layers to the MOF units for different types of MOF network: MOF-5, HKUST-1 and MIL-100 [26]. (right) Schematic bonding formation between MOF network (top) and graphene layer (bottom) [127].	67
Figure 3-1. The formation of MOF-carbon composites in <i>in situ</i> synthesis of the types of ship-in-a-bottle method; (i) before and (ii) after, and, (iii) bottle-around-ship method. MOF unit and doping material are presented in blue and brown, respectively [26].	79
Figure 3-2. Schematic figure of solvothermal synthesis of this work with repeating washing processes or with additional centrifugal separations.	81
Figure 3-3. Schematic figure of solvothermal <i>in situ</i> synthesis of MOF-carbon composites of this work.	83
Figure 3-4. Schematic figure of the extraction of graphene oxide from water suspension.	84
Figure 3-5. Thermogravimetric curve and its derivative curve of the synthesized Mg-MOF-74.	87
Figure 3-6. CO <sub>2</sub> adsorption isotherms of Mg-MOF-74 samples from the first-batch synthesis after washing repetitions (red) and the second-batch synthesis with centrifugation 1 (blue) and centrifugations 1 and 2 (green), at 1 bar and 25 °C.	89
Figure 3-7. FTIR spectra of Mg-MOF-74 samples before centrifugation (red), after centrifugation 1 (blue), and after centrifugations 1 and 2 (green), with the spectrum of 2,5-dihydroxyterephthalic acid linker (brown).	90
Figure 3-8. (left) PXRD reflections of Mg-MOF-74 from the first-batch synthesis (red) and the second-batch synthesis with centrifugations 1 and 2 (green). (right) Results of Rietveld refinement of the second-batch sample. Green, yellow, and blue lines represent experimental data, indexed reflections of molecular structure of Mg-MOF-74, and difference plot, respectively.	92

Figure 3-9. PXRD reflections of M-MOF-74 series of this work, where M=Mg, Ni, Zn, Co.....	94
Figure 3-10. FTIR spectra of M-MOF-74 series of this work, where M=Mg, Ni, Zn, Co. ....	94
Figure 3-11. CO <sub>2</sub> adsorption isotherm of M-MOF-74 series of this work at 1 bar and 25 °C, where M=Mg, Ni, Zn, Co.....	95
Figure 3-12. PXRD reflections of Mg-MOF-74@nGO series, where n = 0–6 wt%. ....	98
Figure 3-13. (left) CO <sub>2</sub> adsorption isotherms and (right) CO <sub>2</sub> adsorption capacity of Mg-MOF-74@nGO series, at 1 bar and 25 °C where n = 0–6 wt%.....	98
Figure 3-14. PXRD reflections of Mg-MOF-74@nGO series, where n = 0–0.6 wt%. ....	99
Figure 3-15. FTIR spectra of Mg-MOF-74@nGO series, where n = 0–0.6 wt%.....	99
Figure 3-16. (left) CO <sub>2</sub> adsorption isotherms and (right) CO <sub>2</sub> adsorption capacity of Mg-MOF-74@nGO series, at 1 bar and 25 °C where n = 0–0.6 wt%.....	100
Figure 3-17. The images of the synthesized (i) Mg-MOF-74, (ii) Mg-MOF-74@CNT and (iii) Mg-MOF-74@GO. The composites were prepared with ≈0.3 wt% of carbon doping agent.....	100
Figure 3-18. PXRD reflections of (a) Mg-MOF-74, (b) Mg-MOF-74@CNT and (c) Mg-MOF-74@GO. Blue, red and green lines represent experimental data, fitting of profile refinement and difference plot, respectively. ....	102
Figure 3-19. FTIR spectra of (a) Mg-MOF-74, (b) Mg-MOF-74@CNT, (c) Mg-MOF-74@GO and (d) 2,5-dihydroxyterephthalic acid linker.....	104
Figure 3-20. The coordination of DOT ligands joining by metal oxide SBUs to form 3D MOF-74 crystal structure with 1D hexagonal channels [167]. ....	105
Figure 3-21. (i) Raman spectra of (a) Mg-MOF-74, (b) Mg-MOF-74@CNT, (c) Mg-MOF-74@GO and (d) 2,5- dihydroxyterephthalic acid linker and (ii) characteristic bands of carbonaceous materials in Raman spectra of GO and CNT.....	105
Figure 3-22. Micrograph images of Mg-MOF-74, Mg-MOF- 74@CNT and Mg-MOF-74@GO. ....	107
Figure 3-23. (i) Thermogravimetric curves and (ii) their derivative curves of (a) Mg-MOF-74, (b) Mg-MOF-74@CNT and (c) Mg-MOF-74@GO.....	109
Figure 3-24. (i) N <sub>2</sub> ads/desorption isotherms at 77 K, (ii) their derivative curves and (iii) cumulative N <sub>2</sub> adsorbed volume of (a) Mg-MOF-74, (b) Mg-MOF-74@CNT and (c) Mg-MOF-74@GO. Solid and open symbols represent the adsorption and desorption of N <sub>2</sub> , respectively. ....	112
Figure 3-25. PXRD reflections of (a) Mg-MOF-74, (b) Mg-MOF-74@CNT and (c) Mg-MOF-74@GO. Blue and red lines represent the analysis right after their synthesis and 18 months after their synthesis, respectively. ....	114
Figure 4-1. Descriptive schema of mass transfers from bulk gas phase to nanoporous solid surface. ....	120
Figure 4-2. Van der Waals forces of intermolecular interactions of CO <sub>2</sub> from type (i) Keesom polar force, (ii) Debye polar force and (iii) London dispersive force. ....	121
Figure 4-3. Lennard-Jones–John schema of intermolecular potential energy versus distance of adsorbate molecules from the substrate. ....	122
Figure 4-4. (left) Metal sites and framework sites for CO <sub>2</sub> adsorption in Mg-MOF-74 one-unit cell and (right) the coordination of CO <sub>2</sub> binding at primary site (metal) and secondary site (framework). The figure is modified from [178]. ....	125
Figure 4-5. (i) Binding energy of CO <sub>2</sub> at different adsorption sites in Mg-MOF-74 one-unit cell: metal sites marked 1-2-3 and framework site marked 4 [178]. <sup>39</sup> (ii) A maximum loading of CO <sub>2</sub> in Mg-MOF-74 one-unit cell: primary adsorption site marked 1 <sup>st</sup> and secondary adsorption site marked 2 <sup>nd</sup> [24]. ....	125
Figure 4-6. Detail of the electrostatic potential of Mg-MOF-74 mapped on the electron charge density isosurface (0.003 a.u.) together with the electrostatic potential of CO <sub>2</sub> . Red, green, and blue represent negative, zero, and positive values in a.u., respectively [16].....	126
Figure 4-7. Physisorption isotherms classification based on IUPAC Recommendations 2015.....	128

Figure 4-8. Schematic representation of configuration of (A) monolayer adsorption, (B) multilayer adsorption, (C) pore condensation, (D) pore saturation and (E) pore evaporation in a single pore [176]. ..	129
Figure 4-9. The method of calculation of isosteric heat of adsorption using Clausius–Clapeyron approach. ....	130
Figure 4-10. Illustration of gas mixture in an adsorption system. ....	133
Figure 4-11. Recapitulative of the IAST selectivity calculation method, assuming for an equimolar binary mixture of species A and B whose adsorption isotherm of the pure component is described by Langmuir model at the same operational conditions. ....	137
Figure 4-12. Schematic figure giving the configuration of manometric apparatus in which the sample cell temperature equals to the reservoir temperature. ....	138
Figure 4-13. Schematic configuration of the manometric system taking into consideration the gradient of temperature between the sample cell and the gas reservoir. ....	141
Figure 4-14. Different reference states for determining dead volume in (i) net adsorption, (ii) excess adsorption and (iii) absolute adsorption [213]. ....	144
Figure 4-15. A schematic diagram illustrating the concept of Gibbs excess adsorbed quantity and absolute adsorbed quantity on an open planar surface [209]. ....	145
Figure 4-16. A schematic representation of the difference between excess and absolute adsorption capacities as a function of pressure at constant temperature [210]. ....	147
Figure 4-17. The configuration of the manometric equipment at low pressures. The pressure transducer and thermocouples are marked P and T, respectively. ....	150
Figure 4-18. The configuration of the manometric equipment at high pressures. The pressure transducers and thermocouples are marked LP (low pressure), HP (high pressure) and T, respectively. ....	151
Figure 4-19. CO <sub>2</sub> adsorption/desorption isotherms on (a) Mg-MOF-74, (b) Mg-MOF-74@CNT, (c) Mg-MOF-74@GO, pure CNT and pure GO up to 1 bar at 25 °C. Solid and open symbols represent the adsorption and desorption of CO <sub>2</sub> , respectively. ....	152
Figure 4-20. CO <sub>2</sub> adsorption isotherms on (a) Mg-MOF-74, (b) Mg-MOF-74@CNT and (c) Mg-MOF-74@GO up to 1 bar at 25 °C, fitted to (i) Langmuir model and (ii) dual-site Langmuir, with their respective coefficient of determination, R <sup>2</sup> . ....	154
Figure 4-21. CO <sub>2</sub> adsorption isotherms of (a) Mg-MOF-74, (b) Mg-MOF-74@CNT, and, (c) Mg-MOF-74@GO up to 1 bar at 25 °C, normalized to the BET specific surface area of the materials. ....	156
Figure 4-22. CH <sub>4</sub> adsorption/desorption isotherms on (a) Mg-MOF-74, (b) Mg-MOF-74@CNT and (c) Mg-MOF-74@GO up to 1 bar at 25 °C, fitted to Henry’s law isotherm (dashed line). ....	157
Figure 4-23. IAST adsorption uptake for an equimolar mixture of CO <sub>2</sub> and CH <sub>4</sub> on (a) Mg-MOF-74, (b) Mg-MOF-74@CNT and (c) Mg-MOF-74@GO up to 1 bar at 25 °C. ....	159
Figure 4-24. IAST selectivity of CO <sub>2</sub> /CH <sub>4</sub> for an equimolar mixture on (a) Mg-MOF-74, (b) Mg-MOF-74@CNT and (c) Mg-MOF-74@GO up to 1 bar at 25 °C. ....	160
Figure 4-25. IAST selectivity of CO <sub>2</sub> /CH <sub>4</sub> versus IAST capacity in mmol·g <sup>-1</sup> of CO <sub>2</sub> for an equimolar mixture on Mg-MOF-74, Mg-MOF-74@CNT and Mg-MOF-74@GO at 1 bar, 25 °C. ....	160
Figure 4-26. Cycling performance of CO <sub>2</sub> adsorption/desorption isotherms on (i) a: MgMOF-74, (ii) b: MgMOF-74@CNT and (iii) c: MgMOF-74@GO up to 1 bar at 25 °C. Solid and open symbols represent the adsorption and desorption of CO <sub>2</sub> , respectively. ....	161
Figure 4-27. CO <sub>2</sub> adsorption/desorption isotherms of (i) a: Mg-MOF-74, (ii) b: Mg-MOF-74@CNT and (iii) c: Mg-MOF-74@GO up to 35 bar at 25 °C with absolute errors bars, fitted to an average curve providing coefficient of determination, R <sup>2</sup> , and average relative errors, ARE. Solid and open symbols represent the adsorption and desorption of CO <sub>2</sub> , respectively. ....	163
Figure 4-28. CO <sub>2</sub> adsorption/desorption isotherms of (i) a: Mg-MOF-74, (ii) b: Mg-MOF-74@CNT and (iii) c: Mg-MOF-74@GO up to 35 bar at 50 °C with absolute errors bars, fitted to an average curve providing coefficient of determination, R <sup>2</sup> , and average relative errors, ARE. Solid and open symbols represent the adsorption and desorption of CO <sub>2</sub> , respectively. ....	164

Figure 4-29. CO <sub>2</sub> adsorption/desorption isotherms of (i) a: Mg-MOF-74, (ii) b: Mg-MOF-74@CNT and (iii) c: Mg-MOF-74@GO up to 35 bar at 75 °C with absolute errors bars, fitted to an average curve providing coefficient of determination, R <sup>2</sup> , and average relative errors, ARE. Solid and open symbols represent the adsorption and desorption of CO <sub>2</sub> , respectively. ....	165
Figure 4-30. Average curve of CO <sub>2</sub> adsorption isotherms of (a) Mg-MOF-74, (b) Mg-MOF-74@CNT and (c) Mg-MOF-74@GO up to 35 bar with average relative errors bars, ARE, for different temperatures: (i) 25 °C, (ii) 50 °C and (iii) 75 °C, fitted to dual-site Langmuir until 10 bar. ....	167
Figure 4-31. Average curve of CO <sub>2</sub> adsorption isotherms of (a) Mg-MOF-74, (b) Mg-MOF-74@CNT and (c) Mg-MOF-74@GO up to 10 bar with average relative errors bars, ARE, fitted to dual-site Langmuir model providing coefficient of determination, R <sup>2</sup> , for different temperatures: (i) 25 °C, (ii) 50 °C and (iii) 75 °C. ....	171
Figure 4-32. CH <sub>4</sub> adsorption/desorption isotherms of (i) a: Mg-MOF-74, (ii) b: Mg-MOF-74@CNT and (iii) c: Mg-MOF-74@GO up to 35 bar at 25 °C with absolute errors bars, fitted to an average curve providing coefficient of determination, R <sup>2</sup> , and average relative errors, ARE. Solid and open symbols represent the adsorption and desorption of CH <sub>4</sub> , respectively. ....	173
Figure 4-33. CH <sub>4</sub> adsorption/desorption isotherms of (i) a: Mg-MOF-74, (ii) b: Mg-MOF-74@CNT and (iii) c: Mg-MOF-74@GO up to 35 bar at 50 °C with absolute errors bars, fitted to an average curve providing coefficient of determination, R <sup>2</sup> , and average relative errors, ARE. Solid and open symbols represent the adsorption and desorption of CH <sub>4</sub> , respectively. ....	174
Figure 4-34. CH <sub>4</sub> adsorption/desorption isotherms of (i) a: Mg-MOF-74, (ii) b: Mg-MOF-74@CNT and (iii) c: Mg-MOF-74@GO up to 35 bar at 75 °C with absolute errors bars, fitted to an average curve providing coefficient of determination, R <sup>2</sup> , and average relative errors, ARE. Solid and open symbols represent the adsorption and desorption of CH <sub>4</sub> , respectively. ....	175
Figure 4-35. Average curve of CH <sub>4</sub> adsorption isotherms of (a) Mg-MOF-74, (b) Mg-MOF-74@CNT and (c) Mg-MOF-74@GO up to 35 bar with average relative errors bars, ARE, for different temperatures: (i) 25 °C, (ii) 50 °C and (iii) 75 °C, fitted to Langmuir model until 10 bar providing coefficient of determination, R <sup>2</sup> , for different temperatures: (iv) 25 °C, (v) 50 °C and (vi) 75 °C. ....	177
Figure 4-36. (i) Intrinsic selectivity of CO <sub>2</sub> /CH <sub>4</sub> and (ii) PSA adsorbent selection parameter of CO <sub>2</sub> /CH <sub>4</sub> of (a) Mg-MOF-74, (b) Mg-MOF-74@CNT and (c) Mg-MOF-74@GO at 10 bar as a function of temperatures. ....	178
Figure 4-37. IAST adsorption uptake of CO <sub>2</sub> and CH <sub>4</sub> for an equimolar mixture on (a) Mg-MOF-74, (b) Mg-MOF-74@CNT, and, (c) Mg-MOF-74@GO up to 10 bar for different temperatures: (i) 25 °C, (ii) 50 °C and (iii) 75 °C. ....	180
Figure 4-38. IAST selectivity of CO <sub>2</sub> /CH <sub>4</sub> for an equimolar mixture on (a) Mg-MOF-74, (b) Mg-MOF-74@CNT, and, (c) Mg-MOF-74@GO up to 10 bar for different temperatures: (i) 25 °C, (ii) 50 °C and (iii) 75 °C. ....	181
Figure 4-39. IAST selectivity of CO <sub>2</sub> /CH <sub>4</sub> versus IAST capacity in mmol·g <sup>-1</sup> of CO <sub>2</sub> adsorption for an equimolar mixture on (a) Mg-MOF-74, (b) Mg-MOF-74@CNT and (c) Mg-MOF-74@GO at 10 bar for different temperatures: 25 °C, 50 °C and 75 °C. ....	182
Figure 4-40. CO <sub>2</sub> adsorption isotherms of (a-i) Mg-MOF-74, (b-i) Mg-MOF-74@CNT, and, (c-i) Mg-MOF-74@GO up to 35 bar and at different temperatures, and, (a-ii) (b-ii) (c-ii) their respective Arrhenius plot for the calculation of isosteric heat of adsorption with the coefficient of determination, R <sup>2</sup> , for each amount adsorbed, q, in mmol·g <sup>-1</sup> . ....	183
Figure 4-41. CH <sub>4</sub> adsorption isotherms of (a-i) Mg-MOF-74, (b-i) Mg-MOF-74@CNT, and, (c-i) Mg-MOF-74@GO up to 35 bar and at different temperatures, and, (a-ii) (b-ii) (c-ii) their respective Arrhenius plot for the calculation of isosteric heat of adsorption with the coefficient of determination, R <sup>2</sup> , for each amount adsorbed, q, in mmol·g <sup>-1</sup> . ....	184
Figure 4-42. Isosteric heat of adsorption, Q <sub>st</sub> , of (i) CO <sub>2</sub> and (ii) CH <sub>4</sub> on (a) Mg-MOF-74, (b) Mg-MOF-74@CNT and (c) Mg-MOF-74@GO as a function of amount adsorbed. ....	186
Figure 5-1. Illustration of different mechanisms of internal diffusion of molecules in pore capillary: (i) Poiseuille, (ii) Knudsen, (iii) molecular and (iv) surface diffusions. ....	197
Figure 5-2. Combination of internal diffusional resistance according to a resistor network model [172]. ...	199

Figure 5-3. Configuration of ZLC equipment.....	212
Figure 5-4. (i) Fractional adsorption uptakes and (ii) adsorption uptakes of CO <sub>2</sub> on Mg-MOF-74@CNT at 0.2 bar and 25 °C for different outgassing conditions. ....	214
Figure 5-5. Fractional adsorption uptakes of CO <sub>2</sub> on Mg-MOF-74 with their profile temperature at 0.2 bar, 0.5 bar and 1.5 bar for different temperatures: (i) 25 °C, (ii) 50 °C and (iii) 75 °C.....	216
Figure 5-6. Fractional adsorption uptakes of CO <sub>2</sub> on Mg-MOF-74@CNT with their profile temperature at 0.2 bar, 0.5 bar and 1.5 bar for different temperatures: (i) 25 °C, (ii) 50 °C and (iii) 75 °C.....	217
Figure 5-7. Fractional adsorption uptakes of CO <sub>2</sub> on Mg-MOF-74@GO with their profile temperature at 0.2 bar, 0.5 bar and 1.5 bar for different temperatures: (i) 25 °C, (ii) 50 °C and (iii) 75 °C.....	218
Figure 5-8. Fractional adsorption uptakes of CO <sub>2</sub> on Mg-MOF-74 at 0.2 bar, fitted to Linear Driving Force (LDF) model and Fickian diffusion model for (i) 25 °C, (ii) 50 °C and (iii) 75 °C with their respective coefficient of determination, R <sup>2</sup> , and, linear form of fractional adsorption uptakes of CO <sub>2</sub> on Mg-MOF-74 at 0.2 bar and 0.5 bar, fitted to LDF model for (iv) 25 °C, (v) 50 °C and (vi) 75 °C. ....	222
Figure 5-9. Fractional adsorption uptakes of CO <sub>2</sub> (compared to CH <sub>4</sub> ) on Mg-MOF-74@CNT at 0.2 bar, fitted to Linear Driving Force (LDF) model and Fickian diffusion model for (i) 25 °C, (ii) 50 °C and (iii) 75 °C, and, linear form of fractional adsorption uptakes of CO <sub>2</sub> on Mg-MOF-74@CNT at 0.2 bar, 0.5 bar and 1.5 bar, fitted to LDF, LDF-Darken and LDF-Darken-Arrhenius models for (iv) 25 °C, (v) 50 °C and (vi) 75 °C, with their respective coefficient of determination, R <sup>2</sup> . ....	223
Figure 5-10. Fractional adsorption uptakes of CO <sub>2</sub> (compared to CH <sub>4</sub> ) on Mg-MOF-74@GO at 0.2 bar, fitted to Linear Driving Force (LDF) model and Fickian diffusion model for (i) 25 °C, (ii) 50 °C and (iii) 75 °C, and, linear form of fractional adsorption uptakes of CO <sub>2</sub> on Mg-MOF-74@GO at 0.2 bar, 0.5 bar and 1.5 bar, fitted to LDF, LDF-Darken and LDF-Darken-Arrhenius models for (iv) 25 °C, (v) 50 °C and (vi) 75 °C, with their respective coefficient of determination, R <sup>2</sup> . ....	224
Figure 5-11. Arrhenius plot of diffusivity time constants, D/r <sub>c</sub> <sup>2</sup> , of CO <sub>2</sub> adsorption on (i) Mg-MOF-74@CNT and (ii) Mg-MOF-74@GO at 0.2 bar, 0.5 bar and 1.5 bar for 25 °C, 50 °C and 75 °C, calculated using Linear Driving Force (LDF), LDF-Darken and LDF-Darken-Arrhenius models. ....	227
Figure 5-12. Arrhenius plots of diffusivity time constant at nearly zero coverage, D <sub>0</sub> /r <sub>c</sub> <sup>2</sup> , of (i) CO <sub>2</sub> and (ii) CH <sub>4</sub> adsorptions on (a) Mg-MOF-74, (b) Mg-MOF-74@CNT and (c) Mg-MOF-74@GO for 25 °C, 50 °C and 75 °C. The value was calculated on average from the measurements at 0.2 bar, 0.5 bar and 1.5 bar using Linear Driving Force (LDF) and LDF-Darken-Arrhenius models. ....	227
Figure 5-13. Logarithmic fractional desorption curves of (i) CO <sub>2</sub> and (ii) CH <sub>4</sub> on Mg-MOF-74 for a purge gas flow rate of 150 ml·min <sup>-1</sup> at 25 °C. Adsorption equilibrium was initially achieved for mixtures of different concentration of gas adsorbate (in mol%) in helium. ....	229
Figure 5-14. Fractional desorption curves of CO <sub>2</sub> on Mg-MOF-74 as a function of purge gas volume for different purge gas flow rates at (i) 25 °C, (ii) 50 °C and (iii) 75 °C, and, (iv) logarithmic fractional desorption curves of CO <sub>2</sub> on Mg-MOF-74 for a purge gas flow rate of 150 ml·min <sup>-1</sup> for different temperatures. Adsorption equilibrium was initially achieved for a mixture of 2% mol CO <sub>2</sub> in helium.....	232
Figure 5-15. Fractional desorption curves of CO <sub>2</sub> on Mg-MOF-74@CNT as a function of purge gas volume for different purge gas flow rates at (i) 25 °C, (ii) 50 °C and (iii) 75 °C, and, (iv) logarithmic fractional desorption curves of CO <sub>2</sub> on Mg-MOF-74@CNT for a purge gas flow rate of 150 ml·min <sup>-1</sup> at different temperatures. Adsorption equilibrium was initially achieved for a mixture of 2% mol CO <sub>2</sub> in helium. ....	233
Figure 5-16. Fractional desorption curves of CO <sub>2</sub> on Mg-MOF-74@GO as a function of purge gas volume for different purge gas flow rates at (i) 25 °C, (ii) 50 °C and (iii) 75 °C, and, (iv) logarithmic fractional desorption curves of CO <sub>2</sub> on Mg-MOF-74@GO for a purge gas flow rate of 150 ml·min <sup>-1</sup> at different temperatures. Adsorption equilibrium was initially achieved for a mixture of 2% mol CO <sub>2</sub> in helium. ....	234
Figure 5-17. Fractional desorption curves of CO <sub>2</sub> on Mg-MOF-74 in kinetic regime (purge gas flow rates of 140 ml·min <sup>-1</sup> and 150 ml·min <sup>-1</sup> ) at (i) 25 °C, (ii) 50 °C and (iii) 75 °C, and, (sub-figures) logarithmic fractional desorption curves, fitted to Zero Length Column–Fickian diffusion model with their respective coefficient of determination, R <sup>2</sup> . Adsorption equilibrium was initially achieved for a mixture of 2% mol CO <sub>2</sub> in helium. ....	235
Figure 5-18. Fractional desorption curves of CO <sub>2</sub> on Mg-MOF-74@CNT in kinetic regime (purge gas flow rates of 140 ml·min <sup>-1</sup> and 150 ml·min <sup>-1</sup> ) at (i) 25 °C, (ii) 50 °C and (iii) 75 °C, and, (sub-figures) logarithmic	

---

fractional desorption curves, fitted to Zero Length Column–Fickian diffusion model with their respective coefficient of determination, $R^2$ . Adsorption equilibrium was initially achieved for a mixture of 2% mol $\text{CO}_2$ in helium.....	236
Figure 5-19. Fractional desorption curves of $\text{CO}_2$ on Mg-MOF-74@GO in kinetic regime (purge gas flow rates of $140 \text{ ml}\cdot\text{min}^{-1}$ and $150 \text{ ml}\cdot\text{min}^{-1}$ ) at (i) $25^\circ\text{C}$ , (ii) $50^\circ\text{C}$ and (iii) $75^\circ\text{C}$ , and, (sub-figures) logarithmic fractional desorption curves, fitted to Zero Length Column–Fickian diffusion model with their respective coefficient of determination, $R^2$ . Adsorption equilibrium was initially achieved for a mixture of 2% mol $\text{CO}_2$ in helium.....	237
Figure 5-20. Arrhenius plots of diffusivity time constant, $D_0/r_c^2$ , of $\text{CO}_2$ on (a) Mg-MOF-74, (b) Mg-MOF-74@CNT and (c) Mg-MOF-74@GO at $25^\circ\text{C}$ , $50^\circ\text{C}$ and $75^\circ\text{C}$ , deduced by Zero Length Column method.....	239

## List of tables

Table 2-1. CO <sub>2</sub> content from various natural gas fields around the world in volume percent basis. ....	33
Table 2-2. Typical compositions of biogas according to its source in volume percent basis. ....	36
Table 2-3. Requirements and challenges of the most industrially applied CO <sub>2</sub> capture technologies [7, 8, 55, 87, 88].....	41
Table 2-4. Operation conditions and available technologies of CO <sub>2</sub> capture for natural gas production. ....	43
Table 2-5. Comparison of different pilot and commercial biogas upgrading technologies [102].....	47
Table 2-6. Different types of carboxylate ligands used in the synthesis of MOFs. ....	52
Table 2-7. Different MOF families produced from octahedral Zn <sub>4</sub> O(CO <sub>2</sub> ) <sub>6</sub> SBU.....	55
Table 2-8. Other MOF families produced from divers SBUs and linkers. ....	56
Table 2-9. MOFs with the highest CO <sub>2</sub> uptake capacity reported to date.....	60
Table 2-10. Published works on MOF-74 reported to date for CO <sub>2</sub> adsorption (2008–present). ....	63
Table 2-11. Published works on MOF-74-membrane hybrid system reported to date for CO <sub>2</sub> separation (2008–present). ....	63
Table 2-12. Published works on MOF–carbon composite using CNT and GO reported to date for various gas adsorption (2009–present). ....	71
Table 2-13. Published works on MOF–carbon composites using CNT and GO reported to date for specific materials removal (2009–present). ....	72
Table 3-1. The most common techniques of preparation of MOFs. ....	76
Table 3-2. Possible variation of parameters for the preparation of MOFs.....	77
Table 3-3. Crystallographic data of the synthesized Mg-MOF-74 deduced from Rietveld refinement. ....	92
Table 3-4. Stages of improvement of washing processes in solvothermal synthesis in this work. ....	93
Table 3-5. Comparison results of CO <sub>2</sub> adsorption capacity of MOF-74 series of this work at 1 bar and 25 °C to the literature data. The values are presented in mmol·g <sup>-1</sup> . ....	96
Table 3-6. Crystallographic data of Mg-MOF-74, Mg-MOF-74@CNT and Mg-MOF-74@GO. ....	102
Table 3-7. Average particle sizes of single specimen and atomic percentage of elements of Mg-MOF-74, Mg-MOF-74@CNT and Mg-MOF-74@GO.....	108
Table 3-8. BET specific surface area of Mg-MOF-74, Mg-MOF-74@CNT and Mg-MOF-74@GO.....	113
Table 3-9. BET specific surface area of Mg-MOF-74, Mg-MOF-74@CNT and Mg-MOF-74@GO as a function of time after their production. The values are presented in m <sup>2</sup> ·g <sup>-1</sup> . ....	113
Table 4-1. Recapitulative of mass transfer phenomena from bulk gas phase to nanoporous solid surface [16, 24, 95, 96, 170, 172-181].....	120
Table 4-2. List of calculation modes of the IAST module [204]. ....	133
Table 4-3. The forms of the reduced spreading pressure equation, initial guess, and constraint for the different modes of calculation [204]. ....	135
Table 4-4. Fitted parameters of Langmuir and dual-site Langmuir models for CO <sub>2</sub> adsorption isotherms of Mg-MOF-74, Mg-MOF-74@CNT and Mg-MOF-74@GO up to 1 bar at 25 °C. ....	155
Table 4-5. Fitted parameters of Henry’s law and Langmuir models for CH <sub>4</sub> adsorption isotherms of Mg-MOF-74, Mg-MOF-74@CNT, and, Mg-MOF-74@GO up to 1 bar at 25 °C.....	157
Table 4-6. Selectivity parameters of CO <sub>2</sub> /CH <sub>4</sub> for Mg-MOF-74, Mg-MOF-74@CNT and Mg-MOF-74@GO at 1 bar and at 25 °C. ....	159
Table 4-7. CO <sub>2</sub> adsorption capacities of Mg-MOF-74, Mg-MOF-74@CNT and Mg-MOF-74@GO at 10 bar for different temperatures: 25 °C, 50 °C and 75 °C.....	166

---

Table 4-8. Fitted parameters of dual-site Langmuir for CO <sub>2</sub> adsorption isotherms of Mg-MOF-74, Mg-MOF-74@CNT and Mg-MOF-74@GO up to 10 bar at different temperatures: 25 °C, 50 °C and 75 °C. ....	170
Table 4-9. CH <sub>4</sub> adsorption capacities of Mg-MOF-74, Mg-MOF-74@CNT and Mg-MOF-74@GO at 10 bar at different temperatures: 25 °C, 50 °C and 75 °C. ....	172
Table 4-10. Fitted parameters of Langmuir model for CH <sub>4</sub> adsorption isotherms of Mg-MOF-74, Mg-MOF-74@CNT and Mg-MOF-74@GO up to 10 bar at different temperatures: 25 °C, 50 °C and 75 °C. ....	176
Table 4-11. Isosteric heats of CO <sub>2</sub> and CH <sub>4</sub> adsorptions $Q_{st}$ in kJ·mol <sup>-1</sup> on Mg-MOF-74, Mg-MOF-74@CNT and Mg-MOF-74@GO at an adsorbed amount of 1 mmol·g <sup>-1</sup> . ....	186
Table 5-1. Setting parameters for kinetic modelling of non-isothermal diffusion system using manometric method. ....	221
Table 5-2. Diffusivities of CO <sub>2</sub> and CH <sub>4</sub> adsorptions on Mg-MOF-74, Mg-MOF-74-CNT and Mg-MOF-74-GO at 25 °C, 50 °C and 75 °C. The values are deduced by manometric method. ....	226
Table 5-3. Kinetic selectivity of CO <sub>2</sub> /CH <sub>4</sub> on Mg-MOF-74, Mg-MOF-74-CNT and Mg-MOF-74-GO at 25 °C, 50 °C and 75 °C. The values deduced by manometric method. ....	228
Table 5-4. Determination of parameter $K_H \cdot V_s$ for CO <sub>2</sub> adsorption on Mg-MOF-74, Mg-MOF-74@CNT and Mg-MOF-74@GO. ....	230
Table 5-5. Setting parameters for kinetic modelling of linear isothermal diffusion system using Zero Length Column method. ....	230
Table 5-6. Diffusivities times constant of CO <sub>2</sub> adsorption on Mg-MOF-74, Mg-MOF-74-CNT and Mg-MOF-74-GO at 25 °C, 50 °C and 75 °C, deduced by Zero Length Column method. ....	238
Table 5-7. Comparison of the values of zero coverage diffusivity time constant, $D_0/r_c^2$ , of CO <sub>2</sub> adsorption on Mg-MOF-74, Mg-MOF-74@CNT and Mg-MOF-74@GO deduced using manometric method and Zero Length Column method. The values are presented in s <sup>-1</sup> . ....	241

## CHAPTER 1

# Introduction

## CHAPTER 1: INTRODUCTION

### 1.1. General introduction

Global energy demand has shifted to natural gas due to burning energy efficiency and low carbon emissions [1-3] while the European Union has encouraged biogas production due to renewable energy policies in addition to economic, environmental and climate benefits [4]. Therefore, researchers are working on finding ways to increase the economic feasibility in exploiting these resources. Carbon dioxide (CO<sub>2</sub>) which is the major gaseous contaminant found in natural gas and biogas streams for averagely 0.5–10 vol.% (with peaks up to 70 vol.%) [5], should be removed from methane (CH<sub>4</sub>) for industrial importance and commercial value. In CO<sub>2</sub> removal technologies, adsorption is viewed as an emerging alternative to contend with traditional amine scrubbing where the use of solvents is controversial [6, 7]. In adsorption technologies such as Pressure Swing Adsorption (PSA), solid-state sorbents like zeolites, activated carbon, graphene oxide and alumina are being widely developed for industrial application [8].

In the past decades, a new family of porous solid called metal-organic frameworks (MOF) firstly reported by Yaghi's group in 1999 [9] have been the focus of intense research owing to the ability to provide large microporous volumes and immense specific surface areas. MOFs are the assembly of metal-containing nodes coordinated to organic bridging ligands giving rise to characteristic three-dimensionally ordered crystalline structures [10]. Since MOFs may develop specific surface area as high as 6240 m<sup>2</sup>·g<sup>-1</sup> [11], one of their most promising applications is the processes of gas storage and separation relying on adsorption [12]. By reason of well-defined structure of micropore walls, MOFs are recognized for the possibility of fine and controlled tuning of gas adsorption properties by performing ligand design, metallic center substitution or functionality adjustment [13]. This allows to rich gas adsorption capacity and separation selectivity that cannot be achieved by other porous materials [14].

To date, MOF-74 family and particularly Mg-MOF-74 material figure among the most promising adsorbents for CO<sub>2</sub> separation from CH<sub>4</sub>/CO<sub>2</sub> and CH<sub>4</sub>/CO<sub>2</sub>/N<sub>2</sub> gas streams in the context natural gas and biogas purification [15-18]. Characterized by BET specific surface area close to 1200 m<sup>2</sup>·g<sup>-1</sup> [19] and one-dimensional pores of approximately 10 Å [20], this material features exceptional density and accessibility of open metal sites which are the preferential adsorptive centers for gas molecules [21, 22]. The ratio of Henry's

constants of CO<sub>2</sub> and CH<sub>4</sub> adsorptions exhibited by Mg-MOF-74 is reported as high as 330 at 1 bar and 25 °C, allowing one of the best CO<sub>2</sub>/CH<sub>4</sub> separation efficiency by MOF materials [23]. This excellent selectivity towards CO<sub>2</sub> originates from a strong intermolecular interaction of this gas with the exposed metallic centers leading to the stabilization of their coordination sphere and thus high ordering of adsorbed CO<sub>2</sub> molecules within unit cell as revealed by in-situ characterization techniques [16, 20, 24].

The possible structural variation of MOF-based materials or composites in terms of constitutes functionalities, particle size, geometry and topology has led to more than 20000 different types of reported MOFs [25]. Further improvement of gas adsorption performances of MOF materials can be attained by optimizing the texture and morphology of the solid creating an additional microporosity and interstitial porosity [26-28]. This facilitates the gas transport to adsorption sites and increases total accessible pore volumes and specific surface areas. Recently, researches on incorporation of MOFs with carbon-based compounds to produce MOF-carbon composites are continuously being conducted. Owing to the formation of secondary micro and mesoporosity within the composites nanostructure, the carbon-doped MOFs have been reported able to increase gas adsorption capacity and separation efficiency in comparison to their parent material [29-42].

Carbon nanotubes (CNT) and graphene oxide (GO) are considered as the most common carbon-based doping agents used in the synthesis of MOF-carbon composites for various applications [27]. CNTs which are an allotropic form of carbon related to fullerene family can be divided into single-walled and multiwalled CNTs according to their structure [43]. CNT walls are inert with chemical reaction but organic ligands or functional organic agents can easily attach or cover on CNT walls in CNT-hybrid composites [44]. This is advantageous for MOF materials. Meanwhile, GO contains high density of atoms and oxygen functionalities in the arrangement of layered-structure [45]. These functionalities from type hydroxyl, carboxyl, epoxy and ketone groups are able to coordinate with the metallic centers of MOFs, leading to the growth of MOF crystals onto graphene layers [46, 47]. This formation can be described as an alternate structure of MOF units and GO layers [48].

## 1.2. Problem statements

Since MOF-74 has been introduced in 2005 [15], no published work has reported on the development of MOF-74-carbon composites despite of potential advantages the new

materials can offer for selective separation of CO<sub>2</sub> and CH<sub>4</sub>. Literature review also shows that the performance of MOF-74 materials for CO<sub>2</sub> capture at high pressures in regard to natural gas streams at processing plant that can reach 75–100 bar [49] has received less attention. Most published works of MOF-74 have experimentally performed the adsorption at mild pressures which are more relevant for CO<sub>2</sub> captures at natural gas power plants [17-19, 23, 37, 50-54]. To fill these research gaps, the present study proposes a potential novelty in adsorption technologies by developing other types of MOF–carbon composite from Mg-MOF-74 template for CO<sub>2</sub> and CH<sub>4</sub> adsorptions at high pressures.

In order to assess the performances of the synthesized materials, isotherm studies are necessary to establish equilibrium correlation of adsorbent–adsorbate to predict the behavior of the adsorption system under different operational conditions, especially temperature. The isotherm data also provides the information on adsorption capacities per unit mass of adsorbent and its regeneration which influence the operational cost. Meanwhile, the importance to study the kinetics of adsorption processes is for economic reason because fast processes will reduce operational cost, and also, for fundamental reason which involves the understanding of transport phenomena, porosity and connectivity in adsorbent materials to improve the diffusion. Therefore, equilibrium and kinetic data are essential to provide the information required for a fundamental design of a PSA unit for specific application.

### 1.3. Objectives of the study

This study is directed from the potential of MOF-74–carbon composite as the effective adsorbent for CO<sub>2</sub>/CH<sub>4</sub> separation for a widely developed PSA technology. The aim is to assess the performances of these materials in a laboratory scale in order to provide the equilibrium and kinetic adsorption data, that are the input for PSA cycle simulation. However, PSA development remains as the future work and is not covered in this study. For that reason, the objectives of the study are:

1. To develop these MOF-74–carbon composites with an optimum concentration of doping agent (GO or CNT) and to understand the properties of these composites with respect to the pristine MOF-74 through a comprehensive characterization.
2. To evaluate and understand the equilibrium isotherm behaviour of pure CO<sub>2</sub> and CH<sub>4</sub> on these synthesized materials at high pressures for different temperatures. These data

provide the information on the adsorption capacities, energies and equilibrium selectivities.

3. To evaluate and understand the diffusion behaviour of pure CO<sub>2</sub> and CH<sub>4</sub> on these synthesized materials in and out of Henry law region for different temperatures, also when the diffusion is controlled by internal or external mass transfer resistance.

#### 1.4. Scopes of the study

**Synthesis and characterization:** The pristine MOF-74 and its carbon composites were synthesized using conventional solvothermal technique. The doping agent was added by an *in situ* synthesis and its concentration was optimized. The synthesized materials were characterized for the studies of crystal structure (PXRD analysis), chemical functionalities (FTIR analysis), morphology (FESEM analysis), thermal stability (TG analysis) and pore textural properties (nitrogen physisorption analysis).

**Adsorption equilibria:** The synthesized materials were firstly tested for the equilibrium measurement of pure CO<sub>2</sub> and CH<sub>4</sub> at low pressure (up to 1 bar) at 25 °C for a preliminary study. After that, they were tested for the adsorption of pure CO<sub>2</sub> and CH<sub>4</sub> at high pressure (up to 35 bar) for different adsorption temperatures; 25 °C, 50 °C and 75 °C. The adsorption cycling performance and isotherm reproducibility were also studied. For high-temperature and high-pressure adsorption conditions, the effects of temperature gradient of the instrument and surface excess mass of adsorbed gas molecules were taken into consideration.

**Adsorption kinetics:** The synthesized materials were firstly tested for the kinetic measurement of pure CO<sub>2</sub> and CH<sub>4</sub> by using manometric method at different pressures (0.2 bar, 0.5 bar and 1.5 bar) for different adsorption temperatures; 25 °C, 50 °C and 75 °C. The sorption rate was estimated accounting for the influence of temperature and adsorption coverage on the diffusion, especially for concentration distributions out of Henry's law region. After that, they were tested for the kinetic measurement of pure CO<sub>2</sub> in a diluted system of Helium flux (2 mol% of CO<sub>2</sub>) by using Zero Length Column method for different adsorption temperatures; 25 °C, 50 °C and 75 °C. The sorption rate was estimated and designated as the diffusivity at zero adsorption coverage.

## **CHAPTER 2**

# **Context of the Study**

## CHAPTER 2: CONTEXT OF THE STUDY

### 2.1. Global energy demands

#### 2.1.1. Natural gas

As reported in International Energy Outlook 2016 forecast, natural gas is the fastest-growing primary energy resource with the projection to 2040 as seen in Figure 2-1 (left) [1] and its production increases nearly double between 2001 and 2025 [2]. Natural gas is favorable energy resource for many countries in terms of greenhouse effect since its combustion emits lower quantities of CO<sub>2</sub> and other greenhouse gases as seen in Figure 2-1 (right) [2, 6]. Although natural gas is relatively low in energy content per unit volume due to its gaseous state, it exhibits higher energy conversion efficiencies for power generation comparatively to other hydrocarbon resources [3]. Natural gas is distributed to several sectors including industry, residential and commercial users, transportation and electrical power generation [1].

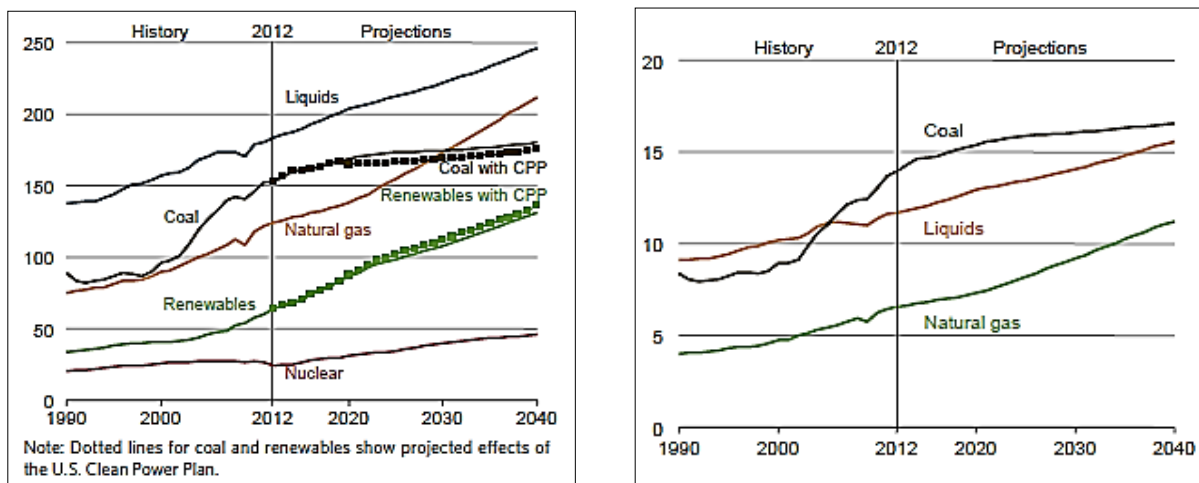


**Figure 2-1.** (left) World energy consumption by energy resource in quadrillion British Thermal Unit (BTU) from 1990 with the projection to 2040 [1]. (right) World energy-related CO<sub>2</sub> emissions by fuel type in billion metric tons from 1990 with the projection to 2040 [1].

Pure state natural gas which is colorless and odorless can be categorized into conventional gas and unconventional gas based on the origin and chemical compositions [55]. The conventional gas that occurs in deep hydrocarbon reservoirs coexisting with natural gas liquids (NGL) and crude oil is referred as the “associated gas” [56]. While the conventional gas that originates from the deposits containing small amount or none of NGLs and crude oil is referred as the “non-associated gas” [56]. NGLs are made of higher

hydrocarbons ( $C_{2+}$  products) while crude oil contains gasoline condensates ( $C_{5+}$  products) [55]. The unconventional gas exists in several forms such as shale gas, coal-bed methane, deep aquifer gas and gas hydrates. The treatment of natural gas involves the removal of NGLs, crude oil, moisture, acid gases such as  $CO_2$  and hydrogen sulphide ( $H_2S$ ), and, trace components such as nitrogen, oxygen, helium, mercury, arsenic compounds, radioactive materials and volatile organic compounds [55-57].

Natural gas composition is influenced by the type, depth and geological area of the underground reservoir [7]. In any cases,  $CO_2$  appears as the largest gaseous impurity in natural gas for averagely 0.5-10 vol.% (with peaks up to 70 vol.%) [5]. Natural gas with high  $CO_2$  concentration is encountered in South China Sea, Gulf of Thailand, Central European Pannonian basin, Australian Cooper-Eromanga basin, Colombian Putumayo basin, Ibleo platform, Sicily, Taranaki basin, New Zealand and South Viking Graben [58]. Table 2-1. shows  $CO_2$  content in volume percent basis from various natural gas fields around the world. Russia which is the world's largest gas exporter has the purest methane-containing gas up to 98% with almost zero content of  $CO_2$  [59]. Russia supplies natural gas from  $47.8 \cdot 10^6 m^3$  reservoirs that represent 24% of world proven reserves [1]. Over 25% of European natural gas consumption is supplied by Russia alone [59], following by the second largest gas exporter, Norway, for almost 20% of European demands [60].

**Table 2-1.**  $CO_2$  content from various natural gas fields around the world in volume percent basis.

Natural gas field	$CO_2$ content	Ref.
Urengoy, Russia	~ 0%	[61]
Cortemaggiore, Italy	0.2%	[62]
Hassi R'Mel, Algeria	0.2%	[62]
Heimdal, Norway	0.4%	[62]
Groningen, the Netherlands	0.9%	[7]
Ardjuna, Indonesia	4.1%	[7]
Lacq, France	9.3%	[7]
Uthmaniyah, Saudi Arabia	8.9%	[7]
Telaga Bergading, Malaysia	23.5%	[63]
Uch, Pakistan	46.2%	[7]

In Southeast Asia, Malaysia ranks third-largest natural gas market through the activities of Malaysian oil and gas company, PETRONAS [64]. It is also one of the countries having the most gas penetration where 38% of the fuel mix is derived from natural gas [64]. Malaysia has approximately  $285 \cdot 10^{10} \text{ m}^3$  of total natural gas volume with  $212 \cdot 10^6 \text{ m}^3$  reserves that are able to last up to 40 years [2, 65]. PETRONAS Floating Liquefied Natural Gas (LNG) Satu terminal is the first world floating LNG project having the production capacity of 1.2 million tons per year [65]. This terminal has achieved an industry breakthrough in 2016 with the successful production completing its first gas milestone: made its 2,120 nautical mile journey from Okpo, South Korea to Kanowit gas field, Malaysia for its offshore phase of commissioning [65, 66]. Thus, natural gas is predicted to continue as an important role in empowering the economy and energy supply in Malaysia until 2050 [65].

### 2.1.2. Biogas and biomethane

Meanwhile, Europe has different perspectives of energy consumption where biogas has received more attention in these recent years being widely used for electricity, heat and transport. Biogas production has increased in the European Union (EU) and its Member States reaching 18 billion  $\text{m}^3$  of methane in 2015 representing half of the global biogas production [4], as seen in Figure 2-2 (left). This is encouraged by the renewable energy policies in addition to economic, environmental and climate benefits [4]. Recently the upgrading of biogas to biomethane has started for the direct use of the biogas for heat and power, and it is progressively used for vehicle fuel or injection into natural gas network [4, 67]. Figure 2-2 (right) illustrates the number of existing upgrading plant producing biomethane worldwide in 2019.

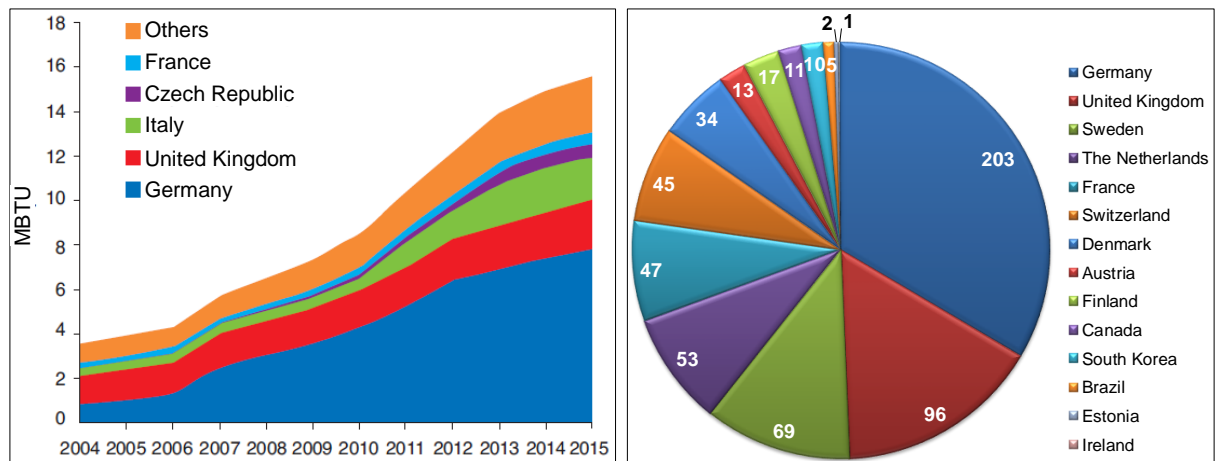


**Figure 2-2.** (left) Development of biogas production in European countries in mega British Thermal Unit (MBTU) from 2004 to 2015 [68]. (right) The number of existing upgrading plant producing biomethane worldwide in 2019 [69].

France, despite having abundant shale gas deposits, it no longer has a major production of natural gas whereby 84% of the consumed natural gas is imported by cross-border pipelines from other interconnected countries and the remaining 16% from LNG terminals of the middle-east countries [70]. This situation is explained by the French government's ban on fracking in 2011 [71]. France is the first country to prohibit hydraulic fracturing to explore natural gas resources due to the potential impact on the environment [71]. Instead, France by this time has 685 biogas plants of which 76 are supplying injecting biogas into the natural gas distribution systems while the rest of them are locally producing heat or electricity [72]. In 2018, the number of biomethane plants in France has increased by 73% and the quantity of biomethane injected into French distribution networks has increased by 76% in comparison to 2017 [72].

Biogas is defined as a mixture of gases produced by the breakdown of organic matter in anoxic conditions (anaerobic digestion). It is produced in biogas plants by fermentation of renewable raw materials such as agricultural waste, manure, municipal waste, plant material, sewage, green waste and food waste. It primarily consists of methane and CO<sub>2</sub>, the average amount of methane in raw biogas is 60% [73]. biogas composition depends on the type of plant biomass used [74]. Different sources of production lead to different specific compositions, Figure. CO<sub>2</sub> content appears as the largest impurity composition for averagely 30–40 vol% (with peaks up to 50 vol%) in biogas [73]. The treatment of biogas

includes the removal of moisture, acid gases such CO<sub>2</sub> and H<sub>2</sub>S, and, traces components such as nitrogen, oxygen, hydrogen, carbon monoxide, ammonia and siloxanes [73, 75].

**Table 2-2.** Typical compositions of biogas according to its source in volume percent basis.

Components	Agricultural waste [73]	Industrial waste [75]	Landfills [73]	Sludge [75]
Methane, CH <sub>4</sub>	50–80	50–70	45–65	50–80
Carbon dioxide, CO <sub>2</sub>	30–50	30–50	20–50	20–50
Hydrogen sulphide, H <sub>2</sub> S	0.70	0–8	0.10	0–1
Hydrogen, H <sub>2</sub>	0–2	0–2	0–5	0–5
Nitrogen, N <sub>2</sub>	0–1	0–1	0–3	0–3
Oxygen, O <sub>2</sub>	0–1	0–1	0–1	0–1
Carbon monoxide, CO	0–1	0–1	0–1	0–1
Ammonia, NH <sub>3</sub>	Traces	Traces	Traces	Traces
Siloxanes	Traces	Traces	Traces	Traces

## 2.2. CO<sub>2</sub> problems in natural gas and biogas productions

For the utilization of these resources, the methane content is the most important parameter. The purification of both gas resources is indispensable for some reasons: (i) to meet the specification of pipelines, (ii) to obtain environmentally clean-burning gas, (iii) to maximize the efficiency of combustion, (iv) to remove the components that inhibit the use the gaseous fuel for residential and industrial purposes, (v) to separate valuable components from the raw gas such as propane (fuels), ethane and helium (industrial gases), and, (vi) to enable liquefaction of the gases for transportation and storage [55, 57].

The selling price of the gases is determined by their calorific value. Therefore, CO<sub>2</sub> must be removed since it degrades the energy content of the fuel gas [7]. This consequently reduces the efficiencies of fuels conversion into energy power during combustion. The heating value of commercial gas should be in the order of 38–39 MJ·m<sup>-3</sup> (United States, United Kingdom and Australia), 37 MJ·m<sup>-3</sup> (Canada), 35 MJ·m<sup>-3</sup> (Malaysia) and 34 MJ·m<sup>-3</sup> (Russia) containing less than 2–3 vol.% of CO<sub>2</sub> [76-78]. Others also mentioned that natural gas with more than 3 vol.% of CO<sub>2</sub> is considerably unmarketable whereby the production demands can only tolerate until 2.5% [79, 80].

The concentrations of acidic gas such as CO<sub>2</sub> and H<sub>2</sub>S across gas pipelines and distribution networks are also strictly enforced and must be kept at low levels due to their corrosive properties. Aside from wasting pipeline capacities, CO<sub>2</sub> is reactive with moisture which is also the traces component in the gas to form carbonic acids that can threaten steel pipelines and equipment system. On the other hand, traces of acidic gases can give a passivating effect causing the formation of sulphides and carbonites of iron (Fe) on the internal walls of the pipeline, which can further protect the surface against corrosion [81]. In LNG processing aiming for the separation of light hydrocarbons from methane operating at 150–160 °C, CO<sub>2</sub> will be condensed or solidified causing the blockage of the pipelines and consequently disrupting the transportation [7]. For instance, U.S. pipeline specification limits the amount of those components at <2 mol% for CO<sub>2</sub>, <4 ppm for H<sub>2</sub>S and <120 ppm for moisture [7]. However, the standard quality of the gas varies depending on the design of the pipeline system and the markets that it serves.

The removal of CO<sub>2</sub> is also primordial to obtain environmentally clean-burning gas knowing that CO<sub>2</sub> is the primary anthropogenic contributor to irreversible climate changes [6]. It is estimated that 30 Giga tons of CO<sub>2</sub> is generated per year from the combustion of fossil fuels which is the major source of CO<sub>2</sub> emissions [6, 82]. One-third of the total CO<sub>2</sub> release is equivalent to the emissions of other greenhouse gases such as methane, nitrous oxide, hydrofluorocarbons, perfluorocarbons and sulfur hexafluoride [82, 83]. Meanwhile, the carbon climate response defined as the change in temperature per cumulative carbon emissions is predicted to be 1.0–2.1 °C per 1 Terra tons of carbon emitted [84]. Biomethane fuel is one of the cleanest fuels in the transportation sector in which greenhouse gases emissions from the combustion of 100% biomethane are estimated 5 g of CO<sub>2</sub>-eq/km, 25 times less than those of fossil natural gas (124 g of CO<sub>2</sub>-eq/km), while mixtures of 20% biomethane with natural gas emits 100 g of CO<sub>2</sub>-eq/km [67].

## **2.3. CO<sub>2</sub> removal technologies**

### **2.3.1. CO<sub>2</sub> removal from natural gas streams**

CO<sub>2</sub> removal from natural gas streams is effectuated at processing plants in both onshore and offshore fields, and also, at power plants comprising of post-combustion, pre-combustion and oxy-fuel combustion captures. Natural gas power plants includes integrated coal gasification combined cycle (IGCC) plant, natural gas combined cycle

(NGCC) plant or supercritical pulverized coal combustion (SC/PCC) plant [85]. The intensification level of CO<sub>2</sub> removal depends on the market that the natural gas serves and the pipeline limits for transportation.

In natural gas processing plant, since the reservoirs are normally in miles distance from the final marketplaces, the gas needs to be transported either by pipelines as gaseous mixture with >75 vol.% of methane or by tankers in LNG form with >85 vol% of methane [5]. The purification at onshore or offshore sites is the first step of natural gas treatment before being transported where a certain amount of CO<sub>2</sub> is reinjected in geological form. At wellhead of the reservoirs, natural gas is available at very high pressure where the rising gas itself supplies the wellhead with under pressure [86]. The average pressure of natural gas streams for the treatment at processing plant can reach 75–100 bar [49]. The schematic figure of natural gas treatment at processing plant is presented in Figure 2-3.

Figure 2-4 represents schematic pathways of CO<sub>2</sub> capture approaches in fuel-fired power plants. Concurrently, the pre-combustion capture of CO<sub>2</sub> is adopted in IGCC and NGCC power plants [85]. It removes fuel carbon content before the fuel is burned. Before the separation process, coal and other solid/liquid fuels such as oil and biomass undergo gasification process whereas natural gas is reformed, both of which are to produce synthesis gas or “syngas”. After gasification process, the produced syngas is drained to a water-gas shift reactor before being fed to a CO<sub>2</sub> capture for separation process. CO<sub>2</sub> is removed from the gas stream before the extraction of the fuel gas for gas combustion. Hydrogen gas goes on to participate in the combustion process. The pre-combustion capture occurs at much more high pressure in comparison to that of post-combustion.

The post-combustion capture involves CO<sub>2</sub> removal from flue gas in NGCC and SC/PCC power plants [85]. The conversion of fossil fuel to energy is carried out in prior to the CO<sub>2</sub> separation. The major challenge is to separate the low concentration of CO<sub>2</sub> (~16%) from the high concentration of N<sub>2</sub> gas (73–77%) [87]. At this stage, the pressure of CO<sub>2</sub> flow is lower when compared to other gas streams. It requires a balance between the selectivity towards CO<sub>2</sub> over other gases and its ability to desorb [87]. This process occurs at ambient pressure. The exhaust gas that comes out from post-combustion chamber is termed as “flue gas”.

The oxy-fuel combustion capture to which pure oxygen is fed is also adopted in NGCC and SC/PCC power plants [85]. It is a nitrogen-free technique producing flue gas

stream with high concentration of CO<sub>2</sub> with the aim of minimizing energy provided for the separation to occur. During the process, fossil fuel is combusted with pure oxygen to produce almost pure CO<sub>2</sub> that can be easily captured [85]. Although this technique is considerably expensive due to the generation of oxygen by separating it from the air and needs further advancement, it can reduce CO<sub>2</sub> emissions significantly and ease CO<sub>2</sub> separation, storage and utilization. The exhaust gas that comes out from oxy-fuel combustion chamber is also termed as “flue gas”.

The recapitulative of operation conditions such as separation task, CO<sub>2</sub> concentration, pressure and temperature of natural gas stream at different stages of treatment are tabulated in Section 2.3.3.

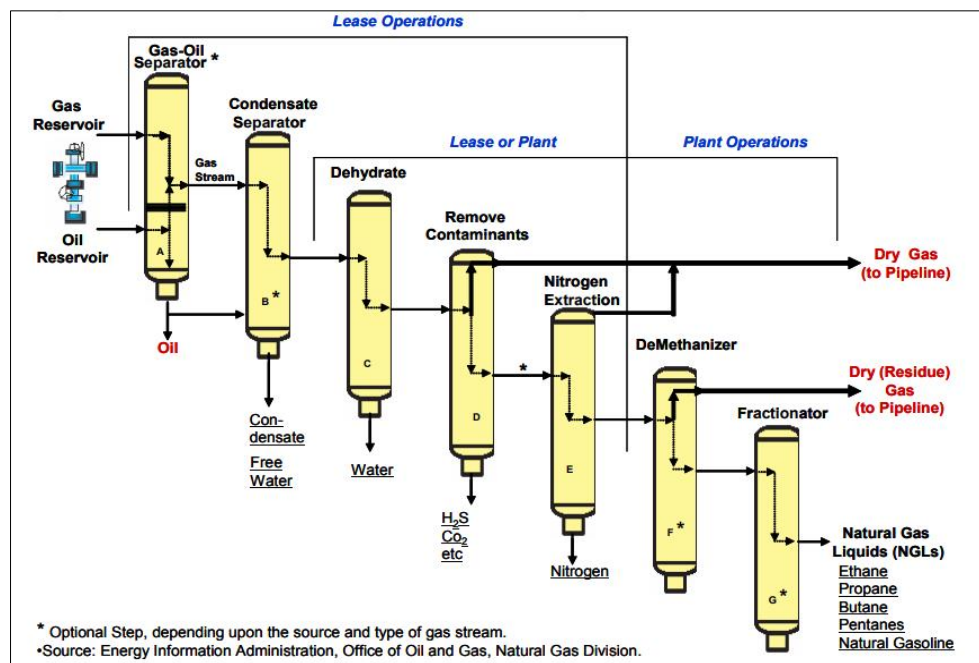
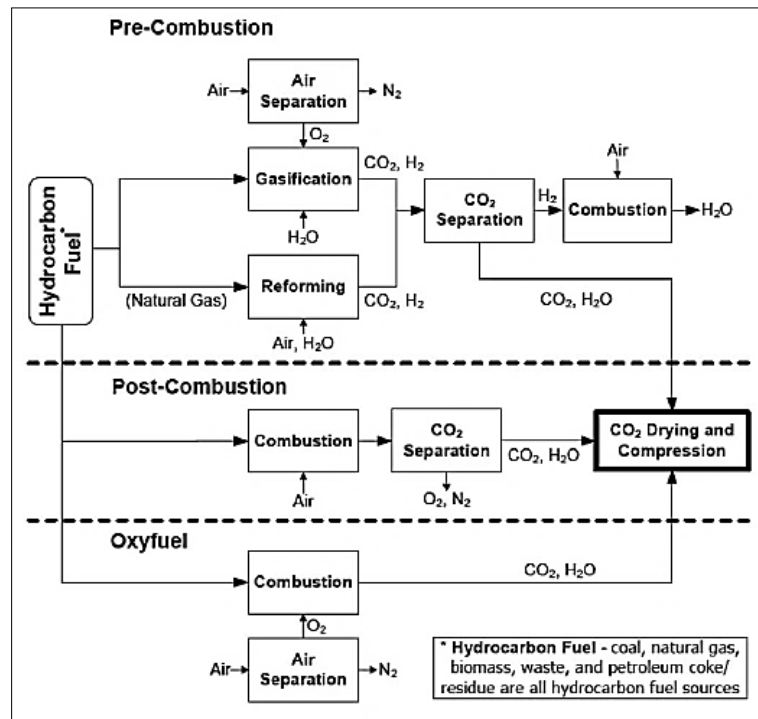


Figure 2-3. Schematic figure of natural gas treatment at processing plant [49].



**Figure 2-4.** Schematic pathways of CO<sub>2</sub> capture approaches in fuel-fired power plants [6].<sup>1</sup>

### 2.3.2. Comparison of different technologies: Advantages and challenges

Acid gas removal units serve to purify natural gas and biogas from acidic contaminants such as CO<sub>2</sub>, H<sub>2</sub>S, remaining moisture and inert gases through a sweetening process. The techniques that are already widely used and developed for gas treatment includes absorption, adsorption, cryogenic distillation, membranes, gas hydrates and chemical looping [87]. The most renowned process, amine-based scrubbing (absorption), has been taking place in industry for over 70 years but it is uncertain if this technology is able to cater the scale of worldwide CO<sub>2</sub> emitted which is 30 Giga tons per year [6]. The use of solvents in absorption technique is controversial because of environmental hazards of their disposal, aside from the risks of corrossions of the units, damages of pump suctions when the solvents vaporize, and high operating cost due to chemical absorption regeneration [7].

For that reason, other techniques have been also taking place to mitigate CO<sub>2</sub> emissions aside from the traditional absorption [8]. Researches are continuously being conducted to make improvement in the existing technologies and discover new effective

<sup>1</sup> Reprinted from Carbon Capture, J. Wilcox, Chapter 1: Introduction to carbon capture, pp. 1-34, Copyright 2012, with permission from Springer Nature.

solvents or adsorbents for CO<sub>2</sub> capture. Some factors need to be considered in selecting an appropriate CO<sub>2</sub> removal technology. Firstly, the nature and conditions of the feed gas such as the gas volume to be treated, CO<sub>2</sub> concentration, other hydrocarbons concentrations, and, pressure and temperature where the feed gas is available. Secondly, the operating outcome to achieve considering the end-markets and demands, pipelines specification, final acceptable CO<sub>2</sub> concentration and the tolerance between CO<sub>2</sub> removal capacities and desired selectivity. Thirdly, the operating limitations including energy consumption, capital and operating costs, maintenance cost, easy-handling operation, and, modulation in regard to weight and footprint of the units.

Every technology exhibits its own advantages and limitations relatively to others. In these recent years, adsorption in which solid-state sorbents are used is viewed as a competitive technology with many potential advantages, especially in terms of low negative environmental impacts, over the use of liquid sorbents in absorption [7, 8, 55, 87, 88]. Adsorption also attracts attention for its superiority to other techniques in some applications such as the removal of hazardous materials, fossil fuels purification and gas capture and storage, in terms of high capacity per module, high chemical resistivity, low capacity of heat and low capital cost [7, 8, 55, 87, 88]. However, in many cases, the gas stream should be cooled and dried before being fed into adsorption unit which limits the attractiveness of adsorption compared to chemical absorption [8]. Besides membranes and cryogenic techniques, adsorption can be implemented at both natural gas processing plant and power plant with high purity of produced gas [55, 88]. The requirements to meet and challenges to overcome by the most industrially applied CO<sub>2</sub> capture technologies are summarized in Table 2-3.

**Table 2-3.** Requirements and challenges of the most industrially applied CO<sub>2</sub> capture technologies [7, 8, 55, 87, 88].

<b>Technology</b>	<b>Requirements</b>	<b>Limitations/challenges</b>
Absorption	Solvent must have: <ul style="list-style-type: none"> <li>- High gas solubility</li> <li>- High solvent selectivity</li> <li>- High volatility</li> <li>- Low effects on product and environment</li> <li>- High chemical stability</li> </ul>	<ul style="list-style-type: none"> <li>• Amines and Benfield solution causes corrosion of the units</li> <li>- Solvents cannot be recycled and its disposal cause environmental hazards</li> <li>- Regenerated solvent vaporize in the pump suction, resulting in vibration and excessive wear of pump impellers</li> <li>• Not recommended at low partial pressures</li> </ul>

	<ul style="list-style-type: none"> <li>- Non-corrosive</li> <li>- Low viscosity</li> <li>- Non-flammable</li> <li>- Low freezing point</li> </ul>	
Adsorption	<p>Solid sorbents must have:</p> <ul style="list-style-type: none"> <li>- High selectivity <ul style="list-style-type: none"> <li>o Depends on adsorption equilibrium and kinetics</li> </ul> </li> <li>- High capacity <ul style="list-style-type: none"> <li>o Surface area per volume</li> </ul> </li> <li>- High transfer rates</li> <li>- Facile regeneration</li> <li>- Long service life</li> </ul>	<ul style="list-style-type: none"> <li>• Adsorption loading decreases with increasing temperature</li> <li>• Adsorption loading decreases with decreasing partial pressure</li> <li>• Normally the feed gas needs to be cooled and dried in prior to adsorption</li> </ul>
Cryogenic distillation	<p>Conditions required are:</p> <ul style="list-style-type: none"> <li>- High concentrations of CO<sub>2</sub> (50-70%)</li> <li>- Very low temperature CO<sub>2</sub> (-73.3°C)</li> </ul> <p>Cryogenic fluids must have boiling point of &lt;120 K.</p>	<ul style="list-style-type: none"> <li>• Not economical for low concentration of CO<sub>2</sub></li> <li>• High energy intensive for regeneration</li> <li>• High tendency for blockage of equipment</li> <li>• Some cryogenic fluids are flammable and toxic</li> <li>• Uneasy operation under different feed streams due to highly integrated and enclosed system</li> </ul>
Membranes	<p>Selection of materials:</p> <ul style="list-style-type: none"> <li>- High perm-selectivity (in tolerance with high permeability)</li> <li>- High chemical resistance</li> <li>- Ability to form asymmetric morphology</li> <li>- Good mechanical strength</li> </ul>	<ul style="list-style-type: none"> <li>• Compromise between product purity and productivity</li> <li>• Mainly used for moderate-volume gas streams</li> <li>• Cannot compete with standard amine absorption for large-scale volume gas streams <ul style="list-style-type: none"> <li>- Flux and selectivity of membrane are too low</li> </ul> </li> <li>• Must be protected from heavier C<sub>5+</sub> hydrocarbons to prevent irreversible damages</li> </ul>

### 2.3.3. Operation conditions at different stages of gas treatment

Table 2-4 summarizes the operation conditions and available technologies of CO<sub>2</sub> capture for natural gas production. Different from natural gas, biogas and biomethane are normally available at  $\approx 1$  atm and at a temperature range of 35–55 °C [89].

**Table 2-4.** Operation conditions and available technologies of CO<sub>2</sub> capture for natural gas production.

	Natural gas processing	Pre-combustion	Post-combustion	Oxy-fuel combustion	Ref.
Type of power plant		IGCC	NGCC	NGCC	[85]
		NGCC	SC/PCC	SC/PCC	
Feed gas	Raw natural gas	Syngas	Flue gas (with low CO <sub>2</sub> )	Flue gas (with high CO <sub>2</sub> )	[87]
Separation task	CO <sub>2</sub> /CH <sub>4</sub>	CO <sub>2</sub> /H <sub>2</sub>	CO <sub>2</sub> /N <sub>2</sub>	CO <sub>2</sub> /N <sub>2</sub>	[8]
Feed gas pressure	75–100 bar <sup>1</sup>	20–40 bar <sup>2</sup> (for auto-thermal reforming)	≈1 atm <sup>3</sup>	≈1 atm <sup>3</sup>	<sup>1</sup> [49] <sup>2</sup> [90] <sup>3</sup> [18]
Feed gas temperature	15–43 °C <sup>4</sup>	>100 °C <sup>5</sup> (especially IGCC)	40–60 °C <sup>6</sup>	40–60 °C <sup>6</sup>	<sup>4</sup> [91] <sup>5</sup> [92] <sup>6</sup> [93]
CO <sub>2</sub> content in volume %	Av. 0.5–10% <sup>7</sup> (peaks up to 70%)	15–60% <sup>8</sup>	3–15% <sup>8</sup>	>80% <sup>8</sup>	<sup>7</sup> [5] <sup>8</sup> [94]
Available CO <sub>2</sub> capture technologies for industry	Absorption				[87]
	Adsorption				
	Cryogenic techniques				
	Membrane				
		Gas hydrates			
		Chemical looping		Chemical looping	
Available solvents for industry	Physical absorption solvents				[8]
	Chemical absorption solvents				
Available adsorbents for industry	Zeolites				[8]
	Activated carbon / carbonaceous materials				
		Alumina / silicates			
Available membranes for industry	Polymeric membranes				[8]
	Ceramic membranes				
				Ion-transport	
Available cryogenic for industry	Ryan-Holmes	Liquefaction	Liquefaction	Distillation	

## 2.4. Pressure Swing Adsorption (PSA)

### 2.4.1. Introduction to adsorption

Adsorption in general is defined as the deposition of molecular species (adsorbate) onto a solid surface (adsorbent) due to imbalance intermolecular interaction. Adsorption is an exothermic process due to energy released when the molecules lose the degree of freedom after being adsorbed, thus the adsorption loading decreases with increasing temperature [95]. Adsorbents, which normally exist in spherical pellets, are porous materials preferably having a large surface area per unit mass. The adsorption process takes place when an adsorbent is put in contact with a fluid stream resulting in an equilibrium state after a sufficient time to allow a dynamic balance between the adsorbate concentration in the bulk gas phase and that at the solid interface [95, 96]. The amount of adsorbate taken up per unit mass of adsorbent (adsorption capacity) indicates the thermodynamic limit of the solid to load the adsorbate at specific operation conditions such as molecular concentration, applied pressure and temperature. The adsorption separation is based on three distinct mechanisms: (i) steric mechanism, the porous solid has pores having certain dimension that allows small molecules to enter while excluding large molecules from entry, (ii) equilibrium mechanism, the solid has different abilities to accommodate different species in the way that the stronger adsorbing species is preferentially captured by the solid, (iii) kinetic mechanism, the different rates of diffusion of different species into the pore control the time of exposure thus the faster diffusing species is preferentially captured by the solid [95]. In this study, we discuss the adsorption of the gas phase of different molecular species by which their separation on the adsorbent material is determined by the different properties they exhibit in relation to these mechanisms. In the case of co-adsorption, the less-adsorbed (“light”) species will easily breakthrough the adsorption column while the more-adsorbed (“heavy”) species loads the adsorption bed. The bed is then regenerated by desorbing the adsorbed molecules. The regeneration process is carried out by reversing the adsorbate–adsorbent equilibrium by pressure or temperature change and it normally takes shorter than the adsorption process.

#### 2.4.2. Pressure Swing Adsorption

Knowing that the equilibrium of adsorption is determined by thermodynamic states of the system such as pressure and temperature, different techniques of regeneration are established by changing one of these parameters. The most widely used technique in adsorption technologies is Pressure Swing Adsorption (PSA) in which the total pressure of the system is swung from high pressure in feed to low pressure in regeneration in order to desorb the heavy molecules. There are two ways to conduct the PSA process by which the adsorbate concentration is modified: (i) changing the total pressure of the system, or, (ii) injecting an inert gas to the column while maintaining the pressure. Both methods will lead to the decreased adsorbate partial pressure or concentration in the column allowing the reversibility of equilibrium where the desorption process takes place. Another regeneration technique is known as Thermal Swing Adsorption (TSA) which involves the increment in temperature of the isotherm system, changing the equilibrium constant allowing the reversibility for desorption. The temperature for desorption must be higher than the adsorption temperature.

For the efficiency reason, PSA is more preferable than TSA when the concentration of the heavy component is considered important (more than a few percent) [97]. This is due to the balance between the quite short time taken to accomplish the loading of the heavy component in the column and the short time required to change the total pressure of the system for regeneration [97]. At low concentration of heavy component, the adsorption step takes much longer and regeneration under TSA can be considered since the change in temperature is much slower than the pressure swing [97]. Although TSA is applicable for both gases and liquids, the thermal ageing of the adsorbent and the heat loss of energy usage must be taken into consideration [7]. However, PSA in which very low pressure is needed for regeneration requires mechanical energy that is more expensive than the heat supply in TSA [7]. Anyhow, based on the real application, PSA process is normally related to an attractive technology due to compactness of the equipment, low energy requirements, low capital costs and simple operation [97, 98].

PSA technology separates the different gasses from biogas based on their molecular characteristics and the affinity of the adsorbent material [99]. The main principle of PSA technology relies on the properties of pressurized gasses to be attracted to solid surfaces [99]. Therefore, under high pressure, large amounts of gas will be adsorbed, while, a decrease (a swing) of pressure will result in gas release [99]. The PSA process follows four

equal or different duration steps (Skarstrom Cycle): (i) pressurization, adsorption, blow-down and purge [98, 100]. In industrial practice, multiple adsorption columns are installed (usually four) to ensure the maintenance of a continuous operation of PSA with complex and improved cycles while two-column units rather give the operating principle for the utilization in the laboratory scale [99].

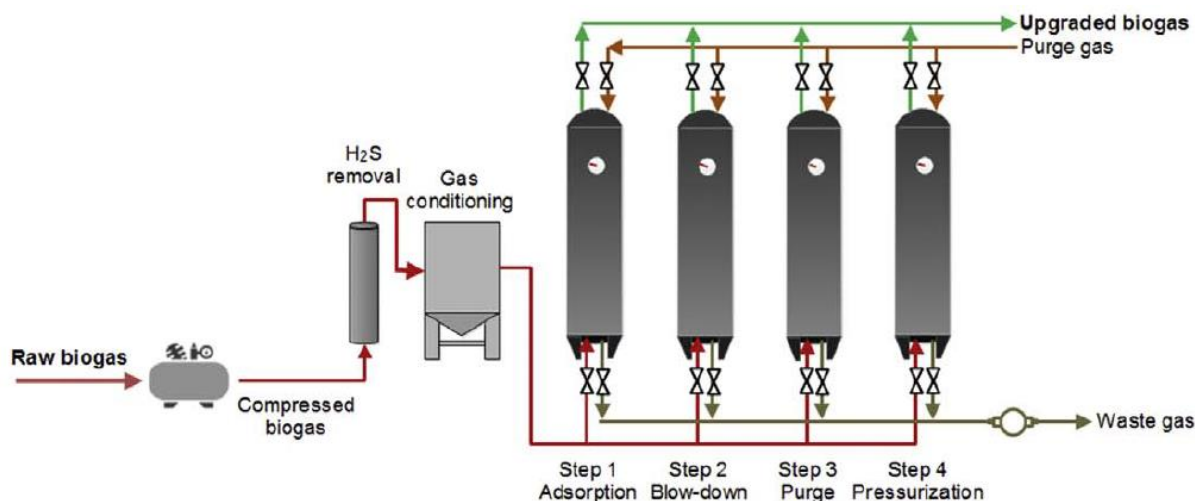


**Figure 2-5.** Pressure swing adsorption technology for biogas production [99].<sup>2</sup>

The following is described for the real PSA operation for biogas upgrading:

- **Pressurization:** The raw biogas is pressurized into an adsorption vessel (column) to 4–10 bar [100], in which the adsorbent material will selectively retain the targeted compounds e.g. CO<sub>2</sub>, while the methane is able to flow through it and can be collected from the top of the column by decreasing the pressure. The flow rate ranges from small scale at 10 m<sup>3</sup>·h<sup>-1</sup> to larger scale at 10,000 m<sup>3</sup>·h<sup>-1</sup> [101].
- **Adsorption/feed:** The raw biogas is fed into the tank and the targeted compounds start to become attracted to the solid adsorption surface as the methane flows through the column. When the adsorption bed is saturated, the feed is closed and the blowdown phase is initiated.
- **Blowdown:** Once the adsorption bed is saturated, and the upgraded methane was moved through, the feed is closed. The pressure inside the vessel is lowered considerable to desorb the CO<sub>2</sub> from the adsorbent and the CO<sub>2</sub>-rich gas is pumped out of the vessel.

<sup>2</sup> Reprinted from *Biotechnology Advances*, I. Angelidaki *et al.*, Biogas upgrading and utilization: Current status and perspectives, vol. 36, no. 2, pp. 452-466, Copyright 2018, with permission from Elsevier.

- **Purge:** At the lowest column pressure, the purge is initiated.

Table 2-5 compares the properties of Pressure Swing Adsorption with other pilot and commercial biogas upgrading technologies [99].

**Table 2-5.** Comparison of different pilot and commercial biogas upgrading technologies [102].

	<b>PSA</b>	<b>Cryogenic</b>	<b>Membrane separation</b>	<b>Physical scrubbing</b>	<b>Chemical absorption</b>
<b>Operation pressure (bar)</b>	3–10	80	5–8	4–8	Atm.
<b>Pressure at outlet (bar)</b>	4–5	8–10	4–6	1.3–7.5	4–5
<b>CH<sub>4</sub> recovery (%)</b>	96–98	97–98	96–98	96–98	96–99
<b>Consumption for raw biogas (kWh·N<sup>-1</sup>·m<sup>-3</sup>)</b>	0.23–0.30	0.76	0.18–0.20	0.2–0.3	0.05–0.15
<b>Consumption for clean biogas (kWh·N<sup>-1</sup>·m<sup>-3</sup>)</b>	None	-	0.14–0.26	0.4	0.05–0.25
<b>Heat consumption (kWh·N<sup>-1</sup>·m<sup>-3</sup>)</b>	None	-	None	<0.2	0.50–0.75
<b>Heat demand (°C)</b>	None	-196	None	55–80	100–180
<b>Cost</b>	Medium	High	High	Medium	High
<b>Pre-purification</b>	Yes	Yes	Recommended	Recommended	Yes
<b>H<sub>2</sub>S co-removal</b>	Possible	Yes	Possible	Possible	No
<b>N<sub>2</sub> and O<sub>2</sub> co-removal</b>	Possible	Yes	Partial	No	No

#### 2.4.3. MOFs for Pressure Swing Adsorption

As seen in Section 2.3.3, the adsorbents that are currently used in PSA for industrial CO<sub>2</sub> removal are zeolites, activated carbon, carbonaceous materials, alumina and silicates

[8]. A new class of porous solids, metal-organic frameworks (MOF) are categorized as an emerging adsorbent for PSA technology [55, 87]. In this regard, the performances of MOF materials in CO<sub>2</sub> capture technologies have not been fully evaluated for adsorption processes at large scale in real industrial conditions. Recently, several research groups have reported the encouraging performance of MOF in pilot scale PSA extrapolated for industrial scale [103-105].

Majchrzak-Kuceba *et al.* (2016) presented the potential of two kind of MOFs, Cu-BTC and MIL-53(Al), for flue gas CO<sub>2</sub> capture using Vacuum Pressure Swing Adsorption (VPSA) [105]. The CO<sub>2</sub> sorption process was conducted isothermally at a temperature of 30 °C under atmospheric pressure with a flow rate of 50 cm<sup>3</sup>·min<sup>-1</sup> to evaluate the maximum equilibrium capacity. The results showed that Cu-BTC and MIL-53(Al) had the sorption capacity of 160 mg·g<sup>-1</sup> and 53 mg·g<sup>-1</sup>, respectively, which confirmed the higher sorption capacity of MOF materials under working pressure conditions compared to zeolites and activated carbons [105]. The cyclic stability of the adsorbents was tested by performing multistage CO<sub>2</sub> adsorption/desorption cycles: (i) pure CO<sub>2</sub> was passed with a flow rate of 50 cm<sup>3</sup>·min<sup>-1</sup> for a period of 15 min at 30 °C, (ii) then, the CO<sub>2</sub> sorption capacity was determined based on the mass increment during this stage, and, (iii) after completion of CO<sub>2</sub> sorption, a regeneration process was carried out under a 10 kPa abs vacuum [105]. The sorption/desorption cycles were repeated five times in a continuous manner by which the duration of a single sorption/desorption cycle was 30 min [105]. The results revealed a complete desorption of CO<sub>2</sub> from both MOF samples, which confirmed the reversible nature of the process and the ability to use the materials in multiple cycles in VPSA unit [105].

Also by using VPSA unit, Grande *et al.* (2017) evaluated the utilization of other type of MOFs, UTSA-16, for pre-combustion CO<sub>2</sub> capture [104]. Quaternary breakthrough curves of a gas mixture of 76% H<sub>2</sub>, 17% CO<sub>2</sub>, 3% CH<sub>4</sub> and 4% CO assimilating to the off-gas of a typical steam-methane reformer were measured in a 4-column PSA unit, with the aim of selectively capture CO<sub>2</sub> while allowing H<sub>2</sub> and other components to pass through the column [104]. The experiments were carried out under a total pressure of 16 bar at a temperature of 33 °C while varying the flowrates to understand the effect of dispersion and diffusion [104]. As the results, CO<sub>2</sub> is strongly adsorbed on UTSA-16 much more than the other gases, and in addition, it was possible to desorb the CO<sub>2</sub> only by reducing its partial pressure without requiring thermal treatments [104]. Besides that, the adsorption capacity

of this material was also high when compared with zeolites which makes it advantageous for simultaneous production of H<sub>2</sub> and capture of CO<sub>2</sub> [104].

In another work, Ferreira *et al.* (2014) investigated the utilization of MIL-53(Al) for CO<sub>2</sub>/CH<sub>4</sub> separation using PSA by dynamic experiments in a fixed-bed reactor of two columns at pressures up to 3.5 bar and a temperature of 30 °C [103]. The material presented an adsorption capacity of 4.3 mol·kg<sup>-1</sup> at 3.5 bar for CO<sub>2</sub> [103]. The adsorption/desorption experiments in helium flow revealed high selectivity of MIL-53(Al) for CO<sub>2</sub>, with a separation factor of 4.1 at the same operation conditions, thus showing to be promising for a PSA process [103]. Two industrial-scale PSA processes were designed and optimized by simulations, a case similar to natural gas upgrade and biogas upgrade [103]. The results demonstrated that CH<sub>4</sub> recoveries were determined as 92.8% and 72.9%, respectively, and these obtained purity values allowed the distribution via pipelines of upgraded CH<sub>4</sub> [103]. Besides that, the productivities were estimated as 2.09 mol·kg<sup>-1</sup>·h<sup>-1</sup> and 2.78 mol·kg<sup>-1</sup>·h<sup>-1</sup>, respectively [103].

The feasibility of scale-up also includes the upgrade of MOF synthesis method to higher technological readiness to supply a large production. Interestingly, to fulfil the need, a new company founded in Switzerland in 2017 known as novoMOF has been established to focus on MOF synthesis and production for a wide scale of application. In parallel to this advancement, an efficient MOF synthesis for large production is slowly being conducted including the work of Oh *et al.* (2017) [106].

Figure 2-6 compares experimental results of different materials in adsorption technologies for biogas separation. It shows that, in terms of adsorption performances: working capacity and separation selectivity, different MOF families appear as competitive adsorbents to zeolites 13 (NaX) and activated carbon (AC35) which have been adopted for PSA in industrial scale.

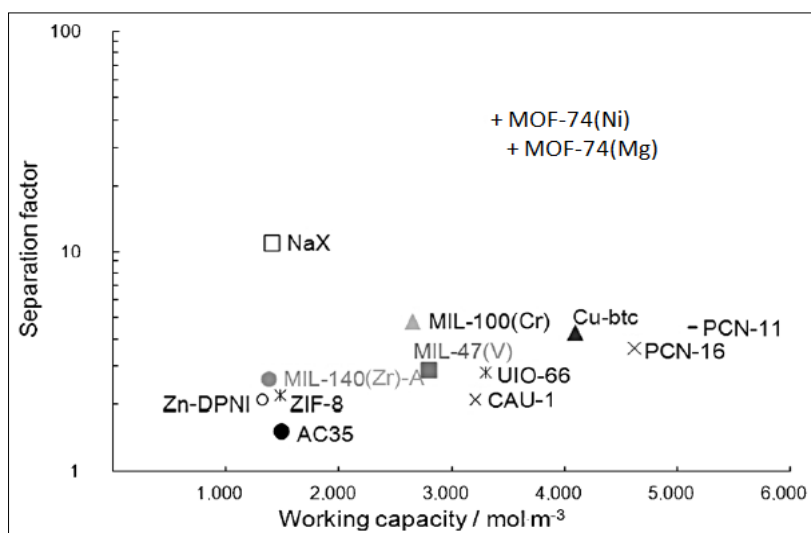


**Figure 2-6.** Separation factor vs. working capacity of different adsorbents for biogas separation of 50:50 mixtures of CO<sub>2</sub>/CH<sub>4</sub>. The adsorption was carried out at  $p_{\text{ads}}=10$  bar and  $p_{\text{des}}=1$  bar [107].<sup>3</sup>

## 2.5. Metal-organic frameworks (MOF) for CO<sub>2</sub> capture

### 2.5.1. Selection of MOFs over other adsorbents

MOFs have picked up the significant attention ever since they were introduced to the world of porous materials two decades ago. In 1989, Hoskins and Robson claimed that open frameworks were possible to be constructed in the presence of metal nodes such as tetrahedral Zn<sup>2+</sup> and spacers [108]. The first MOF family, MOF-5, known also as IRMOF-1, which is constructed from octahedral Zn-O-C cluster and benzene-based linker was introduced by Yaghi's group in 1999 for the application of methane storage [9]. Since then, the research area of these materials has grown tremendously leaving behind other porous solids due to their superior potential advantages.

MOFs are recognized for their ability to provide large microporous volumes and immense specific surface areas for numerous applications. MOF pore structures are able to act as catalytic sites allowing their application in nanocatalysis [109]. MOF magnetic properties and their different adsorption behavior towards various gases allow their application in gas sensing [12, 110]. MOF excellent biocompatibility and their ability to afford high amount of drug loading allow their application in drug delivery [111]. MOFs also can be employed for removal of hazardous substances [112] and key odorants [113],

<sup>3</sup> Reprinted from ChemSusChem, G. D. Pirngruber *et al.*, A method for screening the potential of MOFs as CO<sub>2</sub> adsorbents in pressure swing adsorption processes, vol. 5, no. 4, pp. 762-776, Copyright 2012, with permission from John Wiley and Sons.

development of electrode materials for electrochemical detectors and energy storage devices [114], and as luminescent materials in the application of lighting, organic pigments, drug tracer and many others [115].

Since MOFs may develop specific surface area as high as  $6240 \text{ m}^2 \cdot \text{g}^{-1}$  [11], one of their most promising applications is gas capture, storage and separation relying on adsorption [12]. Owing to their well-defined structure of micropore walls, MOFs are recognized for the possibility of fine and controlled tuning of gas adsorption properties by performing ligand design, metallic center substitution or functionality adjustment [13]. This allows to rich gas adsorption capacity and separation selectivity that cannot be achieved by other porous materials [14].

Other than their exceptional capacity, tunable structure and adjustable functionality, MOFs also exhibit permanent porosity and high thermal stability allowing their adaptation to different operation conditions for gas treatment [14, 112, 113, 116]. The application of MOFs in gas adsorption ranges many specific domains knowing that different MOFs have different affinity towards various gases. The common domains involve the capture and storage of  $\text{CO}_2$ , hydrogen, methane, carbon monoxide (CO) and nitrogen oxide (NO) [12].

In the application of  $\text{CO}_2$  capture, adsorbents can be classified as low-temperature or high-temperature adsorbents. Porous materials such as zeolites, molecular sieve, carbon molecular sieve and MOFs are categorized as low-temperature adsorbents which can function at temperature below  $400 \text{ }^\circ\text{C}$  [55]. Using thermogravimetric analysis Mg-MOF-74 was found stable up to  $400 \text{ }^\circ\text{C}$  [23]. Otherwise, the adsorbents that are able to remove  $\text{CO}_2$  at high temperature ( $400\text{-}600 \text{ }^\circ\text{C}$ ), for example for the treatment of hot flue gas, are calcium oxide, magnesium oxide, activated carbon, lithium compounds, silicates, dry carbonates and hydrotalcite [55].

### 2.5.2. MOF structure and families

MOFs are the assembly of metal-containing nodes coordinated to organic bridging ligands giving rise to characteristic three-dimensionally ordered crystalline structures [10]. The repeating crystalline structures make them easier to be characterized. Different metal nodes can be used for MOF synthesis including transition metals<sup>4</sup>, alkaline earth elements<sup>5</sup>,

---

<sup>4</sup> E.g. cobalt (Co), nickel (Ni), copper (Cu), zinc (Zn).

<sup>5</sup> E.g. strontium (Sr), barium (Ba).

p-block elements<sup>6</sup>, actinides<sup>7</sup> and mix metals [12]. Possible linkers (or spacers or ligands) that can be used to make bonding with the metal ion nodes are polycarboxylates, phosphonates, sulfonates, imidazoles, amines, pyridyl, phenolates [116]. The most common used linkers come from carboxylate-based family as listed in Table 2-6. Their chemical structures, some with Langmuir specific surface area they can offer, are presented in Figure 2-7 (for linear ligands) and Figure 2-8 (for trigonal and imidazolate ligands).

These nanostructural materials offer the liberty to design the frameworks by tuning the metal ions or the linkers adapting to the desired application [117]. The possible structural variation of these materials has led to more than 20000 different types of reported MOFs [25]. However, MOF synthesis does not only involves the selection of the connecting units for the desired modules, but also the prediction of their final coordination after complete formation [13]. For that reason, Baerlocher *et al.* (2001) has introduced a structural entity called Secondary Building Unit (SBU) in the analysis of zeolites framework [118]. The SBU idea has then been adopted by other researchers in order to describe MOF crystalline framework.

SBU (or paddlewheel) is a one-dimensional chain of organic-inorganic structure of metal nodes and ligands where the connection between SBUs will be formed with the help of the organic ligands to create an expanded three-dimensional framework. For a better picture, Figure 2-9 illustrates the formation of SBU and consequently the framework from the metal ions and the linkers. Table 2-7 summarizes the possible linkers to bind with the most common studied SBU, octahedral  $Zn_4O(CO_2)_6$  which is formed from tetrahedral  $ZnO_4$  cluster, specifying the produced MOF families. Also, Table 2-8 summarizes other types of SBUs with the possible organic ligands to create other types of MOF family.

**Table 2-6.** Different types of carboxylate ligands used in the synthesis of MOFs.

Acid form		Base form (anion)	
<b>H<sub>2</sub>BDC</b>	Benzene-1,4-dicarboxylic acid	<b>BDC</b>	1,4-benzenedicarboxylate
<b>H<sub>2</sub>BPDC</b>	4,4-biphenyldicarboxylic acid	<b>BPDC</b>	4,4-biphenyldicarboxylate
<b>H<sub>2</sub>NDC</b>	1,4-naphthalenedicarboxylic acid	<b>NDC</b>	1,4-naphthalenedicarboxylate

<sup>6</sup> E.g. indium (In), gallium (Ga).

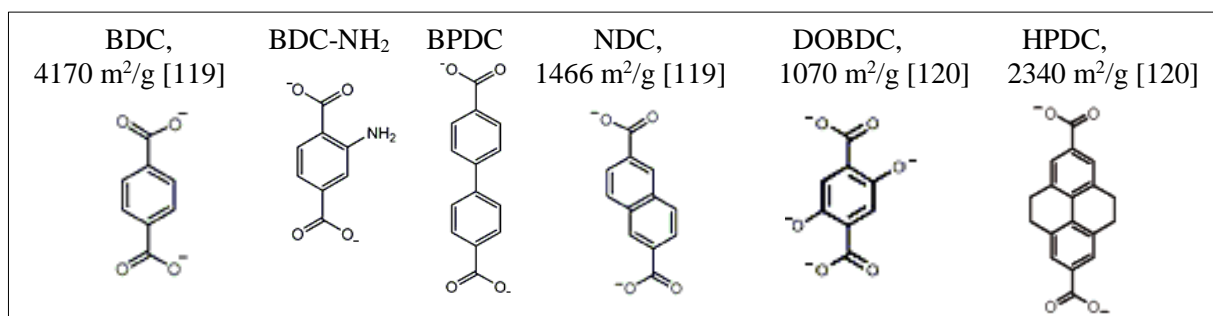
<sup>7</sup> E.g. uranium (U), thorium (Th).

<b>H<sub>2</sub>DHBDC/</b> <b>H<sub>4</sub>DOBDC</b> <sup>8</sup>	2,5-dihydroxy-1,4-benzene- dicarboxylic acid	<b>DHBDC/</b> <b>DOBDC</b> <sup>9</sup>	2,5-dioxido-1,4-benzene- dicarboxylate
<b>H<sub>2</sub>PDC</b> <sup>10</sup>	Pyridine-2,6-dicarboxylic acid	<b>HPDC</b>	Pyridine-2,6-dicarboxylate
<b>H<sub>3</sub>BTB</b>	1,3,5-tri(4carboxyphenyl)benzene	<b>BTB</b>	1,3,5-benzenetriyltribenzoate
<b>H<sub>3</sub>BTC</b>	Benzene-1,3,5-tricarboxylic acid	<b>BTC</b>	1,3,5-benzenetricarboxylate
<b>H<sub>3</sub>BTE</b>	1,3,5-triscarboxyphenylethynyl benzene	<b>BTE</b>	1,3,5-triscarboxyphenylethynyl benzoate
<b>H<sub>3</sub>BBC</b>	1,3,5-tris(4'-carboxy[1,1'- biphenyl]-4-yl)benzene	<b>BBC</b>	1,3,5-tris(4'-carboxy[1,1'- biphenyl]-4-yl)benzoate

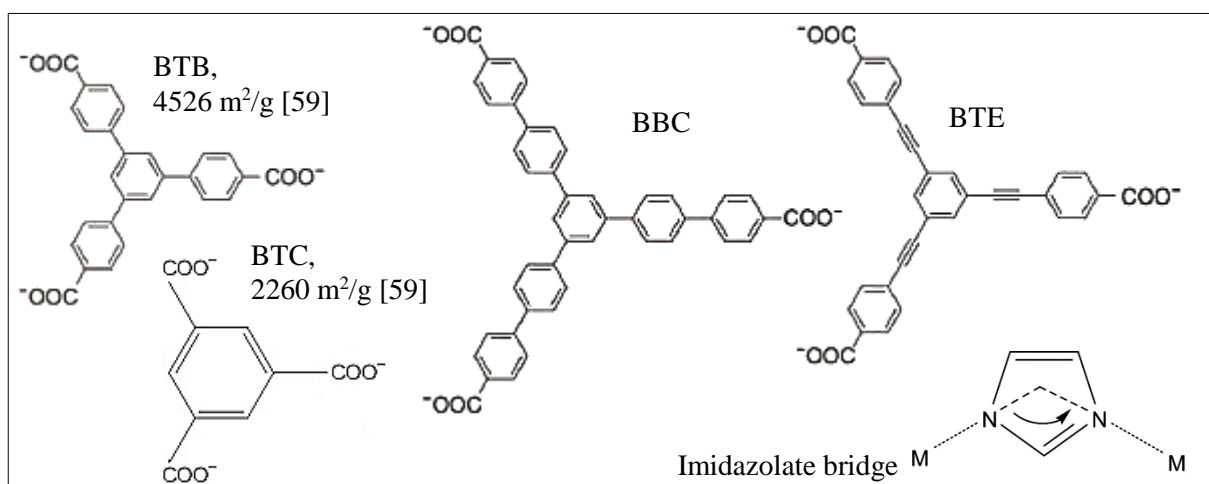
<sup>8</sup> H<sub>2</sub>DHBDC or H<sub>4</sub>DOBDC is also known as 2,5-dihydroxyterephthalic (DHTP) acid.

<sup>9</sup> DHBDC or DOBDC is also known as 2,5-dioxydoterephthalate (DOT) ligand.

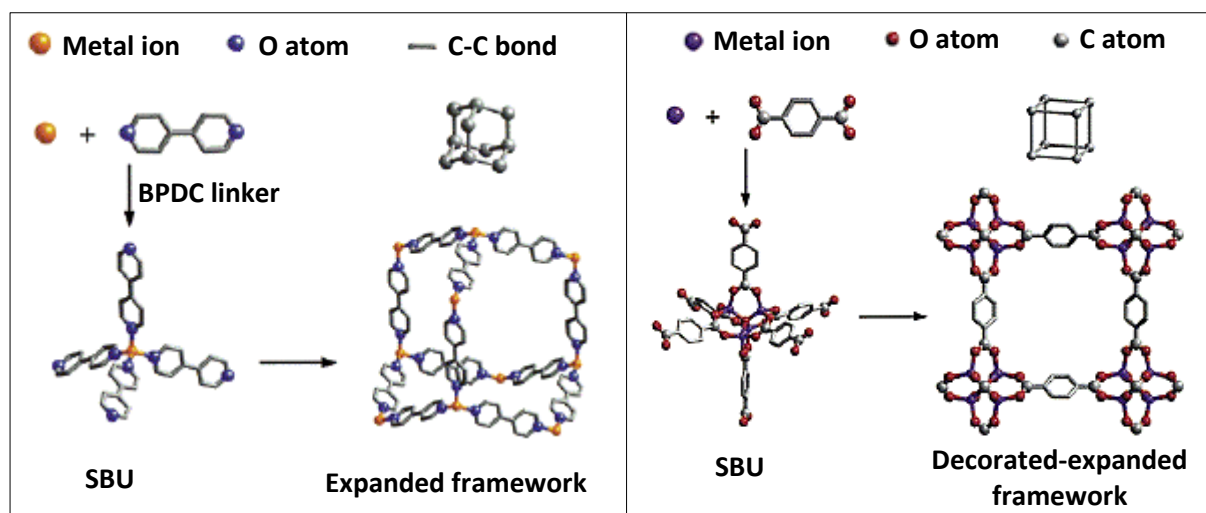
<sup>10</sup> H<sub>2</sub>PDC can be partially or completely deprotonated to form HPDC<sup>-</sup> or PDC<sup>2-</sup> anions to bridge metal ions.



**Figure 2-7.** Chemical structure of linear carboxylate ligands used in MOF synthesis.



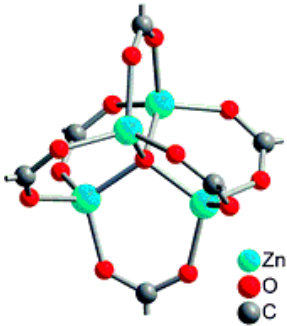
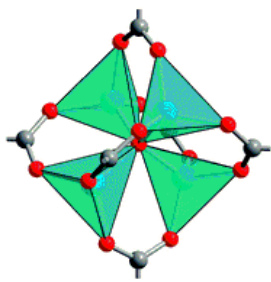
**Figure 2-8.** Chemical structure of trigonal and imidazolate carboxylate ligands used in MOF synthesis.



**Figure 2-9.** The formation of SBU and consequently the framework by copolymerization of metal ions with organic linkers [14, 121].<sup>11</sup>

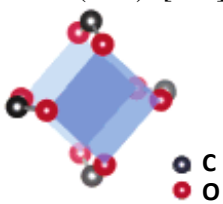
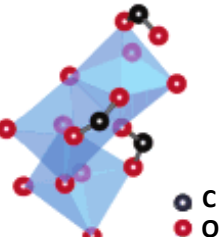
<sup>11</sup> Reprinted from Chemical Engineering Science, T. G. Glover *et al.*, MOF-74 building unit has a direct impact on toxic gas adsorption, vol. 66, no. 2, pp. 163-170, Copyright 2011, with permission from Elsevier.

**Table 2-7.** Different MOF families produced from octahedral  $Zn_4O(CO_2)_6$  SBU.

SBU / Paddlewheel	Organic ligand	Type of produced MOFs	MOF chemical formula
Octahedral $Zn_4O(CO_2)_6$ [122]  	Triangular BTB	MOF-177	$Zn_4O(BTB)_3$
	Triangular BTE	MOF-180	$Zn_4O(BTE)_2$
	Triangular BBC	MOF-200	$Zn_4O(BBC)_2(H_2O)_3$
	Triangular BTB + Linear NDC	MOF-205	$Zn_4O(BTB)_{4/3}(NDC)$
	Triangular BTE + Linear BPDC	MOF-210 <sup>12</sup>	$Zn_4O(BTE)_{4/3}(BPDC)$
	Linear BDC	MOF-2	$Zn_4O(BDC)_2$
		MOF-5 <sup>13</sup> (IRMOF-1)	$Zn_4O(BDC)_3$
	Linear BDC-NH <sub>2</sub>	IRMOF-3	$Zn_4O(NH_2BDC)_3$
	Linear BDC-C <sub>2</sub> H <sub>4</sub>	IRMOF-6	$Zn_4O(C_2H_4BDC)_3$
Linear HPDC	IRMOF-11	$Zn_4O(HPDC)_3$	

<sup>12</sup> MOF-210 exhibits highest specific surface area known to date.<sup>13</sup> Since reported in 1999, MOF-5 (or IRMOF-1) became the most intensively studied MOFs due to its stable framework and high porosity.

**Table 2-8.** Other MOF families produced from divers SBUs and linkers.

SBU / Paddlewheel	Organic ligand	Type of produced MOFs	MOF chemical formula
Tetrahedral $\text{Cr}_3\text{OF}(\text{CO}_2)_6$ or Tetrahedral $\text{Al}_3\text{OF}(\text{CO}_2)_6$	Linear BDC	MIL-101(Cr) or MIL-101(Al)	$\text{Cr}_3\text{F}(\text{H}_2\text{O})_2\text{O}(\text{BDC})_3$ or $\text{Al}_3\text{F}(\text{H}_2\text{O})_2\text{O}(\text{BDC})_3$
Tetrahedral $\text{ZnN}_4$ or Tetrahedral $\text{CoN}_4$	Imidazolate bridge	ZIF <sup>14</sup>	$\text{ZnIm}_2$ or $\text{CoIm}_2$
Cubic $\text{Cu}_2(\text{CO}_2)_4$ [120] 	Linear BPTC <sup>15</sup>	MOF-505	$\text{Cu}_2(\text{BPTC})$
	Triangular BTC	HKUST-1	$\text{Cu}_3(\text{BTC})_2$
Tetrahedral $\text{Ti}(\text{OiPr})_4$ <sup>16</sup>	Linear BDC + Linear BDC-NH <sub>2</sub>	MIL-125(Ti)	$\text{Ti}_8\text{O}_8(\text{OH})_4$ ( $\text{C}_6\text{H}_3\text{C}_2\text{O}_4\text{NH}_2$ ) <sub>6</sub>
$[\text{M}_3\text{O}_3(\text{CO}_2)_3]_\infty$ helices [120] 	Linear DOBDC	MOF-74(M)	$\text{M}_2(\text{DOBDC})$ M = Mg, Zn, Co, Ni, Fe, Cu or Mn (see Figure 2-10)

### 2.5.3. Selection of MOF-74 for CO<sub>2</sub>/CH<sub>4</sub> separation

MOF-74 family is the assembled hexagonal crystalline framework built from the copolymerization of one-dimensional helical channels of  $\text{M}_2\text{O}_2(\text{CO}_2)_2$  SBU with linear DOBDC linker as illustrated in Figure 2-10. This MOF family is also known as CPO-27-M<sup>17</sup>,  $\text{M}_2(\text{DOBDC})$ <sup>18</sup>, M/DOBDC,  $\text{M}_2(\text{DOT})$ <sup>4</sup> and  $\text{M}_2(\text{DHTP})$ <sup>19</sup> representing isostructural series that may contain one-type or mixed-type of metal cations  $\text{M}^{2+}$  such as  $\text{Ni}^{2+}$ ,  $\text{Zn}^{2+}$ ,  $\text{Mg}^{2+}$ ,  $\text{Mn}^{2+}$ ,  $\text{Co}^{2+}$ ,  $\text{Fe}^{2+}$ ,  $\text{Mn}^{2+}$  and  $\text{Cu}^{2+}$ .

<sup>14</sup> ZIF is a plain framework and it is not the final product of its kind.

<sup>15</sup> BPTC is a deprotonated form of 3,3',5,5'-biphenyltetracarboxylic acid ( $\text{H}_4\text{BPTC}$ ).

<sup>16</sup>  $\text{Ti}(\text{OiPr})$ : Titanium isopropoxide.

<sup>17</sup> CPO: Coordination Polymer of Oslo.

<sup>18</sup> DOBDC: 2,5-dioxido-1,4-benzene-dicarboxylate = DOT: 2,5-dioxidoterephthalate.

<sup>19</sup> DHTP: 2,5-dihydroxyterephthalic acid.

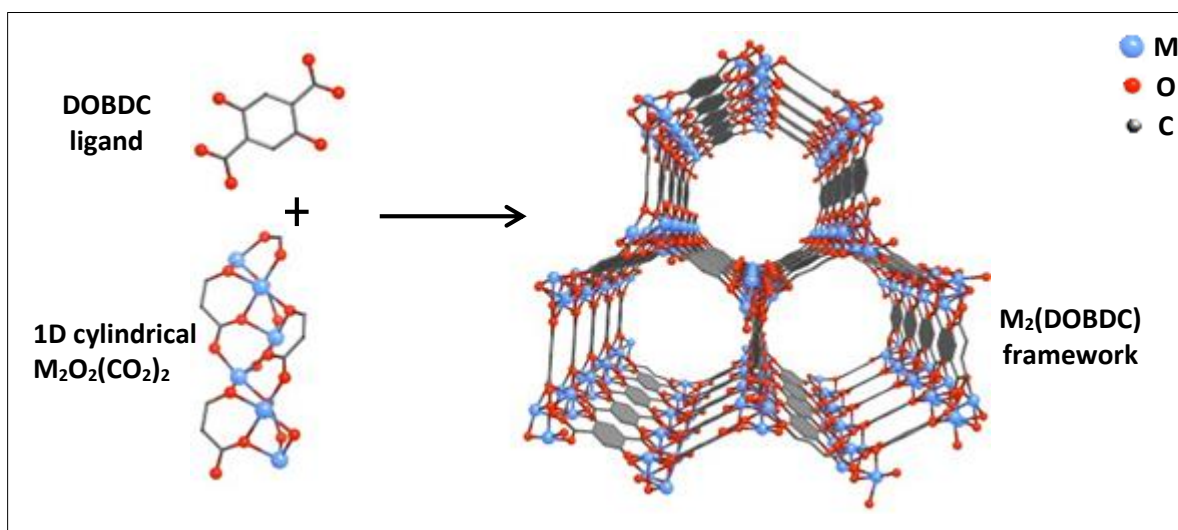


**Figure 2-10.** The formation of hexagonal array of M-MOF-74 formed from one-dimensional channels of  $M_2O_2(CO_2)_2$  SBU and DOBDC linker [121].<sup>20</sup>

MOF-74 family was firstly introduced by Yaghi's group in 2005 representing a Zn-based framework called CPO-27-Zn, later called Zn/DOBDC [15]. After that, Caskey *et al.* (2008) were the first who studied on the dramatic tuning of the metal cations on the performance of  $CO_2$  and  $CH_4$  adsorptions [18]. The comparative observation by performing metal nodes diversity in MOF-74 revealed that Mg-based MOF-74 exhibited the highest dynamic capacity of  $CO_2$  uptake as seen in Figure 2-11 (left), aside from the best selectivity over  $CH_4$  [18]. The result was attributed to the ability of Mg-MOF-74 to afford highest number of  $CO_2$  molecules per unit cell: Mg (12) > Ni (7), Co (7) > Zn (4) [18]. The difference in  $CO_2$  adsorption uptake of these four M-MOF-74 series was reported elsewhere [18, 37, 123], resulting from the different specific surface areas ranging from  $599 \text{ m}^2 \cdot \text{g}^{-1}$  to  $1525 \text{ m}^2 \cdot \text{g}^{-1}$  due to the different metal atomic weight. In parallel to the study, MOF-74 family was also leading in  $CO_2$  adsorption uptake performance in comparison to other typical MOF families such as IRMOF-1, HKUST-1, ZIF-8, MIL-47, etc. as seen in Figure 2-11 (right). Since then, MOF-74 family and especially Mg-MOF-74 figure as among the most promising adsorbents for  $CO_2$  separation from  $CH_4/CO_2$  and  $CH_4/CO_2/N_2$  gas streams in the context natural gas and biogas purification [15-17].

<sup>20</sup> Reprinted from Chemical Engineering Science, T. G. Glover *et al.*, MOF-74 building unit has a direct impact on toxic gas adsorption, vol. 66, no. 2, pp. 163-170, Copyright 2011, with permission from Elsevier.

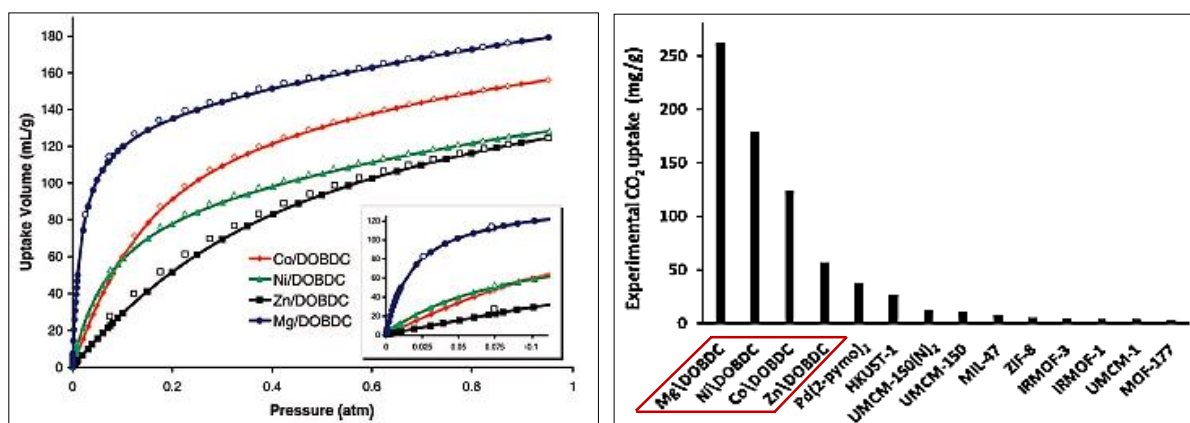


**Figure 2-11.** (left) CO<sub>2</sub> sorption isotherm at 296 K and 1 atm (main figure) and 0.1 atm (sub-figure) by comparing M/DOBDC series (filled markers: adsorption points; open markers: desorption points) [18].<sup>21</sup> (right) CO<sub>2</sub> uptake of various MOF families at 0.1 bar at 293-298 K [123].<sup>22</sup>

Other than high CO<sub>2</sub> uptake capacity, Mg-MOF-74 is well-known for the ability to perform an excellent thermodynamic selectivity for an effective separation of CO<sub>2</sub> and CH<sub>4</sub> [18, 23]. Characterized by BET specific surface area close to 1200 m<sup>2</sup>·g<sup>-1</sup> [19] and one-dimensional pores of approximately 10 Å [20], this material features exceptional density and accessibility of open metal sites which are the preferential adsorptive centers for gas molecules [21, 22]. The ratio of Henry's constants,  $K$ , of CO<sub>2</sub> and CH<sub>4</sub> adsorptions on Mg-MOF-74 ( $K$  is expressed as a proportionality factor of adsorbed amount per unit mass of adsorbent to adsorbate gas pressure at equilibrium in mol·g<sup>-1</sup>·bar<sup>-1</sup>) is reported as high as 330 in a pressure range of Henry's law region at 25 °C, allowing one of the best CO<sub>2</sub>/CH<sub>4</sub> separation efficiency by MOF materials [23]. This excellent selectivity towards CO<sub>2</sub> originates from a strong intermolecular interaction of this gas with the exposed metallic centers leading to the stabilization of their coordination sphere and thus high ordering of adsorbed CO<sub>2</sub> molecules within unit cell as revealed by in-situ characterization techniques [16, 20, 24]. The same reason explains the maximum number of CO<sub>2</sub> molecules that Mg-MOF-74 can afford in comparison to other metal nodes in MOF-74 series, as mentioned above [18]. Figure 2-12 shows the occupation of CO<sub>2</sub> molecules in Mg-MOF-74 unit cell

<sup>21</sup> Reprinted from Journal of the American Chemical Society, S. R. Caskey *et al.*, Dramatic tuning of carbon dioxide uptake via metal substitution in a coordination polymer with cylindrical pores, vol. 130, no. 33, pp. 10870-10871, Copyright 2008, with permission from American Chemical Society.

<sup>22</sup> Reprinted from Journal of the American Chemical Society, O. Yazaydin *et al.*, Screening of metal-organic frameworks for carbon dioxide capture from flue gas using a combined experimental and modelling approach, vol. 131, no. 51, pp. 18198-18199, Copyright 2009, with permission from American Chemical Society.

and different interactions of CO<sub>2</sub>, N<sub>2</sub> and CO molecules with open Mg<sup>2+</sup> sites in the material.

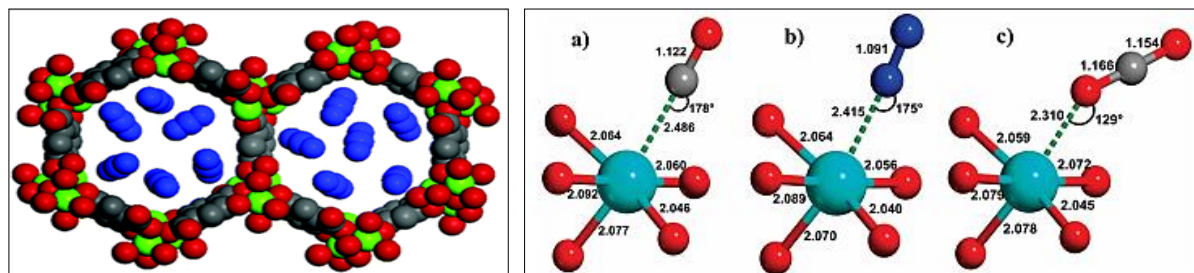


**Figure 2-12.** (left) One unit cell of Mg-MOF-74 occupied by 12 molecules of CO<sub>2</sub>; Mg (green), O (red), C (grey) and CO<sub>2</sub> (blue) [18].<sup>23</sup> (right) The geometry of adsorption of (a) CO, (b) N<sub>2</sub> and (c) CO<sub>2</sub> in Mg-MOF-74; Mg (cyan), O (red), C (grey) and N (blue); distances in Å [16].<sup>24</sup>

Moreover, Britt *et al.* (2009) was the first who investigated the dynamic separation of an equal gas mixture of CO<sub>2</sub> and CH<sub>4</sub> in Mg-MOF-74 under breakthrough experiment [23]. It was observed that there was no concentration of CO<sub>2</sub> effluent in the CH<sub>4</sub> flow at the exit of the sample cell before the CO<sub>2</sub> saturation in the material, indicating as well the excellent dynamic selectivity Mg-MOF-74 can perform [23]. Although there were several MOF families that exceed the specific surface area of Mg-MOF-74 and demonstrated higher CO<sub>2</sub> uptake as shown in Table 2-9, Liu *et al.* (2012) stated in their review paper “Recent Advances in Carbon Dioxide Capture with Metal-Organic Frameworks”, that Mg-MOF-74 was among the best candidate for CO<sub>2</sub> separation owing to its excellent balance between high CO<sub>2</sub> uptake capacity and high CO<sub>2</sub>/CH<sub>4</sub> selectivity [28]. It thus makes a significant difference between Mg-MOF-74 and other typical ultra-highly porous MOF families. In other way around, there was another type of developed MOFs called Cu-BTTri-mmen<sup>25</sup> having among the highest selectivity factor of CO<sub>2</sub>/CH<sub>4</sub> which is 327, but the material could only adsorb 5.5 wt% of CO<sub>2</sub> at 1 bar [124], much lower than 35.2 wt% achieved by Mg-MOF-74, due to their low specific surface area [23]. Therefore, the selection of Mg-MOF-74 for the present study is strongly based on these reasons knowing

<sup>23</sup> Reprinted from Journal of the American Chemical Society, S. R. Caskey *et al.*, Dramatic tuning of carbon dioxide uptake via metal substitution in a coordination polymer with cylindrical pores, vol. 130, no. 33, pp. 10870-10871, Copyright 2008, with permission from American Chemical Society.

<sup>24</sup> Reprinted from The Journal of Physical Chemistry C, L. Valenzano *et al.*, Computational and experimental studies on the adsorption of CO, N<sub>2</sub>, and CO<sub>2</sub> on Mg-MOF-74, vol. 114, no. 25, pp. 11185-11191, Copyright 2010, with permission from American Chemical Society.

<sup>25</sup> Cu-BTTri-mmen is formed by incorporation of N,N'-dimethylethylenediamine (mmen) and Cu-BTTri MOFs. BTTri = 1,3,5-tri(1,2,3-triazol-4-yl)benzene.

that it is impossible to produce an adsorbent having both high capacity and selectivity to the fullest.

**Table 2-9.** MOFs with the highest CO<sub>2</sub> uptake capacity reported to date.

Type of MOF families	BET surface area (m <sup>2</sup> ·g <sup>-1</sup> )	CO <sub>2</sub> uptake capacity (wt%)	Pressure (bar)	Temperature (K)	Ref.
MOF-210	6,240	70.6	50	298	[11]
MOF-200	4,530	70.9	50	298	[11]
Mg-MOF-74	1,542	62.9	33	298	[54]
MOF-177	4,508	60.0	35	298	[11]
MOF-205	4,460	59.9	50	298	[11]

Besides that, Mg-MOF-74 was also reported having an excellent balance between high capacity and facile regeneration [18, 23]. Although Mg-MOF-74 family exhibited one of the highest CO<sub>2</sub> uptake capacities among adsorbents in presence [18, 123], the adsorption energy of CO<sub>2</sub> molecules on Mg sites in MOF-74 was reported as a strong physisorption based on the isosteric heat value of 39 kJ·mol<sup>-1</sup> which remained below the energy of a chemical bond [18]. Therefore, the regeneration of Mg-MOF-74 required only minimum energy to release the adsorbed CO<sub>2</sub> despite of its outstanding CO<sub>2</sub> capacity [23]. In comparison to the conventional amine-based scrubbing, the adsorption energy in Mg-MOF-74 was much lower than the heat of interaction in amine solution (30% MEA<sup>26</sup>) which was of 84 kJ·mol<sup>-1</sup>, indicating far milder regeneration conditions for Mg-MOF-74 [23]. The regeneration temperature to desorb CO<sub>2</sub> from Mg-MOF-74 was suggested at only mild temperature which was 80 °C [23]. By comparing the recovery ability of Mg-MOF-74 with the most performed zeolites for CO<sub>2</sub> adsorption, Mg-MOF-74 could regain 87% (7.8 wt%) of its original adsorption capacity After regeneration while zeolites NaX could only regain 71% (6.4 wt%) [23]. More rigorous study on cycling adsorption performance of MOF-74 stated that there was no diminution in the original adsorption capacity after eight consecutive adsorption-desorption cycles [50]. This proves that MOF-74 is a robust compound with permanent porosity.

In addition, MOF-74 was also reported having a better stability in humidity relatively to other typical MOF families [23, 53, 124, 125]. A dynamic simulation study

<sup>26</sup> MEA: Monoethanolamine.

showed that Mg-MOF-74 has superior water-resistance in comparison to the most studied MOFs such as MOF-5<sup>27</sup> and IRMOF-10<sup>8</sup> [125]. However, there are few papers that discussed on the degradation of Mg-MOF-74 capacity with regard to water dissociation reaction [28, 126-128]. By investigating the water reaction mechanism in MOF-74 series and its effect on H<sub>2</sub> adsorption, Tan *et al.* (2014) discovered that the adsorption capacity was adversely affected by water for two reasons as follows [126]. Firstly, after dissociating at the metal center in MOFs, the water molecules liberated OH<sup>-</sup> species that remains bonded with the metal sites and thus led to the passivation of the adsorptive sites. Secondly, based on the binding energy values, the bonding of H atom of H<sub>2</sub> with O atom of the framework became weaker after the water dissociation. Nevertheless, it was found that water dissociation in MOF-74 took place only at temperatures between 150 °C and 200 °C, therefore the implementation of MOF-74 must be kept at condition below the temperature range [126].

Meanwhile, Kizzie *et al.* (2014) compared the effect of humidity on the adsorption performance of MOF-74 series with different metal nodes [129]. Based on the result, Mg-MOF-74 and Zn-MOF-74 showed a significant decrease in CO<sub>2</sub> uptake after being exposed to 70% relative humidity, where they respectively lost 78% and 84% of the initial adsorption capacity [129]. However, under the same humidity exposure, Ni-MOF-74 and Co-MOF-74 respectively lost only 15% and 39% of their initial CO<sub>2</sub> adsorption capacity [129]. This showed that different metal nodes in MOF-74 had different stability towards hydrolysis reflected by the different degree of recovered adsorption capacity after humidification. Although the passivation of metal adsorptive sites in MOF-74 during the exposition to water vapor deteriorated the CO<sub>2</sub> uptake, some structural modification has been proposed to improve the energy barrier to water dissociation and thus controlling their stability under humid conditions [127, 128]. For example, Jiao *et al.* (2015) proved that little substitution of Ni or Co into Mg-MOF-74 structure at 16% remarkably enhanced the water stability of the material because both Ni and Co were less vulnerable to hydrolysis [127]. Besides that, Zuluaga *et al.* (2016) found that the modification of Zn-MOF-74 by S-ligands<sup>28</sup> functionalization improved the water stability of the material since the ligands could lead to the suppression of water dissociation [128].

---

<sup>27</sup> MOF-5 (also known as IRMOF-1) and IRMOF-10 are in the same isorecticular MOFs series of IRMOF-n with n=1– 18. IRMOF-n is a cubic-structured framework having a surface area from 700 to 1000 m<sup>2</sup>·g<sup>-1</sup>.

<sup>28</sup> H<sub>4</sub>DSBDC: 2,5- disulfhydrylbenzene-1,4-dicarboxylic acid.

Several advanced studies on MOF-74 modification to improve CO<sub>2</sub> adsorption performances have been conducted to date [37, 52, 130]. In CO<sub>2</sub> and N<sub>2</sub> separation study, Ni-MOF-74 was coated with cordierite monolith via bottom-up film growth technique in which the MOF crystals underwent nucleation and growth on the monolithic walls [52]. As the result, the monolith-coated Ni-MOF-74 exhibited higher affinity towards CO<sub>2</sub> relatively to N<sub>2</sub> with faster kinetics but lower CO<sub>2</sub> capacity in comparison to Ni-MOF-74 powders [52]. In another study, Ni-MOF-74 and Co-MOF-74 were doped with palladium (Pd)-containing activated carbon to enhance the separation efficiencies of CO<sub>2</sub> and N<sub>2</sub> knowing that Pd was the low-electronegative atom [37]. The breakthrough curves showed a complete separation of CO<sub>2</sub> from N<sub>2</sub> stream resulting from the interaction between partially negative-charged O atom of polarized CO<sub>2</sub> and partially positive-charged Pd metal [37]. This finding was comforted in an earlier study stating that the polarization effects were important in describing CO<sub>2</sub> adsorption in Mg-MOF-74 [131].

Furthermore, another study investigated the adsorption behavior of CO<sub>2</sub> and H<sub>2</sub>O in Mg-MOF-74 functionalized by TEPA<sup>29</sup> via post-synthetic modification [130]. The result demonstrated that the increased CO<sub>2</sub> adsorption uptake was attributed to the additional amine sites improving Lewis acid-base interaction with CO<sub>2</sub> molecules [130]. It was also proven that post-synthetic functionalization preserved Mg-MOF-74 crystalline structure and did not block the original pores despite being substituted with amino adsorption sites [130]. In another modified MOF-74 study, hybrid metal nanocrystal-MOF was synthesized by encapsulating copper nanocrystal in Cu-MOF-74 to produce Cu@Cu-MOF-74 [132]. Although their performance in CO<sub>2</sub> adsorption has not been tested yet, the BET specific surface areas of Cu@Cu-MOF-74 was reported 985 m<sup>2</sup>·g<sup>-1</sup>, higher than that of pristine Cu-MOF-74 which was only 394 m<sup>2</sup>·g<sup>-1</sup> [132]. Another interesting innovation about MOF-74 is the development of hybrid system that combines MOF-74 with membrane technology in which the mass transfer mechanism is not only based on adsorption but also permeation [133, 134]. In different studies, Ni-MOF-74 membrane and amine-modified Mg-MOF-74 were invented for CO<sub>2</sub> separation from various gases to enhance their selectivity ratio [133, 134].

Table 2-10 and Table 2-11 summarize the published works on the development of MOF-74 and modified MOF-74 reported to date, specifically for CO<sub>2</sub> adsorption studies.

---

<sup>29</sup> TEPA: Tetraethylenepentamine.

**Table 2-10.** Published works on MOF-74 reported to date for CO<sub>2</sub> adsorption (2008–present).

Ref.	Type of MOF-74	Hybrid agents	Adsorption (PSA, DVS <sup>30</sup> , etc...)	
			Task	Operation conditions
2008 Caskey [18]	M-MOF-74 (M=Mg,Ni,Co,Zn)	-	CO <sub>2</sub>	0.1 and 1 bar 23 °C
2009 Britt [23]	Mg-MOF-74	-	CO <sub>2</sub> /CH <sub>4</sub>	1 bar 25 °C
2009 Dietzel [54]	Mg-MOF-74 Ni-MOF-74	-	CO <sub>2</sub> CO <sub>2</sub> /CH <sub>4</sub>	33 – 39.8 bar 5 – 200 °C
2010 Bao [19]	Mg-MOF-74	-	CO <sub>2</sub> /CH <sub>4</sub>	1 bar 5, 25 and 45 °C
2011 Cho [50]	Co-MOF-74	-	CO <sub>2</sub>	1 bar 25 °C
2014 Lou [51]	Fe(II)-MOF-74	-	CO <sub>2</sub>	10 bar 25 °C
2014 Chen [17]	Ni-MOF-74	-	CO <sub>2</sub> /CH <sub>4</sub>	10 bar 25, 50 and 75 °C
2016 Rezaei [52]	Monoliths-coated Ni-MOF-74	Cordierite monolith	CO <sub>2</sub>	1 bar 25 °C
2016 Adhikari [37]	AC(Pd)-doped Ni-MOF-74 AC(Pd)-doped Co-MOF-74	Palladium Activated carbon	CO <sub>2</sub> /N <sub>2</sub>	31 bar 25 °C
2017 Su [53]	Amino-Mg-MOF-74	TEPA	CO <sub>2</sub> /H <sub>2</sub> O	1 bar 25 °C

**Table 2-11.** Published works on MOF-74-membrane hybrid system reported to date for CO<sub>2</sub> separation (2008–present).

Ref.	Type of MOF-74	Hybrid system	Adsorption + permeation
2012 Lee [133]	Ni-MOF-74 membrane	Membrane	H <sub>2</sub> , N <sub>2</sub> , CH <sub>4</sub> and CO <sub>2</sub>
2014 Wang [134]	Amine-modified Mg-MOF-74 membrane	Membrane Amine groups	H <sub>2</sub> /CO <sub>2</sub>

<sup>30</sup> DVS: Dynamic Vapour Sorption vacuum.

#### 2.5.4. Performance of MOF–carbon composites for gas separation

The possible structural variation of MOF-based materials or composites in terms of constitutive functionalities, particle size, geometry and topology has led to more than 20000 different types of reported MOFs [25]. The presence of open metal nodes in MOFs is very advantageous to allow the embedding of other molecules into the crystalline structure [135]. The functionality of the organic linker offers the possibility of grafting during or after synthesis [111]. This molecular alteration can create additional adsorptive sites for guest molecules and is possible to be conducted without perturbing the crystal [31, 53]. Recent advancement in MOF studies shows that MOFs are also being used as the template in fabricating new MOF-derived materials [109]. Various types of doping agents such as metal nanocrystal [109, 132], carbon-based compounds [31, 37, 38], palladium [136, 137], salt ions [138], indium [139] and silica [140] have been incorporated into MOF structure to improve MOF properties for different purposes.

Recently, researches on incorporation of MOFs with carbon-based compounds to produce MOF–carbon composites are continuously being conducted. This refers to a further improvement of gas adsorption performances of MOF materials by optimizing the texture and morphology of the solid to create an additional microporosity and interstitial porosity [26-28]. This facilitates the gas transport to the adsorption sites and increases total accessible pore volumes and specific surface areas. Owing to the formation of secondary micro and mesoporosity within the composites nanostructure, the carbon-doped MOF composites have been reported able to increase gas adsorption capacity and separation efficiency in comparison to their parent material [29-42]. As seen in Figure 2-13, carbon nanotubes (CNT) and graphene oxide (GO) are considered as the most common carbon-based doping agents used in the synthesis of MOF–carbon composites for various applications [27]. CNTs which are an allotropic form of carbon related to fullerene family can be divided into single-walled and multiwalled CNTs according to their structure [43]. CNT walls are inert with chemical reaction but organic ligands or functional organic agents can easily attach or cover on CNT walls in CNT-hybrid composites [44]. This is advantageous for MOF materials. Meanwhile, GO contains high density of atoms and oxygen functionalities in the arrangement of layered-structure [45]. These functionalities from type hydroxyl, carboxyl, epoxy and ketone groups are able to coordinate with the metallic centers of MOFs, leading to the growth of MOF crystals onto graphene layers [46,

47]. This formation can be described as an alternate structure of MOF units and GO layers [48].

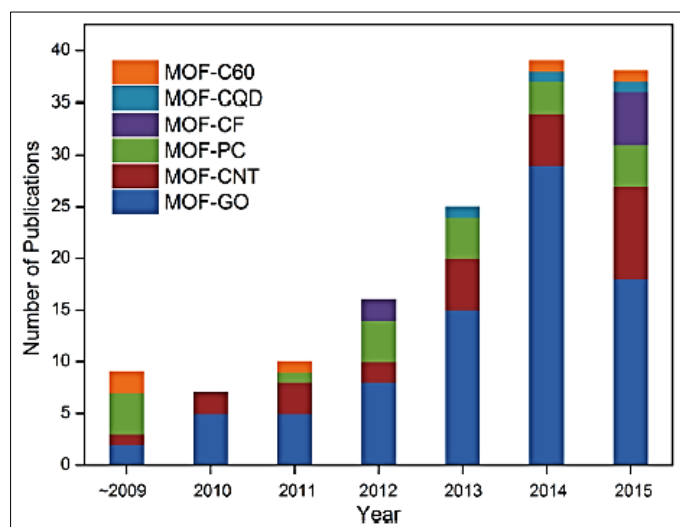


**Figure 2-13.** Statistic of publication number on MOF-carbon composites according to carbonaceous doping agent from 2009 to 2015 [27].<sup>31</sup>

Yang *et al.* (2009) were the first who synthesized a hybrid composite of multiwalled CNT-incorporated MOF-5 denoted as CNT@MOF-5 for the application of H<sub>2</sub> storage [35]. The CNT was well-dispersed in DMF<sup>32</sup> before being mixed with another DMF solution containing zinc nitrates [35]. Although both MOF-5 and its composite CNT@MOF-5 had the same crystal structure and morphology, the result showed that the composite exhibited higher specific surface area from 2160 m<sup>2</sup>·g<sup>-1</sup> to 3550 m<sup>2</sup>·g<sup>-1</sup> and higher H<sub>2</sub> storage capacity from 1.2 wt% to 1.52 wt% at 77 K and 1 bar [35]. The increased surface area was attributed to the formation of new nanopores by the presence of doped carbonaceous compound [35]. Besides that, it was also found that MOF/CNT cooperation improved the hydro-stability of the material in ambient moisture [35]. The same finding was later supported by Chen *et al.* (2016) stating that the combination of MOF-505 with GO enhanced the moisture stability of the material [31]. As an analogue to CNT@MOF-5 composite, Yang *et al.* (2010) in his continuous study on H<sub>2</sub> adsorption, have embedded Pt-loaded CNT into MOF-5 crystal to form in-situ Pt-loaded CNT@MOF-5 composite [34]. The result demonstrated that the H<sub>2</sub> storage capacity was improved from 1.2 wt% to 1.89 wt% at 77 K and 1 bar [34]. In both

<sup>31</sup> Reprinted from Journal of Materials Chemistry A, X.-W. Liu *et al.*, Composites of metal-organic frameworks and carbon-based materials: Preparations, functionalities and applications, vol. 4, no. 10, pp. 3584-3616, Copyright 2016, with permission from Royal Society of Chemistry.

<sup>32</sup> DMF: Dimethylformamide, is an organic solvent used in MOF synthesis.

studies, the CNT substrate played an important role as an efficient primary receptor of H<sub>2</sub> and secured the porosity of MOF-5 that acted as the secondary receptor [34].

In ammonia (NH<sub>3</sub>) adsorption study, Petit *et al.* from Bandosz's group have performed a number of MOF-carbon composites studies such as MOF-5/GO (2010) [48], HKUST-1/graphene (2010) [32], MIL-100(Fe)/GO (2011) [141] and HKUST-1/GO (2012) [142]. In the first study, MOF-5/GO was tested for NH<sub>3</sub> removal under dry atmosphere in which a panel of samples at different ratio of MOF:GO was synthesized [48]. The amount of NH<sub>3</sub> adsorbed was found increasing with the amount of loaded GO [48]. By adding 50 wt% of GO, the capacity of NH<sub>3</sub> uptake was increased to 82 mg/g from 6 mg/g achieved by the virgin MOF-5 at ambient conditions [48]. It was observed that NH<sub>3</sub> interacted with tetrahedral zinc oxide cluster in the framework via hydrogen bonding and was also intercalated between GO layers [143]. The second study showed that HKUST-1/graphene was able to enhance NH<sub>3</sub> adsorption capacity under both dry and moist condition as it was water-stable unlikely MOF-5/GO composites [32]. The higher NH<sub>3</sub> uptake was attributed to the presence of graphene layers that increased the material porosity and improved its surface dispersive forces [32]. However, the increasing in NH<sub>3</sub> adsorption capacity with the increasing amount of embedded graphene was observed only until 18 wt% of graphene loading [32]. After that specific composition, the material decreased in its performance as the amount of graphene increased [32]. It was also found that the NH<sub>3</sub> adsorption in HKUST-1 composite was more favorable under wet atmosphere although the adsorption mechanism was slow in regards to the competition of NH<sub>3</sub> and H<sub>2</sub>O to make binding with Cu adsorptive sites [32]. The same finding was demonstrated by Yazaydin *et al.* (2009) who had earlier studied on the removal of CO<sub>2</sub> from flue gas by using HKUST-1 [123]. It was stated that the pre-adsorption of H<sub>2</sub>O onto Cu open sites enhanced the selectivity of CO<sub>2</sub> over CH<sub>4</sub> and N<sub>2</sub> gases [123]. Cu-based MOF, HKUST-1, was reported having a better water-stability compared to Zn-based type, MOF-5 [144], and the presence of water allowed the dissolution of certain adsorbates such as NH<sub>3</sub> [32] and H<sub>2</sub>S [33]. These factors allowed a higher NH<sub>3</sub> and H<sub>2</sub>S loading under humid condition by using HKUST-1-based material.

Considering the different topology and geometry of MOFs, the doping of carbonaceous agent was not necessarily favorable for pore textural formation and thus gas adsorption. Another study on NH<sub>3</sub> adsorption was later conducted by using Fe (III) terephthalate-based MOFs as the template and GO as the hybrid agent to produce MIL-

100(Fe)/GO composite [141]. The GO powder was added to the mixture of MOF precursors at different percentage of substitution (4 and 9 wt%) before being sonicated and undergoing heat treatment [141]. Unfortunately, the result of  $\text{NH}_3$  adsorption was not encouraging where the breakthrough capacity decreased with the loading of GO at both dry and moist conditions [141]. This observation was related to the formation of the composite that was not favored since the attachment of GO layers to the spherical cage of MIL-100(Fe) (via coordination between the O atoms of GO and the metallic sites of the framework) prevented the proper formation of the MOF structure [141]. As the consequence, a higher GO loading composite had a lower porosity and a smaller  $\text{NH}_3$  uptake capacity [141]. Figure 2-14 (left) illustrates that the growth of spherical MIL-100 is hindered by the presence of GO layers unlikely MOF-5 and HKUST-1 crystals whose growth were not affected by the GO.

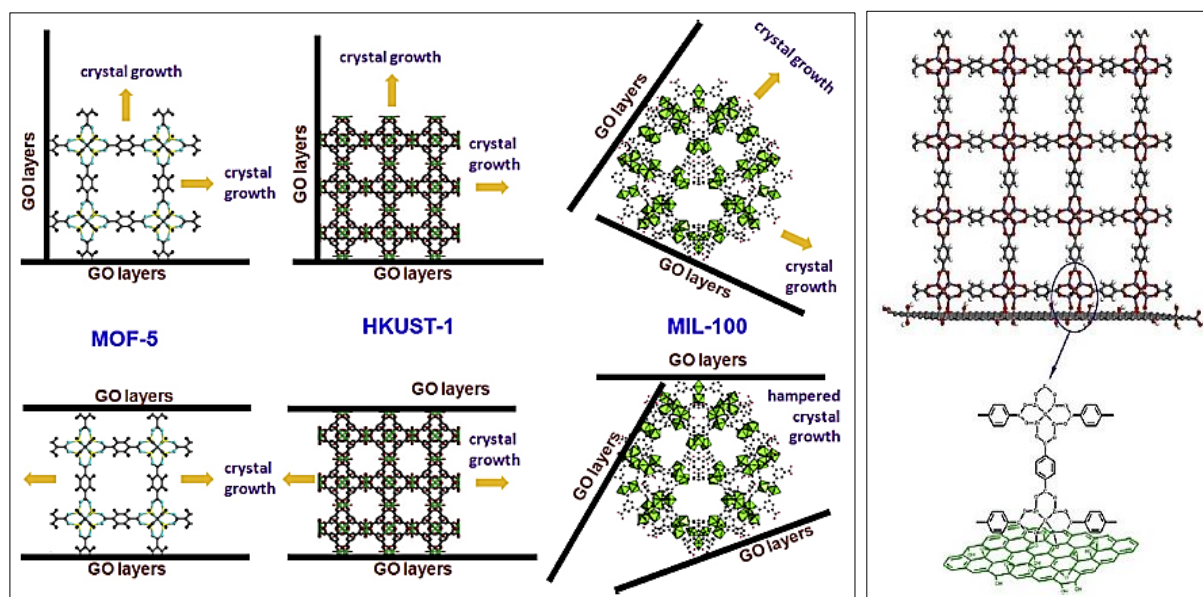


**Figure 2-14.** (left) Schematic comparison of the coordination between GO layers to the MOF units for different types of MOF network: MOF-5, HKUST-1 and MIL-100 [26].<sup>33</sup> (right) Schematic bonding formation between MOF network (top) and graphene layer (bottom) [127].<sup>34</sup>

The most adopted MOFs in MOF–carbon composite studies, HKUST-1, was also incorporated with GO denoted as HKUST-1/GO composite for the adsorptive removal of

<sup>33</sup> Reprinted from *Materials Today*, I. Ahmed *et al.*, Composites of metal-organic frameworks: Preparation and application in adsorption, vol. 17, no. 3, pp. 136-146, Copyright 2014, with permission from Elsevier.

<sup>34</sup> Reprinted from *Industrial & Engineering Chemistry Research*, Y. Jiao *et al.*, Tuning the kinetic water stability and adsorption interactions of Mg-MOF-74 by partial substitution with Co or Ni, vol. 54, no. 49, pp. 12408-12414, Copyright 2015, with permission from American Chemical Society.

acidic gases namely H<sub>2</sub>S [33, 142] and NO<sub>2</sub> [142, 145] at ambient conditions. In two different studies, it was proved that the increment of 50% of H<sub>2</sub>S adsorption capacity under both dry [33] and moist [142] atmospheres was achieved by inserting 5 wt% of GO into the pristine HKUST-1. However, the performance of HKUST-1/GO for H<sub>2</sub>S adsorption diminished with the amount of GO substituted unlikely the adsorption of NH<sub>3</sub> in HKUST-1/graphene that needed until 18 wt% of graphene as the limit concentration to attain the maximum uptake [32, 33, 142]. Besides that, by using the same optimized concentration of GO at 5 wt%, Levasseur *et al.* (2010) and Petit *et al.* (2012) conducted adsorption studies of NO<sub>2</sub> gas [142, 145]. The results showed that the adsorption uptake of NO<sub>2</sub> was slightly enhanced from 106 mg/g to 134 mg/g under dry condition owing to the increased MOF porosity [142, 145].

In those studies [33, 142, 145], it was found that the increased uptake capacity of H<sub>2</sub>S and NO<sub>2</sub> were resulting from both physical and reactive adsorptions. The physisorption of H<sub>2</sub>S and NO<sub>2</sub> took place in the pore spaces that were formed at the interface between MOF units and GO layers at which the dispersive forces were stronger than those in MOFs [33, 142]. The synergetic effects of GO and MOFs were related to the formation of those new small pore spaces providing the strongest force of surface dispersion within the composite [33, 142]. Meanwhile, the reactive adsorption which was the main retention mechanism has taken place when H<sub>2</sub>S and NO<sub>2</sub> molecules created bindings to the Cu open centers and carboxylate ligands of the framework [33, 145]. The reaction of H<sub>2</sub>S with the metal sites lead to the formation of copper sulphide whereas the same reaction of NO<sub>2</sub> produced bidentate and monodentate copper nitrates [142, 145]. The material exhibited high adsorption loading of H<sub>2</sub>S even in the presence of humidity but did not performed well for NO<sub>2</sub> due the competition of NO<sub>2</sub>/H<sub>2</sub>O to adsorb on Cu sites [33, 142, 145]. Although the presence of the new micropores gave benefits to both H<sub>2</sub>S and NO<sub>2</sub> adsorptions, the trend in their adsorption capacities did not follow the trend in the porosity of the composites [142]. This indicated that the physisorption was not the only mechanism of H<sub>2</sub>S or NO<sub>2</sub> retention but there was also reactive adsorption that contributed [142]. Surprisingly, it was also reported that the progressive reactions with Cu sites and the framework ligands led to the destruction of MOF structure causing the permanent loss of the material porosity [33].

In a wider application, HKUST-1-based composite containing GO was developed for selective separation of binary mixture gas; CO<sub>2</sub>/CH<sub>4</sub> [42] and CO<sub>2</sub>/N<sub>2</sub> [30]. For CO<sub>2</sub> removal from CH<sub>4</sub> gas stream, Huang *et al.* (2014) demonstrated that the combination of

Cu-BTC MOFs and 1 wt% of GO in one framework called GO@Cu-BTC gave rise to the amount of CO<sub>2</sub> uptake by 26% at 273 K, 1 bar, and, intensified 2.5 times the selectivity of CO<sub>2</sub> over CH<sub>4</sub> [42]. Based on the higher value of desorption activation energy of CO<sub>2</sub> from the composite deduced by Temperature-Programmed Desorption experiments, the interaction of CO<sub>2</sub> molecules in GO@Cu-BTC was reported superior than that in the pristine Cu-BTC, explaining the higher amount of CO<sub>2</sub> uptake [42]. The same result was found by Zhao *et al.* (2014) who studied the separation of CO<sub>2</sub> and N<sub>2</sub> also by using HKUST-1/GO [30]. At 305 K and 5 atm, it was stated that the CO<sub>2</sub> storage capacity increased by 38% for 10 wt% of GO substitution whereby the N<sub>2</sub> uptake was found almost similar in both materials [30]. The encouraging result was obtained despite of having a lower specific surface area of the composite due to the excessive amount of GO that caused the deterioration and defects in the composite structure, such as fracture and breakage of the framework [30]. The XRD analysis demonstrated that the composite had the same octahedral-shape as the virgin HKUST-1 but with smaller particle sizes since the incorporation of GO retarded the growth of MOF crystallite [30]. Different studies made hypothesis that the reaction between Cu sites in HKUST-1 and O-containing groups in GO allowed the embedment of GO layers in MOF blocks [30, 141].

Chen *et al.* (2017) conducted a study of MOF-505@GO composite for selective separation of different binary gases, CO<sub>2</sub>/CH<sub>4</sub> and CO<sub>2</sub>/N<sub>2</sub> [31]. By estimating their selectivities on the basis of Ideal Adsorbed Solution Theory, the quality of the separation was improved to 8.6 and 37.2 at 289 K and 1 bar for CO<sub>2</sub>/CH<sub>4</sub> and CO<sub>2</sub>/N<sub>2</sub>, respectively, by using the composite with 5 wt% of GO loading [31]. It was found that the improvement in the material performance was not only caused by the new formation of micropores and open metal sites in MOFs but also by the enhanced surface dispersive force in the composite, both of which were the result of the synergetic effects between MOF-505 and GO [31]. This finding was also claimed by Jabbari *et al.* (2016) in producing Cu-BTC@GO where the synergetic effects between Cu-BTC MOFs and GO were defined by the increased surface dispersive forces within the framework [38]. This created different morphologies and sizes of MOF crystals and led to the formation of small pores between the MOF units and GO layers, resulting to the enhanced gas uptake in the composite [38]. Not only using GO, the same finding was also stated in another CO<sub>2</sub> adsorption study where MIL-101(Cr) was doped with multiwalled CNT to produce hybrid CNT@MIL-101(Cr) [36]. With 10 wt% of CNT loading, Anbia *et al.* (2014) discovered that the CO<sub>2</sub> adsorption was increased

nearly 60% at 298K and 10 bar by the reason of increased micropores volume in the composite without perturbing the crystal structure and morphology [36]. Interestingly, it was also observed that the thermal stability of MIL-101(Cr) was enhanced after the incorporation with CNT [36].

The cycling performance of MOF–carbon composite was examined by Zhao *et al.* (2014). It showed that the re-adsorption isotherm of CO<sub>2</sub> in HKUST-1 after desorption by vacuum was similar to the first adsorption while the re-adsorption in HKUST-1/GO was higher than the first cycle [30]. The result indicated that HKUST-1 exhibited good structure stability where some pores between MOF units and GO layers in HKUST-1/GO were activated under the first adsorption [30]. In different area of studies, other forms of MOF–carbon composites using CNT and GO were also developed for the adsorption of specific compounds; MIL-101(Cr)/GO for n-hexane adsorption [146], CNT@MIL-68(Al) for phenol adsorption [147], and, Cu-BTC@GO and Fe<sub>3</sub>O<sub>4</sub>/Cu-BTC@GO for organic pollutants removal [38].

Table 2-12 summarizes the published works on MOF–carbon composites using GO and CNT reported to date for various gas adsorption. Table 2-13 summarizes the published works on other types of MOF–carbon composites also using GO and CNT reported to date for specific materials removal.

**Table 2-12.** Published works on MOF–carbon composite using CNT and GO reported to date for various gas adsorption (2009–present).

Ref.	Type of MOF template	Type of doping agent	Application	Performances
2009 Yang [35]	MOF-5	CNT	H <sub>2</sub> storage	<u>At 77 K and and 1 bar:</u> H <sub>2</sub> storage was improved from 1.2 to 1.52 wt%. <u>At 298 K and 95 bar:</u> H <sub>2</sub> storage was improved from 0.3 to 0.61 wt%.
2010 Petit [48]	MOF-5	GO	NH <sub>3</sub> adsorption	<u>At ambient conditions:</u> NH <sub>3</sub> adsorption was increased from 6 to 82 mg/g for 50 wt% of GO loading.
2010 Petit [32]	HKUST-1	Graphene	NH <sub>3</sub> adsorption	<u>At ambient conditions (dry):</u> NH <sub>3</sub> adsorption was enhanced from 115 to 149 mg/g for 18 wt% of graphene. <u>At ambient conditions (moist):</u> NH <sub>3</sub> adsorption was enhanced from 172 to 182 mg/g for 18 wt% of graphene.
2010 Petit [33]	HKUST-1	GO	H <sub>2</sub> S adsorption	<u>At ambient conditions:</u> H <sub>2</sub> S adsorption was improved from 92 to 199 mg/g for 5 wt% of GO.
2010 Yang [34]	MOF-5	Pt(CNT)	H <sub>2</sub> storage	<u>At 77 K and and 1 bar:</u> H <sub>2</sub> storage was improved from 1.2 to 1.89 wt%.
2010 Levasseur [145]	HKUST-1	GO	NO <sub>2</sub> adsorption	<u>At ambient conditions (dry):</u> NO <sub>2</sub> adsorption increased from 106 to 134 mg/g for 5 wt% of GO. <u>At ambient conditions (moist):</u> NO <sub>2</sub> adsorption increased from 54 to 59 mg/g for 18 wt% of GO.
2011 Petit [141]	MIL-100(Fe)	GO	NH <sub>3</sub> adsorption	<u>At ambient conditions (dry):</u> NH <sub>3</sub> adsorption decreased with the amount of GO added; from 55.7 to 48.6 mg/g (for 4 wt% of GO) and 44 mg/g (for 9 wt% of GO). <u>At ambient conditions (moist):</u>

				NH <sub>3</sub> adsorption increased from 39.8 to 42.2 mg/g (for 4 wt% of GO) and decreased to 28.4 mg/g (for 9 wt% of GO).
2012 Petit [142]	HKUST-1	GO	H <sub>2</sub> S and NO <sub>2</sub> adsorption	<u>At ambient conditions (dry):</u> NO <sub>2</sub> adsorption was enhanced from 106 to 134 mg/g for 5 wt% of GO. <u>At ambient conditions (moist):</u> H <sub>2</sub> S adsorption was enhanced from 95 to 195 mg/g for 5 wt% of GO.
2012 Anbia [36]	MIL-101(Cr)	CNT	CO <sub>2</sub> storage	<u>At 298 K and 10 bar:</u> CO <sub>2</sub> uptake was enhanced from 0.84 to 1.34 mmol·g <sup>-1</sup> for 10 wt% of CNT (60% of increment).
2014 Huang [42]	Cu-BTC	GO	CO <sub>2</sub> /CH <sub>4</sub> separation	<u>At 273 K and 1 bar:</u> CO <sub>2</sub> adsorption was improved from 6.49 to 8.19 mmol·g <sup>-1</sup> for 1 wt% of GO. The selectivity of CO <sub>2</sub> /CH <sub>4</sub> was improved 2.5 times (14 at 1 bar).
2014 Zhao [30]	HKUST-1	GO	CO <sub>2</sub> /N <sub>2</sub> separation	<u>At 305 K and 5 atm:</u> CO <sub>2</sub> adsorption increased from 1.8 to 2.5 mmol·g <sup>-1</sup> for 10 wt% of GO. The selectivity of CO <sub>2</sub> /N <sub>2</sub> was also enhanced.
2017 Chen [31]	MOF-505	GO	CO <sub>2</sub> /CH <sub>4</sub> and CO <sub>2</sub> /N <sub>2</sub> separation	<u>At 298 K and 1 bar:</u> CO <sub>2</sub> uptake was increased from 2.87 to 3.94 mmol·g <sup>-1</sup> for 5 wt% of GO (37.3% of increment). The selectivity of CO <sub>2</sub> /CH <sub>4</sub> and CO <sub>2</sub> /N <sub>2</sub> were up respectively to 8.6 and 37.2.

**Table 2-13.** Published works on MOF–carbon composites using CNT and GO reported to date for specific materials removal (2009–present).

Ref.	Type of MOF	Type of composing material	Application
2013, Sun [146]	MIL-101(Cr)	GO	n-hexane adsorption
2015, Han [147]	MIL-68(Al)	CNT	Phenol adsorption
2016, Jabbari [38]	Cu-BTC	GO	Organic pollutants adsorption

## 2.6. Conclusion

This research is judiciously directed from the global energy and environmental issues to the potential application of MOF carbon-based adsorbents for CO<sub>2</sub> and CH<sub>4</sub> separation. The selection of Mg-MOF-74 as the basis for the development of new MOF-carbon composite adsorbents is grounded on the encouraging features that the material can offer for CO<sub>2</sub> and CH<sub>4</sub> separation: (i) excellent balance between high CO<sub>2</sub> adsorption capacity and high selectivity towards CO<sub>2</sub> over CH<sub>4</sub>, and, (ii) excellent balance between high adsorption capacity and facile regeneration. Since MOF-74 has been introduced to MOF world in 2005, no published work has reported on the development of MOF-74-carbon composites despite of potential advantages the carbon-doped materials can offer to improve CO<sub>2</sub> adsorption capacity. Literature review also shows that the performance of MOF-74 materials for CO<sub>2</sub> capture at high pressures in regard to natural gas streams at processing plant that can reach 75–100 bar has received less attention. Most published works on MOF-74 have experimentally performed the adsorption at mild pressures which are more relevant for CO<sub>2</sub> captures at natural gas power plants. To fill these research gaps, the present study proposes a potential novelty in adsorption technologies by developing other types of MOF-carbon composite from Mg-MOF-74 template and CNT or GO as the counterpart doping agent for CO<sub>2</sub> and CH<sub>4</sub> adsorptions. For experimental studies, pure CO<sub>2</sub> adsorption at 25 °C can only be performed to the pressure limit up to 40 bar due to supercritical pressure, which represents approximately 40–53 vol.% of CO<sub>2</sub> content in 75–100 bar of CH<sub>4</sub>/CO<sub>2</sub> gas stream.

**CHAPTER 3**

**Synthesis and  
Characterization  
of Materials**

---

**CHAPTER 3: SYNTHESIS AND CHARACTERIZATION OF MATERIALS****3.1. Synthesis of MOFs and MOF composites: Review**

There are six common preparation routes of MOFs that can be classified: solvothermal synthesis, microwave assisted synthesis, sonochemical synthesis, mechanochemical synthesis, electrochemical synthesis, and, slow evaporation synthesis [12, 20, 50, 73, 148, 149]. Solvothermal synthesis is the most preferable method being used in approximately 70% of published works on MOF materials [12, 149]. In general, solvothermal preparation of MOFs consists of employing soluble metal salts, organic linkers, and organic high-boiling solvent in a sealed vessel and heated above the boiling point of the solvent to undergo the reaction. Then, the product is recovered and washed, followed by the evacuation of solvent in MOF pores. Owing to the fast reaction kinetics in solvothermal reaction, this technique allows production of uniform MOF particles with high crystallinity, high phase purity, and small crystallite size distribution, requiring however thorough optimization of experimental conditions [149, 150]. One should notice that for different applications of MOF materials involving the processes of mass transfer, aside from highly specific surface area and microporous volume, average particle size and size distribution are important parameters determining the kinetics of the process and diffusion barriers. In the particular case of gas adsorption, the diffusion barrier of mass transfer decreases with crystallite sizes [151].

However, solvothermal synthesis undeniably exhibits some shortcomings, such as the use of expensive stainless steel autoclaves and Teflon reactors, environmental hazards with the use of solvents, limitation of mass production per synthesis, and difficulties of product washing processes [150]. The latter involves the use of solvents such as dimethylformamide, diethylformamide, acetonitrile, acetone, ethanol, and methanol, where the mixtures of solvents have also been used in many cases to avoid problems of different solubility for the different reactants [12]. The chemical reaction takes place between inorganic and organic components leading to the formation of frameworks of the material contoured by the solvent molecules that act as a “pore template”, and will be removed during washing and evacuation processes at high temperatures [18]. Depending on the operational conditions, the processes may involve the blockage of pores due to the incomplete removal of reactive media from MOF product such as solvents of the reaction, residual reactants, and side products [18]. Other preparation routes of MOFs are also continuously being developed as summarized in Table 3-1 and become more interesting in

some aspects, provided that they can produce the same high-quality MOF crystals as offered by solvothermal synthesis. As described in Table 3-2, a number of parameters can be varied during the synthesis in order to control the final products such as types of metal soluble salts [152], types of organic linker [152], types of organic solvent [132, 152], ligand-to-metal molar ratios [132], reactants concentrations [151], reaction times [132, 151, 152] and reaction temperatures [132].

**Table 3-1.** The most common techniques of preparation of MOFs.

Synthesis technique	% of published work [12]	Required energy	Synthesis duration	Synthesis conditions	Advantages and limitations	Ref.
Solvothermal / Hydrothermal synthesis	≈69.9% ≈13.5%	Heat energy	48 hours to 96 hours	80 °C to 180 °C	Production of high-quality MOF crystals, but difficult washing processes with small production of MOFs.	Many
Microwave assisted synthesis	≈6.1%	Microwave	4 min to 4 hours	30 °C to 100 °C	Very rapid synthesis with good-quality MOF crystals. Preferable technique after solvothermal synthesis.	[50] [148]
Sonochemical synthesis	≈4.9%	Intensive ultrasonic radiation	30 min to 3 hours	20 kHz to 10 MHz	Generation of homogenous nucleation centers and possibility of reducing crystallization time.	[20]
Mechanochemical synthesis	≈4.3%	Mechanical force	30 min to 2 hours	Room T	Solvent-free synthesis thus become economical and environmentally friendly.	[31]
Electrochemical synthesis	≈1.2%	Electrical energy	10 min to 30 min	Room T, pH change	Continuous production of MOF crystals, but with large crystal sizes. Possibility of large-scale production, but	[149]

					the development is ongoing.	
Slow evaporation	≈0%	No energy required	7 days to 7 months	Room T	No external energy is required with the use of low-boiling solvent, but very slow synthesis.	[12]

**Table 3-2.** Possible variation of parameters for the preparation of MOFs.

Parameters	Effects of variation of the parameters	Ref.
Types of soluble metal salt	MOF types and geometries.	[152]
Types of organic linker	MOF pore sizes; for example, the isoreticular series of IRMOF-n contain different linkers producing different pore sizes: IRMOF-1 (linker: H <sub>2</sub> BDC), IRMOF-10 (linker: H <sub>2</sub> BPDC) and IRMOF-16 (linker: H <sub>2</sub> TPDC).	[152]
Types of organic solvent	MOF types and geometries.	[152]
	Reaction kinetics; different solvents induce different reaction kinetics.	[132]
Ligand-to-metal molar ratios	Reaction kinetics; the higher the ligand-to-metal molar ratio, the faster the conversion takes place.	[132]
Reactants concentrations (by fixing reactants amount and changing solvents volume)	MOF crystallite sizes.	[151]
Reaction times	MOF types and geometries.	[152]
	MOF crystallite sizes; the longer the reaction time, the smaller the particle size distribution.	[151] [132]
Reaction temperatures	Reaction kinetics; the higher the temperature, the faster the reaction kinetics, however, an optimal temperature must be chosen for the reaction. In the synthesis of MOF composites, a fine control of hybrid material formation cannot be achieved if the rate of reaction kinetics is too high.	[132]

Specifically for the application of gas adsorption, the ways of preparing MOF composites including MOF-carbon composites must involve the formation of MOF units in continuous phase applying either three common approaches: (i) post-synthesis, and, *in situ* synthesis of the types of (ii) ship-in-a-bottle or (iii) bottle-around-ship methods [26]. The first approach, post-synthetic modification, can be effectuated by the procedures of

simple loading (impregnation), insolubilization (coprecipitation), encapsulation, chemical conversion, infiltration or functionalization as recently reported by Ullah *et al.* (2020) in preparing MOF-200/GO composite [153]. The second approach, *in situ* synthesis of the type of ship-in-a-bottle method, refers to the formation of a composite from “pre-formed MOFs” and “doping agent precursors” during the reaction in the synthesis procedure. Described as the encapsulation of doping material by MOF units, the doping agent precursors penetrate into MOF pores via diffusion by the help of a solvent system. The composite is formed after the stabilization of the formation of the particles of the doping material inside MOF pores using chemical or thermal method. Due to the increase in size, the final particles of the doping material remain stable inside MOF pores. This method was early well-known for zeolite composites [154] and recently adopted for zeolite-like MOF composites [155]. Different from the previous approach, the third approach, *in situ* synthesis of the type of bottle-around-ship method can be carried out by direct mixing “MOF precursors” with “doping agent particles” before the reaction in the synthesis procedure. The MOF units are built from their precursors around the particles of the doping material leading to the trapped and immobilized large particles of the doping material within MOF units after complete formation.

Adopted for this work, the third approach is widely published for the preparation of MOF-carbon composites for the application of gas adsorption [29-42, 48, 141, 142, 145]. Petit *et al.* (2010-2012) et Levasseur *et al.* (2011) from Bandosz's group have produced a number of MOF/graphene-based material composites by using this technique for different studies such as HKUST-1/GO [29, 33, 142, 145], HKUST-1/graphene [32], MOF-5/GO [48] and MIL-100(Fe)/GO [141]. Figure 3-1 describes different formations of MOF units and carbon doping material prepared using *in situ* synthesis approaches. One should note that for an *in situ* synthesis, an appropriate amount of carbon doping material is required to prevent excessive interference with the coordination reactions of MOFs that may ruin the structure of MOF-carbon composites and adversely affect the performance of the material [27]. Therefore, an optimization study of substitution percentage of the doping material is primordial in order to obtain the most performing material having the best concentration.

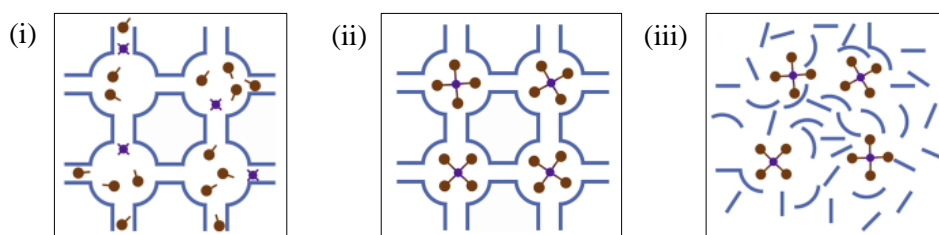


**Figure 3-1.** The formation of MOF-carbon composites in *in situ* synthesis of the types of ship-in-a-bottle method; (i) before and (ii) after, and, (iii) bottle-around-ship method. MOF unit and doping material are presented in blue and brown, respectively [26].<sup>35</sup>

## 3.2. Synthesis of MOF-74: Materials and methodology

### 3.2.1. Materials

All reagents were commercially available and consumed as received. Magnesium nitrate hexahydrate [ $\text{Mg}(\text{NO}_3)_2 \cdot 6\text{H}_2\text{O} \geq 99\%$ , Merck], nickel (II) nitrate hexahydrate [ $\text{Ni}(\text{NO}_3)_2 \cdot 6\text{H}_2\text{O} \geq 99\%$ , Merck], cobalt (II) nitrate hexahydrate [ $\text{Co}(\text{NO}_3)_2 \cdot 6\text{H}_2\text{O} \geq 99\%$ , Merck], zinc nitrate hexahydrate [ $\text{Zn}(\text{NO}_3)_2 \cdot 6\text{H}_2\text{O} 98\%$ , Acros], 2,5-dihydroxyterephthalic acid (DOT 98%, Aldrich), *n,n*-dimethylformamide (DMF 99.8%, Merck) and ethanol absolute (99.8%, BDH), methanol (99.9%, Merck) were all purchased from Portray (M) Sdn Bhd (Petaling Jaya, Malaysia).

### 3.2.2. Solvothermal synthesis technique

The following preparation is the typical procedure of solvothermal synthesis of MOF-74 materials reported elsewhere [17-19, 23, 37, 51, 54], noting that the synthesis parameters might differ. In detail for this work, soluble metal salt  $\text{Mg}(\text{NO}_3)_2 \cdot 6\text{H}_2\text{O}$  (0.712 g, 2.78 mmol) and DOT linker (0.167 g, 0.84 mmol) were completely dissolved in a 15:1:1 (v/v/v) mixture of DMF (67.5 ml), ethanol (4.5 ml) and distilled water (4.5 ml) using ultrasonication at 37 kHz for 15 minutes. The homogeneous solution was then transferred into a 125-ml Teflon reactor and stainless steel autoclave (Kean Seng Engineering Works, Pusing, Malaysia), tightly capped and put in the oven at 125 °C for 26 h [19]. The Teflon reactor was removed and cooled at room temperature. The mother liquor of the reaction was gently separated from the product. The product was washed by immersion in methanol

<sup>35</sup> Reprinted from Materials Today, I. Ahmed *et al.*, Composites of metal-organic frameworks: Preparation and application in adsorption, vol. 17, no. 3, pp. 136-146, Copyright 2014, with permission from Elsevier.

in a petri dish for 3 days with a 6-time replenishment of fresh methanol. The remaining solvents were evacuated under a dynamic vacuum at 250 °C for 15 h [19]. The synthesis processes are summarized in Figure 3-2. The produced Mg-MOF-74 was the pristine material in this work and denoted as the sample of the first-batch synthesis (basic synthesis without improvement).

### 3.2.3. Improvement of conditions of solvent evacuation

Due to the significant color change of Mg-MOF-74 powder from yellowish to deep dark after solvent removal process, it was noticed that the product was degraded by the applied temperature which was 250 °C. Thus, an optimum temperature at which the solvents could be removed without destroying the organic components in the material was determined as 150 °C. In terms of the evacuation time of the solvents, it was conducted under a dynamic vacuum for a certain period until the stabilization of the residual pressure was reached within 20–72 hours.

### 3.2.4. Improvement of washing processes

For the first-batch synthesis, the washing processes were repeated to improve the separation of MOF product from the reactive media, marked green in Figure 3-2. For the second-batch synthesis, the centrifugal separations were introduced in the synthesis routes (without washing repetitions) at two different points, marked red in Figure 3-2: (1) between reaction and product washing, and (2) between product washing and solvent evacuation. Methanol was used as the washing solvent in centrifugation. A solution of 360 mg of MOF powder and fresh methanol was poured into six centrifuge tubes for 50 ml each. An optimization study of centrifugal time and rotation speed was carried out to obtain the best separation quality. It consisted of varying the parameters one by one and observing the separation between MOF products and methanol after each centrifugation. The incomplete separation was indicated by the dispersion of MOF particles in methanol shown by murky methanol colour, indicating that both centrifugal parameters were insufficient. A good separation was observed by total sedimentation of MOFs, but without any detachment of MOF “flakes” from the sedimentation, failing which either centrifugal time or rotation speed was overestimated. As a result, the optimized centrifugal time and rotation speed for 50 ml solution of 60 mg MOFs in methanol were determined as 7 min and 8000 rpm, respectively. The produced Mg-MOF-74 was denoted as the sample of the second-batch

synthesis (improved synthesis). The adsorption performance of CO<sub>2</sub> was evaluated for Mg-MOF-74 of the first-batch synthesis without and with washing repetitions, and also, for Mg-MOF-74 of the second batch synthesis with centrifugation 1 and both centrifugations 1 and 2.

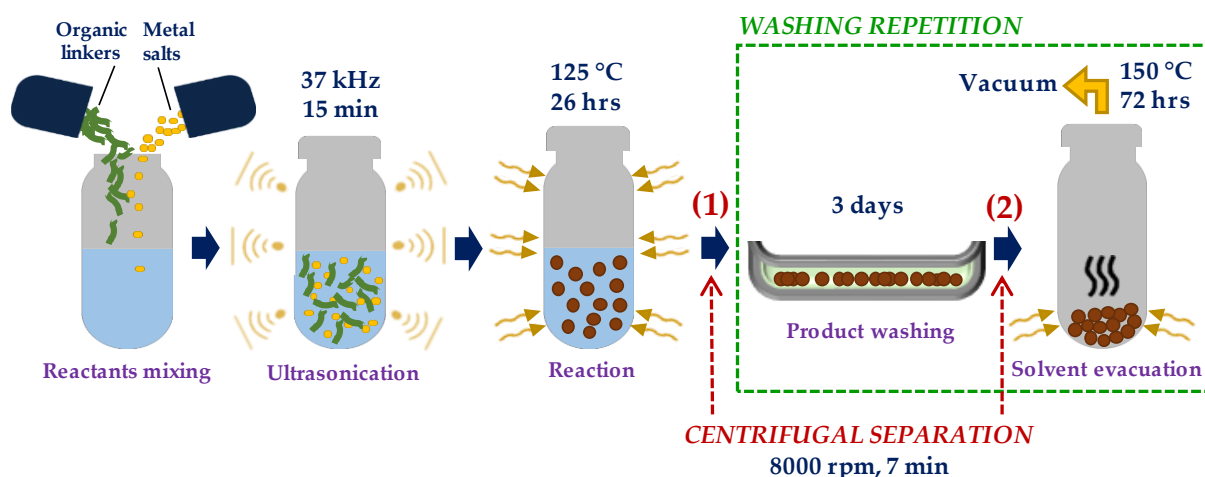


**Figure 3-2.** Schematic figure of solvothermal synthesis of this work with repeating washing processes or with additional centrifugal separations.

### 3.2.5. Metal nodes tuning

By using the improved synthesis routes and the same synthesis parameters, other M-MOF-74 series were prepared using soluble metal salts Ni(NO<sub>3</sub>)<sub>2</sub>·6H<sub>2</sub>O, Zn(NO<sub>3</sub>)<sub>2</sub>·6H<sub>2</sub>O and Co(NO<sub>3</sub>)<sub>2</sub>·6H<sub>2</sub>O in order to produce Ni-MOF-74, Zn-MOF-74 and Co-MOF-74, respectively. The best metal node was determined from the best sample performing the highest CO<sub>2</sub> adsorption.

### 3.2.6. Reproducibility and storage

Each reaction batch of the synthesized material was first characterized using powder X-ray diffraction analysis to confirm the success of reproducibility of MOF-74. All samples were stored in a sealed vacuum bag with the presence of silica gel and kept in desiccators. The ageing effect of the samples were also evaluated after 18 months of their production.

### 3.3. Synthesis of MOF-74-carbon composites: Materials and methodology

#### 3.3.1. Materials

All reagents were commercially available and consumed as received. Magnesium nitrate hexahydrate [ $\text{Mg}(\text{NO}_3)_2 \cdot 6\text{H}_2\text{O} \geq 99\%$ , Merck], 2,5-dihydroxyterephthalic acid (DOT, 98%, Aldrich), *n,n*-dimethylformamide (DMF, 99.8%, Merck), ethanol absolute (99.8%, BDH), methanol (99.9%, Merck), graphene oxide (GO monolayer content  $>95\%$ , oxygen content  $\geq 36\%$ , 4  $\text{mg} \cdot \text{ml}^{-1}$ , dispersion in  $\text{H}_2\text{O}$ , Sigma-Aldrich) and carbon nanotubes (multiwalled CNT  $>7.5\%$  basis, 7-15 nm diameter, 0.5-10  $\mu\text{m}$  length,  $>99\%$  purity, Sigma-Aldrich) were all purchased from Portray (M) Sdn Bhd (Petaling Jaya, Malaysia).

#### 3.3.2. *In situ* synthesis method

As seen in Section 3.1, *in situ* synthesis of the type of bottle-around-ship method can be carried out by direct mixing “MOF precursors” with “doping agent particles” before the reaction as reported elsewhere [29-42, 48, 141, 142, 145]. CNT and GO were used as the carbon doping agents to produce Mg-MOF-74-carbon composites. CNT and GO were measured in mass-basis to obtain  $n^{36}$  wt% of the weight of the pristine Mg-MOF-74 deduced in the previous synthesis which was 350 mg. In detail, soluble metal salt  $\text{Mg}(\text{NO}_3)_2 \cdot 6\text{H}_2\text{O}$  (0.712 g, 2.78 mmol), DOT linker (0.167 g, 0.84 mmol) and carbon doping agent (either CNT or GO) were completely dissolved in a 15:1:1 (v/v/v) mixture of DMF (67.5 ml), ethanol (4.5 ml) and distilled water (4.5 ml) using ultrasonication at 37 kHz for 2 hours<sup>37</sup>. The homogeneous solution was then transferred into a 125-ml Teflon reactor and stainless steel autoclave (Kean Seng Engineering Works, Pusing, Malaysia), tightly capped and put in the oven at 125 °C for 26 h. The Teflon reactor was removed and cooled at room temperature. The mother liquor of the reaction was gently separated from the product. The product was then dissolved in methanol and the solution was poured into six centrifuge tubes for 50 ml each, and then, separated by centrifugal technique at 8000 rpm for 7 minutes. Another fresh methanol was added into the centrifuge tube, shaken and underwent another centrifugal separation. The same procedure was repeated for three times. The product was collected and immersed in methanol in a petri dish for 3 days with a 6-

<sup>36</sup> The optimization of the substituted composition of carbon doping agent is detailed in Section 3.3.4.

<sup>37</sup> The ultrasonication time was increased to have a complete dissolution of the carbonaceous material.

time replenishment of fresh methanol. After that, the same centrifugal procedure was repeated for three times. The remaining solvent was evacuated under a dynamic vacuum at 150 °C for 72 h. The synthesis procedure is schematized in Figure 3-3. The composites were denoted as Mg-MOF-74@CNT and Mg-MOF-74@GO.

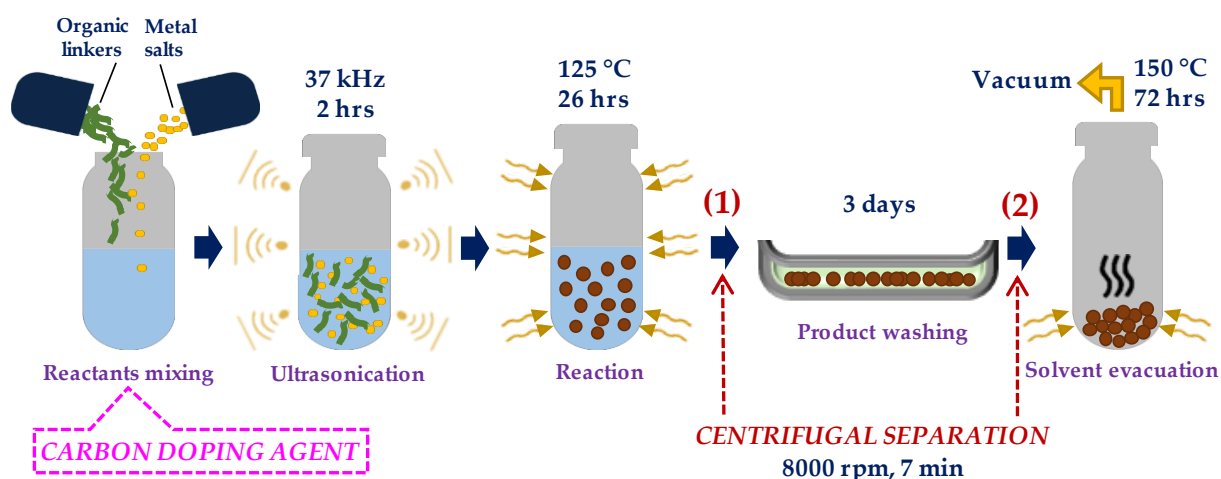


**Figure 3-3.** Schematic figure of solvothermal *in situ* synthesis of MOF-carbon composites of this work.

### 3.3.3. Extraction of graphene oxide

Unlike the commercial CNT that existed in powder form, the commercial GO was provided in water suspension. Thus, the extraction of GO from the water was necessary to study the properties and adsorption behavior of pure GO to be compared with Mg-MOF-74@GO composites. Knowing that GO was soluble in acetone which was a low-boiling solvent, the following procedure was carried out. 100 ml of 4 mg·ml<sup>-1</sup> GO suspension was dissolved in 260 ml of acetone and stirred to obtain precipitation. The solution was then poured into six centrifuge tubes for 30 ml each. GO was then separated from the acetone by centrifugal technique using the optimized centrifugal time and rotation speed which were 30 minutes and 7000 rpm, respectively. The optimization methodology of centrifugal parameters was the same as applied for MOFs in Section 3.2.4. The sediment of wet GO solid was then collected and dried in the oven at 80 °C overnight. As the product, GO flakes were obtained. These processes are summarized in Figure 3-4.

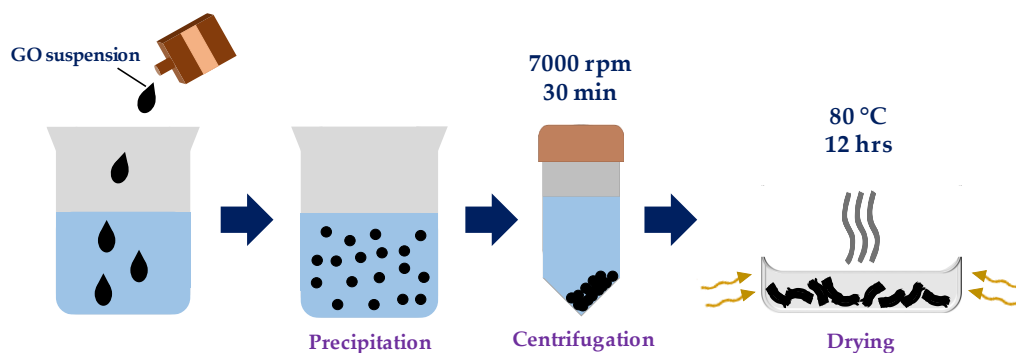


**Figure 3-4.** Schematic figure of the extraction of graphene oxide from water suspension.

#### 3.3.4. Optimization of concentration of carbon doping agent

The concentration of carbon doping agent embedded into MOF-74-carbon composite was optimized by fixing firstly 10–20 wt%, secondly 1–6 wt% and thirdly 0.1–0.6 wt%. These weight percentages were referred to the weight of the pristine Mg-MOF-74 deduced in the previous synthesis which was 350 mg. An optimum concentration was determined from the best sample performing the highest CO<sub>2</sub> adsorption.

### 3.4. Characterization of synthesized materials: Methodology

#### *a. Powder X-ray diffraction (PXRD) analysis*

The crystalline structure of the synthesized sample was analyzed using powder X-ray diffraction (PXRD). The patterns were recorded by using a Bruker AXS-D8 Advance Diffractometer (Massachusetts, U.S.) with a Cu K $\alpha$  radiation ( $\lambda = 1.5406 \text{ \AA}$ ), a step size of  $0.02^\circ$  in  $2\theta$  ranging from  $5^\circ$  to  $45^\circ$  and a scan rate of  $1^\circ/\text{min}$ . A novaculite was used as the standard material to determine instrumental resolution of the diffractometer.

#### *b. Fourier transform infrared spectroscopy (FTIR) analysis*

Fourier-transform infrared spectroscopy (FTIR) analysis via potassium bromide (KBr) method was used to generate spectra with patterns that provide structural insights by using a Thermo Nicolet IS5 Spectrometer (Massachusetts, U.S.). The spectra with a resolution of  $4 \text{ cm}^{-1}$  were acquired in Attenuated Total Reflection mode allowing direct measurement of powder samples under ambient conditions within 32 runs (scans) in a wavenumber range of  $4000\text{--}500 \text{ cm}^{-1}$ . For every sample, the background scanning was performed to recognize the presence of air impurities such as CO<sub>2</sub> peak.

**c. Raman spectroscopy analysis**

Raman spectroscopy analysis was carried out using a Thermo Scientific DXR Smart RAMAN System (Massachusetts, U.S.) with a He–Ne laser ( $\lambda = 700$  nm) and spectrograph aperture of 25  $\mu\text{m}$  slit. The laser power was controlled below 30 mW for an exposure time of 30 s and a spectra resolution of 1  $\text{cm}^{-1}$  in a Raman shift range of 500–4000  $\text{cm}^{-1}$ . A 50 objective lens was used in the experiments.

**d. Field emission scanning electron microscopy (FESEM) analysis**

Zeiss SUPRA 55VP instrument (Arlington, U.S.) was used to study the morphology of the samples under field emission scanning electron microscopy (FESEM) analysis. The sample powder was deposited onto a conductive carbon double-sided adhesive tape on a specimen stub. The loose material was removed. The sample coating was effectuated with a platinum sputter coater for 60 s. The sample was placed in a vacuum chamber where the applied vacuum reached an optimum value of  $p=2 \cdot 10^{-5}$  bar before the imaging was run. The micrographs were visualized from 1k to 100k magnification using secondary electrons detector. Energy dispersive X-ray spectroscopy (EDXS) analysis was carried out to access the concentration of different elements on sample surfaces.

**e. Thermogravimetric analysis (TGA)**

Thermogravimetric measurements were performed on a Setaram LabSys evo TGA-DTA instrument (Caluire, France) with temperature ramp from 50  $^{\circ}\text{C}$  to 600  $^{\circ}\text{C}$  at 2  $^{\circ}\text{C} \cdot \text{min}^{-1}$  under flow of helium gas to homogenize heat transfer, protect the balance and avoid sample oxidation. In order to account for mass variation induced by factors other than sample weight loss, the thermogram measured for an empty crucible is systematically subtracted from that of the sample.

**f.  $\text{N}_2$  adsorption/desorption isotherm analysis**

Textural properties of the materials were characterized by using  $\text{N}_2$  adsorption/desorption isotherm at 77 K. The isotherms were obtained using 3Flex manometric adsorption analyzer from Micromeritics (Unterschleißheim, Germany). The instrument is equipped with pressure transducers allowing measurements in the domain of  $\text{N}_2$  relative pressure ( $p/p^{\circ}$ ) ranging between  $10^{-7}$  and 1 with 0.15% precision of absolute pressure reading, where  $p^{\circ}$  is the saturation pressure. The acquisition was performed in a

fixed-dose mode until  $p/p^\circ=0.03$  and then incrementing  $N_2$  relative pressure. The periodicity of equilibration time measurement in the domain of micropore filling was set to 90 s in order to achieve a complete equilibrium. Before isotherm measurement, the sample was outgassed using Smart VacPrep degas station from Micromeritics (Unterschleißheim, Germany) under  $10^{-6}$  bar dynamic vacuum at  $150\text{ }^\circ\text{C}$  with heating rate of  $1\text{ }^\circ\cdot\text{min}^{-1}$  until residual pressure stabilization for at least 20 h. The volumes of cell non-occupied by sample were determined at ambient temperature and at 77 K by helium expansion. Apparent specific surface area was determined using BET method ( $N_2$  cross section= $0.162\text{ nm}^2$ ) at  $0.005\leq p/p^\circ\leq 0.05$  in the way to obtain a positive BET constant.

#### ***g. CO<sub>2</sub> adsorption isotherm measurement***

The efficiency of MOF pore activation in the synthesis was evaluated by the performance of the produced sample for  $CO_2$  adsorption, which was the interested application of this material. This method of evaluation was also performed by Das *et al.* (2016) when improving the synthesis of MOF-74 by varying the type of solvents [156].  $CO_2$  adsorption isotherm was obtained at 1 bar and at  $25\text{ }^\circ\text{C}$  using BELSORP mini II from MicrotracBEL (Osaka, Japan). Prior to the measurement, the sample was outgassed using BET pre-treatment equipment BelprepII from MicrotracBEL (Osaka, Japan) under a dynamic vacuum at  $150\text{ }^\circ\text{C}$  for at least 20 h.

### **3.5. Synthesis of MOF-74: Results and discussions**

#### **3.5.1. Characterization for improving the synthesis**

##### ***a. Improvement of conditions of solvent evacuation***

Based on the thermogravimetric curve of the synthesized Mg-MOF-74 (blue) in Figure 3-5, the required temperature to completely remove the humidity, guest molecules and solvents from the material is  $250\text{ }^\circ\text{C}$ , which lies after the first weight loss presented by the derivative curve (red). However, it was noticed that the product was degraded by the applied temperature due to the significant color change of the material from yellowish to deep dark after solvent evacuation or outgassing. Therefore, an optimum temperature at which the solvents could be removed without destroying the organic components in the material was estimated as  $150\text{ }^\circ\text{C}$ , close to the boiling point of DMF ( $153\text{ }^\circ\text{C}$  at 1 bar). The duration of the heating under the dynamic vacuum must be though prolonged to reach a

complete evacuation since the temperature was reduced. Also, one should note that the heating ramp must be slow, suggested as  $1\text{ }^{\circ}\text{C}\cdot\text{min}^{-1}$  [18], in order to prevent the rupture of the organic fragments by sudden evaporation of the solvent (or humidity in the case of outgassing). The advancement of solvent evaporation was followed by the pressure change in the vacuum line system. The experiments showed that it required 20–72 hours to have a relative pressure stabilization, indicating a complete solvent removal and MOF pore activation. Therefore, for the future synthesis, the solvent evacuation or the outgassing processes were effectuated at  $150\text{ }^{\circ}\text{C}$  for at least 20 hours.

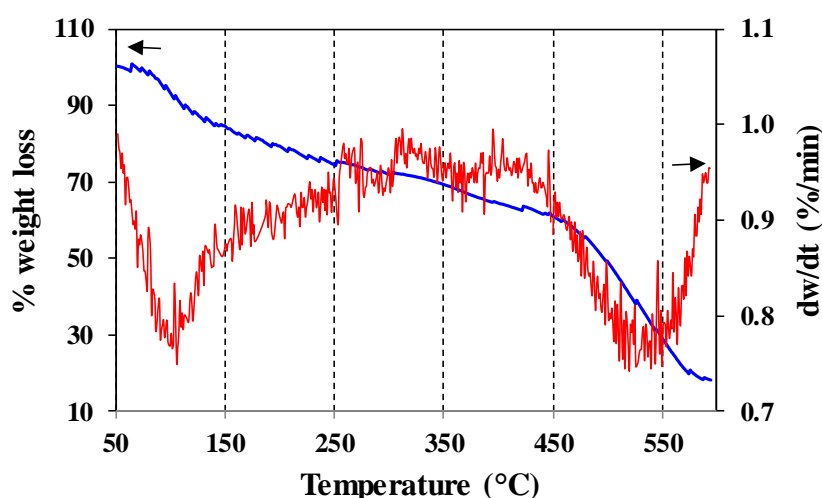


**Figure 3-5.** Thermogravimetric curve and its derivative curve of the synthesized Mg-MOF-74.

### ***b. Improvement of washing processes***

Mg-MOF-74 powder was successfully synthesized and confirmed by the PXRD result, which was in agreement with the diffractions calculated from the reference structure available in Cambridge Crystallographic Data Centre (CCDC, FIJDOS 265095) [25]. In order to assess the quality of the material produced from the first-batch synthesis, ensuring the efficiency of MOF pore activation,  $\text{CO}_2$  adsorption isotherms were measured at 1 bar and  $25\text{ }^{\circ}\text{C}$ . It is observed that the  $\text{CO}_2$  uptake of the first adsorption cycle is  $0.34\text{ mmol}\cdot\text{g}^{-1}$  at 1 bar, which is far below the reported value of  $5.08\text{ mmol}\cdot\text{g}^{-1}$  of the well-known work of Caskey *et al.* (2008) at the same operational conditions [18]. The sample was outgassed and the following adsorption/desorption cycles were performed resulting in the slight progressive increment in  $\text{CO}_2$  uptakes:  $0.38\text{ mmol}\cdot\text{g}^{-1}$  (second) and  $0.85\text{ mmol}\cdot\text{g}^{-1}$  (third). This observation figures that the solvent evacuation has been incomplete during the synthesis procedure because some micropores have been activated in the progressive

outgassing upon multiple adsorption/desorption cycles. It means that the washing processes of MOFs in which the reactive media, especially DMF “pore template”, which should have been removed, was not carried out properly. Then, the washing processes were repeated for the same sample followed by solvent evacuation. It is observed that the CO<sub>2</sub> uptake has increased to 1.22 mmol·g<sup>-1</sup>, but the value is still further away from the expectation even after successive washing repetitions. It is understood that the technique of the washing processes needs improvement.

For the second-batch synthesis, centrifugal separations were introduced at two different points as shown in Figure 3-2: (1) between reaction and product washing, with the aim of removing the reactive media from the MOF powder after the reaction, and, (2) between product washing and solvent evacuation, with the aim of separating the polluted methanol from the MOF powder after the product washing. Two Mg-MOF-74 samples were synthesized in the second-batch synthesis; one was prepared with the addition of centrifugation 1 and another one with centrifugations 1 and 2. The effect of centrifugal separations on the pore activation of the MOFs was then assessed by performing CO<sub>2</sub> adsorption measurement at 1 bar and 25 °C. The results were presented in Figure 2 comparing the isotherm of the first-batch sample with washing repetitions (red). At 1 bar, the second-batch samples display higher CO<sub>2</sub> uptake with 3.70 mmol·g<sup>-1</sup> for centrifugation 1 (blue) and 5.80 mmol·g<sup>-1</sup> for centrifugations 1 and 2 (green). The final value is comparable to the above-mentioned literature data. It shows that the introduction of the centrifugal separation technique to the synthesis routes at two points has evidently improved the separation in the washing processes.

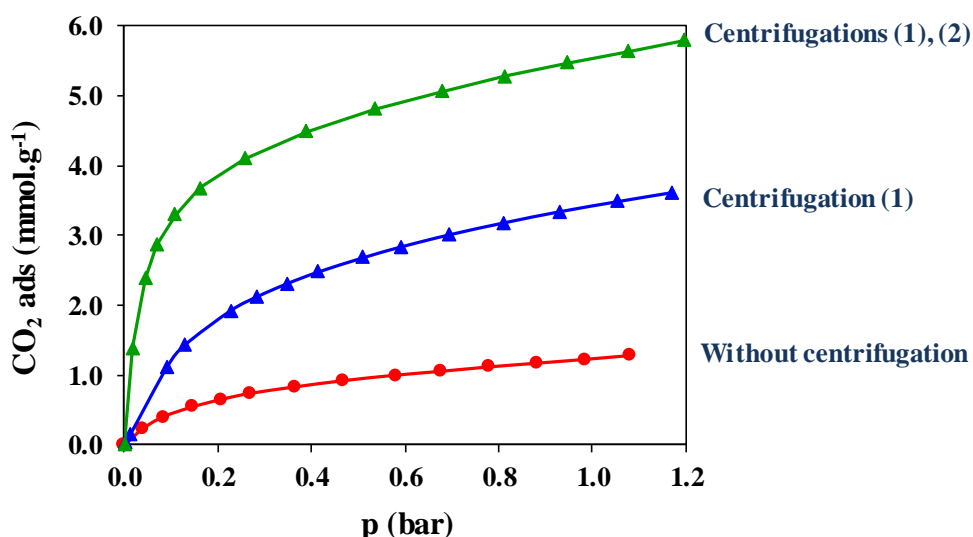


**Figure 3-6.** CO<sub>2</sub> adsorption isotherms of Mg-MOF-74 samples from the first-batch synthesis after washing repetitions (red) and the second-batch synthesis with centrifugation 1 (blue) and centrifugations 1 and 2 (green), at 1 bar and 25 °C.

The characterization of materials was carried out using FTIR to analyze the organic chemical structure of the samples as a function of centrifugal separation as presented in Figure 3-7. The red, blue, and green spectra represent the reaction products before centrifugation, after centrifugation 1, and after centrifugations 1 and 2, respectively. All samples have the same characteristic peaks of symmetric (1570 cm<sup>-1</sup>) and asymmetric (1430 cm<sup>-1</sup>) stretching vibrations of carboxylate groups [157], which are the functional groups of DOT linkers that act as organic fragments in MOF-74 materials. By applying the same resolution and conditions of acquisition of the analysis, it is noticed that the green and blue spectra produce peaks with higher intensities whereby the intensity in FTIR spectroscopy is directly proportional to the concentration of molecules of interest in a sample [158]. The equation that relates concentration to absorbance is known as Beer's law which is presented below [159]:

$$A = \varepsilon \cdot l \cdot c$$

where  $A$  is absorbance,  $\varepsilon$  is absorptivity,  $l$  is path length, and  $c$  is concentration. Thus, it indicates that the concentrations of molecules of MOFs in the sample are significantly improved after centrifugal separation. The reason behind this is probably due to the loss of impurities (residual reactants and remaining solvents) that had been separated by centrifugal separation, leading to higher purity or concentration of MOFs in the sample. The feeble intensities in the red spectrum give rise to the oscillating small peaks in C–H bending regions, so that the two characteristic peaks of Mg-MOF-74 at 1120 cm<sup>-1</sup> (in-plane

bending) and  $590\text{ cm}^{-1}$  (out-of-plane bending) are not visible. Despite exhibiting different values of adsorption capacity, it can be seen that there was no significant difference in FTIR spectra between the second-batch samples after centrifugation 1 and after centrifugations 1 and 2, indicating that the impurities have been largely removed from both samples. The impurities that were present after centrifugation 1 were considerably negligible to the overall concentration of MOFs, producing similar spectra as the sample after centrifugations 1 and 2. On the other hand, it can be understood that the step of classical product washing (immersion in methanol for 3 days) was not able to “wash” the contaminated MOF products as it was the case for the first-batch sample.

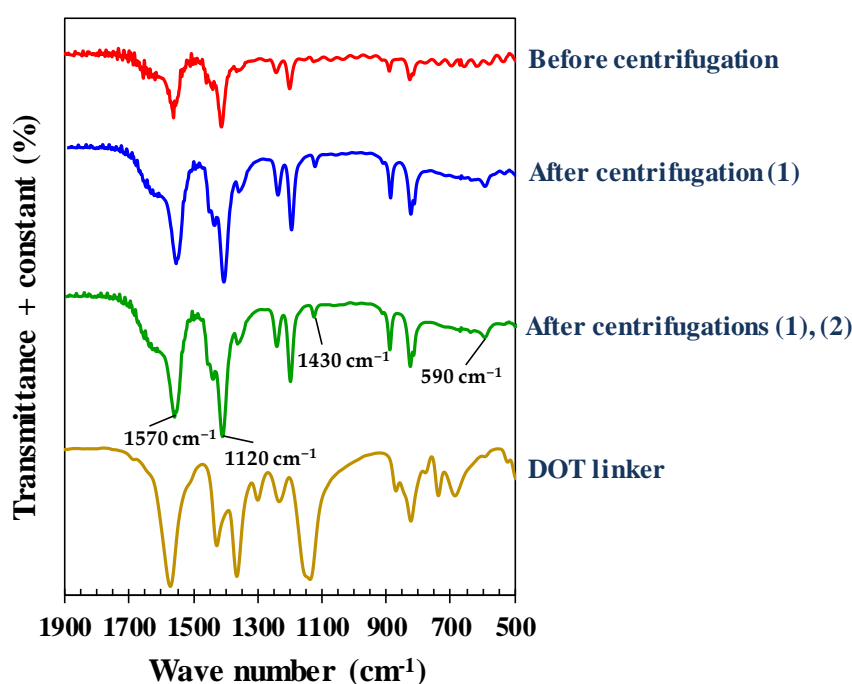


**Figure 3-7.** FTIR spectra of Mg-MOF-74 samples before centrifugation (red), after centrifugation 1 (blue), and after centrifugations 1 and 2 (green), with the spectrum of 2,5-dihydroxyterephthalic acid linker (brown).

PXRD analysis was performed to analyze the crystalline structure of Mg-MOF-74 samples prepared before and after the optimization of the synthesis routes. As presented in Figure 3-8, the samples from the first-batch synthesis and the second-batch synthesis with centrifugation 1 and 2, produce similar reflections characteristic of Mg-MOF-74. However, it is observed that the level of background noises indicating the amount of amorphous phases in the sample have been significantly decreased after centrifugations, indicating the enhancement in crystallinity of the frameworks [30, 41, 42, 146, 160, 161]. The relative

amorphicity in the first-batch sample may be attributed to the presence of residual reactants, especially soluble salts and DOT linkers that consist of similar diffraction atoms with those in the frameworks. It is reported in various fields of application of MOFs that the intensity of XRD reflections of MOFs charged with organic compounds decreased in comparison to the bare MOFs due to the increment in amorphicity [30, 41, 42, 146, 160, 161]. Besides that, the presence of some reflections in the first-batch samples, which do not belong to Mg-MOF-74 (marked with blue triangles), signify the interference of impurities. This observation is in accordance with FTIR analysis as well as CO<sub>2</sub> adsorption measurements whereby the centrifugations have improved the separation leading to the effective MOF pore activation and thus satisfy gas adsorption uptake. In order to assess the crystallographic data of the final sample from the second-batch synthesis, Rietveld refinement of the unit cell was carried out using PANalytical X'Pert HighScore Plus software, which was done by the least squares fit method through the angular differences between measured reflections (green) and indexed reflections (yellow). The procedure of the refinement using the software is detailed by Scott A. Speakman from MIT Center for Materials Science and Engineering [162]. The results reveal the best fit simulation affording a nearly perfect-zero difference plot (blue) with an acceptable value of fitting goodness. As presented in Table 3-3, the final sample exhibits comparable values of lattice parameters of the unit cell to the reference structure, which are given in Angstrom (Å) and considered accurate to  $\pm 3$  (for  $a$  and  $b$ ) and  $\pm 1$  (for  $c$ ) in the last reported decimal.

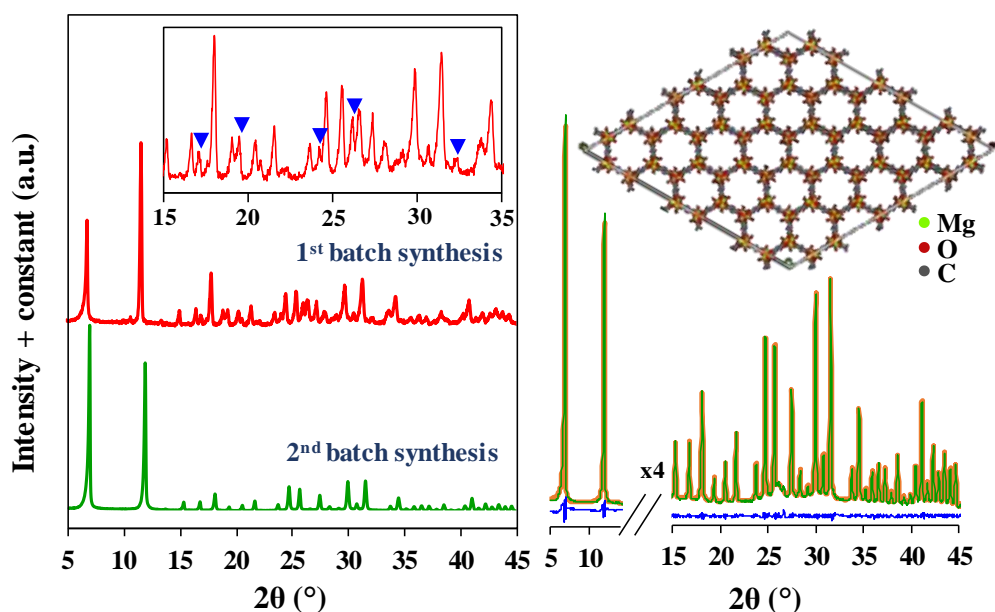


**Figure 3-8.** (left) PXRD reflections of Mg-MOF-74 from the first-batch synthesis (red) and the second-batch synthesis with centrifugations 1 and 2 (green). (right) Results of Rietveld refinement of the second-batch sample. Green, yellow, and blue lines represent experimental data, indexed reflections of molecular structure of Mg-MOF-74, and difference plot, respectively.

**Table 3-3.** Crystallographic data of the synthesized Mg-MOF-74 deduced from Rietveld refinement.

	Mg-MOF-74 of the second-batch synthesis	Calculated from molecular structure [25]
<b>Crystal system</b>	Trigonal (hexagonal axes)	
<b>Angles</b>	$\alpha = \beta = 90^\circ, \gamma = 120^\circ$	
<b>Space group</b>	R-3	
<b>Lattice parameters:</b>		
$a = b$ (Å)	26.009 ( $\pm 3$ )	26.026
$c$ (Å)	6.777 ( $\pm 1$ )	6.759
<b>Unit cell volume (Å<sup>3</sup>)</b>	3970	3965
<b>R<sub>exp</sub></b>	2.39	
<b>R<sub>p</sub></b>	3.32	
<b>R<sub>wp</sub></b>	4.67	
<b>Goodness of fitting</b>	1.95	

**Table 3-4.** Stages of improvement of washing processes in solvothermal synthesis in this work.

Stage	Synthesis	CO <sub>2</sub> adsorption capacity at 1 bar and 25 °C	Observation
1	First-batch synthesis	From 0.34 mmol·g <sup>-1</sup> to 0.85 mmol·g <sup>-1</sup> after three successive adsorption cycles	Activation of some micropores by progressive outgassing.
2	First-batch synthesis with washing repetitions	1.22 mmol·g <sup>-1</sup>	Activation of some micropores by more times of washing.
3	Second-batch synthesis with centrifugation 1	3.70 mmol·g <sup>-1</sup>	Good separation of reactive media from MOF powder.
4	Second-batch synthesis with centrifugations 1 and 2	5.80 mmol·g <sup>-1</sup>	Good separation of reactive media and washing solvents from MOF powder.

### *c. Metal nodes tuning*

Based on the literature review in Section 2.5.3, Mg-MOF-74 appears as the most performing material for CO<sub>2</sub> adsorption among other MOF-74 series, thus it was selected and synthesized as the experimental material for the purpose of improving the synthesis. By using the improved synthesis routes and the same synthesis parameters, other M-MOF-74 series namely Ni-MOF-74, Zn-MOF-74 and Co-MOF-74 were prepared to ensure the reproducibility of the synthesis processes for other MOF materials and to confirm the selection of Mg-MOF-74. The characterization results show that all synthesized samples exhibit similar crystallography and chemical structure with those of Mg-MOF-74 as shown by their PXRD reflections in Figure 3-9 and FTIR spectra in Figure 3-10.

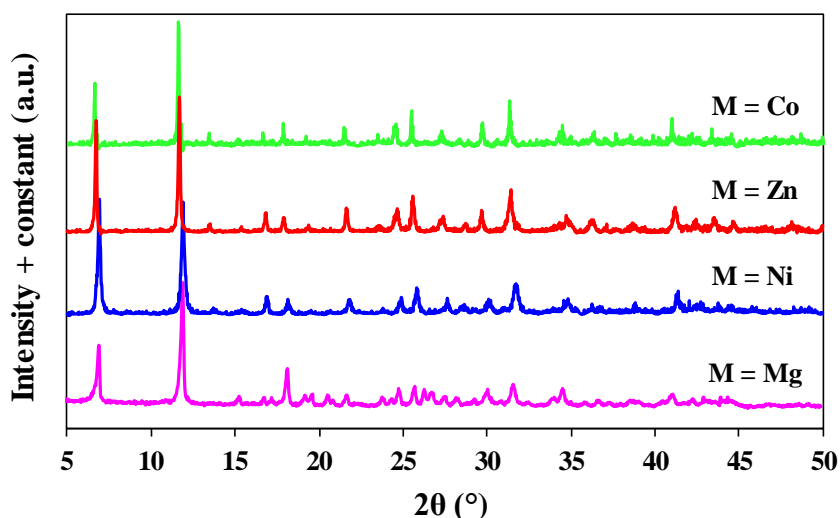


**Figure 3-9.** PXRD reflections of M-MOF-74 series of this work, where M=Mg, Ni, Zn, Co.

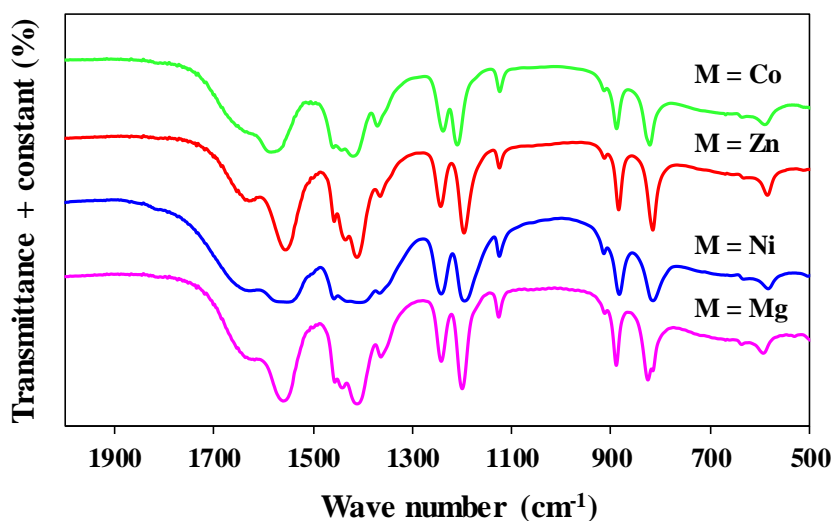


**Figure 3-10.** FTIR spectra of M-MOF-74 series of this work, where M=Mg, Ni, Zn, Co.

A screening study of CO<sub>2</sub> adsorption performance of the M-MOF-74 series was performed at 1 bar and 25 °C. The results presented in Figure 3-11 shows that Ni-MOF-74 achieves the highest CO<sub>2</sub> adsorption uptake among the MOF-74 series with 5.80 mmol·g<sup>-1</sup>, followed by Mg-MOF-74 with 5.61 mmol·g<sup>-1</sup>, and, both Zn-MOF-74 and Co-MOF-74 with 4.60 mmol·g<sup>-1</sup>. The difference in CO<sub>2</sub> adsorption uptake of these four M-MOF-74 series was reported elsewhere [18, 37, 123], resulting from two reasons: (i) different specific surface areas ranging from 599 to 1525 m<sup>2</sup>·g<sup>-1</sup> due to the different metal atomic weight, and also, (ii) different metal affinity towards CO<sub>2</sub> affording different number of adsorbed CO<sub>2</sub> per unit cell.

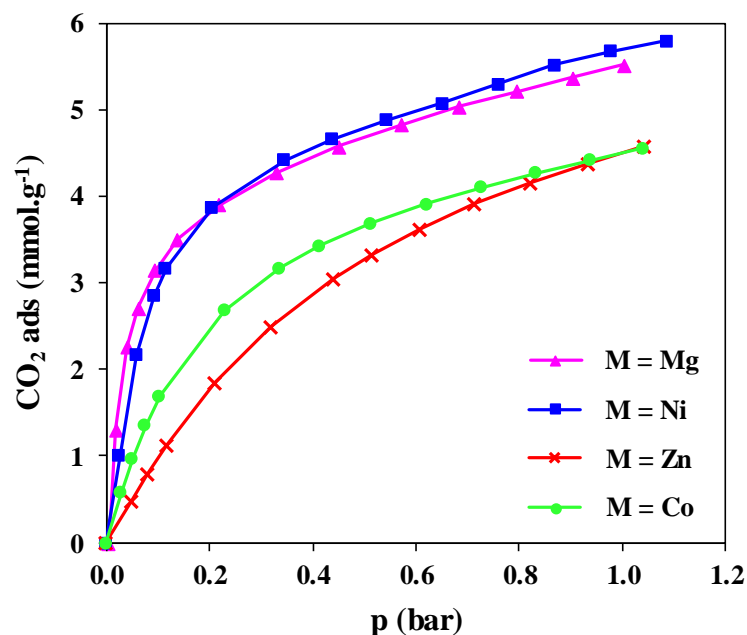


**Figure 3-11.** CO<sub>2</sub> adsorption isotherm of M-MOF-74 series of this work at 1 bar and 25 °C, where M=Mg, Ni, Zn, Co.

Table 3-5 summarizes the comparison results of CO<sub>2</sub> adsorption uptake of MOF-74 series of this work to the literature data for different metal nodes at 1 bar and 25 °C. It can be seen that the synthesized materials figure the encouraging results and competitive to the existing reported data. The result achieved by Ni-MOF-74 of this work is higher than that reported by the well-known work of Caskey *et al.* (2008) [18] (5.08 mmol·g<sup>-1</sup>) and some others' data, indicating the effectiveness of the improved synthesis routes. Meanwhile, despite being denoted as the landmark for CO<sub>2</sub> adsorption, this work was not able to reproduce Mg-MOF-74 with the satisfying adsorption uptake and it was far below the literature data. One of the challenges of developing MOF materials is the reproducibility of adsorption results and the high sensitivity of synthesis outcome to minor changes of experimental conditions including not only the concentration of reactive media but also homogeneity and heating rate, generated pressure and agitation. Exposed Mg sites inside MOF-74 micropores are highly reactive, especially to humidity, owing to the strong interaction towards O atom from H<sub>2</sub>O to complete the coordination sphere of Mg. Thus even exposure and manipulating MOF materials can influence their properties at different time scales. In any cases, Mg-MOF-74 is still preferable as the pristine material for this work seen that its CO<sub>2</sub> adsorption (5.61 mmol·g<sup>-1</sup>) is very close to that of Ni-MOF-74 (5.80 mmol·g<sup>-1</sup>), with the commercial price of Mg (II) nitrate hexahydrate (RM0.36/g) is four times cheaper than that of Ni (II) nitrate hexahydrate (RM1.38/g). Therefore, specifically

for this work, Mg-MOF-74 is more economic in terms of production cost when compared to Ni-MOF-74 with the slightest difference in gas adsorption capacity.

**Table 3-5.** Comparison results of CO<sub>2</sub> adsorption capacity of MOF-74 series of this work at 1 bar and 25 °C to the literature data. The values are presented in mmol·g<sup>-1</sup>.

Ni-MOF-74	Mg-MOF-74	Zn-MOF-74	Co-MOF-74	Ref.
5.80	5.61	4.60	4.60	This work
5.08	7.52	6.30	5.00	[18]
4.00	-	-	3.38	[37]
3.75	8.50	-	-	[148]
2.50	-	-	-	[17]
-	7.99	-	-	[23]
-	8.41	5.45	-	[123]

### 3.5.2. Production yield

As the product, Mg-MOF-74 was obtained in light yellowish fine powder which agreed with reported elsewhere [19]. After washing and solvent evacuation process, approximately 350 mg of final MOF sample was produced in one-batch reaction with a basic yield calculation showing that the production reached 85%, presented as follows:

Theoretical:



Experimental:



Production yield:

$$(1.66/1.96) \cdot 100\% = 85\%, \text{ considering the product was purely MOFs.}$$

## 3.6. Synthesis of MOF-74-carbon composites: Results and discussions

### 3.6.1. Characterization for optimizing the concentration

As mentioned previously, for an *in situ* synthesis of MOF-based materials, an appropriate amount of carbon doping material must be determined to avoid excessive

interference that may ruin MOF structure and adversely affect the performance of the material. Therefore, by using only GO as the doping agent, the same synthesis parameters and the improved synthesis routes, the following study was conducted. In the first stage, the amount of GO substitution was varied from 10 wt% to 20 wt% of the weight of the produced composites. As the results, some observations were noted after the reaction: (i) there was no formation of MOF particles because there was no solid attached to the wall of the reactor as MOFs should, (ii) there was a lot of remaining GO in form of suspension which did not undergo chemical reaction, and, (iii) there was some unidentified precipitation which was white in color, not sticky to the wall and less dense unlikely MOF particles. Thus, it was understood that the GO substitution amount was too excessive retarding the reaction to take place. In the second stage, the GO amount was varied from 1 wt% to 6 wt% of the weight of the produced composites. MOF particles were successfully produced after the reaction with the presence of the remaining GO. The materials were then characterized using PXRD analysis in which the measurement was done for three times of different samplings to confirm the reproducibility of the results for all MOF powders. Their PXRD reflections in Figure 3-12 show that they exhibit Mg-MOF-74 crystal structure, but the defects occur progressively by the increasing amount of GO. Although the crystallinity of the materials is explained by the sharpness of XRD reflections, not the intensity of the reflections, the diminution in XRD reflections intensities due to the loading of organic compounds in MOFs has been mentioned in many published works [30, 41, 42, 146, 160, 161]. They reported that MOF composites doped with carbonaceous agent present lower intensity of XRD reflections compared to the pristine material. Knowing that carbonaceous agents are amorphous, thus in certain cases such as in this study, the diminution in intensities can be related to the properties of less crystallinity of MOFs, by which the reduced intensities give higher ratio value of background noise to XRD reflections intensities. The CO<sub>2</sub> adsorption was then performed on the samples at 1 bar and 25 °C for three times each measurement. Figure 3-13 display that their CO<sub>2</sub> isotherms are inferior to the pristine Mg-MOF-74, demonstrating that the GO amount should be further reduced.

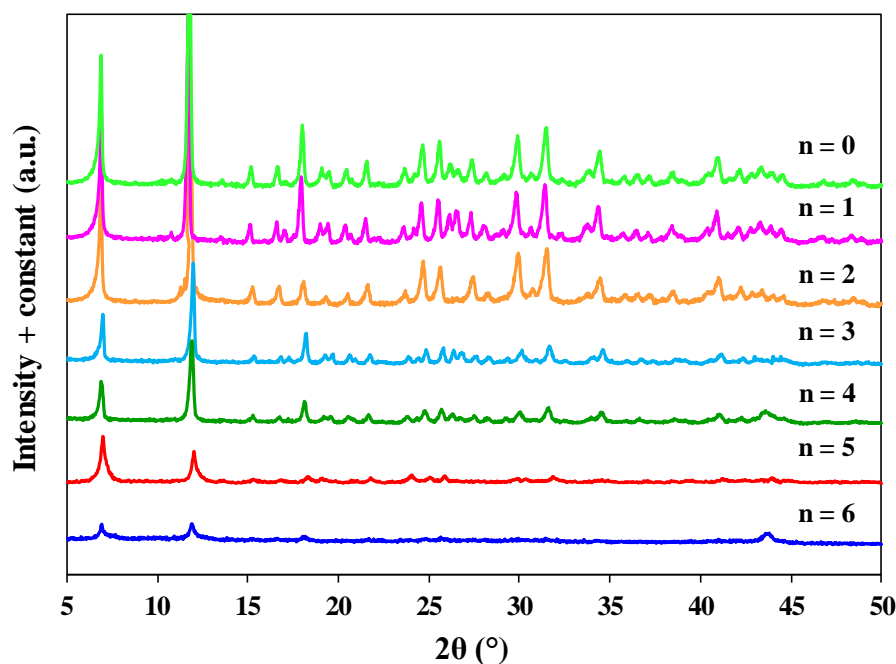


Figure 3-12. PXRD reflections of Mg-MOF-74@nGO series, where  $n = 0-6$  wt%.

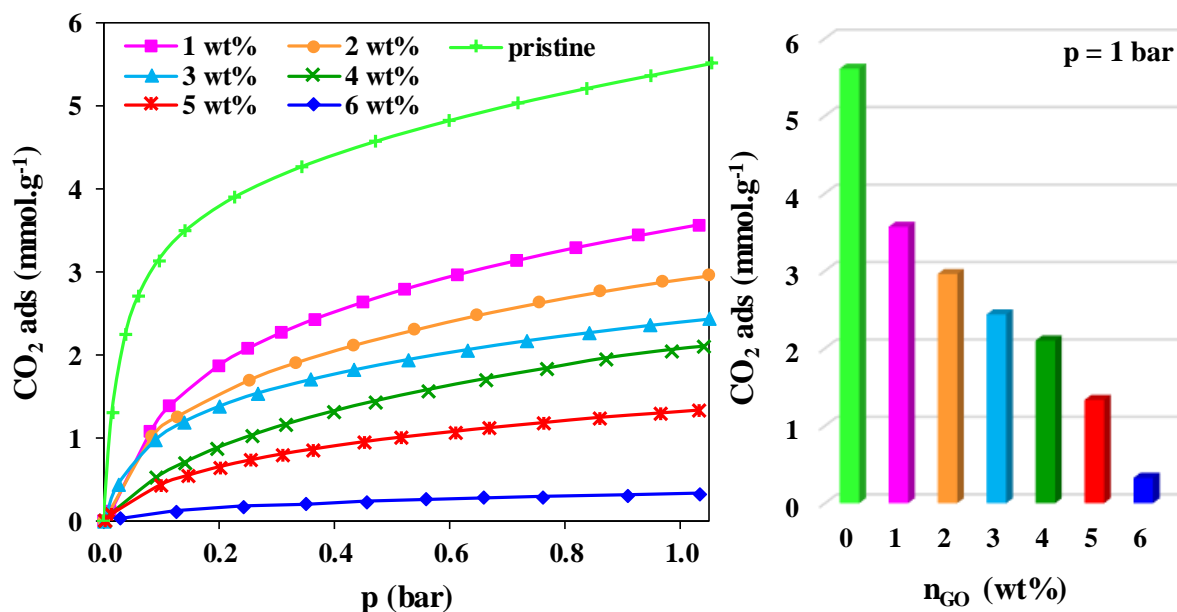
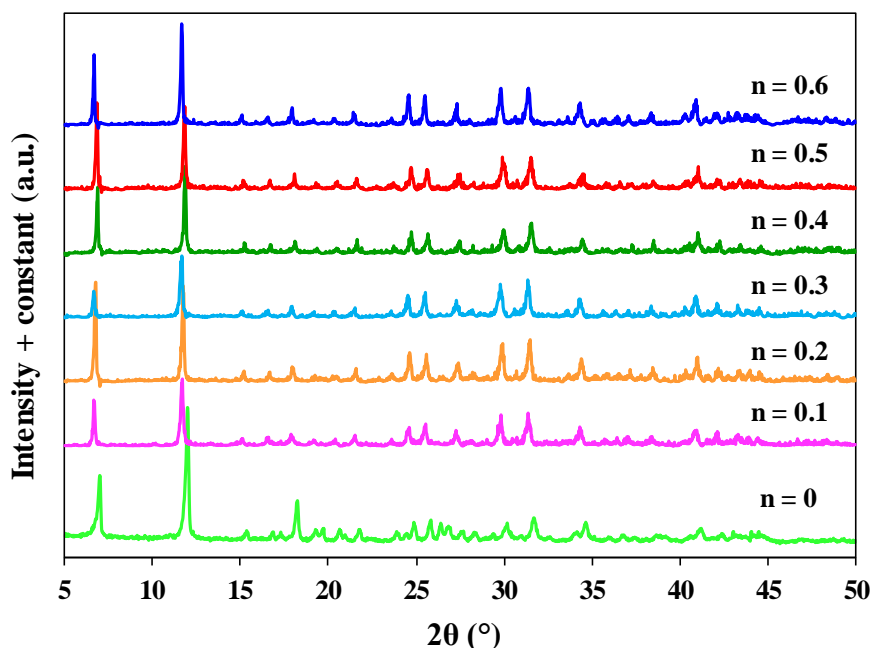


Figure 3-13. (left)  $\text{CO}_2$  adsorption isotherms and (right)  $\text{CO}_2$  adsorption capacity of Mg-MOF-74@nGO series, at 1 bar and  $25^\circ\text{C}$  where  $n = 0-6$  wt%.

In the third stage, the GO amount was varied from 0.1 wt% to 0.6 wt% of the weight of the produced composites. Their PXRD reflections in Figure 3-14 and FTIR spectra in Figure 3-15 show that they have the same Mg-MOF-74 crystal structure and chemical functionality. Interestingly, the results of their  $\text{CO}_2$  adsorption isotherms at 1 bar and  $25^\circ\text{C}$  in Figure 3-16 were encouraging, whereby some were superior to the pristine Mg-MOF-74, with the optimum amount of approximately 0.3 wt%. As the conclusion,  $\approx 0.3$  wt%

(equivalent to 30 mol%) was employed as the substitution concentration for producing Mg-MOF-74@CNT and Mg-MOF-74@GO composites in this work. The same incorporation amount for CNT was decided for the purpose of comparison. One should keep in mind that it is the optimum concentration on the basis of GO determined from a single criterion; CO<sub>2</sub> adsorption capacity.



**Figure 3-14.** PXRD reflections of Mg-MOF-74@nGO series, where n = 0–0.6 wt%.

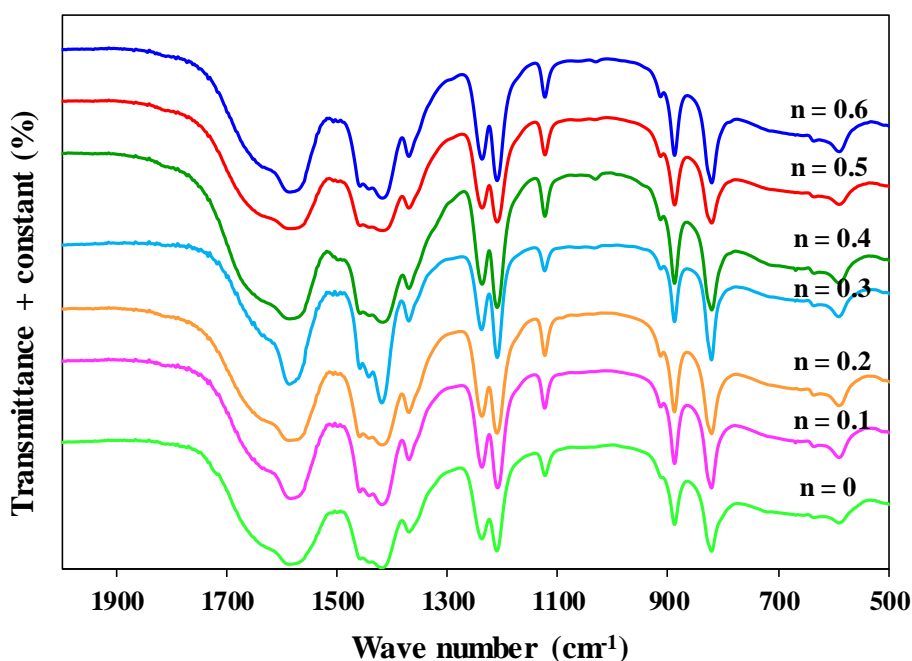


**Figure 3-15.** FTIR spectra of Mg-MOF-74@nGO series, where n = 0–0.6 wt%.

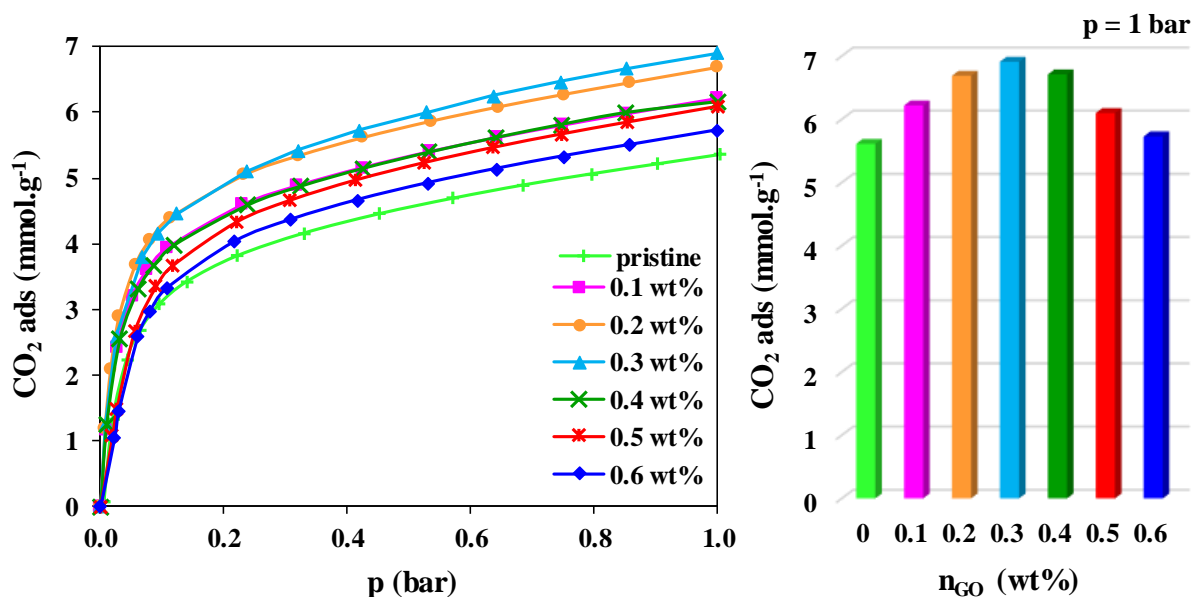


**Figure 3-16.** (left) CO<sub>2</sub> adsorption isotherms and (right) CO<sub>2</sub> adsorption capacity of Mg-MOF-74@nGO series, at 1 bar and 25 °C where n = 0–0.6 wt%.

### 3.6.2. Production yield

As the products, Mg-MOF-74@CNT and Mg-MOF-74@GO embedded with  $\approx 0.3$  wt% of carbon doping agent representing 1.05 mg of approximately 350 mg of the materials, were obtained in slightly dark yellowish powder exhibiting as same production yield as the pristine Mg-MOF-74 which was 85%. Figure 3-17 shows the images of the synthesized MOF powder.

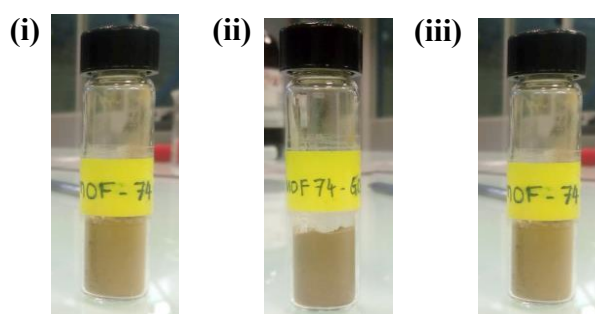


**Figure 3-17.** The images of the synthesized (i) Mg-MOF-74, (ii) Mg-MOF-74@CNT and (iii) Mg-MOF-74@GO. The composites were prepared with  $\approx 0.3$  wt% of carbon doping agent.

## 3.7. Characterization of selected materials: Results and discussions

### 3.7.1. Crystal structure of materials

As shown in Figure 3-18, the XRD reflections of the pristine Mg-MOF-74 and its

carbon composites, Mg-MOF-74@CNT and Mg-MOF-74@GO, exhibit sharp characteristic peaks at  $6.9^\circ$ ,  $11.9^\circ$ ,  $13.7^\circ$ ,  $15.3^\circ$ ,  $16.8^\circ$ ,  $18.1^\circ$ ,  $19.4^\circ$ ,  $20.5^\circ$ ,  $21.7^\circ$ ,  $23.8^\circ$ ,  $24.7^\circ$ ,  $25.7^\circ$ ,  $26.6^\circ$ ,  $27.5^\circ$ ,  $28.4^\circ$ ,  $29.2^\circ$ ,  $30.0^\circ$ ,  $30.8^\circ$ ,  $31.6^\circ$ ,  $33.8^\circ$  and  $34.5^\circ$  being in a perfect agreement with those calculated from the reference structure (CCDC, FIJDOS 265095) [25]. Well-defined sharp peaks of XRD reflection of all three samples confirm that Mg-MOF-74 and its composites have good crystallinity. However, qualitative comparison of experimental data for the Mg-MOF-74 composites with that of the pristine material reveals a light narrowing and intensity diminishing of principal peaks at  $6.9^\circ$  and  $11.9^\circ$  suggesting that the doping implies some structural defects. The presence of CNT and GO featuring characteristic XRD signals at  $11.9^\circ$  and  $26.1^\circ$ , respectively, could not be detected in the Mg-MOF-74 composites by this analysis. In order to get access to lattice parameters, Rietveld refinement of XRD reflections was performed using PANalytical X'Pert HighScore Plus software, which was done by the least squares fit method through the angular differences between measured reflections (blue) and indexed reflections (red). The profile fitting requires the best fit simulation affording nearly perfect-zero difference plot (green) and the results are as summarized in Table 3-6 together with their fitting goodness parameters. All synthesized materials exhibit the values of lattice parameters close to those calculated from reference molecular structure from the database. It means that the original lattice structure is well-preserved, indicating that the formation of Mg-benzenedicarboxylate (Mg-BDC) was not ruptured by the carbon doping agents. Also presented in Table 3-6, the average crystal size and micro strain of the materials were calculated using Williamson-Hall plot method available in the software. In terms of crystal size, the Mg-MOF-74 composites appear with larger average crystallite in compared to the pristine material suggesting that the carbonaceous doping agent does influence the crystal growth processes. Both Mg-MOF-74 composites have slightly higher micro strain in comparison to the pristine material, but the difference are not really significant to definitely conclude. The procedure of Rietveld refinement and Williamson-Hall plot using the software are detailed by Scott A. Speakman from MIT Center for Materials Science and Engineering [162, 163]. In view of numerous challenges associated with atomic position refinement that might be related to the existence of defects in large-volume lattice cells or the occurrence of preferential orientation of crystallites, a thorough Rietveld refinement [164, 165] of XRD reflections could not be performed.

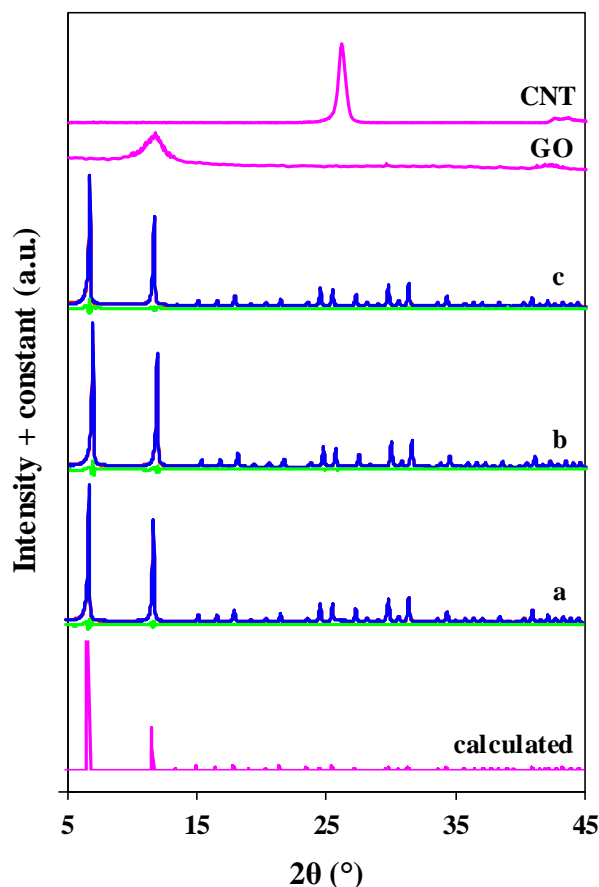


**Figure 3-18.** PXRD reflections of (a) Mg-MOF-74, (b) Mg-MOF-74@CNT and (c) Mg-MOF-74@GO. Blue, red and green lines represent experimental data, fitting of profile refinement and difference plot, respectively.

**Table 3-6.** Crystallographic data of Mg-MOF-74, Mg-MOF-74@CNT and Mg-MOF-74@GO.

	Pristine Mg-MOF-74	Mg-MOF-74 @CNT	Mg-MOF-74 @GO	Calculated from molecular structure [25]
<b>Crystal system</b>	Trigonal (hexagonal axes)			
<b>Angles</b>	$\alpha=\beta=90^\circ, \gamma=120^\circ$			
<b>Space group</b>	R-3			
<b>Lattice parameters</b>				
$a=b$ (Å)	26.009	26.002	25.986	26.026
$c$ (Å)	6.777	6.782	6.777	6.759
<b>Unit cell volume (Å<sup>3</sup>)</b>	3970	3971	3963	3965
<b>Average crystal size (nm)</b>	66.6	72.5	81.7	
<b>Crystal micro strain (%)</b>	0.022	0.041	0.042	
<b>Goodness of fitting</b>	1.95	1.99	1.96	

### 3.7.2. Chemical functionality of materials

The synthesized materials were also characterized by FTIR analysis and interpreted according to Gauglitz *et al.* (2003) [158] and Stuart *et al.* (2004) [157]. Figure 3-19 shows IR spectra of the pristine Mg-MOF-74, both Mg-MOF-74 composites and DOT linker used in the synthesis. The absence of DMF strong peaks in 3000–2700  $\text{cm}^{-1}$  region in MOF spectra confirm that all MOF samples were well-washed from the trace of mother liquor of the reaction. The carboxylate-based DOT linker exhibits broader O–H stretching band in 3700–2340  $\text{cm}^{-1}$  region and stronger C–H alkane stretching vibrations between 3200 and 2500  $\text{cm}^{-1}$ . Both O–H and C–H stretching bands progressively fade during the formation of MOFs. A marginal peak at 1760  $\text{cm}^{-1}$  situated in carbonyl region (1840–1740  $\text{cm}^{-1}$ ) indicates the presence of anhydrides (–CO–O–CO–) before the reaction. A significant peak in DOT linker at 1500  $\text{cm}^{-1}$  is referred to aromatic stretching band of the linker and almost disappears in all MOF spectra. All peaks appeared in 1370–1000  $\text{cm}^{-1}$  region signify in-plane C–H bending whereas those in the lower wavenumber region (1000–500  $\text{cm}^{-1}$ ) indicate out-of-plane C–H bending [157]. It is also observed that symmetric stretching vibrations of carboxylate groups in all samples are shifted to 1590  $\text{cm}^{-1}$  from a lower wavenumber in DOT linker, 1650  $\text{cm}^{-1}$ . Meanwhile, asymmetric stretching vibrations of carboxylate groups in DOT and all samples are observed almost at the same wavelength (1430  $\text{cm}^{-1}$ ). These carboxylate peaks remain visible in all MOF spectra but with a slight shifting and a significant reduced intensity, and also, are more pronounced in the pristine Mg-MOF-74 than those of the composites. A small component of symmetric peak at 1590  $\text{cm}^{-1}$  which is the only characteristic peak distinguishing the DOT linker from MOF samples is observed in Mg-MOF-74 spectrum, indicating the presence of remaining linkers in the sample. In order to study the coordination of carboxylate groups with Mg metal sites, the separation values between the symmetric and asymmetric peaks were calculated,  $\Delta = \lambda_{sym}(\text{COO}^-) - \lambda_{assym}(\text{COO}^-)$  [166]. For  $\Delta > 200 \text{ cm}^{-1}$  and  $\Delta < 110 \text{ cm}^{-1}$ , monodentate and bidentate ligands are respectively expected, while  $\Delta$  in the order of 138–200  $\text{cm}^{-1}$  represents bridging ligands [166]. The calculated value of  $\Delta$  (DOT) is 220 whereas  $\Delta$  (Mg-MOF-74, Mg-MOF-74@CNT, Mg-MOF-74@GO) is 160. It is concluded that the carboxylate groups in DOT linker existed in form of monodentate ligands while in MOFs, the carboxylate groups were deduced binding with Mg cations to form bridging ligands of the framework. Therefore, the formation of the pristine Mg-MOF-74 and the composites were confirmed having similar chemical structure of BDC ligands which differed from that of

DOT before the reaction. The coordination of DOT ligands joining by metal oxide SBUs to form three-dimensional MOF-74 crystal structure with one-dimensional hexagonal channels was described by Deng *et al.* (2012) in Figure 3-20 [167].

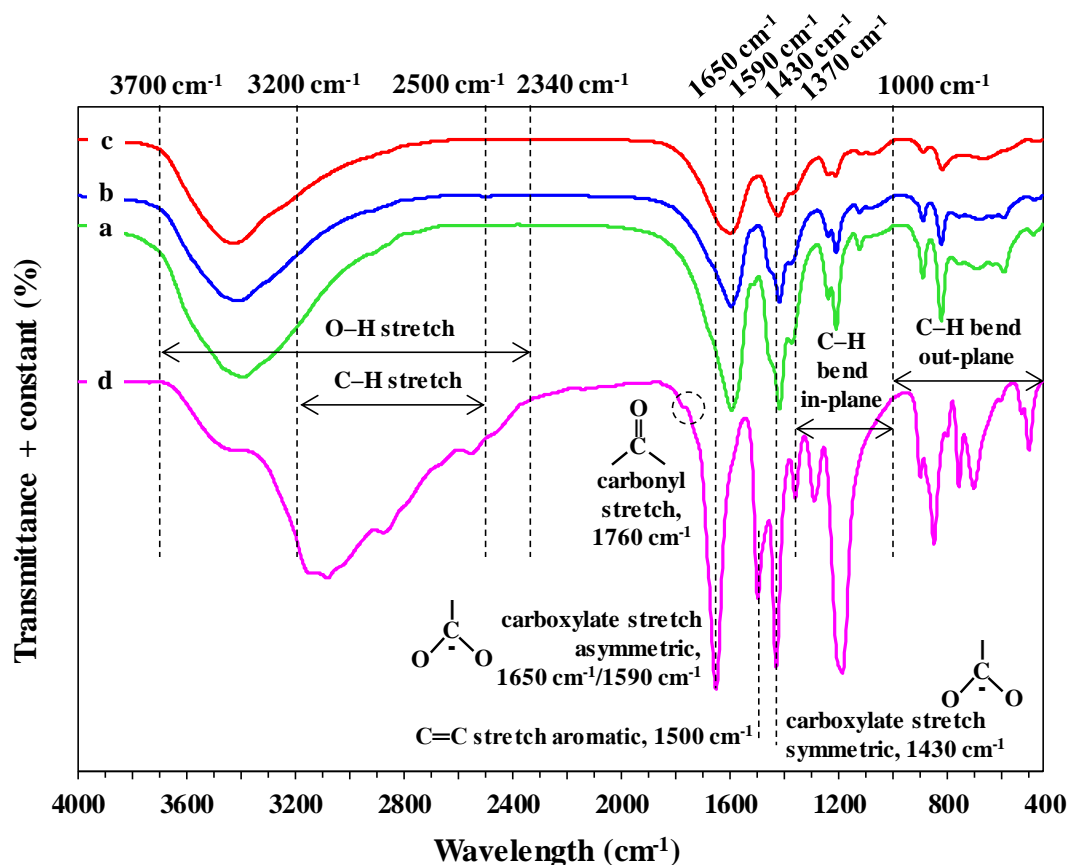


**Figure 3-19.** FTIR spectra of (a) Mg-MOF-74, (b) Mg-MOF-74@CNT, (c) Mg-MOF-74@GO and (d) 2,5- dihydroxyterephthalic acid linker.

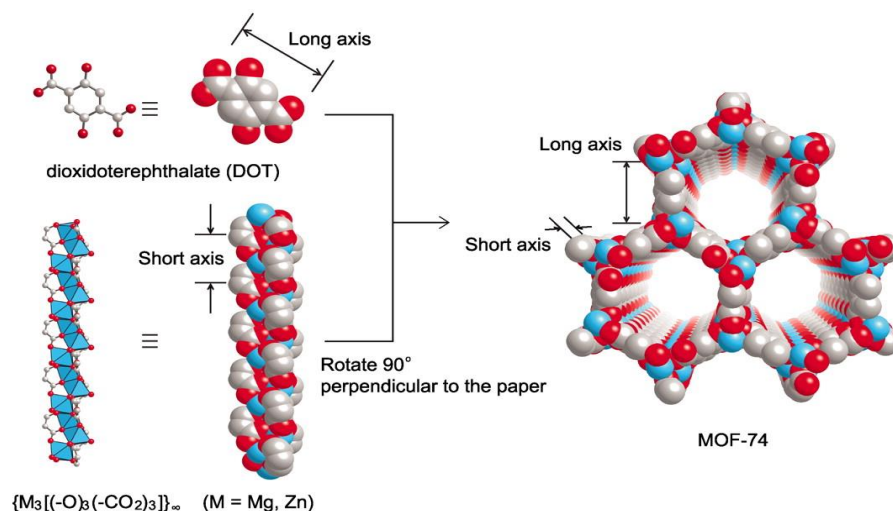


**Figure 3-20.** The coordination of DOT ligands joining by metal oxide SBUs to form 3D MOF-74 crystal structure with 1D hexagonal channels [167].<sup>38</sup>

Another chemical structure characterization, Raman spectroscopy analysis, also was performed with the aim of detecting the presence of carbon doping agent in Mg-MOF-74 composites. Knowing that both CNT and GO should have characteristic bands of carbonaceous materials: G-band, D-band and G'-band in Raman spectra, the analysis was carried out for CNT, GO, DOT linker and all MOF samples. The results are presented in Figure 3-21. Unfortunately, the same characteristic bands were already present in DOT linker spectrum and thus in the MOF spectra. Therefore, as same as FTIR and PXRD analysis, Raman analysis was also not able to detect the presence of doping materials.

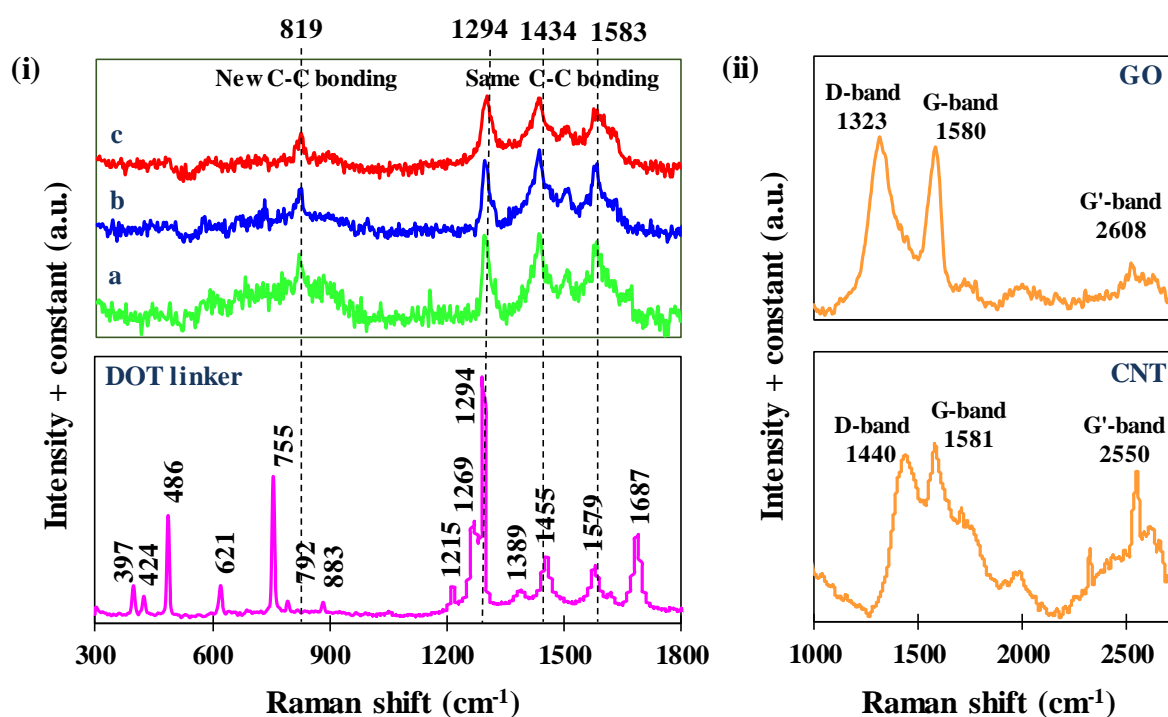


**Figure 3-21.** (i) Raman spectra of (a) Mg-MOF-74, (b) Mg-MOF-74@CNT, (c) Mg-MOF-74@GO and (d) 2,5- dihydroxyterephthalic acid linker and (ii) characteristic bands of carbonaceous materials in Raman spectra of GO and CNT.

<sup>38</sup> Reprinted from Science, H. Deng *et al.*, Large-pore apertures in a series of metal-organic frameworks, vol. 336, no. 6084, pp. 1018-1023, Copyright 2012, with permission from American Association for the Advancement of Science.

### 3.7.3. Morphology of materials

As seen in Table 3-6, the increase of average crystal size indicates the addition of carbonaceous material has altered physical morphology of Mg-MOF-74. However, the amount of substitution is too low to be detected by spectroscopy measurement as well as X-ray diffractometer. Therefore, to further investigate and confirm the success of substitution of carbon doping agent, the morphology of the synthesized materials was studied using FESEM analysis. The micrograph images are shown in Figure 3-22. They exhibit irregular sizes of hexagonal cylindrical crystallite-like particles which are supposedly referred to the original shape of Mg-MOF-74 (Figure 3-22-i,ii,iii). However, particle size distribution in the samples is notably different where MOF particles grow a bit larger with the addition of CNT and much larger with GO. The estimation over 30 particles in 83x114  $\mu\text{m}$  image showed that the samples display very wide population of particle sizes of 10–40  $\mu\text{m}$ . Average particle sizes of single specimen of Mg-MOF-74 (Figure 3-22-i), Mg-MOF-74@CNT (Figure 3-22-ii) and Mg-MOF-74@GO (Figure 3-22-iii) are presented in Table 3-7. Interestingly, a cross-section of the pristine Mg-MOF-74 particle (Figure 3-22-vii) exhibits a complex pattern resembling circular staking of plate-like domains with the characteristic thickness of approximately 60 nm corresponding to crystallite size determined from XRD reflections. Meanwhile, the interdomain voids in Figure 3-22-viii feature the size of mesopores which are in the order of tens of nm. In both Mg-MOF-74 composites, it is noticed that the secondary nucleation of MOF units prevails over the primary growth resulting in pronounced agglomeration of individual particles (Figure 3-22-iv,v,vi). In Mg-MOF-74@CNT, some specimens are found randomly agglomerated due to CNT cross-binding through in-and-out of the framework interlocked with the bridging ligands (Figure 3-22-v). The substitution of CNT occurs along with the formation of Mg–BDC units which made them homogenous and forms agglomerated polycrystalline structure of MOF/CNT (Figure 3-22-ix). The average diameter of the embedded CNT was measured close to 17 nm in accordance with manufacturer's specification (Figure 3-22-x). The micrograph image of pure GO used in the synthesis is shown in Figure A-1 in Annex I. In Mg-MOF-74@GO, some specimens tend to form a choral-like agglomeration of crystallites (Figure 3-22-vi) in which GO layers stack in between the planar cage structure of hexagonal MOF crystallites. The attachment of GO layers at crystallite edges causes their architecture became less sharp (Figure 3-22-xi,xii). Two hypotheses of the synergetic effects between Mg-MOF-74 and GO can be deduced: (i) the growth of some crystals take

place on the layers of GO, and, (ii) oxygen-functional groups in GO interact with Mg-sites, both of which gave rise to polycrystalline formation MOF/GO. In earlier studies, the interaction of O atoms of GO with Cu-sites of octahedral HKUST-1 was mentioned by Zhao *et al.* (2014) [30] and Petit *et al.* (2011) [46] when developed HKUST-1/GO composites. In a bigger picture, MOF/CNT composite figures aleatory morphology which may represent heterogeneous adsorption sites while MOF/GO composite figures more regular morphology which may represent homogenous adsorption sites.

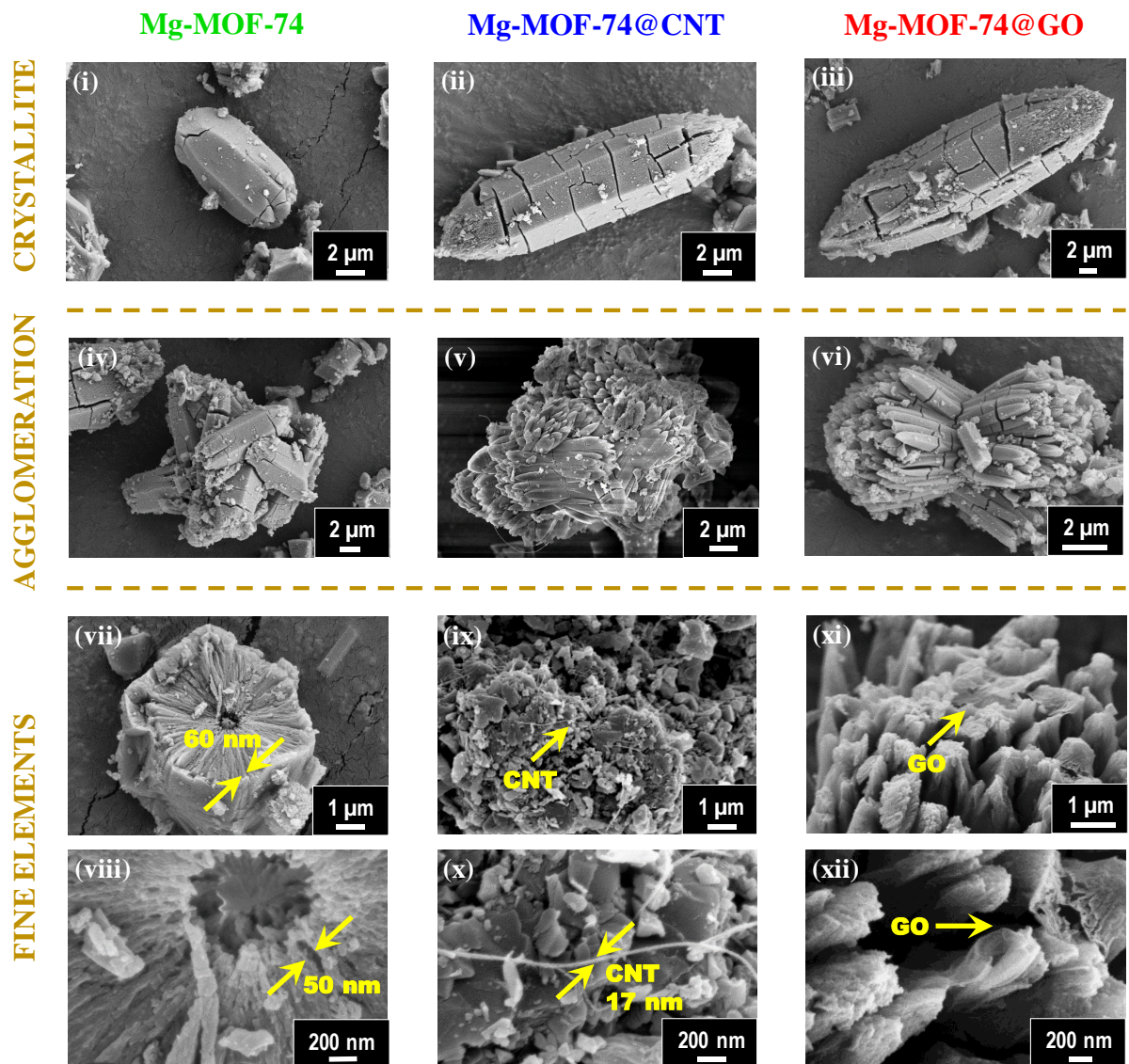


**Figure 3-22.** Micrograph images of Mg-MOF-74, Mg-MOF- 74@CNT and Mg-MOF-74@GO.

EDXS analysis on the surface of the synthesized material reveals slight variances in elementary concentration between the different samples. Passing from the pristine Mg-MOF-74 to the composites, a slight increase in Mg atomic content is observed. It can be

supposed as the result of crystallite external surfaces functionalization with carbon doping agents which explains the modification of their morphology. The atomic concentration of O increases by 6–8% in the composites in comparison to the pristine Mg-MOF-74 while C atomic content diminishes by 7–8%. Knowing that the accuracy of quantitative EDXS analysis of the instrument is given by the order of  $\pm 5\%$ , and that it especially requires specific sample preparation for the case of “light” elements, so this observation cannot be definitely interpreted. However, higher C content in the pristine Mg-MOF-74 may be due to the presence of residual amount of free ligands enclosed in the micropores which agreed with FTIR results (a small peak component at  $1590\text{ cm}^{-1}$  in the pristine material). Meanwhile, higher O content along with higher Mg content in the composites may be due to adsorbed water molecules completing the coordination sphere of additional Mg cations in the composites.

**Table 3-7.** Average particle sizes of single specimen and atomic percentage of elements of Mg-MOF-74, Mg-MOF-74@CNT and Mg-MOF-74@GO.

	Average particle size of single specimen ( $\mu\text{m}$ )	Mg (at%)	O (at%)	C (at%)
<b>Mg-MOF-74</b>	10	8.32	38.73	52.95
<b>Mg-MOF-74@CNT</b>	23	8.77	46.39	44.84
<b>Mg-MOF-74@GO</b>	37	9.74	44.59	45.66

#### 3.7.4. Thermal properties of materials

Thermogravimetric analysis was effectuated in order to evaluate the thermal stability of the synthesized materials. Figure 3-23 illustrates the thermogravimetric plots of all samples which agree well with the profile of the same pristine material in other literature [18]. The derivative curves indicate two notable weight loss steps: (i) 50–250 °C, due to the removal of moisture and guest molecules present in the micropores, and, (ii) above 450 °C, attributed to the decomposition of DOT organic fragments in the material. High thermal stability of Mg-MOF-74 was earlier claimed by Britt *et al.* (2009) stating that it could sustain high temperatures up to 400 °C [23], but the conditions of the intended application may not reach to this level. Regarding the high-temperature domain where the material rupture occurs, it can be realized that the pristine material having more steep trend degrades more rapidly in comparison to carbon-doped composites. The slight nanostructure

modification or defects in Mg-MOF-74@CNT and Mg-MOF-74@GO as revealed in the qualitative and morphological analysis may give advantage on the thermal stability behavior of the composites in comparison to the pristine material.

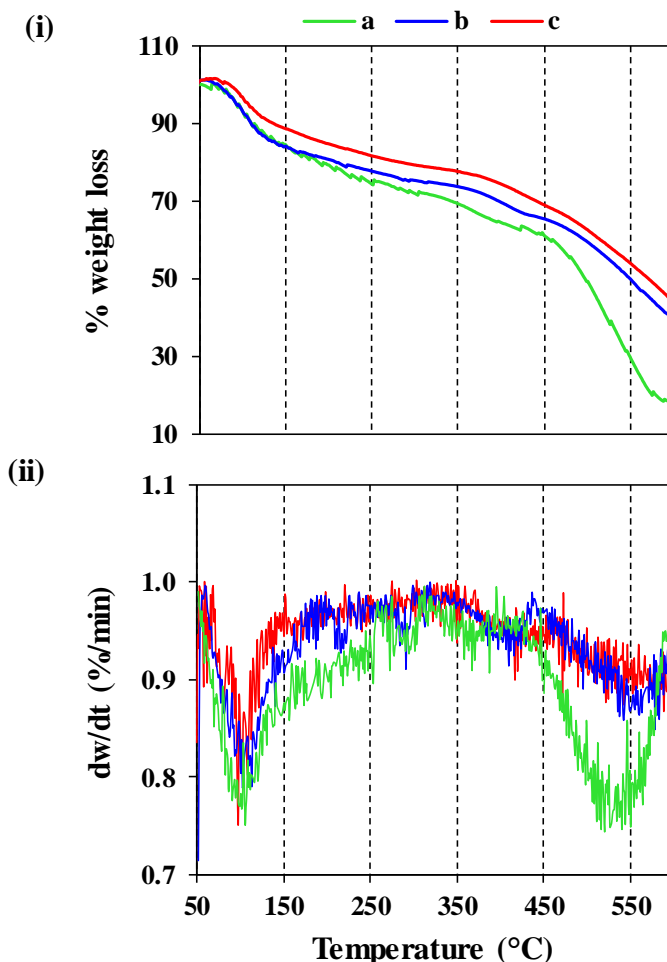


**Figure 3-23.** (i) Thermogravimetric curves and (ii) their derivative curves of (a) Mg-MOF-74, (b) Mg-MOF-74@CNT and (c) Mg-MOF-74@GO.

### 3.7.5. Pore textural properties of materials

N<sub>2</sub> physisorption analysis at 77 K was carried out to assess specific surface areas and pore volumes of the synthesized materials. Figure 3-24-i presents N<sub>2</sub> adsorption/desorption isotherms of all synthesized materials acquired at  $10^{-7} \leq p/p^{\circ} \leq 1$ . The measured data features Type I-Type IV isotherm with a pseudo-plateau at  $10^{-7} \leq p/p^{\circ} \leq 0.1$  suggesting the completion of micropore filling, and marginal hysteresis loop between adsorption and desorption isotherms at  $0.4 \leq p/p^{\circ} \leq 1$  due to the occurrence of capillary condensation which is the characteristic of mesopores. The standard method BET (Brunauer, Emmett, and Teller) model is continuously being used to assess specific surface areas of microporous

materials. The model is reliable to give the apparent value of specific surface area of microporous materials if three consistency criteria are applied (Rouquerol (2007) [168]): (i) the BET constant must be positive indicating the valid range of the BET equation, (ii) the application of the fitting must be limited to the range where  $V(1-p/p^0)$  continuously increases with  $p/p^0$  (where  $V$  is the volume of  $N_2$  adsorbed at STP per unit mass of adsorbent), and, (iii) the BET monolayer capacity must fall within the pressure region selected for the calculation. In Annex I, Figure A-2 shows the fitting for the pristine Mg-MOF-74 in forms of BET plot to visualize the pressure domain of BET equation application and Rouqueurol plot to determine the highest relative pressure  $p/p^0$  to use for the fitting. As the results, the BET model affords the apparent values of  $1111 \text{ m}^2 \cdot \text{g}^{-1}$ ,  $1340 \text{ m}^2 \cdot \text{g}^{-1}$  and  $1393 \text{ m}^2 \cdot \text{g}^{-1}$  for Mg-MOF-74, Mg-MOF-74@CNT and Mg-MOF-74@GO, respectively. By introducing CNT and GO, the surface area of MOF-74 materials has been increased by 20.6% and 25.4%, respectively. The specific surface area of Mg-MOF-74 is comparable to the values reported elsewhere:  $1030 \text{ m}^2 \cdot \text{g}^{-1}$  [164],  $1174 \text{ m}^2 \cdot \text{g}^{-1}$  [19, 148] and  $1206 \text{ m}^2 \cdot \text{g}^{-1}$  [121, 169], all of which used the same technique of characterization. The slight difference between the values may be due to the range of the pressure domain in which the BET equation was applied. In the same figure, raw data of  $N_2$  adsorption at 77 K of the produced materials are directly compared to literature data of Mg-MOF-74 reported by Glover *et al.* (2011) [121] from Yaghi's group and Bae *et al.* (2012) [169].  $N_2$  physisorption analysis at 77 K was also conducted for pure carbon doping agents, CNT and GO, in a pressure domain of  $0.01 \leq p/p^0 \leq 1$  to reveal their respective specific surface area. The isotherms are presented in Figure A-3 in Annex I giving the values of BET specific surface area of  $16 \text{ m}^2 \cdot \text{g}^{-1}$  and  $1.2 \text{ m}^2 \cdot \text{g}^{-1}$  for CNT and GO, respectively. Despite having feeble surface areas, both carbon doping agents have considerably improved the porosity of MOF-74 composite materials although at only  $\approx 0.3 \text{ wt}\%$  which represents 1.05 mg of 350 mg of the sample in one-batch synthesis.

Characterization of micropore size and volume distribution using gas adsorption relies exclusively on isotherm modelling accounting for solid surface–gas molecule interaction, gas molecule–gas molecule interaction and confinement of pore size [170]. Since MOF feature a large range of electronic properties and energies of adsorption sites, to date, the accurate determination of their micropore sizes from gas adsorption isotherms is difficult due to the lack of adequate models. In this work, we will mainly rely on the raw data of  $N_2$  adsorption for describing micropore evolution and filling processes. In Figure

3-24-ii, high-resolution  $N_2$  adsorption isotherms in semi-logarithmic coordinates and their derivative curves in the pressure range of  $10^{-7} \leq p/p^o \leq 0.1$  offer higher sensitivity to adsorbed amount variation. At least three well-defined components in micropore filling domain can be distinguished: (i) a narrow contribution with the maximum at  $p/p^o = 5 \cdot 10^{-7} - 8 \cdot 10^{-7}$  and two broad contributions with the maxima at (ii)  $p/p^o = 5 \cdot 10^{-5} - 8 \cdot 10^{-5}$  and (iii)  $p/p^o = 10^{-3}$ . According to the crystallographic structure, Mg-MOF-74 features a unique size of micropore close to  $10 \text{ \AA}$  [20]. Comparing the literature data for MOF-74 and other well-crystallized MOF materials with pore size close to  $10 \text{ \AA}$  [171], their micropore filling with  $N_2$  at 77 K is usually completed before  $p/p^o = 10^{-4} - 10^{-3}$ , so the first two contributions lied in “low-pressure” domain are assigned to structural microporosity. The origin of the splitting of micropore filling processes into two components with nearly close population could be due to the coexistence of two adsorption sites with different binding energy values referred as “near-metal” and “near-ligand” featuring one-to-one ratio [16, 20, 24]. However more thorough experimental and molecular modelling studies are needed to verify this hypothesis. For both Mg-MOF-74 composites, the  $N_2$  adsorption isotherms are shifted to lower relative pressures suggesting higher adsorbates–adsorbent interaction energies. The origins of this difference are not clear and supposedly due to the structural defects revealed by FESEM analysis and the slightly higher Mg concentration estimated by EDXS analysis, resulting in higher adsorption energies of “near-metal” adsorption sites. Meanwhile, the “high-pressure” contributions with the maximum at  $p/p^o = 10^{-3}$  are assigned to larger intercrystallites pores. Comparing the results of cumulative adsorbed volume for the pristine material and both composites in Figure 3-24-iii, it can be realized that the doping of Mg-MOF-74 with carbon-based materials favors the growth of structural micropore volume inside the material. This tendency is in line with the finding of different works reported that carbonaceous agents such as GO and CNT act as binders favoring the development of new micropores [29-42].

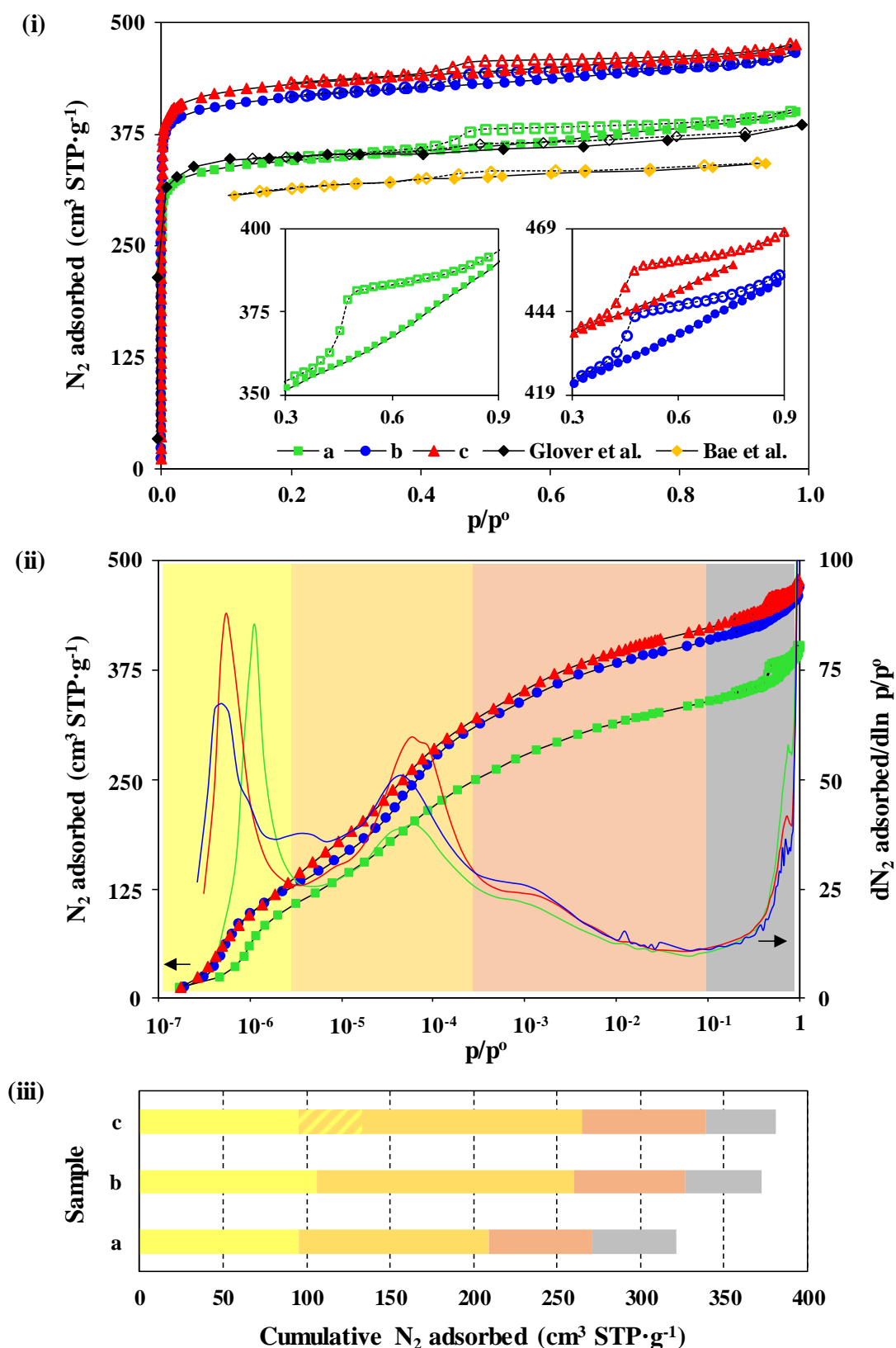


**Table 3-8.** BET specific surface area of Mg-MOF-74, Mg-MOF-74@CNT and Mg-MOF-74@GO.

	<b>Pristine Mg-MOF-74</b>	<b>Mg-MOF-74 @CNT</b>	<b>Mg-MOF-74 @GO</b>
<b>BET equation<sup>1</sup></b>			
<b>Specific surface area (m<sup>2</sup>·g<sup>-1</sup>)</b>	1111 ± 0.6	1340 ± 1.8	1393 ± 0.8
<b>ARE (%)</b>	5.3%	4.8%	4.4%

<sup>1</sup>For  $0.005 \leq p/p^0 \leq 0.05$

### 3.7.6. Ageing effects of materials

All synthesized materials were stored in a sealed vacuum bag with the presence of silica gel and kept in desiccators. After 18 months of their production, the samples were re-characterized using powder X-ray diffraction and N<sub>2</sub> physisorption analysis with the same operational conditions, to study the ageing effect of the materials. Fortunately, as presented in Figure 3-25 and Table 3-9, the consistency of the analysis results can be observed between the measurements right after synthesis and after a long storage period, demonstrating the durability of the materials.

**Table 3-9.** BET specific surface area of Mg-MOF-74, Mg-MOF-74@CNT and Mg-MOF-74@GO as a function of time after their production. The values are presented in m<sup>2</sup>·g<sup>-1</sup>.

	<b>After synthesis</b>	<b>18 months after synthesis</b>
<b>Mg-MOF-74</b>	1111 ± 0.6	1085 ± 0.7
<b>Mg-MOF-74@CNT</b>	1340 ± 1.8	1327 ± 0.4
<b>Mg-MOF-74@GO</b>	1393 ± 0.8	1370 ± 0.5

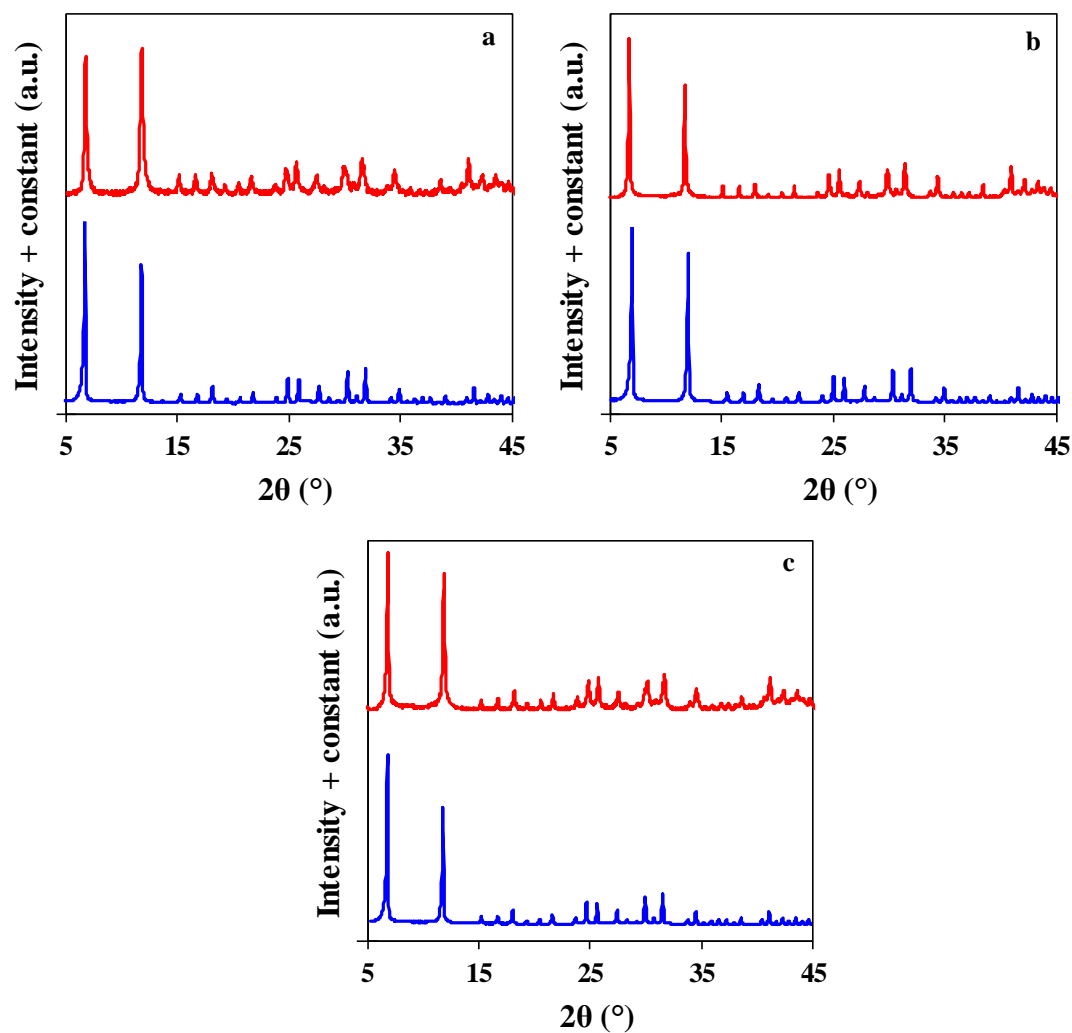


**Figure 3-25.** PXRD reflections of (a) Mg-MOF-74, (b) Mg-MOF-74@CNT and (c) Mg-MOF-74@GO. Blue and red lines represent the analysis right after their synthesis and 18 months after their synthesis, respectively.

### 3.8. Conclusion

Mg-MOF-74 and its carbon composites, Mg-MOF-74@CNT and Mg-MOF-74@GO, were successfully synthesized using the improved solvothermal *in situ* synthesis method with the optimized substitution of carbon doping agent which was  $\approx 0.3$  wt%. Based on X-ray diffraction analysis, the crystallinity of Mg-MOF-74 was well preserved in both composites but Mg-MOF-74@CNT and Mg-MOF-74@GO appeared with larger average crystallite sizes, 82 nm and 73 nm, respectively, compared to 67 nm for the pristine material. The electron microscopy images showed that Mg-MOF-74@CNT and Mg-MOF-74@GO displayed larger average particle sizes of single specimen, 23  $\mu\text{m}$  and 37  $\mu\text{m}$  respectively compared to 10  $\mu\text{m}$  for the pristine material. CNT or GO promoted

agglomeration of polycrystalline structure of Mg-MOF-74 during the crystal growth by interlocking with the framework and stacking to the crystallites surface. The structure modification in the Mg-MOF-74 composites not only gave advantage on thermal stability but also popularized new formation of micropores inside MOFs. The BET specific surface area increased from  $1111 \text{ m}^2 \cdot \text{g}^{-1}$  measured for the pristine Mg-MOF-74 to  $1340 \text{ m}^2 \cdot \text{g}^{-1}$  (increased by 20.6%) and  $1393 \text{ m}^2 \cdot \text{g}^{-1}$  (by 25.4%) for Mg-MOF-74@CNT and Mg-MOF-74@GO, respectively. These data together with the analysis of the experimental isotherm components and their modelling based on a Density Functional Theory approach indicate that Mg-MOF-74 composites are characterized with larger micropore volumes, estimated from  $0.40 \text{ cm}^3 \cdot \text{g}^{-1}$  for the pristine Mg-MOF-74 to  $0.48 \text{ cm}^3 \cdot \text{g}^{-1}$  (by 18.0%) and  $0.49 \text{ cm}^3 \cdot \text{g}^{-1}$  (by 23.9%) for Mg-MOF-74@CNT and Mg-MOF-74@GO, respectively. This current work proved that by doping with carbonaceous agents although only at a very low percentage of substitution, pore textural properties of Mg-MOF-74 for gas adsorption could be significantly improved, not to mention their better thermal stability.

For future work of synthesis of materials, seeing that CNT substitution follows the optimum concentration on the basis of GO for the purpose of comparison between MOF/GO and MOF/CNT composites, thus another optimization study to determine CNT concentration in MOF/CNT composite can be proposed. Moreover, pore textural properties can be characterized as a function of doping agent concentration to better understand their role in development of micropore in the composites. For industrial application, simplicity of synthesis and upscaling of MOF production must be further explored to produce larger amount of MOFs (by increasing reactants amount) with the same solvent volume, but having the same quality as the present synthesis. In order to reduce the resistance to external mass transfer, MOF materials which are produced in powder form must be shaped into pallets. The research on this work is ongoing at Universiti Teknologi PETRONAS for MOF-74 material. It is also interesting to study the influence of compactness density of MOF crystals on  $\text{CO}_2$  adsorption capacity. Moreover, some modifications of MOF structure can also be proposed to improve their resistivity to humidity.

For future work of characterization of materials, in order to confirm a complete pore activation of MOFs, it is suggested to verify the absence of DMF solvent in the MOF samples by detecting a significant characteristic peak of DMF at wavenumber  $1650 \text{ cm}^{-1}$  using FTIR analysis. Besides that, more in-depth morphological study can be done using high-resolution TEM to better understand their crystal growth and carbon incorporation. In

addition, knowing that GO is a graphite form while CNT is a fullerene form of carbon that give different synergetic effects with the MOF crystal, so another form of carbon allotropic such as cubic diamond (e.g. carbon fiber) can be suggested. Furthermore, the micropore of the synthesized materials can be further characterized using argon physisorption analysis, having less polarity compared to nitrogen, to study the effect of polarizability on the adsorption sites. Based on our preliminary study, the exploitation of raw isotherm data at high resolution shows that the adsorption sites having the same interaction with both nitrogen and argon. Regarding the estimation of dead volumes, method of extrapolation using Dubinin-Radushkevitch model can be proposed to compare with the present method.

**CHAPTER 4**

**Adsorption  
Equilibria**

## CHAPTER 4: ADSORPTION EQUILIBRIA

### 4.1. Adsorption mechanisms: Principles

#### 4.1.1. Mass transfer phenomena from bulk gas phase to solid surface

The mass transfer phenomena of a probe molecule from the bulk gas phase to the adsorption sites in porous solid is described as follows according to Figure 4-1 and Table 4-1. In the case of MOFs, a solid particle consists of an assembly of crystallites having different types of nanopores (usually meso- and micropores) and also the formation of secondary nanopores within the crystallites (intercrystallite porosity).

The mass transfer firstly involves (1) the transport of the gas molecule from the fluid phase to the boundary layer surrounding the solid particle to which the axial dispersion in the gas phase become the barrier [172]. Considered as extra-granular diffusion, the transfer results from the concentration gradient between the bulk phase and the boundary film, and also from Brownian molecular motion (called self-diffusion) [172].

It also includes (2) the diffusion of the gas molecule in the film (or boundary layer) surrounding the external surface of the solid particle [172, 173]. The film thickness is related to hydrodynamic gas flow conditions whereby it decreases with increasing superficial velocity of highly turbulent regime. The following phenomenon involves (3) the mass transfer of the gas molecule in the “particle skin” [172, 174]. The “particle skin” is described as the interface between the exterior and the interior of the solid representing the change in energy environment undergone by the gas molecule when passing from the outside to the inside [172, 174]. Both phenomena (2) and (3) are accounted for external diffusions.

The phenomena (4) and (5) are the mass transfer of the gas molecule in the macro- and mesoporous volumes of the solid particle, which mainly route by molecular diffusion and Knudsen diffusion. Molecular diffusion is driven by collisions between the gas molecules and their kinetic energy due to intermolecular interactions and predominantly occurs when the pore size is significantly larger than the mean free path of the gas molecule [172, 174, 175]. While Knudsen diffusion is driven by collisions between the gas molecule and the pore walls due to electrostatic interactions and predominantly occurs when the pore size is comparable to the mean free path of the gas molecule [172, 174, 175]. Both phenomena (4) and (5) are accounted for the internal diffusions.

The internal diffusions specifically in MOFs can be understood in regard to three different terms: (i) the intraparticle diffusion representing the ensemble of diffusion phenomena taking place within the solid particle, (ii) the interstitial diffusion which occurs in the voids outside the crystallites in the solid particle, and, (iii) the intracrystalline diffusion which occurs within the crystallites [172].

Along with those internal phenomena, a sufficient difference in total pressure between the ends of the pore capillary will give rise to (6) the longitudinal Poiseuille diffusion of the gas phase inside the pore capillary, controlled by the viscous flow [172].

Meanwhile, (7) the adsorption equilibrium is established when the gas molecule has been in contact with the solid surface for a sufficient time to allow a dynamic balance between the adsorbate concentration in the bulk gas phase and at the solid interface [95, 96]. This state of equilibrium depends on: (i) the interplay between the strength of the gas molecule–gas molecule interaction and gas molecule–solid surface interactions (or chemical reaction), (ii) confined geometry effects, and, (iii) the thermodynamic state of pore and bulk gas phases [170, 176]. It can be described as the balance between the energy of interactions with the solid phase and the kinetic energy of the gas molecule; the equilibrium is achieved in longer time when the kinetic is slower.

A phenomenon that can principally occur in heterogeneous adsorbents such as MOFs [16, 24, 177, 178], is (8) the displacement of the molecule from one adsorption site to another site while remaining adsorbed due the energy landscapes of the solid surface [172, 179, 180]. This mass transfer is called surface diffusion or surface mobility [172, 179, 180]. The heterogeneity in topography (concentration and structure) of an adsorbent leads to the variation of electron charge densities and energy distributions of the adsorption sites on the solid surface [16, 181]. This process predominates in micropores.

Lastly, the phenomenon (9) indicates the release of heat following the above-mentioned adsorption processes.

For a deeper understanding on interactions mechanisms of gas–gas and gas–solid, the following sections in this chapter describe mechanisms of intermolecular interactions of CO<sub>2</sub> and binding interactions of CO<sub>2</sub> in Mg-MOF-74. The equilibrium of CO<sub>2</sub> adsorption in the system in comparison to CH<sub>4</sub> is studied in this chapter whereas the kinetics of intraparticle diffusion of the gases in the adsorption system is addressed in Chapter 5.

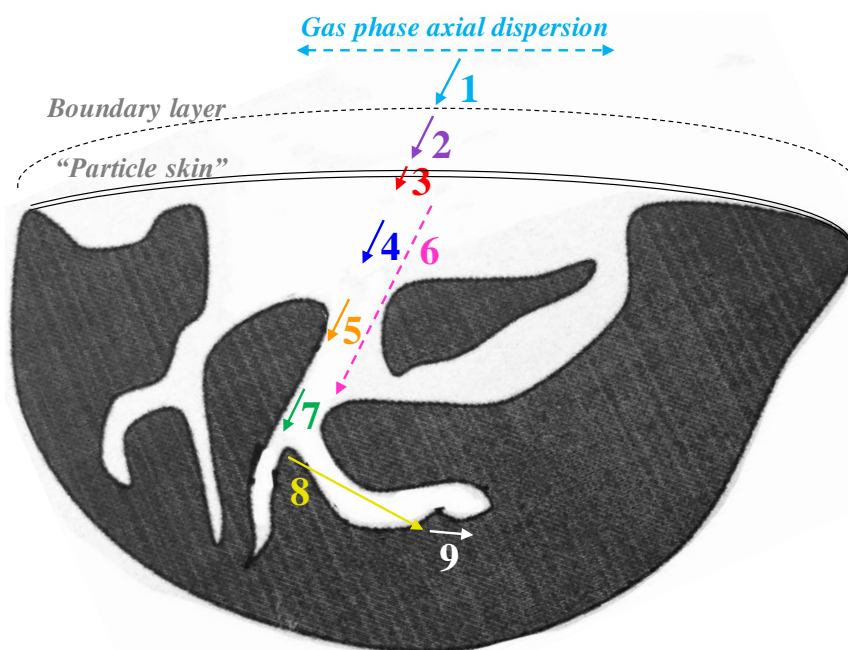


**Figure 4-1.** Descriptive schema of mass transfers from bulk gas phase to nanoporous solid surface.

**Table 4-1.** Recapitulative of mass transfer phenomena from bulk gas phase to nanoporous solid surface [16, 24, 95, 96, 170, 172-181].

No.	Mass transfer	Medium	Driving force	Barrier
1	Extra-granular diffusion	Gas phase	Gas concentration gradient Brownian molecular motion	Axial dispersion in gas phase
2	External diffusions	Boundary layer	Gas concentration gradient	External film barrier
3		"Particle skin"	Change in energy environment	External surface barrier
4	Internal diffusions	Macropores (predominated by molecular diffusion)	Collision between gas molecule–gas molecule	Macropores confinement barrier
5		Mesopores (predominated by Knudsen diffusion)	Collision between gas molecule–pore wall	Mesopores confinement barrier
6	Poiseuille diffusion	Pore capillary	Viscous flow	Pores confinement barrier
7	Adsorption	Adsorption site	Balance between interactions energy and kinetic energy	Kinetic energy of the gas molecule

8	Surface diffusion	Micropores adsorption site–adsorption site	Energy landscapes of the solid surface	Homogeneity of the solid surface
---	-------------------	--	--	----------------------------------

#### 4.1.2. Intermolecular interactions of CO<sub>2</sub>

CO<sub>2</sub> is a non-polar molecule having zero net moment value ( $\mu=0$ ) due to its linear geometry ( $O^{\delta-}=C^{\delta+}=O^{\delta-}$ ). Although C–O bond exhibits a covalent bond with delocalized charge due to the difference in electronegativity between C and O atoms and the availability of polarizable pi electrons of double bond, the dipole moment in both C–O orbitals are magnitudinally directed opposite to each other, resulting to an even charge distribution and no dipole moment. Meanwhile, a symmetric CO<sub>2</sub> molecule has a permanent electrical quadrupole moment that can be described as two electrical dipoles sitting back-to-back and pointing in opposite directions. For that reason, the weak attractive electrostatic forces called Van der Waals that give rise to CO<sub>2</sub> intermolecular interactions can be divided into three: (i) the permanent quadrupole moment–permanent quadrupole moment force, Keesom 1915 [182], in Figure 4-2-i, (ii) the permanent dipole moment–induced dipole moment force, Debye 1921 [183], in Figure 4-2-ii, and, (iii) the instantaneous dipole moment–induced dipole moment force, London 1937 [184], in Figure 4-2-iii. Both Keesom and Debye are the polar forces in which at least one permanent dipole is needed to act on the second dipole to produce an electrostatic field of attractive interaction. London is described as a dispersive force of attractive interaction that can be present between molecules of all substances whether or not having a permanent dipole. It is usually predominant over Keesom and Debye interactions.

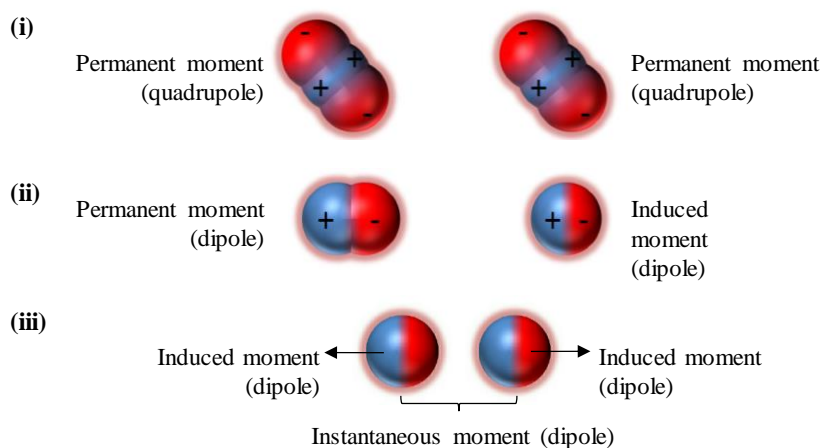


**Figure 4-2.** Van der Waals forces of intermolecular interactions of CO<sub>2</sub> from type (i) Keesom polar force, (ii) Debye polar force and (iii) London dispersive force.

For a physical CO<sub>2</sub> adsorption, gas molecule–gas molecule and gas molecule–solid surface interactions arise from those intermolecular forces creating a surface tension between the interacted molecules. The total potential energy of the interaction between an adsorbate and a substrate accounts for the difference between the sum of the Van der Waals forces (attractive interactions) and the intermolecular repulsive electrostatic forces, Lennard-Jones–John 1937 [185], as schematized in Figure 4-3. The electrostatic force can be repulsive at a very close distance of interaction which is smaller than the minimum distance of Van der Waals,  $2r_{vdw}$ , of which  $r_{vdw}$  value depends on the interacted molecules. The heat of adsorption at zero adsorption coverage is released at the strongest point of attractive interaction between the gas molecule and the solid surface.

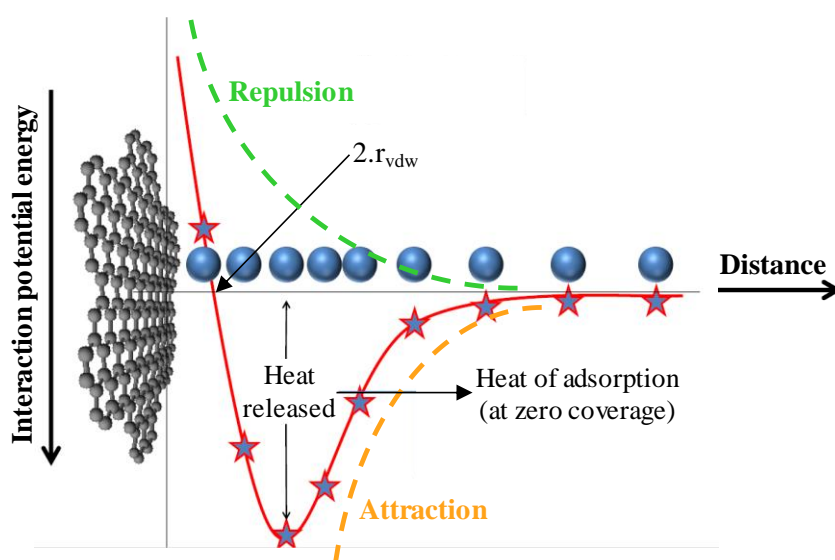


**Figure 4-3.** Lennard-Jones–John schema of intermolecular potential energy versus distance of adsorbate molecules from the substrate.

#### 4.1.3. Equilibrium interactions of CO<sub>2</sub> in MOF-74

The different mechanisms of CO<sub>2</sub> equilibrium interactions in Mg-MOF-74 have been reported by various investigations. By using neutron powder diffraction measurements, Wu *et al.* (2010) identified that the primary binding sites of CO<sub>2</sub> in Mg-MOF-74 were the open metal ions due to strong electrostatic interaction [186]. A vibrational mode analysis showed that one of the O atoms of the adsorbed CO<sub>2</sub> molecule was strongly attached to the Mg sites while the rest of the molecule was relatively free [186]. Interestingly, the calculation of a small angle of bend of Mg-CO<sub>2</sub> bond suggested that the CO<sub>2</sub> adsorption at the metal site was still largely physisorption, and the overall binding strength was right in the range that

facilitates both adsorption and desorption [186]. In another study using X-ray absorption spectroscopy and First Principle calculations, Drisdell *et al.* (2013) mentioned that the open metal sites created local electronic interaction during the molecular adsorption with CO<sub>2</sub> [187]. The open (or exposed) metal sites, also known as coordinatively unsaturated metal sites [21], are defined as five-coordinate metal cations that behave as Lewis acids to adsorb CO<sub>2</sub> [187]. The organic frameworks in Mg-MOF-74 is able to constrain the bond angles at the Mg sites to ensure a significant portion of the Mg coordination sphere is available for adsorbing CO<sub>2</sub> molecules [187]. The effect of the presence/absence of open metal sites in MOF-74 on the adsorption performances of CO<sub>2</sub> and CH<sub>4</sub> was investigated by Lou *et al.* (2014) [51]. Two MOF-74 materials were tested namely Fe<sub>2</sub>(DOBDC) containing open Fe sites and its oxidized analogue Fe<sub>2</sub>(O<sub>2</sub>)(DOBDC) that no longer had any unsaturated Fe sites [51]. The result showed that Fe<sub>2</sub>(DOBDC) exhibited higher CO<sub>2</sub> and CH<sub>4</sub> adsorption capacities with 144.5 cm<sup>3</sup>/g (CO<sub>2</sub>) and 75.8 cm<sup>3</sup>/g (CH<sub>4</sub>) in comparison to 98.1 cm<sup>3</sup>/g (CO<sub>2</sub>) and 36.8 cm<sup>3</sup>/g (CH<sub>4</sub>) measured for Fe<sub>2</sub>(O<sub>2</sub>)(DOBDC) at 298 K and 10 bar [51]. Using Ideal Adsorbed Solution Theory calculations, the separation factor of CO<sub>2</sub>/CH<sub>4</sub> on Fe<sub>2</sub>(DOBDC) for an equimolar gas mixture was deduced 18, much higher than 7 calculated for Fe<sub>2</sub>(O<sub>2</sub>)(DOBDC) at 298 K and 1 bar, and it was stable as a function of pressure [51]. The open metal sites preferentially adsorb CO<sub>2</sub> over CH<sub>4</sub> due to its larger quadrupole moment and greater polarizability.

Also by using neutron powder diffraction analysis as previous Wu *et al.* (2010) [186], Queen *et al.* (2014) deduced that the framework (the linker fragment) in Mg-MOF-74 became the secondary binding sites for CO<sub>2</sub> adsorption after the primary metal adsorption sites [188]. The data were collected at low temperature revealing two CO<sub>2</sub> adsorption sites on the pore surface followed by multiple changes in the framework as a function of CO<sub>2</sub> loading [188]. By systematically increasing the amount of adsorbed CO<sub>2</sub>, the detailed structural analysis of Mg-MOF-74 displayed the population of secondary CO<sub>2</sub> adsorption sites associated with the framework, in which the subsequent adsorbed CO<sub>2</sub> was forced to form a second layer since the current intermolecular distances did not permit any further direct adsorption onto the framework surface [188].

In a computational study using Density Functional Theory and Grand-Canonical Monte Carlo simulation, Hou *et al.* (2012) explored that the CO<sub>2</sub> adsorption in Mg-MOF-74 was attributed to the strong Lewis acid and base interactions: (i) between metal ions and O atom of CO<sub>2</sub>, (ii) between O atom of the framework and C atom of CO<sub>2</sub>, and, (ii)

between C atom of the framework and O atom of CO<sub>2</sub> [177]. The same observation was also discovered and described in details by Liu *et al.* (2016) in their molecular simulation study in which the molecular structure of CO<sub>2</sub>-adsorbed Mg-MOF-74 was constructed from its experimental X-ray powder diffraction [178]. The primary binding with the metal ions occurred when a CO<sub>2</sub> molecule took the position vertically to the plane of a –OOMgOO– cluster at the metal site whereby: (i) O atom of CO<sub>2</sub> pointing to Mg ion with a Mg–OCO interaction distance of approximately 2.33 Å, and, (ii) C atom of the same CO<sub>2</sub> molecule interacted with O atom of the same –OOMgOO– cluster with a O–COO distance of approximately 3.36 Å, as described in Figure 4-4 [178]. The bond angle of Mg–OCO in Mg-MOF-74 was identified as 129° which deviated from the linear bond angle of the same interaction undergone by other typical gases, such as CO and N<sub>2</sub> [16]. Meanwhile, the secondary binding occurred when a CO<sub>2</sub> molecule was in a vertical position to the plane of –C<sub>6</sub>H<sub>2</sub> cluster at the framework site whereby O atom of CO<sub>2</sub> pointing to central C atom of the cluster with a C–OCO distance of approximately 3.42 Å, as also described in Figure 4-4 [178]. From the established molecular structure, the binding energy of the interactions at the two adsorption sites in kJ·mol<sup>-1</sup> were estimated using Density Functional Theory calculations [178], and defined as: binding energy =  $E_{MOF+CO_2} - (E_{MOF} + E_{CO_2})$ , where  $E_{MOF}$  is the total energy of the substrate,  $E_{CO_2}$  is the total energy of the adsorbate and  $E_{MOF+CO_2}$  is the total energy of adsorbate/substrate system in the equilibrium state. In average, the binding energy of the primary and secondary binding sites were -55.5 kJ·mol<sup>-1</sup> and -27.1 kJ·mol<sup>-1</sup>, respectively, resulting to the variation of electrostatic environment in one-unit cell as shown in Figure 4-5-i [178]. In an earlier study, the calculation of binding energy with the same definition at the two adsorption sites was conducted by Lopez *et al.* (2013) by calculating the carbon nuclear magnetic resonance shielding for CO<sub>2</sub> inside Mg-MOF-74 [24]. The results revealed that the adsorption energy reached -48 kJ·mol<sup>-1</sup> and -44.3 kJ·mol<sup>-1</sup> for the primary and secondary adsorption sites, respectively, at a maximum loading (12 molecules per unit cell), as shown in Figure 4-5-ii [24]. Several different CO<sub>2</sub> loadings were also described: (i) at low loading, less than 6 molecules per unit cell occupy the primary binding sites, (ii) at high loading, 6 molecules per unit cell completely saturate all available primary sites, (iii) at very high loading, 6 molecules per unit cell completely saturate all primary sites and less than 6 molecules per unit cell occupy the secondary sites, and, (iv) at maximum loading, 12 molecules per unit cell occupy all available primary and secondary sites [24].

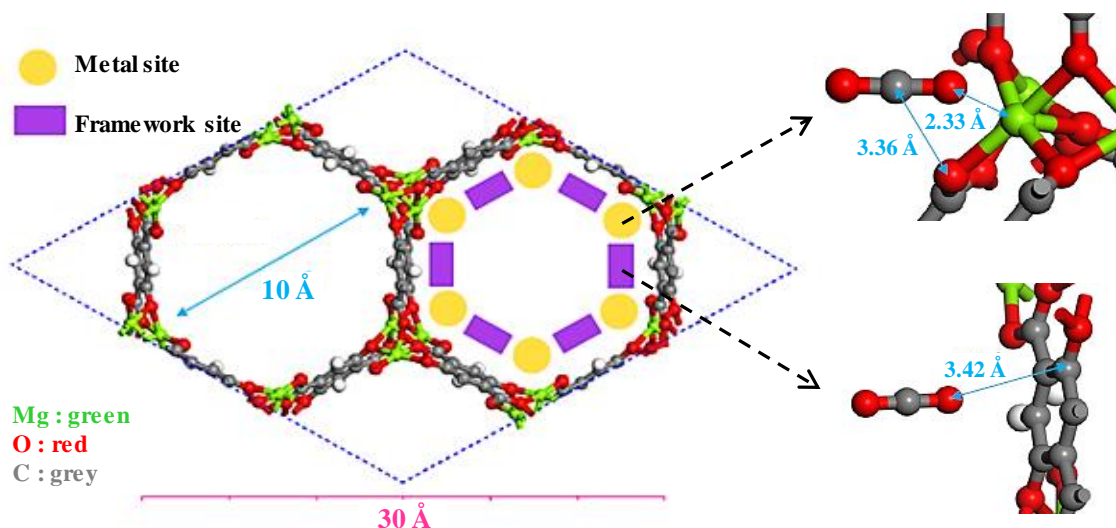


**Figure 4-4.** (left) Metal sites and framework sites for CO<sub>2</sub> adsorption in Mg-MOF-74 one-unit cell and (right) the coordination of CO<sub>2</sub> binding at primary site (metal) and secondary site (framework). The figure is modified from [178].<sup>39</sup>

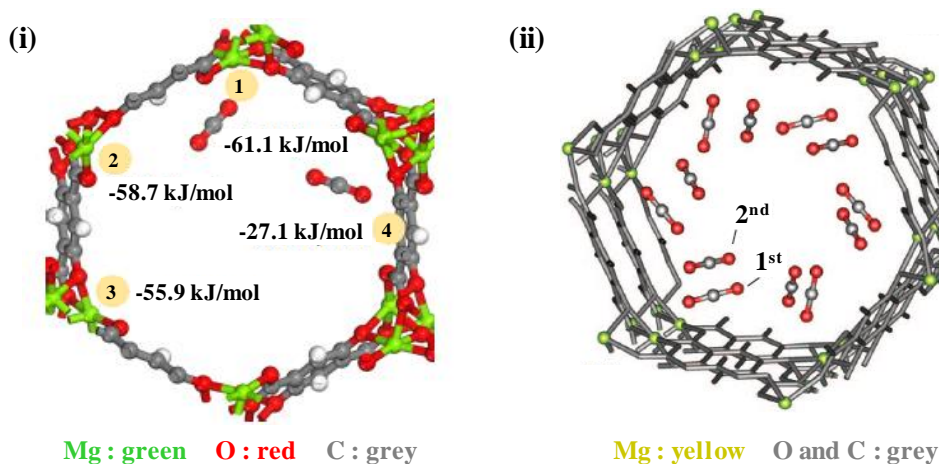


**Figure 4-5.** (i) Binding energy of CO<sub>2</sub> at different adsorption sites in Mg-MOF-74 one-unit cell: metal sites marked 1-2-3 and framework site marked 4 [178].<sup>39</sup> (ii) A maximum loading of CO<sub>2</sub> in Mg-MOF-74 one-unit cell: primary adsorption site marked 1<sup>st</sup> and secondary adsorption site marked 2<sup>nd</sup> [24].<sup>40</sup>

In addition to these findings, Valenzano *et al.* (2010) discovered that about one-half of adsorption enthalpy of CO<sub>2</sub> in Mg-MOF-74, representing gas molecule-solid surface interaction energy, was attributed to weak dispersive interactions (London) between the adsorbed molecules and the surrounding framework [16]. This kind of interaction energy

<sup>39</sup> Reprinted from Fuel, Y. Liu *et al.*, Mechanism of CO<sub>2</sub> adsorption on Mg/dobdc with elevated CO<sub>2</sub> loading, vol. 181, pp. 340-346, Copyright 2016, with permission from Elsevier.

<sup>40</sup> Reprinted from The Journal of Chemical Physics, M. Lopez *et al.*, NMR study of small molecule adsorption in MOF-74-Mg, vol. 138, no. 15, pp. 154704, Copyright 2013, with permission from American Institute of Physics.

was also designated as “surface dispersive force” [16], and several published works claimed that the energy could be improved by doping carbon-based materials into MOF structure [29-31, 33, 38, 142]. Figure 4-6 shows the distribution of electrostatic potential on the surface of Mg-MOF-74 and also the electrostatic potential of CO<sub>2</sub> molecule.

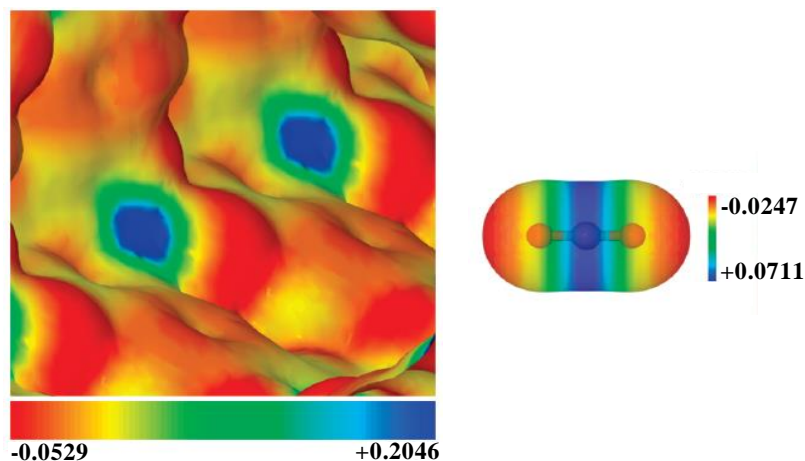


**Figure 4-6.** Detail of the electrostatic potential of Mg-MOF-74 mapped on the electron charge density isosurface (0.003 a.u.) together with the electrostatic potential of CO<sub>2</sub>. Red, green, and blue represent negative, zero, and positive values in a.u., respectively [16].<sup>41</sup>

## 4.2. Adsorption isotherms: Principles

### 4.2.1. IUPAC adsorption isotherm types

In these recent years, major advances have been made in understanding the adsorption and phase behavior of fluids confined in ordered nanoporous materials. Defined by the International Union of Pure and Applied Chemistry (IUPAC), nanoporous materials consist of <100 nm pore widths within the ranges of macropores (>50 nm), mesopores (2-50 nm) and micropores (<2 nm) that can be divided into supermicropores (0.7-2 nm) and ultramicropores (<0.7 nm) [189]. Measurements of physisorption isotherms allow one to assess micro- and mesopores while mercury porosimetry is widely employed for textural analysis of macropores [189]. IUPAC has published in their technical report (IUPAC Recommendations 2015 [190]), the updated classification of physisorption isotherms of a single component in micro- and mesoporous materials. The shape of the adsorption

<sup>41</sup> Reprinted from The Journal of Physical Chemistry C, L. Valenzano *et al.*, Computational and experimental studies on the adsorption of CO, N<sub>2</sub>, and CO<sub>2</sub> on Mg-MOF-74, vol. 114, no. 25, pp. 11185-11191, Copyright 2010, with permission from American Chemical Society.

isotherm is representative of the adsorption mechanisms of gas–solid stem from the interplay between the strength of the gas–gas and gas–solid interactions, pore confinement and the thermodynamic state of pore and bulk gas phases, as mentioned previously [170, 176]. The different isotherm shapes are described as follows referring to Thommes *et al.* (2004) [176] (2014) [170] (2015) [190] (2017) [189], and according to Figure 4-7 and Figure 4-8.

Type I isotherm generally represents the adsorption in microporous adsorbents whereby (X) the gas molecules commence to occupy the micropores at low relative pressures,  $p/p^0$ , governed by the strong gas molecule–solid surface interactions at  $p/p^0 < 0.01$ , and, the cooperative mechanism depending on gas molecule size and nature, pore geometry and effective pore width at  $p/p^0 = 0.01-0.15$ . The micropores filling capacity depends on the accessibility of the pores for the gas molecules and consequently reaches the plateau after (Y) the pores filling completion. The adsorption in micropores in most cases is assimilated to a monolayer adsorption due to the micro-confinement the molecular-size capillaries, but multi-molecular adsorption can also take place in super-micropores. Type I isotherm can be observed either, for ultramicropores filling (Type Ia isotherm) having a very sharp inflexion point before the plateau, or, for supermicropores filling (Type Ib isotherm) having a moderate inflexion point before the plateau.

Type II and Type III isotherms are typically obtained in an adsorbent with a broad pore size distribution. The gradual progression can be observed from (A) monolayer adsorption to (B) multilayer adsorption, and, to (C) pore (or capillary) condensation. The difference between these two is that Type III isotherm displays very small amount adsorbed at low relative pressures indicating relatively weak interactions between the adsorbate and the adsorbent, thus the gas molecules are not completely “wetting” the surface. After the multilayer adsorption reaches a critical film thickness, pore condensation occurs in the core of the mesopores indicating a gas–liquid phase transition. The mesopores filling via pore condensation is described as a phenomenon whereby the gas condenses to a liquid-like phase in the pores under the influence of the attractive gas molecule–solid surface interactions at a pressure less than the saturation pressure of the bulk gas phase.

Also for an adsorbent with mesoporous sites, Type IV isotherm is another variation of Type II isotherm exhibiting a final saturation plateau that indicates the complete transition between processes (C) and (D). (D) reflects the situation where the mesopores are completely filled with liquid, and sometimes produces a sharp inflexion point before

the plateau. The pore liquid is separated from the bulk gas phase by a hemispherical meniscus. When the meniscus recedes at a pressure less than the condensation pressure of the pore, (E) pore evaporation takes place and the isotherm returns to (B). If the mesopores diameter exceeds a certain critical width which is dependent on adsorbate–adsorbent system and temperature, the pore condensation will be accompanied by a hysteresis (irreversible isotherm) from (E) to (B) which occurs in most cases, called Type IV-a isotherm. Hence, for smaller-width mesopores which is normally for the case of conical and cylindrical pores, a complete reversible isotherm from (E) to (B) can be observed after the pore condensation, called Type IV-b isotherm.

Lastly, Type V isotherm is another variation of Type III isotherm featuring a relatively much stronger intermolecular interaction between the adsorbed gas molecules with the presence of mesopores. Thus, the isotherm exhibits more rapid (C) pore condensation followed by (D) pore saturation and (E) pore evaporation with a hysteresis returning to (B) as described previously.

In addition, all isotherm types will end with interparticle voids condensation when  $p/p^0$  is approaching 1 displayed by a sudden increase in amount adsorbed (not shown in the figure). There is also a rare Type VI isotherm published by IUPAC for non-porous homogeneous materials which is not concerned by this study.

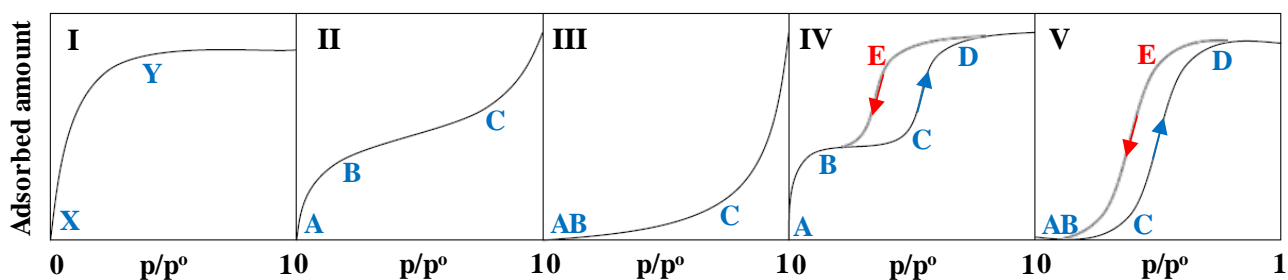
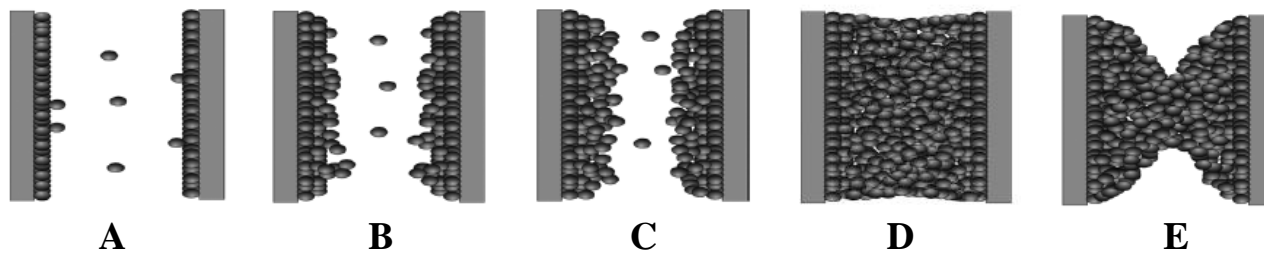


Figure 4-7. Physisorption isotherms classification based on IUPAC Recommendations 2015.



**Figure 4-8.** Schematic representation of configuration of (A) monolayer adsorption, (B) multilayer adsorption, (C) pore condensation, (D) pore saturation and (E) pore evaporation in a single pore [176].<sup>42</sup>

#### 4.2.2. Isotheric heat of adsorption

Heat of adsorption, usually expressed in  $\text{kJ}\cdot\text{mol}^{-1}$ , represents the amount of heat released when the adsorption takes place. It reflects the strength of the interactions between adsorbate and adsorbent, and it is often assumed that at least this the same amount of heat must be applied to the system to regenerate the adsorbent [19, 95, 191]. The information on heat release is important in the kinetic studies because the heat produced by adsorption is partly absorbed by the solid adsorbent and partly dissipated to the surroundings [95]. The amount of heat absorbed by the solid increases the particle temperature, and consequently reduces the adsorption rate because the amount of gas adsorbed at equilibrium decreases with increasing temperature [95, 192]. Similarly, a large temperature drop may also occur in the desorption step, making adsorbate components freeze out onto the adsorbent [193].

Heat of adsorption can be defined as the integral heat of adsorption corresponds to the total amount of heat released as experimentally measured in a calorimeter, when setting initial pressure and temperature conditions until equilibrium is reached in the system. At constant temperature and volume, the derivative heat of adsorption is derived from the derivative of the total adsorption heat curve per amount of gas adsorbed. The isotheric heat of adsorption,  $Q_{st}$ , actually corresponds to a change in the enthalpy of the system, and is defined as the ratio of the infinitesimal change in the adsorbate enthalpy to the infinitesimal change in the amount adsorbed at constant volume and temperature [192]. Isotheric heat is one of the most practically used quantities in adsorption studies as it can be easily derived from experimental isotherms determined at different temperatures and assuming this quantity as not dependent on temperature and pressure [95]. It may however vary or not with adsorption loading. Derived from Gibbs Free Energy<sup>43</sup> equation, supposing an ideal gas, isotheric heat of adsorption can be calculated from Van't Hoff thermodynamic equation which is assimilated to Clausius–Clapeyron-type relation (Eq. 4-1) for a fixed amount of adsorbate,  $q$  [19, 95]. The integral of this equation is expressed in form of linear function

<sup>42</sup> Reprinted from Nanoporous Materials: Science and Engineering, M. Thommes *et al.*, Physical adsorption characterization of ordered and amorphous mesoporous materials, pp. 317-364, Copyright 2004, with permission from World Scientific Publishing Co.

<sup>43</sup> Gibbs Free Energy equation:  $\Delta G^o = \Delta H^o - T \cdot \Delta S^o$ . Physisorption is spontaneous and exothermic, thus the Gibbs free energy  $\Delta G^o < 0$ , the entropy  $\Delta S^o > 0$  and the enthalpy  $\Delta H^o < 0$ .

of  $\ln p$  versus  $1/T$  as shown in Eq. 4-2 and described in Figure 4-9. It consists of interpolating  $q$  points from adsorption isotherms of different temperatures and isosteric heat of adsorption is deduced from the slope of linear fit of  $\ln p$  versus  $1/T$ . This method of measurement is known as sorption isosteric technique [194, 195], in which virial-thermal equation [196] and spline function [197] approaches can also be employed in place of Clausius–Clapeyron. Besides sorption isosteric technique, calorimetry is another well-known technique of measurement of heat of adsorption that has been widely used for the same purpose [198-200]. In this study, we focus on the first technique and make use of Clausius–Clapeyron classical approach.

$$Q_{st} = -R \cdot \left( \frac{\partial \ln p}{\partial \frac{1}{T}} \right)_q \quad (\text{Eq. 4-1})$$

$$\ln p = \frac{Q_{st}}{R} \left( \frac{1}{T} \right) + C \quad (\text{Eq. 4-2})$$

where,  $Q_{st}$  ( $\text{kJ} \cdot \text{mol}^{-1}$ ) is the isosteric heat of adsorption,  $R$  is the gas constant,  $T$  (K) is the temperature of adsorption,  $p$  (Pa) is the gas pressure of adsorbate in equilibrium with adsorbed phase,  $q$  ( $\text{mol} \cdot \text{kg}^{-1}$ ) is the amount of adsorbate adsorbed per unit mass of adsorbent at equilibrium and  $C$  is a constant.

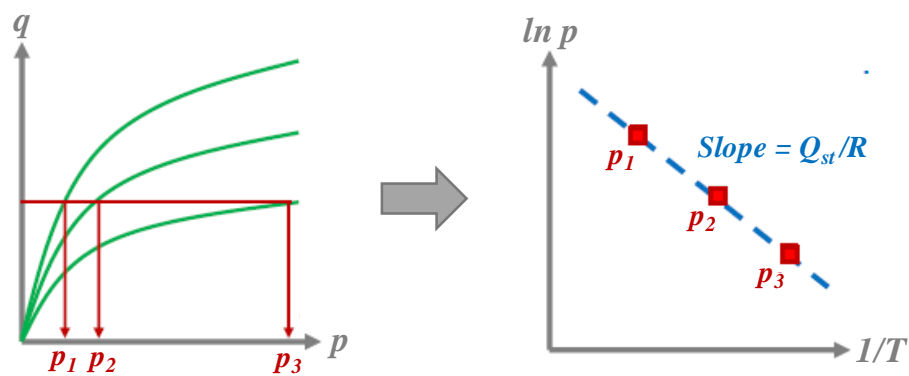


**Figure 4-9.** The method of calculation of isosteric heat of adsorption using Clausius–Clapeyron approach.

### 4.2.3. Equilibrium selectivities for gas separation

#### *a. Intrinsic selectivity at zero adsorption coverage*

Intrinsic selectivity,  $\alpha^{INT}$ , which is defined at zero adsorption coverage [201], is commonly used by several published works [19, 23] to calculate the selectivity of binary gas mixture of CO<sub>2</sub> and CH<sub>4</sub> from the ratio of their Henry's constants deduced from the isotherms. As discussed in Annex III, several isotherm models have linear properties at low pressures (reduced to Henry's law) such as Henry, Langmuir, Toth and dual-site Langmuir isotherms. Thus, they display their own expression of Henry's constant at low-pressure region which is the product of affinity parameter,  $b_{model}$ , and saturation capacity,  $q_{sat}$ , as summarized in Table A-2. The higher is the selectivity value, the larger is the difference in the affinity of the adsorbent between two adsorbate molecules. The definition of the intrinsic selectivity is presented as follows:

$$\alpha_{A/B}^{INT} = \frac{K_A}{K_B} \quad (\text{Eq. 4-3})$$

where,  $\alpha^{INT}$  is the intrinsic selectivity and  $K_A$  and  $K_B$  (mol·kg<sup>-1</sup>·bar<sup>-1</sup>) are the Henry's constant of species A and B, respectively, of which the expression depends on the isotherm model presented in Table A-2.

#### *b. Selectivity parameter for Pressure Swing Adsorption (PSA)*

For the design of PSA separation processes, a dimensionless adsorbent selection parameter,  $S^{PSA}$ , is useful for adsorbent choice and is defined as the ratio of the difference in the equilibrium capacities of each gas species at high and low pressures (also called working or useable capacity),  $\Delta q$ , times the intrinsic selectivity,  $\alpha^{INT}$ , as shown in Eq. 4-4 [19, 201, 202]. The adsorption capacity difference is calculated within specific pressure region, which is from adsorption pressure to desorption pressure of PSA, as presented in Eq. 4-5 [19, 201, 202]. For a given separation, the adsorbent that yields the highest  $S^{PSA}$  value is an indicator of the most performing adsorbent provided that the pressure swing is conducted under conditions close to the limits where equilibrium theory is valid [201], by considering other factors such as the adsorbent ageing effects, thermal stability, etc.

$$S_{A/B}^{PSA} = \frac{\Delta q_A}{\Delta q_B} \alpha_{A/B}^{INT} \quad (\text{Eq. 4-4})$$

$$\Delta q = q_{p_{ads}} - q_{p_{des}} \quad (\text{Eq. 4-5})$$

where,  $S^{PSA}$  is the adsorbent selection parameter in PSA,  $\Delta q_A$  and  $\Delta q_B$  are the working adsorption capacity for gas species A and B, respectively,  $q_{p_{ads}}$  ( $\text{mol}\cdot\text{kg}^{-1}$ ) is the amount of adsorbate adsorbed per unit mass of adsorbent at equilibrium at adsorption pressure while  $q_{p_{des}}$  ( $\text{mol}\cdot\text{kg}^{-1}$ ) is the amount of adsorbate adsorbed per unit mass of adsorbent at equilibrium at desorption pressure.

### c. *Ideal adsorption solution theory (IAST) selectivity*

Ideal adsorbed solution theory (IAST) was developed by Myers and Prausnitz in 1965 [203], and provides a theoretical foundation to obtain adsorption isotherm data of a multicomponent gaseous mixture from individual pure component equilibrium data [204]. IAST supposes that the gas phase is an ideal gas mixture and that the adsorbed phase is an ideal solution in which the activity coefficient of each phase equals to unity [204]. IAST assumes that: (i) the temperature is fixed and that the pure-component isotherms are measured at the same temperature as the gaseous mixture, (ii) the change in each thermodynamic property of the adsorbent when gas molecules adsorb is negligible compared to the change for the adsorbate, (iii) each adsorbed species has access to the same area of the adsorbent surface, and, (iv) Gibbs dividing surface equation<sup>44</sup> defines an adsorbed phase accounting for the amount of adsorbate condensed in the pores in excess and the amount of gaseous adsorptive occupying the intra-particle voids at a density equals to the bulk [95, 203, 205]. Therefore, the term spreading pressure,  $\pi$ , representing two-dimensional pressure of adsorbed phase is introduced as the adsorbed phase is considered as a solution. IAST is thermodynamically consistent and precise at the limit of zero pressure [95]. Thus, the success of IAST calculations depends on the fitting goodness of the pure component isotherm, especially in the low-pressure region as well as in the high-pressure region [95]. An error in these regions, can cause a large error in the multicomponent calculations [95].

The idea of IAST is described as follows, summarized from [95, 203-205]. Considering a multicomponent gaseous mixture of  $N$  species at a system pressure,  $p_T$ , in

<sup>44</sup> "Gibbs diving surface" equation of (two-dimensional) adsorbed phase of pure component at constant temperature:  $A \cdot d\pi + n \cdot d\mu = 0$ , where  $A$  is the solid specific surface area,  $\pi$  is the spreading pressure,  $n$  is the amount of adsorbate adsorbed and  $\mu$  is the chemical potential of adsorbate.

equilibrium with an adsorbate phase on a solid surface with the a total uptake,  $q_T$ , as described in Figure 4-10, let: (i)  $y_i$  and  $x_i$  be mole fractions (or compositions) in the gas phase and adsorbed phase, respectively, for  $i = 1, 2, \dots, N$ , (ii)  $p$  be the pressure of species  $i$  in the gas phase of the mixture, and, (iii)  $q_i^o(p)$  be the amount of species  $i$  adsorbed on the surface when in equilibrium with the gas phase of pure species  $i$  as a function of its pressure. The term  $q_i^o(p)$  can be expressed in the form of isotherm model equation that fit best the data of each species. By using  $q_i^o(p)$  for  $i = 1, 2, \dots, N$ , the goal is to predict the amount of each species adsorbed on the surface when in equilibrium with the gas phase of the mixture,  $q_i^o(p_T)$  where  $q_i^o(p_T) = q_T \cdot x_i$ . Finally, the IAST selectivity of the species is deduced from these calculated individual amount adsorbed.

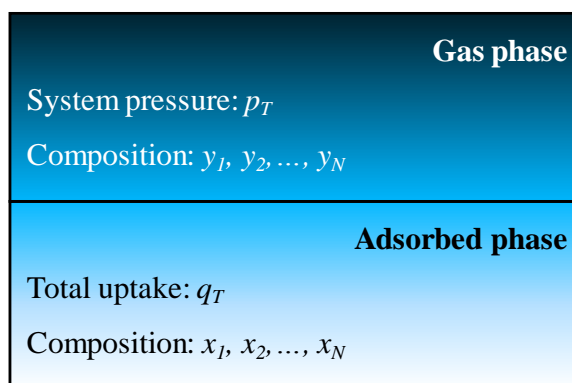


**Figure 4-10.** Illustration of gas mixture in an adsorption system.

The possible input variables given to IAST calculation system and their respective output variables can be divided into 3 modes as summarized in Table 4-2. In this particular study, IAST calculations were performed according to Mode 1, considering the only direct measurements of pure component pressure data. We firstly provided the equilibrium system pressure,  $p_T$ , which lies in the pressure region at which the adsorption isotherms of pure components are measured and fitted to the appropriate isotherm models. Secondly, we fixed the compositions of species in gas phase as equimolar, so that in the case of a binary gas mixture,  $y_1 = y_2 = 0.5$ . These two inputs allow the calculation of the amount of each species adsorbed when in equilibrium with the gas mixture,  $q_i^o(p_T)$ , deduced from the product of  $q_T$  and  $x_i$  which are the output variables of Mode 1.

**Table 4-2.** List of calculation modes of the IAST module [204].

Mode	Input variables	Output variables
1	$p_T, y_1, y_2, \dots, y_N.$	$q_T, x_1, x_2, \dots, x_N.$
2	$p_T, x_1, x_2, \dots, x_N.$	$q_T, y_1, y_2, \dots, y_N.$
3	$q_T, x_1, x_2, \dots, x_N.$	$p_T, y_1, y_2, \dots, y_N.$

As mentioned previously about the assumptions for IAST, this approach treats the adsorbed phase as a single entity in which Gibbs adapted the classical thermodynamics of the bulk phase and applied it to the adsorbed phase [95]. For that reason, the concept of volume in the bulk phase is replaced by the area, and the pressure is replaced by the so-called spreading pressure [95]. In order to solve the equation system, the spreading pressure,  $\pi$ , was introduced and expressed according to Eq. 4-17, in which the pressure of species  $i$  in the gas phase,  $p$ , varies from zero to hypothetical pressure,  $p_i^o$ . Hypothetical pressure  $p_i^o$  is defined as the equilibrium pressure of species  $i$  in the single-component system at the same spreading pressure  $\pi$  as that of the mixture. Thus, IAST is based on the thermodynamic equivalence of the spreading pressure  $\pi$  of each adsorbed species at equilibrium.

$$\pi_i = \frac{R \cdot T}{A} \int_0^{p_i^o} \frac{q_i^o(p)}{p} dp, \quad (\text{Eq. 4-6})$$

where,  $\pi_i$  (Pa·m) is the spreading (or surface) pressure of species  $i$ ,  $R$  (kJ·mol<sup>-1</sup>·kg<sup>-1</sup>) is the gas constant,  $T$  (K) is the temperature of adsorption,  $A$  (m<sup>2</sup>·kg<sup>-1</sup>) is the solid specific surface area,  $p_i^o$  (Pa) is the hypothetical pressure of species  $i$ ,  $q_i^o(p)$  (mol·kg<sup>-1</sup>) is the amount of pure component  $i$  adsorbed per unit mass of adsorbent at equilibrium of which the expression follows the fitted isotherm model, and,  $p$  (Pa) is pressure of species  $i$  in the gas phase.

Knowing that  $T$ ,  $R$  and  $A$  are the same whatever the adsorbed species, another term which is the reduced form of the spreading pressure can be defined as follows:

$$\pi_i^* = \frac{\pi_i \cdot A}{R \cdot T} = \int_0^{p_i^o} \frac{q_i^o(p)}{p} dp. \quad (\text{Eq. 4-7})$$

where,  $\pi_i^*$  is the reduced spreading pressure of species  $i$ .

The relation between the molar compositions of both gas and adsorbed phases is presented in Eq. 4-8:

$$p \cdot y_i = p_i^o \cdot x_i \quad \leftrightarrow \quad p_i^o = \frac{p \cdot y_i}{x_i} \quad (\text{Eq. 4-8})$$

where,  $y_i$  and  $x_i$  are the mole fractions of species  $i$  in the gas phase and adsorbed phase, respectively.

From Eq. 4-8, the hypothetical pressure,  $p_i^o$ , can be expressed as a function of  $x_i$  and  $y_i$ . Therefore, the reduced spreading pressure,  $\pi_i^*$ , can also be expressed as a function of  $x_i$  and  $y_i$  instead of  $p_i^o$ . Table 4-3 shows the different forms of the reduced spreading pressure together with the proposed initial guesses and constraints of the equation variable ( $y_i$ ,  $x_i$  or  $p_i^o$ ).

**Table 4-3.** The forms of the reduced spreading pressure equation, initial guess, and constraint for the different modes of calculation [204].

Mode	Reduced spreading pressure	Initial guess	Constraint
1	$\pi_i^*(x_i) = \int_0^{\frac{p \cdot y_i}{x_i}} \frac{q_i^o(p)}{p} dp$	$x_i = \frac{q_i^o(p \cdot y_i)}{\sum_i^N q_i^o(p \cdot y_i)}$	$\sum_i x_i = 1$
2	$\pi_i^*(y_i) = \int_0^{\frac{p \cdot y_i}{x_i}} \frac{q_i^o(p)}{p} dp$	$y_i = x_i$	$\sum_i y_i = 1$
3	$\pi_i^*(p_i^o) = \int_0^{p_i^o} \frac{q_i^o(p)}{p} dp$	Solution of $q_T \cdot x_i = q_i^o(p_i^o)$	$\sum_i \frac{q_T \cdot x_i}{q_i^o(p_i^o)} = 1$

Based on the thermodynamic equivalence of the spreading pressure  $\pi_i^*$  of each adsorbed species at equilibrium, the thermodynamic state of the system can be obtained by solving Eq. 4-9 with the help of initial guess and constraint equation in Table 4-3 to calculate the pure component hypothetical pressure  $p_i^o$ . The iterations computes the output variables at each points of equilibrium:  $q_T, x_1, x_2, \dots, x_N$  for Mode 1.

$$\pi_1^* = \pi_2^* = \dots = \pi_N^* \quad (\text{Eq. 4-9})$$

The calculation can be effectuated by different ways such as using Visual Basic for Applications (VBA) which is an implementation of Microsoft in Excel, Math Lab or

available software such as pyIAST [205] and IAST++ (used in this study) [204]. In VBA or Math Lab, the calculation can be done by using dichotomy or other methods to solve Eq. 4.21 with the help of analytical expressions of reduced spreading pressure and pure component hypothetical pressure provided by Do 1998 [95]. However, one should note that some isotherms such as Langmuir and Freundlich do have analytical expressions for the spreading pressure as well as for the pure component hypothetical pressure [95]. Other isotherm models such as Toth only has analytical expression for the spreading pressure, but the pure component hypothetical pressure expressed in terms of the reduced pressure must be determined from a numerical method [95]. And for other general isotherm such as Dubinin–Radushkevitch, a numerical method must be resorted to obtain the spreading pressure as well as the pure component hypothetical pressure [95]. Therefore, analytical IAST calculation cannot be done using VBA for Toth, Dubinin–Radushkevitch and some other isotherm models.

The adsorption selectivity of a binary gas mixture is usually calculated based on the definition of the equilibrium separation factor introduced by Ruthven 1984 [206] as shown below:

$$\alpha_{A/B} = \frac{q_A/q_B}{p_A/p_B} \quad \leftrightarrow \quad \alpha_{A/B} = \frac{x_A/x_B}{y_A/y_B} \quad (\text{Eq. 4-10})$$

where,  $q_A$  and  $q_B$  ( $\text{mol}\cdot\text{kg}^{-1}$ ) are the amount of species  $A$  and  $B$  adsorbed per unit mass of adsorbent at equilibrium at their respective partial pressures,  $p_A$  and  $p_B$ .

By using the values of adsorbed molar fractions,  $x_i$ , deduced from IAST calculations, the IAST selectivity can so be expressed as in Eq. 4-11:

$$\alpha_{A/B}^{IAST} = \frac{x_A^{IAST}/x_B^{IAST}}{y_A/y_B} \quad (\text{Eq. 4-11})$$

Figure 4-11 recapitulates the method of IAST selectivity calculations, assuming for: (i) an equimolar binary mixture of species  $A$  and  $B$  ( $y_A = y_B = 0.5$ ), and, (ii) both adsorption isotherms of each pure component are described by Langmuir model (Eq. A-2) at the same operational conditions.

In another approach called Real Adsorbed Solution Theory, the non-ideality of the system is taken into account: (i) for the gas phase by replacing the pressure,  $p$ , in the above equations with the fugacity, and, (ii) for the adsorbed phase by replacing the adsorbed phase

mole fractions  $x_i$  with  $x_i \cdot a_i$  where  $a_i$  is the activity coefficient of species  $i$  [95, 203-205]. However, in this study, only ideal systems (IAST) were assumed.

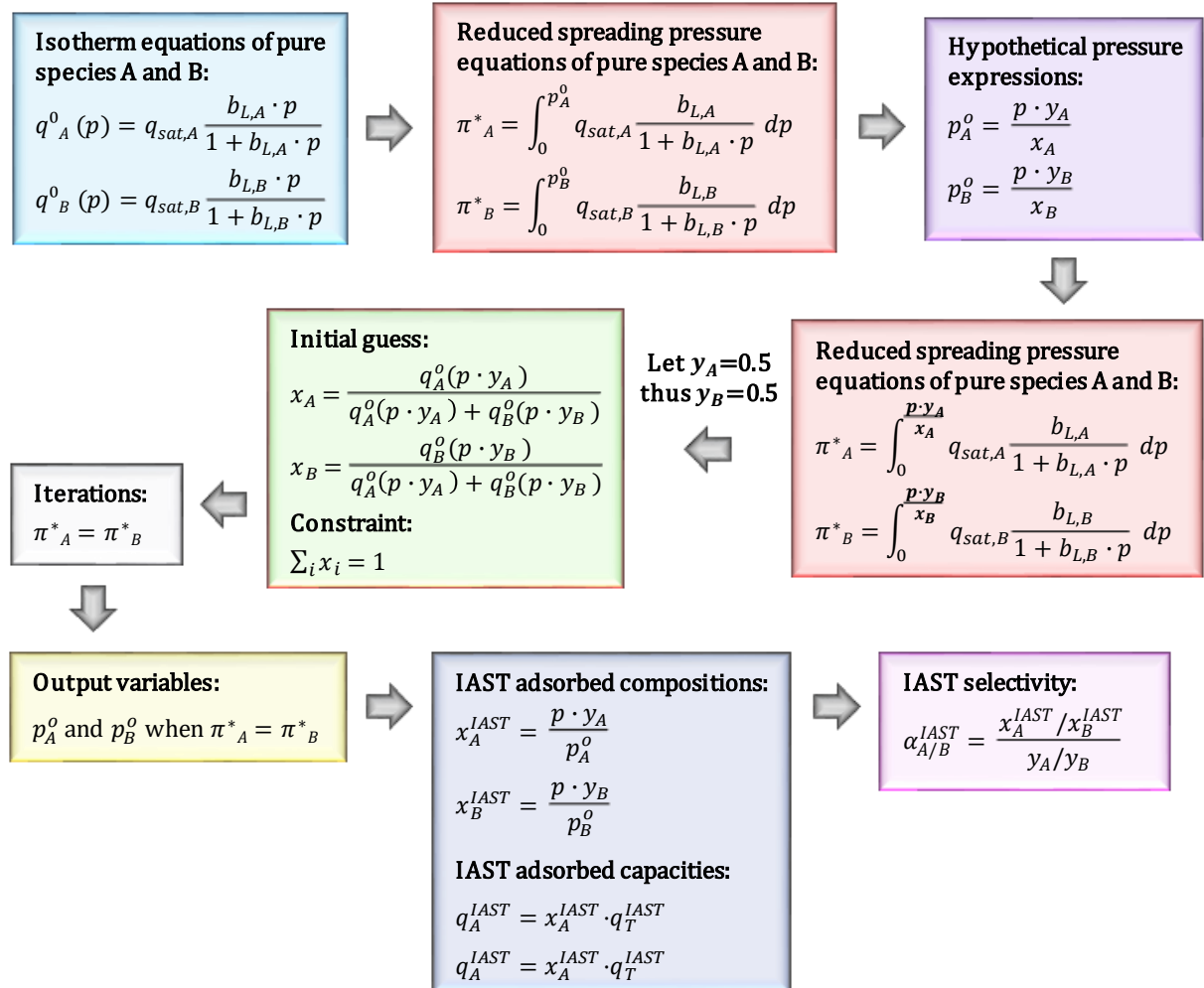


**Figure 4-11.** Recapitulative of the IAST selectivity calculation method, assuming for an equimolar binary mixture of species A and B whose adsorption isotherm of the pure component is described by Langmuir model at the same operational conditions.

### 4.3. Manometric measurements: Methodology

#### 4.3.1. Experimental approaches and data treatment

Manometric measurement was the earliest approach for determining gas adsorption capacities [207]. This technique measures the amount of gas removed from the gas phase in static (non-flowing) mode by performing the measurement of either: (i) the pressure drop  $\Delta P$  in a fixed volume  $V$  (method used in this study), or (ii) the change in volume  $\Delta V$  at a fixed pressure  $P$ , or (iii) the gas molar flow rate using a mass flow meter [208]. A number

of different terms are employed to describe the method of measurement of the pressure drop in a fixed volume system, such as manometric, volumetric, piezometric method, constant-volume-variable-pressure method and Sieverts technique [209]. Figure 4-12 describes the configuration of a manometric apparatus which enables the adsorption of a single gas component and consists of two compartments, a reservoir and a sample cell (or an adsorption system). This schema considers in the first place the situation where the sample cell temperature equals to the reservoir temperature.

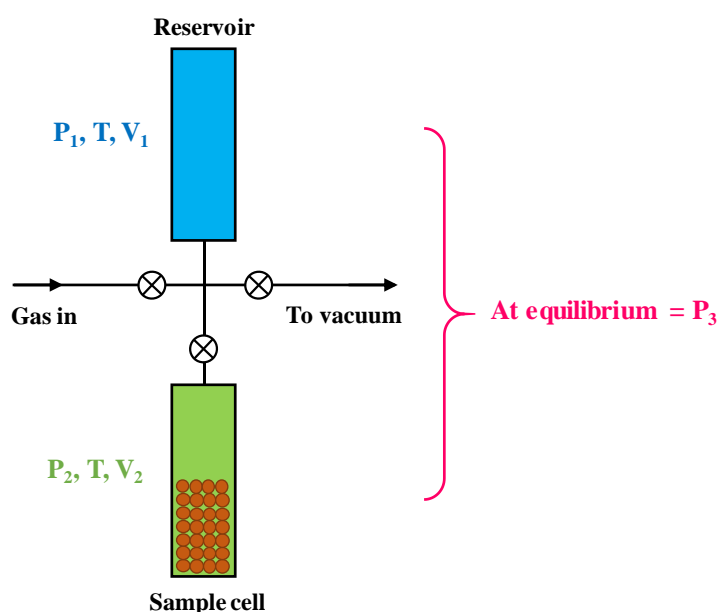


**Figure 4-12.** Schematic figure giving the configuration of manometric apparatus in which the sample cell temperature equals to the reservoir temperature.

The manometric experiments make use of the real gas law as presented in Eq. 4-12 [192, 208]. If  $V$  and  $T$  are known, the measurement of  $P$  allows the derivation of the number of moles of gas present.

$$P \cdot V = n \cdot Z \cdot R \cdot T \quad (\text{Eq. 4-12})$$

where  $P$  (Pa) is the gas pressure,  $V$  ( $\text{m}^3$ ) is the gas volume,  $n$  is the number of moles in the gas phase,  $Z$  is the gas compressibility factor ( $Z=1$  for an ideal gas,  $Z \neq 1$  for a real gas),  $R$  ( $\text{J} \cdot \text{mol}^{-1} \cdot \text{K}^{-1}$ ) is the gas constant and  $T$  (K) is the temperature.

The instrument is firstly evacuated whereby volume  $V_2$  is held under vacuum at  $P_2$ , and volume  $V_1$  is then pressurised to an initial pressure in reservoir,  $P_1$ . In order to dose the gas filling the sample cell, the separating valve is opened and the final pressure  $P_3$  is

measured after equilibration delay. Eq. 4-12 is used to derive the mass balance equation in an instrument of known internal volumes  $V_1$  and  $V_2$ . For the first isotherm point, the number of moles adsorbed is then given by Eq. 4-13 [192, 208]:

$$\Delta n = \frac{P_1 \cdot V_1}{Z_{P_1,T} \cdot R \cdot T} - \frac{P_3(V_1 + V_2)}{Z_{P_3,T} \cdot R \cdot T} \quad (\text{Eq. 4-13})$$

where  $\Delta n$  is the number of moles adsorbed,  $Z_{P_1,T}$  and  $Z_{P_3,T}$  are the gas compressibility factors at  $T$  and at  $P_1$  and  $P_3$ , respectively, and  $V_2$  is the dead volume in the sample cell, which includes free space non-occupied by the sample, the interparticle voids of granular sample as well as the internal particular porosity of the sample which is not filled with the adsorbate.

The dosing volume is initially pressurized in  $V_1$  until the pressure of the reservoir reaches  $P_1$ . A period of stabilization is then required to allow accurate calculation. The dosing is expanded to  $V_2$  in which the sample cell pressure is initially at the pressure of the previous adsorption equilibrium point,  $P_2$ , and then is allowed to decrease until equilibrium is achieved at  $P_3$ . The amount of gas adsorbed is calculated in the region of  $\Delta P = P_2 - P_3$ . Therefore, the adsorption uptake at point  $m$  of an isotherm can be given by the following equation, let  $j$  be instantaneous points of adsorption equilibrium where  $1 \leq j \leq m$ :

$$n_{ads,m} = \sum_{j=1}^m \left[ \underbrace{\frac{P_{1,j} \cdot V_1}{Z_{P_{1,j},T} \cdot R \cdot T}}_{\substack{\text{Moles in } V_1 \\ \text{before dosing}}} + \underbrace{\frac{P_{2,j} \cdot V_2}{Z_{P_{2,j},T} \cdot R \cdot T}}_{\substack{\text{Moles in } V_2 \\ \text{before dosing}}} - \underbrace{\frac{P_{3,j} \cdot (V_1 + V_2)}{Z_{P_{3,j},T} \cdot R \cdot T}}_{\substack{\text{Moles in } V_1+V_2 \text{ at} \\ \text{the end of sorption}}} \right] \quad (\text{Eq. 4-14})$$

One should note that  $P_{2,j} = P_{3,j-1}$ . For the data treatment,  $n_{ads,m}$  is deduced from measurements of  $P$  and  $T$  values, accounting for the compressibility factors  $Z$  dependent on  $P$  and  $T$ . At pressures close to ambient, most gases behave as “ideal” thus the compressibility factor  $Z = 1$ , while the value of  $Z$  needs to be determined at elevated pressures since it may significantly deviate from 1. For the determination of the gas density  $\rho_g$  as a function of  $P$  and  $T$ , non-ideal Equations of States (EOSs) of various types are available, including a widely used general type corresponding to multiparameter EOSs [210]. Multiparameter EOSs express  $\rho_g$  as a function of  $P$  and  $T$  involving a number of empirical parameters that makes solving the equation quite complicated [210], but there are

several available developed databases that can be used to predict the state properties of non-ideal gases. For example, the best-known NIST REFPROP database can provide the data of non-ideal gases derived from different multiparameter EOSs, e.g. Span and Wagner EOSs which were developed in 1996 for CO<sub>2</sub>, and that were employed in this study [211].

The volume  $V_2$  in the sample cell which is filled by the adsorptive molecules either in the gas or in the adsorbed phase can be defined as:  $V_2 = V_{cell} - V_s$ , where  $V_{cell}$  is the empty volume of the sample cell and  $V_s$  the volume occupied by the adsorbent sample, excluding the intraparticle porosity which remains accessible to the adsorbate molecules. Defining  $\rho_s$  as the skeletal density of the adsorbent sample (when the volume measured excludes the pores as well as the void spaces between particles within the bulk sample), thus the volume  $V_s$  can be derived as  $V_s = m_s/\rho_s$ , where  $m_s$  is the mass of the adsorbent sample. Then, Eq. 4-14 can be expressed as follows:

$$n_{ads,m} = \sum_{j=1}^m \left[ \frac{P_{2,j,T} \left( V_{cell} - \frac{m_s}{\rho_s} \right)}{Z_{P_{2,j,T}} \cdot R \cdot T} + \frac{P_{1,j,T} \cdot V_1}{Z_{P_{1,j,T}} \cdot R \cdot T} - \frac{P_{3,j,T} \left( V_1 + \left( V_{cell} - \frac{m_s}{\rho_s} \right) \right)}{Z_{P_{3,j,T}} \cdot R \cdot T} \right] \quad (\text{Eq. 4-15})$$

Any adsorption measurement that relies on volume such as manometric measurements requires the accurate determination of the dead volume,  $V_2$ . The value of  $V_2$  can be calibrated by using two general approaches: direct and indirect [207]. The direct determination of dead volume involves measuring  $V_2$  of the sample cell with the sample inside using an *in situ* Helium gas expansion. This method was actually the one applied for this study. Whereas the indirect determination implies an *ex situ* determination of the true density of the adsorbent by Helium pycnometry [207] or accounting for theoretical crystal density for well-crystallized adsorbents.

The determination of  $V_2$  becomes especially difficult at two following situations. The first situation is when the adsorption experiment is done at a controlled temperature that differs significantly from the set reservoir temperature. The accurate determination of  $V_2$  requires then to account for temperature gradients in the whole system, as discussed in Section 4.3.2. Second situation is when the adsorption experiment is conducted until elevated pressures. The increasing pore volume occupied by the adsorbed phase  $V_{ads}$  must be taken into account in the estimation of  $V_2$ , as discussed in Section 4.3.3.

## 4.3.2. Temperature-dependent dead volumes estimation for high temperatures

The adsorption measurement at high temperatures gives rise to temperature inhomogeneities along the system that affect the value of the dead volume  $V_2$  in the sample cell. Figure 4-13 describes the configuration of the manometric apparatus when a single gas component is adsorbed with a gradient of temperature between the reservoir  $T_1$ , and the sample cell  $T_2$ . Unlike the previous configuration, apparent “up” dead volume  $V_U$ , and “down” dead volume  $V_D$ , are introduced to decompose  $V_2$  into two sub-compartments, where  $V_U$  is the upper compartment in the sample cell assumed at the temperature  $T_1$  of the reservoir, while  $V_D$  is the lower compartment in the sample cell assumed at a uniform temperature  $T_2$ .

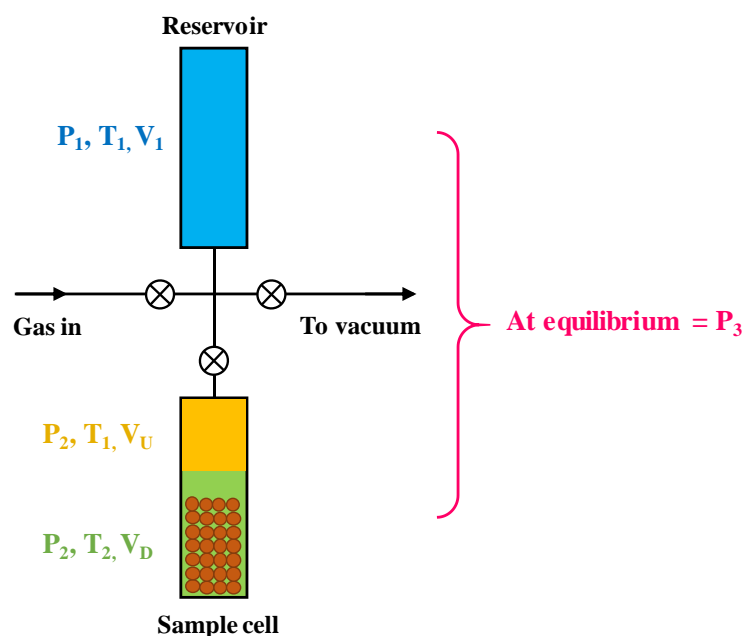


**Figure 4-13.** Schematic configuration of the manometric system taking into consideration the gradient of temperature between the sample cell and the gas reservoir.

The expressions for temperature-dependent dead volumes  $V_U$  and  $V_D$ , are established from helium expansion experiments, assuming no adsorption of helium and the sample cell initially empty of gas ( $P_2 = 0$ ). Departing from the equality in the total number of moles of gas present in the system at the two stationary conditions, before and after gas expansion:

- reservoir initially filled with helium at pressure  $P_1$ ,
- reservoir and sample cell both at equilibrium pressure  $P_3$  after helium expansion.

The gas mass conservation is expressed as Eq. 4-16:

$$\frac{P_1 \cdot V_1}{R \cdot T} = \frac{P_3(V_1 + V_2)}{R \cdot T} \quad (\text{Eq. 4-16})$$

Knowing that  $V_2 = V_U + V_D$ , then Eq. 4-16 becomes:

$$\frac{P_1 \cdot V_1}{R \cdot T} = \frac{P_3(V_1 + V_U + V_D)}{R \cdot T} \quad (\text{Eq. 4-17})$$

Let  $V_{2,T_1}$  and  $V_{2,T_2}$  be the dead volumes of the sample cell containing the adsorbent calibrated using helium at two controlled temperatures  $T_1$  and  $T_2$ , respectively.

When the sample cell volume is at the same temperature as the reservoir  $T_1$ , Eq. 4-17 gives:

$$\frac{P_1 \cdot V_1}{R \cdot T_1} = \frac{P_3(V_1 + V_{2,T_1})}{R \cdot T_1} \quad (\text{Eq. 4-18})$$

When the sample cell volume is at the temperature that  $T_2 \neq T_1$ , then  $V_2 = V_{2,T_2} = V_U + V_D$  (Eq. 4-19). Replacing  $V_2$  with  $V_U$  and  $V_D$  in Eq. 4-18:

$$\begin{aligned} \frac{P_1 \cdot V_1}{R \cdot T_1} &= \frac{P'_3 \cdot V_1}{R \cdot T_1} + \frac{P'_3 \cdot V_U}{R \cdot T_1} + \frac{P'_3 \cdot V_D}{R \cdot T_2} \\ \frac{P_1 \cdot V_1}{R \cdot T_1} &= \frac{P'_3 \cdot (V_1 + V_U)}{R \cdot T_1} + \frac{P'_3 \cdot V_D}{R \cdot T_2} \end{aligned} \quad (\text{Eq. 4-20})$$

Then, Eq. 4-18 + Eq. 4-20:

$$\begin{aligned} \frac{P_3(V_1 + V_{2,T_1})}{R \cdot T_1} &= \frac{P'_3(V_1 + V_U)}{R \cdot T_1} + \frac{P'_3 \cdot V_D}{R \cdot T_2} \\ \frac{V_{2,T_1} - V_U}{T_1} &= \frac{V_D}{T_2} \end{aligned} \quad (\text{Eq. 4-21})$$

From Eq. 4-19,  $V_U = V_{2,T_2} - V_D$ . By injecting  $V_U$  of Eq. 4-19 into Eq. 4-21:

$$V_D = \frac{V_{2,T_1} - (V_{2,T_2})^{fictive}}{\left(\frac{T_1}{T_2} - 1\right)} \quad (\text{Eq. 4-22})$$

Eq. 4-22 is used to calculate  $V_D$  from the helium-calibrated values of  $V_{2,T_1}$  and  $V_{2,T_2}$  and consequently Eq. 4-19 can be used to calculate  $V_U$ .

When a large temperature difference between the reservoir and the sample cell needs to be taken into account in dead volume calibration, the calculation of amount adsorbed of an adsorptive component onto the sample can be determined by the following equation elaborated from the previous Eq. 4-14:

$$\begin{aligned}
 n_{ads,m} = \sum_{j=1}^m & \left[ \underbrace{\frac{P_{1,j} \cdot V_1}{Z_{P_{1,j},T_1} \cdot R \cdot T_1}}_{\text{Moles in } V_1 \text{ before dosing}} + \underbrace{\frac{P_{2,j} \cdot V_U}{Z_{P_{2,j},T_1} \cdot R \cdot T_1}}_{\text{Moles in } V_U \text{ before dosing}} + \underbrace{\frac{P_{2,j} \cdot V_D}{Z_{P_{2,j},T_2} \cdot R \cdot T_2}}_{\text{Moles in } V_D \text{ before dosing}} - \underbrace{\frac{P_{3,j} \cdot V_1}{Z_{P_{3,j},T_1} \cdot R \cdot T_1}}_{\text{Moles in } V_1 \text{ at the end of sorption}} \right. \\
 & \left. - \underbrace{\frac{P_{3,j} \cdot V_U}{Z_{P_{3,j},T_1} \cdot R \cdot T_1}}_{\text{Moles in } V_U \text{ at the end of sorption}} - \underbrace{\frac{P_{3,j} \cdot V_D}{Z_{P_{3,j},T_2} \cdot R \cdot T_2}}_{\text{Moles in } V_D \text{ at the end of sorption}} \right] \quad (\text{Eq. 4-23})
 \end{aligned}$$

At each point of equilibrium: (i) the instrument measures and provides the values of  $P_1$ ,  $P_2$ ,  $P_3$ ,  $T_1$  and  $T_2$ , (ii)  $V_1$  is fixed depending on reservoir size, (iii)  $V_{2,T_1}$  and  $V_{2,T_2}$  are calibrated with helium in prior to adsorption measurements, (iv)  $V_U$  and  $V_D$  are determined based on  $V_{2,T_1}$  and  $V_{2,T_2}$  as well as  $T_1$  and  $T_2$ , and, (v)  $Z_{P_1,T_1}$ ,  $Z_{P_2,T_1}$ ,  $Z_{P_2,T_2}$ ,  $Z_{P_3,T_1}$  and  $Z_{P_3,T_2}$  are calculated as functions of  $P_1$ ,  $P_2$ ,  $P_3$ ,  $T_1$  and  $T_2$  using developed EOSs database.

#### 4.3.3. Pressure-dependent dead volumes estimation for high pressures

The measured adsorbed quantities in manometric experiments (and other volume-basis measurement techniques) can be related to net, absolute and excess adsorption concepts [190, 209, 212, 213]. Adsorption capacities are defined according to these different concepts requiring different corrections in the calibration of the dead volume  $V_2$  [190, 209, 212, 213].

Net adsorption capacity,  $n_{net}$ , proposed by Gumma and Talu (2013) [213] accounts for all the quantity of adsorptive molecules filling the sample cell volume  $V_{cell}$ , ignoring any distinction between the fractions contained in the adsorbed phase and in the bulk gas phase. Therefore  $V_2 = V_{cell}$  (Figure 4-14-i). This procedure has the advantage of eliminating uncertainties in the evaluation of the volumes respectively occupied by the adsorbent sample and the adsorbed phases,  $V_s$  and  $V_{ads}$ . For nanoporous adsorbents (pore sizes <100 nm by IUPAC definition),  $V_s$  is difficult to be accurately measured due to the

possible existence of non-accessible pores in the adsorbent particle, meaning that adsorbate molecules may not “see” the same pores as those “seen” by helium molecules because of the difference in their kinetic diameters, thus provoking some uncertainties in the calibration of  $V_g$  [190]. Meanwhile, the estimation of the volume of the adsorbed phase  $V_{ads}$ , which is crucial for experiments performed at high pressures, is also difficult especially because the estimation of the pore volume accessible to adsorptive molecules relies on the interpretation of physisorption isotherms, carrying some dependency with the nature of the probe molecule, the operational pressure and temperature applied and the assumption made to describe the state of the condensed molecules within the pores (considered as a liquid). For crystalline adsorbents such as MOFs and zeolites, the assumption of  $V_{ads} \approx V_{pore}$  presents less uncertainties than for amorphous porous materials [209, 212, 213], however these cannot be fully eliminated.

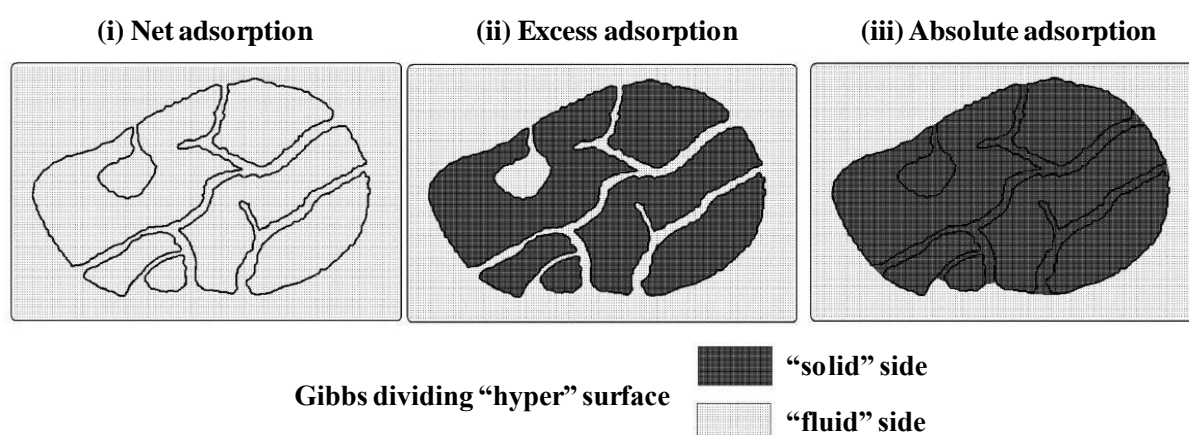


**Figure 4-14.** Different reference states for determining dead volume in (i) net adsorption, (ii) excess adsorption and (iii) absolute adsorption [213].<sup>45</sup>

Excess adsorption, also known variously as surface excess, Gibbs excess or Gibbsian surface excess, is a standard concept dated back to work by Gibbs in 1878. Gibbs proposed to make a distinction between excess adsorbed quantity and absolute adsorbed quantity assuming the system divided into two regions by an imaginary line called “the Gibbs dividing surface”,  $x_{Gibbs}$ , placed parallel to the surface of the adsorbent (Figure 4-15). One of these two regions is filled with the gaseous adsorptive at a density equal to the bulk gas, whereas the other fraction is occupied by the adsorbed phase of volume  $V_a$  which lies between the solid surface

<sup>45</sup> Reprinted from The Journal of Physical Chemistry C, O. Talu *et al.*, Net adsorption of gas/vapor mixtures in microporous solids, vol. 117, no. 25, pp. 13059-13071, Copyright 2013, with permission from American Chemical Society.

(at  $x = 0$ ) and the dividing line,  $x_{Gibbs}$ . The upper diagram in Figure 4-15 represents the volume of the solid (adsorbent skeleton including potential non-accessible pores)  $V_S$ , the volume of the adsorbed phase (filling the accessible intraparticle porosity)  $V_{ads}$ , and that of the bulk gas phase  $V_g$ . The bottom plot shows the change in the density of the adsorptive molecules as a function of the distance from the solid surface  $x$ , varying continuously between a high and a low density equaling that to the bulk  $\rho_g$ .

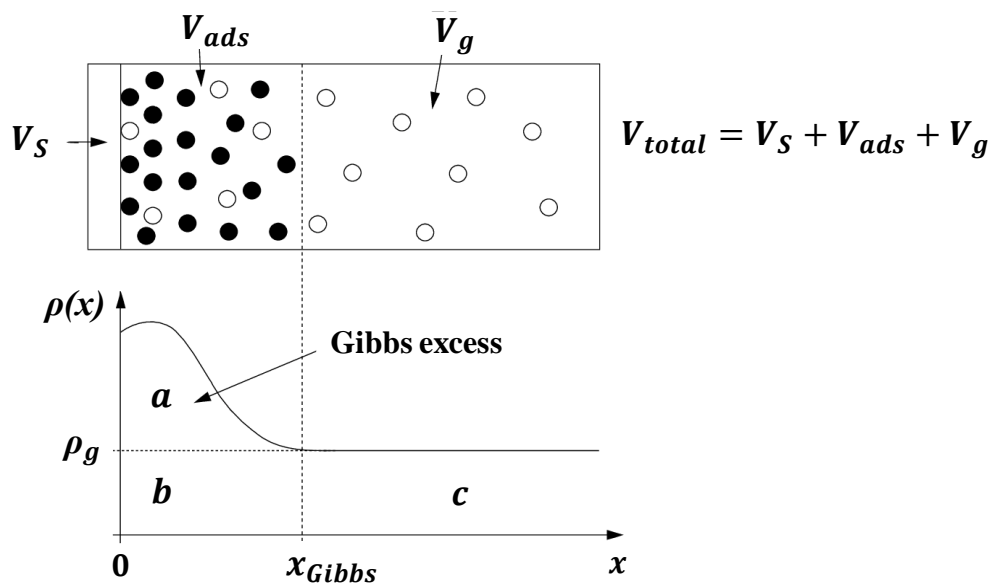


**Figure 4-15.** A schematic diagram illustrating the concept of Gibbs excess adsorbed quantity and absolute adsorbed quantity on an open planar surface [209].<sup>46</sup>

The total quantity of adsorbates contained in the sample cell is described in the bottom plot as the regions ( $a + b + c$ ): (i) Gibbs excess adsorbed quantity  $n_{ex}$ , corresponds to the condensed fraction in region ( $a$ ), (ii) absolute adsorbed quantity  $n_{abs}$ , accounts for regions ( $a + b$ ), and, (iii) the amount of gas present in the absence of adsorption is shown as region ( $b + c$ ). In the upper diagram, black circles indicate molecules that are attributed to region ( $a$ ), while white circles indicate molecules that are attributed to region ( $b + c$ ). As shown in the bottom plot, supposing that the condensed adsorbed molecules (black) in region ( $a$ ) is liquid-like phase, then its density appears higher than  $\rho_g$ , while supposing that the non-adsorbed molecules (white) in adsorbed phase in region ( $b$ ) is gas phase thus it has the same density as bulk gas phase,  $\rho_g$ . But as adsorption pressure increases,  $\rho_g$  increases

<sup>46</sup> Reprinted from JRC Scientific Technical Reports, D. P. Broom *et al.*, Hydrogen sorption measurements on potential storage materials, Copyright 2008, with permission from European Commission.

and as the pressure decreases,  $\rho_g$  decreases. Thus at very low pressures, region (b) may become negligible compared to region (a) which refers to the case where  $n_{abs} \approx n_{ex}$ . While at higher pressures, the contribution of region (b) to absolute adsorbed quantity becomes increasingly significant, therefore  $n_{abs} > n_{ex}$ . At elevated pressures, it may also happen that the contribution of region (a) becomes far less compared to that of region (b), so that Gibbs excess adsorbed quantity may become zero or negative.

Consequently, as the measured adsorption capacity from manometric experiments accounting for dead volume calibration as exposed previously, actually reflects an excess adsorption capacity  $n_{ex}$  (Figure 4-14-ii), it may be observed a decrease in the reported experimental data at increasing pressures because  $V_2 = V_{cell} - V_s$ , includes  $V_{ads}$  as seen in Section 4.3.1. For that reason, at high pressures, a correction must be done to derive data representative of the absolute (or total) uptakes  $n_{abs}$  (or  $n_{total}$ ), taking into account both  $V_s$  and  $V_{ads}$  in the sample cell (Figure 4-14-iii).

$n_{abs}$  can be computed from  $n_{ex}$  using Eq. 4-24 [209, 212, 214] where  $n_{ex}$  is considered as equivalent to the measured adsorbed amount ( $n_{ads}$ ) as derived from Eq. 4-23,  $V_{pore}$  (cm<sup>3</sup>) is the pore volume and  $\rho_g$  (mol·cm<sup>-3</sup>) is the bulk gas density.

$$n_{abs} = n_{ex} + V_{pore} \cdot \rho_g \quad (\text{Eq. 4-24})$$

Figure 4-16 describes the variations in the relative contributions of the excess adsorption amount and  $V_{pore} \cdot \rho_g$  term to absolute adsorption amount as a function of pressure at constant temperature [210]. On the left side of the diagram, the pores are shown filling up with pressure increase, where blue and orange regions represent the magnitudes of excess adsorption and  $V_{pore} \cdot \rho_g$  term, respectively. At low pressures, (A) absolute adsorption amount results mainly from excess adsorption ( $n_{abs} \approx n_{ex}$ ); while at high pressures, (D) a significant part of the absolute adsorption amount is attributed to  $V_{pore} \cdot \rho_g$  term ( $n_{abs} > n_{ex}$ ).

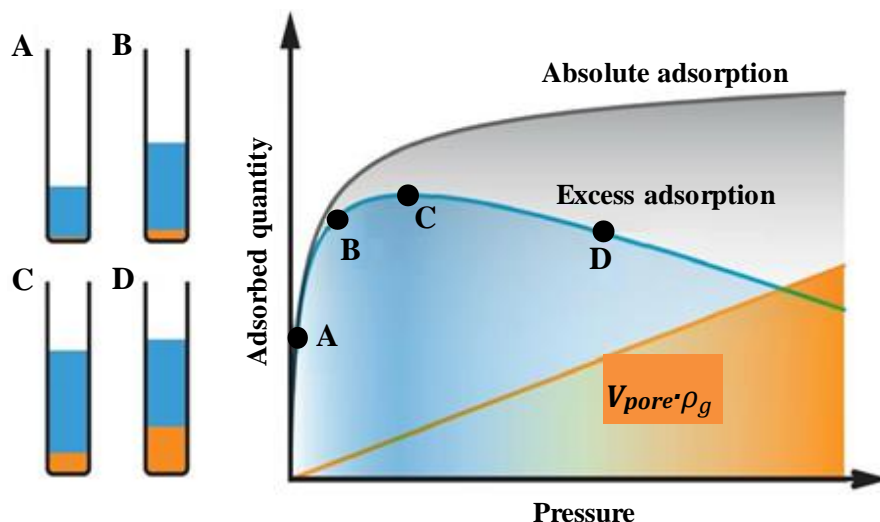


**Figure 4-16.** A schematic representation of the difference between excess and absolute adsorption capacities as a function of pressure at constant temperature [210].<sup>47</sup>

Eq. 4-24 can be solved by assuming that  $V_{ads} = V_{pore}$  at saturation of the adsorbent [209, 212]. Meanwhile,  $V_{pore}$  only accounts for the open porosity determined by  $N_2$  ads/desorption analysis at 77 K in Section 3.7.5. As mentioned previously, this assumption is reasonable for crystalline microporous materials including MOFs. Thus, the amount of gas adsorbed in this study was corrected using Eq. 4-24 in which  $n_{ex} = n_{ads}$  as derived from experimental data in Eq. 4-23. The expression of gas density  $\rho_g$  at each point of equilibrium is presented in Eq. 4-25. However, there are also a number of published works focusing on MOFs and zeolites high-pressure adsorptions studies who consider that  $\rho_{ads} = \rho_{liquid}$  [209, 212, 215-217]. Anyhow, it is undeniable that there are still disagreements in the literature in regard to which definition is the best to use [209].

$$\rho_g = \frac{P_3 \cdot M}{Z_{P_3, T_2} \cdot R \cdot T_2} \quad (\text{Eq. 4-25})$$

#### 4.3.4. Absolute and relative experimental errors

The absolute experimental errors of an adsorption measurement depends on the inaccuracy of the instrument in measuring all parameters;  $P, T, V$ . The errors need to be estimated for each measurement point to evaluate the accuracy of equilibrium data which

<sup>47</sup> Reprinted from MRS Bulletin, D. P. Broom and K. M. Thomas, Gas adsorption by nanoporous materials: future applications and experimental challenges, vol. 38, no. 5, pp. 412-421, Copyright 2013, with permission from Springer Nature.

concerns especially the measurements at elevated temperatures and (or) elevated pressures because the absolute errors exhibit more important and significant values. The calculations of cumulative variances of absolute experimental errors of measurement at point  $m$ ,  $\sigma_{cum}^2(n_{ads,m})$ , are shown in Eq. 4-26 departing from the equation of the adsorbed amount (Eq. 4-23).

Recall of Eq. 4-23:

$$n_{ads,m} = \sum_{j=1}^m \left[ \frac{P_{1,j} \cdot V_1}{Z_{P_{1,j},T_1} \cdot R \cdot T_1} + \frac{P_{2,j} \cdot V_U}{Z_{P_{2,j},T_1} \cdot R \cdot T_1} + \frac{P_{2,j} \cdot V_D}{Z_{P_{2,j},T_2} \cdot R \cdot T_2} - \frac{P_{3,j} \cdot V_1}{Z_{P_{3,j},T_1} \cdot R \cdot T_1} - \frac{P_{3,j} \cdot V_U}{Z_{P_{3,j},T_1} \cdot R \cdot T_1} - \frac{P_{3,j} \cdot V_D}{Z_{P_{3,j},T_2} \cdot R \cdot T_2} \right]$$

Thus,  $\sigma_{cum}^2(n_{ads,m})$  can be defined as follows. Eq. 4-26 represents the errors propagation of Eq. 4-23 which is obtained by partially deriving each term of Eq. 4-26 with respect to each variable for which the uncertainty is accounted: (i)  $P$  supposing  $\sigma^2(P) = \sigma^2(P_1) = \sigma^2(P_2)$ , (ii)  $V_1$ , (iii)  $V_U$  and (iv)  $V_D$ .

$$\begin{aligned} \sigma_{cum}^2(n_{ads,m}) = & \sum_{j=1}^m \left[ \left( \frac{V_1}{Z_{P_{1,j},T_1} \cdot R \cdot T_1} \right)^2 + \left( \frac{V_U}{Z_{P_{2,j},T_1} \cdot R \cdot T_1} \right)^2 + \left( \frac{V_D}{Z_{P_{2,j},T_2} \cdot R \cdot T_2} \right)^2 \right. \\ & \left. - \left( \frac{V_1}{Z_{P_{3,j},T_1} \cdot R \cdot T_1} \right)^2 - \left( \frac{V_U}{Z_{P_{3,j},T_1} \cdot R \cdot T_1} \right)^2 - \left( \frac{V_D}{Z_{P_{3,j},T_2} \cdot R \cdot T_2} \right)^2 \right] \sigma^2(P) \\ & + \left[ \left( \frac{P_{1,j}}{Z_{P_{1,j},T_1} \cdot R \cdot T_1} \right)^2 - \left( \frac{P_{3,j}}{Z_{P_{3,j},T_1} \cdot R \cdot T_1} \right)^2 \right] \sigma^2(V_1) \\ & + \left[ \left( \frac{P_{2,j}}{Z_{P_{2,j},T_1} \cdot R \cdot T_1} \right)^2 - \left( \frac{P_{3,j}}{Z_{P_{3,j},T_1} \cdot R \cdot T_1} \right)^2 \right] \sigma^2(V_U) \\ & + \left[ \left( \frac{P_{2,j}}{Z_{P_{2,j},T_2} \cdot R \cdot T_2} \right)^2 - \left( \frac{P_{3,j}}{Z_{P_{3,j},T_2} \cdot R \cdot T_2} \right)^2 \right] \sigma^2(V_D) \quad (\text{Eq. 4-26}) \end{aligned}$$

where  $\sigma^2(P)$ ,  $\sigma^2(V_1)$ ,  $\sigma^2(V_U)$  and  $\sigma^2(V_D)$  represents the variances of measurement errors of  $P$ ,  $V_1$ ,  $V_U$  and  $V_D$ , respectively.

The expressions for  $\sigma^2(V_D)$  in Eq. 4-27 and  $\sigma^2(V_U)$  in Eq. 4-28 are presented below deduced from partial differentiation of Eq. 4-22 and Eq. 4-19, respectively, with respect to variables  $V_{2,T_1}$  and  $V_{2,T_2}$ , and,  $V_D$ , respectively.

$$\sigma^2(V_D) = \frac{V_{2,T_2}}{\left(\frac{T_1}{T_2} - 1\right)} \sigma^2(V_{2,T_1}) + \frac{V_{2,T_1}}{\left(\frac{T_1}{T_2} - 1\right)} \sigma^2(V_{2,T_2}) \quad (\text{Eq. 4-27})$$

$$\sigma^2(V_U) = \sigma^2(V_{2,T_2}) + \sigma^2(V_D) \quad (\text{Eq. 4-28})$$

With the aim of reducing the experimental mistakes, a few aspects must be applied to the measurement method, involving the number of experimental recorded isotherm data and the equilibration time. The number of measurement points must be high enough to accurately describe the isotherm curve, but a large number of data also increases the accumulated errors. Besides that, it is important to allow sufficient equilibration time at each isotherm point. As discussed in Section 4.1, adsorption equilibrium is dependent on  $T$ ,  $P$  and interactions strength, but diffusion kinetics imposes the duration of the equilibration times. The sample cell temperature  $T$  can be affected by the release of heat in the course of adsorption. The pressure change threshold ( $\Delta P/\Delta t$ ) must be monitored as a function of  $t$  at each isotherm step to ensure sufficient equilibration time [208].

In addition, a number of measurement repetitions must be carried out to estimate relative experimental errors and to evaluate the consistency of the experimental equilibrium data.

#### 4.3.5. Procedure of measurements

##### *a. Adsorption isotherms at low pressures*

The sorption isotherms at low pressures for CO<sub>2</sub> and CH<sub>4</sub> on the synthesized samples were measured using automated manometric analyzers: BELSORP mini II from MicrotracBEL (Osaka, Japan) at Universiti Teknologi PETRONAS and 3Flex from Micromeritics (Unterschleißheim, Germany) at IMT Atlantique. Ultrahigh purity CO<sub>2</sub> and CH<sub>4</sub> gases (>99.995 vol%) supplied by Linde Gas Malaysia Sdn Bhd and Air Liquide were used for the study. The adsorption equilibrium data were collected by varying gas probe set pressure,  $p$ , rising to 1 bar (equivalent to  $p/p^\circ=0.0156$  for CO<sub>2</sub> at 25 °C, where  $p^\circ$  is the saturation pressure) in a fixed dose mode. The sample temperature was controlled by water

bath in a Dewar vessel. From 50 to 200 mg of MOF material was placed in a sample cell and further outgassed under a dynamic vacuum at 150 °C for at least 20 h using BelprepII degas stations from MicrotracBEL (Osaka, Japan) at Universiti Teknologi PETRONAS and Smart VacPrep degas stations from Micromeritics (Unterschleißheim, Germany) at IMT Atlantique. The sample cell was then installed to manometric equipment. The determination of dead volume was carried out at 25 °C by helium expansion. More details in the operational procedure is described in Annex VI.

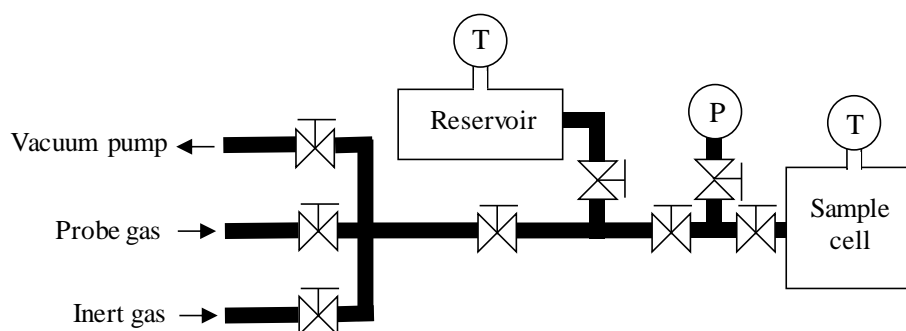


**Figure 4-17.** The configuration of the manometric equipment at low pressures. The pressure transducer and thermocouples are marked P and T, respectively.

#### ***b. Adsorption isotherms at high pressures***

The sorption isotherms at high pressures for CO<sub>2</sub> and CH<sub>4</sub> on the synthesized samples were measured using PCT-Pro manometric equipment from SETARAM (Caluire, France) at IMT Atlantique. Ultrahigh purity CO<sub>2</sub> and CH<sub>4</sub> gases (>99.995 vol%) supplied by Air Liquide were used for the study. The adsorption equilibrium data were collected by varying the increment in gas probe set pressure,  $\Delta P$ , for charging (or pressurizing) the reservoir gradually rising to 40 bars at three different temperatures; 25 °C, 50 °C and 75 °C. The sample temperature was controlled by heating jacket with a thermocouple and isolation coating. About 1.5 g of MOF material was placed in the 40 cm<sup>3</sup> sample holder, cylindrical stainless steel spacers were used to fill in the remaining volume. Gas supply pipelines and adsorption system were evacuated and purged using gas probe. Prior to the measurement, the sample was *in situ* outgassed under vacuum at 150 °C with gradual temperature increment and left overnight under dynamic vacuum until residual pressure stabilization was achieved. Sample holder dead volume was measured using helium expansion at reservoir temperature (27 °C) and at analysis temperature (25 °C, 50 °C and 75 °C), noted  $V_{2,T_1}$  and  $V_{2,T_2}$  respectively (the calculations are detailed in Section 4.3.2).

Then, the equilibrium measurement was run. In order to evaluate the reproducibility of the experimental data and to calculate relative experimental errors, the isotherm was measured 3 times for every operational conditions. More details in the operational procedure including the control of the measurement parameters in the course of the adsorption experiment are described in Annex VI.

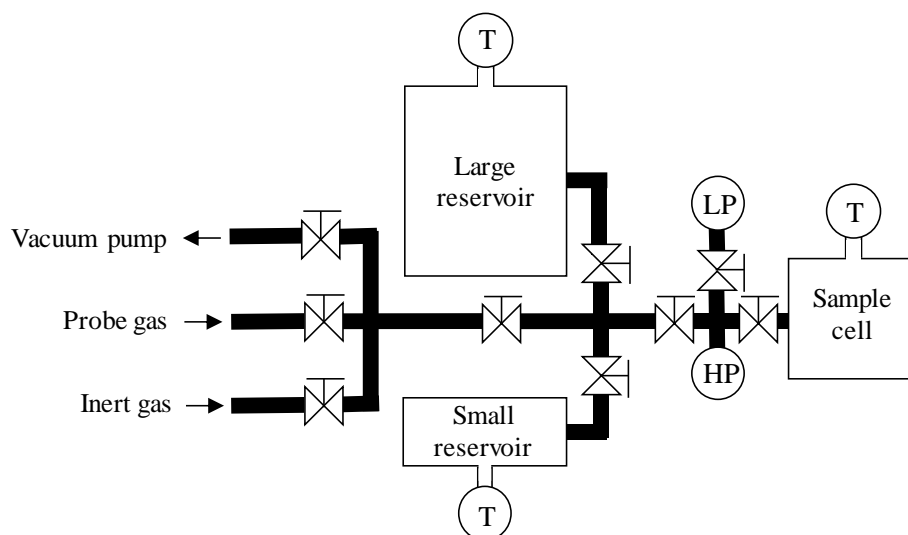


**Figure 4-18.** The configuration of the manometric equipment at high pressures. The pressure transducers and thermocouples are marked LP (low pressure), HP (high pressure) and T, respectively.

#### 4.4. Adsorption isotherms at low pressures: Results and discussions

##### 4.4.1. CO<sub>2</sub> adsorption isotherms and modelling

The adsorption equilibrium data of single component CO<sub>2</sub> were measured on Mg-MOF-74, Mg-MOF-74@CNT and Mg-MOF-74@GO using 3Flex manometric equipment up to 1 bar at 25°C. As presented in Figure 4-19, the produced CO<sub>2</sub> isotherms reveal the improvement in CO<sub>2</sub> uptake at 1 bar from 5.61 mmol·g<sup>-1</sup> (22.4 wt%) measured for the pristine Mg-MOF-74 to 6.62 mmol·g<sup>-1</sup> (26.5 wt%) and 6.91 mmol·g<sup>-1</sup> (27.6 wt%) for Mg-MOF-74@CNT and Mg-MOF-74@GO, respectively. Even if these values remain in the upper range of adsorption capacities reported for MOF-74 family (2.5 mmol·g<sup>-1</sup> and 8.5 mmol·g<sup>-1</sup>) [18-20, 23, 54, 123, 148], they are lower than the data published for Mg-MOF-74. The improvement of CO<sub>2</sub> uptake by 18 mol% and 23 mol% for Mg-MOF-74@CNT and Mg-MOF-74@GO, respectively, compared to the pristine Mg-MOF-74, is in accordance with the changes observed in pore textural properties of both composites. As seen in Section 3.7.5, both composites exhibit larger BET specific surface areas than the

pristine Mg-MOF-74, 21% and 25% more for Mg-MOF-74@CNT and Mg-MOF-74@GO, respectively, and, higher micropore volumes, 18% and 24% more for Mg-MOF-74@CNT and Mg-MOF-74@GO, respectively. The development of microporosity in composite materials offers more adsorption sites for gas molecules which results in higher CO<sub>2</sub> uptakes. The shape of CO<sub>2</sub> isotherms of all samples can be assimilated to Type I isotherm representing adsorption process in microporous adsorbents, demonstrating the ability of CO<sub>2</sub> molecules to diffuse into micropores in addition to strong CO<sub>2</sub>–Mg-MOF-74 interactions. It can also be observed that the isotherms never reach the plateau in this low-pressure region, indicating that micropore filling has not been completed yet at 1 bar. In the same figure, the adsorption of CO<sub>2</sub> up to 1 bar at 25 °C on pure carbon doping agents, CNT and GO, reveals an uptake capacity of 0.021 mmol·g<sup>-1</sup> and 0.125 mmol·g<sup>-1</sup>, respectively.

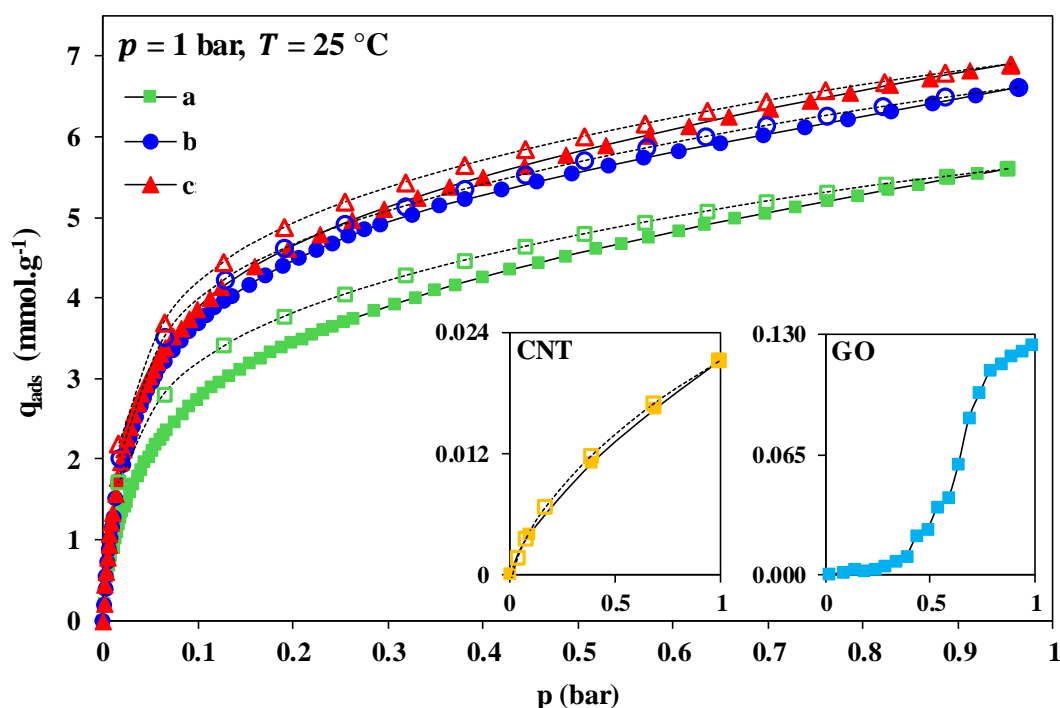


**Figure 4-19.** CO<sub>2</sub> adsorption/desorption isotherms on (a) Mg-MOF-74, (b) Mg-MOF-74@CNT, (c) Mg-MOF-74@GO, pure CNT and pure GO up to 1 bar at 25 °C. Solid and open symbols represent the adsorption and desorption of CO<sub>2</sub>, respectively.

The equilibrium data of CO<sub>2</sub> adsorption of all samples were fitted to different isotherm models: Langmuir (Eq. A-2), dual-site Langmuir (Eq. A-8), Sips (Eq. A-4), dual-site Sips (Eq. A-9), Toth (Eq. A-5), Dubinin–Radushkevitch (Eq. A-6) and BET (Eq. A-7). Isotherm modelling becomes the crucial aspect in this study because IAST calculations are

very sensitive to type of goodness of fitting of pure component isotherm model [95]. Thus, the selection of isotherm model must be appropriately done. The fitting goodness were evaluated considering coefficient of determination,  $R^2$ , (Eq. A-10) and sum squares errors,  $ERRSQ$ , (Eq. A-11). In general, based on  $R^2$  and  $ERRSQ$  values, dual-site Langmuir appears to be the best model in general to describe CO<sub>2</sub> isotherms on the synthesized MOF-74 materials for low- and high-pressure adsorptions and for all temperatures. Therefore, dual-site Langmuir was selected and employed for IAST modelling of CO<sub>2</sub> adsorption under all pressure and temperature conditions in order to have a good comparison of the results. Figure 4-20 proposes that the CO<sub>2</sub> adsorption data up to 1 bar at 25 °C were well adjusted to dual-site Langmuir model but not to Langmuir model. The results show that the isotherms respect the hypothesis made behind Langmuir except they figure two sites of adsorption. Langmuir assumes localized and monolayer adsorption, no interaction between the adsorbed molecules, no interaction with neighboring sites and no transmigration of the adsorbate in the plane of the solid surface [95, 96]. Dual-site Langmuir indicates that all samples consist of two distinctive types of adsorption sites, each of them are energetically not identical and unequal in affinity for the adsorbate [95, 96]. This result is in line with the data derived from N<sub>2</sub> adsorption/desorption isotherms at 77 K in semi-logarithmic coordinates in Section 3.7.5, where two major adsorption volume contributions were observed for all samples. The contributions were expected for near-metal and near-ligand adsorption sites at which equilibrium interactions between CO<sub>2</sub> and Mg-MOF-74 take place [24, 51, 177, 178, 186-188]. Based on the fitted parameters for dual-site Langmuir in Table 4-4, applicable for all samples, the first adsorption site (supposedly near-metal) displays a much stronger theoretical affinity for CO<sub>2</sub>,  $b_L$ , with a higher  $q_{sat}$ , a parameter representative of the theoretical monolayer adsorption capacity almost doubled in comparison to the one corresponding to the second adsorption site (supposedly near-ligand). Physically, adsorbate molecules prefer to adsorb onto sites with high energy and as the adsorption progresses, molecules then adsorb onto the sites with lower energy, resulting in a slower rise in the amount adsorbed versus pressure. Dual-site Langmuir also reveals that both composites exhibit higher total monolayer capacity  $q_{sat,TOT}$  when compared to the pristine material: 7.87 mmol·g<sup>-1</sup> (Mg-MOF-74), mmol·g<sup>-1</sup> (Mg-MOF-74@CNT) and 9.26 mmol·g<sup>-1</sup> (Mg-MOF-74@GO).

In Annex IV, the fitting of isotherm modelling of CO<sub>2</sub> adsorption up to 1 bar at 25 °C using other isotherm models are presented in Figure A-6 and the fitted parameters are

summarized Table A-3. Based on Dubinin–Radushkevitch model that satisfies well the fitting, especially in the relative pressure range larger than 0.01, the characteristic energies of adsorption of solid surface towards CO<sub>2</sub> are estimated slightly higher in both composites compared to the pristine material: 14.38 kJ·mol<sup>-1</sup> (Mg-MOF-74), 15.53 kJ·mol<sup>-1</sup> (Mg-MOF-74@CNT) and 15.61 kJ·mol<sup>-1</sup> (Mg-MOF-74@GO). Based on Toth model that is also acceptable in fitting, heterogeneity factor of solid surface for all samples are close to the order of magnitude of typical zeolites materials ( $3 \leq n \leq 6$ ) or ( $0.17 \leq 1/n \leq 0.33$ ), being the standard for homogenous adsorbents having narrow micropore size distribution [95]. This assumption is in line with the calculated narrow bimodal pore size distribution for all samples using Density Functional Theory and Horvath–Kawazoe in Annex III. In addition to this, BET isotherm model which involves considering two types of interactions with different energies on the surface of the solid and with the adsorbed molecules, may be considered in agreement with the experimental data.

$p = 1 \text{ bar}, T = 25 \text{ }^\circ\text{C}$

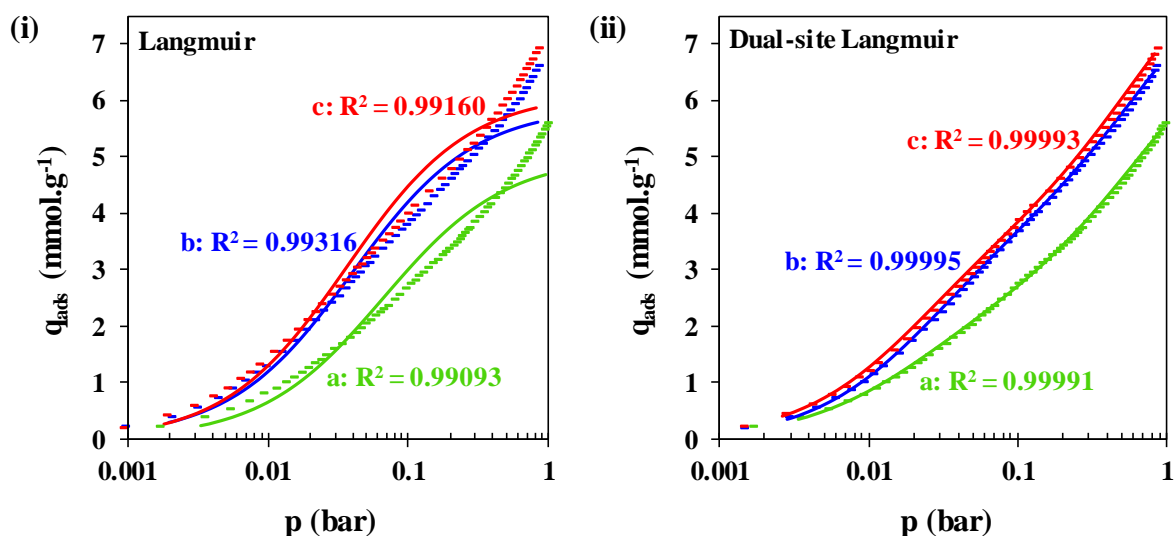


**Figure 4-20.** CO<sub>2</sub> adsorption isotherms on (a) Mg-MOF-74, (b) Mg-MOF-74@CNT and (c) Mg-MOF-74@GO up to 1 bar at 25 °C, fitted to (i) Langmuir model and (ii) dual-site Langmuir, with their respective coefficient of determination, R<sup>2</sup>.

**Table 4-4.** Fitted parameters of Langmuir and dual-site Langmuir models for CO<sub>2</sub> adsorption isotherms of Mg-MOF-74, Mg-MOF-74@CNT and Mg-MOF-74@GO up to 1 bar at 25 °C.

Isotherm model	Fitted parameters	Mg-MOF-74	Mg-MOF-74@CNT	Mg-MOF-74@GO
Langmuir (L)	<i>ERRSQ</i>	0.10872	0.11932	0.15491
	$R^2$	0.99093	0.99316	0.99160
	$q_{sat}$ (mmol·g <sup>-1</sup> )	5.03	5.88	6.14
	$b_L$ (bar <sup>-1</sup> )	14.96	21.72	23.35
Dual-site Langmuir	<i>ERRSQ</i>	0.00106	0.00084	0.00121
	$R^2$	0.99991	0.99995	0.99993
	$q_{sat,1}$ (mmol·g <sup>-1</sup> )	5.36	5.09	5.51
	$b_{L,1}$ (bar <sup>-1</sup> )	45.82	43.99	53.17
	$q_{sat,2}$ (mmol·g <sup>-1</sup> )	2.51	3.82	3.75
	$b_{L,2}$ (bar <sup>-1</sup> )	1.40	1.25	1.39
	$q_{sat,TOT}$ (mmol·g <sup>-1</sup> )	7.87	8.92	9.26

In Figure 4-21, CO<sub>2</sub> adsorption capacities of all samples were normalized to their respective BET specific surface area to give the number of moles adsorbed per unit area of solid surface. It can be observed that in general, all samples display almost the same uptake of CO<sub>2</sub> molecules per unit area, meaning that the composites can afford more CO<sub>2</sub> molecules due to higher surface area. It confirms that the increment of CO<sub>2</sub> uptake capacity is attributed to the development of the micropore volume (all samples have similar metal-to-ligand ratio in the frameworks) resulting an extension of the specific surface area, not to the presence of additional Mg sites or other unexpected functionalities. It also tends to prove that the higher atomic percentage of Mg in both composites detected using surface morphology analysis in Section 3.4.4, does not have any significant influence on CO<sub>2</sub> adsorption capacities.

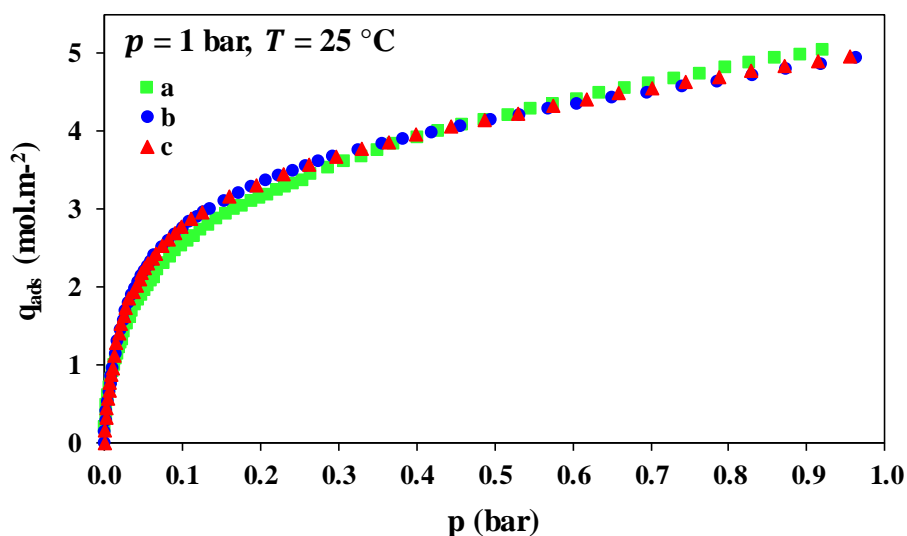


**Figure 4-21.** CO<sub>2</sub> adsorption isotherms of (a) Mg-MOF-74, (b) Mg-MOF-74@CNT, and, (c) Mg-MOF-74@GO up to 1 bar at 25 °C, normalized to the BET specific surface area of the materials.

#### 4.4.2. CH<sub>4</sub> adsorption isotherms and modelling

At the same operational conditions, the adsorption equilibrium data of single component CH<sub>4</sub> were measured on Mg-MOF-74, Mg-MOF-74@CNT and Mg-MOF-74@GO using BELSORP-mini II manometric equipment up to 1 bar at 25°C. As presented in Figure 4-22, the experimental CH<sub>4</sub> isotherms reveal the slight increment in CH<sub>4</sub> uptake at 1 bar from 0.44 mmol·g<sup>-1</sup> (0.70 wt%) measured for the pristine Mg-MOF-74 to 0.56 mmol·g<sup>-1</sup> (0.90 wt%) and 0.60 mmol·g<sup>-1</sup> (0.96 wt%) for Mg-MOF-74@CNT and Mg-MOF-74@GO, respectively. The CH<sub>4</sub> uptake capacities are far below those of CO<sub>2</sub> which is the gas of interest. It indicates that the affinity of the solid surface of Mg-MOF-74 is preferential for CO<sub>2</sub> thanks to the interplay between CO<sub>2</sub>-CO<sub>2</sub> and CO<sub>2</sub>-Mg-MOF-74 electrostatic interactions, which is not the case for CH<sub>4</sub>, a non-polar molecule with no dipole moment in its C-H orbitals. However, the increment by 27 mol% and 36 mol% for Mg-MOF-74@CNT and Mg-MOF-74@GO, respectively, is unavoidable seen that the higher specific surface area in both composites promotes more gas retention. The equilibrium data of CH<sub>4</sub> adsorption of all samples were simply fitted to Henry's law and Langmuir isotherms. Table 4-5 recapitulates the fitted parameters of the models. The errors functions,  $R^2$  and  $ERRSQ$ , indicate a satisfying fitting due to linear shape of the experimental isotherm curves, signifying that CH<sub>4</sub> adsorption is not influenced by the affinity with the solid surface, also proven by feeble affinity values of Langmuir isotherm relatively to CO<sub>2</sub>. The value of Henry's constant represents proportionality factor of the

amount of CH<sub>4</sub> adsorbed and its pressure at equilibrium. Unsurprisingly, CH<sub>4</sub> adsorption on Mg-MOF-74@GO exhibits the highest proportionality (0.615 mmol·g<sup>-1</sup>·bar<sup>-1</sup>), followed by Mg-MOF-74@CNT (0.571 mmol·g<sup>-1</sup>·bar<sup>-1</sup>) and the pristine Mg-MOF-74 (0.429 mmol·g<sup>-1</sup>·bar<sup>-1</sup>). The data was fitted to Langmuir for the purpose of determining the equilibrium selectivities of CO<sub>2</sub>/CH<sub>4</sub> knowing that Henry's law isotherm does not have saturation limit which is not recommended for IAST calculations.

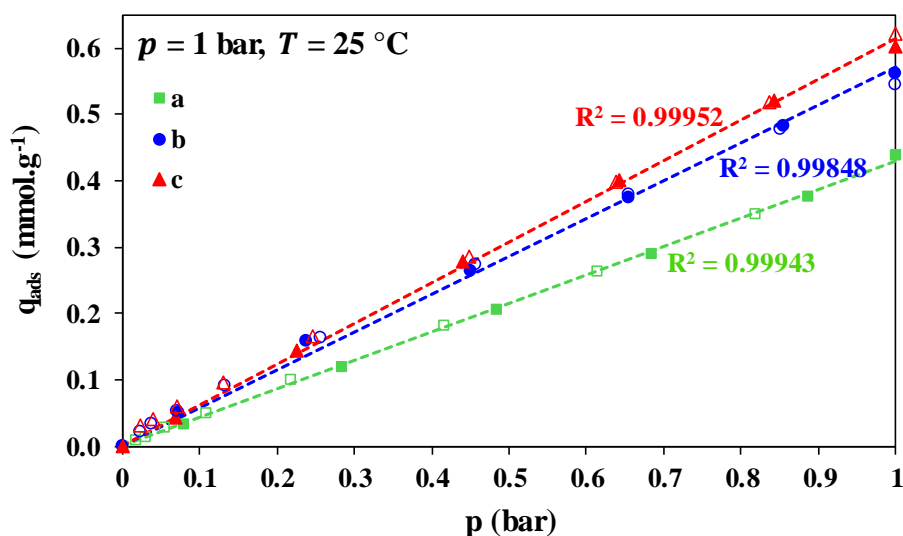


**Figure 4-22.** CH<sub>4</sub> adsorption/desorption isotherms on (a) Mg-MOF-74, (b) Mg-MOF-74@CNT and (c) Mg-MOF-74@GO up to 1 bar at 25 °C, fitted to Henry's law isotherm (dashed line).

**Table 4-5.** Fitted parameters of Henry's law and Langmuir models for CH<sub>4</sub> adsorption isotherms of Mg-MOF-74, Mg-MOF-74@CNT, and, Mg-MOF-74@GO up to 1 bar at 25 °C.

Isotherm model	Fitted parameters	Mg-MOF-74	Mg-MOF-74 @CNT	Mg-MOF-74 @GO
Henry (H)	$ERRSQ$	0.00003	0.00013	0.00005
	$R^2$	0.99943	0.99848	0.99952
	$K_H$ (mmol·g <sup>-1</sup> ·bar <sup>-1</sup> )	0.42915	0.57103	0.61541
Langmuir (L)	$ERRSQ$	0.00007	0.00006	0.00001
	$R^2$	0.99932	0.99928	0.99991
	$q_{sat}$ (mmol·g <sup>-1</sup> )	5.62	6.76	7.32
	$b_L$ (bar <sup>-1</sup> )	0.08	0.09	0.09

#### 4.4.3. Equilibrium selectivities of CO<sub>2</sub>/CH<sub>4</sub>

Despite not being able to perform co-adsorption of CO<sub>2</sub> and CH<sub>4</sub> to observe their dynamic separation, the equilibrium selectivities of CO<sub>2</sub>/CH<sub>4</sub> of different definitions were calculated to evaluate the separation factor up to 1 bar at 25 °C. Intrinsic selectivity,  $\alpha_{CO_2/CH_4}^{INT}$ , (Eq. 4-3) which represents the selectivity at Henry's law region (zero adsorption coverage) was deduced from the ratio of Henry's constants of dual-site Langmuir isotherm of CO<sub>2</sub> adsorption and Langmuir isotherm of CH<sub>4</sub> adsorption. By using the same isotherm models, PSA adsorbent selection parameter,  $S_{CO_2/CH_4}^{PSA}$ , (Eq. 4-4) and IAST selectivity,  $\alpha_{CO_2/CH_4}^{IAST}$ , (Eq. 4-11) were calculated as well. Both Langmuir isotherms are the best candidates for IAST calculations having asymptotic properties at low pressures as well as at high pressures. The results are summarized in Table 4-6. Mg-MOF-74@GO figures the highest intrinsic selectivity (336), followed by Mg-MOF-74@CNT (306) and the pristine Mg-MOF-74 (285), all of which are comparable to 330 from the well-known work of Yaghi's group, Britt *et al.* (2009) [23] and to 283 from Bao *et al.* (2011) [19] for Mg-MOF-74 at the same operational conditions. The results prove that Mg-MOF-74 material is one of the promising adsorbents to separate CO<sub>2</sub> from CH<sub>4</sub>, as denoted in several review articles [28, 117, 218-221]. But one should note that the values are not representative for all pressure regions because the adsorption coverage progresses with the increasing pressure. Regarding  $S_{A/B}^{PSA}$  results, which is defined as the ratio of working capacities  $\Delta q$  of CO<sub>2</sub> and CH<sub>4</sub> times intrinsic selectivity  $\alpha_{CO_2/CH_4}^{INT}$ , the pristine Mg-MOF-74 appears as the best adsorbent having the highest value of separation factor (956), followed by Mg-MOF74@GO (741) and Mg-MOF-74@CNT (696). The values are comparable to 834 published by Bao *et al.* (2011) [19] for Mg-MOF-74 at the same operational conditions. Based on this definition, the selectivity of CO<sub>2</sub> over CH<sub>4</sub> is adversely affected by the increment in adsorption uptake of the gases onto the composites. Also in Table 4-6, IAST selectivity are calculated with help of IAST++ using fitted pure isotherm models (dual-site Langmuir for CO<sub>2</sub> and Langmuir for CH<sub>4</sub>) of the same pressure region by fixing the gases compositions. All samples display almost the same values of IAST separation factor of CO<sub>2</sub>/CH<sub>4</sub>, precisely at 1 bar and at 25 °C for an equimolar mixture: Mg-MOF-74 (50), Mg-MOF-74@CNT (46) and Mg-MOF-74@GO (49). Figure 4-23 shows the adsorption uptakes of each CO<sub>2</sub> and CH<sub>4</sub> as well as the total gas uptake of the materials based on IAST calculations, as a function of pressure. It can be seen that despite having almost the same

selectivity value at 1 bar, both composites can afford larger production of gas separation which are more advantageous. Figure 4-24 presents the calculated IAST selectivity of all samples as a function of pressure. The selectivity decreases as the pressure progresses, which is in line with the shape of pure CO<sub>2</sub> and CH<sub>4</sub> isotherms (slower rise of CO<sub>2</sub> adsorption versus pressure while constant linear of CH<sub>4</sub> adsorption versus pressure). One can consider that all samples offer almost the same value of IAST selectivity as a function of pressure. The performances of the materials are evaluated in Figure 4-25, in which Mg-MOF-74@GO appears as the best adsorbent having a good balance between CO<sub>2</sub>/CH<sub>4</sub> selectivity and CO<sub>2</sub> adsorption capacity at 1 bar and at 25 °C, followed by Mg-MOF-74@CNT and Mg-MOF-74.

**Table 4-6.** Selectivity parameters of CO<sub>2</sub>/CH<sub>4</sub> for Mg-MOF-74, Mg-MOF-74@CNT and Mg-MOF-74@GO at 1 bar and at 25 °C.

Selectivity parameters	Mg-MOF-74	Mg-MOF-74@CNT	Mg-MOF-74@GO
$\alpha_{CO_2/CH_4}^{INT}$	285	306	336
$S_{CO_2/CH_4}^{PSA}$	956	696	741
$\alpha_{CO_2/CH_4}^{IAST}$ for 50:50 (mol·mol <sup>-1</sup> )	50	46	49

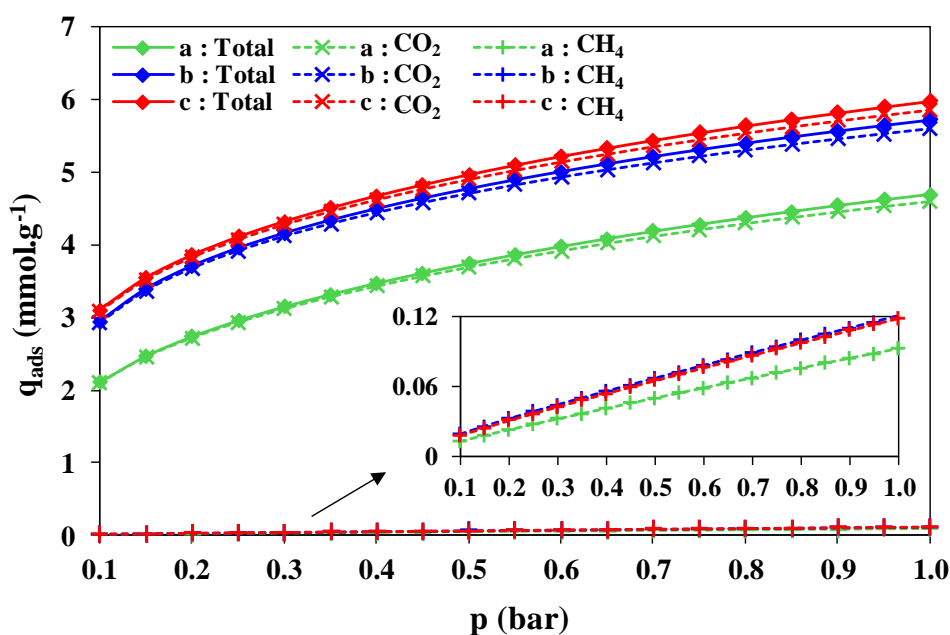


**Figure 4-23.** IAST adsorption uptake for an equimolar mixture of CO<sub>2</sub> and CH<sub>4</sub> on (a) Mg-MOF-74, (b) Mg-MOF-74@CNT and (c) Mg-MOF-74@GO up to 1 bar at 25 °C.

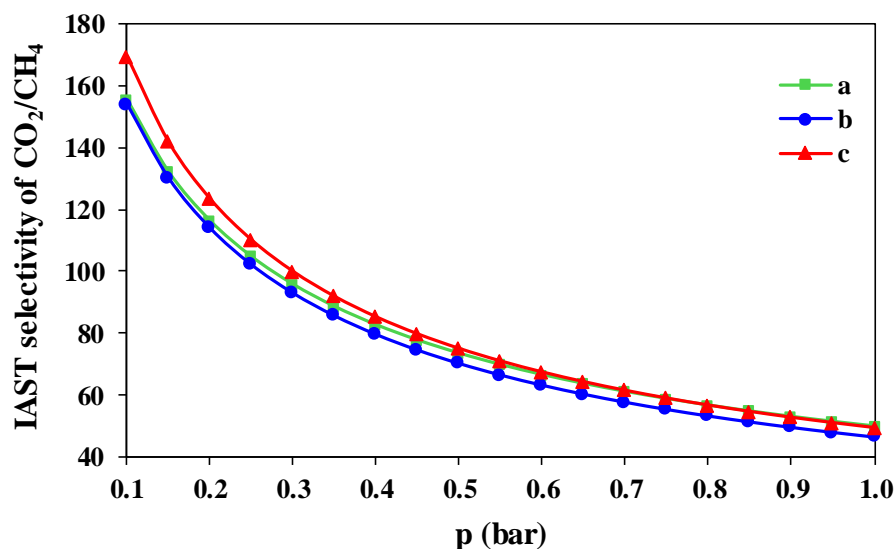


**Figure 4-24.** IAST selectivity of CO<sub>2</sub>/CH<sub>4</sub> for an equimolar mixture on (a) Mg-MOF-74, (b) Mg-MOF-74@CNT and (c) Mg-MOF-74@GO up to 1 bar at 25 °C.

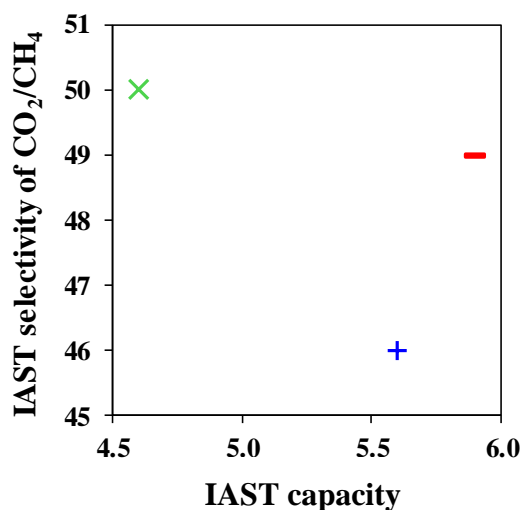


**Figure 4-25.** IAST selectivity of CO<sub>2</sub>/CH<sub>4</sub> versus IAST capacity in mmol·g<sup>-1</sup> of CO<sub>2</sub> for an equimolar mixture on Mg-MOF-74, Mg-MOF-74@CNT and Mg-MOF-74@GO at 1 bar, 25 °C.

#### 4.4.4. Cycling performance of CO<sub>2</sub> adsorption/desorption

The adsorption/desorption cycle of CO<sub>2</sub> on Mg-MOF-74, Mg-MOF-74@CNT and Mg-MOF-74@GO was repeated using the same sample for four consecutive cycles using BELSORP-mini II up to 1 bar at 25°C. Prior to each measurement, the outgassing process was performed under a dynamic vacuum with heating at 150 °C for 72 h. The results are shown in Figure 4-26. CO<sub>2</sub> adsorption isotherms on all samples are observed stable and consistent from the first to the fourth cycles, indicating the robustness of the materials subjected to multiple regeneration processes. In an earlier study, it was claimed that there

was no diminution in CO<sub>2</sub> uptake capacity on Mg-MOF-74 after eight consecutive adsorption/desorption cycles [50].

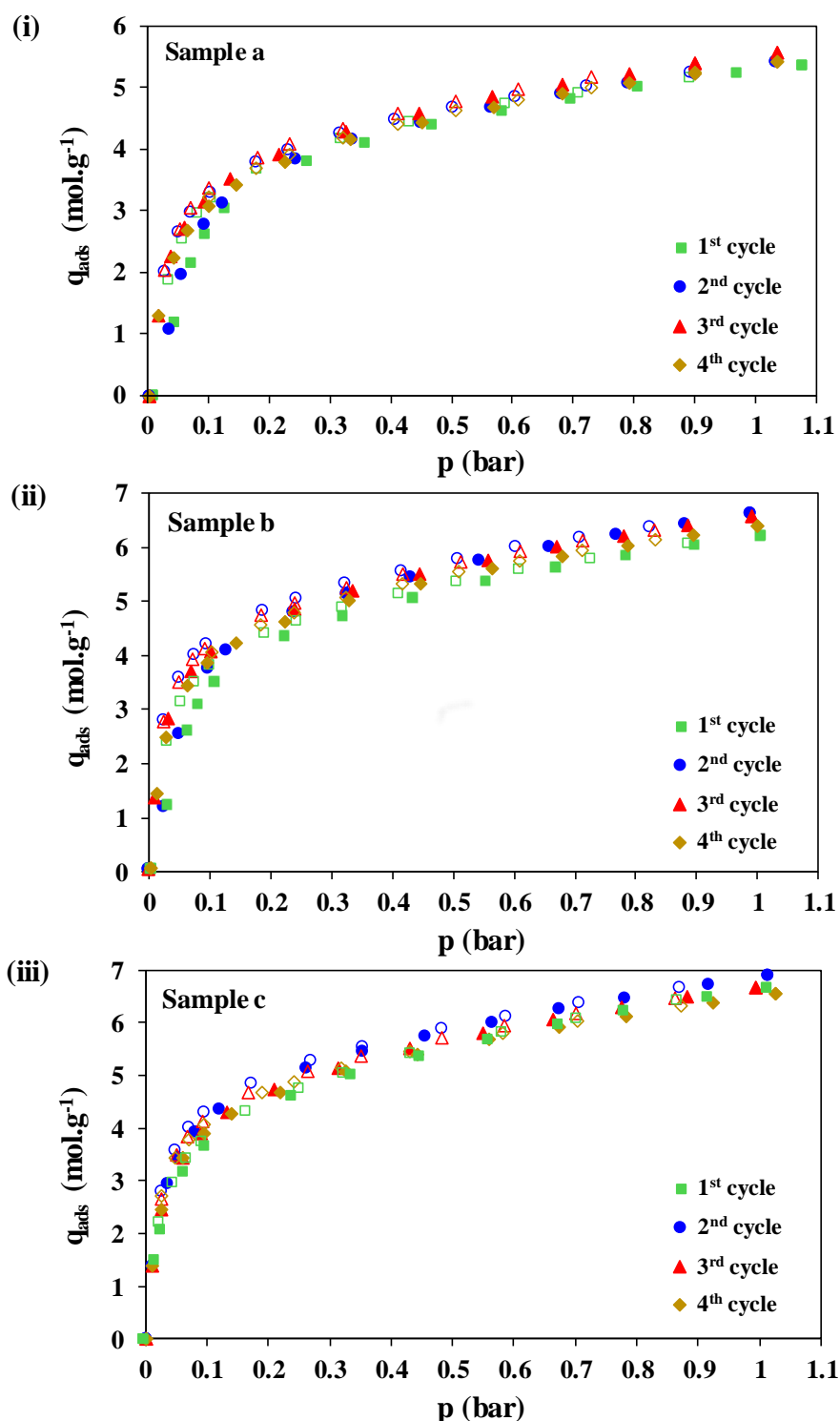


**Figure 4-26.** Cycling performance of CO<sub>2</sub> adsorption/desorption isotherms on (i) a: MgMOF-74, (ii) b: MgMOF-74@CNT and (iii) c: MgMOF-74@GO up to 1 bar at 25 °C. Solid and open symbols represent the adsorption and desorption of CO<sub>2</sub>, respectively.

## 4.5. Adsorption isotherms at high pressures: Results and discussions

### 4.5.1. CO<sub>2</sub> adsorption isotherms and modelling

The equilibrium data of high-pressure adsorption of single component CO<sub>2</sub> were measured on Mg-MOF-74, Mg-MOF-74@CNT and Mg-MOF-74@GO using PCT-Pro manometric equipment up to 40 bar for three different temperatures: 25 °C, 50 °C and 75 °C. Considering the significant experimental errors that might be produced in high-pressure and (or) high-temperature adsorption, the measurement was repeated 3 times for each operational conditions (sample, temperature). Prior to each measurement, the outgassing process was performed under a dynamic vacuum with heating at 150 °C for 72 h. The CO<sub>2</sub> adsorption/ desorption isotherms are presented in Figure 4-27 (25 °C), Figure 4-28 (50 °C) and Figure 4-29 (75 °C), with absolute experimental errors bars (Eq. 4-26), fitted to an average curve providing coefficient of determination,  $R^2$ , and average relative errors,  $ARE$  (%). Due to the difficulties in collecting data over 35 bar at 25 °C, which is a regular case when the gas is approaching its critical pressure, the isotherms are presented for this limited feasible pressure range. Overall, the equilibrium data of CO<sub>2</sub> adsorption were well-produced in the range of the absolute errors bars, displaying a good accuracy of measurements. The data also show an acceptable consistency of averagely  $R^2=0.99067$  and  $ARE=5.5\%$ . The shape of CO<sub>2</sub> isotherms of all samples can be interpreted as: (i) micropore filling at low pressures with different rates of increasing adsorbed amount, (ii) completion of micropore filling or saturation of monolayer adsorption capacity at  $\approx 10$  bar (plateau-like isotherm), (iii) multilayer adsorption in mesopores followed by capillary condensation (a small portion of mesopores was observed in these materials in Section 3.7.5), and, (v) accompanied by a hysteresis in mode desorption, indicating the irreversibility of the isotherms. The equilibration time had to be long enough to avoid diffusion-controlled hysteresis, in which the desorption curve went higher than the adsorption curve abnormally producing a parabolic curve, which was the case in the first experiments we conducted. This phenomenon is explained by Ravikovitch and Neimark (2005) [222]. For a given equilibration time, when the diffusion of the adsorbates is too slow, part of them are not be able to reach adsorption sites where they would adsorb at particular equilibrium pressure. Consequently, upon desorption, part of the adsorbent is not saturated at the respective pressure, so it will adsorb more instead of desorbing, which results in higher adsorbed amount. The following data were produced after optimizing the equilibration time, noting that CO<sub>2</sub> adsorption in the synthesized materials exhibited slow kinetics.

$p = 35 \text{ bar}$ ,  $T = 25 \text{ }^\circ\text{C}$

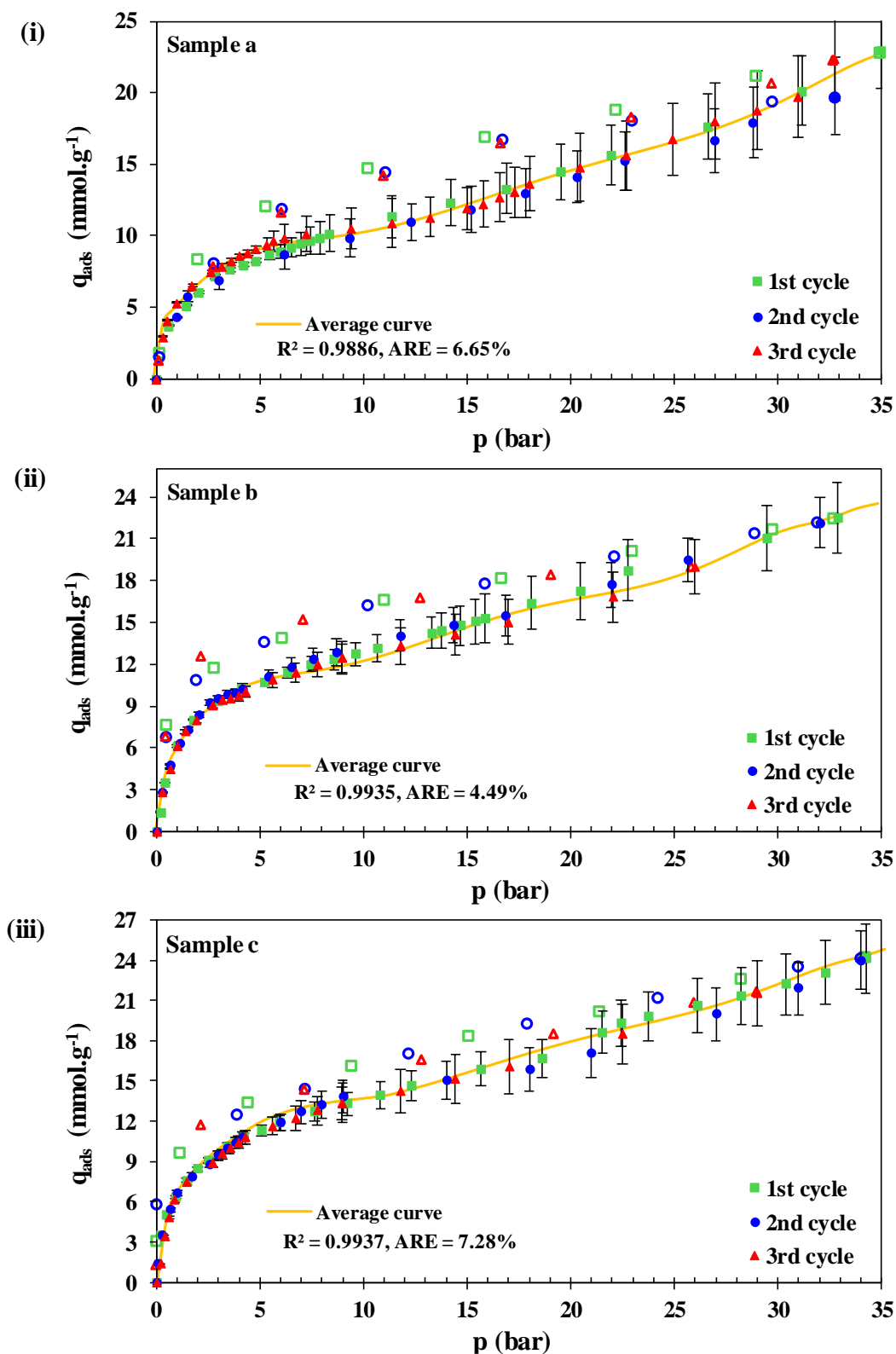


**Figure 4-27.** CO<sub>2</sub> adsorption/desorption isotherms of (i) a: Mg-MOF-74, (ii) b: Mg-MOF-74@CNT and (iii) c: Mg-MOF-74@GO up to 35 bar at 25 °C with absolute errors bars, fitted to an average curve providing coefficient of determination,  $R^2$ , and average relative errors, ARE. Solid and open symbols represent the adsorption and desorption of CO<sub>2</sub>, respectively.

$p = 35 \text{ bar}$ ,  $T = 50 \text{ }^\circ\text{C}$

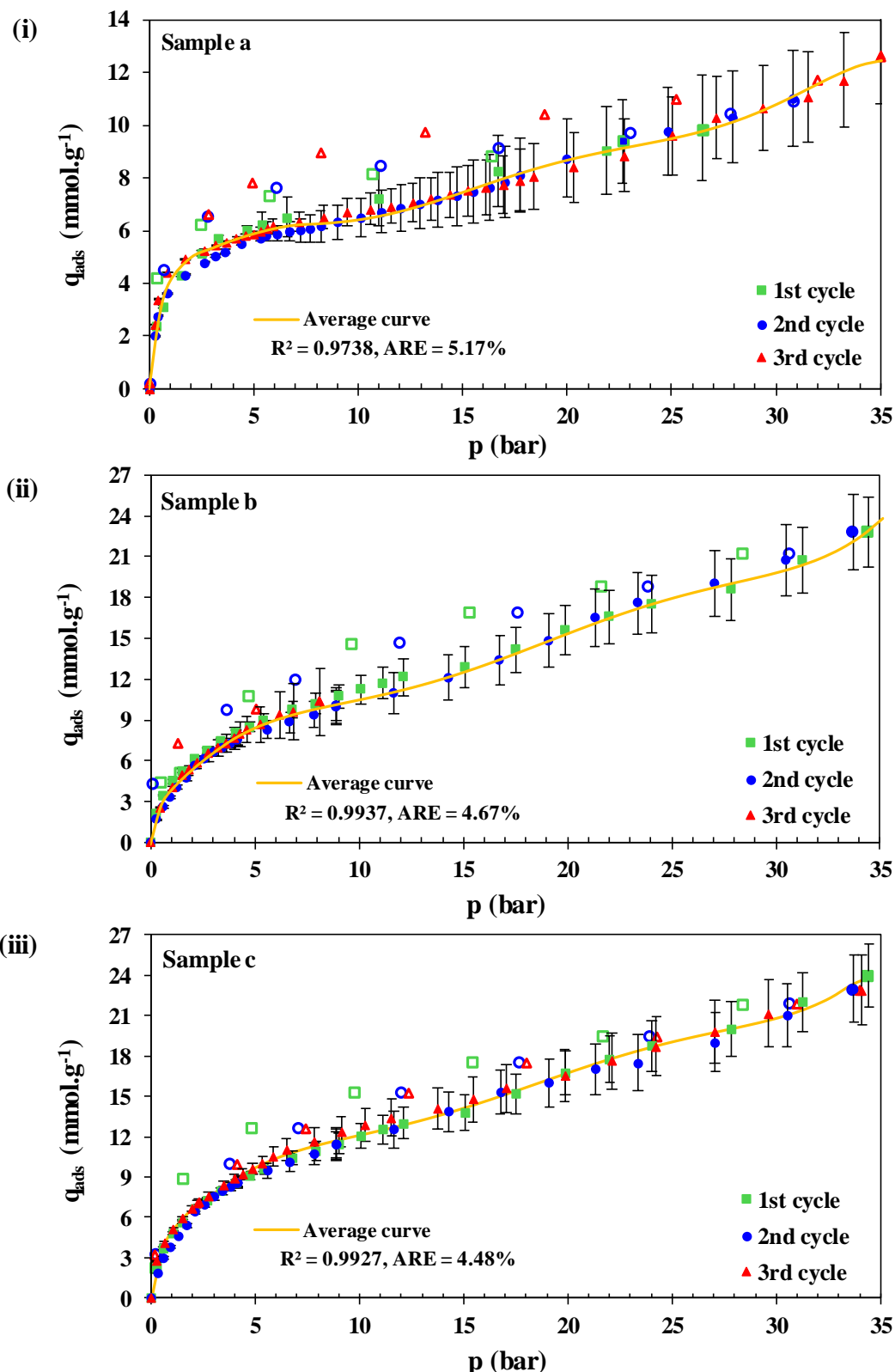


**Figure 4-28.** CO<sub>2</sub> adsorption/desorption isotherms of (i) a: Mg-MOF-74, (ii) b: Mg-MOF-74@CNT and (iii) c: Mg-MOF-74@GO up to 35 bar at 50 °C with absolute errors bars, fitted to an average curve providing coefficient of determination,  $R^2$ , and average relative errors, ARE. Solid and open symbols represent the adsorption and desorption of CO<sub>2</sub>, respectively.

$p = 35 \text{ bar}$ ,  $T = 75 \text{ }^\circ\text{C}$

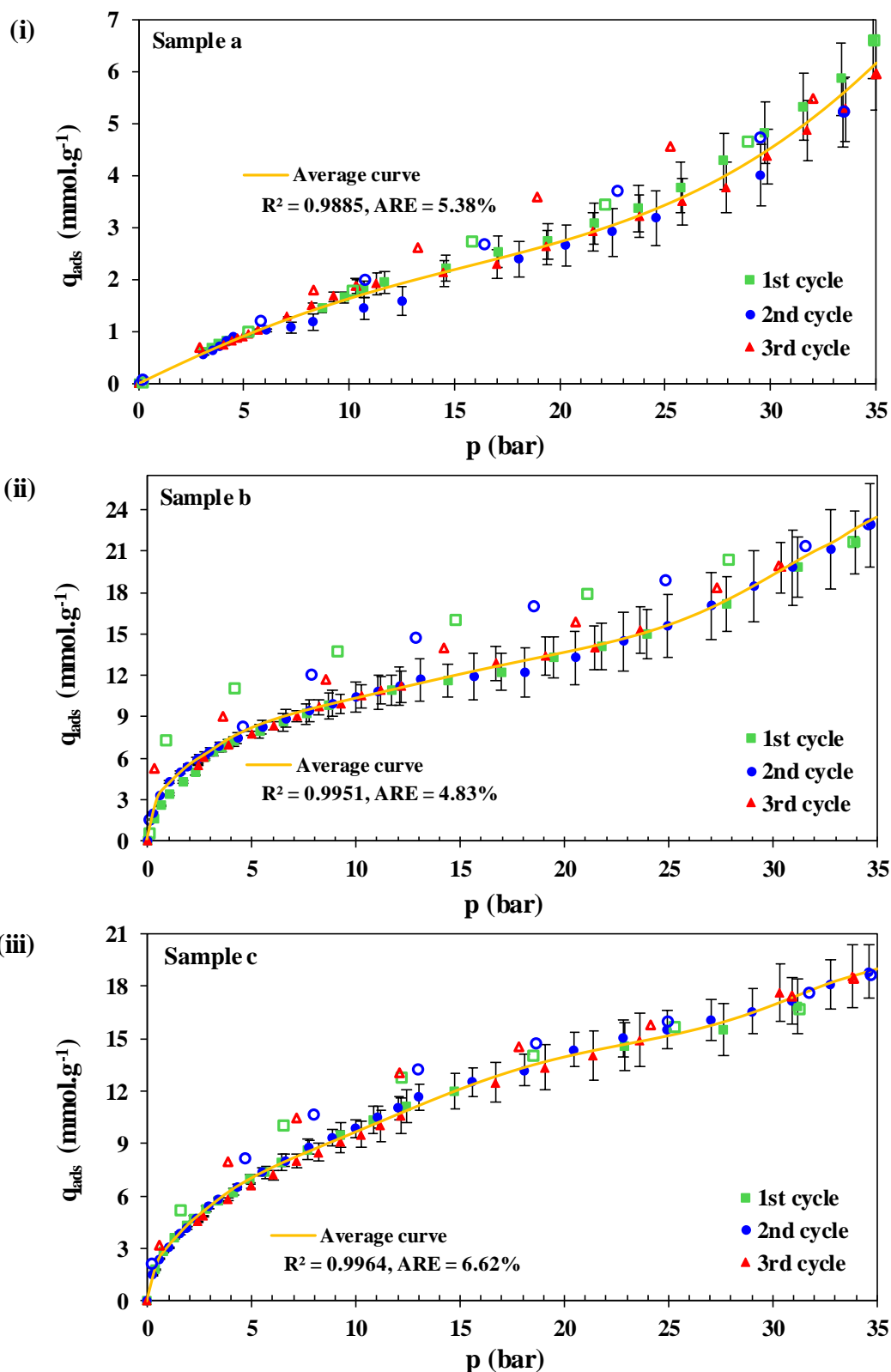


**Figure 4-29.** CO<sub>2</sub> adsorption/desorption isotherms of (i) a: Mg-MOF-74, (ii) b: Mg-MOF-74@CNT and (iii) c: Mg-MOF-74@GO up to 35 bar at 75 °C with absolute errors bars, fitted to an average curve providing coefficient of determination,  $R^2$ , and average relative errors, ARE. Solid and open symbols represent the adsorption and desorption of CO<sub>2</sub>, respectively.

The average curve of CO<sub>2</sub> adsorption isotherms on Mg-MOF-74, Mg-MOF-74@CNT and Mg-MOF-74@GO up to 35 bar are presented in Figure 4-30 for 25 °C, 50 °C and 75 °C. At all temperatures, both composites exhibit higher CO<sub>2</sub> adsorption uptakes compared to the pristine Mg-MOF-74 which is in agreement with the measurements at low-pressure region. The CO<sub>2</sub> uptake for the pristine Mg-MOF-74 at 30 bar and at 25 °C is measured as 18.5 mmol·g<sup>-1</sup> comparable to 16 mmol·g<sup>-1</sup> reported in the well-known work of Dietzel *et al.* (2009) [54] for the same material and operational conditions, noting that their value refers to excess adsorption capacity. CO<sub>2</sub> adsorption uptakes at 10 bar are recapitulated in Table 4-7. It can be seen that the percentage of improvement of CO<sub>2</sub> uptake capacity increases as the temperature increases, revealing that the adsorption behaviour in the pristine Mg-MOF-74 is significantly adversely affected by the temperature while for both composites, it is less affected.

**Table 4-7.** CO<sub>2</sub> adsorption capacities of Mg-MOF-74, Mg-MOF-74@CNT and Mg-MOF-74@GO at 10 bar for different temperatures: 25 °C, 50 °C and 75 °C.

Temperature	Adsorption at 10 bar	Mg-MOF-74	Mg-MOF-74 @ CNT	Mg-MOF-74 @ GO
25 °C	CO <sub>2</sub> uptake (mmol·g <sup>-1</sup> )	10.1	12.6	13.5
	CO <sub>2</sub> uptake (mmol·cm <sup>-3</sup> )	1.82	2.27	2.43
	CO <sub>2</sub> uptake (wt%)	40.4	50.4	54.0
	Improvement (mol%)	-	25	34
50 °C	CO <sub>2</sub> uptake (mmol·g <sup>-1</sup> )	6.4	10.7	12.1
	CO <sub>2</sub> uptake (mmol·cm <sup>-3</sup> )	1.15	1.93	2.18
	CO <sub>2</sub> uptake (wt%)	25.6	42.6	48.4
	Improvement (mol%)	-	67	89
75 °C	CO <sub>2</sub> uptake (mmol·g <sup>-1</sup> )	2.7	10.2	9.67
	CO <sub>2</sub> uptake (mmol·cm <sup>-3</sup> )	0.49	1.84	1.74
	CO <sub>2</sub> uptake (wt%)	10.8	40.9	38.7
	Improvement (mol%)	-	279	258

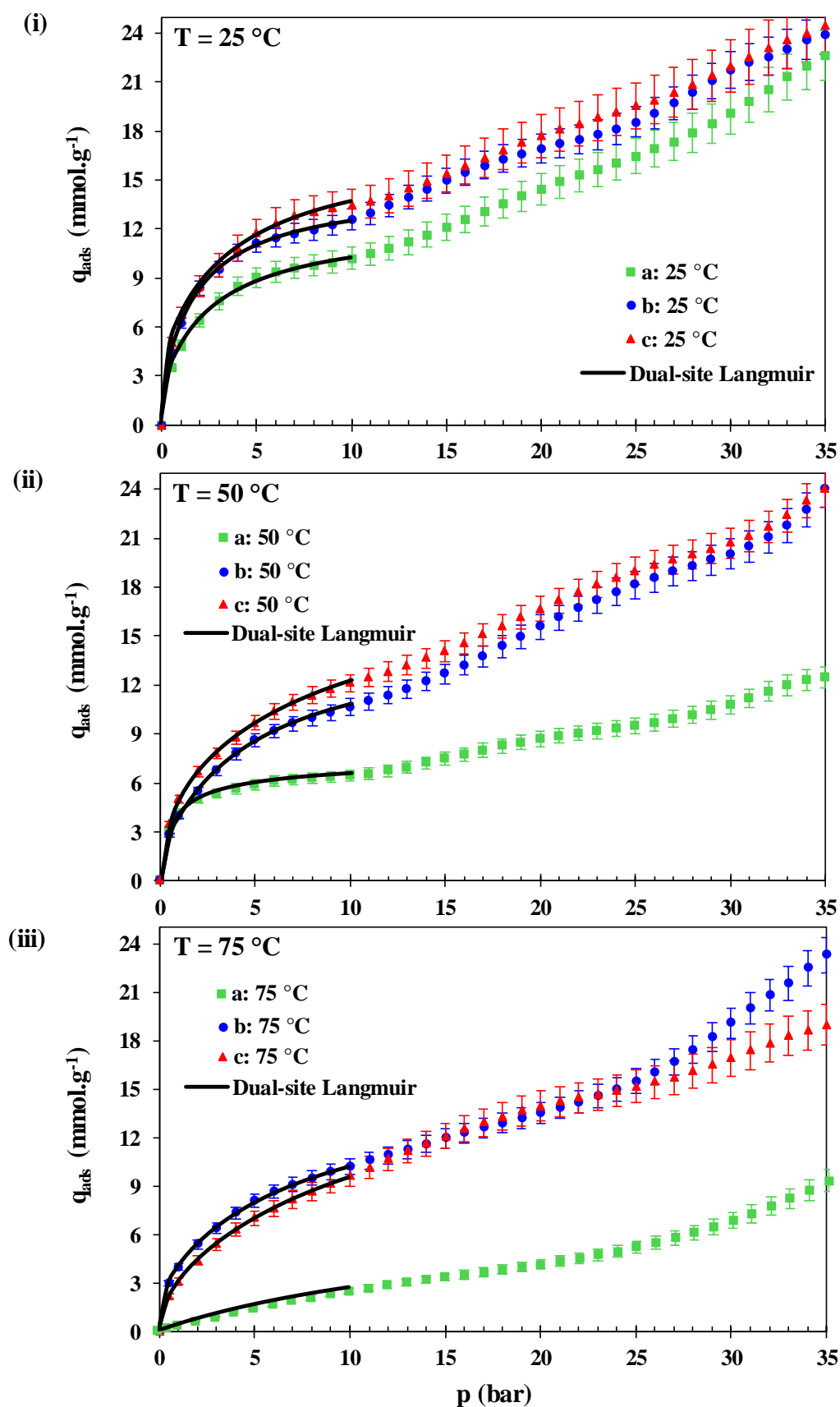


**Figure 4-30.** Average curve of  $\text{CO}_2$  adsorption isotherms of (a) Mg-MOF-74, (b) Mg-MOF-74@CNT and (c) Mg-MOF-74@GO up to 35 bar with average relative errors bars, ARE, for different temperatures: (i)  $25\text{ }^{\circ}\text{C}$ , (ii)  $50\text{ }^{\circ}\text{C}$  and (iii)  $75\text{ }^{\circ}\text{C}$ , fitted to dual-site Langmuir until 10 bar.

The equilibrium data of all samples were fitted to the same previous isotherm models: Langmuir (Eq. A-2), dual-site Langmuir (Eq. A-8), Sips (Eq. A-4), dual-site Sips (Eq. A-9), Toth (Eq. A-5), Dubinin–Radushkevitch (Eq. A-6) and BET (Eq. A-7), but the models can only fit the equilibrium in the domain of validity of the isotherm model, which is before the inflexion of the isotherm shape at 10 bar for 25 °C [95]. It was proven during the modelling that the isotherm models cannot fit the data beyond this pressure limit. As mentioned previously, seeing that dual-site Langmuir appears to be the best model in general to describe CO<sub>2</sub> isotherms for low- and high-pressure adsorptions and for all temperatures, thus this model was employed for IAST modelling of CO<sub>2</sub> adsorption under all operational conditions. Since the fitted experimental data were the data of the average isotherm curve of the three measurements, the model to be observed lies in the range of average relative errors bars. The fitting of dual-site Langmuir model on the isotherms of CO<sub>2</sub> adsorption up to 10 bar is presented in Figure 4-31 and the fitted parameters are recapitulated in Table 4-8. Based on the parameters value, applicable for all samples at all temperatures, we can see the consistency of the first adsorption site (supposedly near-metal) displaying stronger theoretical affinity  $b_L$  for CO<sub>2</sub> and higher theoretical monolayer capacity  $q_{sat}$  in comparison to the second adsorption site (supposedly near-ligand). Also, both composites consistently have higher total monolayer capacity  $q_{sat,TOT}$  when compared to that of the pristine Mg-MOF-74.

In Annex IV, the fitting of isotherm modelling of CO<sub>2</sub> adsorption up to 10 bar using other isotherm models are presented in Figure A-7 (25 °C), Figure A-8 (50 °C) and Figure A-9 (75 °C) and the fitted parameters are summarized in Table A-4 (25 °C), Table A-5 (50 °C) and Table A-6 (75 °C). By comparing low-pressure (up to 1 bar) and high-pressure (up to 10 bar) CO<sub>2</sub> adsorptions at the same temperature (25 °C), dual-site Sips isotherm model is able to describe the equilibrium data better than dual-site Langmuir at high pressures based on  $R^2$  and  $ERRSQ$  values. It means that the isotherms at high-pressure region are more likely influenced by the heterogeneity factor of the adsorption system ( $1/n$ ) complementing by Freundlich expression in the Sips equation. The deviation from Langmuir may be attributed to adsorption sites energies and adsorbate intermolecular interactions [223] at that higher pressure range. BET isotherm which is designed for multilayer adsorption is not suitable to fit the equilibrium data (<10 bar) well for all temperatures, suggesting that the adsorption in this pressure region is probably not a multilayer adsorption, but it would certainly occur in the small portion of mesopores of the

---

materials revealed in Section 3.7.5. With acceptable fitting goodness, Dubinin–Radushkevitch model estimates that the characteristic energy of adsorption of both composites are higher than the pristine Mg-MOF-74 for all temperatures, all of which are decreasing with increasing temperature. A particular remark is observed for CO<sub>2</sub> isotherm on the pristine Mg-MOF-74 at 75 °C whereby the adsorption is nearly linear, dissimilar to others, due to relatively very low CO<sub>2</sub> uptake. Seeing that all models can fit this isotherm well due to its “simple” form, the most relevant model, Langmuir, is selected to represent CO<sub>2</sub> isotherm at 75 °C for selectivity calculations.

**Table 4-8.** Fitted parameters of dual-site Langmuir for CO<sub>2</sub> adsorption isotherms of Mg-MOF-74, Mg-MOF-74@CNT and Mg-MOF-74@GO up to 10 bar at different temperatures: 25 °C, 50 °C and 75 °C.

Temperature	Fitted parameters	Mg-MOF-74	Mg-MOF-74 @CNT	Mg-MOF-74 @GO
25 °C	<i>ERRSQ</i>	0.03772	0.02164	0.01599
	<i>R</i> <sup>2</sup>	0.99976	0.99995	0.99987
	<i>q</i> <sub>sat,1</sub> (mmol·g <sup>-1</sup> )	10.11	12.45	12.76
	<i>b</i> <sub>L,1</sub> (bar <sup>-1</sup> )	8.37	5.86	6.79
	<i>q</i> <sub>sat,2</sub> (mmol·g <sup>-1</sup> )	2.42	2.08	4.67
	<i>b</i> <sub>L,2</sub> (bar <sup>-1</sup> )	0.34	0.51	0.25
	<i>q</i> <sub>sat,TOT</sub> (mmol·g <sup>-1</sup> )	12.53	14.54	17.43
50 °C	<i>ERRSQ</i>	0.00116	0.00442	0.00518
	<i>R</i> <sup>2</sup>	0.99996	0.99994	0.99994
	<i>q</i> <sub>sat,1</sub> (mmol·g <sup>-1</sup> )	5.67	13.42	14.21
	<i>b</i> <sub>L,1</sub> (bar <sup>-1</sup> )	2.11	22.60	22.58
	<i>q</i> <sub>sat,2</sub> (mmol·g <sup>-1</sup> )	1.83	1.70	4.93
	<i>b</i> <sub>L,2</sub> (bar <sup>-1</sup> )	0.13	0.21	0.11
	<i>q</i> <sub>sat,TOT</sub> (mmol·g <sup>-1</sup> )	7.49	15.12	19.14
75 °C	<i>ERRSQ</i>	0.00016	0.00303	0.00355
	<i>R</i> <sup>2</sup>	0.99995	0.99994	0.99998
	<i>q</i> <sub>sat,1</sub> (mmol·g <sup>-1</sup> )	7.71	13.01	15.59
	<i>b</i> <sub>L,1</sub> (bar <sup>-1</sup> )	0.05	4.94	1.99
	<i>q</i> <sub>sat,2</sub> (mmol·g <sup>-1</sup> )	0.00	3.00	2.80
	<i>b</i> <sub>L,2</sub> (bar <sup>-1</sup> )	0.00	0.13	0.08
	<i>q</i> <sub>sat,TOT</sub> (mmol·g <sup>-1</sup> )	7.71	16.01	18.39

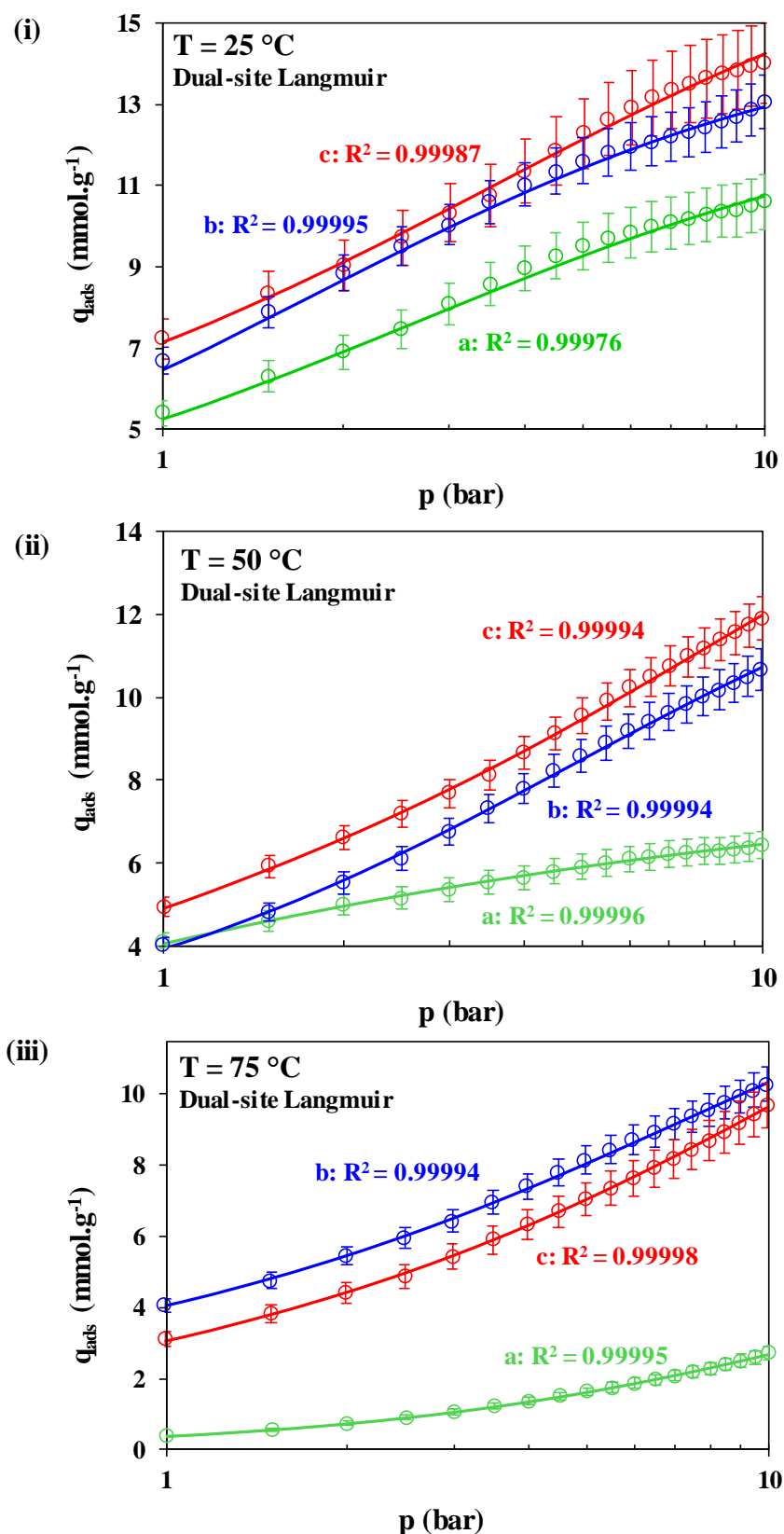


**Figure 4-31.** Average curve of  $\text{CO}_2$  adsorption isotherms of (a) Mg-MOF-74, (b) Mg-MOF-74@CNT and (c) Mg-MOF-74@GO up to 10 bar with average relative errors bars, ARE, fitted to dual-site Langmuir model providing coefficient of determination,  $R^2$ , for different temperatures: (i)  $25\text{ }^{\circ}\text{C}$ , (ii)  $50\text{ }^{\circ}\text{C}$  and (iii)  $75\text{ }^{\circ}\text{C}$ .

4.5.2. CH<sub>4</sub> adsorption isotherms and modelling

The equilibrium data of high-pressure adsorption of single component CH<sub>4</sub> were measured on Mg-MOF-74, Mg-MOF-74@CNT and Mg-MOF-74@GO using PCT-Pro manometric equipment up to 35 bar for three different temperatures: 25 °C, 50 °C and 75 °C. Similar to CO<sub>2</sub>, the measurement was repeated 3 times for each operational conditions, between which the outgassing process was performed under a dynamic vacuum with heating at 150 °C for 72 h. The CH<sub>4</sub> adsorption/desorption isotherms are presented in Figure 4-32 (25 °C), Figure 4-33 (50 °C) and Figure 4-34 (75 °C), with absolute errors bars and average curves providing  $R^2$  and  $ARE$ . As same observation as CO<sub>2</sub> adsorption, the equilibrium data of CH<sub>4</sub> display good accuracy of measurement in the range of errors bars with acceptable consistency of averagely  $R^2=0.99570$  and  $ARE=5.8\%$ . The shape of the isotherms and the adsorbed amounts demonstrate that Mg-MOF-74 materials are evidently less favourable for CH<sub>4</sub> retention which is the same case for low-pressure adsorption. CH<sub>4</sub> adsorption uptakes at 10 bar are recapitulated in Table 4-9. In the same pattern as CO<sub>2</sub> adsorption, the percentage of increment of CH<sub>4</sub> adsorption uptake increases as the temperature increases, meaning that it is as well less affected by the temperature rise for both composites.

**Table 4-9.** CH<sub>4</sub> adsorption capacities of Mg-MOF-74, Mg-MOF-74@CNT and Mg-MOF-74@GO at 10 bar at different temperatures: 25 °C, 50 °C and 75 °C.

Temperature	Adsorption at 10 bar	Mg-MOF-74	Mg-MOF-74 @CNT	Mg-MOF-74 @GO
25 °C	CH <sub>4</sub> uptake (mmol·g <sup>-1</sup> )	3.9	5.2	4.4
	CH <sub>4</sub> uptake (wt%)	6.2	8.3	7.0
	Increment (mol%)	-	33	12
50 °C	CH <sub>4</sub> uptake (mmol·g <sup>-1</sup> )	2.5	3.5	3.0
	CH <sub>4</sub> uptake (wt%)	4.0	5.6	4.8
	Increment (mol%)	-	40	20
75 °C	CH <sub>4</sub> uptake (mmol·g <sup>-1</sup> )	0.7	1.6	1.8
	CH <sub>4</sub> uptake (wt%)	1.1	2.6	2.8
	Increment (mol%)	-	150	133

$p = 35 \text{ bar}$ ,  $T = 25 \text{ }^\circ\text{C}$

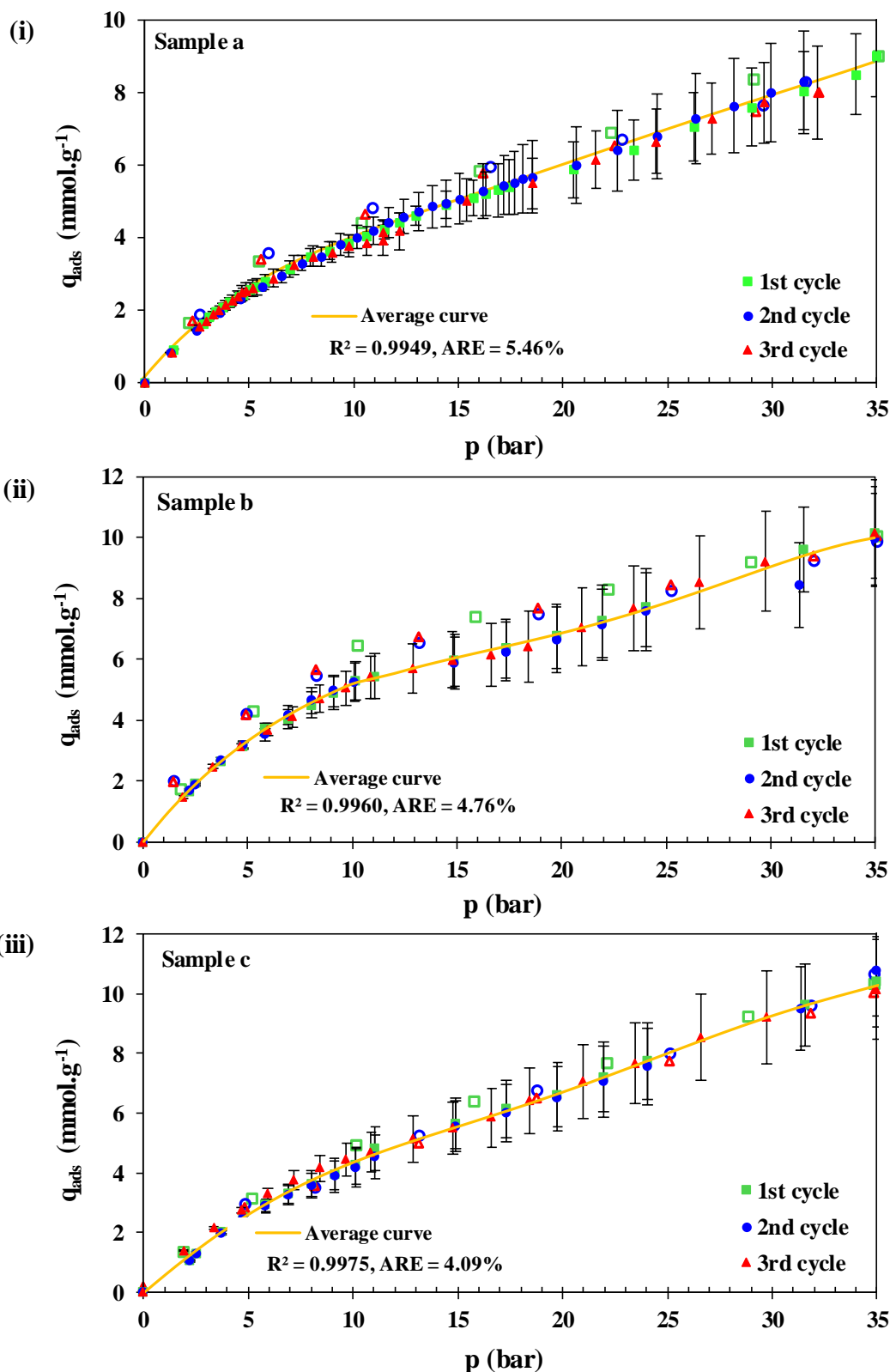


**Figure 4-32.** CH<sub>4</sub> adsorption/desorption isotherms of (i) a: Mg-MOF-74, (ii) b: Mg-MOF-74@CNT and (iii) c: Mg-MOF-74@GO up to 35 bar at 25 °C with absolute errors bars, fitted to an average curve providing coefficient of determination,  $R^2$ , and average relative errors, ARE. Solid and open symbols represent the adsorption and desorption of CH<sub>4</sub>, respectively.

$p = 35 \text{ bar}$ ,  $T = 50 \text{ }^\circ\text{C}$

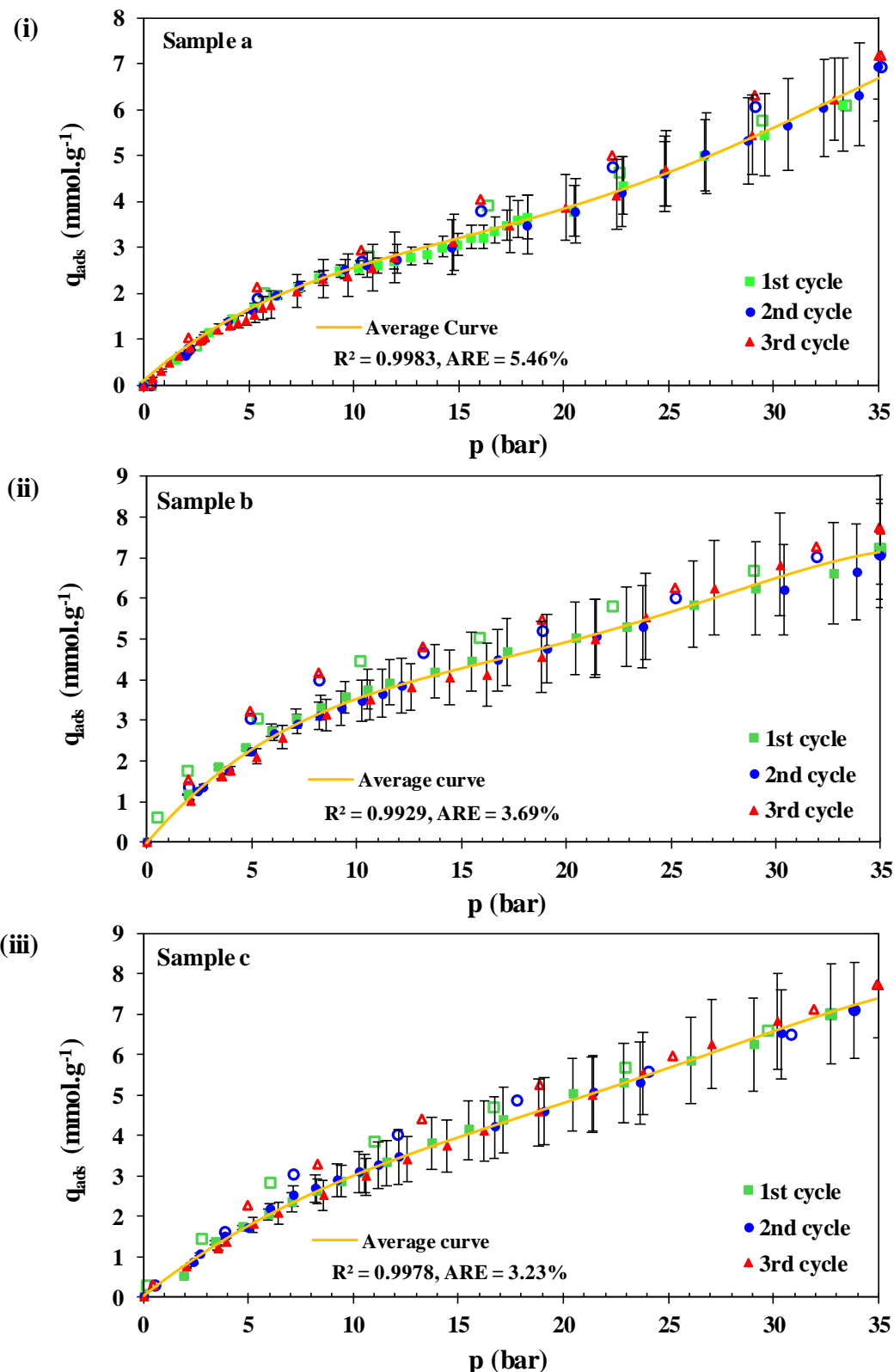


**Figure 4-33.**  $\text{CH}_4$  adsorption/desorption isotherms of (i) a: Mg-MOF-74, (ii) b: Mg-MOF-74@CNT and (iii) c: Mg-MOF-74@GO up to 35 bar at  $50 \text{ }^\circ\text{C}$  with absolute errors bars, fitted to an average curve providing coefficient of determination,  $R^2$ , and average relative errors, ARE. Solid and open symbols represent the adsorption and desorption of  $\text{CH}_4$ , respectively.

$p = 35 \text{ bar}$ ,  $T = 75 \text{ }^\circ\text{C}$

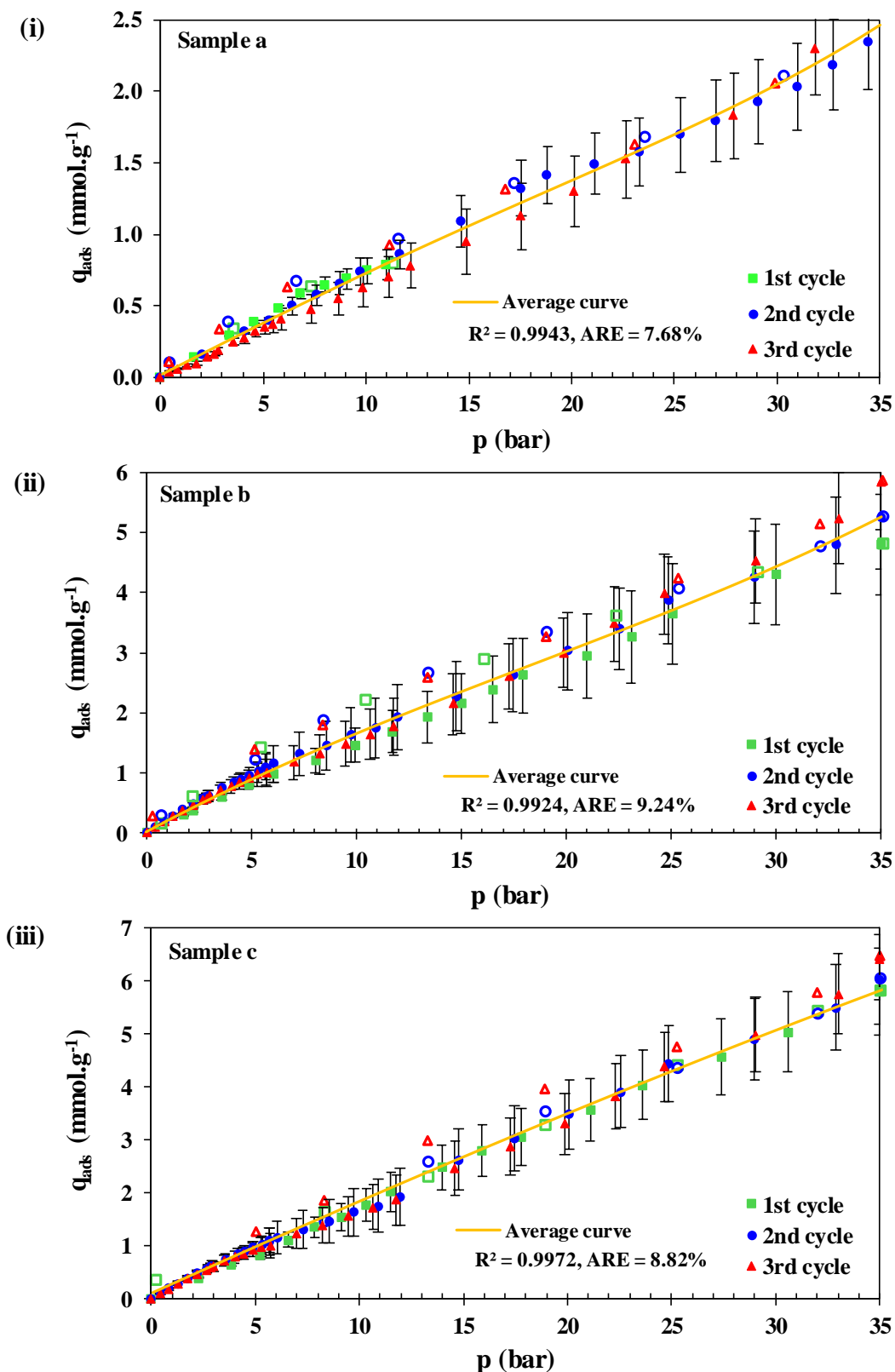


**Figure 4-34.** CH<sub>4</sub> adsorption/desorption isotherms of (i) a: Mg-MOF-74, (ii) b: Mg-MOF-74@CNT and (iii) c: Mg-MOF-74@GO up to 35 bar at 75 °C with absolute errors bars, fitted to an average curve providing coefficient of determination,  $R^2$ , and average relative errors, ARE. Solid and open symbols represent the adsorption and desorption of CH<sub>4</sub>, respectively.

The average curve of the isotherms are presented in Figure 4-35, fitted with Langmuir model in the pressure region below 10 bar, providing the best value of fitting goodness. It means that Langmuir model is able to describe the data adequately and it is unnecessary to test the other isotherm models. The fitted parameters of Langmuir model in Table 4-10 indicate that all samples exhibit almost the same feeble affinity for CH<sub>4</sub> at all temperatures, while Mg-MOF-74@GO has the highest saturation limit of CH<sub>4</sub> followed by Mg-MOF-74@CNT and the pristine Mg-MOF-74 at all temperatures.

**Table 4-10.** Fitted parameters of Langmuir model for CH<sub>4</sub> adsorption isotherms of Mg-MOF-74, Mg-MOF-74@CNT and Mg-MOF-74@GO up to 10 bar at different temperatures: 25 °C, 50 °C and 75 °C.

Temperature	Fitted parameters	Mg-MOF-74	Mg-MOF-74 @CNT	Mg-MOF-74 @GO
25 °C	<i>ERRSQ</i>	9.01x10 <sup>-6</sup>	1.72x10 <sup>-4</sup>	5.34x10 <sup>-4</sup>
	<i>R</i> <sup>2</sup>	1.00000	0.99999	0.99993
	<i>q</i> <sub>sat</sub> (mmol·g <sup>-1</sup> )	8.83	12.42	14.76
	<i>b</i> <sub>L</sub> (bar <sup>-1</sup> )	0.08	0.07	0.04
50 °C	<i>ERRSQ</i>	1.69x10 <sup>-5</sup>	1.81x10 <sup>-4</sup>	5.34x10 <sup>-6</sup>
	<i>R</i> <sup>2</sup>	0.99999	0.99997	1.00000
	<i>q</i> <sub>sat</sub> (mmol·g <sup>-1</sup> )	6.20	8.23	10.72
	<i>b</i> <sub>L</sub> (bar <sup>-1</sup> )	0.07	0.08	0.04
75 °C	<i>ERRSQ</i>	1.25x10 <sup>-7</sup>	4.85x10 <sup>-7</sup>	7.02x10 <sup>-9</sup>
	<i>R</i> <sup>2</sup>	1.00000	1.00000	1.00000
	<i>q</i> <sub>sat</sub> (mmol·g <sup>-1</sup> )	18.52	12.89	19.08
	<i>b</i> <sub>L</sub> (bar <sup>-1</sup> )	0.004	0.015	0.012

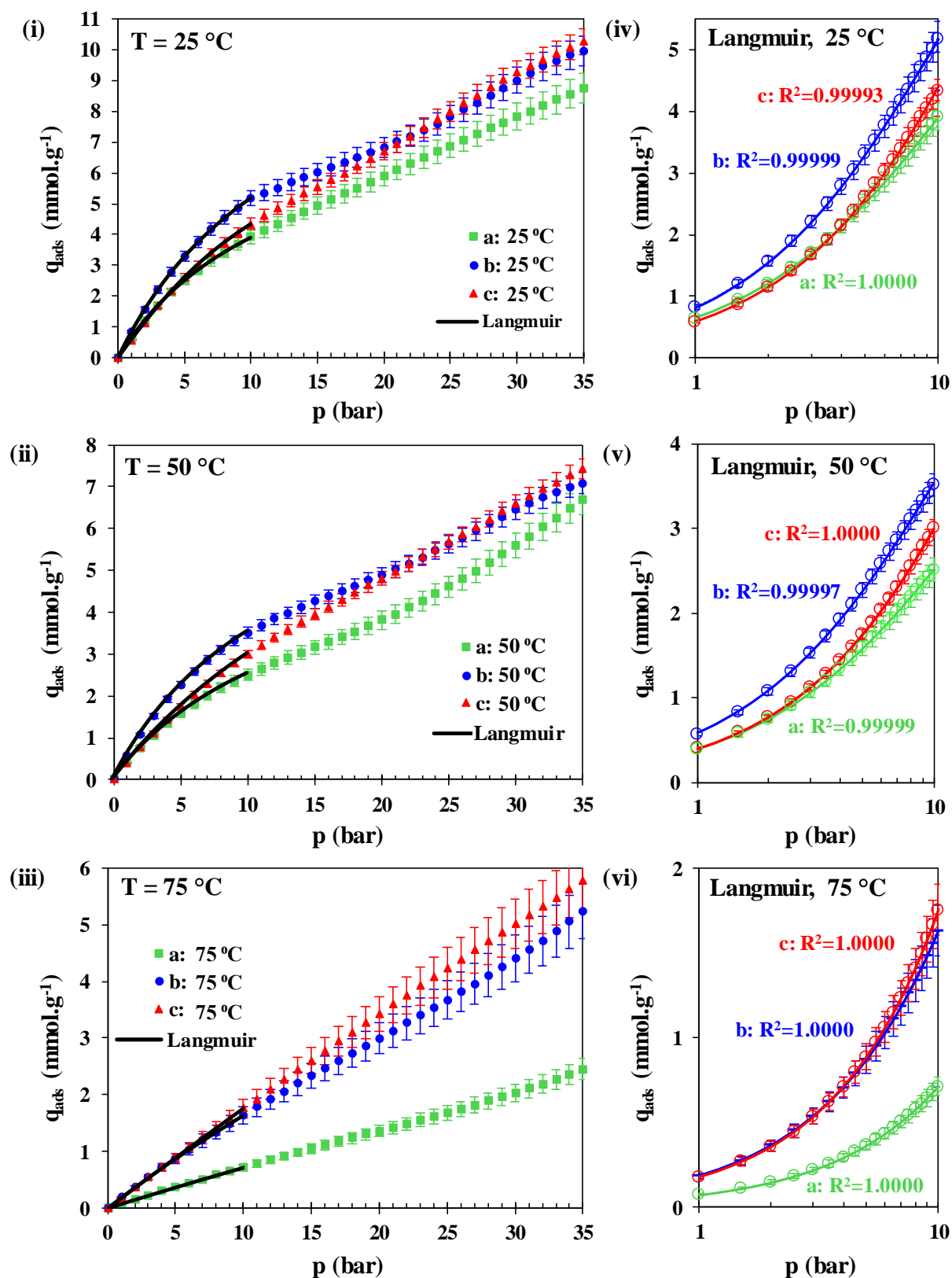


**Figure 4-35.** Average curve of CH<sub>4</sub> adsorption isotherms of (a) Mg-MOF-74, (b) Mg-MOF-74@CNT and (c) Mg-MOF-74@GO up to 35 bar with average relative errors bars, ARE, for different temperatures: (i) 25 °C, (ii) 50 °C and (iii) 75 °C, fitted to Langmuir model until 10 bar providing coefficient of determination, R<sup>2</sup>, for different temperatures: (iv) 25 °C, (v) 50 °C and (vi) 75 °C.

4.5.3. Equilibrium selectivities of CO<sub>2</sub>/CH<sub>4</sub>

Similar to the calculations for low-pressure adsorption, the intrinsic selectivity,  $\alpha_{CO_2/CH_4}^{INT}$ , (Eq. 4-3) and PSA adsorbent selection parameter,  $S_{CO_2/CH_4}^{PSA}$ , (Eq. 4-4) were deduced from the ratio of Henry's constants of dual-site Langmuir isotherm of CO<sub>2</sub> adsorption and Langmuir isotherm of CH<sub>4</sub> adsorption. The results of  $\alpha_{CO_2/CH_4}^{INT}$  and  $S_{CO_2/CH_4}^{PSA}$  are summarized in Figure 4-36. It can be seen that the selectivity values of all samples increase as a function of temperature except the values drop for the pristine Mg-MOF-74 at 75 °C. For adsorption in Henry's law region (or zero coverage), the pristine material is a reasonable adsorbent for the separation at 25 °C aside from Mg-MOF-74@GO, while Mg-MOF-74@GO itself and Mg-MOF-74@CNT exhibits the highest selectivity for adsorptions 50 °C and 75 °C, respectively. By comparing the selectivity values at 25 °C with those of the same temperature at low-pressure adsorptions, the selectivities remarkably diminish, indicating that the separation becomes more difficult for larger quantity of adsorbed gases.

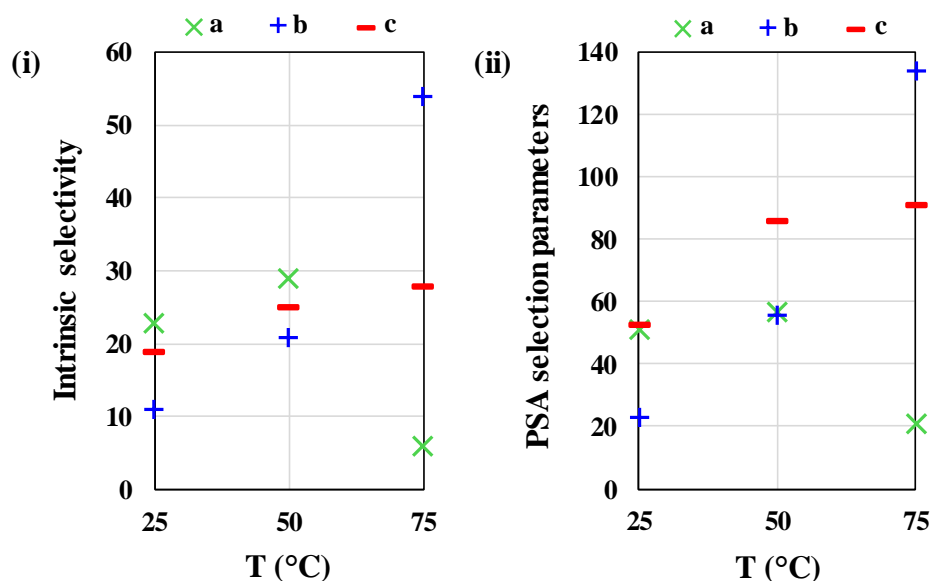


**Figure 4-36.** (i) Intrinsic selectivity of CO<sub>2</sub>/CH<sub>4</sub> and (ii) PSA adsorbent selection parameter of CO<sub>2</sub>/CH<sub>4</sub> of (a) Mg-MOF-74, (b) Mg-MOF-74@CNT and (c) Mg-MOF-74@GO at 10 bar as a function of temperatures.

By using dual-site Langmuir isotherm of CO<sub>2</sub> adsorption and Langmuir isotherm of CH<sub>4</sub> adsorption, IAST selectivity,  $\alpha_{CO_2/CH_4}^{IAST}$ , (Eq. 4-11) were also calculated. Both Langmuir isotherms are the best candidates for IAST calculations having asymptotic

---

properties at low and high pressures. Based on IAST calculations as a function of pressure, the adsorption uptakes of CO<sub>2</sub>, CH<sub>4</sub> and the total gases are shown in Figure 4-37 while IAST selectivities are shown in Figure 4-38. Both composites remain the best adsorbents in terms of separation ability except a slight decrease is observed with the temperature, with more stable adsorption uptakes compared to the pristine Mg-MOF-74. In general, it is observed that the selectivity of all samples do not vary largely with the pressure in the 0–10 bar range. At 25 °C, all samples demonstrate comparable selectivity data as similarly noticed in the low-pressure adsorption. At 50 °C, Mg-MOF-74@GO demonstrates the best selectivity followed by Mg-MOF-74@CNT and Mg-MOF-74. At 75 °C, the selectivity of the pristine Mg-MOF-74 is significantly disfavoured and remains constant as the pressure progresses. Mg-MOF-74@CNT appears with the highest selectivity at this temperature, followed by Mg-MOF-74@GO.

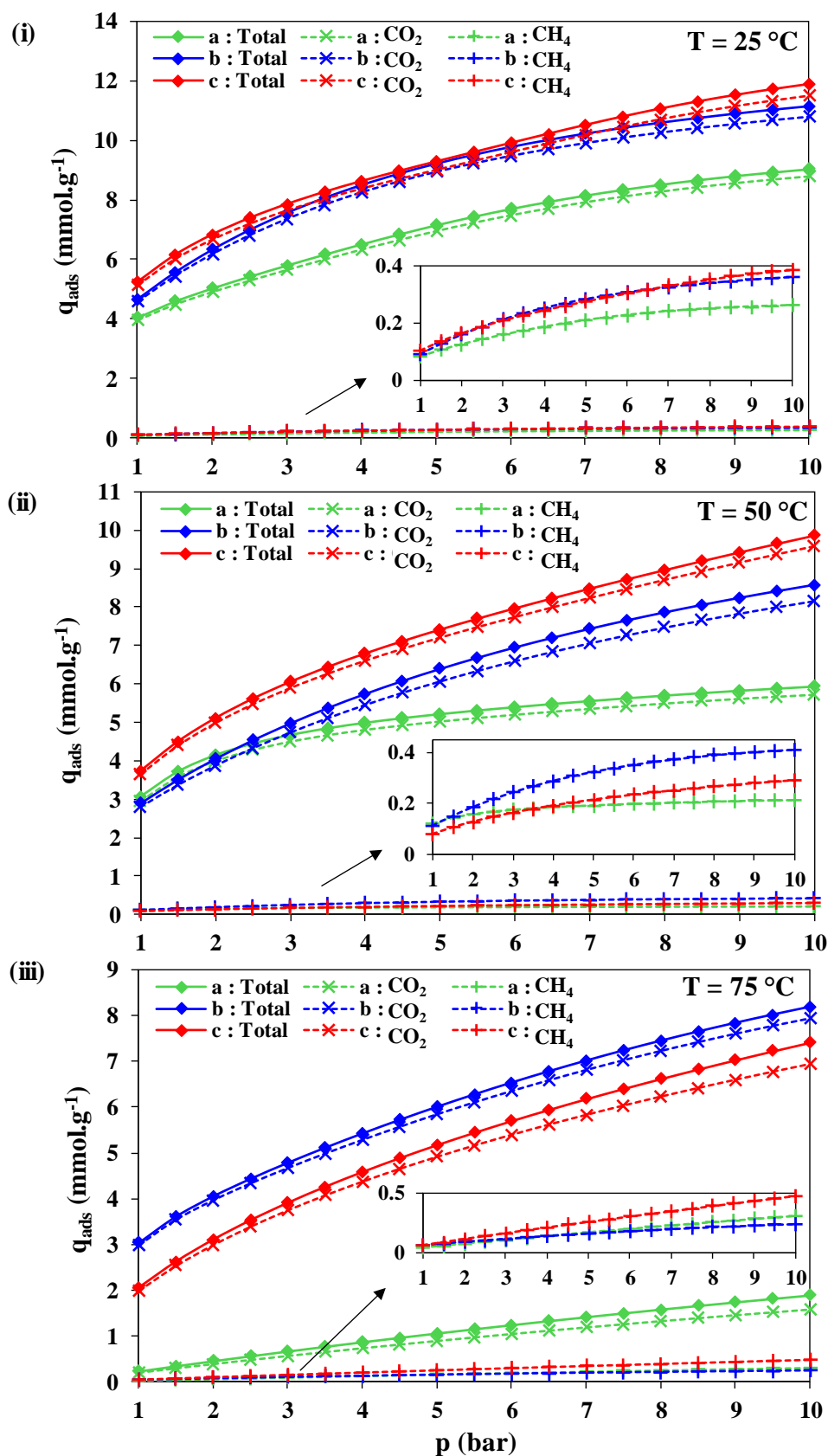


**Figure 4-37.** IAST adsorption uptake of  $\text{CO}_2$  and  $\text{CH}_4$  for an equimolar mixture on (a) Mg-MOF-74, (b) Mg-MOF-74@CNT, and (c) Mg-MOF-74@GO up to 10 bar for different temperatures: (i) 25 °C, (ii) 50 °C and (iii) 75 °C.

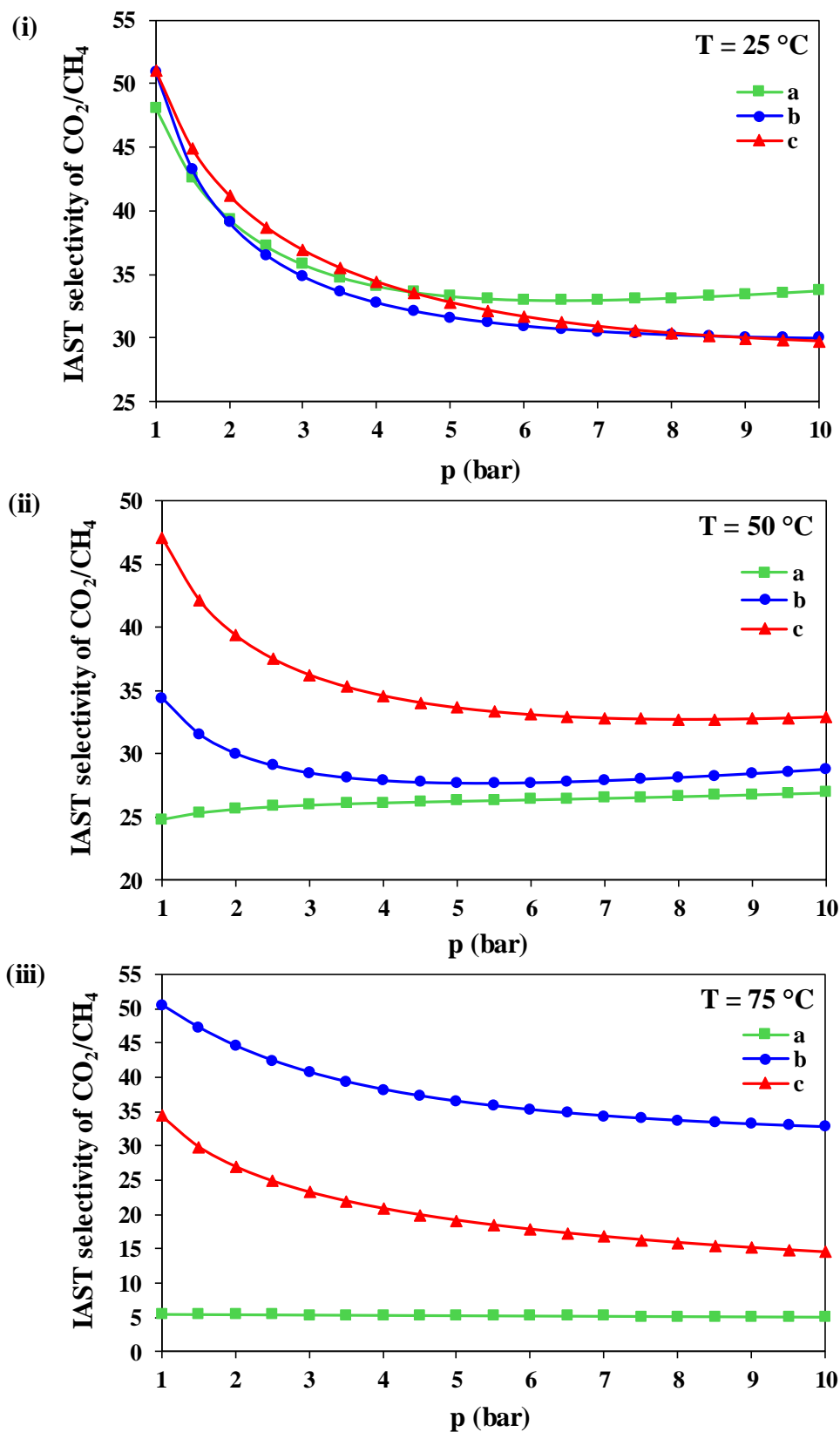


**Figure 4-38.** IAST selectivity of CO<sub>2</sub>/CH<sub>4</sub> for an equimolar mixture on (a) Mg-MOF-74, (b) Mg-MOF-74@CNT, and, (c) Mg-MOF-74@GO up to 10 bar for different temperatures: (i) 25 °C, (ii) 50 °C and (iii) 75 °C.

The performances of the materials based on IAST capacity and selectivity is evaluated in Figure 4-39. At 25 °C, none of the materials display the best balance between these two benchmarks thus the tolerance must be decided between the deviations observed in CO<sub>2</sub> adsorption capacity or CO<sub>2</sub>/CH<sub>4</sub> selectivity. At 50 °C and 75 °C, Mg-MOF-74@GO and Mg-MOF-74@CNT respectively can be considered as best adsorbents affording the highest CO<sub>2</sub> capture rate with the highest separation quality.

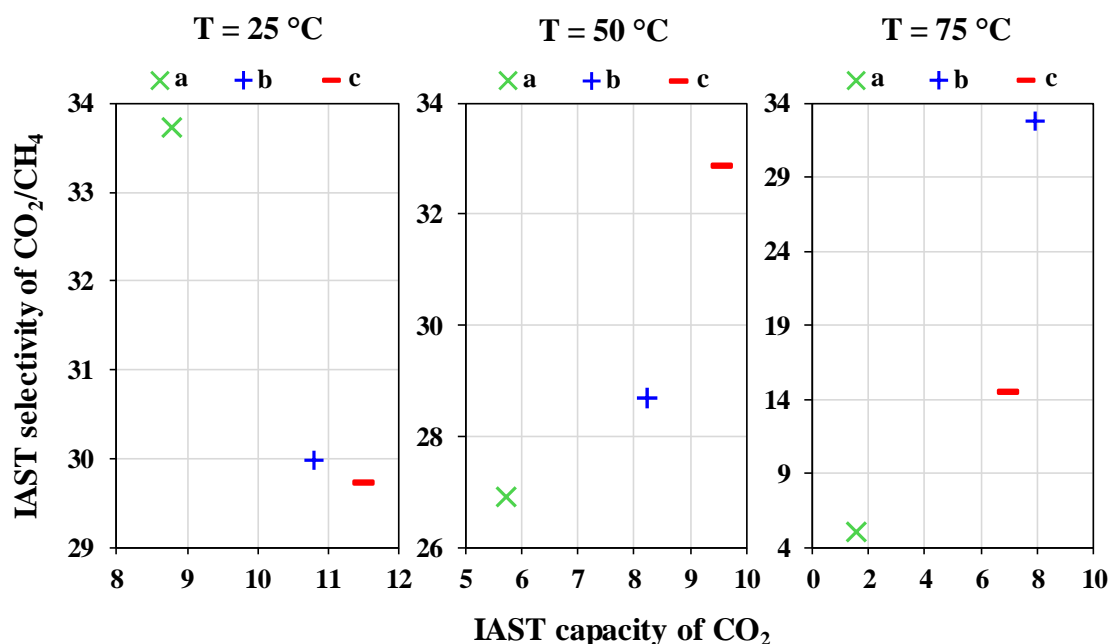


**Figure 4-39.** IAST selectivity of CO<sub>2</sub>/CH<sub>4</sub> versus IAST capacity in mmol·g<sup>-1</sup> of CO<sub>2</sub> adsorption for an equimolar mixture on (a) Mg-MOF-74, (b) Mg-MOF-74@CNT and (c) Mg-MOF-74@GO at 10 bar for different temperatures: 25 °C, 50 °C and 75 °C.

#### 4.5.4. Isosteric heat of adsorption

The effect of adsorption temperature on adsorption uptakes for all samples are presented in Figure 4-40 (CO<sub>2</sub>) and Figure 4-41 (CH<sub>4</sub>). The adsorption capacity of the gases in all samples decreases with the increasing temperature demonstrating the mechanism of physical adsorption (exothermic). However, the adsorption behavior of CO<sub>2</sub> in both composites along the pressure region up to 35 bar is much more stable and less affected by the temperature in comparison to the pristine Mg-MOF-74, as noticed previously. This outcome becomes interesting and advantageous for the implementation of both Mg-MOF-74 composites for high-temperature adsorption.

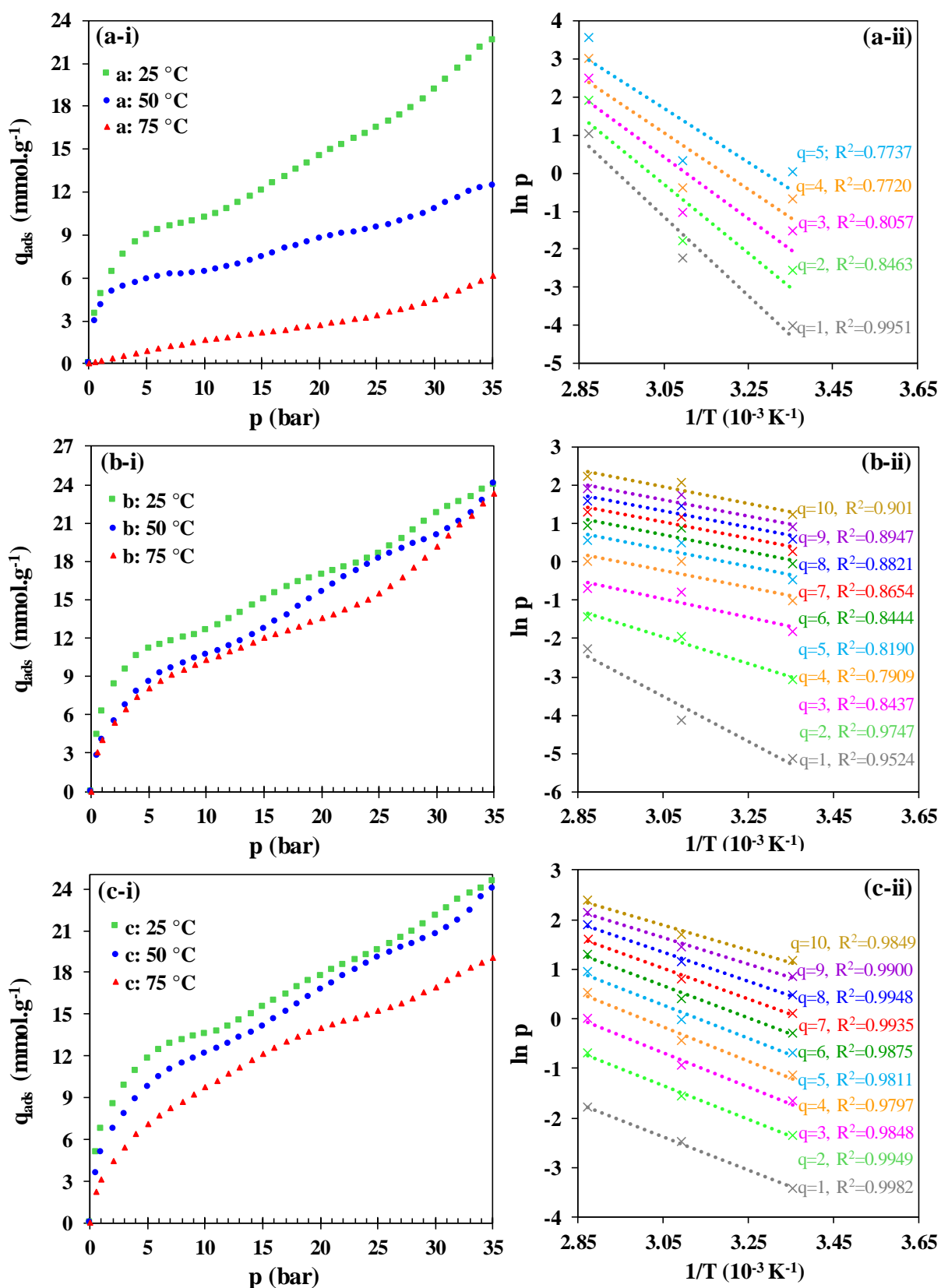


**Figure 4-40.** CO<sub>2</sub> adsorption isotherms of (a-i) Mg-MOF-74, (b-i) Mg-MOF-74@CNT, and, (c-i) Mg-MOF-74@GO up to 35 bar and at different temperatures, and, (a-ii) (b-ii) (c-ii) their respective Arrhenius plot for the calculation of isosteric heat of adsorption with the coefficient of determination,  $R^2$ , for each amount adsorbed,  $q$ , in  $\text{mmol}\cdot\text{g}^{-1}$ .

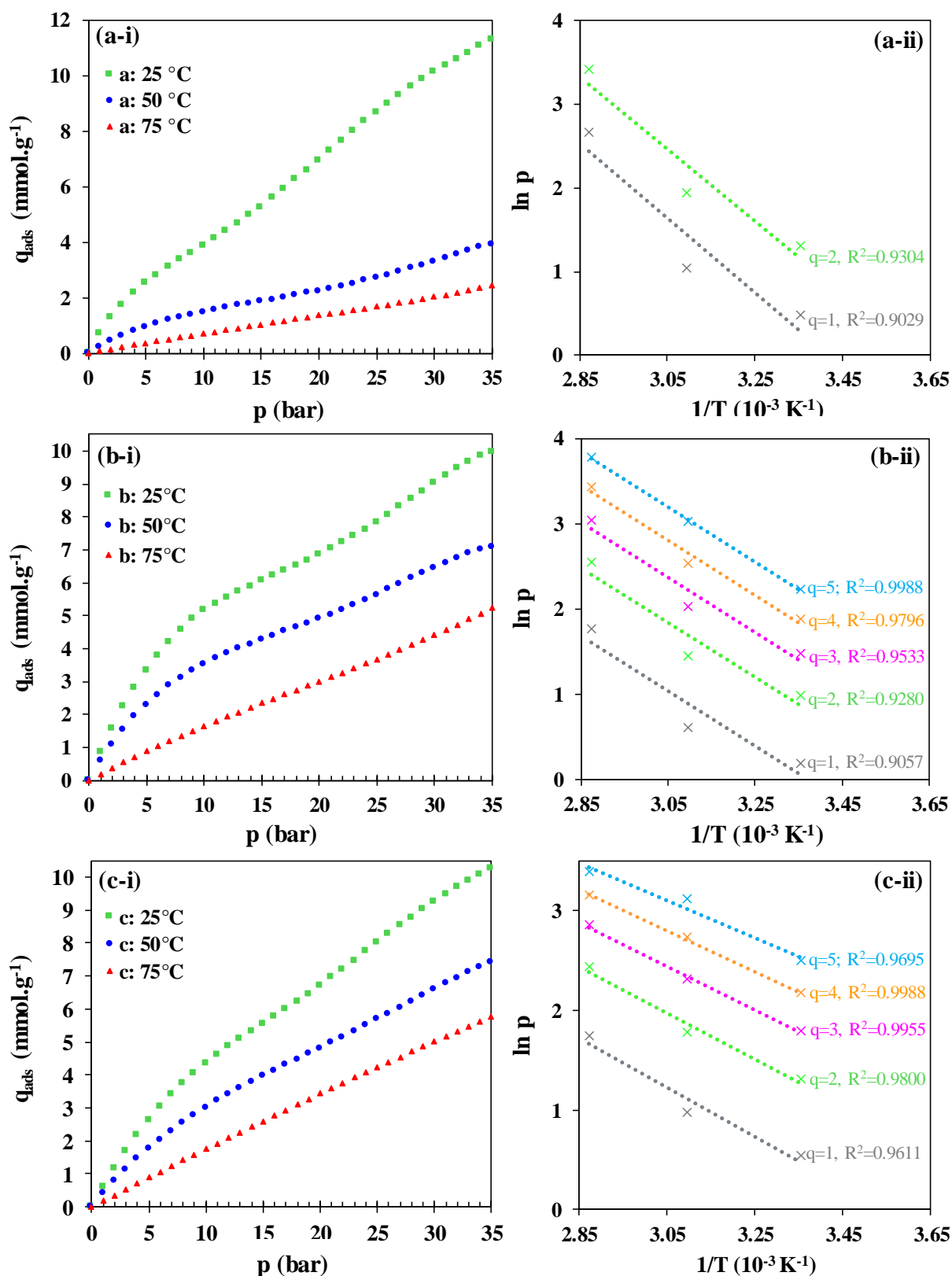


**Figure 4-41.** CH<sub>4</sub> adsorption isotherms of (a-i) Mg-MOF-74, (b-i) Mg-MOF-74@CNT, and, (c-i) Mg-MOF-74@GO up to 35 bar and at different temperatures, and, (a-ii) (b-ii) (c-ii) their respective Arrhenius plot for the calculation of isosteric heat of adsorption with the coefficient of determination, R<sup>2</sup>, for each amount adsorbed, q, in mmol.g<sup>-1</sup>.

The experimental values of isosteric heat of adsorption  $Q_{st}$  were calculated using Clausius–Clapeyron approach (Eq. 4-2) for  $q = 1–10 \text{ mmol}\cdot\text{g}^{-1}$ . Knowing that the value is very sensitive to the regression of equilibrium data, thus the coefficient of determination,  $R^2$ , for each  $q$  must be well-defined to evaluate the accuracy of the calculation. As shown by Arrhenius plots also in Figure 4-40 and Figure 4-41, heats of adsorption were deduced with the average  $R^2$  of: 0.83856 (Mg-MOF-74,  $\text{CO}_2$ ), 0.87684 (Mg-MOF-74@CNT,  $\text{CO}_2$ ), 0.98884 (Mg-MOF-74@GO,  $\text{CO}_2$ ), 0.91665 (Mg-MOF-74,  $\text{CH}_4$ ), 0.95308 (Mg-MOF-74@CNT,  $\text{CH}_4$ ) and 0.98098 (Mg-MOF-74@GO,  $\text{CH}_4$ ). The results are then presented in Figure 4-42 for each mole of adsorbed amount. The values of isosteric heat of  $\text{CO}_2$  adsorption on the pristine Mg-MOF-74 lie in the range of physisorption and are comparable to different experimental and calculated literature data from  $39 \text{ kJ}\cdot\text{mol}^{-1}$  to  $73 \text{ kJ}\cdot\text{mol}^{-1}$  [16, 18, 19, 186]. It becomes beneficial in terms of energy cost for adsorbent regeneration in addition of having excellent capacity of gas uptake. The composites appear with lower isosteric heat values displaying easier regeneration of the materials after the adsorption. The hypothesis that can be proposed is that the lower energy adsorption sites in MOF composites are more easily accessible than those in pristine MOF. Therefore, the apparent adsorption energy (isosteric heat) is lower for the composites covering the adsorption sites with higher energy.

For all samples, the difference between the isosteric heat values for  $\text{CO}_2$  and  $\text{CH}_4$  are large enough to facilitate gas separation in the case of co-adsorption which has been proven previously in selectivity calculations. In general, the values of  $Q_{st}$  appear stronger when the adsorption commences, indicating stronger affinity of adsorption sites with higher energy that are preferable for the adsorbates. After certain adsorbed amount, the adsorption energies of  $\text{CO}_2$  seem to be constant even though the adsorption coverage keep on increasing. Remarkably,  $\text{CH}_4$  adsorption energies in Mg-MOF-74@CNT are weakly influenced by the adsorption coverage unlike those in the pristine Mg-MOF-74 and Mg-MOF-74@GO which decreases as a function of adsorbed amount. The values of  $Q_{st}$  considerably at the beginning of the adsorption ( $q = 1 \text{ mmol}\cdot\text{g}^{-1}$ ) on the synthesized materials are recapitulated in Table 4-11.

**Table 4-11.** Isothermic heats of CO<sub>2</sub> and CH<sub>4</sub> adsorptions  $Q_{st}$  in kJ·mol<sup>-1</sup> on Mg-MOF-74, Mg-MOF-74@CNT and Mg-MOF-74@GO at an adsorbed amount of 1 mmol·g<sup>-1</sup>.

Mg-MOF-74		Mg-MOF-74@CNT		Mg-MOF-74@GO	
CO <sub>2</sub>	CH <sub>4</sub>	CO <sub>2</sub>	CH <sub>4</sub>	CO <sub>2</sub>	CH <sub>4</sub>
76.6	37.2	57.2	26.7	57.2	20.5

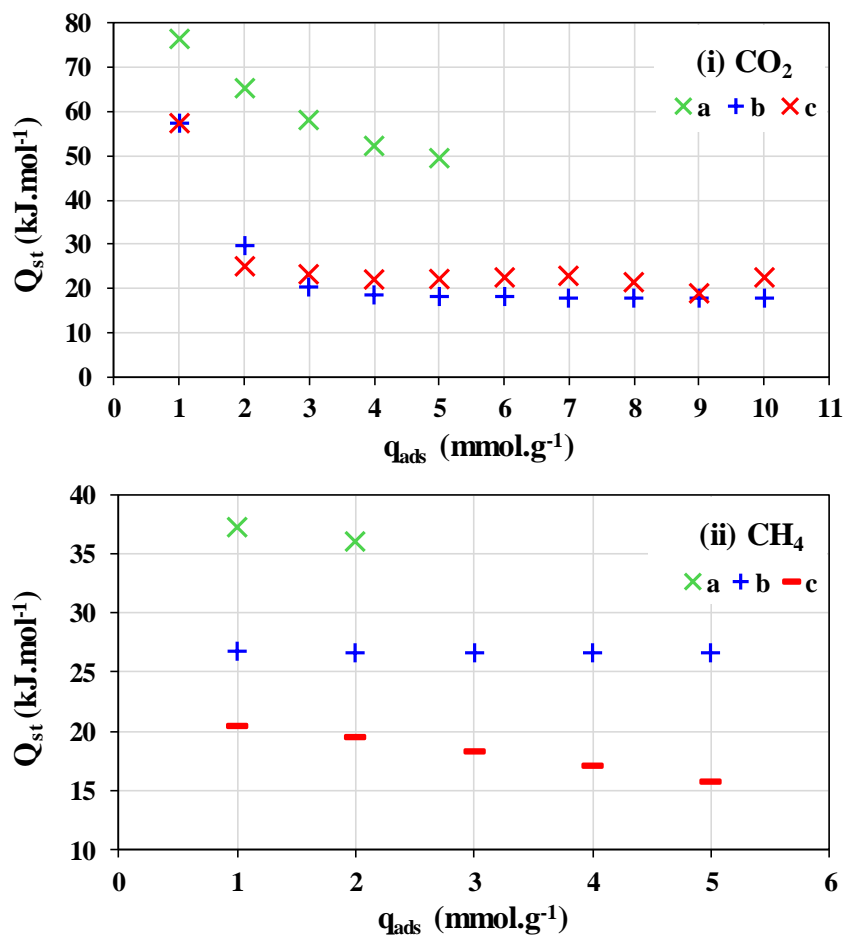


**Figure 4-42.** Isothermic heat of adsorption,  $Q_{st}$ , of (i) CO<sub>2</sub> and (ii) CH<sub>4</sub> on (a) Mg-MOF-74, (b) Mg-MOF-74@CNT and (c) Mg-MOF-74@GO as a function of amount adsorbed.

#### 4.6. Conclusion

The adsorption equilibrium of CO<sub>2</sub> which is the gas of interest was studied all along with CH<sub>4</sub> adsorption on the synthesized Mg-MOF-74 and its carbon composites, Mg-MOF-74@CNT and Mg-MOF-74@GO. The equilibrium data at low pressures (up to 1 bar) at 25 °C indicate the improvement of CO<sub>2</sub> uptake by 18 mol% and 23 mol% for Mg-MOF-74@CNT and Mg-MOF-74@GO, respectively, compared to the pristine Mg-MOF-74. The adsorption capacities are proportional to the enhancement in specific surface area and micropore volume of both composites. The increment in CH<sub>4</sub> adsorption by 27 mol% and 36 mol% for Mg-MOF-74@CNT and Mg-MOF-74@GO, respectively, compared to the pristine Mg-MOF-74, is inevitable because pore texture of the composite materials promotes more gas retention. The performances of the materials for gas separation are evaluated in terms of the ability to provide large production volume and high separation quality. Based on IAST calculations, Mg-MOF-74@GO appears as the best adsorbent having a good balance between CO<sub>2</sub> capacity and CO<sub>2</sub>/CH<sub>4</sub> selectivity up to 1 bar at 25 °C, followed by Mg-MOF-74@CNT and Mg-MOF-74. The equilibrium measurements were then performed at high pressures (up to 35 bar) for different temperatures: 25 °C, 50 °C and 75 °C. The consistency of the improvement of CO<sub>2</sub> uptake in both composites compared to the pristine Mg-MOF-74 is observed in this pressure region, and the improvement gets higher with the increasing temperature. CO<sub>2</sub> adsorption behaviour in the pristine Mg-MOF-74 is significantly adversely affected by the temperature while it is less affected for both composites. It makes both carbon composites superior to the pristine Mg-MOF-74 for the implementation of a dynamic adsorption process, even at temperature above ambient. The performances of the materials were evaluated based on IAST but the modelling is limited up to 10 bar due to the isotherm shape. At 25 °C, none of the materials display the best balance between CO<sub>2</sub> capacity and CO<sub>2</sub>/CH<sub>4</sub> selectivity thus the tolerance must be decided between the deviations in the value of these two benchmarks. At 50 °C and 75 °C, Mg-MOF-74@GO and Mg-MOF-74@CNT respectively are the best adsorbent affording the highest CO<sub>2</sub> capture capacity with the highest separation quality. The experimental values of isosteric heats of adsorption of the gases lie in the range of physisorption which is advantageous for regeneration in addition of having excellent gas uptake capacity. The higher adsorption energies of CO<sub>2</sub> compared to CH<sub>4</sub> are attributed to the polarizability and accessibility of CO<sub>2</sub> molecules inside the micropores, resulting in higher adsorption uptake.

For future work of adsorption equilibria, more appropriate isotherm modelling can be proposed by fixing only one reference temperature and finding the correct relation between the constants of the isotherm model and temperature. In a bigger perspective, co-adsorption of CO<sub>2</sub> and methane can be performed so that we do not only depend on the IAST system to evaluate the selectivity and working capacity of the adsorbent. It is important to study the influence of humidity on adsorption sites passivation and to include the presence of water vapor during CO<sub>2</sub> adsorption to examine their competition.

**CHAPTER 5**

**Adsorption**

**Kinetics**

## CHAPTER 5: ADSORPTION KINETICS

## 5.1. Mass transfer by diffusions: Principles

## 5.1.1. Fick's laws

*a. Fick's first law*

In the period 1850–1855, Thomas Graham and Adolf Fick were the first who verified the proportionality between the diffusive flux and concentration gradient. On this basis, Fick's first law of diffusion was formulated as Eq. 5-1 [172] in which  $D$  ( $\text{m}^2 \cdot \text{s}^{-1}$ ) signifies no more than the diffusivity in general:

$$J = -D \cdot \frac{\partial c}{\partial z} \quad (\text{Eq. 5-1})$$

where  $J$  ( $\text{mol} \cdot \text{m}^{-2} \cdot \text{s}^{-1}$ ) is the diffusive flux,  $c$  ( $\text{mol} \cdot \text{m}^{-3}$ ) the species concentration in fluid phase and  $z$  (m) is the distance coordinate in the space.

*b. Fick's second law*

Fick's second law is demonstrated from the following material balance, supposing for a diffusion of species in a volume between position  $z$  and  $z + \partial z$  inside a column with parallel-sided wall for a duration time  $\partial t$ :

$$\frac{\partial c}{\partial t} \cdot dt \cdot dz = [J(z) - J(z + dz)] \cdot dt$$

$$\frac{\partial c}{\partial t} \cdot dt \cdot dz = -\frac{\partial J}{\partial z} \cdot dz \cdot dt$$

$$\frac{\partial c}{\partial t} = -\frac{\partial J}{\partial z} \quad (\text{Eq. 5-2})$$

where  $t$  (s) is the time and  $\partial c / \partial t$  is the accumulation of species concentration in fluid phase.

By injecting Fick's first law into Eq. 5-2 and supposing that the diffusivity is constant as a function of concentration, Eq. 5-3 can be obtained.

$$\frac{\partial c}{\partial t} = \frac{\partial \left( D \cdot \frac{\partial c}{\partial z} \right)}{\partial z} = D \cdot \frac{\partial^2 c}{\partial z^2} \quad (\text{Eq. 5-3})$$

It is a mass conservation equation commonly known as Fick's second law of "non-stationary" diffusion [172] in which both spatial ( $\partial z$ ) and temporal ( $\partial t$ ) variations of species concentration are defined.

### 5.1.2. Gradient of chemical potential

#### *a. Chemical potential driving force model*

With the aim of describing the mass transfer of adsorbate inside an adsorbent particle, chemical potential driving force (CPDF) model was introduced by Barrer (1971) [224] for pure bulk gas phase. From Fick's first law, it is understood that the driving force of diffusion is the gradient of concentration,  $\partial c$ , which is directly related to the gradient of chemical potential,  $\partial \mu$ , defined by the change in chemical energy in a system per mole of molecules at constant temperature and pressure [172]. Therefore, if the diffusive flux of the adsorbate is considered as a flow driven by the gradient of chemical potential, then the flow must be opposed to frictional forces through a distance  $\partial z$  [172]. So the energy balance for a differential element  $\partial \mu / \partial z$  in a steady state is expressed by Einstein's relation Eq. 5-4 [225]:

$$\frac{\partial \mu}{\partial z} = -f \cdot u \quad (\text{Eq. 5-4})$$

where  $\mu$  ( $\text{J} \cdot \text{mol}^{-1}$ ) is the chemical potential of the adsorbate,  $z$  (m) is the distance coordinate in the space,  $u$  ( $\text{m} \cdot \text{s}^{-1}$ ) is the gas flow velocity and  $f$  (SI unit) is a molecular friction coefficient which equals to  $1/B$  where  $B$  (SI unit) is the molecular mobility.

In order to relate the gradient of chemical potential to the concentration in adsorbed phase, the equilibrium gas phase must be considered as an ideal gas system in which the activity of the adsorbate,  $a$ , is identified by its partial pressure,  $p$ , as shown in Eq. 5-5 [172]:

$$\mu = \mu^0 + R \cdot T \cdot \ln a = \mu = \mu^0 + R \cdot T \cdot \ln p \quad (\text{Eq. 5-5})$$

where  $\mu^0$  is the standard chemical potential for pure phase,  $R$  is the gas constant ( $R=8.314 \text{ J} \cdot \text{mol}^{-1} \cdot \text{K}^{-1}$ ),  $T$  (K) is the temperature,  $a$  is the adsorbate activity and  $p$  (Pa) is the adsorbate partial pressure.

Then, from Eq. 5-5, the differential element  $\partial\mu/\partial z$  is presented as follows, into which the variation of adsorbate concentration in adsorbed phase per unit volume of adsorbent,  $\partial q$  ( $\text{mol}\cdot\text{m}^{-3}$ ), is introduced.

$$\frac{\partial\mu}{\partial z} = R \cdot T \cdot \frac{\partial \ln p}{\partial z} = R \cdot T \cdot \frac{\partial \ln p}{\partial q} \cdot \frac{\partial q}{\partial z} \quad (\text{Eq. 5-6})$$

By injecting Eq. 5-4 into Eq. 5-6:

$$u = -B \cdot R \cdot T \cdot \frac{\partial \ln p}{\partial q} \cdot \frac{\partial q}{\partial z} \quad (\text{Eq. 5-7})$$

Knowing that the diffusive flux in adsorbed phase,  $J$  ( $\text{mol}\cdot\text{m}^{-2}\cdot\text{s}^{-1}$ ), can be defined as the product of  $u$  ( $\text{m}\cdot\text{s}^{-1}$ ) and  $q$  ( $\text{mol}\cdot\text{m}^{-3}$ ), then the following expression can be obtained:

$$J = u \cdot q = -B \cdot R \cdot T \cdot q \cdot \frac{\partial \ln p}{\partial q} \cdot \frac{\partial q}{\partial z}$$

$$J = -B \cdot R \cdot T \cdot \frac{\partial \ln p}{\partial \ln q} \cdot \frac{\partial q}{\partial z} \quad (\text{Eq. 5-8})$$

### ***b. Darken corrective factor***

By assimilating Eq. 5-8 to Fick's first law (Eq. 5-1), for a given temperature, we can deduce that [172, 180]:

$$D = B \cdot R \cdot T \cdot \left( \frac{\partial \ln p}{\partial \ln q} \right)_T = D_0 \cdot \left( \frac{\partial \ln p}{\partial \ln q} \right)_T \quad (\text{Eq. 5-9})$$

where  $D$  ( $\text{m}^2\cdot\text{s}^{-1}$ ) is the Fickian diffusivity in adsorbed phase and  $D_0$  ( $\text{m}^2\cdot\text{s}^{-1}$ ) is the Fickian diffusivity in adsorbed phase at nearly zero adsorption coverage (corrected diffusivity) [172, 180] and  $\partial \ln p/\partial \ln q$  is the thermodynamic corrective factor which follows adsorption coverage, known as Darken corrective factor.

If the system is considered thermodynamically ideal ( $p \propto q$ ) where the isotherm is linear following Henry's law ( $q = K \cdot p$ ) which is usually the case for diluted systems, the corrective factor  $\partial \ln p/\partial \ln q \approx 1$  and thus  $D \approx D_0$  [172, 180].

If the adsorption occurs beyond Henry's law region, the Fickian diffusivity is not constant as a function of concentration in adsorbed phase (adsorption coverage), thus it is

seen to be the product of  $D_0$  coefficient and Darken corrective factor,  $\partial \ln p / \partial \ln q$  [172, 180]. The evolution of adsorption coverage in Darken corrective factor depends on equilibrium isotherm, for instance, Langmuir and Toth isotherms, that have both asymptotic properties at zero coverage and at saturation.

If the adsorption equilibrium follows Langmuir isotherm (Eq. A-2), for single-component system, the fractional adsorption loading will follow Eq. 5-10 [172].

$$q(p) = q_{sat} \frac{b_L \cdot p}{1 + b_L \cdot p} \quad (\text{Recall of Eq. A-2})$$

$$\theta = \frac{q}{q_\infty} = \frac{b_L \cdot p}{1 + b_L \cdot p} \quad (\text{Eq. 5-10})$$

where  $\theta$  is the surface coverage ratio,  $q$  ( $\text{mol} \cdot \text{m}^{-3}$ ) is adsorbate concentration in adsorbed phase per unit volume of adsorbent and  $q_\infty$  ( $\text{mol} \cdot \text{m}^{-3}$ ) is the final value of  $q$  as  $t \rightarrow \infty$  meaning that when the equilibrium is achieved ( $\theta \approx 1$ ). At zero adsorption coverage,  $q \rightarrow K \cdot p$  where  $K = b_L \cdot q_{sat}$ , and at saturation,  $q_\infty \rightarrow q_{sat}$ .

The Darken corrective factor for Langmuir isotherm can be expressed as Eq. 5-11 [172]:

$$\frac{\partial \ln p}{\partial \ln q} = \frac{1}{1 - \theta} = \frac{1}{1 - \frac{q}{q_\infty}} \quad (\text{Eq. 5-11})$$

If the adsorption equilibrium follows Toth isotherm (Eq. A-5), for single-component system, the adsorption coverage will follow Eq. 5-12. At zero adsorption coverage,  $q \rightarrow K \cdot p$  where  $K = b_T \cdot q_{sat}$ , and at saturation,  $q_\infty \rightarrow q_{sat}$ .

$$q(p) = q_{sat} \frac{b_T \cdot p}{[1 + (b_T \cdot p)^{\frac{1}{n}}]^n} \quad (\text{Recall of Eq. A-5})$$

$$\theta = \left( \frac{q}{q_\infty} \right)^{\frac{1}{n}} = \frac{(b_T \cdot p)^{\frac{1}{n}}}{1 + (b_T \cdot p)^{\frac{1}{n}}} \quad (\text{Eq. 5-12})$$

The Darken corrective factor for Toth isotherm can be expressed as Eq. 5-13:

$$\frac{\partial \ln p}{\partial \ln q} = \frac{1}{1 - \theta} = \frac{1}{1 - \left(\frac{q}{q_{\infty}}\right)^{\frac{1}{n}}} \quad (\text{Eq. 5-13})$$

### 5.1.3. Non-isothermal diffusion system

In order to take into account the change in temperature for a non-isothermal adsorption in a diffusion model, the affinity coefficient of isotherm model,  $b$ , can be linked to the temperature by Eq. 5-14, supposing that the isosteric heat of adsorption is constant at any stage of adsorption coverage.

$$b(T) = b_0 \cdot \exp\left(-\frac{Q_{st}}{R \cdot T_0} \left(1 - \frac{T_0}{T}\right)\right) \quad (\text{Eq. 5-14})$$

where  $b_0$  ( $\text{Pa}^{-1}$ ) is the affinity constant at a reference temperature,  $Q_{st}$  ( $\text{kJ} \cdot \text{mol}^{-1}$ ) is the isosteric heat of adsorption,  $R$  is the gas constant,  $T_0$  (K) is a reference temperature and  $T$  (K) is the temperature.

Besides that, the diffusivity in adsorbed phase at zero adsorption coverage,  $D_0$ , can also be related to the temperature by Eq. 5-15 according to Arrhenius law:

$$D_0(T) = D_{0,T_{\infty}} \cdot \exp\left(-\frac{E_a}{R \cdot T}\right) \quad (\text{Eq. 5-15})$$

where  $D_{0,T_{\infty}}$  ( $\text{m}^2 \cdot \text{s}^{-1}$ ) is the diffusivity at zero adsorption coverage at infinite temperature and  $E_a$  ( $\text{kJ} \cdot \text{mol}^{-1}$ ) is the activation energy of diffusion.

Eq. 5-15 can be expressed as the following equation to have the diffusivity corresponding to a reference temperature,  $T_0$ :

$$D_0(T) = D_{0,T_0} \cdot \exp\left(-\frac{E_a}{R \cdot T_0} \left(1 - \frac{T_0}{T}\right)\right) \quad (\text{Eq. 5-16})$$

where  $D_{0,T_0}$  ( $\text{m}^2 \cdot \text{s}^{-1}$ ) is the diffusivity at zero adsorption coverage at a reference temperature.

## 5.2. Diffusion mechanisms in porous solid: Principles

### 5.2.1. External mass transfers

External mass transfers of adsorption from bulk gas phase to adsorbed phase involve: (i) external film barrier (or boundary layer or laminar sublayer) of adsorbent particle quantified by film mass transfer coefficient,  $k_f$ , and, (ii) external surface barrier of adsorbent particle quantified by surface permeability coefficient,  $k_s$ .

#### a. External film mass transfer coefficient

Mass transfer in external film barrier of adsorbent particle is driven by concentration gradient between bulk gas phase and the surface of adsorbent particle, in the way that the thicker is the film, the smaller is the mass transfer coefficient,  $k_f$  [172, 173]. The diffusive flux in the film of adsorbent particle,  $J$  ( $\text{mol}\cdot\text{m}^{-2}\cdot\text{s}^{-1}$ ), can be defined as Eq. 5-17 [172] based on Fick's first law:

$$J = k_f(c - c_s^*) \quad (\text{Eq. 5-17})$$

where  $k_f$  ( $\text{m}\cdot\text{s}^{-1}$ ) is the film mass transfer coefficient,  $c$  ( $\text{mol}\cdot\text{m}^{-3}$ ) is the adsorbate concentration in gas phase and  $c_s^*$  ( $\text{mol}\cdot\text{m}^{-3}$ ) is the adsorbate concentration in gas phase that would be in equilibrium with the concentration at the surface of adsorbent particle.

In general,  $k_f$  is known as the external mass transfer coefficient based on fluid phase concentration difference as the driving force. Depending on the hydrodynamic conditions of the fluid phase, the value of  $k_f$  can be deduced from different functions of dimensionless numbers namely Sherwood, Reynolds and Schmidt,  $k_f = f(Sh, Re, Sc)$  [206]. A correlation was developed by Wakao and Kaguei (1982) [226] which is valid for a packed bed with a void fraction  $\varepsilon \approx 0.4$  in order to estimate the external gas film coefficient:

$$Sh = 2 + 1.1 \cdot Re^{0.6} \cdot Sc^{\frac{1}{3}} \quad (\text{Eq. 5-18})$$

$$Sh = k_f \frac{d_p}{D_{A,B}}, \quad Re = \frac{v \cdot d_p \cdot \rho}{\eta}, \quad Sc = \frac{\eta}{p \cdot D_{A,B}}$$

where  $d_p$  (m) is the adsorbent particle diameter,  $D_{A,B}$  ( $\text{m}^2\cdot\text{s}^{-1}$ ) is the molecular diffusivity in a binary mixture of species A and B,  $v$  ( $\text{m}\cdot\text{s}^{-1}$ ) is the velocity of the bulk gas flow in the bed,  $\rho$  ( $\text{kg}\cdot\text{m}^{-3}$ ) is the density of the fluid and  $\eta$  ( $\text{Pa}\cdot\text{s}$ ) is the fluid dynamic viscosity.

**b. External surface permeability coefficient**

Mass transfer in the external surface barrier (or “particle skin”) is described as the diffusion in the interface between the exterior and the interior of the solid due to the change in energy environment [172, 174]. Also based on Fick’s first law, the diffusive permeability in the surface of adsorbent particle,  $J$  ( $\text{mol}\cdot\text{m}^{-2}\cdot\text{s}^{-1}$ ), can be defined as Eq. 5-19 [172]:

$$J = k_s(q_\infty - q_s) \quad (\text{Eq. 5-19})$$

where  $k_s$  ( $\text{m}\cdot\text{s}^{-1}$ ) is the external surface permeability coefficient,  $q_\infty$  ( $\text{mol}\cdot\text{m}^{-3}$ ) is the equilibrium adsorbate concentration and  $q_s$  ( $\text{mol}\cdot\text{m}^{-3}$ ) is the adsorbate actual boundary (surface) concentration within the particle.

**5.2.2. Internal mass transfers**

Different mechanisms of internal mass transfer control the diffusion of an adsorbate in different regions of porosity (macro-, meso- and micropores) in nanoporous materials [172]. In micropore range, surface dispersive forces are dominant which makes an adsorbed molecule never escapes from the force field of the solid surface, and the gas fluid within the micropores can be considered as a “single” adsorbed phase [172]. In mesopores, capillary forces become important for the diffusion while macropores contribute very little to adsorption capacity but have their own role for the mass transfer [172]. Internal mass transfer mechanisms involve: (i) Poiseuille flow in Figure 5-1-i, (ii) Knudsen diffusion in Figure 5-1-ii, (iii) molecular diffusion in Figure 5-1-iii, and, (iv) surface diffusion in Figure 5-1-iv [95, 172, 174, 175, 179, 206, 227].

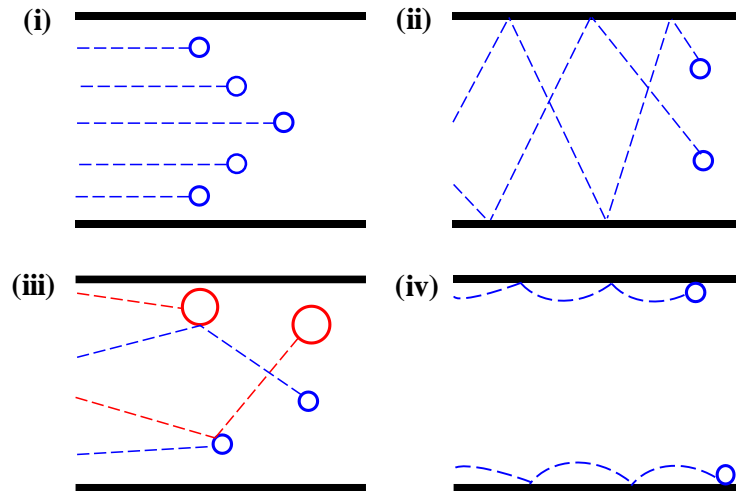


**Figure 5-1.** Illustration of different mechanisms of internal diffusion of molecules in pore capillary: (i) Poiseuille, (ii) Knudsen, (iii) molecular and (iv) surface diffusions.

### a. Poiseuille diffusivity

Poiseuille (or viscous or streamline) flow describes a steady laminar flow of incompressible and Newtonian fluid, driven by a total pressure gradient between the ends of the pore capillary [95, 172]. The flow is due to the viscosity of the fluid with the assumption of no slip at the surface of the wall [95]. In the case of fluid mixture, the molecules move through the capillary without separation because all species move at the same speed [95]. The diffusivity by Poiseuille flow,  $D_p$ , can be expressed as Eq. 5-20 [172]:

$$D_p = \frac{p \cdot r_{pore}^2}{8 \cdot \eta} \quad (\text{Eq. 5-20})$$

where  $D_p$  ( $\text{m}^2 \cdot \text{s}^{-1}$ ) is the Poiseuille (or viscous) diffusivity,  $p$  (Pa) is the gas total pressure,  $r_{pore}$  (m) is the pore radius and  $\eta$  (Pa·s) is the fluid dynamic viscosity.

### b. Knudsen diffusivity

Knudsen diffusion describes the diffusion in which the collisions between gas molecule and pore wall are frequent [172, 174, 175]. It occurs predominantly when mean free path of gas molecule,  $\lambda$ , (Eq. 5-21 [95]) is comparable with or even greater than pore diameter,  $d_{pore}$ , and characterized by Knudsen number,  $Kn$  which is always  $\geq 1$  (Eq. 5-22 [95]).

$$\lambda = \frac{k_b \cdot T}{\pi \cdot d_{pore}^2 \cdot p \cdot \sqrt{2}} \quad (\text{Eq. 5-21})$$

where  $\lambda$  (m) is the mean free path of gas molecule,  $k_b$  is the Boltzmann constant ( $k_b=1.38 \times 10^{-23} \text{ m}^2 \cdot \text{kg} \cdot \text{s}^{-2} \cdot \text{K}^{-1}$ ),  $d_{pore}$  (m) is the pore diameter and  $p$  (Pa) is the total gas pressure.

$$Kn = \frac{\lambda}{d_{pore}} \quad (\text{Eq. 5-22})$$

where  $Kn$  is the Knudsen number.

Knudsen diffusivity,  $D_K$ , can be expressed as Eq. 5-23 [172]:

$$D_K = 97 \cdot r_{pore} \cdot \left(\frac{T}{M}\right)^{0.5} \quad (\text{Eq. 5-23})$$

where  $D_K$  ( $\text{m}^2 \cdot \text{s}^{-1}$ ) is the Knudsen diffusivity and  $M$  ( $\text{g} \cdot \text{mol}^{-1}$ ) is the molar mass of gas molecule.

### c. Molecular diffusivity

Molecular diffusion describes the diffusion in which the collisions between gas molecule–gas molecule are frequent when the diffusing gas contains two or more different molecular species [172, 174, 175]. It occurs predominantly when mean free path of gas molecule,  $\lambda$ , is shorter than pore diameter,  $d_{pore}$  ( $Kn < 1$ ). Whether this mechanism is significant depends on  $Kn$  value which determines the relative frequency of intermolecular collisions and molecule–wall collisions [172]. Molecular diffusivity,  $D_m$ , has no effect for the mass transfer of a single gas component [1] while for the case of binary gas mixture of species A and B, the molecular diffusivity (or  $D_{A,B}$ ) can be expressed as Eq. 5-24 [228]:

$$D_m = \frac{0.0018583 \cdot T^{1.5}}{p \cdot \sigma_{AB}^2 \cdot \Omega_D} \left(\frac{1}{M_A} + \frac{1}{M_B}\right)^{0.5} \quad (\text{Eq. 5-24})$$

where  $\sigma_{AB}$  ( $\text{\AA}$ ) is the arithmetic average diameter of Lennard-Jones collision between molecules A and B ( $\sigma_{AB} = 0.5\sigma_A + 0.5\sigma_B$ ),  $\Omega_D$  is the dimensionless Lennard-Jones parameter ( $\Omega_D = k_b T / \varepsilon_{AB}$ ) and  $\varepsilon_{AB}$  (K) is the maximum energy of attraction between molecules A and

B ( $\varepsilon_{AB} = \sqrt{\varepsilon_A \varepsilon_B}$ ) noting that  $\sigma_{CO_2} = 3.996 \text{ \AA}$ ,  $\sigma_{CH_4} = 3.780 \text{ \AA}$ ,  $\varepsilon_{CO_2}/k_b = 190 \text{ K}$  and  $\varepsilon_{CH_4}/k_b = 154 \text{ K}$  [228].

#### d. Internal surface diffusivity

Surface diffusion corresponds to the motion of adsorbed phase jumping from one adsorption site to another vacant site. The mechanism is proportionally correlated to adsorption coverage by Darken corrective factor as well as to system temperature by Arrhenius law as presented in Eq. 5-25, derived based on Eq. 5-9 and Eq. 5-16.

$$D_s = D_{s,0,T_0} \cdot \left( \frac{\partial \ln p}{\partial \ln q} \right)_T \cdot \exp \left( - \frac{E_{a,s}}{R \cdot T_0} \left( 1 - \frac{T_0}{T} \right) \right) \quad (\text{Eq. 5-25})$$

where  $D_{s,0,T_0}$  ( $\text{m}^2 \cdot \text{s}^{-1}$ ) is the surface diffusivity at zero adsorption coverage for a reference temperature and  $E_{a,s}$  ( $\text{J} \cdot \text{mol}^{-1}$ ) is the activation energy related to surface diffusion.

#### e. Combined internal diffusivities

The combination of internal diffusional resistances is described in Figure 5-2 according to a resistor network model. Knudsen and molecular resistances are positioned in series while being parallel to surface resistance and Poiseuille resistance, respectively.

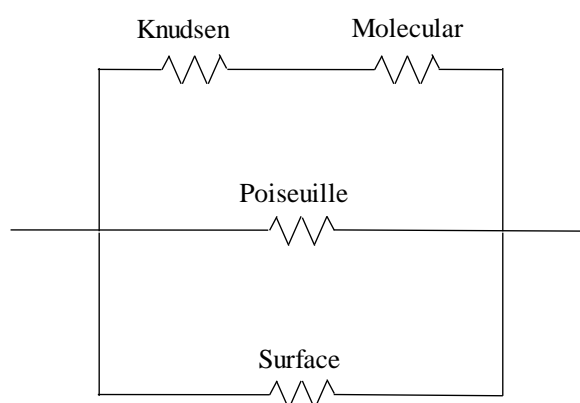


**Figure 5-2.** Combination of internal diffusional resistance according to a resistor network model [172].<sup>48</sup>

<sup>48</sup> Reprinted from Diffusion in Nanoporous Materials, J. Kärger *et al.*, Diffusion mechanisms, vol. 2, Copyright 2012, with permission from John Wiley and Sons.

Based on Figure 5-2, the internal diffusivities which are inversely proportional to the internal diffusion resistances ( $D = 1/R$ ) are correlated by the following equations [172]:

$$D_{macropores} = D_p \quad (\text{Eq. 5-26})$$

$$\frac{1}{D_{mesopores}} = \frac{1}{D_K} + \frac{1}{D_m} \quad (\text{Eq. 5-27})$$

$$D_{meso-micropores} = D_{mesopores} + K'_H \cdot \left( \frac{1 - \varepsilon_p}{\varepsilon_p} \right) \cdot D_s \quad (\text{Eq. 5-28})$$

where  $K'_H$  is the dimensionless Henry's constant based on solid volume defined as  $q_\infty/c$  in  $\text{mol} \cdot \text{m}^{-3} / \text{mol} \cdot \text{m}^{-3}$  and  $\varepsilon_p$  is the internal porosity of adsorbent particle. For the diffusive transport of a single-component system,  $D_m$  can be eliminated thus  $D_{mesopores} = D_K$  [172]. Therefore:

$$D_{meso-micropores} = D_K + K'_H \cdot \left( \frac{1 - \varepsilon_p}{\varepsilon_p} \right) \cdot D_s \quad (\text{Eq. 5-29})$$

By injecting Eq. 5-29 into Fick's first law (Eq. 5-1), a combined diffusive flux for internal mass transfers,  $J$  ( $\text{mol} \cdot \text{m}^{-2} \cdot \text{s}^{-1}$ ), can be expressed as Eq. 5-30. Knudsen diffusivity  $D_K$  is associated to the variation of adsorbate concentration in gas phase  $\partial c$  while surface diffusivity  $D_s$  is associated to the variation of average adsorbate concentration in adsorbed phase  $\partial q$  both of which vary with respect to  $\partial z$ .

$$J = -\varepsilon_p \cdot D_K \cdot \frac{\partial c}{\partial z} - (1 - \varepsilon_p) \cdot K'_H \cdot D_s \cdot \frac{\partial q}{\partial z} \quad (\text{Eq. 5-30})$$

### 5.3. Sorption kinetic based on the context of the study

The above-described diffusive fluxes are developed from the basis of Fick's first law of diffusion while sorption kinetic (or rate) involves temporal concentration variation in adsorbed phase,  $\partial q / \partial t$ , which implicates Fick's second law. The external mass transfer resistances of adsorbate may be attributed to external film and external surface of the adsorbent particle (or crystal) in addition to axial dispersion, if significant. A solid particle of MOFs consists of an assembly of nanoporous crystals, creating a secondary, interstitial porosity within the crystals. Therefore, the internal mass transfers of adsorbate in MOFs

can be understood in regard to: (i) intraparticle diffusion representing the ensemble of diffusion phenomena in an adsorbent particle, (ii) intercrystalline (or interstitial) diffusion which occurs within the crystals in the adsorbent particle, and, (iii) the intracrystalline diffusion which occurs in the crystals [172]. Pore textural characterization of MOFs materials may reveal different distributions of porosity but physically, it is undetermined which pore distribution belongs to which body in a MOFs particle; either interstitial or crystalline nanopores. In a study by Kärger's group, Chmelik *et al.* (2009) [227], ensemble measurement of molecular diffusion using interference microscopy and infrared micro-imaging was conducted on bulk crystals of Zn(tbip)<sup>49</sup> MOFs. A flux of molecules from bulk gas phase passes through the crystal surface due to the difference between counter-directed fluxes leaving and entering the crystal through the surface boundary [227] (no gas flow velocity involved). It is found that out of 20 million molecules colliding with the surface of MOFs crystals, only a single one is able to enter into intracrystalline phase, indicating the existence of external surface resistance which is a thin layer covering the whole crystal surface ("crystal skin") [227]. After the external surface permeation, the concentration reaches exactly the value resulting from the application of Fick's second law and the evolution of diffusion profile of the guest molecule is exclusively controlled by intracrystalline diffusion in the channel direction [227]. The results show that the mass transfers of adsorbate in MOFs materials are controlled initially by external crystal surface resistance and thereafter by intracrystalline nanopores resistance. Therefore, the following approaches are described for this study. By using manometric method, we investigate in the first place, the sorption rate when governed by overall external mass transfer coefficient,  $k_{ext}$  ( $s^{-1}$ ), (Eq. 5-34) that can lead to the determination of effective diffusivity,  $D_{eff}$ , (Eq. 5-35). In that case, the kinetic data will follow Linear Driving Force approximation. If the mass transfer is governed by intracrystalline diffusivity,  $D_c$ , then the kinetic data will follow Quadratic Driving Force approximation based on Fick's second law. By using Zero Length Column method, we investigate in the second place, the sorption rate when governed by intracrystalline diffusivity,  $D_c$ , whereby the external mass transfer resistances are eliminated. The kinetic data will follow Quadratic Driving Force approximation based on Fick's second law adapted for a chromatographic column. In order to remain in the context of the study, the term "intracrystalline diffusion" will be used afterwards instead of

---

<sup>49</sup> tbip: 5-tert-butyl isophthalate.

“intraparticle diffusion”, as well as the term “adsorbent crystal” instead of “adsorbent particle”.

## 5.4. Manometric method: Methodology

### 5.4.1. Experimental approaches

The sorption uptake rate (usually called mass uptake) measurement is carried out by using manometric equipment PCT-Pro from SETARAM which is the same equipment described in Section 4.3 used for equilibrium measurements. In this technique, the uptake of single gas component is recorded as a function of time for a constant pressure variation between the reservoir and the sample cell containing adsorbent material until it reaches the equilibrium concentration in the adsorbed phase. In order to enable the application of kinetic models, the experimental data are exploited to obtain a transient adsorption curve of Eq. 5-31 versus time, supposing that there is no adsorbed amount in the adsorbent before the measurement ( $q_0 = 0$ ).

$$\frac{q(t) - q_0}{q_\infty - q_0} = \frac{q(t)}{q_\infty} = \frac{n_{ads}(t)}{n_{ads,t \rightarrow \infty}} \quad (\text{Eq. 5-31})$$

where  $q$  ( $\text{mol} \cdot \text{mol}^{-3}$ ) is the average adsorbate concentration in adsorbed phase per unit volume of adsorbent,  $q_0$  ( $\text{mol} \cdot \text{mol}^{-3}$ ) is the initial value of  $q$  when  $t < 0$ ,  $q_\infty$  ( $\text{mol} \cdot \text{mol}^{-3}$ ) is the equilibrium value of  $q$  which corresponds to  $t \rightarrow \infty$ , and,  $n_{ads}$  (mol) is the amount of adsorbate adsorbed calculated from Eq. 4-23.

Recall of Eq. 4-23:

$$n_{ads,m} = \sum_{j=1}^m \left[ \frac{P_{1,j} \cdot V_1}{Z_{P_{1,j},T_1} \cdot R \cdot T_1} + \frac{P_{2,j} \cdot V_U}{Z_{P_{2,j},T_1} \cdot R \cdot T_1} + \frac{P_{2,j} \cdot V_D}{Z_{P_{2,j},T_2} \cdot R \cdot T_2} - \frac{P_{3,j} \cdot V_1}{Z_{P_{3,j},T_1} \cdot R \cdot T_1} - \frac{P_{3,j} \cdot V_U}{Z_{P_{3,j},T_1} \cdot R \cdot T_1} - \frac{P_{3,j} \cdot V_D}{Z_{P_{3,j},T_2} \cdot R \cdot T_2} \right]$$

### 5.4.2. Mathematical modelling of sorption kinetic

#### a. Material balance on a packed-bed column

The flow of a fluid containing adsorbate through a packed-bed column can generally be presented by axial dispersed plug flow model, which is a unidimensional model

following z-axis indicating axial position in the column (meaning that the mass transfer in radial position in the column is neglected). Supposing that: (i) the system is isothermal with negligible pressure drop and (ii) the adsorbate concentration is small, so that the gas flow velocity can be considered constant through the column (independent of axial position), then the model can be expressed as Eq. 5-32 [172]. The first, second, third and fourth terms represent axial dispersion, convection, accumulation in gas phase and accumulation in adsorbed phase, respectively.

$$\begin{array}{cccc}
 \text{Axial} & & \text{Accumulation} & \text{Accumulation in} \\
 \text{dispersion} & \text{Convection} & \text{in gas phase} & \text{adsorbed phase} \\
 \underbrace{\hspace{1.5cm}} & \underbrace{\hspace{1.5cm}} & \underbrace{\hspace{1.5cm}} & \underbrace{\hspace{1.5cm}} \\
 -D_L \cdot \frac{\partial^2 c}{\partial z^2} + u \cdot \frac{\partial c}{\partial z} + \frac{\partial c}{\partial t} + \left( \frac{1-\varepsilon}{\varepsilon} \right) \cdot \frac{\partial q}{\partial t} = 0 & & & \text{(Eq. 5-32)}
 \end{array}$$

where  $D_L$  ( $\text{m}^2 \cdot \text{s}^{-1}$ ) is the axial dispersion coefficient and  $\varepsilon$  is the external void fraction corresponding to the volume of column non-occupied by the adsorbent crystals.

### ***b. Material balance in intracrystalline phase of adsorbent***

The term  $\partial q / \partial t$  in Eq. 5-32 represents sorption rate, demonstrated by the material balance expressed for the adsorbate in intracrystalline phase of adsorbent.

#### ***Linear Driving Force model***

If the mass transfer is controlled by external mass transfer barriers, supposing that (i) the adsorbent crystals are spherical of radius  $r_c$  and homogenous<sup>50</sup>, (ii) the adsorbate concentration at the surface of adsorbent crystal is the one that is in equilibrium with bulk gas phase with (iii) linear adsorption equilibrium, (iv) the adsorbate concentration in the material is averaged and uniform at each instant, and, (v) the diffusion system is isothermal, then the sorption rate governed by overall external mass transfer coefficient can be expressed as Eq. 5-35 [172]. This kinetic model was developed by Glueckauf and Coates (1947) [229] based on Linear Driving Force (LDF) approximation. The accumulation in adsorbent crystal is assumed proportionally linear to the difference between concentration in the material,  $q$ , and concentration in the material that would be in equilibrium with bulk

<sup>50</sup>All crystals have the same physical and chemical properties so that there is no preferential axis of gas diffusion.

fluid phase,  $q_\infty$ . This model is also called as surface-barrier model which is assimilated to a diffusion system of a single crystal having a single surface resistance [230].

$$\frac{\partial q}{\partial t} = a_c \cdot k \cdot (q_\infty - q) \quad (\text{Eq. 5-33})$$

where  $k$  ( $\text{m}\cdot\text{s}^{-1}$ ) is the overall external mass transfer coefficient and  $a_c$  ( $\text{m}^{-1}$ ) is the specific surface of an adsorbent crystal ( $a_c = 3/r_c$  supposing a spherical form [230]).

For each step change in concentration, the following initial and boundary conditions are defined for the model:

$$t < 0: \quad c = q = 0$$

$$t \geq 0: \quad c = c_\infty = q_\infty \cdot K'_H$$

$$t \rightarrow \infty: \quad c = c_\infty = q_\infty \cdot K'_H$$

Let  $k_{ext}$  ( $\text{s}^{-1}$ ) be the product of  $a_c$  ( $\text{m}^{-1}$ ) and  $k$  ( $\text{m}\cdot\text{s}^{-1}$ ). Then, the integral of Eq. 5-33 becomes:

$$\frac{q(t)}{q_\infty} = 1 - \exp(-k_{ext} \cdot t) \quad (\text{Eq. 5-34})$$

The correlation between  $k_{ext}$  and effective diffusivity,  $D_{eff}$ , is given by the following diffusion time constant relation for a spherical crystal [172, 230]:

$$k_{ext} = 15 \cdot \frac{D_{eff}}{r_c^2} \quad (\text{Eq. 5-35})$$

where  $D_{eff}/r_c^2$  ( $\text{s}^{-1}$ ) is known as the effective diffusivity time constant.

By injecting Eq. 5-35 into Eq. 5-34, the model can be expressed as follows:

$$\frac{q(t)}{q_\infty} = 1 - \exp\left(-15 \cdot \frac{D_{eff}}{r_c^2} \cdot t\right) \quad (\text{Eq. 5-36})$$

Supposing that the adsorption isotherm is non-linear so that the diffusivity will follow the adsorption coverage (assumption (iii) is not true), then Darken correction can be integrated into the equation. The diffusivity and the kinetic model can therefore be

expressed as Eq. 5-37 and Eq. 5-38, respectively, derived based on Eq. 5-9. In this study, Eq. 5-38 is designated as LDF-Darken model.

$$D_{eff} = D_{eff,0,T_0} \cdot \left( \frac{\partial \ln p}{\partial \ln q} \right)_T \quad (\text{Eq. 5-37})$$

$$\frac{q(t)}{q_\infty} = 1 - \exp \left( -15 \cdot \frac{D_{eff,0,T_0}}{r_c^2} \cdot \left( \frac{\partial \ln p}{\partial \ln q} \right)_T \cdot t \right) \quad (\text{Eq. 5-38})$$

where  $D_{eff,0,T_0}$  ( $\text{m}^2 \cdot \text{s}^{-1}$ ) is the effective diffusivity at zero adsorption coverage for a reference temperature.

If the adsorption equilibrium between the adsorbate concentration at the surface of adsorbent crystal and in bulk gas phase follows Langmuir isotherm, then the Darken corrective factor can be expressed as Eq. 5-39, derived based on Eq. 5-10, Eq. 5-11 and Eq. 5-14, supposing that (vi) the isosteric heat of adsorption is constant at any stage of adsorption coverage:

$$\begin{aligned} \left( \frac{\partial \ln p}{\partial \ln q} \right)_T &= \frac{1}{1 - \frac{q}{q_\infty}} = \frac{1}{1 - \frac{b(T) \cdot p}{1 + b(T) \cdot p}} \\ &= \frac{1}{1 - \frac{b_0 \cdot \exp \left( -\frac{Q_{st}}{R \cdot T_0} \left( 1 - \frac{T_0}{T} \right) \right) \cdot p}{1 + b_0 \cdot \exp \left( -\frac{Q_{st}}{R \cdot T_0} \left( 1 - \frac{T_0}{T} \right) \right) \cdot p}} \end{aligned} \quad (\text{Eq. 5-39})$$

Furthermore, for a non-isothermal system, Arrhenius relationship can also be integrated into Eq. 5-39 to take into account the evolution of temperature. The diffusivity and the kinetic model can therefore be expressed as Eq. 5-41 and Eq. 5-42, respectively, derived based on Eq. 5-16. In this study, Eq. 5-42 is designated as LDF-Darken-Arrhenius model.

$$D_{eff} = D_{eff,0,T_0} \cdot \left( \frac{\partial \ln p}{\partial \ln q} \right)_T \cdot \exp \left( -\frac{E_a}{R \cdot T_0} \left( 1 - \frac{T_0}{T} \right) \right) \quad (\text{Eq. 5-40})$$

$$\frac{q(t)}{q_\infty} = 1 - \exp \left( -15 \cdot \frac{D_{eff,0,T_0}}{r_c^2} \cdot \left( \frac{\partial \ln p}{\partial \ln q} \right)_T \cdot \exp \left( -\frac{E_a}{R \cdot T_0} \left( 1 - \frac{T_0}{T} \right) \right) \cdot t \right) \quad (\text{Eq. 5-41})$$

The above-developed kinetic model will be fitted to experimental data of  $q(t)/q_\infty$  by performing an iterative resolution method to optimize the values of  $D_{eff,0,T_0}/r_c^2$  and  $E_a$  with the aim of having a maximum value of coefficient of determination ( $R^2 \rightarrow 1$ , Eq.A-10), indicative of the quality of the prediction of the model relatively to the experimental data.

### ***Diffusion model based on Fick's second law***

If the mass transfer is controlled by internal mass transfer barriers (micropore diffusion-limited uptake), supposing that (i) the adsorbent crystals are spherical of radius  $r_c$  and homogenous, (ii) the adsorbate concentration at the surface of adsorbent crystal is the one that is in equilibrium with bulk gas phase with (iii) linear adsorption equilibrium, (iv) the adsorbate concentration in the material is averaged and uniform at each instant, and, (v) the diffusion system is isothermal, then the sorption rate can be expressed as the material balance in the crystal for a thickness  $\partial r$  by using the following mass conservation equation based on Fick's second law [172, 231-233]:

$$\frac{\partial q}{\partial t} = D_c \cdot \left( \frac{\partial^2 q}{\partial r^2} + \frac{2}{r} \cdot \frac{\partial q}{\partial r} \right) \quad (\text{Eq. 5-42})$$

where  $D_c$  ( $\text{m}^2 \cdot \text{s}^{-1}$ ) is the intracrystalline diffusivity.

For each step change in concentration, the following initial and boundary conditions are defined for the model, supposing that (vi) the uptake of adsorbate is relatively small to the total amount introduced into the system and (vii) the accumulation of adsorbate at the center of adsorbent crystal is hypothetically zero:

$$t < 0: \quad c = c_0, \quad q(r, t) = q_0$$

$$t \geq 0: \quad c = c_\infty, \quad q(r_c, t) \rightarrow q_\infty$$

$$t \rightarrow \infty: \quad c = c_\infty, \quad q(r, t) \rightarrow q_\infty$$

$$\text{For all } t: \quad \left. \frac{\partial \bar{q}}{\partial t} \right|_{r=0} = 0$$

Based on these assumptions, an analytical solution of Eq. 5-43 can be proposed to solve Eq. 5-42 [172, 230]. This model was developed by Vermeulen (1953) [234] based on Quadratic Driving Force (QDF) approximation.

$$\frac{\partial q}{\partial t} = \pi^2 \cdot \frac{D_c}{r_c^2} \cdot \frac{(q_\infty^2 - q^2)}{2 \cdot q} \quad (\text{Eq. 5-43})$$

where  $D_c/r_c^2$  ( $\text{s}^{-1}$ ) is known as the intracrystalline diffusion time constant.

This model is also called diffusion-barrier model, assimilated to a diffusion system of a batch of crystals having a range of surface resistances [230]. Therefore, the integral of Eq. 5-43 with respect to variable  $t$  can be expressed in Eq. 5-44, in form of the sum of mass transfer of a number of crystals,  $n$ , where  $n = 1, 2, 3, \text{etc.}$ , by supposing that there is no adsorbed amount in the adsorbent before the measurement ( $q_0 = 0$ ).

$$\frac{q - q_0}{q_\infty - q_0} = \frac{q}{q_\infty} = 1 - \frac{6}{\pi^2} \sum_{n=1}^{\infty} \frac{1}{n^2} \cdot \exp\left(-n^2 \cdot \pi^2 \cdot \frac{D_c}{r_c^2} \cdot t\right) \quad (\text{Eq. 5-44})$$

This kinetic model can be corrected as well if some assumptions are not true as demonstrated for LDF. This model will be fitted to experimental data of  $q(t)/q_\infty$  by performing an iterative resolution method to optimize the values of  $D_c/r_c^2$  and  $n$  with the aim of having a maximum value of coefficient of determination ( $R^2 \rightarrow 1$ , Eq. A-10), indicative of the quality of the prediction of the model relatively to the experimental data.

#### 5.4.3. Procedure of measurements

The sorption kinetic for  $\text{CO}_2$  and  $\text{CH}_4$  on the synthesized samples were measured using manometric equipment PCT-Pro from SETARAM. Ultrahigh purity  $\text{CO}_2$  and  $\text{CH}_4$  gases (>99.98 vol%) supplied by Air Liquide were used for the study. The adsorption uptakes were recorded as a function of time by fixing a constant pressure drop,  $\Delta P$ , for a given temperature, until it reach equilibrium. A constant pressure drop was carried out for 0.2 bar, 0.5 bar and 1.5 bar at three different temperatures; 25 °C, 50 °C and 75°C. The sample temperature was controlled by heating jacket with a thermocouple and isolation coating. About 1.5 g of sample was placed in the 40  $\text{cm}^3$  sample holder, and cylindrical stainless steel spacers were used to fill in the remaining volume. Gas supply pipelines and adsorption system were evacuated and purged using gas probe. Prior to each measurement

(one pressure drop = one measurement), the sample was *in situ* outgassed under vacuum at 150 °C with gradual temperature increment and left overnight until residual pressure stabilization was achieved. The reservoir and sample cell were kept pumped under vacuum. The sample temperature was set to reservoir temperature  $T_1$  and left for stabilization followed by dead volume calibration by helium expansion at reservoir temperature, noted  $V_{2,T_1}$ . The sample temperature was then set to operational temperature  $T_2$  and left for stabilization before calibrating the second dead volume by helium expansion at adsorption temperature, noted  $V_{2,T_2}$ . Then, the kinetic measurement was run.

## 5.5. Zero Length Column method: Methodology

### 5.5.1. Experimental approaches

The intracrystalline sorption rate is measured using Zero Length Column (ZLC) technique which was initially developed by Eic and Ruthven (1988) [231]. ZLC equipment consists of a chromatographic column having the inlet and the outlet for the gas flow, containing a small amount of adsorbent (several tens of mg) which is assimilated to an elementary volume of small thickness. The adsorbent material in the column is firstly equilibrated with the diluted adsorbate flow before being purged under certain flow rate of purge gas. The desorption curve is then recorded as a function of time until no more adsorbate concentration is observed. The measurement must be performed under certain gas concentration range where the equilibrium of gas–adsorbent surface can be described by Henry’s law, supposedly for a diluted system. The advantages of having : (i) an elementary volume or “zero-length column” of adsorbent is to eliminate axial dispersion and avoid heat transfer during sorption, (ii) high gas flow velocity is to eliminate external mass transfer resistance related to gradient of concentration (film barrier), so that the mass transfer will be assuredly governed by intracrystalline diffusivity, and, (iii) linear adsorption equilibrium to prevent the dependence of diffusivity on adsorbate concentration in the solid phase [172, 231-233]. In order to enable the application of kinetic models, the experimental data are exploited to obtain a transient desorption curve of  $c(t)/c_0$  versus time where  $c$  is the adsorbate concentration in gas phase and  $c_0$  is the initial adsorbate concentration in gas phase. These concentrations are detected at the outlet of the column using a gas analyzer.

### 5.5.2. Mathematical modelling of sorption kinetic

#### a. Material balance on a chromatographic column

Based on the assumptions mentioned above in addition to that (iv) the adsorbate concentration in the material is averaged and uniform at each instant (assumption of perfectly mixed reactor), the material balance expressed for the adsorbate between the inlet and the outlet of the column during desorption is written as Eq. 5-45 [172, 231-233]. The first, second and third terms represent convection, accumulation in gas phase and accumulation in adsorbed phase, respectively.

$$\begin{array}{c}
 \text{Convection} \quad \text{Accumulation in gas phase} \quad \text{Accumulation in adsorbed phase} \\
 \text{in gas phase} \quad \text{in gas phase} \quad \text{adsorbed phase} \\
 \text{---} \quad \text{---} \quad \text{---} \\
 F \cdot c + V_g \cdot \frac{dc}{dt} + V_s \cdot \frac{dq}{dt} = 0 \quad (\text{Eq. 5-45})
 \end{array}$$

where  $F$  ( $\text{m}^3 \cdot \text{s}^{-1}$ ) is the total volume flow rate of purge gas,  $V_g$  ( $\text{m}^3$ ) is the gas volume in the column and  $V_s$  ( $\text{m}^3$ ) is the adsorbent crystals volume in the column.

#### b. Material balance in intracrystalline phase of adsorbent

The term  $\partial q / \partial t$  in Eq. 5-45 represents sorption rate, demonstrated by the material balance expressed for the adsorbate in intracrystalline phase of adsorbent.

#### *Diffusion model based on Fick's second law adapted for ZLC*

Knowing that the mass transfer in ZLC is controlled by internal mass transfer barriers and supposing that (v) the adsorbent crystals are spherical of radius  $r_c$  and homogenous, (vi) the adsorbate concentration at the surface of adsorbent crystal is the one that is in equilibrium with bulk gas phase, and, (vii) the diffusion system is isothermal, then the material balance in the crystal for a thickness  $\partial r$  can be written by the same mass conservation equation based on Fick's second law, recall of Eq. 5-42:

$$\frac{\partial q}{\partial t} = D_c \cdot \left( \frac{\partial^2 q}{\partial r^2} + \frac{2}{r} \cdot \frac{\partial q}{\partial r} \right)$$

For each step change in concentration, the following initial and boundary conditions are defined for the model [172, 231-233], supposing that (viii) the accumulation of adsorbate at the center of adsorbent crystal is hypothetically zero:

$$t < 0: \quad c = c_0, \quad q(r, t) = q_0 = K'_H \cdot c_0$$

$$t \geq 0: \quad c = c(t), \quad q(r_c, t) = K'_H \cdot c(t)$$

$$t \rightarrow \infty: \quad c = 0, \quad q(r, t) \rightarrow 0$$

$$\text{For all } t: \quad \left. \frac{\partial q}{\partial t} \right|_{r=0} = 0$$

Based on the material balance on the chromatographic column in Eq.5-45, the boundary condition at the surface of adsorbent crystal is presented as follows:

$$D_c \cdot \frac{\partial q}{\partial r}(r_c, t) + \frac{1}{3} \cdot \frac{F \cdot r_c}{V_s \cdot K} \cdot q(r_c, t) = 0$$

Based on these assumptions in addition to that (ix) the hold-up in bulk gas phase,  $V_g$ , is negligible in comparison to adsorbed phase hold-up,  $V_s$ , therefore an analytical solution adapted for ZLC can be proposed as Eq. 5-46. This kinetic model was developed by Eic and Ruthven (1988) [231] to solve Eq. 5-42:

$$\frac{c(t)}{c_0} = \sum_{n=1}^{\infty} \frac{2 \cdot L}{\beta_n^2 + L \cdot (L - 1)} \cdot \exp\left(-\beta_n^2 \cdot \frac{D_c}{r_c^2} \cdot t\right) \quad (\text{Eq. 5-46})$$

where  $n$  is an integer number and  $\beta_n$  is given by the roots of solution of Eq.5-47 where  $\beta_1 \leq \pi$ ,  $\beta_2 \leq 2\pi$ ,  $\beta_3 \leq 3\pi$ , etc and  $L$  is the dimensionless parameter of Eq. 5-48 defined as the ratio of purge gas flow rate to crystal volume.

$$\beta_n \cdot \cot \beta_n + L - 1 = 0 \quad (\text{Eq. 5-47})$$

$$L = \frac{1}{3} \frac{F}{K'_H \cdot V_s} \cdot \frac{r_c^2}{D_c} \quad (\text{Eq. 5-48})$$

The value of  $K'_H \cdot V_s$  can be determined from adsorption equilibrium isotherm of the adsorbate by the following relationship:

$$K'_H \cdot V_s = K_H \cdot \rho_s \cdot \frac{m_s}{\rho_s} = K_H \cdot m_s \quad (\text{Eq. 5-49})$$

where  $K'_H$  is the dimensionless Henry's constant based on solid volume defined as  $q_\infty/c$  in  $\text{mol}\cdot\text{m}^{-3}/\text{mol}\cdot\text{m}^{-3}$ ,  $K_H$  is the Henry's constant based on solid mass defined as  $q_\infty/c$  in  $\text{mol}\cdot\text{kg}^{-1}/\text{mol}\cdot\text{m}^{-3}$ ,  $\rho_s$  ( $\text{kg}\cdot\text{m}^{-3}$ ) is the adsorbent apparent density and  $m_s$  (kg) is the adsorbent mass.

This kinetic model will be fitted to experimental data of  $c(t)/c_0$  by performing an iterative resolution method to optimize the values of  $D_c/r_c^2$ ,  $n$ ,  $\beta_n$  and  $L$  with the aim of having a maximum value of coefficient of determination ( $R^2 \rightarrow 1$ , Eq. A-10), indicative of the quality of the prediction of the model relatively to the experimental data.

### 5.5.3. Procedure of measurements

The desorption curves of  $\text{CO}_2$  and  $\text{CH}_4$  were recorded as a function of time by fixing (i) a diluted concentration of gas probe in helium flux and (ii) total volume flow rate of feed gas, for a given temperature. The measurements were carried out at three different temperatures; 25 °C, 50 °C and 75 °C. The ZLC column was placed in an oven (PerkinElmer Instruments - Autosystem XL) allowing the regulation of temperature from ambient to 350 °C. The gas at the column outlet was sampled via a capillary connected to a mass spectrometer (Pfeiffer Vacuum Omnistar) which measured the concentration in bulk gas phase. About 10 mg of adsorbent material was placed in the column between two small amounts of quartz wool to hold the adsorbent sample. The 316L stainless steel column had an internal diameter of 3 mm. The thickness of the sample of adsorbent material was sufficiently thin to assume that the sample is a perfectly stirred reactor. The procedure of measurement is described as follows according to Figure 5-3.

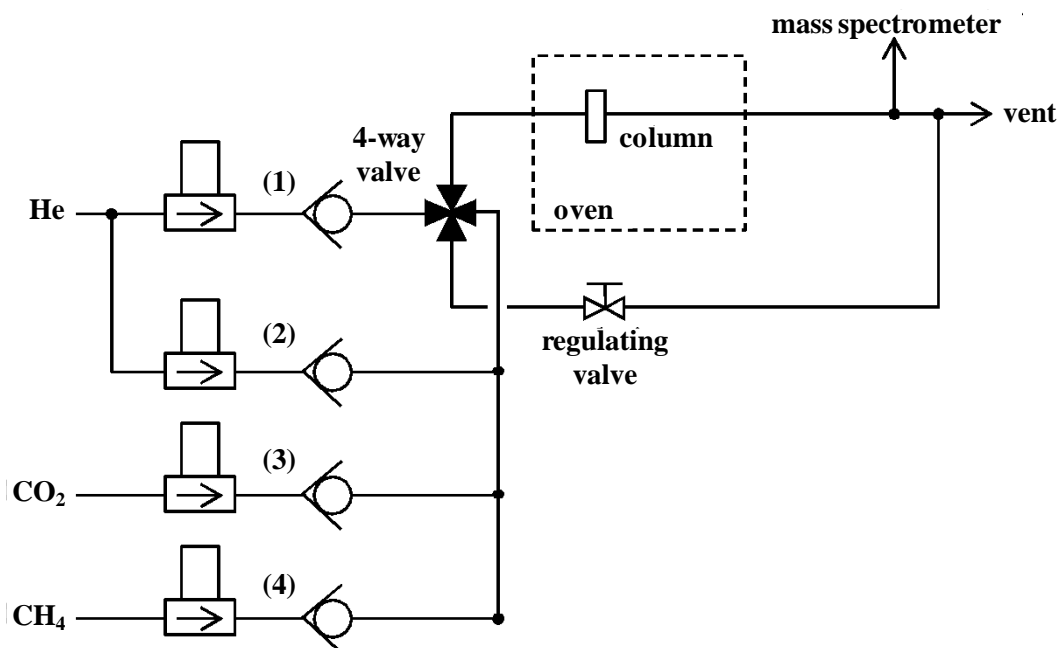


**Figure 5-3.** Configuration of ZLC equipment.

**a. Blank measurement**

1. The column containing quartz wool without sample was placed in the oven and connected to gas pipes.
2. The oven temperature was regulated at operational temperature (25°C, 50°C or 75°C).
3. The flow meters (1) and (2) were opened to sweep the column with helium gas at a maximum flow rate.
4. Adjustment of the opening of micrometric regulating valve: a differential pressure gauge of resolution 1 Pa and full scale [0-700] Pa was placed at the inlet of the 4-way valve which was the outlet of the mixture of the currents (2, 3, 4). The opening of the micrometric regulating valve placed on the bypass flow to the vent was adjusted so that the pressure drop measured by the differential pressure gauge remained the same when helium current (1) fed or did not feed the column. This procedure ensured that the swing of the 4-way valve necessary for the transition between adsorption and desorption stages would not generate any pressure disturbance and fluctuation in total flow rate of the gas.
5. At a fixed diluted concentration of gas probe, the flow rate of gas probe (3) was adjusted as well as the flow rate of helium (2) to ensure the dilution. The total flow rate of feed gas should be equal to the flow rate of purge gas (1).

6. The 4-way valve was initially opened so that the controlled flow of gas stream containing gas probe could pass through the column via currents (2) and (3).
7. The 4-way valve was switched to stop the feed and let the flow of purge gas of pure helium sweep the column via current (1).
8. The concentration of gas probe was measured by mass spectrometer until the gas was no longer detected by the gas analyzer.
9. The procedure 5–8 were repeated for all flow rates chosen for the measurements.

#### ***b. Desorption curves measurement***

10. The adsorbent sample was placed in the column between two quartz wool.
11. A helium flow rate of  $5 \text{ ml}\cdot\text{min}^{-1}$  was fed through the column. The oven was set to operate outgassing temperature.
12. After outgassing, the temperature of the oven was switched to operational temperature.
13. The adsorption of gas probe was carried out by operational procedure 5–6. Since the concentration variations induced by the adsorption were too small, the equilibration time was set at only 15 min.
14. The desorption was then effectuated by operational procedure 7–8.
15. The procedure 5–8 were repeated for all flow rates chosen for the measurements.
16. The experimental data provided by the mass spectrometer gas analyzer was standardized and exploited to provide the concentration change as a function of time  $c(t)/c_0$ .

## **5.6. Manometric method: Results and discussions**

### **5.6.1. Regeneration of adsorbent after CO<sub>2</sub> adsorption**

The regeneration of the synthesized adsorbents after CO<sub>2</sub> adsorption has been studied by performing adsorption uptake measurement at a constant pressure of 0.2 bar and 25 °C for different outgassing conditions as shown in Figure 5-4 (e.g. Mg-MOF-74@CNT). Prior to the outgassing, the adsorption equilibrium of CO<sub>2</sub> on the material was initially achieved at the same pressure. The results show that the diffusion rate becomes more rapid (green and blue curves) if the material has not been outgassed properly because the accessibility of gas adsorbate is limited to the firstly desorbed nanopores which are normally with larger

confinement. As the duration of outgassing increases, there can be more desorption and the adsorption kinetic slows down due to higher accessibility into the micropores. In order to obtain a complete regeneration, the material must be outgassed for at least 20 hours with heating to 150 °C or for a longer period without heating (60 hours). The latter indicates that the regeneration does not necessarily require heat which confirms the absence of chemisorption, in line with the calculated isosteric heat of adsorption of CO<sub>2</sub> ( $\approx 57$  kJ/mol) which demonstrates strong physisorption and remains below chemical energy.

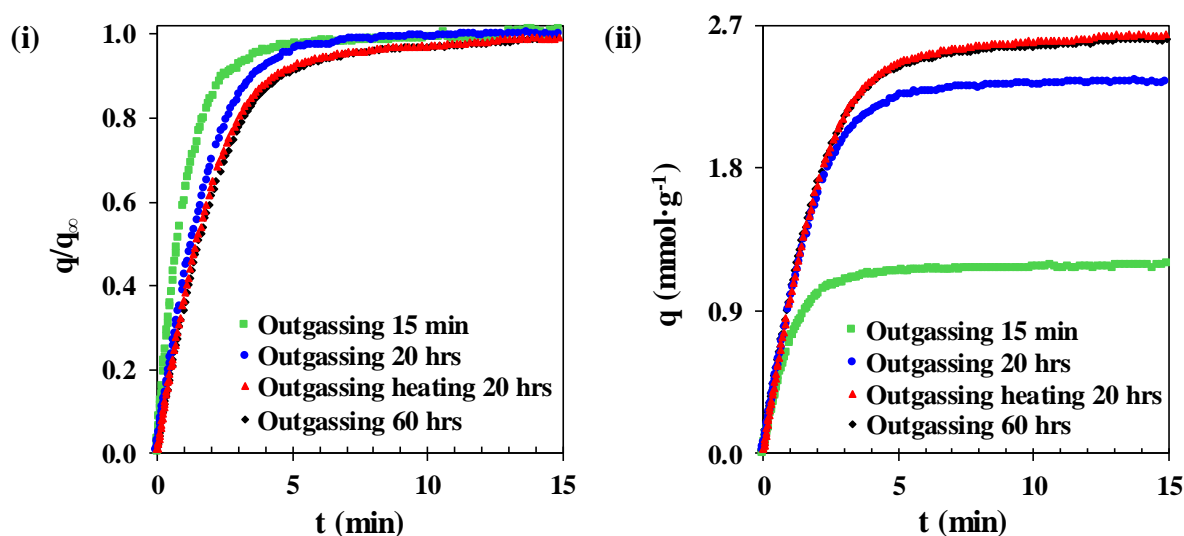


**Figure 5-4.** (i) Fractional adsorption uptakes and (ii) adsorption uptakes of CO<sub>2</sub> on Mg-MOF-74@CNT at 0.2 bar and 25 °C for different outgassing conditions.

### 5.6.2. CO<sub>2</sub> and CH<sub>4</sub> adsorption kinetics at different temperatures

The adsorption kinetics of single component CO<sub>2</sub> and CH<sub>4</sub> were measured on Mg-MOF-74, Mg-MOF-74@CNT and Mg-MOF-74@GO using PCT-Pro manometric equipment at a constant pressure of 0.2 bar, 0.5 bar and 1.5 bar for three different temperatures: 25 °C, 50 °C and 75 °C. The temperature profile following the adsorption processes was also observed. In order to have the parameters of isotherm for kinetic modelling, the adsorption equilibrium was fitted to Langmuir model. The kinetic data of CO<sub>2</sub> adsorption are presented in Figure 5-5 for Mg-MOF-74, Figure 5-6 for Mg-MOF-74@CNT and Figure 5-7 for Mg-MOF-74@GO. In Figure 5-5, for all temperatures, the rate of CO<sub>2</sub> adsorption on Mg-MOF-74 are not really affected by varying the pressure from 0.2 bar to 0.5 bar and appears to be not exploitable at 1.5 bar. Due to the relatively fast kinetic, it actually requires a lower pressure range to clearly see the change in the kinetic of CO<sub>2</sub> diffusion over this material when it is influenced by the adsorption coverage and

the rise in temperature. In Figure 5-6 and Figure 5-7, for all temperatures, the rate of CO<sub>2</sub> adsorption on Mg-MOF-74@CNT and Mg-MOF-74@GO increases as the pressure increases accompanied by the increasing temperature profile as a function of pressure. The rise in temperature following CO<sub>2</sub> adsorption on both composites is more pronounced in comparison to that in the pristine Mg-MOF-74 indicating stronger adsorption processes. Also, for all temperatures, the sorption rate of CO<sub>2</sub> on both composites is evidently slower than that on the pristine Mg-MOF-74 demonstrating slower diffusion kinetic due to higher microporous volume in the composites. In Annex V, the kinetic data of CH<sub>4</sub> adsorption are presented in Figure A-10 for Mg-MOF-74@CNT and Figure A-11 for Mg-MOF-74@GO. Due to very fast kinetic, the experimental data for CH<sub>4</sub> on Mg-MOF-74 were not able to be measured in this pressure range while the sensibility of the pressure transducer of the equipment was limited to a minimum of 0.2 bar. The results show that, for all temperatures, the rate of CH<sub>4</sub> adsorption on Mg-MOF-74@CNT and Mg-MOF-74@GO as well as the temperature profile are not influenced by the pressure. It is due to a very small amount of adsorbed CH<sub>4</sub> on these materials as shown by their equilibrium isotherm so that the diffusion does not depend on the adsorption coverage or on the temperature.

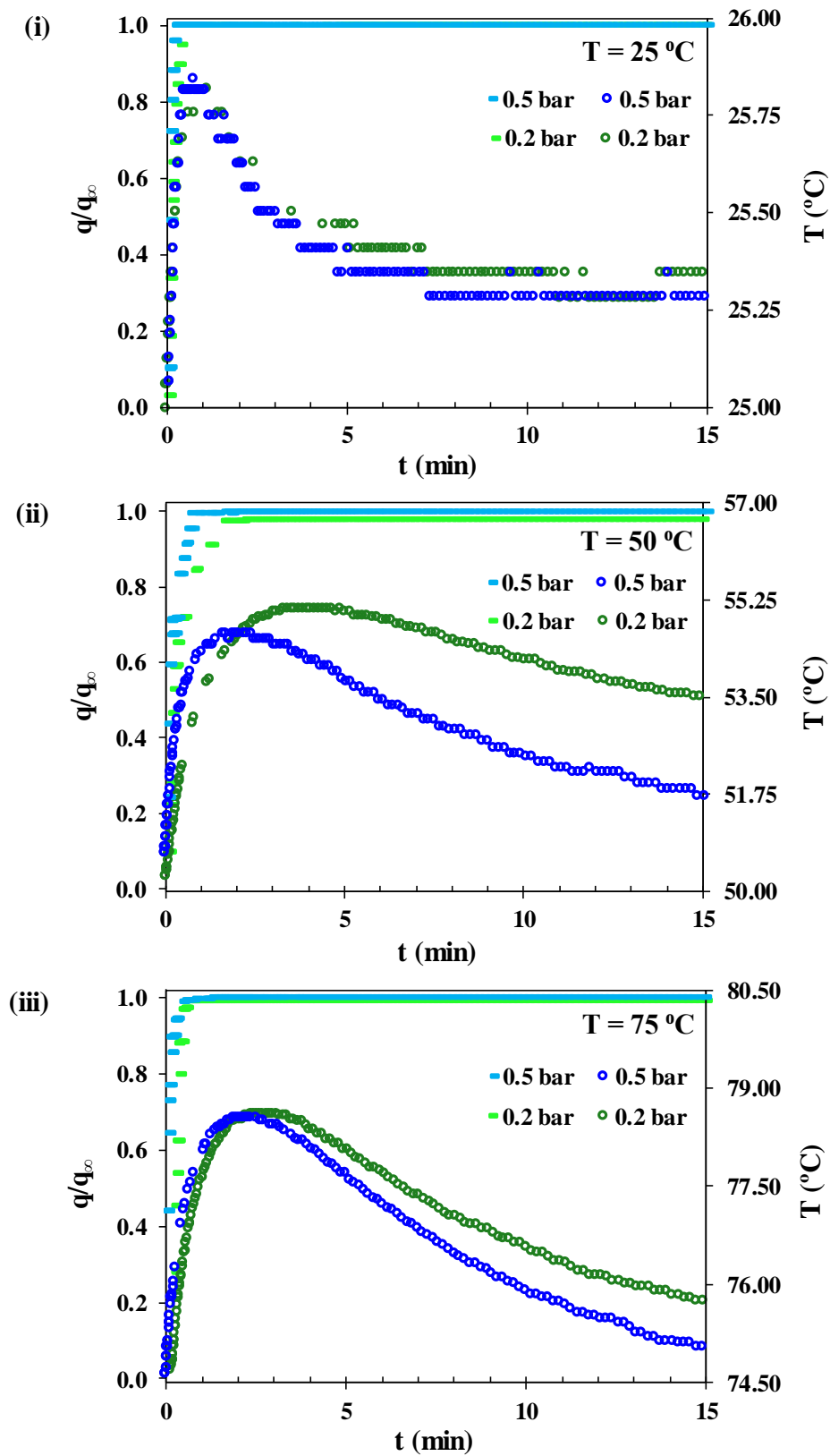


**Figure 5-5.** Fractional adsorption uptakes of  $\text{CO}_2$  on Mg-MOF-74 with their profile temperature at 0.2 bar, 0.5 bar and 1.5 bar for different temperatures: (i)  $25^{\circ}\text{C}$ , (ii)  $50^{\circ}\text{C}$  and (iii)  $75^{\circ}\text{C}$ .

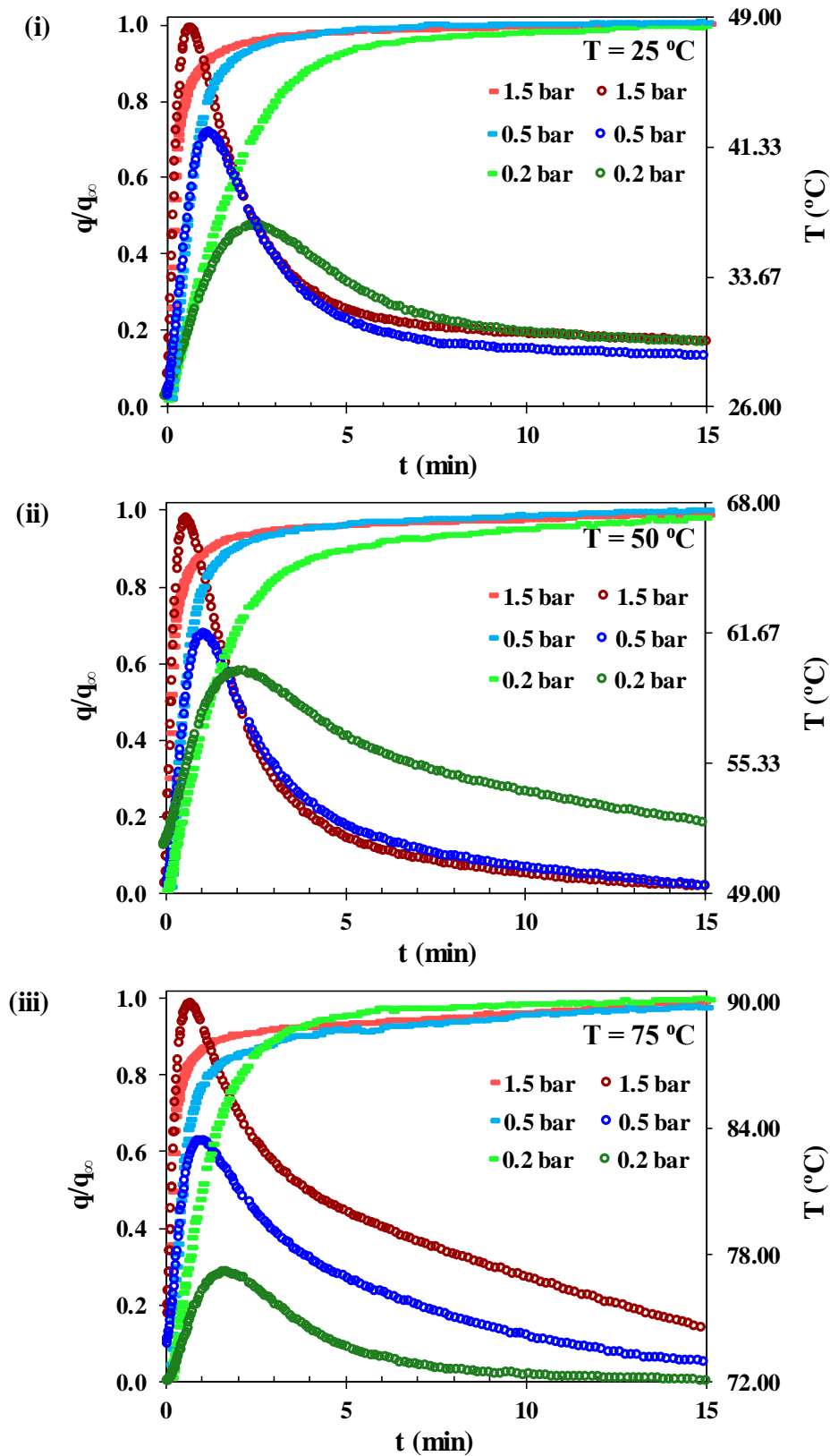


**Figure 5-6.** Fractional adsorption uptakes of  $\text{CO}_2$  on Mg-MOF-74@CNT with their profile temperature at 0.2 bar, 0.5 bar and 1.5 bar for different temperatures: (i)  $25\text{ }^{\circ}\text{C}$ , (ii)  $50\text{ }^{\circ}\text{C}$  and (iii)  $75\text{ }^{\circ}\text{C}$ .

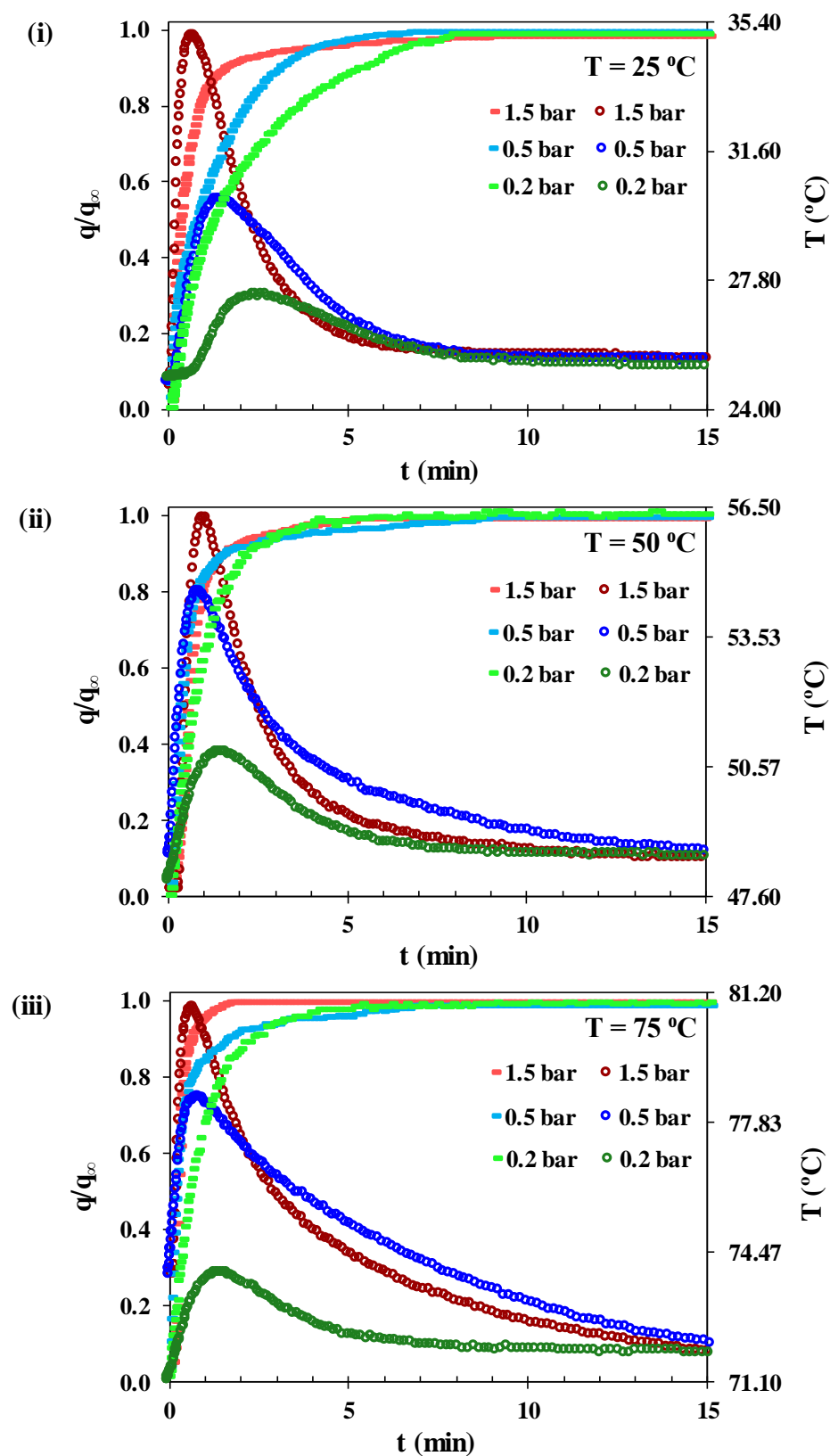


**Figure 5-7.** Fractional adsorption uptakes of CO<sub>2</sub> on Mg-MOF-74@GO with their profile temperature at 0.2 bar, 0.5 bar and 1.5 bar for different temperatures: (i) 25 °C, (ii) 50 °C and (iii) 75 °C.

### 5.6.3. Determination of diffusion coefficients

The kinetic data of CO<sub>2</sub> and CH<sub>4</sub> adsorptions at 0.2 bar for all temperatures were fitted to LDF model for an isothermal diffusion system (Eq. 5-36) and to diffusion model based on Fick's second law (Eq. 5-44). The fitting goodness were evaluated by coefficient of determination,  $R^2$ , (Eq. A-10). The modelling results are presented in Figure 5-8-i,ii,iii (Mg-MOF-74), Figure 5-9-i,ii,iii (Mg-MOF-74@CNT) and Figure 5-10-i,ii,iii (Mg-MOF-74@GO). The results show that LDF model can fit the data better than Fickian diffusion model for all samples, signifying that the mass transfer is controlled by external barriers [230]. Using LDF approximation, the sorption rate is assumed to be proportionally linear to the difference between the concentration in adsorbed phase and the equilibrium concentration at the surface of crystal with bulk gas phase [229]. The external mass transfer resistance in MOF crystal is attributed to the external surface diffusion so that it can be assumed as the single diffusion process within the crystal [227]. The mass transfer described by LDF can be assimilated to a diffusion system of a single crystal having a single surface resistance [230].

At 0.2 bar, a significant difference between the sorption rates of CO<sub>2</sub> and CH<sub>4</sub> can be observed whereby CO<sub>2</sub> takes longer to reach the equilibrium when compared to CH<sub>4</sub> which can facilitate their separation for the case of co-adsorption. By using LDF as the appropriate model, the kinetic data for higher bulk gas pressure was modelled only for CO<sub>2</sub> adsorption seen that CH<sub>4</sub> is not influenced by the pressure. The data were also fitted to LDF models for a non-isothermal diffusion system taking into account the influence of: (i) adsorption coverage, associated with Darken corrective factor and designated as LDF-Darken model (Eq. 5-38), and, (ii) temperature, associated with Arrhenius relationship and designated as LDF-Darken-Arrhenius model (Eq. 5-41). Langmuir model was used to describe all isotherms seen that they can fit the model up to 2 bar with a good coefficient of determination,  $R^2$ . The setting parameters for non-isothermal kinetic modelling are summarized in Table 5-1, noting that the activation energy was optimized for all reference temperatures. The values of Langmuir affinity,  $b(T)$ , were calculated using Eq. 5-14. The results of modelling are presented in Figure 5-8-iv,v,vi (Mg-MOF-74), Figure 5-9-iv,v,vi (Mg-MOF-74@CNT) and Figure 5-10-iv,v,vi (Mg-MOF-74@GO) with their respective coefficient of determination  $R^2$ . The calculated values of diffusivities are presented in Table 5-2, Figure 5-11 and Figure 5-12.

As seen in these figures, at 0.2 bar and for all temperature, the sorption rate of CO<sub>2</sub> on all samples exhibit nearly perfect agreement with LDF displaying the reliability of the diffusivity value deduced at this pressure. Thus, at such a low pressure, taking the temperature and adsorbate concentration changes into account does not improve the modelling agreement. In Figure 5-8, the kinetic data measured on Mg-MOF-74 at 0.5 bar is linear, following LDF approximation for all temperatures, and very close to the sorption rate measured at 0.2 bar, as observed in Figure 5-5. The diffusion time constant,  $D_{0,T_0}/r_c^2$ , of CO<sub>2</sub> adsorption on Mg-MOF-74 is deduced as 0.00832 s<sup>-1</sup> at 25 °C comparable to 0.00811 s<sup>-1</sup> at the same temperature [19] and 0.00947 s<sup>-1</sup> at 50 °C comparable to 0.00893 at 45 °C [19], both of which were reported for the same material by using manometric method at 0.013 bar.

In Figure 5-9 and Figure 5-10, for all temperatures, the deviation of the kinetic data of CO<sub>2</sub> adsorption on both composites from LDF approximation can be observed as the pressure increases, indicating the influence of adsorption coverage and temperature. LDF-Darken model is not able to fit the data measured above 0.2 bar while LDF-Darken-Arrhenius can fit the data for 0.5 bar with an acceptable value of  $R^2$  and 1.5 bar with a moderate value of  $R^2$ . It shows that the release of heat during adsorption, especially pronounced at elevated pressures, affects the sorption rate more than the increasing concentration in adsorbed phase does.

**Table 5-1.** Setting parameters for kinetic modelling of non-isothermal diffusion system using manometric method.

	Mg-MOF-74			Mg-MOF-74@CNT			Mg-MOF-74@GO		
<b>Gas adsorbate</b>	CO <sub>2</sub>			CO <sub>2</sub>			CO <sub>2</sub>		
<b>Initial gas pressure, <math>p_i</math> (bar)</b>	0			0			0		
<b>Bulk gas pressure, <math>p</math> (bar)</b>	0.2 / 0.5 / 1.5			0.2 / 0.5 / 1.5			0.2 / 0.5 / 1.5		
<b>Initial temperature, <math>T_i</math> (°C)</b>	25	50	75	25	50	75	25	50	75
<b>Bulk gas temperature, <math>T</math> (°C)</b>	25	50	75	25	50	75	25	50	75
<b>Reference temperature, <math>T_0</math> (°C)</b>	25	50	75	25	50	75	25	50	75
<b>Langmuir affinity at <math>T_0</math>, <math>b_0</math> (bar<sup>-1</sup>)</b>	1.875	1.872	1.600	1.600	1.597	1.594	1.600	1.597	1.595
<b>Langmuir saturation at <math>T_0</math>, <math>q_{sat,0}</math> (mol·kg<sup>-1</sup>)</b>	7.916	6.226	10.49	10.50	7.823	6.792	11.07	8.447	6.396
<b>Isosteric heat of adsorption, <math>Q_{st}</math> (kJ·mol<sup>-1</sup>)</b>	76			57			57		
<b>Activation energy of diffusion, <math>E_a</math> (kJ·mol<sup>-1</sup>)</b>	-			45			45		

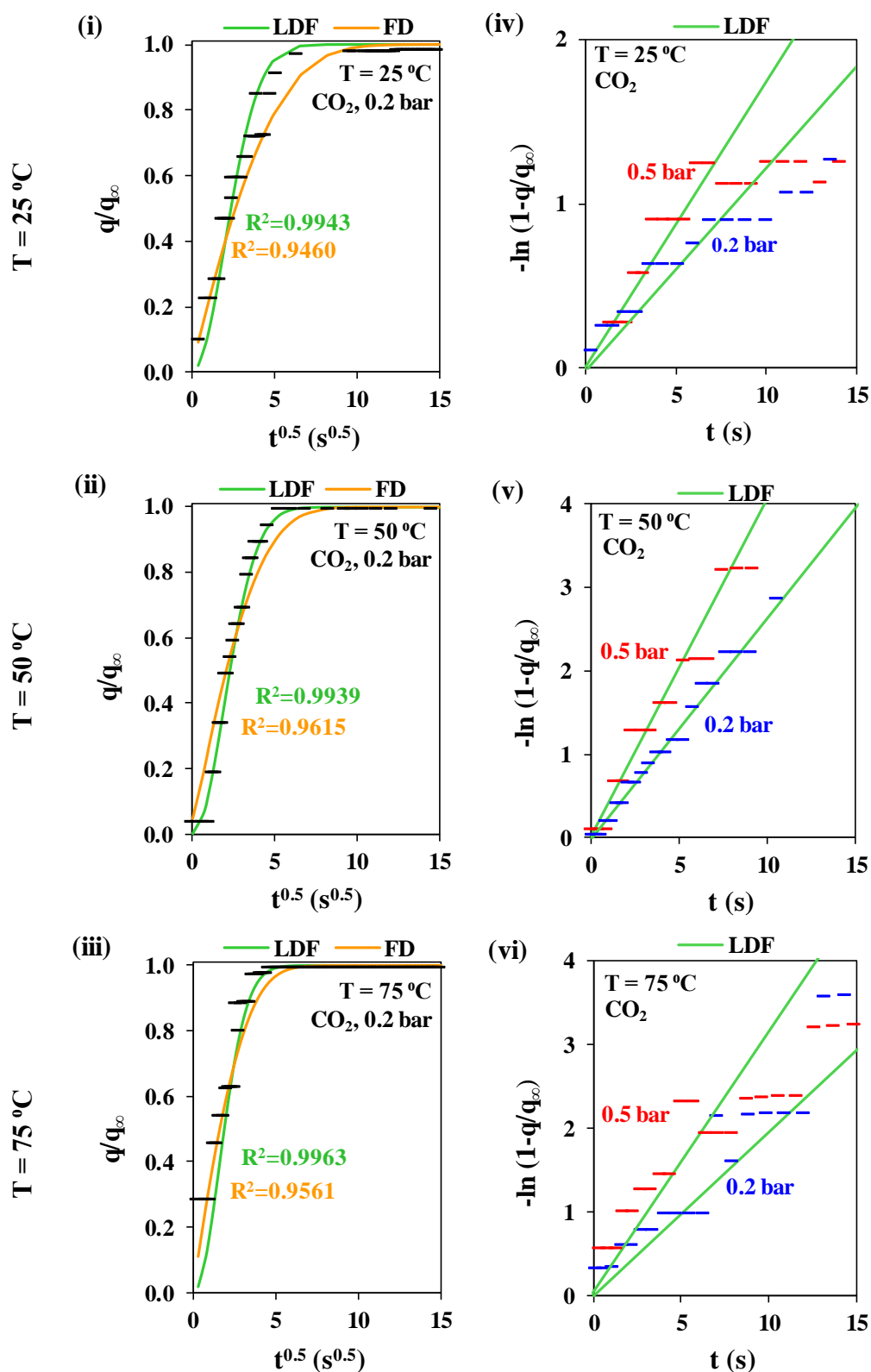


**Figure 5-8.** Fractional adsorption uptakes of CO<sub>2</sub> on Mg-MOF-74 at 0.2 bar, fitted to Linear Driving Force (LDF) model and Fickian diffusion model for (i) 25 °C, (ii) 50 °C and (iii) 75 °C with their respective coefficient of determination,  $R^2$ , and, linear form of fractional adsorption uptakes of CO<sub>2</sub> on Mg-MOF-74 at 0.2 bar and 0.5 bar, fitted to LDF model for (iv) 25 °C, (v) 50 °C and (vi) 75 °C.

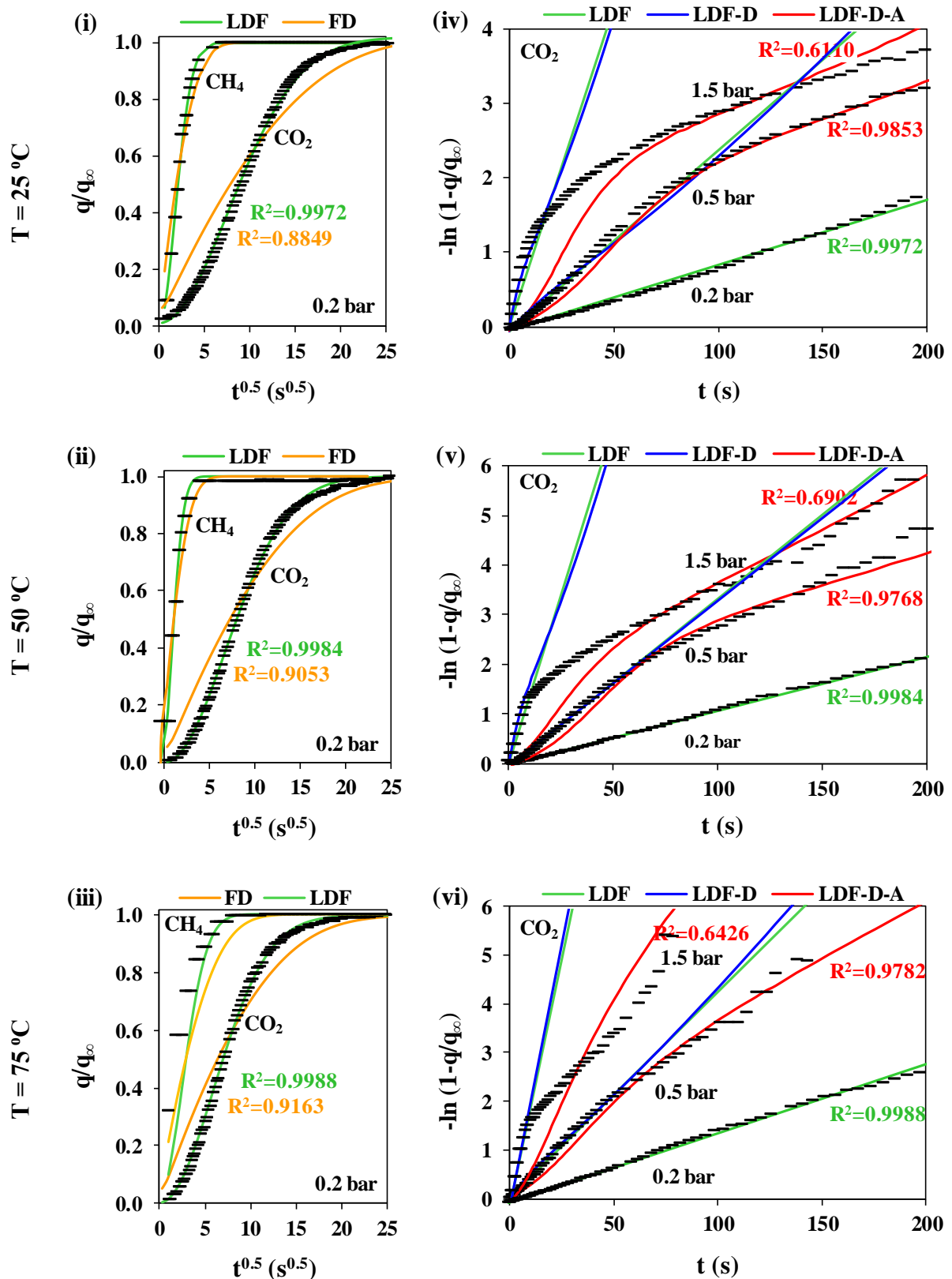


**Figure 5-9.** Fractional adsorption uptakes of  $\text{CO}_2$  (compared to  $\text{CH}_4$ ) on Mg-MOF-74@CNT at 0.2 bar, fitted to Linear Driving Force (LDF) model and Fickian diffusion model for (i) 25 °C, (ii) 50 °C and (iii) 75 °C, and linear form of fractional adsorption uptakes of  $\text{CO}_2$  on Mg-MOF-74@CNT at 0.2 bar, 0.5 bar and 1.5 bar, fitted to LDF, LDF-Darken and LDF-Darken-Arrhenius models for (iv) 25 °C, (v) 50 °C and (vi) 75 °C, with their respective coefficient of determination,  $R^2$ .

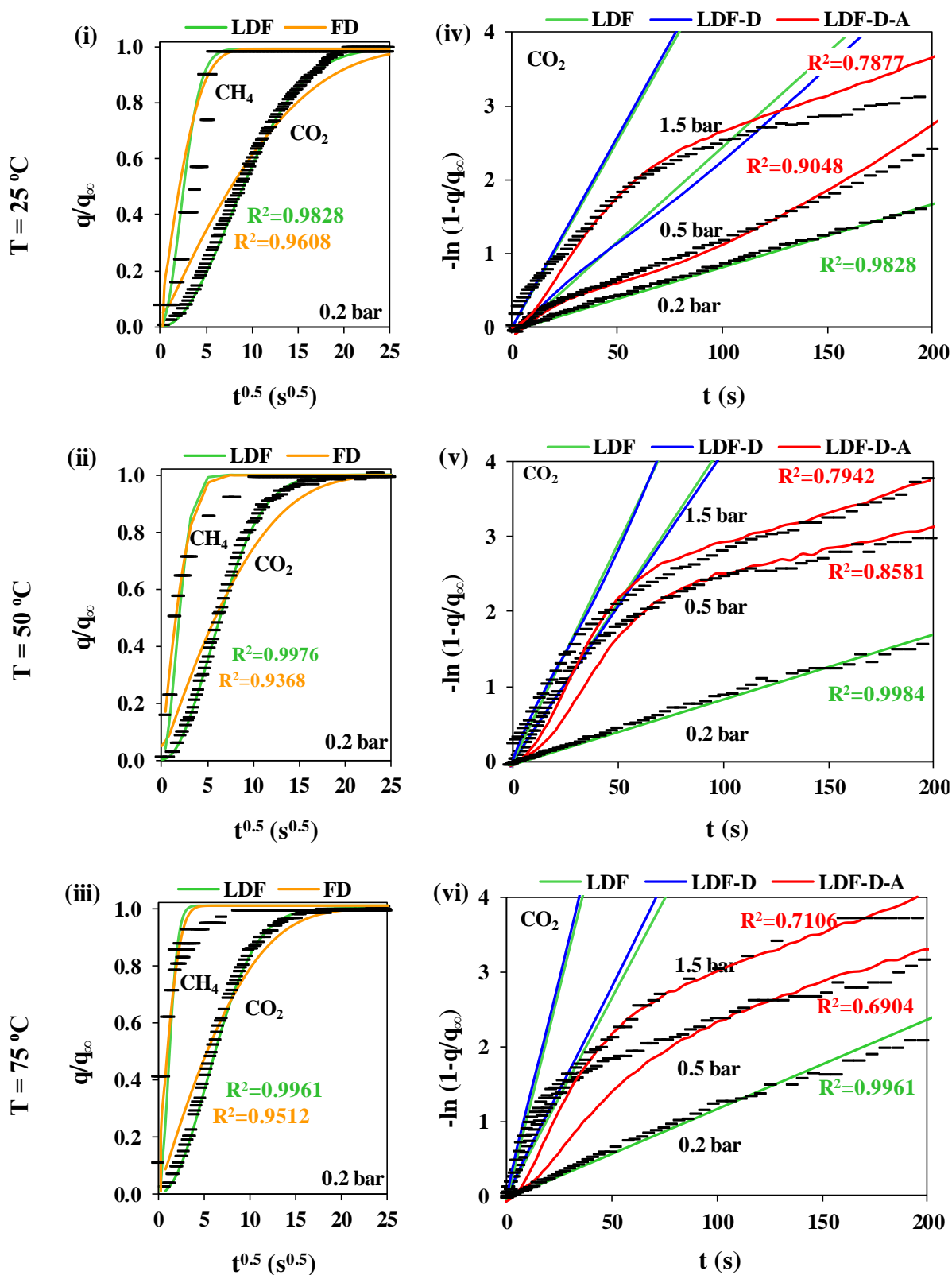


**Figure 5-10.** Fractional adsorption uptakes of CO<sub>2</sub> (compared to CH<sub>4</sub>) on Mg-MOF-74@GO at 0.2 bar, fitted to Linear Driving Force (LDF) model and Fickian diffusion model for (i) 25 °C, (ii) 50 °C and (iii) 75 °C, and, linear form of fractional adsorption uptakes of CO<sub>2</sub> on Mg-MOF-74@GO at 0.2 bar, 0.5 bar and 1.5 bar, fitted to LDF, LDF-Darken and LDF-Darken-Arrhenius models for (iv) 25 °C, (v) 50 °C and (vi) 75 °C, with their respective coefficient of determination,  $R^2$ .

Figure 5-11 summarizes the modelling results in Table 5-2 in form of Arrhenius plot, presenting the outcome of the corrections effectuated in the kinetic models of CO<sub>2</sub> adsorption for Mg-MOF-74@CNT and Mg-MOF-74@GO on the variations observed in the value of the diffusivity time constant  $D/r_c^2$  with the reference temperature  $T_0$  chosen equal to the initial temperature of the system. As the pressure increases, the diffusion coefficient calculated using LDF deviates from the value measured at nearly zero adsorption coverage, as assumed at 0.2 bar. This shows an important influence of heat release on sorption rate of CO<sub>2</sub> in both composites. Figure 5-12 presents the variations of zero coverage diffusivity time constant  $D_{0,T_0}/r_c^2$  determined at different reference temperatures for CO<sub>2</sub> and CH<sub>4</sub>. The zero coverage diffusivities of CO<sub>2</sub> and CH<sub>4</sub> on the synthesized samples vary with the temperature of reference, according to Arrhenius law. The sorption rate of CH<sub>4</sub> is much faster when compared to that of CO<sub>2</sub>. The diffusion rate of CO<sub>2</sub> in both composites is less influenced by the adsorption temperature in comparison to the pristine Mg-MOF-74 which comforts the findings in equilibria studies in Chapter 4: the adsorption capacity of CO<sub>2</sub> on both composites are less adversely affected with temperature when compared to the pristine Mg-MOF-74. It stems from the more complex features of nanoporous body in both composites providing more diffusion channels for the mass transfer of gas adsorbate.

**Table 5-2.** Diffusivities of CO<sub>2</sub> and CH<sub>4</sub> adsorptions on Mg-MOF-74, Mg-MOF-74-CNT and Mg-MOF-74-GO at 25 °C, 50 °C and 75 °C. The values are deduced by manometric method.

		Mg-MOF-74	Mg-MOF-74-CNT			Mg-MOF-74-GO					
Crystal radius, $r_c^2$ (nm) <sup>1</sup>		67	73			82					
Gas adsorbate		CO <sub>2</sub>	CO <sub>2</sub>		CH <sub>4</sub>	CO <sub>2</sub>		CH <sub>4</sub>			
Equilibrium pressure (bar)		0.2	0.2	0.5	1.5	0.2	0.2	0.5	1.5	0.2	
<b><math>T = 25\text{ °C}, (T_0 = 25\text{ °C})</math></b>											
$D/r_c^2$ ( $10^{-4}\text{ s}^{-1}$ )	Fickian diffusion model ( $n=10$ )	71.9	4.71	–	–	82.3	5.16	–	–	116	
	LDF model	LDF	83.2	5.8	16.3	57.0	102	5.74	17.1	33.6	118
		LDF-Darken	–	–	13.7	43.0	–	–	8.44	25.2	–
		LDF-Darken-Arrhenius	–	–	5.35	5.77	–	–	5.93	5.84	–
		Average <sup>2</sup>	83.2	5.64 ± 0.21		102	5.84 ± 0.08		118		
$D_{0,T_0}$ ( $\text{m}^2\cdot\text{s}^{-1}$ )	Average <sup>2</sup>	3.73x10 <sup>-17</sup>	3.01x10 <sup>-18</sup>		5.44x10 <sup>-17</sup>	3.93x10 <sup>-18</sup>		7.93x10 <sup>-17</sup>			
<b><math>T = 50\text{ °C}, (T_0 = 50\text{ °C})</math></b>											
$D/r_c^2$ ( $10^{-4}\text{ s}^{-1}$ )	Fickian diffusion model ( $n=10$ )	80.3	5.86	–	–	152	8.87	–	–	166	
	LDF model	LDF	94.7	7.77	22.6	90.4	223	10.4	28.3	66.1	208
		LDF-Darken	–	–	15	58	–	–	15	43.5	–
		LDF-Darken-Arrhenius	–	–	7.93	7.82	–	–	10.52	10.3	–
		Average <sup>2</sup>	94.7	7.84 ± 0.07		223	10.41 ± 0.09		208		
$D_{0,T_0}$ ( $\text{m}^2\cdot\text{s}^{-1}$ )	Average <sup>2</sup>	4.25x10 <sup>-17</sup>	4.18x10 <sup>-18</sup>		1.19x10 <sup>-16</sup>	7.00x10 <sup>-18</sup>		1.40x10 <sup>-16</sup>			
<b><math>T = 75\text{ °C}, (T_0 = 75\text{ °C})</math></b>											
$D/r_c^2$ ( $10^{-4}\text{ s}^{-1}$ )	Fickian diffusion model ( $n=10$ )	119	7.57	–	–	202	10.9	–	–	210	
	LDF model	LDF	122	9.5	28.2	136	302	12.1	35.4	110	293
		LDF-Darken	–	–	20.2	69.3	–	–	26.8	68.2	–
		LDF-Darken-Arrhenius	–	–	10.2	10.1	–	–	12.3	12.7	–
		Average <sup>2</sup>	122	9.93 ± 0.31		302	12.37 ± 0.25		293		
$D_{0,T_0}$ ( $\text{m}^2\cdot\text{s}^{-1}$ )	Average <sup>2</sup>	5.48x10 <sup>-17</sup>	5.29x10 <sup>-18</sup>		1.61x10 <sup>-16</sup>	8.32x10 <sup>-18</sup>		1.97x10 <sup>-16</sup>			

<sup>1</sup> Calculated using Williamson-Hall plot in PXRD analysis in Section 3.7.1.

<sup>2</sup> Calculated on average from the measurements at 0.2 bar, 0.5 bar and 1.5 bar using Linear Driving Force (LDF) model for 0.2 bar and LDF-Darken-Arrhenius model for 0.5 bar and 1.5 bar (supposedly  $D_{0,T_0}$ ).

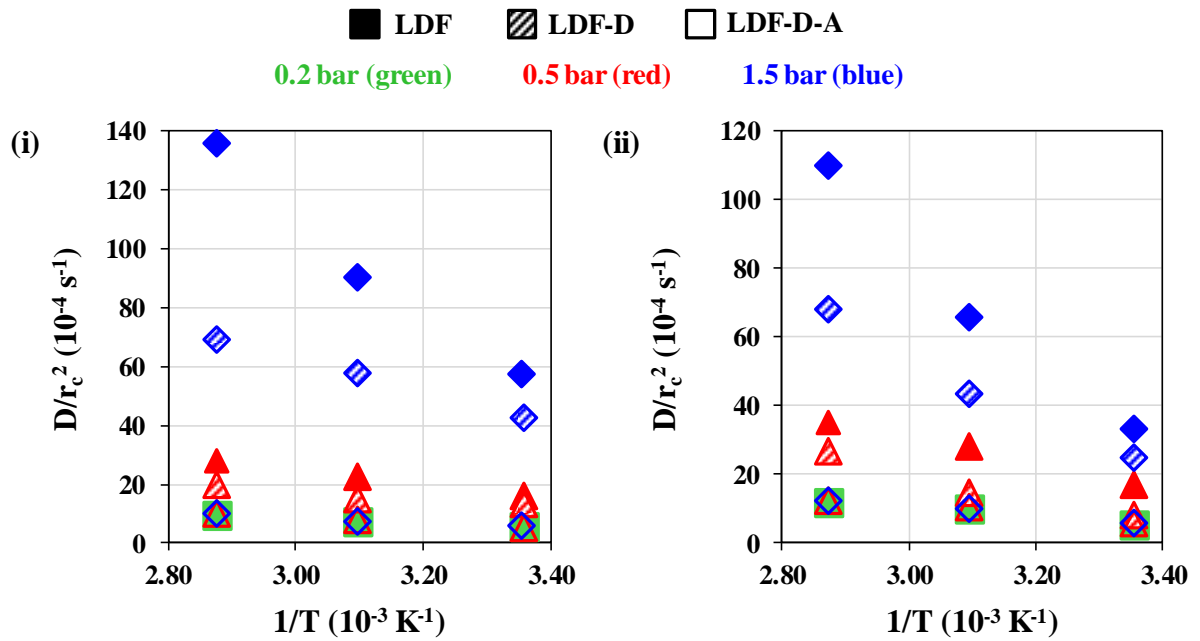


**Figure 5-11.** Arrhenius plot of diffusivity time constants,  $D/r_c^2$ , of  $\text{CO}_2$  adsorption on (i) Mg-MOF-74@CNT and (ii) Mg-MOF-74@GO at 0.2 bar, 0.5 bar and 1.5 bar for 25 °C, 50 °C and 75 °C, calculated using Linear Driving Force (LDF), LDF-Darken and LDF-Darken-Arrhenius models.

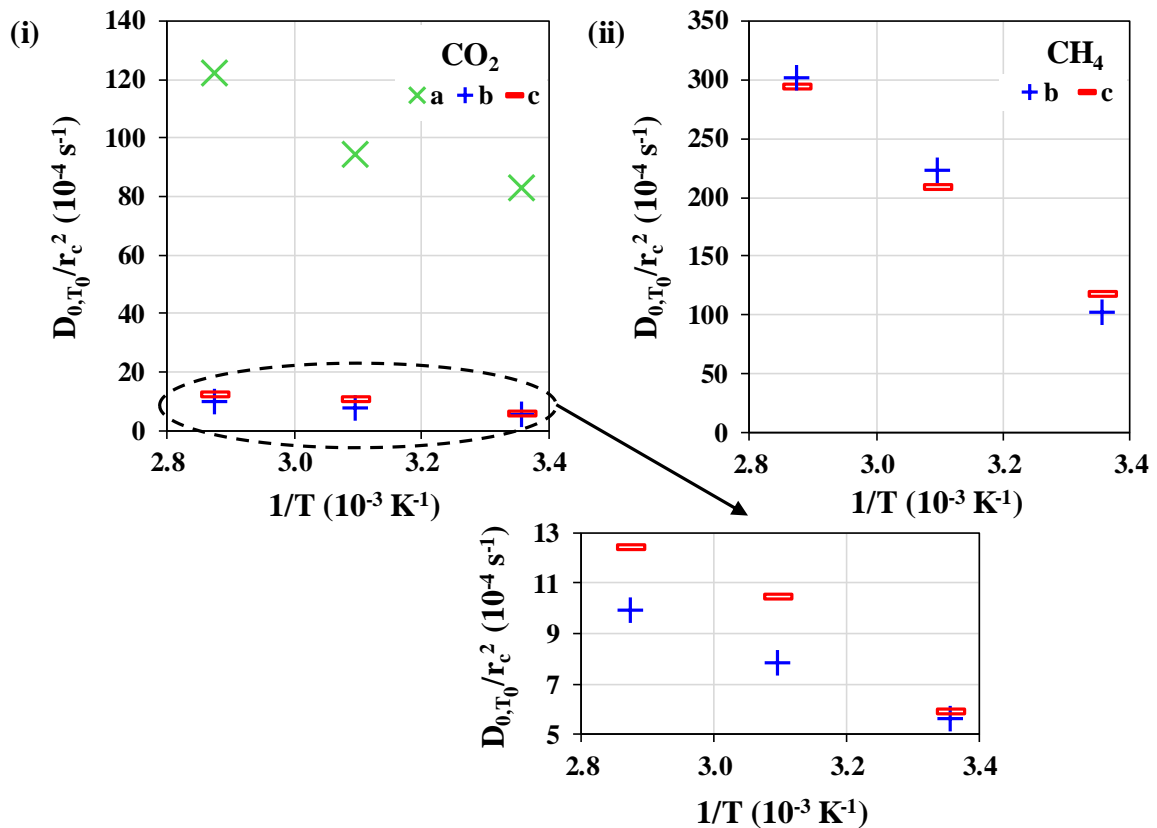


**Figure 5-12.** Arrhenius plots of diffusivity time constant at nearly zero coverage,  $D_0/r_c^2$ , of (i)  $\text{CO}_2$  and (ii)  $\text{CH}_4$  adsorptions on (a) Mg-MOF-74, (b) Mg-MOF-74@CNT and (c) Mg-MOF-74@GO for 25 °C, 50 °C and 75 °C. The value was calculated on average from the measurements at 0.2 bar, 0.5 bar and 1.5 bar using Linear Driving Force (LDF) and LDF-Darken-Arrhenius models.

#### 5.6.4. Kinetic selectivity of CO<sub>2</sub>/CH<sub>4</sub>

The kinetic selectivities of CO<sub>2</sub>/CH<sub>4</sub> on Mg-MOF-74@CNT and Mg-MOF-74@GO for all temperatures were deduced using Eq. 5-50 [192] where the Henry's constants  $K$  were determined from the Langmuir isotherm model. The results are presented in Table 5-3. In the absence of kinetic data of CH<sub>4</sub> adsorption on the pristine Mg-MOF-74, the comparison with the composites cannot be done. However, we can say that both composites exhibit encouraging values of kinetic selectivities favourable to CO<sub>2</sub> over CH<sub>4</sub>. Following the same trend as the equilibrium selectivities determined in Chapter 4, the kinetic selectivity is improved when the adsorption temperature increases which becomes advantageous for the separation at these conditions.

$$\alpha_{CO_2/CH_4}^{KIN} = \frac{K_{H,CO_2}}{K_{H,CH_4}} \cdot \sqrt{\frac{D_{CO_2}}{D_{CH_4}}} \quad (\text{Eq. 5-50})$$

**Table 5-3.** Kinetic selectivity of CO<sub>2</sub>/CH<sub>4</sub> on Mg-MOF-74, Mg-MOF-74-CNT and Mg-MOF-74-GO at 25 °C, 50 °C and 75 °C. The values deduced by manometric method.

Temperature	Mg-MOF-74@CNT	Mg-MOF-74@GO
25 °C	3.54	4.38
50 °C	5.43	6.86
75 °C	8.83	7.74

### 5.7. Zero Length Column method: Results and discussions

#### 5.7.1. CO<sub>2</sub> and CH<sub>4</sub> adsorption kinetics at different temperatures

The adsorption kinetics of single component CO<sub>2</sub> and CH<sub>4</sub> were measured on Mg-MOF-74, Mg-MOF-74@CNT and Mg-MOF-74@GO using Zero Length Column equipment for three different temperatures: 25 °C, 50 °C and 75°C. Prior to the measurement, the first step consists of determining the appropriate concentration of gas adsorbate in condition that the equilibrium is described by Henry's law (diluted enough). However, the concentration must be sufficient to allow the desorption to occur which is identified when the curve can be distinguishable from the blank (measurement without sample). The second step involves the determination of parameter  $K'_H \cdot V_s$  from the equilibrium isotherm of pure gas adsorbate when fitted to Henry's law. The third step

involves the determination of the appropriate purge gas flow rates for desorption measurement which must lie in a kinetic region.

Figure 5-13 shows the logarithmic fractional desorption curves of CO<sub>2</sub> and CH<sub>4</sub> on the pristine Mg-MOF-74 as a function of time for a purge gas flow rate of 150 ml·min<sup>-1</sup> at 25 °C. Adsorption equilibrium was initially achieved for gas mixtures of different concentrations of adsorbate diluted in helium. In Figure 5-13-i, the feed gases containing less than 5 mol% of CO<sub>2</sub> produce overlaid desorption curves (supposedly having same sorption rate) which must be the concentration distributions in Henry's law region. Therefore, any concentration in this range can be used for kinetic measurements. Knowing that CO<sub>2</sub> is more highly adsorbed in both composites compared to the pristine Mg-MOF-74, then 2 mol% was selected as a fixed parameter to prevent working beyond Henry's law region for both composites, noting that the equipment was not able to calibrate the concentrations below 2 mol%. In Figure 5-13-ii, it can be seen that the desorption curves of CH<sub>4</sub> makes no difference from the blank although at a maximum concentration due to very fast diffusion kinetics. The same observation also happened for both composites so that all kinetic data of CH<sub>4</sub> are not exploitable using the available ZLC equipment.

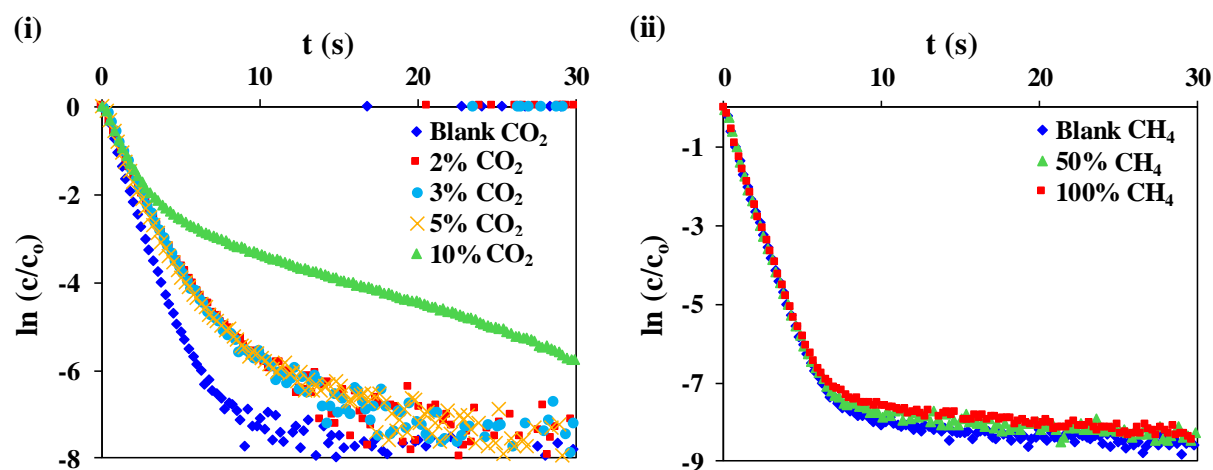


**Figure 5-13.** Logarithmic fractional desorption curves of (i) CO<sub>2</sub> and (ii) CH<sub>4</sub> on Mg-MOF-74 for a purge gas flow rate of 150 ml·min<sup>-1</sup> at 25 °C. Adsorption equilibrium was initially achieved for mixtures of different concentration of gas adsorbate (in mol%) in helium.

The isotherms of equilibrium data of CO<sub>2</sub> at different temperatures allow the estimation of Henry's constant,  $K_H$ , from a linear regression applied in the domain of low adsorbate concentrations (<5 mol%).  $K_H$  (mol·kg<sup>-1</sup>/mol·m<sup>-3</sup>) correlates the adsorbate concentration per unit mass of adsorbent to the concentration in bulk gas phase based on

ideal gas law while  $K'_H$  ( $\text{mol}\cdot\text{kg}^{-1}/\text{mol}\cdot\text{m}^{-3}$ ) appears with the same definition but expressed as per unit volume of adsorbent. The quantity  $K'_H \cdot V_s$  as a function of temperature for the different materials was then deduced using Eq. 5-49 in which  $K'_H \cdot V_s = K_H \cdot m_s$  as presented in Table 5-4. The setting parameters for kinetic model using ZLC method are summarized in Table 5-5.

**Table 5-4.** Determination of parameter  $K'_H \cdot V_s$  for  $\text{CO}_2$  adsorption on Mg-MOF-74, Mg-MOF-74@CNT and Mg-MOF-74@GO.

	Mg-MOF-74			Mg-MOF-74@CNT			Mg-MOF-74@GO		
$m_s$ (mg)	10.2 mg			10.7 mg			10.5 mg		
Gas adsorbate	$\text{CO}_2$			$\text{CO}_2$			$\text{CO}_2$		
Bulk gas pressure range, $p$ (bar)	0–0.5			0–0.5			0–0.5		
Bulk gas temperature, $T$ ( $^\circ\text{C}$ )	25	50	75	25	50	75	25	50	75
$K_H$ ( $\text{mol}\cdot\text{kg}^{-1}/\text{mol}\cdot\text{m}^{-3}$ )	3.97 $\times 10^{-3}$	3.01 $\times 10^{-3}$	1.13 $\times 10^{-4}$	4.43 $\times 10^{-3}$	3.47 $\times 10^{-3}$	3.01 $\times 10^{-3}$	4.96 $\times 10^{-3}$	3.76 $\times 10^{-3}$	2.55 $\times 10^{-3}$
$R^2$	1.000	1.000	1.000	1.000	1.000	1.000	1.000	1.000	1.000

**Table 5-5.** Setting parameters for kinetic modelling of linear isothermal diffusion system using Zero Length Column method.

	Mg-MOF-74			Mg-MOF-74@CNT			Mg-MOF-74@GO		
Crystal radius, $r_c^2$ (nm) <sup>1</sup>	67			73			82		
Concentration of gas adsorbate	2 mol% $\text{CO}_2$ diluted in helium			2 mol% $\text{CO}_2$ diluted in helium			2 mol% $\text{CO}_2$ diluted in helium		
Purge gas	helium			helium			helium		
Purge gas flow rate, $F$ ( $\text{ml}\cdot\text{min}^{-1}$ )	110 / 120 / 130 /140 /150			110 / 120 / 130 /140 /150			110 / 120 / 130 /140 /150		
Bulk gas temperature, $T$ ( $^\circ\text{C}$ )	25	50	75	25	50	75	25	50	75
$K'_H \cdot V_s$ ( $\text{m}^3$ )	4.05 $\times 10^{-8}$	3.07 $\times 10^{-8}$	1.15 $\times 10^{-9}$	4.64 $\times 10^{-8}$	3.72 $\times 10^{-8}$	3.22 $\times 10^{-8}$	5.21 $\times 10^{-8}$	3.95 $\times 10^{-8}$	2.67 $\times 10^{-8}$

<sup>1</sup>Calculated using numerical Williamson-Hall plot in PXRD analysis in Section 3.4.2.

The sorption rates were measured under feed gas flow rates between  $100 \text{ ml}\cdot\text{min}^{-1}$  and  $150 \text{ ml}\cdot\text{min}^{-1}$  in order to identify the kinetic regime of the mass transfer. The kinetic data are presented in the plot of  $c/c_0$  standardized from the ion signals provided by gas analyser as shown in Figure 5-14 (Mg-MOF-74), Figure 5-15 (Mg-MOF-74@CNT) and Figure 5-16 (Mg-MOF-74@GO). In these figures, for all samples and temperatures, the desorption curve is getting closer to each other as the purge gas flow rate increases until they overlay at  $140 \text{ ml}\cdot\text{min}^{-1}$  and  $150 \text{ ml}\cdot\text{min}^{-1}$ , that is when the external film mass transfer resistance is assumed to not contribute significantly to the diffusion rate (when the intracrystalline mass transfer mechanisms control the diffusion kinetics). When an adsorbent crystal is put into contact with a feed gas, an external fluid film was developed at the surface of the crystal. The thickness of the fluid film decreases as a function of the superficial velocity of the gas passing through the adsorbent. Hence, for sufficiently high velocities, the resistance to the external mass transfer of the film becomes negligible to the resistance to the internal transfer in the crystal. In order to measure an intracrystalline diffusivity,  $D_c$ , it is therefore necessary to place the system under the condition of gas velocities for which the kinetic regime can be established. This condition is fulfilled when the variation of desorbed gas concentration,  $c/c_0$ , as a function of the total volume of purge gas introduced into the column,  $F \cdot t$ , are independent to the flow velocities of the purge gas. In other words, the range of gas flow rates for which the intracrystalline diffusivity can be correctly measured in the absence of variation induced by the external mass transfer resistance can be determined when the area under the curve  $c/c_0 = f(F \cdot t)$  is independent to the purge gas flow rate. Therefore, for the concentration of 2 mol%  $\text{CO}_2$  diluted in helium, the kinetic regime is supposed to be achieved for a purge gas flow rate of at least  $140 \text{ ml}\cdot\text{min}^{-1}$  for all desorption temperatures. In Annex V, Figure A-12 presents the desorption curves of 100 mol%  $\text{CH}_4$  at  $25 \text{ }^\circ\text{C}$  for different purge gas flow rates where the kinetic regime can never be established using the available ZLC equipment.

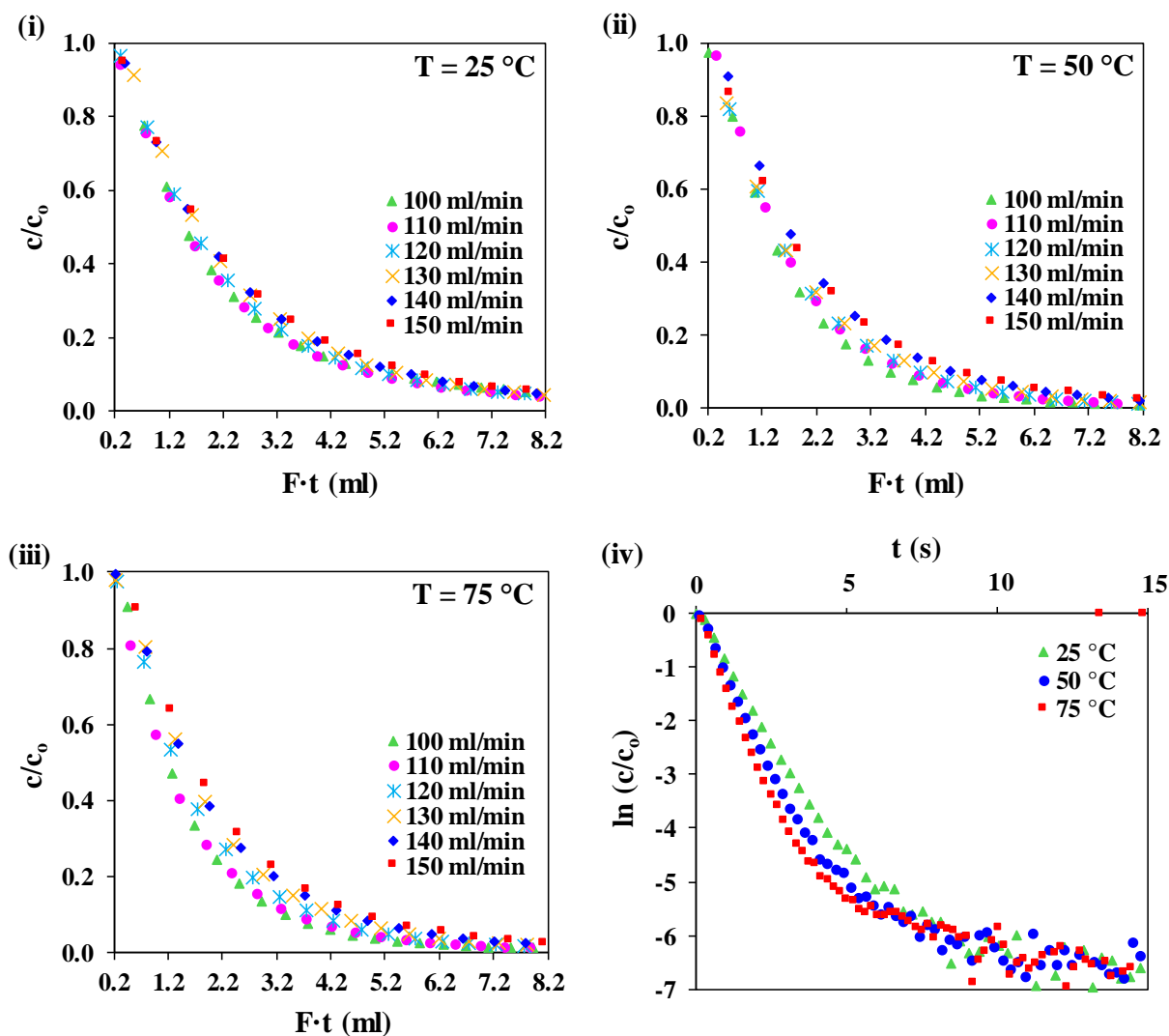


**Figure 5-14.** Fractional desorption curves of CO<sub>2</sub> on Mg-MOF-74 as a function of purge gas volume for different purge gas flow rates at (i) 25 °C, (ii) 50 °C and (iii) 75 °C, and, (iv) logarithmic fractional desorption curves of CO<sub>2</sub> on Mg-MOF-74 for a purge gas flow rate of 150 ml·min<sup>-1</sup> for different temperatures. Adsorption equilibrium was initially achieved for a mixture of 2% mol CO<sub>2</sub> in helium.

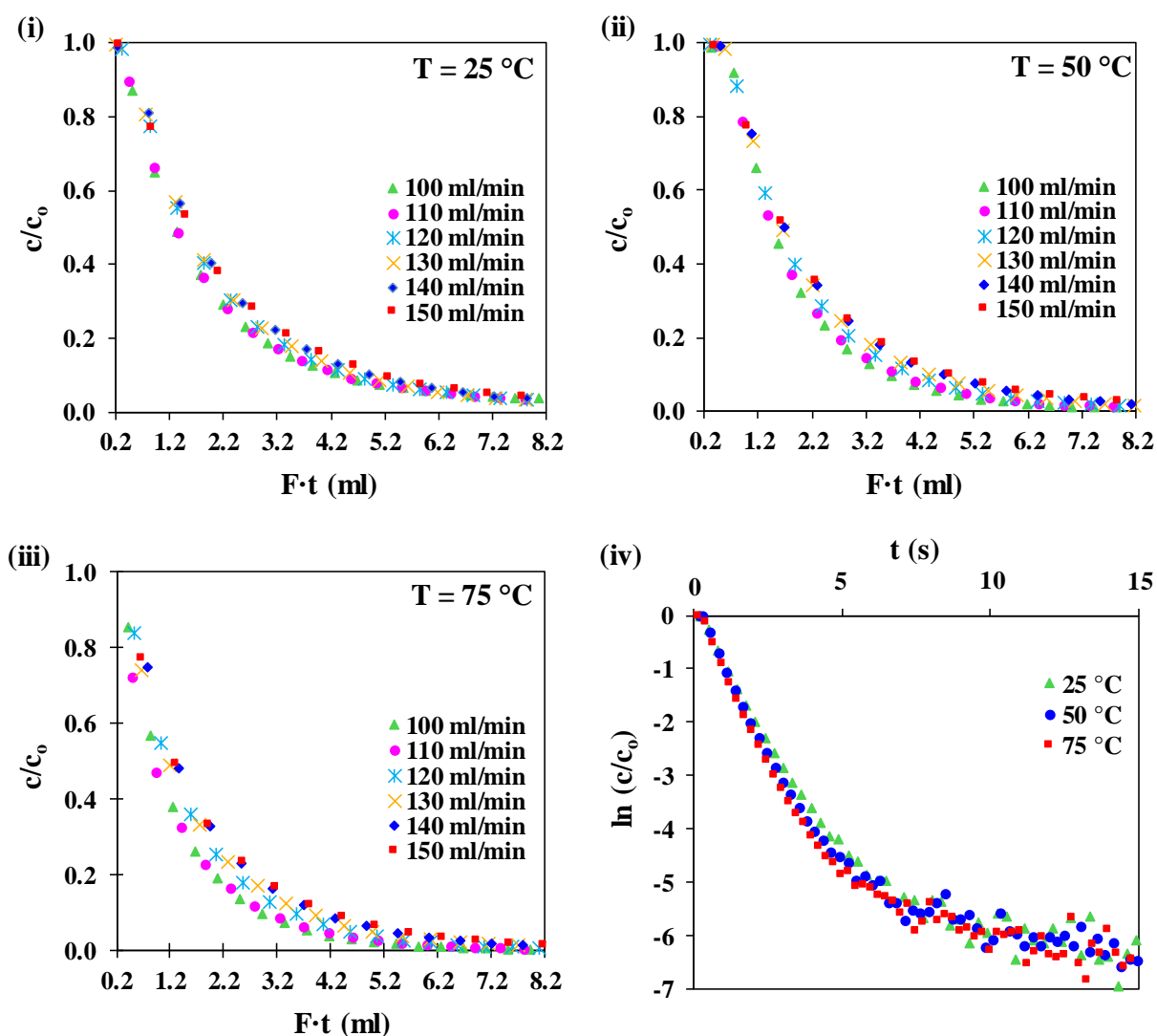


**Figure 5-15.** Fractional desorption curves of CO<sub>2</sub> on Mg-MOF-74@CNT as a function of purge gas volume for different purge gas flow rates at (i) 25 °C, (ii) 50 °C and (iii) 75 °C, and, (iv) logarithmic fractional desorption curves of CO<sub>2</sub> on Mg-MOF-74@CNT for a purge gas flow rate of 150 ml·min<sup>-1</sup> at different temperatures. Adsorption equilibrium was initially achieved for a mixture of 2% mol CO<sub>2</sub> in helium.

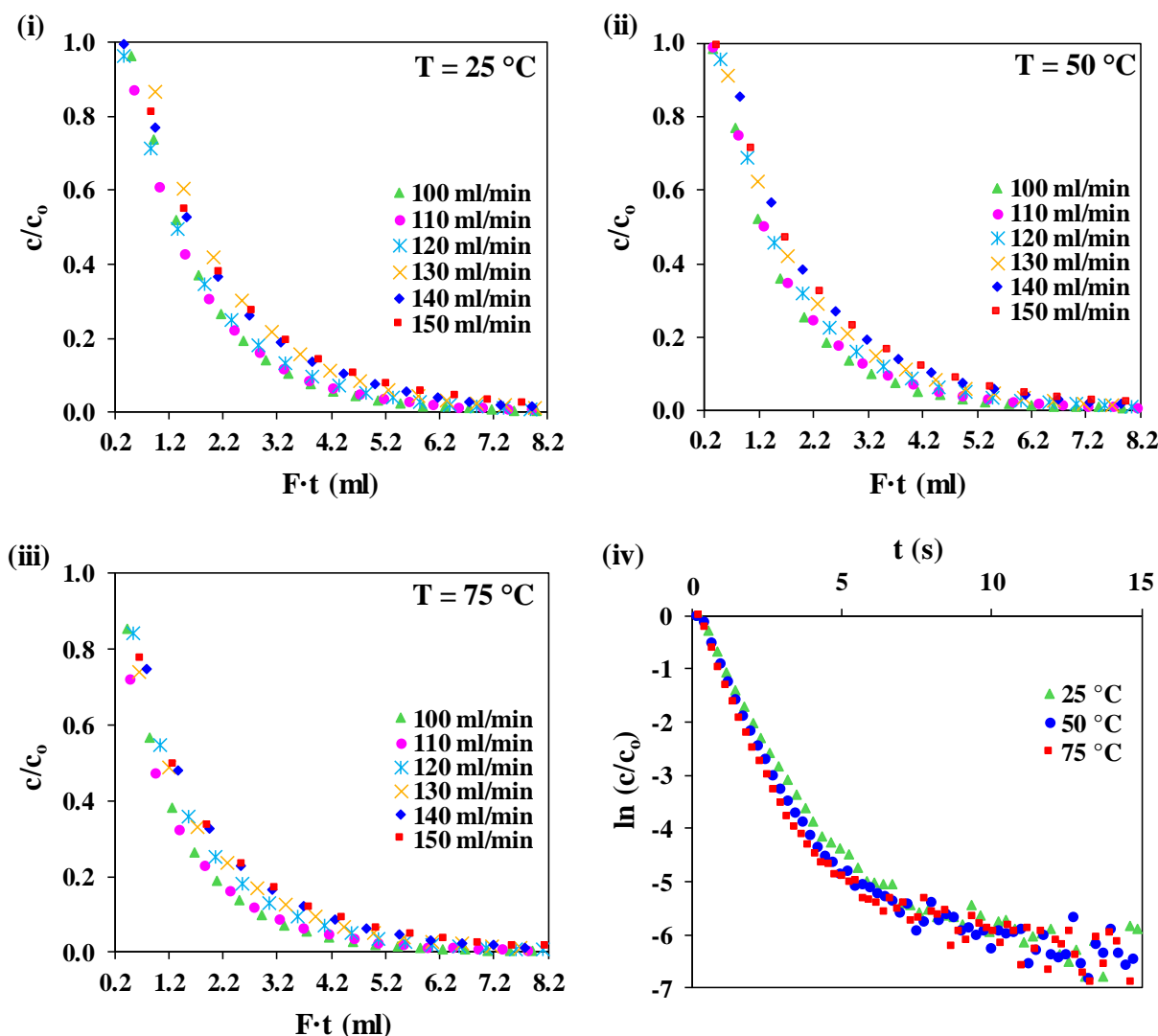


**Figure 5-16.** Fractional desorption curves of CO<sub>2</sub> on Mg-MOF-74@GO as a function of purge gas volume for different purge gas flow rates at (i) 25 °C, (ii) 50 °C and (iii) 75 °C, and, (iv) logarithmic fractional desorption curves of CO<sub>2</sub> on Mg-MOF-74@GO for a purge gas flow rate of 150 ml·min<sup>-1</sup> at different temperatures. Adsorption equilibrium was initially achieved for a mixture of 2% mol CO<sub>2</sub> in helium.

### 5.7.2. Determination of diffusion coefficients

When the kinetic regime was achieved (purge gas flow rates of 140 ml·min<sup>-1</sup> and 150 ml·min<sup>-1</sup>), the intracrystalline diffusivity was determined using diffusion model based on Fick's second law adapted for a chromatographic column. It consisted of performing an iterative resolution method by considering only the first three terms of the sum in Eq. 5-46 ( $n=3$ ), meaning that the contribution of the higher order terms were considered negligible. If the model was not able to fit the data with this assumption,  $n$  could be increased to take into account the higher order terms. The diffusion time constant,  $D/r_c^2$ , and parameter  $L$  were determined by minimizing the square of the difference between the experimental data

and the simulated data. The set of parameters  $\beta_1$ ,  $\beta_2$  and  $\beta_3$  was determined from the root solutions of Eq. 5-47 by adjusting these parameters along with the iteration Eq. 5-46. The modelling results are presented in Figure 5-17 for Mg-MOF-74, Figure 5-18 for Mg-MOF-74@CNT and Figure 5-19 for Mg-MOF-74@GO with their respective coefficient of determination,  $R^2$ . In these figures, the kinetic model describes a linear variation of the function  $\ln c/c_0 = f(t)$  (shown in sub-figures) which indicates that the first term of the series of Eq. 5-46 giving the analytical solution to the mass conservation equation is always predominant.

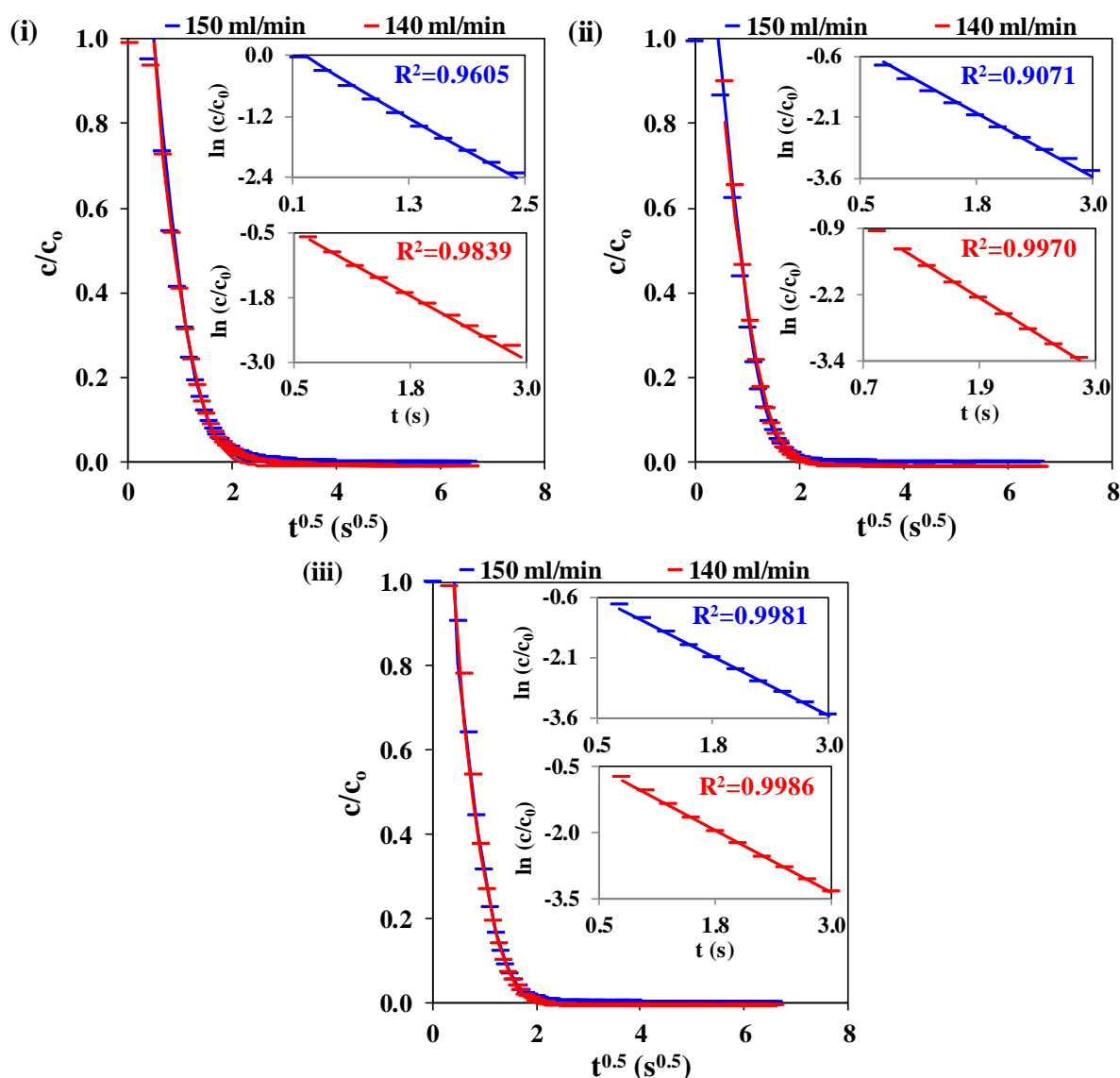


**Figure 5-17.** Fractional desorption curves of CO<sub>2</sub> on Mg-MOF-74 in kinetic regime (purge gas flow rates of 140 ml·min<sup>-1</sup> and 150 ml·min<sup>-1</sup>) at (i) 25 °C, (ii) 50 °C and (iii) 75 °C, and, (sub-figures) logarithmic fractional desorption curves, fitted to Zero Length Column–Fickian diffusion model

with their respective coefficient of determination,  $R^2$ . Adsorption equilibrium was initially achieved for a mixture of 2% mol  $\text{CO}_2$  in helium.

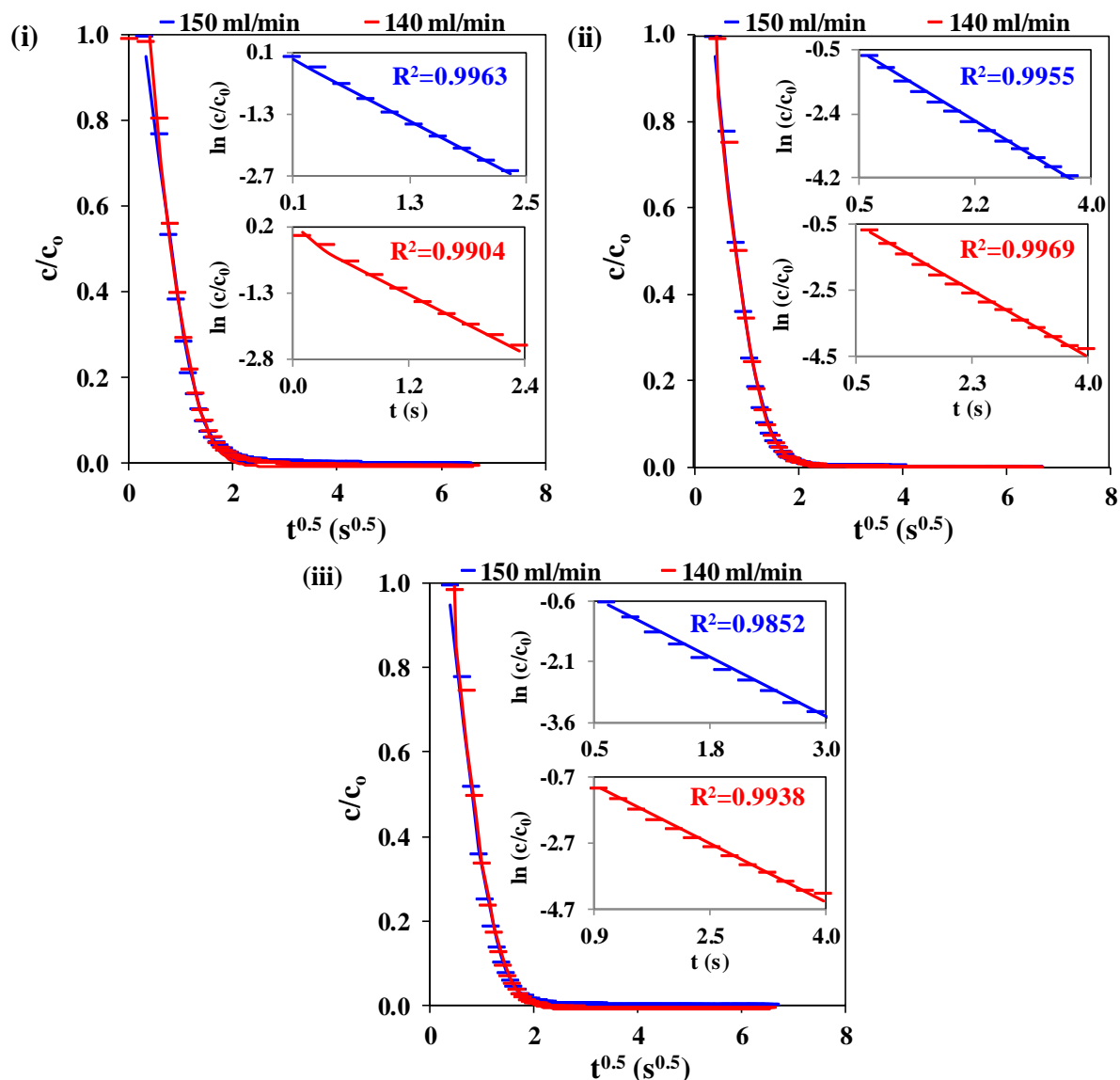


**Figure 5-18.** Fractional desorption curves of  $\text{CO}_2$  on Mg-MOF-74@CNT in kinetic regime (purge gas flow rates of  $140 \text{ ml}\cdot\text{min}^{-1}$  and  $150 \text{ ml}\cdot\text{min}^{-1}$ ) at (i)  $25^\circ\text{C}$ , (ii)  $50^\circ\text{C}$  and (iii)  $75^\circ\text{C}$ , and, (sub-figures) logarithmic fractional desorption curves, fitted to Zero Length Column-Fickian diffusion model with their respective coefficient of determination,  $R^2$ . Adsorption equilibrium was initially achieved for a mixture of 2% mol  $\text{CO}_2$  in helium.

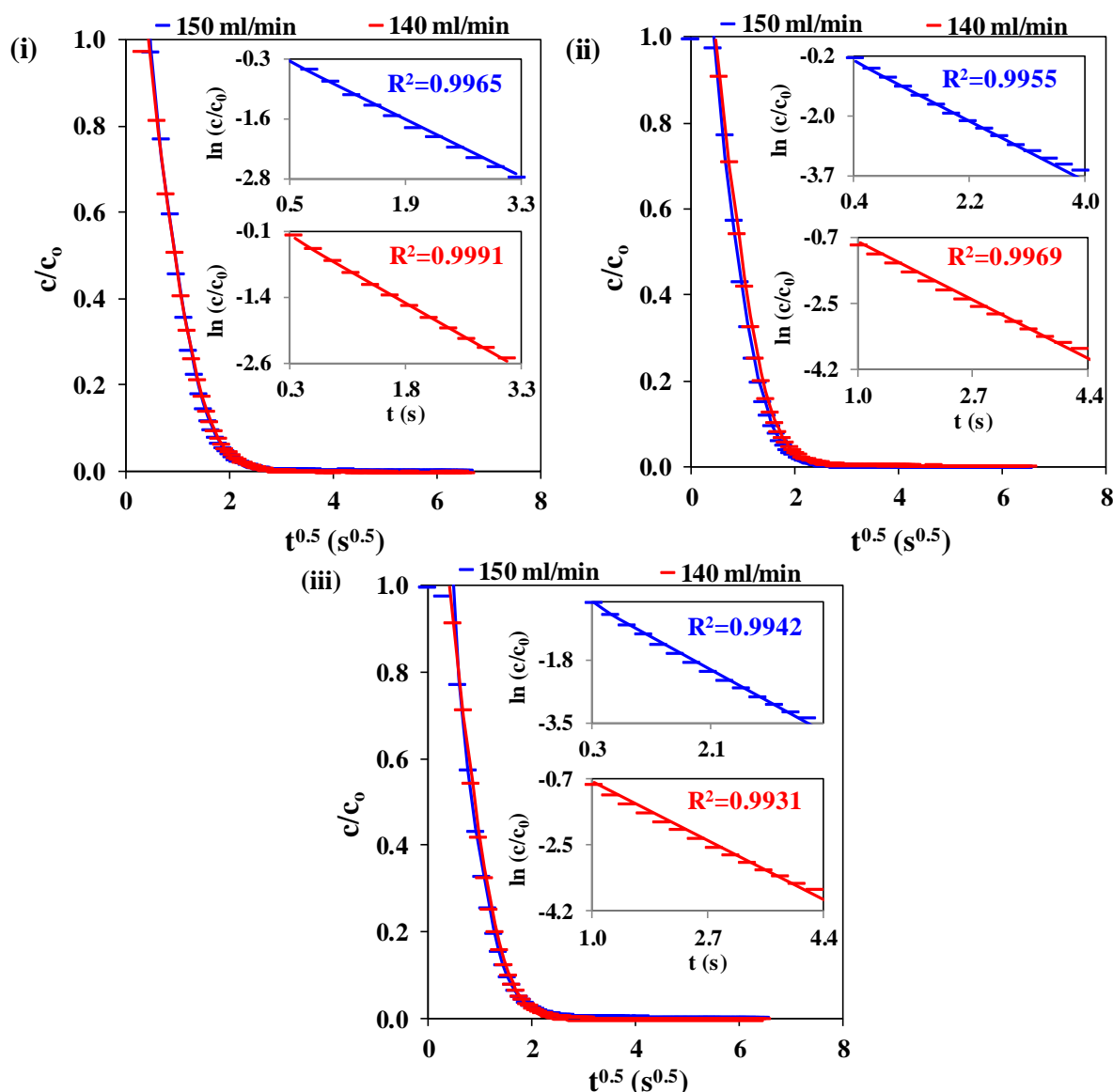


**Figure 5-19.** Fractional desorption curves of CO<sub>2</sub> on Mg-MOF-74@GO in kinetic regime (purge gas flow rates of 140 ml·min<sup>-1</sup> and 150 ml·min<sup>-1</sup>) at (i) 25 °C, (ii) 50 °C and (iii) 75 °C, and, (sub-figures) logarithmic fractional desorption curves, fitted to Zero Length Column–Fickian diffusion model with their respective coefficient of determination,  $R^2$ . Adsorption equilibrium was initially achieved for a mixture of 2% mol CO<sub>2</sub> in helium.

The calculated values of intracrystalline diffusivities are presented in Table 5-6 and summarized in form of Arrhenius plot in Figure 5-20. The diffusion rate of CO<sub>2</sub> on the synthesized samples increases as a function of adsorption temperature whereby the value is less affected for both composites when compared to the pristine Mg-MOF-74. It is in agreement with the trend observed by manometric method. Also, the intracrystalline diffusion of CO<sub>2</sub> is observed much slower on both composites in comparison to the pristine Mg-MOF-74 for all temperatures due to their improved textural properties as mentioned previously for the deduction by manometric method.

**Table 5-6.** Diffusivities times constant of CO<sub>2</sub> adsorption on Mg-MOF-74, Mg-MOF-74-CNT and Mg-MOF-74-GO at 25 °C, 50 °C and 75 °C, deduced by Zero Length Column method.

<b>Mg-MOF-74</b>	<b>25 °C</b>		<b>50 °C</b>		<b>75 °C</b>	
<b><math>F</math> (ml·min<sup>-1</sup>)</b>	<b>140</b>	<b>150</b>	<b>140</b>	<b>150</b>	<b>140</b>	<b>150</b>
<b><math>D_0/r_c^2</math> (s<sup>-1</sup>)</b>	0.683	0.626	0.748	0.749	0.861	0.885
<b>Average<sup>1</sup> <math>D_0/r_c^2</math> (s<sup>-1</sup>)</b>	0.645 ± 0.029		0.749 ± 0.001		0.873 ± 0.012	
<b>Average<sup>1</sup> <math>D_0</math> (m<sup>2</sup>·s<sup>-1</sup>)</b>	2.90 x10 <sup>-15</sup>		3.36 x10 <sup>-15</sup>		3.92 x10 <sup>-15</sup>	
<b><math>L</math></b>	15.34	15.34	16.33	17.43	18.00	18.00
<b><math>\beta_1</math></b>	1.20	2.94	1.15	1.24	1.25	1.23
<b><math>\beta_2</math></b>	3.27	3.50	3.26	4.00	3.79	3.62
<b><math>\beta_3</math></b>	9.29	8.76	9.30	9.25	9.26	9.27
<b><math>R^2</math></b>	0.9839	0.9605	0.9970	0.9071	0.9986	0.9981
<b>Mg-MOF-74@CNT</b>	<b>25 °C</b>		<b>50 °C</b>		<b>75 °C</b>	
<b><math>F</math> (ml·min<sup>-1</sup>)</b>	<b>140</b>	<b>150</b>	<b>140</b>	<b>150</b>	<b>140</b>	<b>150</b>
<b><math>D_0/r_c^2</math> (s<sup>-1</sup>)</b>	0.562	0.582	0.637	0.613	0.687	0.696
<b>Average<sup>1</sup> <math>D_0/r_c^2</math> (s<sup>-1</sup>)</b>	0.572 ± 0.010		0.625 ± 0.002		0.692 ± 0.005	
<b>Average<sup>1</sup> <math>D_0</math> (m<sup>2</sup>·s<sup>-1</sup>)</b>	3.05 x10 <sup>-15</sup>		3.33 x10 <sup>-15</sup>		3.69 x10 <sup>-15</sup>	
<b><math>L</math></b>	14.43	14.43	20.08	21.91	19.21	20.33
<b><math>\beta_1</math></b>	1.30	1.13	1.30	1.31	1.30	1.30
<b><math>\beta_2</math></b>	4.03	5.85	4.07	4.07	4.07	4.07
<b><math>\beta_3</math></b>	9.22	9.11	9.27	9.29	9.27	9.27
<b><math>R^2</math></b>	0.9904	0.9963	0.9943	0.9852	0.9938	0.9852
<b>Mg-MOF-74@GO</b>	<b>25 °C</b>		<b>50 °C</b>		<b>75 °C</b>	
<b><math>F</math> (ml·min<sup>-1</sup>)</b>	<b>140</b>	<b>150</b>	<b>140</b>	<b>150</b>	<b>140</b>	<b>150</b>
<b><math>D_0/r_c^2</math> (s<sup>-1</sup>)</b>	0.556	0.529	0.655	0.629	0.679	0.687
<b>Average<sup>1</sup> <math>D_0/r_c^2</math> (s<sup>-1</sup>)</b>	0.543 ± 0.014		0.642 ± 0.016		0.683 ± 0.029	
<b>Average<sup>1</sup> <math>D_0</math> (m<sup>2</sup>·s<sup>-1</sup>)</b>	3.65 x10 <sup>-15</sup>		4.32 x10 <sup>-15</sup>		4.59 x10 <sup>-15</sup>	
<b><math>L</math></b>	17.97	17.00	20.23	19.00	21.50	21.28
<b><math>\beta_1</math></b>	1.35	1.17	1.35	1.17	1.18	3.14
<b><math>\beta_2</math></b>	4.21	3.44	4.21	3.30	3.31	6.28
<b><math>\beta_3</math></b>	9.25	9.28	9.29	9.15	9.31	9.42
<b><math>R^2</math></b>	0.9991	0.9965	0.9969	0.9955	0.9931	0.9942

<sup>1</sup>Calculated on average from the measurements for purge gas flow rates of 140 ml·min<sup>-1</sup> and 150 ml·min<sup>-1</sup>.

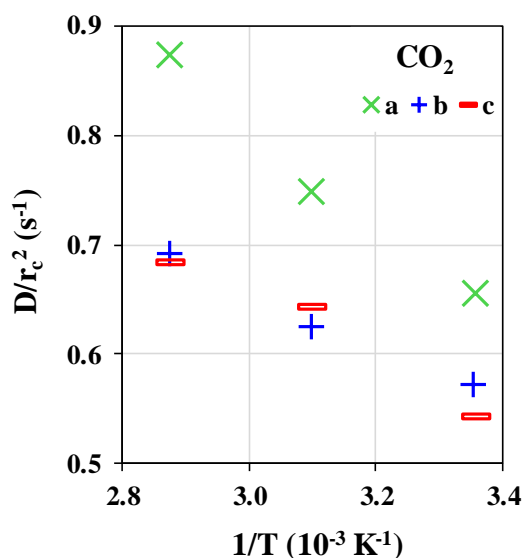


**Figure 5-20.** Arrhenius plots of diffusivity time constant,  $D_0/r_c^2$ , of CO<sub>2</sub> on (a) Mg-MOF-74, (b) Mg-MOF-74@CNT and (c) Mg-MOF-74@GO at 25 °C, 50 °C and 75 °C, deduced by Zero Length Column method.

### 5.7.3. Comparison with manometric method

Table 5-7 compares the values of zero coverage diffusivity time constant  $D_0/r_c^2$  of CO<sub>2</sub> adsorption deduced using manometric method and Zero Length Column method. Despite giving the same arguments such as the sorption rate of CO<sub>2</sub> on both composites is slower than the pristine Mg-MOF-74 and less influenced by the increasing temperature, these two methods produce distinctive order of magnitude of diffusivities. The first explanation that can be proposed is the diffusion coefficient determined by manometric method (designated as effective diffusivity,  $D_{eff}$ ) is modelled by LDF approximation which describes the mass transfer when limited by external barriers. In the case of the mass transfer in MOF crystals, this external resistance is mainly attributed to the external surface (“particle skin” or constriction of pore entry) of the MOF crystals, not to mention the existence of fluid film surrounding the crystals. The kinetic data measured by manometric method cannot satisfied the diffusion model based on Fick’s second law which comes with the assumption that the mass transfer is controlled by the internal resistances, specifically by the micropore barriers in intracrystalline phase of the MOFs. Meanwhile, the advantage of using ZLC method as the measurement technique is that the above-mentioned external barriers are eliminated owing to the elementary volume of adsorbent in addition to the presence of purge gas velocities for which the mass transfer is controlled by a single kinetic regime. Thus, the diffusion coefficient determined by ZLC method can be referred to

intracrystalline diffusivity,  $D_c$ , which is limited by micropore barriers. Secondly, it should be remembered that the sorption rate in manometric measurement is performed in adsorption mode while that in ZLC measurement is performed in desorption mode. In order to have the equality in their values, the adsorption and desorption isotherms should be completely reversible without hysteresis loop indicating the same rate of sorption, which is not the case for the synthesized materials in this study. Earlier in Chapter 4, the hysteresis was observed in the equilibrium isotherms of  $\text{CO}_2$  on all samples even though at low-pressure region. Thirdly, in the desorption mode using ZLC method, the desorbed molecules do not meet the "particle skin" of the solid adsorbent in their diffusion channel, which makes them easier to diffuse outwards. Fourthly, the synthesized materials belong to MOF family which is known with high density of micropores and requires a proper regeneration process to entirely desorb the adsorbate. As investigated in Section 5.6.1, for strongly adsorbed species such as  $\text{CO}_2$ , the synthesized materials need to be outgassed for at least 20 hours with heating or for 60 hours without heating. If the outgassing has not been completed, then the diffusion rate becomes faster due to limited accessibility in the nanoporous body. Knowing that the total desorption of  $\text{CO}_2$  from the materials cannot be accomplished within few seconds, thus the desorption rate measured using ZLC is supposedly attributed to the firstly desorbed molecules which are adsorbed in nanopores with larger confinement. The remaining adsorbate molecules strongly bonded inside micropore take longer to desorb and their desorbing concentration is feeble as a function of time due to slow desorption rate which makes the detection by gas analyser difficult. As a conclusion, both methods of measurement provide valuable results to understand the adsorption kinetics of  $\text{CO}_2$  and  $\text{CH}_4$  on the pristine Mg-MOF-74 as well as its composites for a wide range of pressure and temperature. The difference in the order of magnitude of the calculated diffusion coefficients comes from the different definitions that the parameters represent. Therefore, the diffusivities must be well-defined for the use of more in-depth kinetic studies such as process simulation.

**Table 5-7.** Comparison of the values of zero coverage diffusivity time constant,  $D_0/t_c^2$ , of CO<sub>2</sub> adsorption on Mg-MOF-74, Mg-MOF-74@CNT and Mg-MOF-74@GO deduced using manometric method and Zero Length Column method. The values are presented in s<sup>-1</sup>.

Temperature	Mg-MOF-74		Mg-MOF-74@CNT		Mg-MOF-74@GO	
	Manometric method	ZLC method	Manometric method	ZLC method	Manometric method	ZLC method
25 °C	8.32 x10 <sup>-3</sup>	6.45 x10 <sup>-1</sup>	5.64 x10 <sup>-4</sup>	5.72 x10 <sup>-1</sup>	5.84 x10 <sup>-4</sup>	5.43 x10 <sup>-1</sup>
50 °C	9.47 x10 <sup>-3</sup>	7.49 x10 <sup>-1</sup>	7.84 x10 <sup>-4</sup>	6.25 x10 <sup>-1</sup>	1.04 x10 <sup>-3</sup>	6.42 x10 <sup>-1</sup>
75 °C	1.22 x10 <sup>-2</sup>	8.73 x10 <sup>-1</sup>	9.93 x10 <sup>-4</sup>	6.92 x10 <sup>-1</sup>	1.24 x10 <sup>-3</sup>	6.83 x10 <sup>-1</sup>

## 5.8. Conclusion

The kinetic data of CO<sub>2</sub> and CH<sub>4</sub> adsorptions were first measured on Mg-MOF-74, Mg-MOF-74@CNT and Mg-MOF-74@GO using manometric method at a constant pressure of 0.2 bar, 0.5 bar and 1.5 bar for three different temperatures: 25 °C, 50 °C and 75 °C. The results show that Linear Driving Force (LDF) model can fit the data better than Fickian diffusion model for all samples, signifying that the mass transfer is controlled by external barriers. The diffusion time constant of CO<sub>2</sub> adsorption on Mg-MOF-74 is deduced as 0.00832 s<sup>-1</sup> at 25 °C and 0.00947 s<sup>-1</sup> at 50 °C which are comparable to the literature data. A significant difference between the sorption rates of CO<sub>2</sub> and CH<sub>4</sub> can be observed whereby CO<sub>2</sub> takes longer to reach the equilibrium when compared to CH<sub>4</sub>. As the pressure increases, the diffusion coefficient derived from the LDF model deviates significantly from the value measured at nearly zero adsorption coverage (assumed at 0.2 bar). The values were then corrected by LDF-Darken model and by LDF-Darken-Arrhenius model giving the best agreement with experimental data at pressure above 0.2 bar. This shows an important influence of the release of heat during adsorption on the sorption rate, which appears more significant than slowing caused by progressive occupation of the adsorption sites with increasing concentration of the adsorbed molecules. The kinetic data of CO<sub>2</sub> adsorption were then measured using Zero Length Column method at a fixed concentration of 2 mol% CO<sub>2</sub> diluted in helium for three different temperatures: 25 °C, 50 °C and 75 °C. According to both methods of measurement, the diffusion rate of CO<sub>2</sub> is observed much

slower on both composites in comparison to the pristine Mg-MOF-74 for all temperatures. This can be explained by the more complex features of nanoporous body in both composites providing more heterogeneities in the diffusion channels for the mass transfer of gas adsorbate. The diffusion rate on all synthesized samples increases as a function of adsorption temperature whereby the value is less affected for both composites when compared to the pristine Mg-MOF-74. Both methods of measurement provide valuable results to understand the adsorption kinetics of CO<sub>2</sub> and CH<sub>4</sub> on the synthesized materials for a wide range of pressure and temperature. However, the difference in the order of magnitude of the experimentally deduced diffusivities may be attributed to the different mechanisms controlling the mass transfer during the adsorption and desorption processes, operated under conditions where external barriers may or not have a significant contribution against intracrystalline diffusion. Therefore, more in-depth kinetic studies would be required to implement knowledge-based kinetic models derived from the measured diffusivity data and test their ability to correctly simulate dynamics of adsorption and desorption processes at the bed scale.

For future work of adsorption kinetics, in order to have confirmation on diffusivity at zero adsorption coverage, the diffusion should be measured at very low pressure using manometric method (<1 mbar) which was not feasible by our available instrument. Besides that, in order to have a better comparison to the kinetic data produced by ZLC, the sorption rate of desorption can be also studied using manometric method.

## GENERAL CONCLUSIONS

Carbon dioxide (CO<sub>2</sub>), which is the major contaminant present in raw natural gas and biogas need to be extracted to increase their methane (CH<sub>4</sub>) content and meet the standards of pipeline injection. In recent years, a family of porous materials, magnesium-based metal organic framework (Mg-MOF-74), has opened new perspectives for this purpose thanks to strong adsorption affinity of CO<sub>2</sub> with exposed metallic sites in the crystalline network. This material is a potential good adsorbent candidate for the enrichment in CH<sub>4</sub> of natural gas and biogas by Pressure Swing Adsorption (PSA) processes.

The present study was devoted to examine the CO<sub>2</sub> adsorption performances and separation ability from CH<sub>4</sub> of Mg-MOF-74 materials when doped with carbon nanotubes (CNT) and graphene oxide (GO). The aim was to improve the texture of the materials to promote the diffusion of gas molecules in micropores and their accessibility to the adsorption sites. The thermodynamic and kinetic adsorption properties of the synthesized materials were characterized for the specific cases of CO<sub>2</sub> and CH<sub>4</sub> in a pressure range up to 35 bar and at temperatures between ambient and 75 °C. These data would be necessary in order to assess their performances for the implementation in PSA process that treat mixtures of natural gas or biogas.

Mg-MOF-74 material was synthesized by improved synthesis of solvothermal reaction. Since it was delicate to have a complete evacuation of the reactive medium from MOF product, an improvement to the washing step was proposed by introducing a series of centrifugal separations whose parameters were optimized as well. The sample from the optimized synthesis route showed a significantly higher CO<sub>2</sub> adsorption capacity than that obtained with the sample obtained using the basic protocol. An analogous protocol of optimized synthesis was then applied to the development of the doped materials, Mg-MOF-74@CNT and Mg-MOF-74@GO, in which the reactive precursors was initially mixed with the doping agents. The CNT and GO contents of the composite materials were reported by mass compared to that of the pristine Mg-MOF-74. This content was optimized to a value of ≈0.3 wt%, evaluated by their crystallinity and their adsorption capacity for CO<sub>2</sub> measured at 1 bar and at 25 °C.

The three synthesized materials were characterized by X-ray diffraction, Fourier transform infrared spectrometry, scanning electron microscopy, thermogravimetric analysis and nitrogen physisorption at 77 K. The characterization results showed that the

crystallinity of Mg-MOF-74 was well preserved in the both doped materials. The composites Mg-MOF-74@CNT and Mg-MOF-74@GO showed larger average crystallite sizes, 82 nm and 73 nm respectively compared to 67 nm for the pristine material. Morphological analysis showed that the average particle sizes of Mg-MOF-74@CNT and Mg-MOF-74@GO were also larger, 23  $\mu\text{m}$  and 37  $\mu\text{m}$  respectively compared to 10  $\mu\text{m}$  for the pristine material.

The doping agents consequently favored the agglomeration of polycrystalline structure of the material, combining with the networks of MOFs or stacking on the surface of the crystallites. The modification of the structure by adding carbon-based agents did not only give better thermal stability, but also developed the microporosity of the materials. The BET specific surface area was thus increased from 1111  $\text{m}^2\cdot\text{g}^{-1}$  for Mg-MOF-74 to 1340  $\text{m}^2\cdot\text{g}^{-1}$  (increased by +21%) and 1393  $\text{m}^2\cdot\text{g}^{-1}$  (+25%) for Mg-MOF-74@CNT and Mg-MOF-74@GO, respectively. The analysis of nitrogen adsorption isotherms by the Density Functional Theory (DFT) indicated an increase in the volume of micropores, being consistent with the specific surface area of the materials: from 0.40  $\text{cm}^3\cdot\text{g}^{-1}$  for the Mg-MOF-74 at 0.48  $\text{cm}^3\cdot\text{g}^{-1}$  (+18%) and 0.49  $\text{cm}^3\cdot\text{g}^{-1}$  (+24%) for Mg-MOF-74@CNT and Mg-MOF-74@GO, respectively.

The equilibria of single component adsorption of  $\text{CO}_2$  and  $\text{CH}_4$  were studied on Mg-MOF-74 and its doped materials. The equilibrium data measured at low pressure (at 1 bar) and at 25  $^\circ\text{C}$  indicated an improvement in the  $\text{CO}_2$  adsorption capacity of 18 mol% and 23 mol% for Mg-MOF-74@CNT and Mg-MOF-74@GO, respectively with respect to the pristine material. These improvements were related to the increase in specific surface area and microporous volume in both doped materials. Likewise, a 27 mol% and 36 mol% increase in  $\text{CH}_4$  adsorption capacity was measured for Mg-MOF-74@CNT and Mg-MOF-74@GO, respectively. The performance of the materials for gas separation was evaluated not only in terms of working capacity but also in terms of separation efficiency. Based on Ideal Adsorbed Solution Theory (IAST), the selectivity in equimolar mixture of  $\text{CO}_2$  and  $\text{CH}_4$  was evaluated. Up to 1 bar and at 25  $^\circ\text{C}$ , Mg-MOF-74@GO material appeared to give the best compromise between capacity and high selectivity of adsorption with respect to  $\text{CO}_2$ .

The sorption equilibrium data were then measured at a high-pressure range (up to 35 bar) and for different temperatures: 25  $^\circ\text{C}$ , 50  $^\circ\text{C}$  and 75  $^\circ\text{C}$ . The improvement in terms of adsorption capacity for  $\text{CO}_2$  was observed in this pressure region for both composite

materials compared to the pristine material, and this improvement was increased with the increase in temperature. The adsorption capacity of CO<sub>2</sub> on the pristine material was significantly degraded with the rise in the temperature of the system, while it was less affected for both doped materials. This property became interesting for process implementation, because it indicated a lesser influence of local heating resulting from exothermic adsorption process on the dynamic capacity of the beds.

The selectivity in mixture of CO<sub>2</sub> and CH<sub>4</sub> was predicted from IAST model in the pressure range limited to 10 bars taking into account the shape of the isotherms. At 50 °C and 75 °C, the composite materials simultaneously offered better working capacity combined with better separation efficiency, when compared to the pristine material. The experimental data for isosteric heat of adsorption of gases showed that these were likely to vary depending on the adsorption coverage on the adsorbents and that they were below 76 kJ·mol<sup>-1</sup>. The higher values obtained for CO<sub>2</sub> compared to CH<sub>4</sub> were attributed to the polarizability and the greater accessibility of the CO<sub>2</sub> molecules inside the micropores.

The sorption kinetics of CO<sub>2</sub> and CH<sub>4</sub> on the synthesized materials were studied by using manometric and Zero Length Column experiments, at temperatures of 25 °C, 50 °C and 75 °C. The kinetic data were adjusted to the models of Linear Driving Force and according to Fick's law of diffusion, by taking into account the influence of the temperature and the adsorption coverage which affected the diffusivity of gas in the pressure range beyond the Henry's law region. The results showed that the diffusion rates of the CO<sub>2</sub> molecules in both composite materials were significantly slower than those in the pristine material. This could be explained by the more complex features of nanoporous body in both composites providing more heterogeneities in the diffusion channels for the mass transfer of gas adsorbate. The diffusion rates on all materials increased as a function of adsorption temperature whereby the value was less affected for both composites when compared to the pristine material. On the other hand, both composite materials revealed a higher kinetic selectivity of CO<sub>2</sub> with respect to CH<sub>4</sub> at all temperatures.

Both kinetic measurement methods provided valuable results to understand the adsorption kinetics of CO<sub>2</sub> and CH<sub>4</sub> on the materials for a wide range of pressures and temperatures. However, the difference in the order of magnitude of the experimentally deduced diffusivities might be attributed to the different mechanisms controlling the mass transfer during the adsorption and desorption processes, operated under conditions where external barriers might or not had a significant contribution against intracrystalline

diffusion. Therefore, more in-depth kinetic studies would be required to implement knowledge-based kinetic models derived from the measured diffusivity data and test their ability to correctly simulate dynamics of adsorption and desorption processes at the bed scale.

The performances shown by Mg-MOF-74 doped carbon materials encouraged further research towards a better understanding of these structures and the development of MOF-carbon materials as potential candidates for the separation of CO<sub>2</sub> from CO<sub>2</sub>/CH<sub>4</sub> gas streams in the context of the purification of natural gas and biogas.

Finally, we believe that the findings of this project can contribute to some context in the development of MOF materials for CO<sub>2</sub>/CH<sub>4</sub> separation by PSA.

---

## PERSPECTIVES

As the studies are completed, there are several perspectives that can be highlighted.

In the context of synthesis of materials, seeing that CNT substitution follows the optimum concentration on the basis of GO for the purpose of comparison between MOF/GO and MOF/CNT composites, thus another optimization study to determine CNT concentration in MOF/CNT composite can be proposed. Moreover, pore textural properties can be characterized as a function of doping agent concentration to better understand their role in development of micropore in the composites. For industrial application, simplicity of synthesis and upscaling of MOF production must be further explored to produce larger amount of MOFs (by increasing reactants amount) with the same solvent volume, but having the same quality as the present synthesis. In order to reduce the resistance to external mass transfer, MOF materials which are produced in powder form must be shaped into pallets. The research on this work is ongoing at Universiti Teknologi PETRONAS for MOF-74 material. It is also interesting to study the influence of compactness density of MOF crystals on CO<sub>2</sub> adsorption capacity. Moreover, some modifications of MOF structure can also be proposed to improve their resistivity to humidity.

In the context of characterization of materials, in order to confirm a complete pore activation of MOFs, it is suggested to verify the absence of DMF solvent in the MOF samples by detecting a significant characteristic peak of DMF at wavenumber 1650 cm<sup>-1</sup> using FTIR analysis. Besides that, more in-depth morphological study can be done using high-resolution TEM to better understand their crystal growth and carbon incorporation. In addition, knowing that GO is a graphite form while CNT is a fullerene form of carbon that give different synergetic effects with the MOF crystal, so another form of carbon allotropic such as cubic diamond (e.g. carbon fiber) can be suggested. Furthermore, the micropore of the synthesized materials can be further characterized using argon physisorption analysis, having less polarity compared to nitrogen, to study the effect of polarizability on the adsorption sites. Based on our preliminary study, the exploitation of raw isotherm data at high resolution shows that the adsorption sites having the same interaction with both nitrogen and argon. Regarding the estimation of dead volumes, method of extrapolation using Dubinin-Radushkevitch model can be proposed to compare with the present method.

In the context of adsorption equilibria and kinetics, more appropriate isotherm modelling can be proposed by fixing only one reference temperature and finding the correct

relation between the constants of the isotherm model and temperature. Also, in order to have confirmation on diffusivity at zero adsorption coverage, the diffusion should be measured at very low pressure using manometric method ( $<1$  mbar). Besides that, in order to have a better comparison to the kinetic data produced by ZLC, the sorption rate of desorption can be also studied using manometric method. In a bigger perspective, co-adsorption of  $\text{CO}_2$  and methane can be performed so that we do not only depend on the IAST system to evaluate the selectivity and working capacity of the adsorbent. It is important to study the influence of humidity on adsorption sites passivation and to include the presence of water vapor during  $\text{CO}_2$  adsorption to examine their competition.

In the context of PSA development, breakthrough curves can be simulated based on the appropriate modelling of equilibrium and kinetic adsorption data which were produced experimentally. Besides that, PSA cycle should be optimized by taking into account the real operational conditions in gases production.

## Annex I

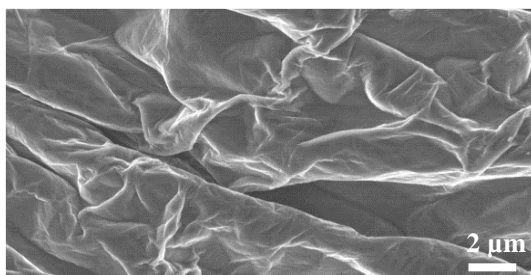


**Figure A-1.** Micrograph image of monolayer graphene oxide used in Mg-MOF-74@GO synthesis.

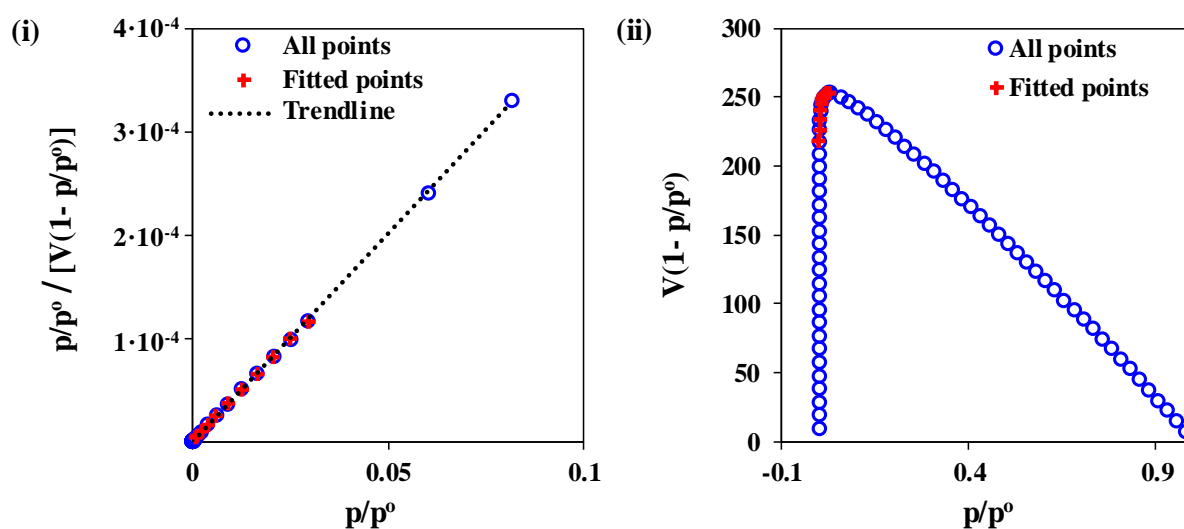


**Figure A-2.** (i) BET plot and (ii) Rouquerol plot of  $N_2$  adsorption isotherm on Mg-MOF-74 at 77 K for the determination of BET specific surface area.

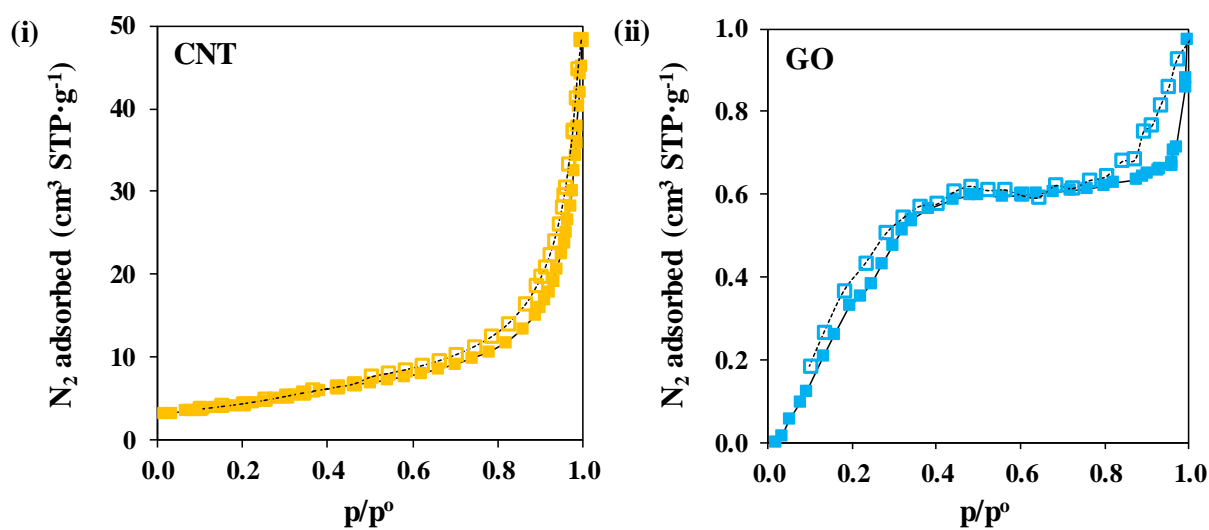


**Figure A-3.**  $N_2$  ads/desorption isotherms at 77 K of (i) CNT and (ii) GO. Solid and open symbols represent the adsorption and desorption of  $N_2$ , respectively

## Annex II

As mentioned in Section 3.7.5, MOF researchers have been using different models to assess micropore size in MOFs from physisorption isotherms seen that no present models were designed for complex features of MOFs. The classical macroscopic thermodynamic models assume that pores are filled with a liquid adsorptive with bulk-like properties which is not the case in micropores [170]. However, this has been addressed in modern approaches that are based on Density Functional Theory (DFT) and molecular simulation, making them reliable to fulfill this purpose [170]. Several published works have proposed to use conventional DFT [146] and Horvath-Kawazoe (HK) [19] models. However, one should keep in mind that these approaches are rather qualitative and can only be used for the sake of results comparison. Here, the average pore sizes and micropore volumes were calculated using DFT for a geometry of cylinder for N<sub>2</sub>-cylindrical pores-oxide surface interaction in the domain of  $10^{-7} \leq p/p^{\circ} \leq 0.99$ , as presented in Figure A-4. The same characterization was carried out using Horvath-Kawazoe for a geometry of Saito-Foley cylinder for zeolite-N<sub>2</sub> interaction with Cheng-Yang correction in the domain of  $10^{-7} \leq p/p^{\circ} \leq 0.1$ , as presented in Figure A-5. Based on DFT calculation, pore size distributions of all synthesized materials show a bimodal micropore distribution and a small fraction of larger micropores. Mg-MOF-74 exhibits the average pore sizes at 7.7 Å/10.9 Å, while the composites display at 7.4 Å/10.6 Å and 7.6 Å/10.6 Å for Mg-MOF-74@CNT and Mg-MOF-74@GO, respectively. Both composites demonstrate higher intensities of pore volumes but improved more for Mg-MOF-74@GO compared to Mg-MOF-74@CNT. These average pore sizes were close to that simulated from Mg-MOF-74 molecular structure as mentioned above. The total pore volumes measured at  $p/p_0=0.99$  showed the increment from  $0.422 \text{ cm}^3 \cdot \text{g}^{-1}$  ( $V_{\text{micropore}}=0.397 \text{ cm}^3 \cdot \text{g}^{-1}$ ) measured for Mg-MOF-74 to  $0.498 \text{ cm}^3 \cdot \text{g}^{-1}$  ( $V_{\text{micropore}}=0.481 \text{ cm}^3 \cdot \text{g}^{-1}$ ) and  $0.523 \text{ cm}^3 \cdot \text{g}^{-1}$  ( $V_{\text{micropore}}=0.486 \text{ cm}^3 \cdot \text{g}^{-1}$ ) for Mg-MOF-74@CNT and Mg-MOF-74@GO, respectively. The same results comparison can be observed using HK model calculation. This comforts the increase in BET specific surface area for both composites as deduced previously. The outcome is attributed to the synergetic incorporation of Mg-MOF-74 and the carbon-based compound creating new formation of structural micropores. Pore textural properties of all synthesized materials are recapitulated in Table A-1.

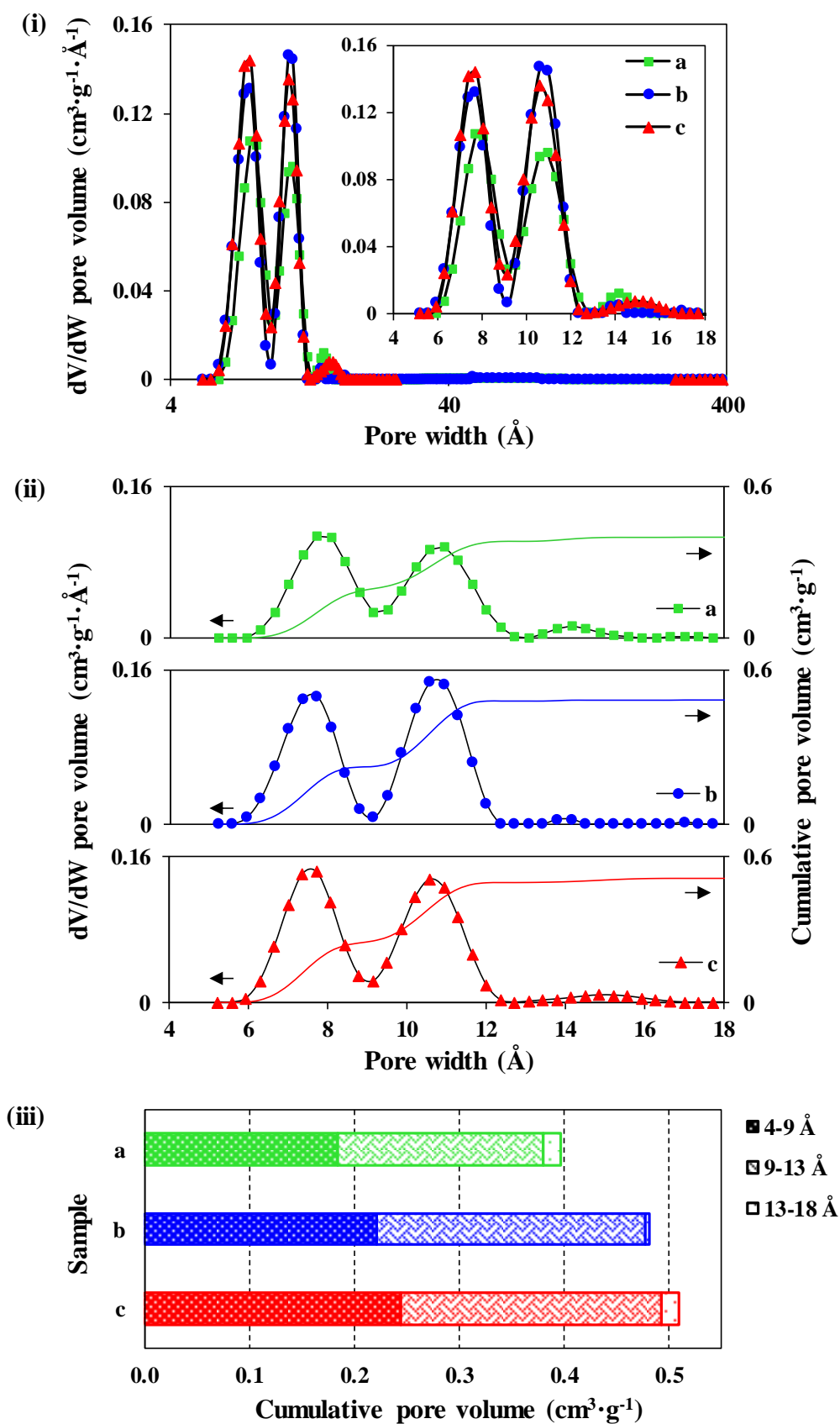


**Figure A-4.** (i)–(ii) Pore size distributions and (iii) cumulative pore volumes of (a) Mg-MOF-74, (b) Mg-MOF-74@CNT and (c) Mg-MOF-74@GO calculated by Density Functional Theory.

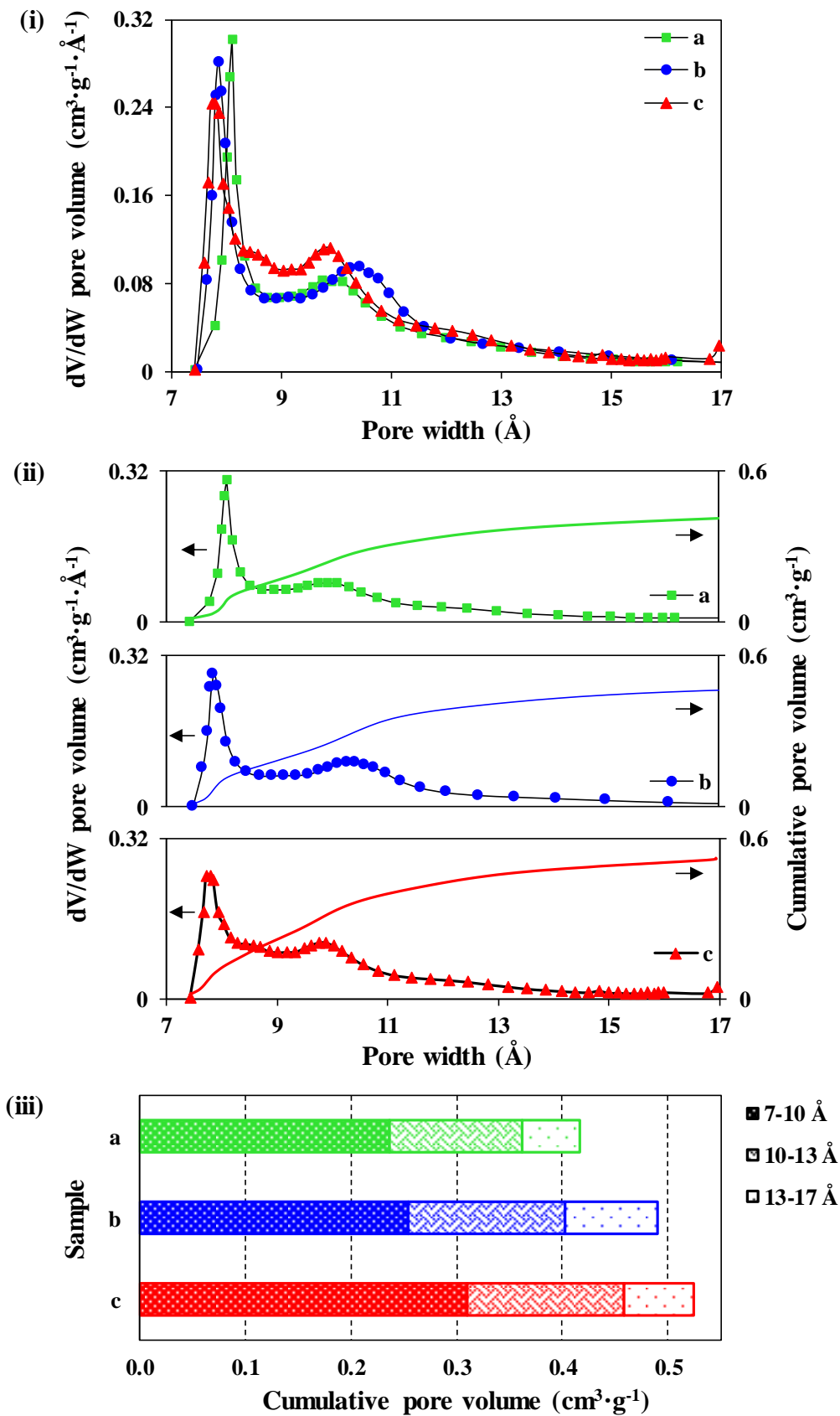


**Figure A-5.** (i)–(ii) Pore size distributions and (iii) cumulative pore volumes of (a) Mg-MOF-74, (b) Mg-MOF-74@CNT and (c) Mg-MOF-74@GO calculated by Horvath-Kawazoe model.

**Table A-1.** Pore textural properties of Mg-MOF-74, Mg-MOF-74@CNT and Mg-MOF-74@GO.

	<b>Pristine Mg-MOF-74</b>	<b>Mg-MOF-74 @CNT</b>	<b>Mg-MOF-74 @GO</b>
<b>Density Functional Theory calculation<sup>1</sup></b>			
<b>Average pore sizes:</b>			
<b>d<sub>1</sub> (Å)</b>	7.7	7.4	7.6
<b>d<sub>2</sub> (Å)</b>	10.9	10.6	10.6
<b>Total pore volumes (cm<sup>3</sup>·g<sup>-1</sup>)</b>	0.422	0.498	0.523
<b>Micropore volumes (cm<sup>3</sup>·g<sup>-1</sup>)</b>	0.397	0.481	0.486
<b>Horvath-Kawazoe calculation<sup>2</sup></b>			
<b>Average pore sizes:</b>			
<b>d<sub>1</sub> (Å)</b>	8.1	7.8	7.8
<b>d<sub>2</sub> (Å)</b>	10.0	10.0	9.8
<b>Micropore volumes (cm<sup>3</sup>·g<sup>-1</sup>)</b>	0.416	0.503	0.525

<sup>1</sup>For  $10^{-7} \leq p/p^0 \leq 0.99$ <sup>2</sup>For  $10^{-7} \leq p/p^0 \leq 0.1$

### Annex III

In general, the analysis of raw isotherms describing gas adsorption by porous solids allows the estimation of adsorption capacity at given pressure for the sake of comparison of different materials and qualitatively determine the type of the isotherm related to the mechanism of adsorption. Much more precious qualitative information about adsorption capacity variation with the pressure and associated energetic parameters determined by the nature of interaction on gas–solid interface can be accessed owing to experimental data modeling. A wide variety of isotherm models have been formulated in terms of three fundamental approaches [95, 96]. The kinetics consideration is the first approach in which the adsorption equilibrium is defined as a state of dynamic equilibrium with both adsorption and desorption rates are equal (e.g. Langmuir isotherm), thus it is known as “Langmuir approach” [95, 96]. The thermodynamics (based on Gibbs thermodynamic equation) is the basis of the second approach from which numerous extended forms of adsorption isotherms have been derived (e.g. Volmer, Fowler-Guggenheim and Hill–de Boer isotherms), and it is also known as “Gibbs approach” [95, 96]. For examples: (i) Langmuir describes localized adsorption with no interaction between molecules, (ii) Volmer describes mobile adsorption with no interaction between molecules, (iii) Fowler-Guggenheim describes localized adsorption with interaction between molecules, and, (iv) Hill–de Boer describes mobile adsorption and interaction between molecules, all of which are the fundamental approaches from which different equations of state are derived, apart from the Henry’s law isotherm [95]. While the third approach comes from the potential theory idea in generating isotherm characteristic curves (e.g. Dubinin–Radushkevitch and Dubinin–Astakhov isotherms) [95, 96].

Besides that, there are a number of empirical or semi-empirical equations that have been derived and employed in adsorption studies for describing adsorption equilibrium. Some equations are reliable to describe the adsorption of gases below the capillary condensation region such as Freundlich, Sips, Toth, Unilan and Dubinin–Radushkevitch, as well as Brunauer–Emmett–Teller for multilayering adsorption [95]. Considering a microporous material with adsorption energy distributions, the following isotherm models are suggested to describe ideal monolayer adsorption on heterogeneous adsorbents [181]: (i) Langmuir, (ii) Freundlich, (iii) Sips, (iv) Toth, and, (v) Dubinin–Radushkevitch. The relevance of these models can also be verified by fitting the experimental data with (vi) multilayer BET isotherm model to prove a non-multilayered adsorption if the fitting is

---

deviated. Moreover, knowing that Mg-MOF-74 exhibits primary and secondary adsorption sites, (vii) dual-site Langmuir and (viii) dual-site Sips isotherms appear as further convenient models to consider. Therefore, the equations, adjustable parameters and asymptotic properties representative of thermodynamic consistency of the isotherm models retained for this study are summarized in Table A-2.

**Table A-2.** Isotherm models tested in this study, summarized from [95, 96, 205, 235, 236].

Isotherm	Equation	Eq.	Adjustable parameter	Asymptotic properties	
				Henry's constant at low $p$	Adsorption maximum at high $p$
Henry's law (H)	$q(p) = K \cdot p$	A-1	$K$	Yes = $K$	No
Langmuir (L)	$q(p) = q_{sat} \frac{b_L \cdot p}{1 + b_L \cdot p}$	A-2	$q_{sat}, b_L$	Yes = $b_L \cdot q_{sat}$	Yes = $q_{sat}$
Freundlich (F)	$q(p) = b_F \cdot p^{1/n}$	A-3	$b_F, n$	No	No
Sips (S)	$q(p) = q_{sat} \frac{(b_S \cdot p)^{1/n}}{1 + (b_S \cdot p)^{1/n}}$	A-4	$q_{sat}, b_S, n$	No	Yes = $q_{sat}$
Toth (T)	$q(p) = q_{sat} \frac{b_T \cdot p}{[1 + (b_T \cdot p)^{1/n}]^n}$	A-5	$q_{sat}, b_T, n$	Yes = $b_T \cdot q_{sat}$	Yes = $q_{sat}$
Dubinin–Radushkevitch (DR)	$q(p) = q_{sat} \exp \left[ - \left( \frac{R \cdot T}{E} \ln \frac{p^0}{p} \right)^{n=2} \right]$ where, $E = \beta \cdot E_o = 1/\sqrt{2 \cdot b_{DR}}$	A-6	$q_{sat}, E$	No	Yes = $q_{sat}$
Multilayer BET (B)	$q(p) = q_{sat} \frac{b_L \cdot p}{(1 - b_B \cdot p) + (1 - b_L \cdot p - b_B \cdot p)}$	A-7	$q_{sat}, b_L, b_B$	Yes = $b_L \cdot q_{sat}$	Yes = $q_{sat}$
Dual-site Langmuir	$q(p) = q_{sat,1} \frac{b_{L,1} \cdot p}{1 + b_{L,1} \cdot p} + q_{sat,2} \frac{b_{L,2} \cdot p}{1 + b_{L,2} \cdot p}$	A-8	$q_{sat,1}, b_{L,1}, q_{sat,2}, b_{L,2}$	Yes = $b_{L,1} \cdot q_{sat,1} + b_{L,2} \cdot q_{sat,2}$	Yes = $q_{sat,1} + q_{sat,2}$
Dual-site Sips	$q(p) = q_{sat,1} \frac{(b_{S,1} \cdot p)^{1/n_1}}{1 + (b_{S,1} \cdot p)^{1/n_1}} + q_{sat,2} \frac{(b_{S,2} \cdot p)^{1/n_2}}{1 + (b_{S,2} \cdot p)^{1/n_2}}$	A-9	$q_{sat,1}, b_{S,1}, n_1, q_{sat,2}, b_{S,2}, n_2$	No	Yes = $q_{sat,1} + q_{sat,2}$

Where,

$q$  (mol·kg<sup>-1</sup>): The amount of adsorbate adsorbed per unit mass of adsorbent at equilibrium

$p$  (bar): The total gas pressure

$K$  (mol·kg<sup>-1</sup>·bar<sup>-1</sup>): The Henry's constant expressed as a proportionality factor of amount of adsorbate adsorbed per unit mass of adsorbent to adsorbate gas pressure at equilibrium

$q_{sat}$  (mol·kg<sup>-1</sup>): The theoretical saturation capacity of adsorbate per unit mass of adsorbent

$b$  (bar<sup>-1</sup>): The isotherm constant representing the theoretical affinity parameter of adsorption site–adsorbate

$1/n$  or  $n$ : The empirical heterogeneity factor of adsorption system

$E$  ( $\text{kJ}\cdot\text{mol}^{-1}$ ): Characteristic energy of adsorption  
 $E_o$  ( $\text{kJ}\cdot\text{mol}^{-1}$ ): Characteristic energy of adsorption towards a reference adsorbate  
 $\beta$ : Similarity constant where  $\beta = 1$  for a reference adsorbate in gas phase  
 $R$  ( $\text{kJ}\cdot\text{mol}^{-1}\cdot\text{K}^{-1}$ ): Gas constant,  $R = 8.314 \text{ J}\cdot\text{mol}^{-1}\cdot\text{K}^{-1}$ .  
 $T$  (K): Temperature  
 $p^o$  (bar): Gas saturation pressure at temperature of adsorption  
Suffix 1 and 2 indicate adsorption sites 1 and 2, respectively

Langmuir isotherm was developed in 1916 [237] assuming: (i) localized adsorption - the molecules adsorb on a fixed number of individual sites, (ii) monolayer (one-molecule thick) adsorption - each site can accommodate one molecule, (iii) all adsorption sites are energetically identical possessing equal affinity for the adsorbate, (iv) no interaction between the adsorbed molecules, and, (v) no interaction with neighboring sites thus no transmigration of the adsorbate in the plane of the solid surface [95, 96]. The deviation of experimental data from Langmuir model was investigated by Barrer *et al.* (1961) proving that it was attributed to adsorption sites heterogeneity and adsorbate intermolecular interactions [223]. At low pressures (or concentrations), Langmuir model reduces to the Henry's law, but it introduces an additional parameter  $b_L$  ( $\text{bar}^{-1}$ ) referred as Langmuir constant that describes the affinity of the adsorbate with the adsorbent [205]. The Henry's constant at zero adsorption coverage  $K$  of a Langmuir isotherm can so be calculated as  $b_L \cdot q_{sat}$  ( $\text{mol}\cdot\text{kg}^{-1}\cdot\text{bar}^{-1}$ ) [95], and this was considered as such in several adsorption studies of  $\text{CO}_2$  and  $\text{CH}_4$  in Mg-MOF-74 [19, 23]. As the occupied adsorption sites increases, the isotherm constant  $b_L$  is inversely related to the increasing pressure [205]. The isotherm model is characterized by a plateau which is the equilibrium saturation point,  $q_{sat}$  ( $\text{mol}\cdot\text{kg}^{-1}$ ), at which no further adsorption can take place after each site being occupied with one molecule [96].

Freundlich isotherm was developed in 1906 [238] being the earliest empirical equation used to describe the equilibrium data [95, 96]. The isotherm assumes a non-ideal and reversible adsorption which is not restricted to the formation of monolayer and can be applied to multilayer adsorption with non-uniform distribution of adsorption affinities over the solid surface [96]. The parameter  $n$  is usually greater than unity so that the closer  $1/n$  gets to unity, the more heterogeneous is the adsorbent system [96]. That heterogeneity could stem from solid surface or adsorbate molecule or a combination of both [95]. Anyhow, Freundlich isotherm exhibits some limitations to its application whereby the equation does not describe the Henry's law for low pressures and does not have a finite

limit with a maximum adsorption capacity for high pressures [95, 235]. Therefore, it is generally valid for a narrow range of the adsorption data.

Recognizing the problem of the continuing increase in the amount adsorbed with an increase in pressure, Langmuir–Freundlich (or Sips) isotherm was developed in 1948 [239] proposing an equation similar to Freundlich isotherm but having a finite saturation limit [95]. Also dedicated for heterogeneous adsorbents, Sips isotherm combines Langmuir and Freundlich models reducing to Freundlich equation at low pressures while predicting a limit for the monolayer adsorption capacity as given by Langmuir isotherm at high pressures [96]. For that reason, Sips isotherm still shares the same disadvantage with Freundlich isotherm as neither of them have the right behavior at low pressures, and do not describe properly the Henry's law domain [95].

In view of the asymptotic limitations of Freundlich and Sips isotherms, Toth equation which is also an extended form of Langmuir was developed in 1971 [240] satisfying both low- and high-end boundaries [95, 235]. Toth isotherm describes an adsorption with sub-monolayer coverage [95], supposing an asymmetrical quasi-Gaussian energy distribution, with most of the sites has an adsorption energy lower than the peak (maximum) or mean value [96]. Exhibiting the same definition of heterogeneity parameter ( $1/n$ ) as the previous isotherms, usually marked as ( $1/t$ ), Toth equation reduces to Langmuir isotherm when  $n$  equals to unity [95]. If the value of  $n$  (or  $t$ ) deviates further away from unity, the adsorbent is said to be more heterogeneous [95]. As same as Langmuir model, the Henry' constant at zero adsorption coverage of a Toth isotherm can be calculated as  $b_T \cdot q_{sat}$  ( $\text{mol} \cdot \text{kg}^{-1} \cdot \text{bar}^{-1}$ ) [95].

The potential theory isotherm, Dubinin–Radushkevitch model, is a semi-empirical equation which was developed in 1960 [241] originally for subcritical vapors in microporous solids where the adsorption process follows a pore filling mechanism [95]. The isotherm is generally applied to express the adsorption mechanism with a Gaussian energy distribution onto a heterogeneous surface [96]. The model fits the data at high pressures and in the intermediate range of pressure as well, but does not predict the Henry's law at low pressures [95, 96, 236]. One of the unique features of Dubinin–Radushkevitch model is that it is a temperature-dependent isotherm having a saturation limit when the equilibrium gas pressure,  $p$  (bar), is close to the gas saturation pressure,  $p^o$  (bar), at the temperature of adsorption,  $T$  (K) [95, 96, 236]. The model also introduces an additional parameter,  $E$  ( $\text{kJ} \cdot \text{mol}^{-1}$ ), which is the characteristic energy of adsorption of the solid surface

defined by the mean free energy per adsorbate molecules for removing the molecules from the adsorption sites [95, 96, 236].

Brunauer–Emmett–Teller (BET) isotherm is a theoretical equation developed in 1938 [242], most widely applied for multilayer physisorption isotherms [96]. As in Langmuir model, the model assumes energetically identical adsorption sites on the surface and no interaction between the adsorbed molecules [95, 205]. The range of validity of this theory is approximately between 0.05 and 0.35 times the gas relative pressure,  $p/p^o$ . Multilayer BET equation consists of two isotherm constants,  $b_L$  ( $\text{bar}^{-1}$ ) representing the Langmuir constant for the first layer of adsorbate molecules in direct contact with the surface, and,  $b_B$  ( $\text{bar}^{-1}$ ) which is the constant for the second and upper layers of adsorbate molecules [205].

In addition, dual-site Langmuir and dual-site Sips isotherms are the attempts to model an adsorbent surface with energetic heterogeneity assuming two different types of adsorption sites [205]. The assumptions made behind dual-site Langmuir (or dual-site Sips) model is the same as those for the single Langmuir (or Sips) model, except that each adsorption site is considered to be independent implying that dual-site Langmuir (or dual-site Sips) model is the sum of the single Langmuir (or Sips) models derived for the two types of sites [205]. Exhibiting an asymptotic property at low pressures just like Langmuir model, the Henry's constant at zero adsorption coverage of the dual-site Langmuir model can be calculated as  $b_{L,1} \cdot q_{sat,1} + b_{L,2} \cdot q_{sat,2}$  ( $\text{mol} \cdot \text{kg}^{-1} \cdot \text{bar}^{-1}$ ). While the saturation capacity of the dual-site Langmuir and dual-site Sips models are expressed as  $q_{sat,1} + q_{sat,2}$  ( $\text{mol} \cdot \text{kg}^{-1}$ ). In different adsorption studies, dual-site Langmuir [218, 243-245] and dual-site Sips [42, 148, 219, 246-249] isotherm models have been demonstrated capable of properly fitting the equilibrium data of various gas components in MOFs, zeolites and silicates.

In order to verify the consistency and theoretical assumptions of an isotherm model to equilibrium experimental data, two errors functions called coefficient of determination,  $R^2$ , (Eq.A-10) and sum squares errors,  $ERRSQ$ , (Eq.A-11) are used in this study and defined as follows [96]. The fitting is adjusted by maximizing  $R^2$  approaching 1, minimizing  $ERRSQ$  approaching 0.

$$R^2 = \frac{\sum(q_{exp} - \overline{q_{model}})^2}{\sum(q_{exp} - \overline{q_{model}})^2 + (q_{exp} - q_{model})^2} \quad (\text{Eq.A-10})$$

$$ERRSQ = \sum_{i=1}^n (q_{exp} - q_{model})_i^2 \quad (\text{Eq. A-11})$$

where,  $q_{exp}$  and  $q_{model}$  ( $\text{mol}\cdot\text{kg}^{-1}$ ) are the amount of adsorbate adsorbed per unit mass of adsorbent at equilibrium measured by experiment and calculated by the model, respectively, while  $\overline{q_{model}}$  is the mean value of  $q_{model}$ .

## Annex IV

The fitting of isotherm modelling of CO<sub>2</sub> adsorption on Mg-MOF-74, Mg-MOF-74@CNT and Mg-MOF-74@GO at different pressures and temperatures using different isotherm models and the summary of their fitted parameters:

- **Figure A-6. Table A-3.** CO<sub>2</sub> adsorption isotherms on Mg-MOF-74, Mg-MOF-74@CNT and Mg-MOF-74@GO up to 1 bar at 25 °C fitted to different isotherm models.
- **Figure A-7. Table A-4.** CO<sub>2</sub> adsorption isotherms on Mg-MOF-74, Mg-MOF-74@CNT and Mg-MOF-74@GO up to 10 bar at 25 °C fitted to different isotherm models.
- **Figure A-8. Table A-5.** CO<sub>2</sub> adsorption isotherms on Mg-MOF-74, Mg-MOF-74@CNT and Mg-MOF-74@GO up to 10 bar at 50 °C fitted to different isotherm models.
- **Figure A-9. Table A-6.** CO<sub>2</sub> adsorption isotherms on Mg-MOF-74, Mg-MOF-74@CNT and Mg-MOF-74@GO up to 10 bar at 75 °C fitted to different isotherm models.

$p = 1 \text{ bar}$ ,  $T = 25 \text{ }^\circ\text{C}$

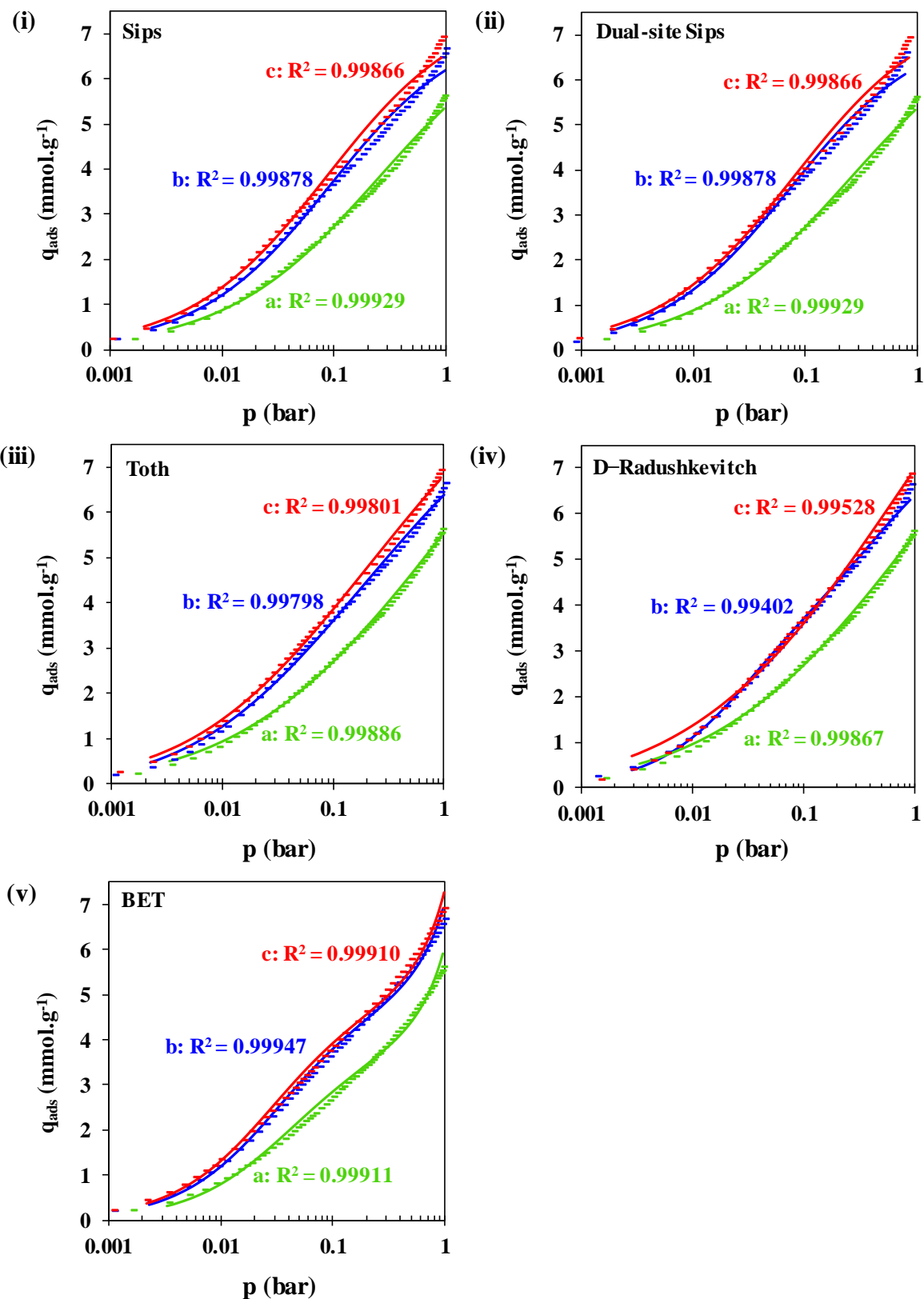


**Figure A-6.** CO<sub>2</sub> adsorption isotherms on (a) Mg-MOF-74, (b) Mg-MOF-74@CNT and (c) Mg-MOF-74@GO up to 1 bar at 25 °C, fitted to different isotherm models providing their respective coefficient of determination,  $R^2$ .

**Table A-3.** Fitted parameters of different models for CO<sub>2</sub> adsorption isotherms of Mg-MOF-74, Mg-MOF-74@CNT and Mg-MOF-74@GO up to 1 bar at 25 °C.

$p = 1 \text{ bar}, T = 25 \text{ }^{\circ}\text{C}$				
Isotherm model	Fitted parameters	Mg-MOF-74	Mg-MOF-74 @CNT	Mg-MOF-74 @GO
BET (B)	<i>ERRSQ</i>	0.01065	0.00923	0.01669
	$R^2$	0.99911	0.99947	0.99910
	$q_{sat}$ (mmol·g <sup>-1</sup> )	3.71	4.71	4.75
	$b_B$ (bar <sup>-1</sup> )	26.58	33.19	38.21
	$b_L$ (bar <sup>-1</sup> )	0.41	0.34	0.37
Sips (S)	<i>ERRSQ</i>	0.00846	0.02133	0.02477
	$R^2$	0.99929	0.99878	0.99866
	$q_{sat}$ (mmol·g <sup>-1</sup> )	7.62	7.23	7.69
	$b_S$ (bar <sup>-1</sup> )	3.99	11.07	10.90
	$1/n$	0.63	0.73	0.71
Dual-site Sips	<i>ERRSQ</i>	0.00846	0.02133	0.02477
	$R^2$	0.99929	0.99878	0.99866
	$q_{sat,1}$ (mmol·g <sup>-1</sup> )	$6.85 \times 10^{-16}$	$2.27 \times 10^{-14}$	$3.37 \times 10^{-14}$
	$b_{S,1}$ (bar <sup>-1</sup> )	0.29	$5.85 \times 10^{-6}$	$5.14 \times 10^{-11}$
	$1/n_1$	$7.71 \times 10^{-4}$	$4.19 \times 10^{-16}$	$2.74 \times 10^{-14}$
	$q_{sat,2}$ (mmol·g <sup>-1</sup> )	7.62	7.23	7.69
	$b_{S,2}$ (bar <sup>-1</sup> )	3.99	11.07	10.90
	$1/n_2$	0.63	0.73	0.71
	$q_{sat,TOT}$ (mmol·g <sup>-1</sup> )	7.62	7.23	7.69
Toth (T)	<i>ERRSQ</i>	0.00272	0.00707	0.00834
	$R^2$	0.99886	0.99798	0.99801
	$q_{sat}$ (mmol·g <sup>-1</sup> )	15.83	10.21	11.39
	$b_T$ (bar <sup>-1</sup> )	55.08	53.61	68.05
	$1/n$	0.27	0.40	0.37
Dubinin–Radushkevitch	<i>ERRSQ</i>	0.00317	0.01954	0.01850
	$R^2$	0.99867	0.99402	0.99528
	$q_{sat}$ (mmol·g <sup>-1</sup> )	9.35	10.35	10.75
	$E$ (kJ·mol <sup>-1</sup> )	14.38	15.53	15.61

$p = 10 \text{ bar}$ ,  $T = 25 \text{ }^\circ\text{C}$

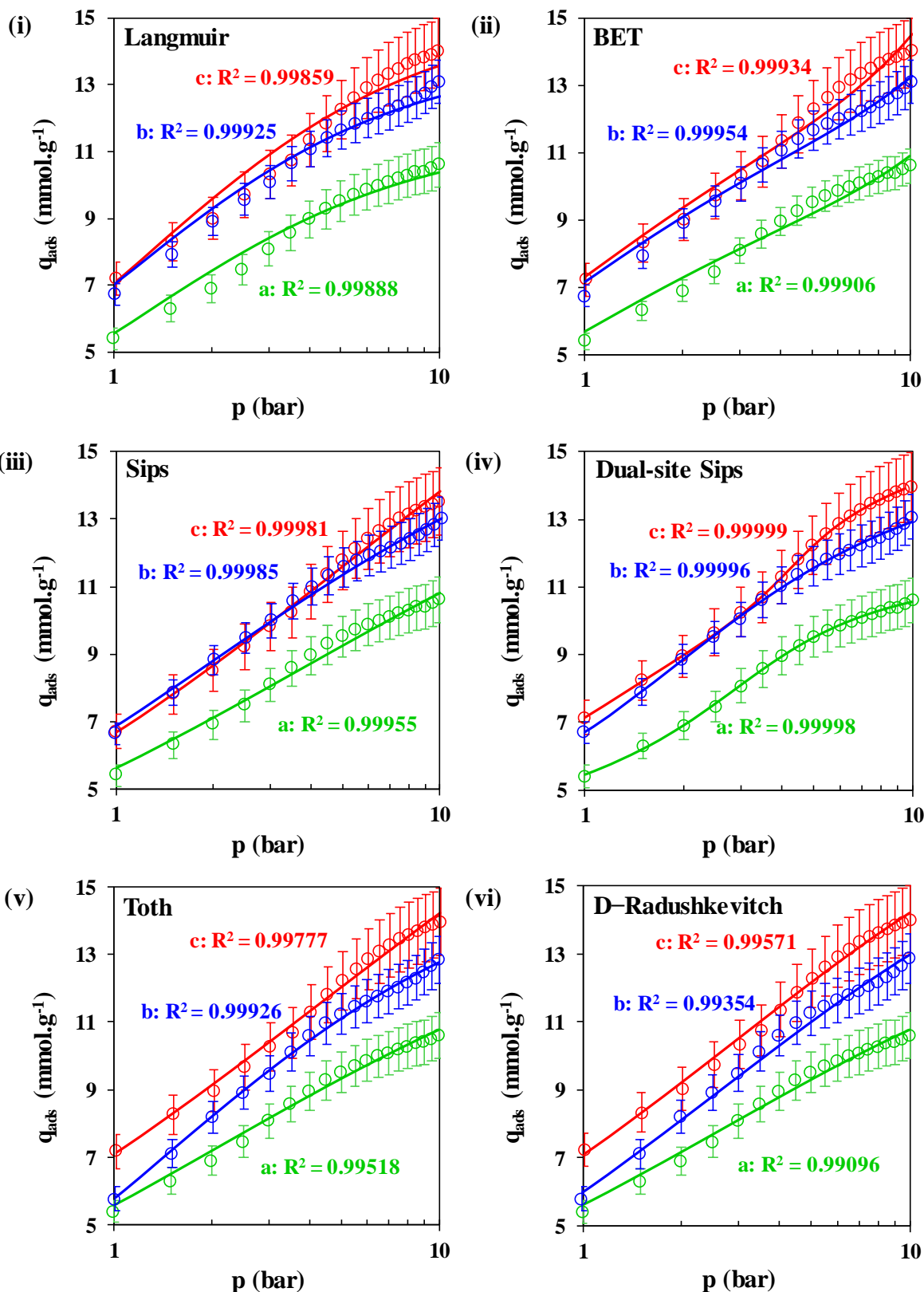


**Figure A-7.** Average curve of CO<sub>2</sub> adsorption isotherms of (a) Mg-MOF-74, (b) Mg-MOF-74@CNT and (c) Mg-MOF-74@GO up to 10 bar at 25 °C with average relative errors bars, ARE, fitted to different isotherm models providing their respective coefficient of determination,  $R^2$ .

**Table A-4.** Fitted parameters of different models for CO<sub>2</sub> adsorption isotherms of Mg-MOF-74, Mg-MOF-74@CNT and Mg-MOF-74@GO up to 10 bar at 25 °C.

<b><math>p = 10 \text{ bar}, T = 25 \text{ }^\circ\text{C}</math></b>				
<b>Isotherm model</b>	<b>Fitted parameters</b>	<b>Mg-MOF-74</b>	<b>Mg-MOF-74 @CNT</b>	<b>Mg-MOF-74 @GO</b>
BET (B)	<i>ERRSQ</i>	0.06826	0.04957	0.08394
	$R^2$	0.99906	0.99954	0.99934
	$q_{sat}$ (mmol.g <sup>-1</sup> )	8.98	11.21	11.43
	$b_B$ (bar <sup>-1</sup> )	1.28	1.36	1.36
	$b_L$ (bar <sup>-1</sup> )	0.02	0.02	0.02
Langmuir (L)	<i>ERRSQ</i>	0.08113	0.06426	0.17957
	$R^2$	0.99888	0.99925	0.99859
	$q_{sat}$ (mmol.g <sup>-1</sup> )	11.06	13.38	14.67
	$b_L$ (bar <sup>-1</sup> )	0.83	0.95	0.82
Sips (S)	<i>ERRSQ</i>	0.03301	0.02025	0.02453
	$R^2$	0.99955	0.99985	0.99981
	$q_{sat}$ (mmol.g <sup>-1</sup> )	16.17	16.74	23.10
	$b_S$ (bar <sup>-1</sup> )	0.27	0.50	0.20
	$1/n$	0.58	0.69	0.56
Dual-site Sips	<i>ERRSQ</i>	0.00131	0.00647	0.00074
	$R^2$	0.99998	0.99996	0.99999
	$q_{sat,1}$ (mmol.g <sup>-1</sup> )	8.12	9.61	14.51
	$b_{S,1}$ (bar <sup>-1</sup> )	1.83	0.66	0.81
	$1/n_1$	0.57	0.39	0.72
	$q_{sat,2}$ (mmol.g <sup>-1</sup> )	3.37	6.51	1.66
	$b_{S,2}$ (bar <sup>-1</sup> )	0.34	0.50	0.23
	$1/n_2$	2.54	1.44	5.05
Toth (T)	<i>ERRSQ</i>	0.03143	0.00732	0.02593
	$R^2$	0.99518	0.99926	0.99777
	$q_{sat}$ (mmol.g <sup>-1</sup> )	15.20	15.35	25.69
	$b_T$ (bar <sup>-1</sup> )	1.55	1.03	2.22
	$1/n$	0.53	0.76	0.40
Dubinin–Radushkevitch	<i>ERRSQ</i>	0.02886	0.03091	0.02510
	$R^2$	0.99096	0.99354	0.99571
	$q_{sat}$ (mmol.g <sup>-1</sup> )	12.25	15.04	16.42
	$E$ (kJ.mol <sup>-1</sup> )	11.05	11.19	10.83

$p = 10 \text{ bar}$ ,  $T = 50 \text{ }^\circ\text{C}$

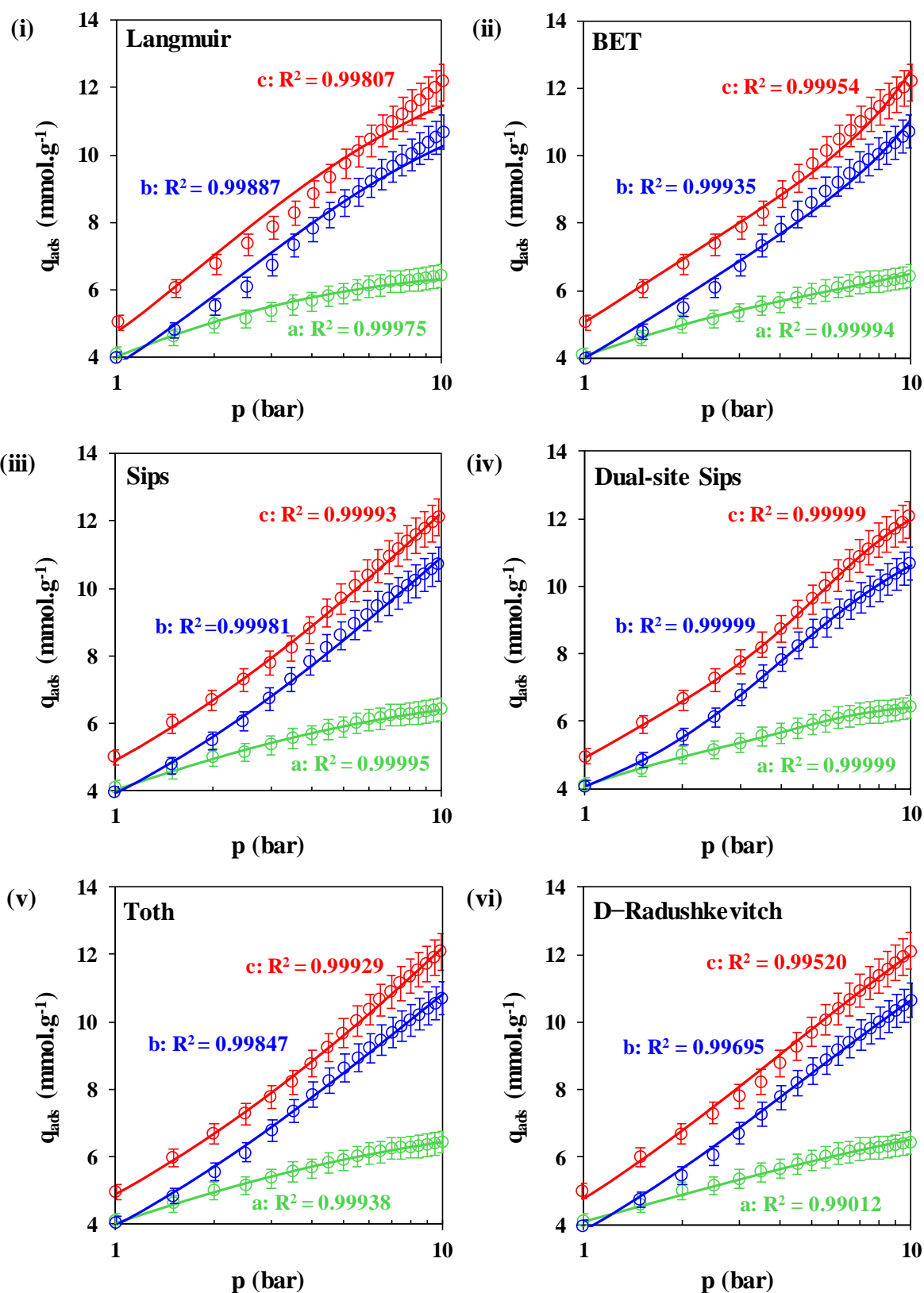


**Figure A-8.** Average curve of  $\text{CO}_2$  adsorption isotherms of (a) Mg-MOF-74, (b) Mg-MOF-74@CNT and (c) Mg-MOF-74@GO up to 10 bar at  $50 \text{ }^\circ\text{C}$  with average relative errors bars,  $ARE$ , fitted to different isotherm models providing their respective coefficient of determination,  $R^2$ .

**Table A-5.** Fitted parameters of different models for CO<sub>2</sub> adsorption isotherms of Mg-MOF-74, Mg-MOF-74@CNT and Mg-MOF-74@GO up to 10 bar at 50 °C.

<b><math>p = 10 \text{ bar}, T = 50 \text{ }^\circ\text{C}</math></b>				
<b>Isotherm model</b>	<b>Fitted parameters</b>	<b>Mg-MOF-74</b>	<b>Mg-MOF-74 @ CNT</b>	<b>Mg-MOF-74 @ GO</b>
BET (B)	<i>ERRSQ</i>	0.00195	0.04525	0.04183
	$R^2$	0.99994	0.99935	0.99954
	$q_{sat}$ (mmol.g <sup>-1</sup> )	6.20	8.81	9.37
	$b_B$ (bar <sup>-1</sup> )	1.84	0.78	1.06
	$b_L$ (bar <sup>-1</sup> )	0.01	0.03	0.03
Langmuir (L)	<i>ERRSQ</i>	0.00802	0.07831	0.17459
	$R^2$	0.99975	0.99887	0.99807
	$q_{sat}$ (mmol.g <sup>-1</sup> )	6.72	12.63	13.54
	$b_L$ (bar <sup>-1</sup> )	1.51	0.43	0.54
Sips (S)	<i>ERRSQ</i>	0.00158	0.01287	0.00647
	$R^2$	0.99995	0.99981	0.99993
	$q_{sat}$ (mmol.g <sup>-1</sup> )	7.25	22.59	27.70
	$b_S$ (bar <sup>-1</sup> )	1.32	0.09	0.07
	$1/n$	0.79	0.63	0.56
Dual-site Sips	<i>ERRSQ</i>	0.00043	0.00086	0.00116
	$R^2$	0.99999	0.99999	0.99999
	$q_{sat,1}$ (mmol.g <sup>-1</sup> )	6.01	8.85	10.31
	$b_{S,1}$ (bar <sup>-1</sup> )	1.99	3.14	0.93
	$1/n_1$	1.09	1.62	2.87
	$q_{sat,2}$ (mmol.g <sup>-1</sup> )	0.64	3.43	3.62
	$b_{S,2}$ (bar <sup>-1</sup> )	0.21	0.24	0.18
	$1/n_2$	3.75	2.25	0.87
Toth (T)	<i>ERRSQ</i>	0.00139	0.01262	0.00709
	$R^2$	0.99938	0.99847	0.99929
	$q_{sat}$ (mmol.g <sup>-1</sup> )	7.46	24.64	51.07
	$b_T$ (bar <sup>-1</sup> )	2.52	0.56	1.56
	$1/n$	0.69	0.45	0.27
Dubinin–Radushkevitch	<i>ERRSQ</i>	0.00752	0.01581	0.02832
	$R^2$	0.99012	0.99695	0.99520
	$q_{sat}$ (mmol.g <sup>-1</sup> )	13.45	13.77	15.14
	$E$ (kJ.mol <sup>-1</sup> )	7.33	9.17	9.60

$p = 10 \text{ bar}$ ,  $T = 75 \text{ }^\circ\text{C}$

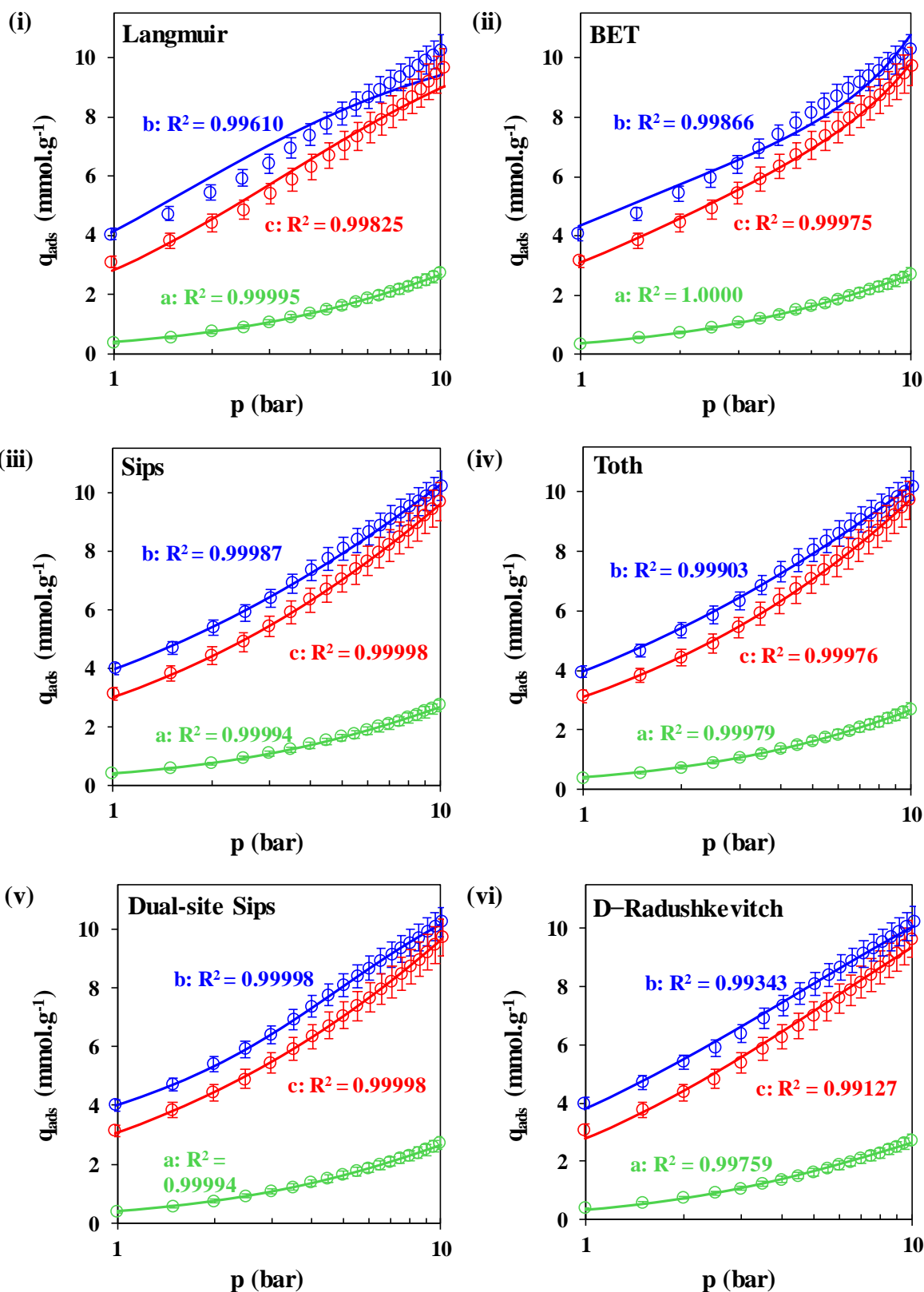


**Figure A-9.** Average curve of  $\text{CO}_2$  adsorption isotherms of (a) Mg-MOF-74, (b) Mg-MOF-74@CNT and (c) Mg-MOF-74@GO up to 10 bar at  $75 \text{ }^\circ\text{C}$  with average relative errors bars,  $ARE$ , fitted to different isotherm models providing their respective coefficient of determination,  $R^2$ .

**Table A-6.** Fitted parameters of different models for CO<sub>2</sub> adsorption isotherms of Mg-MOF-74, Mg-MOF-74@CNT and Mg-MOF-74@GO up to 10 bar at 75 °C.

<b><math>p = 10 \text{ bar}, T = 75 \text{ }^\circ\text{C}</math></b>				
<b>Isotherm model</b>	<b>Fitted parameters</b>	<b>Mg-MOF-74</b>	<b>Mg-MOF-74 @ CNT</b>	<b>Mg-MOF-74 @ GO</b>
BET (B)	<i>ERRSQ</i>	0.00015	0.07879	0.01723
	$R^2$	0.99995	0.99866	0.99975
	$q_{sat}$ (mmol.g <sup>-1</sup> )	6.92	7.02	7.13
	$b_B$ (bar <sup>-1</sup> )	0.06	1.37	0.68
	$b_L$ (bar <sup>-1</sup> )	0.00	0.04	0.03
Langmuir (L)	<i>ERRSQ</i>	0.00016	0.21798	0.09950
	$R^2$	0.99995	0.99610	0.99825
	$q_{sat}$ (mmol.g <sup>-1</sup> )	7.71	11.00	11.96
	$b_L$ (bar <sup>-1</sup> )	0.05	0.59	0.31
Sips (S)	<i>ERRSQ</i>	0.00018	0.00654	0.00336
	$R^2$	0.99994	0.99987	0.99998
	$q_{sat}$ (mmol.g <sup>-1</sup> )	7.28	32.68	30.34
	$b_S$ (bar <sup>-1</sup> )	0.06	0.02	0.03
	$1/n$	1.02	0.52	0.63
Dual-site Sips	<i>ERRSQ</i>	0.00019	0.00109	0.00339
	$R^2$	0.99994	0.99998	0.99998
	$q_{sat,1}$ (mmol.g <sup>-1</sup> )	0.00	8.65	20.31
	$b_{S,1}$ (bar <sup>-1</sup> )	0.06	4.09	0.51
	$1/n_1$	0.00	1.49	0.85
	$q_{sat,2}$ (mmol.g <sup>-1</sup> )	7.27	3.87	4.88
	$b_{S,2}$ (bar <sup>-1</sup> )	0.50	0.20	0.04
	$1/n_2$	1.01	1.24	0.70
Toth (T)	<i>ERRSQ</i>	0.00014	0.00698	0.00160
	$R^2$	0.99979	0.99903	0.99976
	$q_{sat}$ (mmol.g <sup>-1</sup> )	9.72	72.90	1097.86
	$b_T$ (bar <sup>-1</sup> )	0.04	1.60	0.39
	$1/n$	0.86	0.22	0.13
Dubinin–Radushkevitch	<i>ERRSQ</i>	0.00135	0.02891	0.04050
	$R^2$	0.99759	0.99343	0.99127
	$q_{sat}$ (mmol.g <sup>-1</sup> )	4.48	12.90	12.67
	$E$ (kJ.mol <sup>-1</sup> )	6.37	9.35	8.42

## Annex V

The kinetic data of CH<sub>4</sub> adsorption on Mg-MOF-74, Mg-MOF-74@CNT and Mg-MOF-74@GO measured using manometric method and Zero Length Column method:

- **Figure A-10.** Fractional adsorption uptakes of CH<sub>4</sub> on Mg-MOF-74@CNT with their profile temperature at 0.2 bar, 0.5 bar and 1.5 bar for 25 °C, 50 °C and 75 °C using manometric method.
- **Figure A-11.** Fractional adsorption uptakes of CH<sub>4</sub> on Mg-MOF-74@GO with their profile temperature at 0.2 bar, 0.5 bar and 1.5 bar for 25 °C, 50 °C and 75 °C using manometric method.
- **Figure A-12.** Fractional desorption curves of CH<sub>4</sub> on Mg-MOF-74 for different purge gas flow rates at 25 °C using Zero Length Column method. Adsorption equilibrium was initially achieved for a feed gas of 100% mol CH<sub>4</sub>.

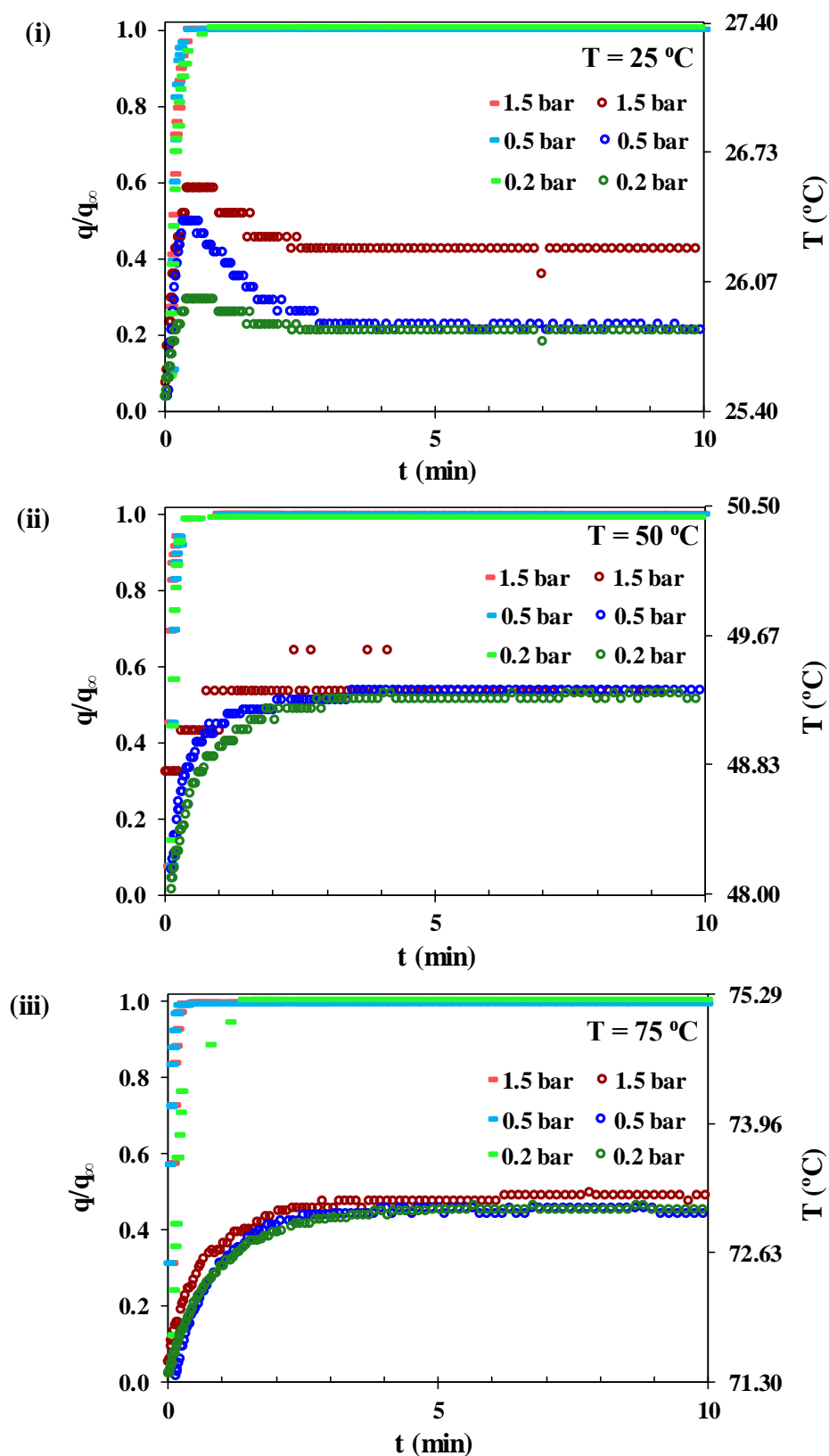


**Figure A-10.** Fractional adsorption uptakes of  $\text{CH}_4$  on  $\text{Mg-MOF-74@CNT}$  with their profile temperature at 0.2 bar, 0.5 bar and 1.5 bar for (i) 25 °C, (ii) 50 °C and (iii) 75 °C.

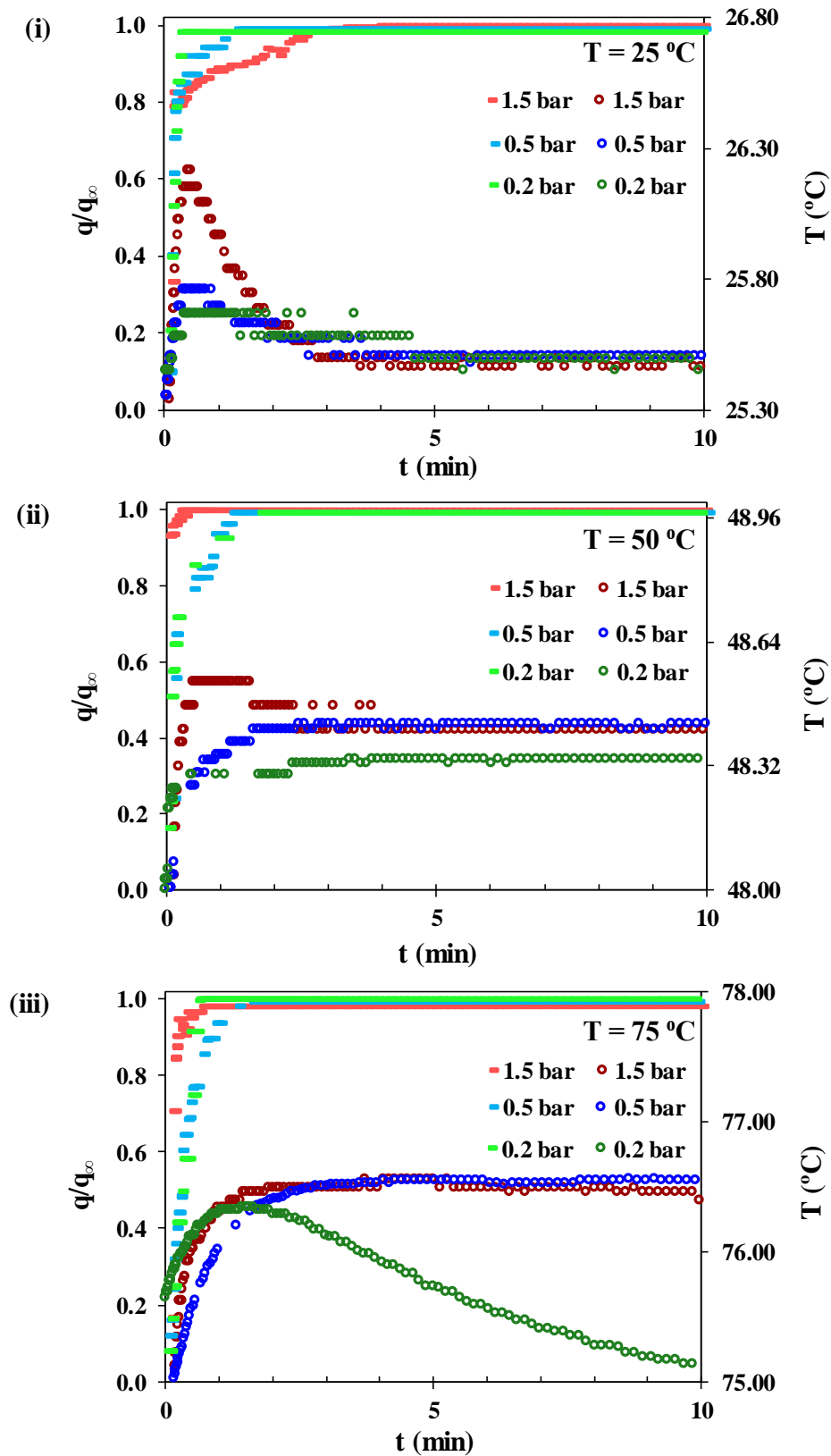


**Figure A-11.** Fractional adsorption uptakes of  $\text{CH}_4$  on Mg-MOF-74@GO with their profile temperature at 0.2 bar, 0.5 bar and 1.5 bar for (i) 25 °C, (ii) 50 °C and (iii) 75 °C.

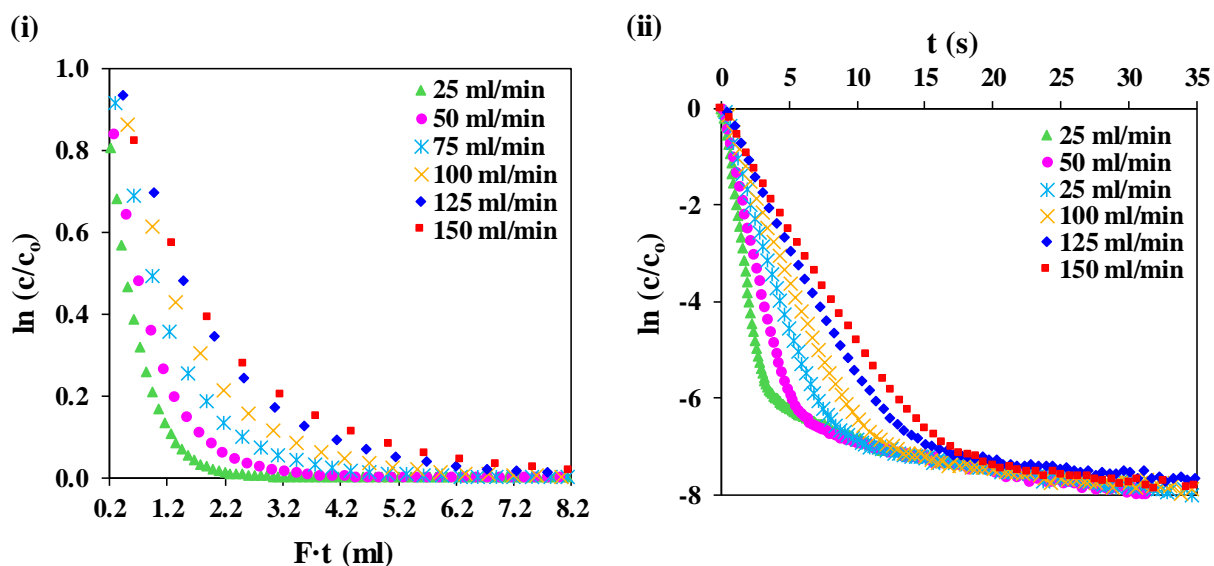


**Figure A-12.** (i) Fractional desorption curves of CH<sub>4</sub> on Mg-MOF-74 as a function of purge gas volume for different purge gas flow rates at 25 °C, and, (ii) logarithmic fractional desorption curves of CH<sub>4</sub> on Mg-MOF-74 as a function of time for different purge gas flow rates at 25 °C. Adsorption equilibrium was initially achieved for a feed gas of 100% mol CH<sub>4</sub>.

## Annex VI

### *a. Measurement of adsorption isotherm at low pressures*

Operational procedure of outgassing using BelprepII degas stations and adsorption isotherms measurement up to 1 bar using BELSORP-mini II manometric equipment from MicrotracBEL:

#### *Sample Outgassing*

1. Mass of sample cell was measured before adding sample.
2. About 200 mg sample was placed in sample cell.
3. Sample cell was connected to vacuum tube and placed inside heater in pre-treatment machine.
4. Heating temperature was set to 150 °C.
5. Heater and vacuum pump were switched on.
6. Leave sample overnight until residual pressure stabilization was achieved.
7. After outgassing was done, heater was switched off.
8. Sample cell was left cooling but not disconnected from vacuum tube.
9. Sample cell was purged by N<sub>2</sub> gas. Vacuum pump was turned off automatically.
10. Sample cell was removed from pre-treatment machine.
11. Mass of sample cell containing sample was measured.
12. Sample mass was calculated:  $m_{\text{cell+sample}} - m_{\text{cell}}$ .

#### *Isotherm Measurement*

1. Sample cell was installed to manometric equipment with addition of reference cell.
2. Gas supply valves were opened for desired gas probe (CO<sub>2</sub> or CH<sub>4</sub>).
3. Gas pipelines and adsorption system was purged manually using CO<sub>2</sub> (or CH<sub>4</sub>).
4. Gas flow valves were adjusted to prevent too-fast or too-slow gas flow.
5. Dead volume of sample cell was calibrated using helium expansion at 25 °C, V<sub>2</sub>.
6. Gas type was selected (CO<sub>2</sub> or CH<sub>4</sub>) and gas temperature was set to 25 °C.
7. A number of measurement points were set by fixing gas set pressure,  $p$ , each point.
8. Dewar vessel was filled in with water at 25 °C.
9. Measurement was run.

### ***b. Measurement of adsorption isotherm at high pressures***

Operational procedure of outgassing and adsorption isotherms measurement up to 35 bar using PCT-Pro manometric equipment from SETARAM:

#### ***Sample Preparation***

1. Sample mass was measured, noted  $m_{\text{before}}$ .
2. About 1.5 g sample was placed in adsorption cell. Spacers were added to fill in the remaining volume.
3. Isolation coating and thermocouple were installed to adsorption cell.

#### ***Gas Supply Lines Purging***

1. New gas was labeled in ***Select Gas*** before purging, after changing feed gas.
2. All gas supply valves and feed gas valve to adsorption cell were closed before purging.
3. Gas supply pipelines were evacuated and purged using gas probe (CO<sub>2</sub> or CH<sub>4</sub>) in automatic mode. Surveillance was required until the end of the process.

#### ***System and Sample Purging***

1. All gas supply valves were closed before purging while feed gas valve to adsorption cell was left opened.
2. Reservoirs, adsorption cell and system pipelines were evacuated and purged using gas probe (CO<sub>2</sub> or CH<sub>4</sub>) in automatic mode. Surveillance was required until the end of the process.

#### ***Sample Outgassing***

1. Adsorption system was pumped and put under vacuum.
2. Heater was switched on. Sample temperature was gradually increased to 150 °C.
3. Sample was left overnight until residual pressure stabilization was achieved.

#### ***Dead Volume Calibration***

1. Direct Measurement was chosen.
2. Dead volumes,  $V_{2,T_1}$  and  $V_{2,T_2}$ , were calibrated by Helium expansion at  $T_1$  and  $T_2$ , respectively, for several cycles to ensure reproducibility.

3. Standard deviation of measurement was also noted.

### *Isotherm Measurement*

- Case A: Adsorption isotherm of CO<sub>2</sub> on MOFs from 0 to 40 bar at T<sub>2</sub>
  - Case B: Desorption isotherm of CO<sub>2</sub> on MOFs from 40 to 0 bar at T<sub>2</sub>
  - Case C: Adsorption isotherm of CH<sub>4</sub> on MOFs from 0 to 40 bar at T<sub>2</sub>
  - Case D: Desorption isotherm of CH<sub>4</sub> on MOFs from 40 to 0 bar at T<sub>2</sub>
1. Sample temperature was set to T<sub>2</sub> and left for stabilization.
  2. Gas supply valves were opened for desired gas probe (CO<sub>2</sub> or CH<sub>4</sub>).
  3. Measurement was executed as follows:
    - Hy-Data window → Measure PCT → Vent and Evacuate System → BYPASS → Measurement → Initial Parameters and Procedures.
    - Initial Parameters and Procedures:
      - ✓ Type of gas:
        - Case A, B: CO<sub>2</sub>
        - Case C, D: CH<sub>4</sub>
      - ✓ Experiment Pressure Settings:
        - Initial sample pressure, P<sub>S,O</sub>:
          - Case A, C: 0 bar
          - Case B, D: 40 bar
        - Reservoir pressure, P<sub>R</sub>:
          - Case A, C: must be > ΔP(t=0)<sup>51</sup>

$$\Delta P_{\text{ADS,CO}_2}(t=0) = 0.5 \text{ bar (optimized)}$$

$$\Delta P_{\text{ADS,CH}_4}(t=0) = 2 \text{ bar (optimized)}$$
          - Case B, D: must be < [P<sub>S,O</sub> - ΔP(t=0)]
 
$$\Delta P_{\text{DES,CO}_2}(t=0) = 4 \text{ bar (can be any)}$$

$$\Delta P_{\text{DES,CH}_4}(t=0) = 4 \text{ bar (can be any)}$$
        - ✓ Concentration Calculation Method: DIRECT
          - V<sub>2,T<sub>2</sub></sub> → calibrated value inserted
          - V<sub>2,T<sub>1</sub></sub> → calibrated value inserted
      - CONTINUE → Set Up window.
      - Set Up window:

<sup>51</sup> ΔP(t=0) is the first increment in gas probe set pressure for pressurizing the reservoir.

- ✓ Mode adsorption (or desorption)
- ✓ Sample ID
- ✓ Data File Name
- ✓ Sample Description
- ✓ Mass sample [g]:  $m_{\text{before}}$
- SELECT → Experimental Parameters Frame.
- Experimental Parameters Frame:
  - ✓ Reservoir volume: 162.89 cc (**selected**) for highly adsorbing system
  - ✓ Asymptotic Time Step<sup>52</sup>:
    - $dt^{53}$  [sec] = 20 (**optimized**)
    - Time Step Constant<sup>54</sup>: 1.5 (**selected**) for poorly kinetic adsorbing system
  - ✓ Equilibrium Test<sup>55</sup>:
    - Rate Limit<sup>56</sup> [wt%/min x 1000]: 0.05 or 0.1 (**optimized**)
    - Test Start<sup>57</sup> [min]: 5, 10, 15 or 20 (**optimized**) depends on ads/des and gas probe
  - ✓ Heater
    - Case A, B, C, D: Adsorption T [°C] =  $T_2$
    - Case A, B, C, D: Desorption T [°C] =  $T_2$
    - Adsorption Tolerance T [°C]: 20°C (**by default**)
    - Desorption Tolerance T [°C]: 20°C (**by default**)
  - ✓ P-Tolerance<sup>58</sup> [%]: 5, 10, 15 or 20, to control (decrease) as  $\Delta P(t)$  increases
  - ✓ PCT Pressure Limit → YES:

<sup>52</sup> Asymptotic Time Step allows to collect data efficiently; data is collected most rapidly at the beginning of measurement when the most rapid sorption occurs, it becomes less and less frequent as time progresses.

<sup>53</sup>  $dt$  represents Time Interval in seconds between pressure measurements.

<sup>54</sup> Time Step Constant determines how quick the Asymptotic Time Step process increases in time between two data points. Time Interval asymptotically approaches  $dt$  as time progresses.

<sup>55</sup> Equilibrium Test parameters act when equilibrium is achieved. The instrument will move on to next aliquot (injection) when a test of equilibrium conditions agrees with Equilibrium Test parameters.

<sup>56</sup> Rate Limit represents average change in the sorption rate over the last ten readings. Once the rate drops below this value, the measurement will stop and move on to next aliquot.

<sup>57</sup> Test Start allows the measurement to stabilize before the Equilibrium Test function is applied. The cycle is described as: Injection of aliquot > sorption reach equilibrium > system stabilize in Test Start duration > Rate Limit applied > move on to next aliquot if sorption rate is below Rate Limit.

<sup>58</sup> P-Tolerance is a parameter that acts before equilibrium and measurement. The instrument will wait until the measured pressure falls within this percentage band around Set Pressure. When achieved, it continues to next step.

- Case A, C:  $P_{LIM} = 40$  bar
  - Case B, D:  $P_{LIM} = 0$  bar
- ✓ Set Pressure  $\rightarrow \Delta P(t)$ :
- Case A:  $\Delta P_{ADS,CO_2}(t=0) = 0.5$  bar (**optimized**)  
 $\Delta P_{ADS,CO_2}(t)$  to control (increase) as time progresses
  - Case B:  $\Delta P_{DES,CO_2}(t=0) = 4$  bar (**can be any**)  
 $\Delta P_{DES,CO_2}(t)$  can fix equal to  $\Delta P_{DES,CO_2}(t=0)$
  - Case C:  $\Delta P_{ADS,CH_4}(t=0) = 1$  bar (**optimized**)  
 $\Delta P_{ADS,CH_4}(t)$  to controlled (increased) as time progresses
  - Case D:  $\Delta P_{DES,CH_4}(t=0) = 4$  bar (**can be any**)  
 $\Delta P_{DES,CH_4}(t)$  can fix equal to  $\Delta P_{DES,CH_4}(t=0)$
- *CONTINUE > CONTINUE > CONTINUE.*
4. After measurement, sample was outgassed and weighted, noted  $m_{after}$ <sup>59</sup>.

---

<sup>59</sup> The value was used to correct the data measured using  $m_{before}$ . Due to sample loss during manipulation which might give inaccurate value of  $m_{after}$ ,  $m_{before} - m_{after}$  which represents humidity loss after outgassing could be compared to TGA weight loss % to confirm the measured value of  $m_{after}$ .

## References

- [1] EIA, *International energy outlook 2016*, Report, United States Energy Information Administration, Forrestal Building, Washington, DC, 2016.
- [2] A. Demirbas, "Chapter 2: Natural gas," *Methane Gas Hydrate*, pp. 57-76: Springer New York, Science & Business Media, 2010.
- [3] M. J. Economides, and D. Wood, "The state of natural gas," *Journal of Natural Gas Science and Engineering*, vol. Vol. 1, no. No. 1-2, pp. 1-13, 2009.
- [4] N. Scarlat, J.-F. Dallemand, and F. Fahl, "Biogas: Developments and perspectives in Europe," *Renewable Energy*, vol. 129, pp. 457-472, 2018.
- [5] M. Tagliabue, D. Farrusseng, S. Valencia, S. Aguado, U. Ravon, C. Rizzo, A. Corma, and C. Mirodatos, "Natural gas treating by selective adsorption: Material science and chemical engineering interplay," *Chemical Engineering Journal*, vol. 155, no. 3, pp. 553-566, 2009.
- [6] J. Wilcox, "Chapter 1 : Introduction to carbon capture," *Carbon Capture*, pp. 1-34, Department of Energy Resources Engineering, Stanford University: Springer New York, 2012.
- [7] S. Biruh, and H. Mukhtar, "Chapter 9: Natural gas purification technologies - Major advances for CO<sub>2</sub> separation and future directions," *Advance in Natural Gas Technology*, H. Al-Megren, ed., pp. 235-270, Universiti Teknologi Petronas: INTECH 2012.
- [8] IPPC, "Chapter 3: Capture of CO<sub>2</sub>," *Special Report: Carbon dioxide Capture and Storage*, B. Metz, O. Davidson, H. C. De Coninck, M. Loos, and L. A. Meyer, ed., pp. 105-178, Cambridge University Press, UK and NY USA Intergovernmental Panel on Climate Change, 2005.
- [9] M. Eddaoudi, J. Kim, N. Rosi, D. Vodak, J. Wachter, M. O'keeffe, and O. M. Yaghi, "Systematic design of pore size and functionality in isorecticular MOFs and their application in methane storage," *Science*, vol. 295, no. 5554, pp. 469-472, 1999.
- [10] I. Choi, Y. E. Jung, S. J. Yoo, J. Y. Kim, H.-J. Kim, C. Y. Lee, and J. H. Jang, "Facile synthesis of M-MOF-74 (M= Co, Ni, Zn) and its application as an electrocatalyst for electrochemical CO<sub>2</sub> conversion and H<sub>2</sub> production," *Journal of Electrochemical Science Technology*, vol. 8, no. 1, pp. 61-68, 2017.
- [11] H. Furukawa, N. Ko, Y. B. Go, N. Aratani, S. B. Choi, E. Choi, A. Ö. Yazaydin, R. Q. Snurr, M. O'Keeffe, and J. Kim, "Ultrahigh porosity in metal-organic frameworks," *Science*, vol. 329, no. 5990, pp. 424-428, 2010.
- [12] C. Dey, T. Kundu, B. P. Biswal, A. Mallick, and R. Banerjee, "Crystalline metal-organic frameworks (MOFs): Synthesis, structure and function," *Acta Crystallographica Section B: Structural Science, Crystal Engineering And Materials*, vol. 70, no. 1, pp. 3-10, 2014.
- [13] J. L. Rowsell, and O. M. Yaghi, "Metal-organic frameworks: A new class of porous materials," *Microporous and Mesoporous Materials*, vol. 73, no. 1, pp. 3-14, 2004.
- [14] M. Hu, "Design, synthesis and applications of metal organic frameworks," Worcester Polytechnic Institute, 2011.
- [15] N. L. Rosi, J. Kim, M. Eddaoudi, B. Chen, M. O'Keeffe, and O. M. Yaghi, "Rod packings and metal-organic frameworks constructed from rod-shaped secondary building units," *Journal of the American Chemical Society*, vol. 127, no. 5, pp. 1504-1518, 2005.
- [16] L. Valenzano, B. Civalieri, S. Chavan, G. T. Palomino, C. O. Areán, and S. Bordiga, "Computational and experimental studies on the adsorption of CO, N<sub>2</sub>, and CO<sub>2</sub> on Mg-MOF-74," *The Journal of Physical Chemistry C*, vol. 114, no. 25, pp. 11185-11191, 2010.
- [17] D.-L. Chen, H. Shang, W. Zhu, and R. Krishna, "Transient breakthroughs of CO<sub>2</sub>/CH<sub>4</sub> and C<sub>3</sub>H<sub>6</sub>/C<sub>3</sub>H<sub>8</sub> mixtures in fixed beds packed with Ni-MOF-74," *Chemical Engineering Science*, vol. 117, pp. 407-415, 2014.
- [18] S. R. Caskey, A. G. Wong-Foy, and A. J. Matzger, "Dramatic tuning of carbon dioxide uptake via metal substitution in a coordination polymer with cylindrical pores," *Journal of the American Chemical Society*, vol. 130, no. 33, pp. 10870-10871, 2008.
- [19] Z. Bao, L. Yu, Q. Ren, X. Lu, and S. Deng, "Adsorption of CO<sub>2</sub> and CH<sub>4</sub> on a magnesium-based metal organic framework," *Journal of Colloid and Interface Science*, vol. 353, no. 2, pp. 549-556, 2011.
- [20] D.-A. Yang, H.-Y. Cho, J. Kim, S.-T. Yang, and W.-S. Ahn, "CO<sub>2</sub> capture and conversion using Mg-MOF-74 prepared by a sonochemical method," *Energy & Environmental Science*, vol. 5, no. 4, pp. 6465-6473, 2012.
- [21] D. Banerjee, H. Wang, B. J. Deibert, and J. Li, "Chapter 4: Alkaline earth metal-based metal-organic frameworks: Synthesis, Properties and Applications," *The chemistry of metal-organic frameworks: Synthesis, characterization, and applications*, S. Kaskel, ed., pp. 73-99, Hoboken, New Jersey, United States: John Wiley & Sons, 2016.

- [22] S. K. Ghosh, "Chapter 2: Metal-organic framework based on carbon capture and purification technologies for clean environment," *Metal-organic frameworks (MOFs) for environmental applications*, pp. 5-49: Elsevier, 2019.
- [23] D. Britt, H. Furukawa, B. Wang, T. G. Glover, and O. M. Yaghi, "Highly efficient separation of carbon dioxide by a metal-organic framework replete with open metal sites," *Proceedings of the National Academy of Sciences*, vol. 106, no. 49, pp. 20637-20640, 2009.
- [24] M. Lopez, P. Canepa, and T. Thonhauser, "NMR study of small molecule adsorption in MOF-74-Mg," *The Journal of Chemical Physics*, vol. 138, no. 15, pp. 154704, 2013.
- [25] H. Furukawa, K. E. Cordova, M. O'Keeffe, and O. M. Yaghi, "The chemistry and applications of metal-organic frameworks," *Science*, vol. 341, no. 6149, pp. 1230444, 2013.
- [26] I. Ahmed, and S. H. Jhung, "Composites of metal-organic frameworks: Preparation and application in adsorption," *Materials Today*, vol. 17, no. 3, pp. 136-146, 2014.
- [27] X.-W. Liu, T.-J. Sun, J.-L. Hu, and S.-D. Wang, "Composites of metal-organic frameworks and carbon-based materials: Preparations, functionalities and applications," *Journal of Materials Chemistry A*, vol. 4, no. 10, pp. 3584-3616, 2016.
- [28] Y. Liu, Z. U. Wang, and H. C. Zhou, "Recent advances in carbon dioxide capture with metal-organic frameworks," *Greenhouse Gases: Science and Technology*, vol. 2, no. 4, pp. 239-259, 2012.
- [29] C. Petit, B. Lévassieur, B. Mendoza, and T. J. Bandoz, "Reactive adsorption of acidic gases on MOF/graphite oxide composites," *Microporous and Mesoporous Materials*, vol. 154, pp. 107-112, 2012.
- [30] Y. Zhao, Y. Cao, and Q. Zhong, "CO<sub>2</sub> capture on metal-organic framework and graphene oxide composite using a high-pressure static adsorption apparatus," *Journal Of Clean Energy Technologies*, vol. 2, no. 1, pp. 34-37, 2014.
- [31] Y. Chen, L. Daofei, W. Junliang, X. Jing, X. Hongxia, X. Qibin, and L. Zhong, "A new MOF-505@GO composite with high selectivity for CO<sub>2</sub>/CH<sub>4</sub> and CO<sub>2</sub>/N<sub>2</sub> separation," *Chemical Engineering Journal*, no. 308, pp. 1065-1072, 2017.
- [32] C. Petit, B. Mendoza, and T. J. Bandoz, "Reactive adsorption of ammonia on Cu-based MOF/graphene composites," *Langmuir*, vol. 26, no. 19, pp. 15302-15309, 2010.
- [33] C. Petit, B. Mendoza, and T. J. Bandoz, "Hydrogen sulfide adsorption on MOFs and MOF/graphite oxide composites," *ChemPhysChem*, vol. 11, no. 17, pp. 3678-3684, 2010.
- [34] S. J. Yang, J. H. Cho, K. S. Nahm, and C. R. Park, "Enhanced hydrogen storage capacity of Pt-loaded CNT@MOF-5 hybrid composites," *International Journal Of Hydrogen Energy*, vol. 35, no. 23, pp. 13062-13067, 2010.
- [35] S. J. Yang, J. Y. Choi, H. K. Chae, J. H. Cho, K. S. Nahm, and C. R. Park, "Preparation and enhanced hydrostability and hydrogen storage capacity of CNT@MOF-5 hybrid composite," *Chemistry of Materials*, vol. 21, no. 9, pp. 1893-1897, 2009.
- [36] M. Anbia, and V. Hoseini, "Development of MWCNT@MIL-101 hybrid composite with enhanced adsorption capacity for carbon dioxide," *Chemical Engineering Journal*, vol. 191, pp. 326-330, 2012.
- [37] A. K. Adhikari, and K.-S. Lin, "Improving CO<sub>2</sub> adsorption capacities and CO<sub>2</sub>/N<sub>2</sub> separation efficiencies of MOF-74 (Ni, Co) by doping palladium-containing activated carbon," *Chemical Engineering Journal*, vol. 284, pp. 1348-1360, 2016.
- [38] V. Jabbari, J. Veleta, M. Zarei-Chaleshtori, J. Gardea-Torresdey, and D. Villagrán, "Green synthesis of magnetic MOF@GO and MOF@CNT hybrid nanocomposites with high adsorption capacity towards organic pollutants," *Chemical Engineering Journal*, vol. 304, pp. 774-783, 2016.
- [39] H. Askari, M. Ghaedi, K. Dashtian, and M. H. A. Azghandi, "Rapid and high-capacity ultrasonic assisted adsorption of ternary toxic anionic dyes onto MOF-5-activated carbon: Artificial neural networks, partial least squares, desirability function and isotherm and kinetic study," *Ultrasonics Sonochemistry*, vol. 37, pp. 71-82, 2017.
- [40] R.-H. Shi, Z.-R. Zhang, H.-L. Fan, T. Zhen, J. Shangguan, and J. Mi, "Cu-based metal-organic framework/activated carbon composites for sulfur compounds removal," *Applied Surface Science*, vol. 394, pp. 394-402, 2017.
- [41] Z. Yu, J. Deschamps, L. Hamon, P. K. Prabhakaran, and P. Pré, "Hydrogen adsorption and kinetics in MIL-101 (Cr) and hybrid activated carbon-MIL-101 (Cr) materials," *International Journal of Hydrogen Energy*, vol. 42, no. 12, pp. 8021-8031, 2017.
- [42] W. Huang, X. Zhou, Q. Xia, J. Peng, H. Wang, and Z. Li, "Preparation and adsorption performance of GrO@Cu-BTC for separation of CO<sub>2</sub>/CH<sub>4</sub>," *Industrial & Engineering Chemistry Research*, vol. 53, no. 27, pp. 11176-11184, 2014.

- [43] G. Herlem, F. Picaud, C. Girardet, and O. Micheau, "Chapter 16: Carbon Nanotubes: Synthesis, Characterization, and Applications in Drug-Delivery Systems," *Nanocarriers for Drug Delivery*, pp. 469-529: Elsevier, 2019.
- [44] C. T. Nguyen, "Review article: Hybrid materials based on carbon nanotubes," *Vietnam Journal of Science and Technology*, vol. 54, pp. 159, 2018.
- [45] S. Eigler, and A. Hirsch, "Chemistry with graphene and graphene oxide - Challenges for synthetic chemists," *Angewandte Chemie International Edition*, vol. 53, no. 30, pp. 7720-7738, 2014.
- [46] C. Petit, J. Burrell, and T. J. Bandoz, "The synthesis and characterization of copper-based metal-organic framework/graphite oxide composites," *Carbon*, vol. 49, no. 2, pp. 563-572, 2011.
- [47] C. Petit, and T. J. Bandoz, "MOF-graphite oxide composites: Combining the uniqueness of graphene layers and metal-organic frameworks," *Advanced Materials*, vol. 21, no. 46, pp. 4753-4757, 2009.
- [48] C. Petit, and T. J. Bandoz, "Enhanced adsorption of ammonia on metal-organic framework/graphite oxide composites: Analysis of surface interactions," *Advanced Functional Materials*, vol. 20, no. 1, pp. 111-118, 2010.
- [49] J. Tobin, and P. Shambaugh, "The crucial link between natural gas production and its transportation to market in: Stages in the production of pipeline-quality natural gas and NGLs. 13.07. 11.," 2006.
- [50] H.-Y. Cho, D.-A. Yang, J. Kim, S.-Y. Jeong, and W.-S. Ahn, "CO<sub>2</sub> adsorption and catalytic application of Co-MOF-74 synthesized by microwave heating," *Catalysis Today*, vol. 185, no. 1, pp. 35-40, 2012.
- [51] W. Lou, J. Yang, L. Li, and J. Li, "Adsorption and separation of CO<sub>2</sub> on Fe(II)-MOF-74: Effect of the open metal coordination site," *Journal of Solid State Chemistry*, vol. 213, pp. 224-228, 2014.
- [52] F. Rezaei, S. Lawson, H. Hosseini, H. Thakkar, A. Hajari, S. Monjezi, and A. A. Rowanghi, "MOF-74 and UTSA-16 film growth on monolithic structures and their CO<sub>2</sub> adsorption performance," *Chemical Engineering Journal*, vol. 313, pp. 1346-1353, 2017.
- [53] X. Su, L. Bromberg, V. Martis, F. Simeon, A. Huq, and T. A. Hatton, "Post-synthetic functionalization of Mg-MOF-74 with tetraethylenepentamine: structural characterization and enhanced CO<sub>2</sub> adsorption," *ACS Applied Materials & Interfaces*, 2017.
- [54] P. D. Dietzel, V. Besikiotis, and R. Blom, "Application of metal-organic frameworks with coordinatively unsaturated metal sites in storage and separation of methane and carbon dioxide," *Journal of Materials Chemistry*, vol. 19, no. 39, pp. 7362-7370, 2009.
- [55] S. Faramawy, T. Zaki, and A.-E. Sakr, "Natural gas origin, composition, and processing: A review," *Journal of Natural Gas Science and Engineering*, vol. 34, pp. 34-54, 2016.
- [56] J. G. Speight, *Natural gas: A basic handbook*: Gulf Publishing Company, 2007.
- [57] A. J. Kidnay, W. R. Parrish, and D. G. McCartney, *Fundamentals of Natural Gas Processing*: CRC Press, 2011.
- [58] N. Azmi, M. Hilmi, and K. M. Sabil, "Removal of high CO<sub>2</sub> content in natural gas by formation of gas hydrates as a potential solution for CO<sub>2</sub> gas emission."
- [59] Alexander's. "Alexander's Gas & Oil Connections - 11 Countries with highest natural gas reserves," <http://www.gasandoil.com/news/2015/08/11-countries-with-highest-natural-gas-reserves>.
- [60] V. S. Nørstebø, K. T. Midthun, T. H. Bjørkvoll, and L. Kolbeinsen, "Use of natural gas with high CO<sub>2</sub> content in an integrated industrial park," *ISIJ International*, vol. 52, no. 8, pp. 1439-1446, 2012.
- [61] GRT, "Composition of natural gas consumed in France," [www.gasinfocus.com](http://www.gasinfocus.com), Gestionnaires de Réseau de Transport de Gaz France and Siapartners, Immeuble Bora, 6, rue Raoul Nordling, 92270 Bois-Colombes (France), 2013.
- [62] B. Clément, É. D. Fosseux, F. Debien, J.-P. Perret, O. Puyraimond, P. D. Renéville, and M. Richard, "Gaz naturel," *Encyclopædia Universalis* [www.universalis.fr](http://www.universalis.fr), É. D. F. Bernard Clément, François Debien, Jean-Pierre Perret, Odile Puyraimond, Patrick De Renéville, Michel Richard, ed., 2016.
- [63] S. Toemen, "Nickel oxide doped noble metals supported catalysts for carbon dioxide methanation and desulfurization reactions," Fakulti Sains, Universiti Teknologi Malaysia, 2011.
- [64] MGA, "Malaysia : Natural gas industry annual review 2012," [www.malaysiangas.com](http://www.malaysiangas.com), Malaysian Gas Association, Etiqa Twins, Level 20, Tower 1, 11, Jalan Pinang, 50450, Kuala Lumpur (Malaysia). 2012.
- [65] MGA, *Malaysia : Natural Gas Industry Annual Report 2016*, Malaysian Gas Association, 2016.
- [66] PETRONAS, "First Gas For PETRONAS' First Floating LNG Facility, PFLNG Satu," *Media, Press Release, PETRONAS*, 2016.
- [67] Sia-partners, "Observatoire du biométhane," *Le Magazine Energies et Environnement de Sia Partners*, April, 2018, 2018.

- [68] IFP-Energies, "Biogas in Europe: Future prospects?. Available on <https://www.ifpenergiesnouvelles.com/article/biogas-europe-future-prospects>", 2017.
- [69] IEA-Bioenergy, "Upgrading Plant List 2019 by IEA Bioenergy. Available on <http://task37.ieabioenergy.com/plant-list.html>," 2019.
- [70] GRT, "Gaz in focus mémo 2016," [www.gasinfocus.com](http://www.gasinfocus.com), Gestionnaires de Réseau de Transport de Gaz France and Siapartners, Immeuble Bora, 6, rue Raoul Nordling, 92270 Bois-Colombes (France), 2016.
- [71] P. Walsh, "France relies on natural gas imports despite having abundant shale gas deposits," *ZE Perspective*, 2013.
- [72] M. Lemonde, "French biogas and biomethane industry in numbers " *Biogas World*, 2019.
- [73] X. Y. Chen, H. Vinh-Thang, A. A. Ramirez, D. Rodrigue, and S. Kaliaguine, "Membrane gas separation technologies for biogas upgrading," *Rsc Advances*, vol. 5, no. 31, pp. 24399-24448, 2015.
- [74] M. Herout, J. Malat'ák, L. Kučera, and T. Dlabaja, "Biogas composition depending on the type of plant biomass used," *Research in Agricultural Engineering*, vol. 57, no. 4, pp. 137-143, 2011.
- [75] J. Reina Hernández, "Landfills: Biogas Cleaning and Conditioning: A Requirement for Optimal Operation of CHP Systems," *Waste Advantage*, September 4, 2015.
- [76] WNA, "Heat values of various fuels," [www.world-nuclear.org](http://www.world-nuclear.org), World Nuclear Association, 2016.
- [77] J. Thaddeus, "Complementary roles of natural gas and coal in Malaysia."
- [78] M. Fuller, *The analysis of carbon dioxide in natural gas*, AMETEK Process Instruments, 150 Freeport Road, Pittsburgh, PA., n.d.
- [79] NERC, "Removal of CO<sub>2</sub> from natural gas processing plant," [www.bgs.ac.uk](http://www.bgs.ac.uk), British Natural Environment Research Council, British Geological Survey, 2017.
- [80] M. A. Arifin, "Experimental study on acid gas removal using absorption-adsorption unit," Final year project thesis, Universiti Malaysia Pahang, 2009.
- [81] D. Davies, and G. Burstein, "The effects of bicarbonate on the corrosion and passivation of iron," *Corrosion*, vol. 36, no. 8, pp. 416-422, 1980.
- [82] IPCC, *Climate change 2014 - Impacts, adaptation, and vulnerability*, Cambridge University Press, University of Cambridge, 32 Avenue of the Americas, New York, USA, 2014.
- [83] M. Meinshausen, N. Meinshausen, W. Hare, S. C. B. Raper, K. Frieler, R. Knutti, D. J. Frame, and M. R. Allen, "Greenhouse-gas emission targets for limiting global warming to 2°C," *Nature*, pp. 1158-1162, 2009.
- [84] H. Matthews, N. Gillet, P. Scott, and K. Zickfield, "The proportionality of global warming to cumulative carbon emissions," *Research Gate*, no. Nature 459(7248), pp. 829-832, July 2009, 2009.
- [85] IEA, "CO<sub>2</sub> capture & storage," [www.iea.org](http://www.iea.org), IEA Energy Technology Essentials, International Energy Agency, 31-35 rue de la Fédération, 75739 Paris Cedex 15 (France), 2006.
- [86] T. Smithson, *Oilfield review 2016: High-pressure, high-temperature wells*, Schlumberger 2016.
- [87] J. Wilcox, "Chapter 2: Compression and Transport of CO<sub>2</sub>," *Carbon Capture*, pp. 35-50, Department of Energy Resources Engineering, Stanford University: Springer New York, 2012.
- [88] MGA, "Malaysia : Natural gas industry annual report 2016," [www.malaysiangas.com](http://www.malaysiangas.com), Malaysian Gas Association, Etiqa Twins, Level 20, Tower 1, 11, Jalan Pinang, 50450, Kuala Lumpur (Malaysia), 2016.
- [89] H. Friedmann. "The Influence of Temperature on the Biogas Production. Available online at <https://friedmann-biogaspraxis.com/en/the-influence-of-temperature-on-the-biogas-production/>."
- [90] L. Eide, and D. Bailey, "Precombustion decarbonisation processes," *Oil & Gas Science And Technology*, vol. 60, no. 3, pp. 475-484, 2005.
- [91] B. Izgec, A. R. Hasan, D. Lin, and C. S. Kabir, "Flow-rate estimation from wellhead-pressure and-temperature data," *SPE Production & Operations*, vol. 25, no. 01, pp. 31-39, 2010.
- [92] A. Lee, G. Xiao, P. Xiao, K. Joshi, R. Singh, and P. A. Webley, "High temperature adsorption materials and their performance for pre-combustion capture of carbon dioxide," *Energy Procedia*, vol. 4, pp. 1199-1206, 2011.
- [93] IEA, "Report: Post-combustion carbon capture from coal fired plants - Solvent scrubbing," [www.iea-coal.org.uk](http://www.iea-coal.org.uk), R. Davidson, ed., IEA Clean Coal Centre, International Energy Agency, Apsley House, 176 Upper Richmond Road, London, SW15 2SH (UK), 2007.
- [94] IPCC, *IPCC Special Report Carbon Dioxide Capture and Storage*, 2005.
- [95] D. D. Do, and R. T. Yang, *Adsorption analysis: equilibria and kinetics*: Imperial College Press London, 1998.

- [96] K. Y. Foo, and B. H. Hameed, "Insights into the modeling of adsorption isotherm systems," *Chemical Engineering Journal*, vol. 156, no. 1, pp. 2-10, 2010.
- [97] C. A. Grande, "Advances in Pressure Swing Adsorption for gas separation," *ISRN Chemical Engineering*, vol. 2012, 2012.
- [98] R. Augelletti, M. Conti, and M. C. Annesini, "Pressure swing adsorption for biogas upgrading. A new process configuration for the separation of biomethane and carbon dioxide," *Journal of Cleaner Production*, vol. 140, pp. 1390-1398, 2017.
- [99] I. Angelidaki, L. Treu, P. Tsapekos, G. Luo, S. Campanaro, H. Wenzel, and P. G. Kougias, "Biogas upgrading and utilization: Current status and perspectives," *Biotechnology Advances*, vol. 36, no. 2, pp. 452-466, 2018.
- [100] F. Bauer, C. Hultberg, and D. T. Persson Tobias, "Biogas upgrading-REVIEW of commercial technologies," *SGC rapport*, vol. 270, pp. 83, 2013.
- [101] C. A. Grande, "Biogas upgrading by pressure swing adsorption," *Biofuel's engineering process technology*, pp. 65-84, 2011.
- [102] J. Langerak. "Biogas-to-Biomethane Conversion Technologies. Available online: <https://www.bioenergyconsult.com/tag/pressure-swing-adsorption/>."
- [103] A. F. Ferreira, A. M. Ribeiro, S. Kulaç, and A. E. Rodrigues, "Methane purification by adsorptive processes on MIL-53 (Al)," *Chemical Engineering Science*, vol. 124, pp. 79-95, 2015.
- [104] C. A. Grande, R. Blom, K. A. Andreassen, and R. Stensrød, "Experimental results of pressure swing adsorption (PSA) for pre-combustion CO<sub>2</sub> capture with metal-organic frameworks," *Energy Procedia*, vol. 114, pp. 2265-2270, 2017.
- [105] I. Majchrzak-Kucęba, and D. Bukalak-Gaik, "Regeneration performance of metal-organic frameworks," *Journal of Thermal Analysis and Calorimetry*, vol. 125, no. 3, pp. 1461-1466, 2016.
- [106] H. Oh, S. Maurer, R. Balderas-Xicohtencatl, L. Arnold, O. V. Magdysyuk, G. Schütz, U. Müller, and M. Hirscher, "Efficient synthesis for large-scale production and characterization for hydrogen storage of ligand exchanged MOF-74/174/184-M (M=Mg<sup>2+</sup>, Ni<sup>2+</sup>)," *International Journal of Hydrogen Energy*, vol. 42, no. 2, pp. 1027-1035, 2017.
- [107] G. D. Pirngruber, L. Hamon, S. Bourrelly, P. L. Llewellyn, E. Lenoir, V. Guillerm, C. Serre, and T. Devic, "A method for screening the potential of MOFs as CO<sub>2</sub> adsorbents in pressure swing adsorption processes," *ChemSusChem*, vol. 5, no. 4, pp. 762-776, 2012.
- [108] B. F. Hoskins, and R. Robson, "Infinite polymeric frameworks consisting of three dimensionally linked rod-like segments," *Journal of the American Chemical Society*, vol. 111, no. 15, pp. 5962-5964, 1989.
- [109] Y. Yusran, D. Xu, Q. Fang, D. Zhang, and S. Qiu, "MOF-derived Co@NC nanocatalyst for catalytic reduction of 4-nitrophenol to 4-aminophenol," *Microporous and Mesoporous Materials*, vol. 241, pp. 346-354, 2017.
- [110] V. Pentyala, P. Davydovskaya, R. Pohle, G. Urban, and O. Yurchenko, "Mg-MOF74 and Co-MOF74 as sensing layers for CO<sub>2</sub> detection," *Procedia Engineering*, vol. 87, pp. 1071-1074, 2014.
- [111] P. Horcajada, C. Serre, M. Vallet-Regi, M. Sebban, F. Taulelle, and G. Férey, "Metal-organic frameworks as efficient materials for drug delivery," *Angewandte Chemie International Edition*, vol. 118, no. 36, pp. 6120-6124, 2006.
- [112] N. A. Khan, Z. Hasan, and S. H. Jung, "Adsorptive removal of hazardous materials using metal-organic frameworks (MOFs): A review," *Journal of Hazardous Materials*, vol. 244, pp. 444-456, 2013.
- [113] E. Ahmed, A. Deep, E. E. Kwon, R. J. C. Brown, and K.-H. Kim, "Performance comparison of MOF and other sorbent materials in removing key odorants emitted from pigpen slurry," *Scientific Reports*, vol. 6, pp. 1-11, 2016.
- [114] B. Liu, H. Shioyama, H. Jiang, X. Zhang, and Q. Xu, "Metal-organic framework (MOF) as a template for syntheses of nanoporous carbons as electrode materials for supercapacitor," *Carbon*, vol. 48, no. 2, pp. 456-463, 2010.
- [115] Y. Cui, Y. Yue, G. Qian, and B. Chen, "Luminescent functional metal-organic frameworks," *Chemical Reviews*, vol. 112, no. 2, pp. 1126-1162, 2011.
- [116] P. Horcajada, R. Gref, T. Baati, P. K. Allan, G. Maurin, P. Couvreur, G. Férey, R. E. Morris, and C. Serre, "Metal-organic frameworks in biomedicine," *Chemical Reviews*, vol. 112, no. 2, pp. 1232-1268, 2011.
- [117] J.-R. Li, Y. Ma, M. C. McCarthy, J. Sculley, J. Yu, H.-K. Jeong, P. B. Balbuena, and H.-C. Zhou, "Carbon dioxide capture-related gas adsorption and separation in metal-organic frameworks," *Coordination Chemistry Reviews*, vol. 255, no. 15, pp. 1791-1823, 2011.
- [118] C. Baerlocher, D. H. Olson, and W. M. Meier, *Atlas of zeolite framework types (formerly: Atlas of zeolite structure types)*: Elsevier, 2001.

- [119] A. Dhakshinamoorthy, M. Alvaro, and H. Garcia, "Commercial metal-organic frameworks as heterogeneous catalysts," *Chemical Communications*, vol. 48, no. 92, pp. 11275-11288, 2012.
- [120] A. G. Wong-Foy, A. J. Matzger, and O. M. Yaghi, "Exceptional H<sub>2</sub> saturation uptake in microporous metal-organic frameworks," *Journal of the American Chemical Society*, vol. 128, no. 11, pp. 3494-3495, 2006.
- [121] T. G. Glover, G. W. Peterson, B. J. Schindler, D. Britt, and O. Yaghi, "MOF-74 building unit has a direct impact on toxic gas adsorption," *Chemical Engineering Science*, vol. 66, no. 2, pp. 163-170, 2011.
- [122] C. Janiak, and J. K. Vieth, "MOFs, MILs and more: Concepts, properties and applications for porous coordination networks (PCNs)," *New Journal of Chemistry*, vol. 34, no. 11, pp. 2366-2388, 2010.
- [123] A. O. Yazaydin, R. Q. Snurr, T.-H. Park, K. Koh, J. Liu, M. D. LeVan, A. I. Benin, P. Jakubczak, M. Lanuza, and D. B. Galloway, "Screening of metal-organic frameworks for carbon dioxide capture from flue gas using a combined experimental and modeling approach," *Journal of the American Chemical Society*, vol. 131, no. 51, pp. 18198-18199, 2009.
- [124] J. J. Low, A. I. Benin, P. Jakubczak, J. F. Abrahamian, S. A. Faheem, and R. R. Willis, "Virtual high throughput screening confirmed experimentally: Porous coordination polymer hydration," *Journal of the American Chemical Society*, vol. 131, no. 43, pp. 15834-15842, 2009.
- [125] S. S. Han, S.-H. Choi, and A. C. van Duin, "Molecular dynamics simulations of stability of metal-organic frameworks against H<sub>2</sub>O using the reaxff reactive force field," *Chemical Communications*, vol. 46, no. 31, pp. 5713-5715, 2010.
- [126] K. Tan, S. Zuluaga, Q. Gong, P. Canepa, H. Wang, J. Li, Y. J. Chabal, and T. Thonhauser, "Water reaction mechanism in metal organic frameworks with coordinatively unsaturated metal ions: MOF-74," *Chemistry of Materials*, 2014.
- [127] Y. Jiao, C. R. Morelock, N. C. Burtch, W. P. Mounfield III, J. T. Hungerford, and K. S. Walton, "Tuning the kinetic water stability and adsorption interactions of Mg-MOF-74 by partial substitution with Co or Ni," *Industrial & Engineering Chemistry Research*, vol. 54, no. 49, pp. 12408-12414, 2015.
- [128] S. Zuluaga, E. M. Fuentes-Fernandez, K. Tan, F. Xu, J. Li, Y. J. Chabal, and T. Thonhauser, "Understanding and controlling water stability of MOF-74," *Journal of Materials Chemistry A*, vol. 4, no. 14, pp. 5176-5183, 2016.
- [129] A. C. Kizzie, A. G. Wong-Foy, and A. J. Matzger, "Effect of humidity on the performance of microporous coordination polymers as adsorbents for CO<sub>2</sub> capture," *Langmuir*, vol. 27, no. 10, pp. 6368-6373, 2011.
- [130] X. Su, L. Bromberg, V. Martis, F. Simeon, A. Huq, and T. A. Hatton, "Postsynthetic functionalization of Mg-MOF-74 with tetraethylenepentamine: Structural characterization and enhanced CO<sub>2</sub> adsorption," *ACS Applied Materials Interfaces*, vol. 9, no. 12, pp. 11299-11306, 2017.
- [131] T. M. Becker, D. Dubbeldam, L.-C. Lin, and T. J. H. Vlugt, "Investigating polarization effects of CO<sub>2</sub> adsorption in Mg-MOF-74," *Journal of Computational Science*, vol. 15, pp. 86-94, 2016.
- [132] I. Luz, "Understanding the formation mechanism of metal nanocrystal@MOF-74 hybrids," *Chemistry of Materials*, vol. 28, no. 11, pp. 3839-3849, 2016.
- [133] D.-J. Lee, Q. Li, H. Kim, and K. Lee, "Preparation of Ni-MOF-74 membrane for CO<sub>2</sub> separation by layer-by-layer seeding technique," *Microporous and Mesoporous Materials*, vol. 163, pp. 169-177, 2012.
- [134] N. Wang, A. Mundstock, Y. Liu, A. Huang, and J. Caro, "Amine-modified Mg-MOF-74/CPO-27-Mg membrane with enhanced H<sub>2</sub>/CO<sub>2</sub> separation," *Chemical Engineering Science*, vol. 124, pp. 27-36, 2015.
- [135] Y. K. Hwang, D. Y. Hong, J. S. Chang, S. H. Jung, Y. K. Seo, J. Kim, A. Vimont, M. Daturi, C. Serre, and G. Férey, "Amine grafting on coordinatively unsaturated metal centers of MOFs: Consequences for catalysis and metal encapsulation," *Angewandte Chemie International Edition*, vol. 47, no. 22, pp. 4144-4148, 2008.
- [136] J. Jin, J. Ouyang, and H. Yang, "Pd nanoparticles and MOFs synergistically hybridized halloysite nanotubes for hydrogen storage," *Nanoscale Research Letters*, vol. 12, no. 1, pp. 240, 2017.
- [137] Z. Liu, W. Dong, S. Cheng, S. Guo, N. Shang, S. Gao, C. Feng, C. Wang, and Z. Wang, "Pd<sub>9</sub>Ag<sub>1</sub>-N-doped-MOF-C: An efficient catalyst for catalytic transfer hydrogenation of nitro-compounds," *Catalysis Communications*, vol. 95, pp. 50-53, 2017.
- [138] Y. Wu, L. Wei, H. Wang, L. Chen, and Q. Zhang, "First principles study of enhanced CO<sub>2</sub> adsorption on MOF-253 by salt-insertion," *Computational Materials Science*, vol. 111, pp. 79-85, 2016.
- [139] C. Yang, X. You, J. Cheng, H. Zheng, and Y. Chen, "A novel visible-light-driven in-based MOF/graphene oxide composite photocatalyst with enhanced photocatalytic activity toward the degradation of amoxicillin," *Applied Catalysis B: Environmental*, vol. 200, pp. 673-680, 2017.
- [140] A. Chakraborty, and T. K. Maji, "Mg-MOF-74@SBA-15 hybrids: Synthesis, characterization, and adsorption properties," *APL Materials*, vol. 2, no. 12, pp. 124107, 2014.

- [141] C. Petit, and T. J. Bandoz, "Synthesis, characterization, and ammonia adsorption properties of mesoporous metal-organic framework (MIL (Fe))-graphite oxide composites: Exploring the limits of materials fabrication," *Advanced Functional Materials*, vol. 21, no. 11, pp. 2108-2117, 2011.
- [142] C. Petit, and T. J. Bandoz, "Exploring the coordination chemistry of MOF-graphite oxide composites and their applications as adsorbents," *Dalton Transactions*, vol. 41, no. 14, pp. 4027-4035, 2012.
- [143] M. Seredych, and T. J. Bandoz, "Mechanism of ammonia retention on graphite oxides: Role of surface chemistry and structure," *The Journal of Physical Chemistry C*, vol. 111, no. 43, pp. 15596-15604, 2007.
- [144] T. J. Bandoz, and C. Petit, "MOF/graphite oxide hybrid materials: Exploring the new concept of adsorbents and catalysts," *Adsorption*, vol. 17, no. 1, pp. 5-16, 2011.
- [145] B. Levasseur, C. Petit, and T. J. Bandoz, "Reactive adsorption of NO<sub>2</sub> on copper-based metal-organic framework and graphite oxide/metal-organic framework composites," *ACS Applied Materials & Interfaces*, vol. 2, no. 12, pp. 3606-3613, 2010.
- [146] X. Sun, Q. Xia, Z. Zhao, Y. Li, and Z. Li, "Synthesis and adsorption performance of MIL-101(Cr)/graphite oxide composites with high capacities of n-hexane," *Chemical Engineering Journal*, vol. 239, pp. 226-232, 2014.
- [147] T. Han, Y. Xiao, M. Tong, H. Huang, D. Liu, L. Wang, and C. Zhong, "Synthesis of CNT@MIL-68(Al) composites with improved adsorption capacity for phenol in aqueous solution," *Chemical Engineering Journal*, vol. 275, pp. 134-141, 2015.
- [148] X. Wu, Z. Bao, B. Yuan, J. Wang, Y. Sun, H. Luo, and S. Deng, "Microwave synthesis and characterization of MOF-74 (M= Ni, Mg) for gas separation," *Microporous and Mesoporous Materials*, vol. 180, pp. 114-122, 2013.
- [149] Y.-R. Lee, J. Kim, and W.-S. Ahn, "Synthesis of metal-organic frameworks: A mini review," *Korean Journal of Chemical Engineering*, vol. 30, no. 9, pp. 1667-1680, 2013.
- [150] T.-F. Yi, L.-J. Jiang, J. Shu, C.-B. Yue, R.-S. Zhu, and H.-B. Qiao, "Recent development and application of Li<sub>4</sub>Ti<sub>5</sub>O<sub>12</sub> as anode material of lithium ion battery," *Journal of Physics and Chemistry of Solids*, vol. 71, no. 9, pp. 1236-1242, 2010.
- [151] C. Larabi, "Surface organometallic chemistry on metal organic frameworks (MOF): Synthesis, characterization and their application in catalysis," Université Claude Bernard-Lyon I, 2011.
- [152] A. S. Munn, "Synthesis and characterisation of metal-organic framework materials with carboxylate ligands," University of Warwick, 2013.
- [153] S. Ullah, M. A. Bustam, A. G. Al-Sehemi, M. A. Assiri, F. A. A. Kareem, A. Mukhtar, M. Ayoub, and G. Gonfa, "Influence of post-synthetic graphene oxide (GO) functionalization on the selective CO<sub>2</sub>/CH<sub>4</sub> adsorption behavior of MOF-200 at different temperatures; an experimental and adsorption isotherms study," *Microporous Mesoporous Materials*, pp. 110002, 2020.
- [154] A. Corma, and H. Garcia, "Supramolecular host-guest systems in zeolites prepared by ship-in-a-bottle synthesis," *European Journal of Inorganic Chemistry*, vol. 2004, no. 6, pp. 1143-1164, 2004.
- [155] M. H. Alkordi, Y. Liu, R. W. Larsen, J. F. Eubank, and M. Eddaoudi, "Zeolite-like metal-organic frameworks as platforms for applications: On metalloporphyrin-based catalysts," *Journal of the American Chemical Society*, vol. 130, no. 38, pp. 12639-12641, 2008.
- [156] A. K. Das, R. S. Vemuri, I. Kutnyakov, B. P. McGrail, and R. K. Motkuri, "An efficient synthesis strategy for metal-organic frameworks: dry-gel synthesis of MOF-74 framework with high yield and improved performance," *Scientific Reports*, vol. 6, no. 1, pp. 1-7, 2016.
- [157] B. H. Stuart, "Chapter 2: Organic molecules," *Infrared spectroscopy: Fundamentals and applications*, pp. 71-93, Hoboken, New Jersey, United States: John Wiley & Sons, 2004.
- [158] G. Gauglitz, and T. Vo-Dinh, *Handbook of spectroscopy*: Wiley Online Library, 2003.
- [159] R. V. Maikala, "Modified Beer's Law—historical perspectives and relevance in near-infrared monitoring of optical properties of human tissue," *International Journal of Industrial Ergonomics*, vol. 40, no. 2, pp. 125-134, 2010.
- [160] M. A. Haydar, H. R. Abid, B. Sunderland, and S. Wang, "Metal organic frameworks as a drug delivery system for flurbiprofen," *Drug Design, Development Therapy*, vol. 11, pp. 2685, 2017.
- [161] R. Dutta, M. N. Rao, and A. Kumar, "Investigation of ionic liquid interaction with ZnBDC-metal organic framework through Scanning eXAFS and inelastic neutron Scattering," *Scientific Reports*, vol. 9, no. 1, pp. 1-11, 2019.
- [162] S. A. Speakman, "Fundamentals of Rietveld Refinement, II. Refinement of a Single Phase," *MIT Center for Materials Science Engineering*, 2011.
- [163] S. A. Speakman, "Profile Fitting for Analysis of XRPD Data using HighScore Plus v3," *Massachusetts Institute of Technology, Cambridge MA*, 2012.

- [164] P. D. Dietzel, R. Blom, and H. Fjellvåg, "Base-induced formation of two magnesium metal-organic framework compounds with a bifunctional tetratopic ligand," *European Journal of Inorganic Chemistry*, vol. 2008, no. 23, pp. 3624-3632, 2008.
- [165] P. D. Dietzel, R. E. Johnsen, R. Blom, and H. Fjellvåg, "Structural changes and coordinatively unsaturated metal atoms on dehydration of honeycomb analogous microporous metal-organic frameworks," *Chemistry—A European Journal*, vol. 14, no. 8, pp. 2389-2397, 2008.
- [166] N. Maksimchuk, M. Timofeeva, M. Melgunov, A. Shmakov, Y. A. Chesalov, D. Dybtsev, V. Fedin, and O. Kholdeeva, "Heterogeneous selective oxidation catalysts based on coordination polymer MIL-101 and transition metal-substituted polyoxometalates," *Journal of Catalysis*, vol. 257, no. 2, pp. 315-323, 2008.
- [167] H. Deng, S. Grunder, K. E. Cordova, C. Valente, H. Furukawa, M. Hmadeh, F. Gándara, A. C. Whalley, Z. Liu, and S. Asahina, "Large-pore apertures in a series of metal-organic frameworks," *Science*, vol. 336, no. 6084, pp. 1018-1023, 2012.
- [168] J. Rouquerol, P. Llewellyn, and F. Rouquerol, "Is the BET equation applicable to microporous adsorbents," *Stud. Surf. Sci. Catal.*, vol. 160, no. 07, pp. 49-56, 2007.
- [169] Y. S. Bae, C. Y. Lee, K. C. Kim, O. K. Farha, P. Nickias, J. T. Hupp, S. T. Nguyen, and R. Q. Snurr, "High propene/propane selectivity in isostructural metal-organic frameworks with high densities of open metal sites," *Angewandte Chemie International Edition*, vol. 51, no. 8, pp. 1857-1860, 2012.
- [170] M. Thommes, and K. A. Cychosz, "Physical adsorption characterization of nanoporous materials: Progress and challenges," *Adsorption*, vol. 20, no. 2-3, pp. 233-250, 2014.
- [171] I. Senkowska, K. A. Cychosz, P. Llewellyn, M. Thommes, and S. Kaskel, "Chapter 19: Adsorption Methodology," *The chemistry of metal-organic frameworks: Synthesis, characterization, and applications*, S. Kaskel, ed., pp. 575-605: John Wiley & Sons, 2016.
- [172] J. Kärger, D. M. Ruthven, and D. N. Theodorou, *Diffusion in nanoporous materials*: John Wiley & Sons, 2012.
- [173] C. Tien, *Adsorption calculations and modeling*, First ed.: Butterworth-Heinemann, Boston, 1994.
- [174] D. M. Ruthven, S. Farouq, and K. S. Knaebel, *Pressure Swing Adsorption*: New York: VCH Publishers, 1994.
- [175] R. M. Roque-Malherbe, *Adsorption and diffusion in nanoporous materials*, Second ed.: CRC press, 2018.
- [176] M. Thommes, "Physical adsorption characterization of ordered and amorphous mesoporous materials," *Nanoporous Materials: Science and Engineering*, pp. 317-364, 2004.
- [177] X.-J. Hou, P. He, H. Li, and X. Wang, "Understanding the adsorption mechanism of C<sub>2</sub>H<sub>2</sub>, CO<sub>2</sub>, and CH<sub>4</sub> in isostructural metal-organic frameworks with coordinatively unsaturated metal sites," *The Journal of Physical Chemistry C*, vol. 117, no. 6, pp. 2824-2834, 2013.
- [178] Y. Liu, J. Hu, X. Ma, J. Liu, and Y. Lin, "Mechanism of CO<sub>2</sub> adsorption on Mg/dobdc with elevated CO<sub>2</sub> loading," *Fuel*, vol. 181, pp. 340-346, 2016.
- [179] G. Ehrlich, and K. Stolt, "Surface diffusion," *Annual Review of Physical Chemistry*, vol. 31, no. 1, pp. 603-637, 1980.
- [180] S. Sircar, and J. Hufton, "Why does the linear driving force model for adsorption kinetics work?," *Adsorption*, vol. 6, no. 2, pp. 137-147, 2000.
- [181] M. Borówko, "Chapter 2: Adsorption on heterogeneous surfaces," *Adsorption*, Surfactant Science Series 107, J. Toth, ed., pp. 105-166, Maria Curie-Skłodowska University: CRC Press, 2002.
- [182] W. Keesom, "The second virial coefficient for rigid spherical molecules, whose mutual attraction is equivalent to that of a quadruplet placed at their centre," *Proc. R. Acad. Sci.*, vol. 18, pp. 636-646, 1915.
- [183] P. Debye, "Molecular forces and their electrical interpretation," *Physikalische Zeitschrift*, vol. 22, pp. 302-308, 1921.
- [184] F. London, "The general theory of molecular forces," *Transactions of the Faraday Society*, vol. 33, pp. 8b-26, 1937.
- [185] J. E. Lennard-Jones, and A. Devonshire, "The interaction of atoms and molecules with solid surfaces VI - The behaviour of adsorbed helium at low temperatures," *Proceedings of the Royal Society of London. Series A-Mathematical Physical Sciences*, vol. 158, no. 894, pp. 242-252, 1937.
- [186] H. Wu, J. M. Simmons, G. Srinivas, W. Zhou, and T. Yildirim, "Adsorption sites and binding nature of CO<sub>2</sub> in prototypical metal-organic frameworks: A combined neutron diffraction and first-principles study," *The Journal of Physical Chemistry Letters*, vol. 1, no. 13, pp. 1946-1951, 2010.
- [187] W. S. Drisdell, R. Poloni, T. M. McDonald, J. R. Long, B. Smit, J. B. Neaton, D. Prendergast, and J. B. Kortright, "Probing adsorption interactions in metal-organic frameworks using x-ray spectroscopy," *Journal of the American Chemical Society*, vol. 135, no. 48, pp. 18183-18190, 2013.

- [188] W. L. Queen, C. M. Brown, D. K. Britt, P. Zajdel, M. R. Hudson, and O. M. Yaghi, "Site-specific CO<sub>2</sub> adsorption and zero thermal expansion in an anisotropic pore network," *The Journal of Physical Chemistry C*, vol. 115, no. 50, pp. 24915-24919, 2011.
- [189] K. A. Cychosz, R. Guillet-Nicolas, J. García-Martínez, and M. Thommes, "Recent advances in the textural characterization of hierarchically structured nanoporous materials," *Chemical Society Reviews*, vol. 46, no. 2, pp. 389-414, 2017.
- [190] M. Thommes, K. Kaneko, A. V. Neimark, J. P. Olivier, F. Rodriguez-Reinoso, J. Rouquerol, and K. S. Sing, "Physisorption of gases, with special reference to the evaluation of surface area and pore size distribution (IUPAC Technical Report)," *Pure Applied Chemistry*, vol. 87, no. 9-10, pp. 1051-1069, 2015.
- [191] S. Mukherjee, A. Kumar, and M. J. Zaworotko, "Metal-organic framework based carbon capture and purification technologies for clean environment," *Metal-Organic Frameworks (MOFs) for Environmental Applications*, pp. 5-61: Elsevier, 2019.
- [192] D. P. Broom, "Characterizing adsorbents for gas separations," *Chem. Eng. Prog.*, vol. 114, pp. 30-37, 2018.
- [193] P. J. Harlick, and F. H. Tezel, "An experimental adsorbent screening study for CO<sub>2</sub> removal from N<sub>2</sub>," *Microporous Mesoporous Materials*, vol. 76, no. 1-3, pp. 71-79, 2004.
- [194] D. Shen, and M. Bülow, "Isothermic study of sorption thermodynamics of single gases and multi-component mixtures on microporous materials," *Microporous Mesoporous Materials*, vol. 22, no. 1-3, pp. 237-249, 1998.
- [195] M. Bülow, D. Shen, and S. Jale, "Measurement of sorption equilibria under isothermic conditions: the principles, advantages and limitations," *Applied Surface Science*, vol. 196, no. 1-4, pp. 157-172, 2002.
- [196] L. Czepirski, and J. Jagiełło, "Virial-type thermal equation of gas-solid adsorption," *Chemical Engineering Science*, vol. 44, no. 4, pp. 797-801, 1989.
- [197] T. J. Bandoz, J. Jagiełło, J. A. Schwarz, and A. Krzyzanowski, "Effect of surface chemistry on sorption of water and methanol on activated carbons," *Langmuir*, vol. 12, no. 26, pp. 6480-6486, 1996.
- [198] P. Llewellyn, J. Coulomb, Y. Grillet, J. Patarin, H. Lauter, H. Reichert, and J. Rouquerol, "Adsorption by MFI-type zeolites examined by isothermal microcalorimetry and neutron diffraction. 1. Argon, krypton, and methane," *Langmuir*, vol. 9, no. 7, pp. 1846-1851, 1993.
- [199] P. L. Llewellyn, and G. Maurin, "Gas adsorption microcalorimetry and modelling to characterise zeolites and related materials," *Comptes Rendus Chimie*, vol. 8, no. 3-4, pp. 283-302, 2005.
- [200] J. Dunne, R. Mariwala, M. Rao, S. Sircar, R. Gorte, and A. Myers, "Calorimetric heats of adsorption and adsorption isotherms. 1. O<sub>2</sub>, N<sub>2</sub>, Ar, CO<sub>2</sub>, CH<sub>4</sub>, C<sub>2</sub>H<sub>6</sub>, and SF<sub>6</sub> on silicalite," *Langmuir*, vol. 12, no. 24, pp. 5888-5895, 1996.
- [201] S. U. Rege, and R. T. Yang, "A simple parameter for selecting an adsorbent for gas separation by pressure swing adsorption," *Adsorption Separation Science Technology*, vol. 36, no. 15, pp. 3355-3365, 2001.
- [202] R. T. Yang, *Gas separation by adsorption processes*: Butterworth-Heinemann, 2013.
- [203] A. L. Myers, and J. M. Prausnitz, "Thermodynamics of mixed-gas adsorption," *AIChE Journal*, vol. 11, no. 1, pp. 121-127, 1965.
- [204] S. Lee, J. H. Lee, and J. Kim, "User-friendly graphical user interface software for ideal adsorbed solution theory calculations," *Korean Journal of Chemical Engineering*, vol. 35, no. 1, pp. 214-221, 2018.
- [205] C. M. Simon, B. Smit, and M. Haranczyk, "pyIAST: Ideal adsorbed solution theory (IAST) Python package," *Computer Physics Communications*, vol. 200, pp. 364-380, 2016.
- [206] D. M. Ruthven, *Principles of adsorption and adsorption processes*: John Wiley & Sons, 1984.
- [207] J. Rouquerol, F. Rouquerol, P. Llewellyn, G. Maurin, and K. S. W. Sing, "Adsorption by powders and porous solids: principles, methodology and applications," 2013.
- [208] D. P. Broom, "Gas sorption measurement techniques," *Hydrogen Storage Materials*, pp. 117-139: Springer, 2011.
- [209] D. P. Broom, "Hydrogen sorption measurements on potential storage materials," *JRC Scientific Technical Reports*, 2008.
- [210] D. P. Broom, and K. M. Thomas, "Gas adsorption by nanoporous materials: future applications and experimental challenges," *MRS bulletin*, vol. 38, no. 5, pp. 412-421, 2013.
- [211] R. Span, and W. Wolfgang, "A new equation of state for carbon dioxide covering the fluid region from the triple-point temperature to 1100 K at pressures up to 800 MPa," *Journal of Physical Chemical Reference Data*, vol. 25, no. 6, pp. 1509-1596, 1996.
- [212] S. Brandani, E. Mangano, and L. Sarkisov, "Net, excess and absolute adsorption and adsorption of helium," *Adsorption*, vol. 22, no. 2, pp. 261-276, 2016.

- [213] O. Talu, "Net adsorption of gas/vapor mixtures in microporous solids," *The Journal of Physical Chemistry C*, vol. 117, no. 25, pp. 13059-13071, 2013.
- [214] A. L. Myers, and P. A. Monson, "Physical adsorption of gases: the case for absolute adsorption as the basis for thermodynamic analysis," *Adsorption*, vol. 20, no. 4, pp. 591-622, 2014.
- [215] J. U. Keller, and R. Staudt, *Gas adsorption equilibria: experimental methods and adsorptive isotherms*: Springer Science & Business Media, 2005.
- [216] H. G. T. Nguyen, L. Espinal, R. D. van Zee, M. Thommes, B. Toman, M. Hudson, E. Mangano, S. Brandani, D. Broom, and M. Benham, "A reference high-pressure CO<sub>2</sub> adsorption isotherm for ammonium ZSM-5 zeolite: results of an interlaboratory study," *Adsorption*, vol. 24, no. 6, pp. 531-539, 2018.
- [217] J. H. Cavka, C. A. Grande, G. Mondino, and R. Blom, "High pressure adsorption of CO<sub>2</sub> and CH<sub>4</sub> on Zr-MOFs," *Industrial Engineering Chemistry Research*, vol. 53, no. 40, pp. 15500-15507, 2014.
- [218] K. Sumida, D. L. Rogow, J. A. Mason, T. M. McDonald, E. D. Bloch, Z. R. Herm, T.-H. Bae, and J. R. Long, "Carbon dioxide capture in metal-organic frameworks," *Chemical Reviews*, vol. 112, no. 2, pp. 724-781, 2011.
- [219] S. Xiang, Y. He, Z. Zhang, H. Wu, W. Zhou, R. Krishna, and B. Chen, "Microporous metal-organic framework with potential for carbon dioxide capture at ambient conditions," *Nature Communications*, vol. 3, no. 1, pp. 1-9, 2012.
- [220] Z. Zhang, Z.-Z. Yao, S. Xiang, and B. Chen, "Perspective of microporous metal-organic frameworks for CO<sub>2</sub> capture and separation," *Energy Environmental Science Technology*, vol. 7, no. 9, pp. 2868-2899, 2014.
- [221] M. Ding, R. W. Flaig, H.-L. Jiang, and O. M. Yaghi, "Carbon capture and conversion using metal-organic frameworks and MOF-based materials," *Chemical Society Reviews*, vol. 48, no. 10, pp. 2783-2828, 2019.
- [222] P. I. Ravikovitch, and A. V. Neimark, "Diffusion-controlled hysteresis," *Adsorption*, vol. 11, no. 1, pp. 265-270, 2005.
- [223] R. M. Barrer, and S. Wasilewski, "Occlusion of iodine in some porous crystals. Part 1. Heat and energy relationships," *Transactions of the Faraday Society*, vol. 57, pp. 1140-1152, 1961.
- [224] R. Barrer, "Intracrystalline diffusion," ACS Publications, 1971.
- [225] A. Einstein, "Zur theorie der brownischen bewegung [adp 19, 371 (1906)]," *Annalen der Physik*, vol. 14, no. S1 1, pp. 248-258, 2005.
- [226] N. Wakao, and S. Kagei, *Heat and mass transfer in packed beds*: Taylor & Francis, 1982.
- [227] C. Chmelik, L. Heinke, P. Kortunov, J. Li, D. Olson, D. Tzoulaki, J. Weitkamp, and J. Kärger, "Ensemble measurement of diffusion: Novel beauty and evidence," *ChemPhysChem*, vol. 10, no. 15, pp. 2623-2627, 2009.
- [228] R. B. Bird, W. E. Stewart, and E. N. Lightfoot, "Transport phenomena (revised second ed.)" *New York*, 2007.
- [229] E. Glueckauf, and J. I. Coates, "241. Theory of chromatography. Part IV. The influence of incomplete equilibrium on the front boundary of chromatograms and on the effectiveness of separation," *Journal of the Chemical Society*, pp. 1315-1321, 1947.
- [230] J. C. Saint Remi, A. Lauerer, C. Chmelik, I. Vandendael, H. Terryn, G. V. Baron, J. F. Denayer, and J. Kärger, "The role of crystal diversity in understanding mass transfer in nanoporous materials," *Nature materials*, vol. 15, no. 4, pp. 401-406, 2016.
- [231] M. Eic, and D. M. Ruthven, "A new experimental technique for measurement of intracrystalline diffusivity," *Zeolites*, vol. 8, no. 1, pp. 40-45, 1988.
- [232] S. Brandani, and D. M. Ruthven, "Analysis of ZLC desorption curves for gaseous systems," *Adsorption*, vol. 2, no. 2, pp. 133-143, 1996.
- [233] D. M. Ruthven, and A. Vidoni, "ZLC diffusion measurements: Combined effect of surface resistance and internal diffusion," *Chemical Engineering Science*, vol. 71, pp. 1-4, 2012.
- [234] T. Vermeulen, "Theory for irreversible and constant-pattern solid diffusion," *Industrial & Engineering Chemistry*, vol. 45, no. 8, pp. 1664-1670, 1953.
- [235] D. G. Kinniburgh, "General purpose adsorption isotherms," *Environmental Science Technology*, vol. 20, no. 9, pp. 895-904, 1986.
- [236] N. D. Hutson, and R. T. Yang, "Theoretical basis for the Dubinin-Radushkevitch (DR) adsorption isotherm equation," *Adsorption*, vol. 3, no. 3, pp. 189-195, 1997.
- [237] I. Langmuir, "The constitution and fundamental properties of solids and liquids. Part I. Solids," *Journal of the American Chemical Society*, vol. 38, no. 11, pp. 2221-2295, 1916.
- [238] H. Freundlich, "Over the adsorption in solution," *J. Phys. Chem*, vol. 57, no. 385471, pp. 1100-1107, 1906.

- [239] R. Sips, "On the structure of a catalyst surface," *The Journal of Chemical Physics*, vol. 16, no. 5, pp. 490-495, 1948.
- [240] J. Toth, "State equation of the solid-gas interface layers," *Acta Chim. Hung.*, vol. 69, pp. 311-328, 1971.
- [241] M. Dubinin, "The potential theory of adsorption of gases and vapors for adsorbents with energetically nonuniform surfaces," *Chemical Reviews*, vol. 60, no. 2, pp. 235-241, 1960.
- [242] S. Brunauer, P. H. Emmett, and E. Teller, "Adsorption of gases in multimolecular layers," *Journal of the American chemical society*, vol. 60, no. 2, pp. 309-319, 1938.
- [243] P. S. B rcia, J. A. C. Silva, and A. E. Rodrigues, "Adsorption equilibrium and kinetics of branched hexane isomers in pellets of BETA zeolite," *Microporous mesoporous materials*, vol. 79, no. 1-3, pp. 145-163, 2005.
- [244] M. Khalighi, S. Farooq, and I. A. Karimi, "Nonisothermal pore diffusion model for a kinetically controlled Pressure Swing Adsorption process," *Industrial Engineering Chemistry Research*, vol. 51, no. 32, pp. 10659-10670, 2012.
- [245] W. Zhu, A. Malekian, M. Eic, F. Kapteijn, and J. Moulijn, "Concentration-dependent diffusion of isobutane in silicalite-1 studied with the ZLC technique," *Chemical Engineering Science*, vol. 59, no. 18, pp. 3827-3835, 2004.
- [246] B. Mu, "Synthesis and gas adsorption study of porous metal-organic framework materials," Georgia Institute of Technology, 2011.
- [247] S.-J. Lee, K. C. Kim, T.-U. Yoon, M.-B. Kim, and Y.-S. Bae, "Selective dynamic separation of Xe and Kr in Co-MOF-74 through strong binding strength between Xe atom and unsaturated Co<sup>2+</sup> site," *Microporous Mesoporous Materials*, vol. 236, pp. 284-291, 2016.
- [248] Y.-S. Bae, O. K. Farha, J. T. Hupp, and R. Q. Snurr, "Enhancement of CO<sub>2</sub>/N<sub>2</sub> selectivity in a metal-organic framework by cavity modification," *Journal of Materials Chemistry*, vol. 19, no. 15, pp. 2131-2134, 2009.
- [249] E. D. Bloch, L. J. Murray, W. L. Queen, S. Chavan, S. N. Maximoff, J. P. Bigi, R. Krishna, V. K. Peterson, F. Grandjean, and G. J. Long, "Selective binding of O<sub>2</sub> over N<sub>2</sub> in a redox-active metal-organic framework with open iron (II) coordination sites," *Journal of the American Chemical Society*, vol. 133, no. 37, pp. 14814-14822, 2011.

**Titre :** Développement de matériaux composites adsorbants réseaux organométalliques–carbones pour la séparation de dioxyde de carbone et de méthane

**Mots clés :** MOF-74, composite MOF–carbone, synthèse, caractérisation, adsorption de gaz, dioxyde de carbone

**Résumé :** Le dioxyde de carbone (CO<sub>2</sub>), principal contaminant des gaz naturels bruts et du biogaz doit être extrait en vue d'un enrichissement en méthane (CH<sub>4</sub>) compatible avec les spécifications d'injection en réseaux de gaz naturel. Au cours des dernières années, une famille de matériaux poreux de type réseaux organométalliques à base de magnésium (Mg-MOF-74) a ouvert une nouvelle perspective à cet effet en raison d'une excellente affinité des sites métalliques exposés au sein de la structure cristalline pour l'adsorption du CO<sub>2</sub>. Ce matériau est un adsorbant potentiellement bon candidat pour l'enrichissement en CH<sub>4</sub> de gaz naturel et de biogaz par des procédés opérant en modulation de pression. La présente étude propose d'examiner l'amélioration des performances d'adsorption du CO<sub>2</sub> en mélange avec le CH<sub>4</sub> par dopage du matériau Mg-MOF-74 avec des nanotubes de carbone et de l'oxyde de graphène. L'objectif est d'améliorer les propriétés texturales pour favoriser la diffusion des molécules des gaz dans

les micropores et leur accessibilité aux sites d'adsorption. Les matériaux ont été synthétisés sous réaction solvothermique et caractérisés par DRX, IRTF, MEB, ATG et physisorption d'azote à 77K. Les équilibres et énergies d'adsorption ont été mesurés suivant une méthode manométrique dans une gamme de pression allant jusqu'à 35 bar et à 25°C, 50°C et 75°C. La cinétique de sorption a été étudiée à partir d'expériences de manométrie et de la méthode dite « Zero Length Column » à 25°C, 50°C et 75°C. A une teneur optimisée à 0,3% en masse d'agent dopant, le modèle de Brunauer–Emmett–Teller montre que la surface spécifique des matériaux dopés est augmentée de plus de 21% par rapport à celle du matériau non-dopé. Les données d'équilibre indiquent que la capacité d'adsorption en CO<sub>2</sub> est sensiblement améliorée pour les matériaux dopés dans toute la gamme opératoire étudiée, tandis qu'ils démontrent une sélectivité comparable ou améliorée, dépendante de la température.

**Title :** Development of metal-organic framework carbon composites for carbon dioxide and methane separation

**Keywords :** MOF-74, MOF–carbon composite, synthesis, characterization, gas adsorption, carbon dioxide

**Abstract :** Carbon dioxide (CO<sub>2</sub>), which is the major contaminant present in raw natural gas and biogas need to be extracted to increase their methane (CH<sub>4</sub>) content and meet the standards of pipeline injection. In recent years, a family of porous materials, magnesium-based Metal Organic Framework (Mg-MOF-74), has opened new perspectives for this purpose thanks to strong adsorption affinity of CO<sub>2</sub> with exposed metallic sites in the crystalline network. This material is a potential good adsorbent candidate for the enrichment in CH<sub>4</sub> of natural gas and biogas by Pressure Swing Adsorption processes. The present study proposes to examine the CO<sub>2</sub> adsorption performances and separation ability from CH<sub>4</sub> of Mg-MOF-74 materials doped with carbon nanotubes and graphene oxide. The objective is to improve the texture of the materials to promote the diffusion of gas molecules into micropores and their accessibility to adsorption sites. The materials were synthesized

under solvothermal reaction and characterized by PXRD, FTIR, FESEM, TGA and physisorption of nitrogen at 77K. The adsorption equilibria and energies were measured using manometric method in a pressure range up to 35 bar and at 25°C, 50°C and 75°C. The sorption kinetics of CO<sub>2</sub> and CH<sub>4</sub> on the materials were studied from manometric experiments and using the Zero Length Column method at 25°C, 50°C and 75°C. At an optimized content of the doping agents of ≈0.3 wt%, Brunauer–Emmett–Teller model shows that the specific surface area is increased for both composites, by more than 21% compared to the pristine material. The equilibrium data indicates that the CO<sub>2</sub> adsorption capacity is significantly improved in the whole range of operating conditions for both composites compared to the pristine material, whereas the CO<sub>2</sub>/CH<sub>4</sub> adsorption selectivity appears either comparable or better as a function of temperature.